A Marine Geophysical Study of the Wilkes Land Rifted Continental Margin, Antarctica

by

David I. Close

Thesis submitted for the Degree of Doctor of Philosophy, University of Oxford

Worcester College &
Department of Earth Sciences

Michaelmas Term 2004

A Marine Geophysical Study of the Wilkes Land Rifted Continental Margin, Antarctica

David I. Close

Worcester College & Department of Earth Sciences

Thesis submitted for the Degree of Doctor of Philosophy to the University of Oxford,

Michaelmas Term 2004

The Wilkes Land margin of East Antarctica, conjugate to the southern Australian margin, is a non-volcanic rifted margin that formed during the Late Cretaceous. During 2000-01 and 2001-02, Geoscience Australia (GA) acquired ∼10,000 line km of seismic reflection, magnetic anomaly, and gravity anomaly data, on the Wilkes Land margin.

Seismic reflection and sonobuoy refraction data provide the first constraints on sediment thickness and images of the deep crustal structure for the extent of the Wilkes Land margin. Two major post-rift seismic-stratigraphic sequences are recognised, separated by a regionally correlatable unconformity. The unconformity is interpreted as Early- to Middle-Eocene (∼50 Ma). This unconformity has previously been interpreted to represent the onset of continent-wide glaciation at ∼34 Ma. A major unconformity at the base of post-rift sediments is interpreted as a breakup unconformity, of approximately Turonian (85-90 Ma) age.

Timing the onset of seafloor spreading using lineated magnetic anomalies within the Australia-Antarctic Basin (AAB) is extremely difficult due to uncertainties in correlating anomalies to the geomagnetic reversal time scale. Modelling indicates that the anomaly commonly correlated to Chron 34y may, in some cases, be associated with high level intrusions and/or serpentinisation of exhumed upper-mantle peridotites.

Process-oriented gravity modelling indicates that the Wilkes Land margin lithosphere is characterised by a relatively high effective elastic thickness (T_e). Isostatic anomalies are most effectively reduced for models utilising T_e = 30 km. Although the margin is broadly characterised by a high T_e, zones of low T_e are inferred from modelling. Spectral analysis of isostatic anomalies indicates that the power of the flexural isostatic anomalies is lower than the free air gravity anomalies.

The margin does not appear to be segmented, at least in regard to its long-term strength. However, a change in initial, zero-elevation crustal thickness (T_c) is inferred from west to east. A T_c of ∼35 km is inferred for western Wilkes Land, whereas eastern Wilkes Land is characterised by T_c =29 to 31 km. Limited seismic refraction data from the conjugate margin indicates a similar trend from southwest to southeast Australia.

Extended Abstract

The Wilkes Land margin of East Antarctica, conjugate to the southern Australian margin, is a non-volcanic rifted margin that formed as a result of intracratonic extension within Gondwana during the Late Cretaceous. The present-day Wilkes Land margin is separated from southern Australia by the ∼3000 km wide southeast Indian and Southern Oceans, contained within the Australia-Antarctica Basin (AAB). The active spreading centre within the AAB is the South East Indian Ridge (SEIR), which is located approximately halfway between the opposing rifted margins.

The SEIR runs broadly east-west at ∼50°S as far east as 140°E, where it is offset to the south by a series of transform faults. A region of anomalously deep oceanic crust, the Australian-Antarctic Discordance (AAD), extends from the SEIR, between ∼120-130°E, to the north and south as far as the margins of Australia and Antarctica respectively. This depth anomaly has been interpreted to represent long-lived asthenospheric downwelling beneath the SEIR.

The morphology of the opposing margins of the AAB is vastly different. The differences reflect the disparate environmental conditions of the Antarctic and Australian continents through the Tertiary. The Wilkes Land margin comprises a rugged and overdeepened shelf associated with glacial erosion during times of glacial expansion. The southern Australian margin comprises a more typical shelf morphology, however, a prominent sediment terrace, the Ceduna Terrace, extends from the upper continental slope for over 100 km off the Great Australian Bight (GAB) margin. No similar terraces are apparent on the conjugate central Wilkes Land margin.

Recently acquired deep-penetrating seismic reflection, sonobuoy refraction, magnetic anomaly, and gravity anomaly data have allowed the structure and evolution of the Wilkes Land margin to be investigated in detail. Interpretation and modelling, where appropriate, of these data provides insights into the age, crustal structure, seismic stratigraphy, subsidence history, and thermo-mechanical evolution of the Wilkes Land margin.

Seismic reflection data, supplemented by sonobuoy refraction data, provide the first constraints on sediment thickness and images of the deep crustal structure for the extent of the Wilkes Land margin. Two major post-rift seismic-stratigraphic sequences are

recognised, separated by a regionally correlatable unconformity. This unconformity is recognised beneath the continental slope and rise by the erosional truncation of underlying strata, and the onlap of overlying reflectors. The unconformity is interpreted as Early- to Middle-Eocene (∼50 Ma) on the basis of correlation with seismic reflection and subsidence data from the conjugate southern Australian margin. This unconformity has previously been interpreted to represent the onset of continent-wide glaciation at ∼34 Ma.

The upper post-rift stratigraphy (Sequence 1) records the change from temperate climatic conditions, to temperate-glacial and then polar-glacial conditions; a major event that was the catalyst for a shift in global climate patterns towards the present-day *ice-house* conditions. No single stratigraphic feature can be correlated with the onset of regional glaciation and the development of the East Antarctic Ice Sheet (EAIS). However, the great thickness of Sequence 1 sediments in some areas (>9 km) is likely an indication of continental erosion and sediment transport, associated with wet-based glaciers, prior to the development of polar-glacial conditions.

An approximately seven-fold reduction in sedimentation rates in the Late Miocene (∼9 Ma) is interpreted to represent the onset of stable, frozen-based, polar glaciers. Inferred sedimentation rates for the ∼34-9 Ma interval are comparable to the highest present-day, observed sedimentation rates at continental margins. Sequence 1, therefore, represents a large load on the rifted Wilkes Land margin lithosphere that was deposited relatively rapidly some 60-80 Ma after rifting.

The Sequence 1 isopach indicates the presence of a major sedimentary basin off the west Wilkes Land margin. The asymmetric distribution of sediments within this basin indicates long-lived west to east sediment transport processes have operated on the Wilkes Land margin continental rise. Present-day observations of deep-marine currents, however, do not indicate the presence of a strong eastward current off the Wilkes Land margin. This may suggest that ocean circulation has changed significantly since the development of polar-glacial conditions.

A major unconformity at the base of Sequence 2 is interpreted as a breakup unconformity, of approximately Turonian age, on the basis of correlation with seismic and well data from the southern Australian margin. The unconformity represents the base of relatively undeformed and unfaulted reflectors for the western and central Wilkes Land margin. However, off eastern Wilkes Land and Terre Adélie, extension-related deformation and faulting is interpreted to have continued until the Early Tertiary. The first evidence of oceanic crust occurs over 400 km from the shelf break off this margin sector, ∼200 km further seaward than off central Wilkes Land. A bathymetric shallowing and cluster of seamounts off eastern Wilkes Land corresponds to this region of heavily

extended continental crust. This region has previously been interpreted as a zone of anomalous oceanic crust.

Underlying the post-rift sediments on the Wilkes Land margin is a combination of extended and deformed continental crust, transition zone crust (typically comprising a number of acoustically transparent basement highs), and oceanic crust. Continental crust is identified on the basis of rotated fault blocks and tilted reflectors in the upper-crust, and a massively thinned, acoustically transparent lower crust that terminates at the landward edge of transitional crust. Oceanic crust exhibits relatively rugged topography, an upper surface characterised by a high-amplitude reflector, and an acoustically transparent internal character. Sonobuoy data indicate that oceanic crust at the Wilkes Land margin comprises a reduced layer 3 thickness and is only ∼75% the thickness of *normal* (i.e. Atlantic and Pacific Ocean) oceanic crust.

The exact breakup age of Australia and Antarctica is difficult to constrain. Subsidence analyses from the southern Australian margin identify two intervals of tectonic subsidence, the younger of which, in the Late Cretaceous, is interpreted to relate to breakup. Accurately timing the onset of seafloor spreading using lineated magnetic anomalies, however, is extremely difficult due to uncertainties in correlating anomalies to the geomagnetic reversal time scale. Initial opening at the incipient SEIR proceeded at very low spreading rates (<10 mm/yr Half Spreading Rate - HSR), which, in combination with hydrothermal alteration associated with sediment blanketing of young, hot oceanic crust, resulted in a poor record of magnetic reversals in Late Cretaceous and Palaeocene aged oceanic crust in the AAB.

The oldest previously interpreted seafloor spreading magnetic anomaly is associated with the end of the Long Cretaceous Normal Polarity period, Chron 34 (i.e. anomaly 34y). However, the form of this anomaly is inconsistent within the AAB and is located within the COT interpreted in seismic reflection data. Magnetic modelling, constrained by the depth to basement interpreted from seismic reflection data, indicates that the anomaly commonly correlated to Chron 34y may, in some cases, be associated with high level intrusions and/or serpentinisation of exhumed upper-mantle peridotites.

It is clear, from interpretation of magnetic anomaly data, that breakup was not synchronous along the length of the SEIR. The lack of recognisable seafloor spreading anomalies older than Chron 21 in the eastern AAB, which correlates to the region of anomalous extension identified in seismic reflection data, indicates that final breakup did not occur there until the Eocene (∼50 Ma). The emplacement of oceanic crust in the eastern AAB correlates to a basin-wide increase in seafloor spreading rates. This change in spreading rates is interpreted to correlate to an increase in thermal subsidence rates identified from well data on the southern Australian margin, and is likely the catalyst for

development of the major unconformity that punctuates the post-rift seismic sequence. Seafloor spreading is interpreted to have remained relatively fast (20-38 mm/yr HSR) since the Eocene, and the associated lineated magnetic anomalies can be confidently correlated to the geomagnetic reversal time scale.

Two-dimensional process-oriented gravity modelling, using depth-converted sediment thickness data, reveals that the Wilkes Land margin lithosphere is characterised by a relatively high effective elastic thickness (T_e). Isostatic anomalies are most effectively reduced for models utilising T_e = 30 km. Process-oriented modelling is most sensitive to T_e variation off west Wilkes Land where the thickest post-rift sediments are located. Although the margin is broadly characterised by a high T_e, zones of low T_e are inferred from modelling. This likely indicates that some sections of extended continental crust were weakened by rifting processes and have not recovered strength equivalent to the relatively unstretched, adjacent continental crust. Multi-layer backstripping does not provide any evidence of major temporal variation in T_e. However, due to the greater relative thickness of Sequence 1 it is difficult to determine this from studies of lithospheric loading.

Three-dimensional modelling also indicates a relatively high T_e for the Wilkes Land margin lithosphere. Isostatic anomalies associated with thick sediments and the continental edge effect are most effectively reduced for models created assuming $T_e = 30 to 45$ km. Spectral analysis of isostatic anomalies indicate that the power of the flexural isostatic anomalies is lower than the free air gravity anomalies.

The margin does not appear to be segmented, at least in regard to its long-term strength. However, a change in initial, zero-elevation crustal thickness (T_c) is inferred from west to east. A T_c of $\sim$35 km is inferred for western Wilkes Land, whereas eastern Wilkes Land is characterised by T_c =29 to 31 km. Limited seismic refraction data from the conjugate margin indicates a similar trend from southwest to southeast Australia.

Process-oriented gravity modelling has also been undertaken on the southern Australian margin. Results broadly indicate a lower T_e relative to the Wilkes Land margin. This is interpreted to indicate that sediment loading in the Late Cretaceous occurred on weakened lithosphere, and that backstripping studies recover this lower T_e because there has been relatively little subsequent loading throughout the Tertiary. Whereas, the major sediment loading interval on the Wilkes Land margin occurred some 60-80 Ma after rifting. This is the first evidence from a conjugate margin pair that continental lithosphere increases in strength following rifting.

Spatially correlated flexural isostatic and free air anomalies, magnetic anomalies, and basement features interpreted in seismic reflection data are observed. On the basis of forward modelling and inversion, these features are interpreted to have a density of

$\sim$3100 kg/m^3, and high magnetic susceptibility. Serpentinised upper-mantle peridotites are inferred on the basis of these results. Upper mantle peridotites have been dredged from a seamount-scarp offshore from eastern Wilkes Land, and similar structures have previously been inferred on the southern Australian margin.

Comparison of seismic reflection data indicate a broad-scale symmetry between the conjugate margins. Additionally, large-scale detachments are not imaged in seismic reflection data, therefore they do not support the lower plate and upper plate margin classifications of simple shear models. Greater depth of bathymetry off the southern Australian margin relative to the Wilkes Land margin is primarily a function of the different Tertiary sedimentation histories of the margins. The gravity and magnetic anomaly sequences are broadly symmetric also.

Depth anomalies of up to 800 m, calculated for the sediment unloaded oceanic crust, confirm greater depths of Wilkes Land oceanic crust relative to that expected from global ocean depth-age trends. This is likely a function of the initially greater depth of oceanic crust extruded at the SEIR, and in particular the AAD. The depth anomalies are not apparent for the possible seafloor spreading anomaly 34y, and for one location the backstripped basement is shallower than the depth predicted for oceanic crust for this anomaly. This provides further evidence that the anomaly previously identified as 34y may not be associated with *normal* oceanic crust.

This thesis provides insight into the evolution of a previously relatively unexplored, frontier, rifted continental margin. The interpretation and modelling results place the Wilkes Land margin in a regional and global context and indicate that it is anomalous with regards to its high lithospheric rigidity. The identification of a sunken marginal plateau or micro-continent off eastern Wilkes Land is important in understanding the breakup and dispersal history of southeast Australia, Tasmania and its associated micro-continents, and eastern Wilkes Land and northern Victoria Land of Antarctica.

Declaration

I hereby declare that this thesis, submitted in fulfilment of the requirements for the degree of Doctorate of Philosophy, represents my own work and is less than 80,000 words in length. This work has not been previously submitted to this or any other institution for any degree, diploma or other qualification.

David I. Close

Acknowledgements

I would like to acknowledge the supervision of Tony Watts over the past three years, particularly for the thorough reviews of this thesis in recent months. I would also like to thank my co-supervisor, Howard Stagg, and the staff of Geoscience Australia for their help, particularly Jim Colwell, Phil Symonds and Fred Kroh.

Many individuals, outside of Oxford, have contributed to various aspects of this project. In particular I would like to thank Takemi Ishihara (JNOC), Jon Childs (USGS), Rob Larter (BAS), Andrew Goodwillie and Bob Fisher (GEBCO), Fred Kroh (GA), all members of the GA Law of the Sea team and Jennie Totterdell, and Nick Direen (Uni. of Adelaide). The financial support of the Rhodes Trust and Shell are also acknowledged.

I would like to thank the staff of the Department of Earth Sciences for helping at every point possible during this project. Thank you also to all the graduate students for providing the high points of each day during the morning and afternoon coffee breaks. In particular I would like to thank my fellow members of the Marine Group over the past three years, especially Natalie Lane, Tiago Cunha, Tom Jordan and Matt Rodger for reading early drafts of several chapters. I would also like to thank Paul Wyer, Mohammed Ali, Marta Perez-Gussinye and John Hillier for discussions on all things marine and geophysical. The assistance of Steve Usher has also been invaluable everytime the computers misbehaved.

Images within this thesis have almost entirely been created using the GMT software of P. Wessel and W. Smith (http://www.soest.hawaii.edu/gmt).

On a personal note, I would like to thank all my friends at Oxford for making my time here so enjoyable. Thankfully, they are too numerous to name individually here. I would particularly like to thank the lovely Eliana, who has been so patient with me over the last year! Lastly, but by no means not least, I want to give huge thanks to my family for all their support over the past 25 years, I would never have got here without them.

Contents

List of Figures

List of Tables

Glossary of terms and abbreviations

The following terms, abbreviations and acronyms are used throughout this thesis.

AAB	Australia-Antarctic Basin
AAD	Australia-Antarctic Discordance
ABC	Aurora Basin Complex
AGC	Automatic Gain Control
ARB	Adelie Rift Block
BAS	British Antarctic Survey
COB	Continent-Ocean Boundary
COT(Z)	Continent-Ocean Transition (Zone)
CMP	Common Midpoint Point
CTB	Continent-Transition Boundary
D_c	Depth of compensation
DSDP	Deep Sea Drilling Program
E	Young's modulus
EAIS	East Antarctic Ice Sheet
EOC	Eocene aged unconformity
FAA	Free-Air Gravity Anomaly
FFID	Field File ID
FFT	Fast Fourier Transform
FIA	Flexural Isostatic Anomaly
FZ	Fracture Zone
g	Gravitational acceleration
G	Gravitational constant
GA	Geoscience Australia
GAB	Great Australian Bight
GMT	Generic Mapping Tools (http://www.soest.hawaii.edu/gmt)
GPS	Global Positioning System

IFP	Institut Francais du Petrole
JNOC	Japanese National Oil Company
KLNP	Cretaceous Long Normal Polarity period
LLCC	Laminated Lower Continental Crust
MCS	Multi-Channel Seismic
MOR	Mid-Ocean Ridge
MORB	Mid-Ocean Ridge Basalt
MQZ	Magnetic Quiet Zone
MSL	Mean Sea Level
NMO	Normal Move-Out
ODP	Ocean Drilling Program
Q	Königsberger Ratio
QZB	Quiet Zone Boundary
RMS	Root Mean Square
SB	Sonobuoy
SCAR	Scientific Committee on Antarctic Research
SDLS	Seismic Data Library Service
SDR	Seaward Dipping Reflector
SEG-Y	Trace sequential seismic recording standard
SEIR	Southeast Indian Ridge
SP	Shot Point
SRS	Southern Rift System
STR	South Tasman Rise
t	Time
T	Temperature
TAM	Transantarctic Mountains
T_c	Zero elevation, initial continental crustal thickness
T_e	Effective elastic thickness of the lithosphere
Tran	Reflector at top of transparent lower crust
TRM	Thermo-Remanent Magnetisation
T_s	Seismogenic thickness
TTS	Total Tectonic Subsidence
Tur	Turonian aged unconformity
TWT	Two-Way Time
USGS	United States Geological Survey
UNCLOS	United Nations Commission on the Law of the Sea

V	Velocity
V_p	P-wave velocity
W	Deflection (flexure)
WEMR	Wave Equation Multiple Rejection
WL	Wilkes Land
YSE	Yield Stress Envelope
Z_{neck}	Depth of Necking
λ	Wavelength
ρ	Density
σ	Poisson's ratio

Units

dB	Decibels
Hz	Hertz
km	kilometre
m	metres
Ma	10^6 years before present
mm	millimetre
ms	millisecond
My	10^6 years
nT	nanoTesla
s	second
yr	year

Chapter 1

Introduction

1.1 Continental Margins

1.1.1 Introduction

The term continental margin describes the region that separates the thick, geologically complex crust of the continents from the relatively thin, less structurally complex and compositionally diverse crust of oceanic basins. Continental and oceanic crust exhibit mean elevations of +0.8 km and -3.7 km relative to sea level, respectively [Kennett, 1982], the continental margin is, therefore, also a prominent morphologic feature.

Suess [1904] recognised that the morphology and geology of continental margins varied greatly, and introduced the descriptive terms, Atlantic margin and Pacific margin. The classifications of Suess [1904] are based on the fundamental differences between the wide coastal plains and thick sediments at the margins of the Atlantic Ocean, and the folded mountain belts, island arcs, volcanism and seismic activity at the margins of the Pacific Ocean.

The Suess [1904] classification of Pacific and Atlantic type margins remains in use today, although a large number of genetically descriptive terms are now also used to describe these margin types. A third major type of continental margin is recognised today, the Transform margin. The differentiation between the major margin types is a function of their relation to plates, plate boundaries, and the presence or absence of seismic and/or volcanic activity. Other common terms for Pacific, Atlantic and Transform type margins are:

- Atlantic: divergent, passive, or rifted.
- Pacific: convergent or active.
- Transform: translational or sheared.

The worldwide distribution of rifted, convergent and transform margins is illustrated in Figure 1.1.

We concentrate here on rifted margins. Rifted margins are old plate edges formed by the extension and eventual *breakup* of continental crust and the emplacement of oceanic crust. *Breakup*, is used here to describe the rifting and drifting stages of continental

Figure 1.1: Worldwide distribution of rifted (divergent), convergent, and transform margins. After Emery [1980].

fragmentation, it is associated with the first generation of new oceanic crust and the initiation of seafloor spreading. Hence, the rifted margin marks the transition to active rifted plate tectonic processes and the formation of an ocean basin. Physiographically, rifted margins are typified by the following conventional morphologic demarcations, after Heezen [1974]. Although such classifications are overly simplistic they provide a term of reference and comparison.

- Continental shelf, the gently dipping region of little relief extending from the coast to the *shelf break*, where the seafloor steepens and the continental slope begins.

- Continental slope, the region where gradients range from 20-4%. In some regions, such as northwest Australia and southeast South America, a *marginal plateau* at a depth of 800-1000 m lies between the continental shelf and slope.

- Continental rise, where typical gradients do not exceed 1%. In some areas the low relief of the continental rise is punctuated by large seamounts or seamount groups, some reaching elevations greater than sea level (e.g. Cape Verde Islands, The Canary Islands).

- Abyssal plain, gradients on the abyssal plain are generally less than 0.1% (a change in microtopography is also characteristic of the abyssal plain regions).

Rifted margins are generally characterised by a wide continental shelf relative to Pacific and Transform type margins. Another common characteristic of rifted margins are submarine channel systems, which dissect the continental shelf and slope regions. These features are associated with the transport of terrigenous sediment, and its subsequent erosion of and deposition on the continental slope and rise. The shelf break varies in depth

as a function of latitude at rifted margins [Heezen, 1974]. Shelf break depths commonly exceed 500 m in polar regions, whereas in more temperate latitudes the average depth is ∼130 m [Kennett, 1982]. This difference is primarily a result of glacial activity at higher latitudes. Shelf *over-deepening* associated with erosion by glaciers or ice-berg keels during times of glacial advance across the continental shelf is considered the primary cause of the greater depth of the shelf break at high latitudes (e.g. and Barnes [1987], Anderson [1991]). However, flexural downwarping, due to ice sheet loading, also contributes to shelf over-deepening (e.g. ten Brink *et al.* [1995]). A bathymetric profile through the Southern and southeast Indian Oceans between Antarctica and Australia (Figure 1.2) illustrates the morphological regions typical of rifted margins.

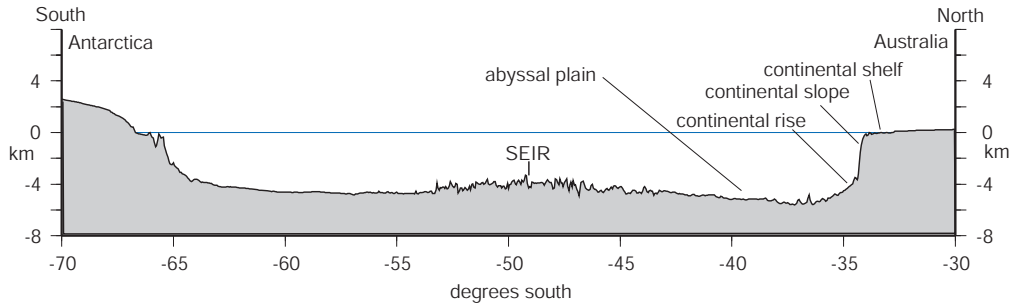

Figure 1.2: Bathymetric transect of the Southern and southeast Indian Oceans, between East Antarctica and southern Australia, at 130°E. SEIR = southeast Indian Ridge.

1.1.2 Structure of Rifted Margins

Crust, Sediment, and Magmatism

The continental crust underlying a rifted margin can be observed in seismic data to thin seawards (e.g. De Charpal *et al.* [1978], Hutchinson *et al.* [1982]). The transition to oceanic crust can occur over a few tens of km up to more than 150 km [Dean *et al.*, 2000]. Continental, cratonic crust at rifted margins is typically altered by stretching, faulting and igneous intrusive activity. However, this deformed crust remains distinct in chemical, structural and geophysical properties from oceanic crust.

Despite the differences in the nature of the crustal types underlying continental margins, the Continent-Ocean Boundary (COB) is an enigmatic geological feature. Geological factors, such as thick sedimentary sequences and masking lithologies (e.g. carbonates, salt, flood basalts) hinder the detailed seismic imaging of underlying crustal features, and typically prevent an absolute determination being made with seismic data alone. Interpretations based on other geophysical data are also rarely unambiguous.

Sedimentary sequences of great thickness, overlying rifted continental and oceanic

crust, occur at many rifted margins, e.g. northeast U.S.A [Hutchinson *et al.*, 1982]. However, some rifted margins are relatively sediment starved and comprise thin sedimentary sequences only, e.g. Hatton Bank [Fowler *et al.*, 1989]. The variations in sediment thickness are primarily a function of climatic conditions and uplift history of adjacent continental areas. Figure 1.3 shows a compilation of bathymetry and sediment thickness at a number of rifted margins, along with the free air gravity anomalies across the margins.

The sedimentary sequence at rifted margins is typically divided into three main units, *pre-rift, syn-rift*, and *post-rift*, as shown in Figure 1.4. The pre-rift sequence describes the deformed and faulted formations that predate rifting. Block rotation along listric normal faults is common within the pre-rift sequences (e.g. Moore *et al.* [2000]). Syn-rift sediments are deposited during active extension, crustal thinning and fault-controlled or tectonic subsidence. They are typically represented by dipping reflectors within fault-bounded rift basins. Rift basins often take the form of half-grabens and syn-rift sediments contained within them are often recognised by reflector divergence (associated with increasing sediment thickness) towards the bounding fault footwall (e.g. Krawczyk *et al.* [1996]). Fault-bounded rift basins and syn-rift sediments are normally blanketed with seaward-dipping, prograded and gently dipping to horizontal, aggraded clastic and carbonate sequences. The base of the post-rift sequence is often clearly marked by a *breakup unconformity* (e.g. Falvey [1974]). Post-rift sediments are typically undeformed and sparsely faulted, as they are deposited during an interval of thermal subsidence (e.g. McKenzie [1978]).

Although most rifted margins exhibit similar sedimentary characteristics, they differ markedly with regards to evidence of magmatic activity during margin evolution. Many margins exhibit evidence of excessive, transient magmatic activity during the final stages of breakup; these are classified as volcanic margins (e.g. Mutter *et al.* [1982], [Eldholm *et al.*, 1995]). Of all rifted margins around the world, 90% are volcanic rifted margins to varying degree, the exceptions being the rifted margins of eastern China, Iberia, the northern Red Sea, southern Australia, the Newfoundland Basin-Labrador Sea, and possibly the Gulf of California [Menzies *et al.*, 2002]. The margins of Antarctica are largely unknown with regards to evidence of rift-related magmatism.

Massive extrusive complexes along rifted margins were first recognised at the Vøring margin of Norway due to the smooth acoustic basement near the COB [Talwani & Eldholm, 1972]. The existence of wedges of seaward dipping, intrabasement reflectors below acoustic basement was later identified (e.g. Eldholm *et al.* [1979]). These Seaward Dipping Reflector (SDR) sequences are commonly used as the basis of identifying volcanic rifted margins (e.g. Coffin & Eldholm [1994]). The global distribution of volcanic margins

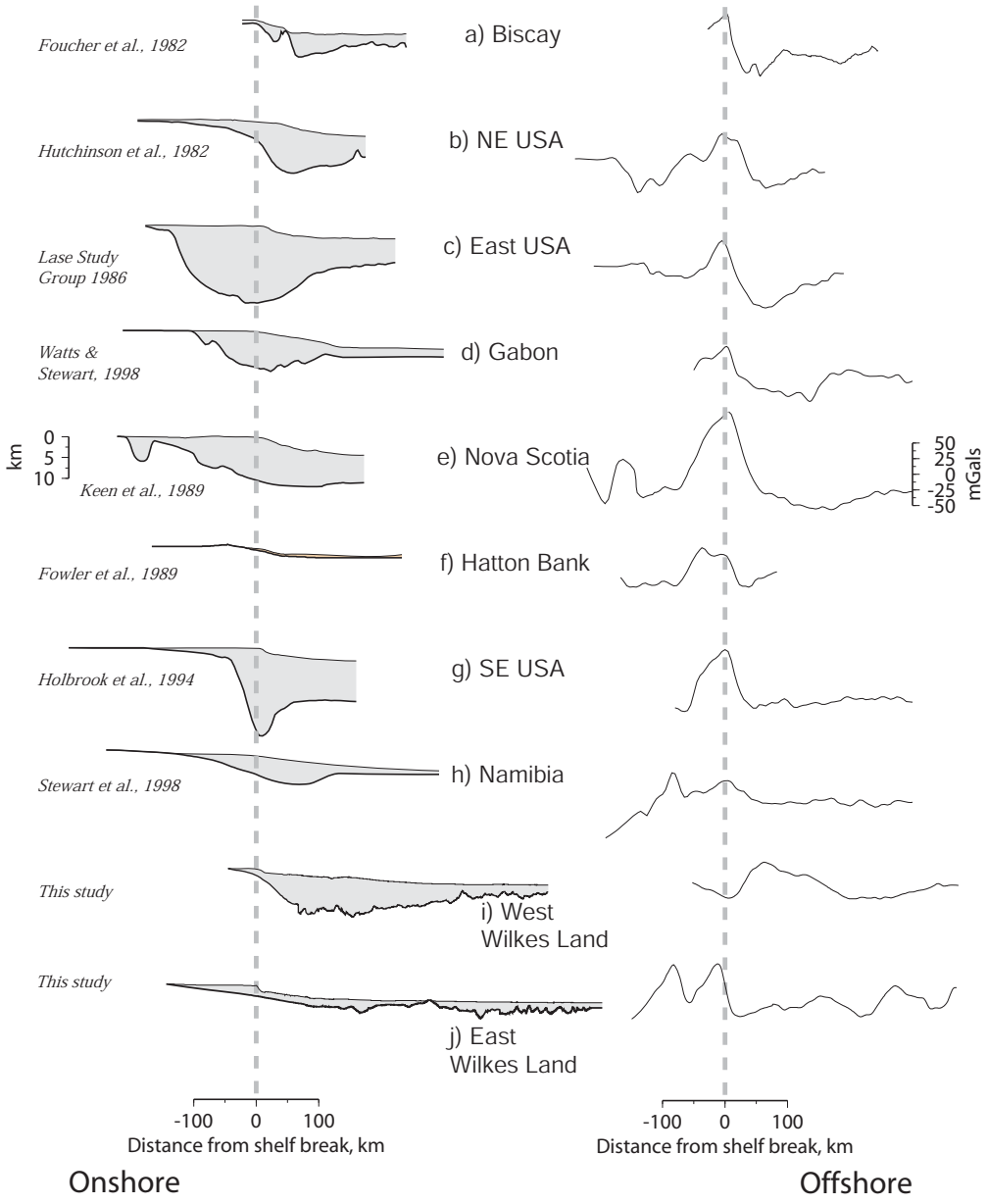

Figure 1.3: (a)-(h)Compilation of published profiles of upper crustal structure, with the grey-shaded area showing the undifferentiated thickness of volcanic and rift sediments above basement, and observed free air gravity anomalies at a number of margins worldwide. (i)-(j) Similar profiles across the western and eastern Wilkes Land margin from this study to enable comparison. Profiles are aligned on the shelf break. References Biscay [Foucher *et al.*, 1982]; USGS32, Carolina Trough [Hutchinson *et al.*, 1982]; LASE 6, Baltimore Canyon Trough [LASE Study Group, 1986]; Gabon [Watts & Stewart, 1998]; Nova Scotia [Keen *et al.*, 1990]; Hatton Bank [Fowler *et al.*, 1989]; EDGE801, US middle Atlantic margin [Holbrook *et al.*, 1994].

Figure 1.4: Seismic reflection section from the Otway Basin, southern Australia, divided into pre-, syn-, and post-rift sequences. After Moore *et al.* [2000].

based on wedges of intrabasement SDR is illustrated in Figure 1.5.

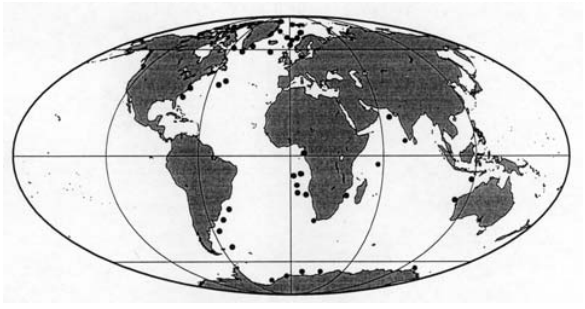

Figure 1.5: Global distribution of volcanic margins based on wedges of intrabasement seaward dipping reflectors, after Eldholm *et al.* [1995].

Eldholm *et al.* [1995] suggested that whether a volcanic margin develops or not during rifting depends on the temperature and fluid content of the asthenosphere along the

incipient plate boundary and the dynamic history of the lithosphere. They recognise a number of geological features by which volcanic margins can be identified, in addition to the commonly used seaward dipping reflector sequences. These include:

1. Onshore continental flood basalts.
2. Voluminous extrusive basaltic complexes along the continent-ocean transition appearing as intrabasement reflectors.
3. Sills and low-angle dikes within pre-rift sediments.
4. Thicker than normal oceanic crust adjacent to the COB.

The presence of thickened crust, commonly referred to as an *underplate*, is a common, but not universal, feature at volcanic rifted margins Eldholm *et al.* [1995]. Figure 1.6 illustrates some of the key geological features used to identify volcanic and non-volcanic margins. The identification or lack of these features allow volcanic margins to be distinguished from non-volcanic rifted margins.

1.1.3 Segmentation and Symmetry

Segmentation can be observed in bathymetry and marine gravity compilations to be a characteristic feature of seafloor spreading along the global mid-ocean ridge system. However, the processes by which an incipient rift and spreading centre develops into a segmented mid-ocean ridge, and how they relate to observed margin segmentation in the present-day is poorly understood [Behn & Lin, 2000].

At slow spreading rates, mid-ocean ridges are known to be highly three-dimensional, with segmentation observed both at active spreading centres and in aged oceanic crust by the presence of fracture zones and off-axis traces of nontransform offsets (e.g. Tucholke & Lin [1994]). In contrast, magma supply at fast spreading ridges, such as the East Pacific Rise, appears to be more two-dimensional [Lin & Phipps Morgan, 1992].

Cochran & Martinez [1988] identify segmentation of both the axial valley of the Red Sea rift basin and its margins on the basis of faulting and basaltic intrusive activity. The identification of segmentation at the axial valley and margins is interpreted to indicate that segmentation has been present in the Red Sea rift since its inception. Segmentation has also been inferred for the West African margin by Watts & Stewart [1998]. The identification of 350-400 km weak zones along-strike of the Gabon margin was interpreted by Watts & Stewart [1998] to indicate that rift margins may be highly segmented as regards their long-term strength. Structural segmentation has also been inferred on the Angolan margin by Hudec & Jackson [2002], where transfer zones associated with breakup are recognised as focal points for post-rift tectonism. Behn & Lin [2000] infer segmentation of the northeast U.S.A margin on the basis of gravity and magnetic anomaly

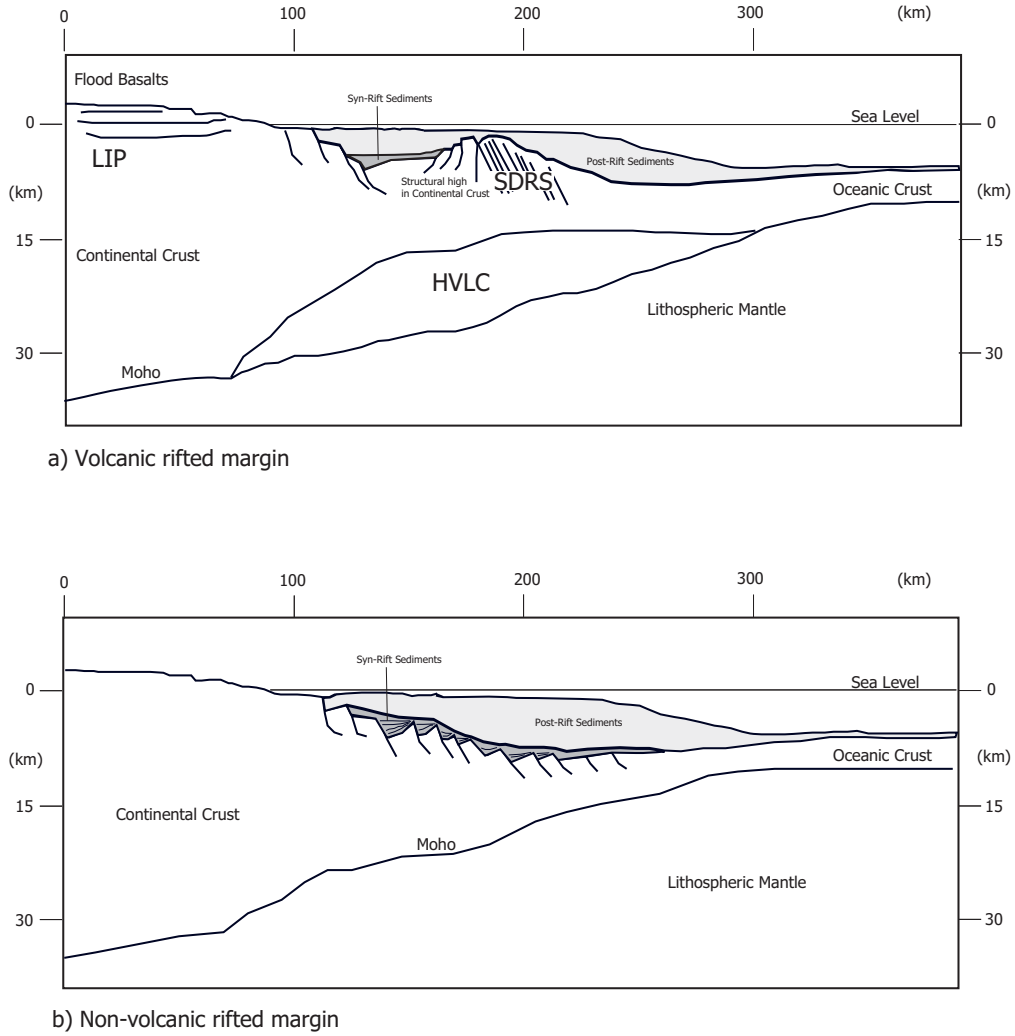

Figure 1.6: a) Schematic volcanic rifted margin. Volcanic rifted margins are characterised by a subaerial flood basalt province (i.e. large igneous province [LIP]) with upper and lower crustal magmatic systems; development of high-velocity lower crust (HVLC) in the transition from continental to oceanic domains; and, formation of a submarine, Seaward Dipping Reflector (SDR) sequence. After Menzies *et al.* [2002] and Symonds *et al.* [2000]. b) Schematic non-volcanic rifted margin. A lack of SDR allows the listric faulting within the rifted continental crust to be imaged in seismic reflection data.

character. They too imply that segmentation observed at mature spreading centres may be directly linked to segmentation during rifting and breakup.

If margin segmentation is related to processes at incipient spreading centres, then such segmentation should be relatively symmetrical for conjugate margin pairs. There is not yet sufficient evidence to determine if this is the case. The symmetry of conjugate margin pairs, however, has been the subject of much debate. Whether conjugate

margins exhibit symmetry with regards to degree of extension, width of extended crust, and lithosphere-scale deformation remains controversial. Pure shear models predict symmetric margins, whereas simple-shear or coupled pure and simple shear models predict asymmetric conjugate margins. Determining which model is more applicable is not trivial. For example, Etheridge *et al.* [1989] interpreted asymmetry between the southern Australia-East Antarctic conjugate margin pair and, therefore, inferred that breakup followed a simple shear process. However, the evidence cited by Etheridge *et al.* [1989] was discounted by Sayers *et al.* [2001] and the interpretation of a simple shear breakup questioned.

1.2 Continental Rifting and Rift Models

Buck *et al.* [1999] observed that *"...the more closely we look at areas of continental extension the more we see that all rifts are not created equal"*. As diverse as the variation in observed structure of rifted margins are the models that seek to explain observed data at these margins. A brief review of a number of the historically important rift models and their assumptions and/or application is given here.

McKenzie [1978] provides a relatively simple, pure shear model of continental extension and rifting. In this model, a section of uniform thickness lithosphere is instantaneously and uniformly extended by a stretching factor, β (Figure 1.7). Crustal thinning associated with the stretching causes an initial subsidence to maintain isostatic equilibrium. Lithospheric thinning in this model also creates an initial temperature perturbation that decays with time according to one-dimensional heat conduction, causing the continued and gradual thermal subsidence of the thinned crust. This model predicts a perfectly symmetrical rift basin (Figure 1.8a) and has been successfully applied in the modelling of many rift basins. However, it assumes a state of local isostasy, and therefore no lithospheric strength, is maintained during extension and rifting.

Wernicke [1985] suggested that subsidence across a rifted margin occurs as a result of simple shear along a low-angle detachment that extends through the crust and lithospheric mantle (Figure 1.8b). In this simple shear model the relative extension of crust and mantle lithosphere is non-uniform along any vertical line. Therefore, this model predicts asymmetric rifting and two broad classes of rifted margins; upper plate margins in the hanging wall of the detachment and lower plate margins in the footwall. A mixed-mode model of extension suggested by Kusznir & Park [1987] invokes brittle faulting above a detachment in the upper lithosphere accompanied by pure shear in the lower lithosphere (Figure 1.8c).

Weissel & Karner [1989] modelled the response of an elastic plate to isostatic forces

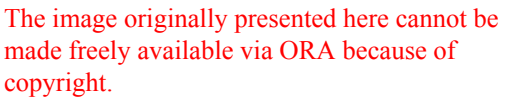

Figure 1.7: Sketch of the principal structural and thermal features from the McKenzie [1978] model of crustal extension, subsidence, and basin formation. β = stretching factor, C = crust, L = lithosphere, A = asthenosphere, a = thickness of the lithosphere.

Figure 1.8: Models of lithospheric extension. a) Symmetrical extension by pure shear, e.g. McKenzie [1978]. b) Asymmetrical extension by simple shear along a low-angle detachment. The thinnest part of the upper lithosphere is offset from the thinnest portion of the lower lithosphere. c) Mixed-mode extension. The lithosphere is cut by a dipping shear zone. Brittle faulting occurs above the detachment; ductile flow takes place at deeper levels. From Jones [1999] after Keen *et al.* [1989].

associated with a simple shear, Wernicke [1985] type, rift. Ebinger *et al.* [1991] applied such a model to explain the observed topography and gravity anomalies of the Western Rift of East Africa, where asymmetry in rift structure is observed. Models of this type have been labelled *flexural cantilever* models by Kusznir & Egan [1990]. In models of this type the lithosphere implicitly retains a finite rigidity during rifting.

Evidence from the continents and oceans suggest that lithospheric strength provides important constraints on crustal structure and, therefore, may influence rift processes. Changes in crustal thickness (i.e. the degree of stretching, β) and in the thickness of the mechanical lithosphere occur across rift margins. This necessarily alters the strength-depth relationships in continental lithosphere, and therefore also the yield strength envelope (YSE).

The YSE is a strength profile of the lithosphere that takes into account brittle and ductile deformation laws based on data from experimental rock mechanics (Figure 1.9). The strength profile increases linearly with depth and then decreases. The increase is given by Byerlee's Law, which varies for tension and compression. The decrease is given by ductile flow laws, which depend on the magnitude of the applied stress and the geotherm. The rate at which extension progresses, the thermal conditions, and mineralogical composition control YSE changes during rifting. Typically, thinned crust exhibits shallower and weaker, crust- and lithosphere-scale strength maxima [Wyer, 2003].

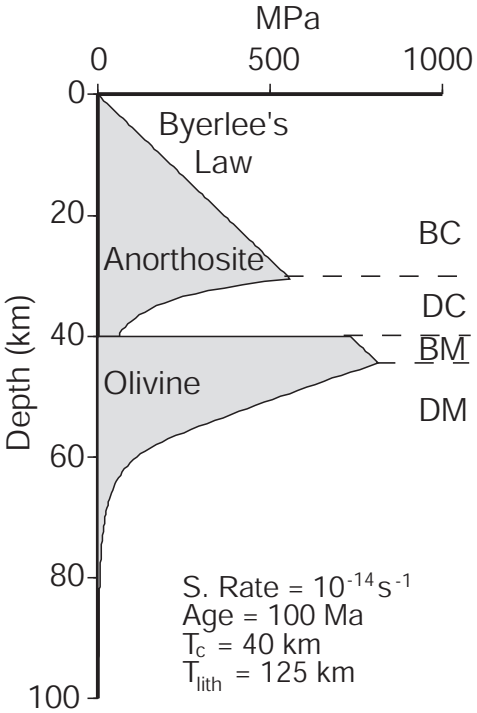

Figure 1.9: Yield Strength Envelope (YSE) profile for continental lithosphere assuming a "standard model" and an anorthosite crust and olivine mantle. The standard model is based on the strain rate (S.Rate), age, crustal thickness (T_c), and lithospheric thickness (T_{lith}) as labelled. BC and DC are brittle and ductile crust respectively, and BM and DM are brittle and ductile mantle respectively. After Watts [2001].

Modelling by Braun & Beaumont [1989] demonstrated that extension was concentrated preferentially at the depth of the maximum yield strength. Kooi *et al.* [1992] introduced the *depth of necking* model, based on the work of Braun & Beaumont [1989], which adapts the rift model of McKenzie [1978] by removing the assumption of Airy isostasy during rifting and allowing the lithosphere to thin preferentially at a depth of necking (Z_{neck}).

A major problem with the depth of necking model, however, is the assumption that Z_{neck} remains constant for the rift duration. Burov & Poliakov [1995] find that mechanical and thermal changes during rifting can cause necking to localise simultaneously and/or successively at multiple depths. Numerical modelling (e.g. Bassi [1995]), and laboratory scale analogue modelling (e.g. Brun & Beslier [1996] and Michon & Merle [2003]), of the rifting of a four layer lithosphere also demonstrate that the depth of the crustal, rheology based, strength maximum is non-constant during rifting (Figure 1.10).

Figure 1.10: Line drawing of an extending lithosphere analogue model composed of sand (brittle layers) and silicon (ductile layers), after Brun & Beslier [1996]. The model is based on rheological yield strength considerations and comprises four layers; Bc = brittle crust, Dc = ductile crust, Bm = brittle mantle, and Dm = ductile mantle.

The rheology based, four layer lithosphere models of Bassi [1995], Brun & Beslier [1996] and Michon & Merle [2003], comprise a plastic/brittle upper crust, a viscous/ductile lower crust, a plastic/brittle upper mantle, and viscous/ductile mantle (Figure 1.10). An important result of Brun & Beslier [1996] is the observation of both pure and simple shear in the same model rift system, although on different scales. They interpret lithospheric necking in their models to indicate pure shear at regional scales. However, within this essentially pure shear environment, they interpret shear components of opposing sense develop at the rheological interfaces within the crust and mantle.

The laboratory analogue experiments of Brun & Beslier [1996] and Michon & Merle

[2003] also indicate the presence of shear zones that control the overall, lithosphere scale thinning and necking. Brun & Beslier [1996] suggest that the final geometry of crustal layers is controlled by the rupture of the brittle mantle layer. The geometry and width of the rift system is also suggested to be a function of extension rate, with lower rates characterised by the formation of a single, asymmetric graben (narrow rift), and higher rates leading to the formation of two grabens (wide rift), as illustrated in Figure 1.11.

Figure 1.11: Comparison of rift geometries for a) slow, and b) fast extension rates. Low rate extension induces the formation of a single, asymmetric graben. In contrast, higher rate extension leads to the formation of two grabens, one asymmetric and one near-symmetric. After Michon & Merle [2003].

The relation between slow extension and narrow rifts suggested by Brun & Beslier [1996] and Michon & Merle [2003] conflicts with the numerical modelling of Bassi [1995]. As Bassi [1995] considers the temperature dependence of rheology and the YSE in her model she finds that slow extension is likely to result in wide rifts. This is because runaway thinning is less likely to occur in slowly extended lithosphere that can thermally equilibrate during rifting.

The relationship between rheology, lithospheric strength, and thermal processes during rifting is clearly complex. The number of variables involved in continental extension and rifting are such that no model, as yet, can adequately incorporate all these variables. Indeed, few rift models exist which do not contradict the assumptions of other rift models, each of which can explain aspects of the same rift system.

1.3 Isostasy and Flexure

Deep margin drilling has revealed sedimentary deposits of shallow water (<200 m) origin at depths of many kilometres (e.g. Totterdell *et al.* [2000]). This provides clear evidence for major subsidence at rifted margins following breakup. Although sediment loading

and thermal relaxation contribute to the observed subsidence at margins, the isostatic compensation of crustal thinning at rifted margins provides a first order control on margin evolution. Each of the above rift models invokes local or regional isostatic compensation to explain rift margin subsidence. A brief history of the concept of isostasy and the salient differences between local and regional isostasy is given here.

Isostasy is the term used to describe a condition to which the Earth's crust and mantle tend, in the absence of disturbing forces [Watts, 2001]. That is, it describes a state of equilibrium between the Earth's crust and the underlying mantle. Due to the dynamic nature of surface Earth, the equilibrium state is constantly shifting; mountain chains are formed and eroded, river deltas grow, ice sheets wax and wane, and volcanoes form and disappear violently. The ideal isostatic state is disturbed by the dynamic and continuously changing mass distribution on surface Earth. Seismic and gravity data, however, suggest that the Earth's outermost layers generally adjust to these disturbances [Watts, 2001].

Early models of isostasy were proposed by Pratt [1855] and Airy [1855] to explain a discrepancy of over $5''$ between survey positions determined using triangulation and astronomical methods in the Himalayas, northern India. Pratt [1855] applied a model based on dividing the Himalayan range into columns of varying densities above a compensation depth at which lithostatic pressure was equal (Figure 1.12a). Pratt's theory failed to correctly predict the observed difference between the astronomical and geodetic calculations.

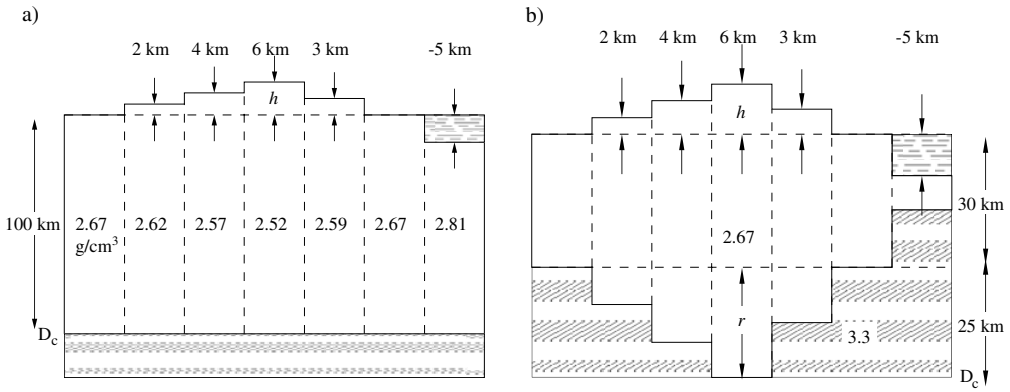

Figure 1.12: a) Pratt's model of isostatic compensation. Topography, h, is supported by density contrasts, above a depth of compensation, D_c, relative to standard density crust. b) The Airy model of isostasy. Topography of height h is supported by a crustal *root*, r, of lower density relative to mantle density. Figure modified from Stewart [1998].

Following the failure of Pratt's theory of isostasy to correctly predict the difference between the astronomical and geodetic calculations in northern India, Airy [1855] pre-

sented an alternative model. Airy demonstrated that if the excess mass of the mountains was supported at depth by a mass deficiency then the discrepancy could be accounted for (Figure 1.12b). He proposed that similarly to icebergs in the ocean, a mountain range was compensated at depth by a root of a relatively lower density than the mantle (or *"lava"* as Airy referred to it) displaced by the root. Which was the more appropriate and applicable model of isostatic compensation remained the subject of ongoing debate for over a century [Watts, 2001].

The Pratt and Airy models of compensation are based on contrasting assumptions, however, they are similar in that they consider compensation to occur on a purely *local* scale. That is, the compensation of topography occurs directly below the topography. If it is assumed that the lithosphere has a finite strength or rigidity, then the compensation of topography or anomalous mass can occur over a greater area as it is supported by the lateral strength of the plate. This is the basic premise of *regional* compensation. The broader wavelength, but smaller peak amplitude, of regional compensation relative to local compensation is illustrated in Figure 1.13.

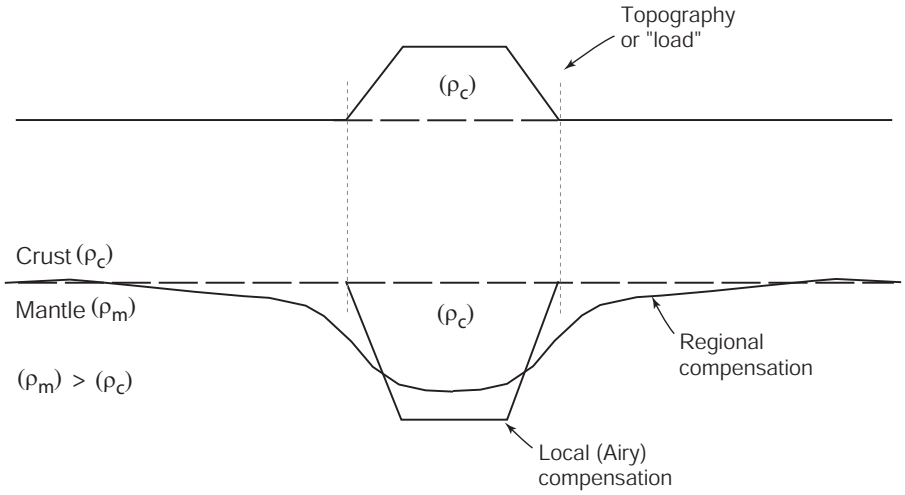

Figure 1.13: Schematic illustration of local and regional modes of compensation. ρ_c = crustal density, ρ_m = mantle density.

The notion of rigid lithospheric plates of finite strength was introduced in a series of papers by J. Barrell [1914] (as summarised by Watts [2001]). Vening Meinesz [1932] and many subsequent workers further developed this concept to incorporate an *elastic lithosphere*, capable of supporting stresses over geological time-scales (>1 My). In this model, the lithosphere is considered as a thin elastic sheet or plate overlying a fluid substratum. The deflection of such a plate is described by the general equation,

$$D\frac{d^4w}{dx^4} + (\rho_m - \rho_{infill})wg = 0 \qquad (1.1)$$

where ρ_m and ρ_{infill} are the densities of the mantle and infilling material, respectively, w is the deflection, and g is the acceleration due to gravity. D is the flexural rigidity of the plate, defined as,

$$D = \frac{ET_e^3}{12(1-\nu^2)} \tag{1.2}$$

where E is Young's modulus, ν is Poisson's ratio, and T_e is the *effective or equivalent elastic thickness*.

Equations 1.1 and 1.2 relate flexural rigidity to deflections of the lithosphere associated with loading forces. They also introduce the concept of effective or equivalent elastic thickness, herein referred to as elastic thickness, T_e. T_e does not represent the physical thickness of the rigid crust or lithosphere, rather it provides an equivalent elastic beam or plate thickness required to produce the observed or predicted deflection of the lithosphere to a given load. Although T_e relates to *rigidity*, it is often interpreted in terms of flexural *strength*, (e.g. Karner & Watts [1982]).

Estimates of T_e have been made in diverse geologic and tectonic environments, such as, the oceans (e.g. [Watts, 1978]), foreland basins (e.g. [Karner & Watts, 1983]), passive margins (e.g. [Stewart *et al.*, 2000]), trenches (e.g. [Parsons & Molnar, 1976]), and cratonic terranes (e.g. [Forsyth, 1985]). Estimates are typically based on spectral methods, such as admittance and coherence, or using forward modelling to fit observed crustal flexure and gravity anomalies.

The T_e evolution of oceanic lithosphere follows a predictable pattern controlled primarily by plate and load age (Figure 1.14), as demonstrated by Watts [1978]. Watts [1978] showed that T_e in the Pacific Ocean conformed to the depth of the $450 \pm 150°C$ isotherm. It is evident that this correspondence applies to most of the worlds ocean basins (see Watts [2001] for summary and references), and the range of T_e estimates for oceanic crust fall almost entirely within ∼2-50 km.

In contrast, T_e estimates from continental interiors are far more varied [Burov & Diament, 1995; Watts, 2001]. T_e values ranging from 7.5-110 km have been recovered using various methods (see Watts [2001] for summary and references). A compilation of continental T_e estimates derived from foreland basin and glacial lake studies (Figure 1.15) shows no systematic correlation between T_e and either age of the load or thermal age of the lithosphere. Many of the larger continental T_e estimates have been determined using the spectral coherence of Bouguer gravity anomalies with topography. The validity of these high estimates has been questioned in recent years.

McKenzie & Fairhead [1997], Maggi *et al.* [2000] and McKenzie [2003] challenge the validity of T_e estimates that exceed the seismogenic thickness (T_s) of ∼10-40 km. They claim that the strength of continents resides in the seismogenic layer within the crust

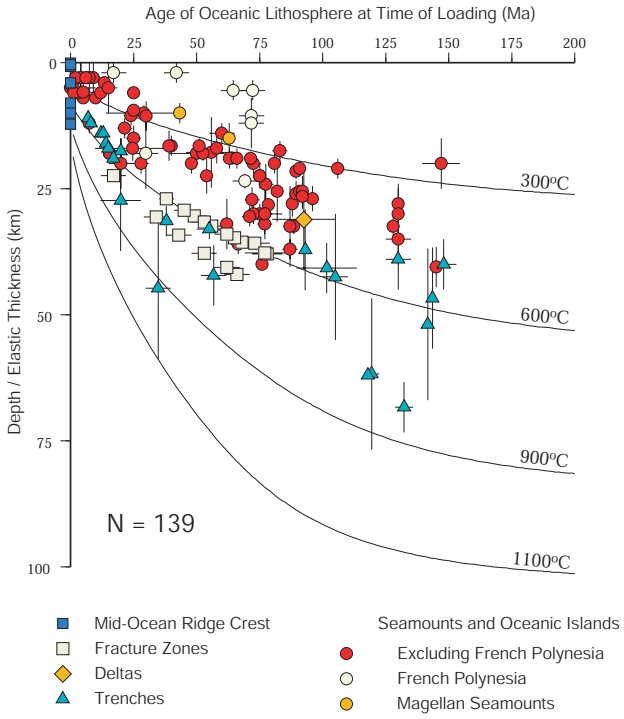

Figure 1.14: Plot of T_e against the age of oceanic lithosphere at the time of loading. T_e estimates are clustered between the depth to the 300 and 600°C isotherms. After Watts [2001].

and that continental mantle lithosphere is relatively weak. Perez-Gussinye *et al.* [2004] demonstrate that the application of spectral methods without adjustment for multi-tapering effects (associated with the size of the window used in spectral analyses) results in downward biased T_e recovery. McKenzie & Fairhead [1997] and McKenzie [2003] fail

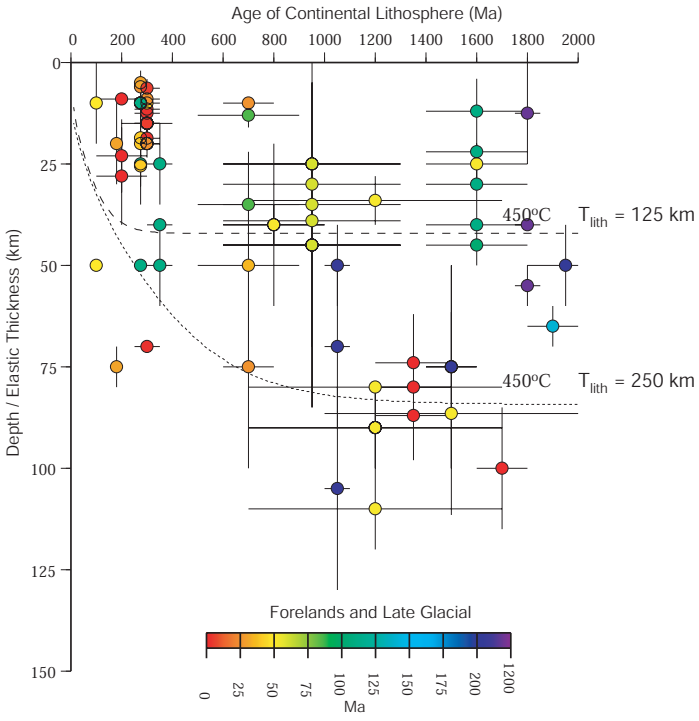

Figure 1.15: Plot of T_e against age of continental lithosphere at the time of loading. No correlation is evident as was the case for oceanic lithosphere and the scatter of estimates is much greater. After Watts [2001].

to make this adjustment in their studies that indicate $T_e \leq T_s$.

Watts & Burov [2003] find that that $T_e >> T_s$ in cratons, many convergent zones and some rifts. Most rifted margins, however, are characterised by low T_e, which is attributed to extensional faulting, thinning, and heating during intra-cratonic rifting, and post-rift sediment loading. Observation of flexure at seamounts has been widely used to constrain T_e estimates in oceanic lithosphere. Estimates of T_e in continental lithosphere are more commonly based on flexure at foreland basins or spectral studies (admittance and coherence). However, at rift margins where large sediment accumulations are common, spectral techniques are not applicable, and gravity modelling is typically used to provide constraints on T_e structure.

1.4 Gravity Modelling

Gravity anomalies can provide important insights into lithospheric structure. The density contrast across the *Moho* makes an important contribution to the gravity field at rifted margins. As models of compensation are intrinsically linked to the *Moho*, isostasy is important in understanding the gravity field at rifted margins. Additionally, analyses of observed and modelled gravity anomalies can elucidate the mode of isostatic compensation, and therefore the thermo-mechanical properties of the lithosphere, at rifted margins.

The initial development of a rift basin (i.e. prior to sediment deposition) causes two main contributions to the free air gravity field. The first is the negative anomaly associated with the replacement of crust by water/air. If the basin is in Airy isostatic equilibrium, the thinned crust and water filled basin are compensated directly beneath the basin by a mantle shallowing (Figure 1.16). The gravitational effect of this mantle shallowing is a positive anomaly. Away from the basin edge, the free air anomalies approach zero. However, over the basin edge a positive-negative couple, often referred to as the *"edge effect"*, occurs (observed edge effect anomalies over a number of rift margins are illustrated in Figure 1.3). The form of the anomaly is a function of the slightly lower magnitude and greater wavelength of the mantle compensation anomaly. This occurs as gravitational force is inversely proportional to the square of the distance to an anomalous mass.

The free air gravity edge effect anomaly at continental margins is one of the most distinctive features of the marine gravity field. It has been modelled and interpreted using various models of isostatic compensation. Worzel [1968] demonstrated the impact on the edge effect anomaly of moving the COB landward or seaward of the shelf break using an Airy isostatic model. Talwani & Eldholm [1973] also attempted to use Airy

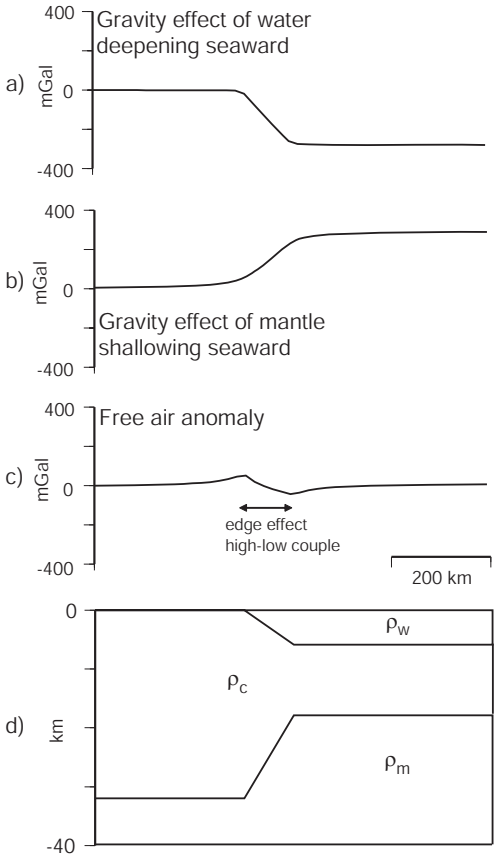

Figure 1.16: Illustration of the contributions of topography and its compensation to the free-air and Bouguer gravity anomalies at a rifted margin. Where $\rho_m = 3300$, $\rho_c = 2800$, and $\rho_w = 1030\,kg/m^{-3}$.

isostatic anomalies to assist in the identification of the continent-ocean transition (COT). This work was extended by Rabinowitz & LaBrecque [1977] to compensate the overlying sediments using an Airy model. They showed that the outer high isostatic anomaly, recognised by Talwani & Eldholm [1973], was not reduced by considering the sediments to be locally compensated. Both Talwani & Eldholm [1973] and Rabinowitz & LaBrecque [1977] interpreted this outer high anomaly to be associated with density differences within the crust and used it, along with other geological and geophysical features, as one criteria diagnostic of the COB.

Walcott [1972] and Cochran [1973], realising the potential importance of flexure at margins, employed the thin elastic plate model in gravity studies of the Mississippi and Amazon river deltas respectively. The results of these studies suggested an important role for flexure at rifted margins. Watts & Ryan [1976] also recognised that sediments at rifted margins represent a surface load that likely cause flexure of the crust and lithosphere. Accordingly, they surmised that an Airy model of isostasy, that assumes local rather than regional compensation, may not be appropriate in such environments.

In an attempt to quantify the effect of flexure on the edge-effect anomaly, Karner & Watts [1982] used spectral techniques (admittance) to estimate T_e in a rift margin

setting. They demonstrated that the outer high anomaly of Talwani & Eldholm [1973] could be explained by lithospheric flexure associated with sediment loading. As a result of this development, studies have been conducted, using seismic data where available to constrain sediment loading and crustal structure, to evaluate the spatial and temporal variation of T_e at rifted margins [Watts, 1988].

Watts & Marr [1995] present synthetic gravity models of *weak* ($T_e = 0$) and *strong* ($T_e = 25$) rifted margins to relate observed differences in edge effect anomalies to flexural strength. They illustrated that the edge effect anomaly is strongly dependent on the mode of compensation, local or flexural, of the sediment load. Watts & Marr [1995] show that a *"double"* edge effect anomaly is diagnostic of a weak margin, whereas a *"single"* edge effect anomaly indicates a strong margin.

Watts [1988] introduced a process-oriented approach to gravity modelling at rifted margins that accounts for the individual processes (i.e. crustal thinning, sedimentation, magmatic underplating) that contribute to the final form of the edge effect anomaly. This technique uses the observed gravity anomaly to constrain flexural rigidity of the lithosphere across rifted margins. Process-oriented modelling was also successfully applied in three-dimensions offshore west Africa, allowing segmentation of lithospheric strength to be inferred [Watts & Stewart, 1998].

Variation in T_e across a rifted margin is likely due to the formative processes involved in rift margin evolution. Continental margins comprise, by definition, continental, rifted continental, and oceanic lithosphere. The rheological and YSE changes associated with rifting of continental crust and the magmatic activity associated with seafloor spreading are likely to affect the long-term rigidity of the rifted continental crust. Therefore, T_e boundaries may represent fundamental changes in the underlying lithosphere and assist in identifying the COB.

Process oriented modelling differs fundamentally from object oriented modelling; a term used here to refer to gravity models that comprise bodies of varying (within a reasonable range as determined from empirical petrophysical measurements) density and geometry as required to model observed data. Object-oriented models provide constraints on the present-day mass distribution only, whereas process-oriented modelling allows the gravity contributions of geological processes to be investigated along with the mass distribution. Typically it is possible to achieve much closer fits to observed data (i.e. lower root mean square (RMS)) with object oriented models. However, due to the large number of bodies and parameters often utilised they are very sensitive to user input.

1.5 Thesis Outline

This thesis primarily analyses and integrates the results of three recently acquired, independent, geophysical datasets on the Wilkes Land margin of East Antarctica. These data were acquired by Geoscience Australia (GA) during two surveys (GA-228 and GA-229) carried out in the Austral summers of 2000-01 and 2001-02. The major geographic and morphologic features of the southeast Indian Ocean and East Antarctica are illustrated in Figure 1.17. The Wilkes Land sector of the East Antarctic margin extends from approximately 100-140°E and is conjugate to the southern margin of Australia. The conjugate margin pair is separated by an uninterrupted ocean basin, however, two oceans (the Southern Ocean[1] and the southeast Indian Ocean) are defined between Australia and Antarctica.

Interpretation and modelling, where appropriate, of seismic reflection, magnetic anomaly, and gravity anomaly data from surveys GA-228 and GA-229, and from previous surveys for which data is available, has been carried out to help understand the evolution of this rifted margin. Previous constraints on the crustal structure, age, seismic stratigraphy, subsidence history and thermomechanical evolution of the Wilkes Land margin are limited relative to the margins of all other continents. The primary reason for this lack of knowledge has been the absence of deep-penetrating, regional seismic reflection data. Sectors of the Wilkes Land margin had remained entirely unsurveyed prior to surveys GA-228 and GA-229.

As this thesis incorporates the analysis, or modelling and interpretation, of three independent datasets, it is split into three main chapters. The structure is as follows:

- Chapter 2 reviews the tectonic, geological and geophysical setting of the Antarctic continent, with specific focus on the Wilkes Land margin. A review of previous work is also included.

- Chapter 3 summarises the acquisition and processing of seismic reflection data offshore Wilkes Land.

- Chapter 4 describes the seismic stratigraphy of the Wilkes Land margin sedimentary section and the crustal structure as determined from seismic reflection data. The first sediment isopach for the Wilkes Land margin illustrates a major sedimentary basin off west Wilkes Land. Due to the almost total ice sheet cover of Antarctica, the marine sedimentary record of the Antarctic margin provides the only accessible record of palaeoevolution of the continental mass. The post-rift stratigraphy is of particular importance as it records the climatic transition from temperate to polar-glacial. A frag-

[1] In 2000, the International Hydrographic Organization delimited the Southern Ocean, it is defined as the ocean that surrounds Antarctica and extends to 60°S

ment of continental crust (?microcontinent), located at abyssal depths, that extends over 450 km from the shelf break is also identified off east Wilkes Land.

- Chapter 5 outlines the seafloor spreading magnetic modelling undertaken to constrain the timing of breakup between Antarctica and Australia. Modelling of magnetic anomaly data in relation to the geomagnetic time scale is crucial in further constraining the timing of breakup and the location of the COB. Problems associated with identifying the oldest true isochron are discussed critically.

- Chapter 6 contains the theoretical background of the backstripping process and process oriented gravity modelling. Modelling is conducted to create isostatic anomaly profiles and grids, and to constrain flexural rigidity variation across and along the margin. Primarily modelling is two-dimensional, using seismic reflection data to constrain model geometry, however, three-dimensional modelling is also completed. Gravity modelling herein provides the first insights into the lithospheric rigidity or strength of this rifted margin.

- Chapter 7 contains analyses and discussion of crustal structure and subsidence. Object oriented gravity modelling (forward and inverse) is completed to constrain the properties of bodies associated with isostatic anomalies calculated in the previous chapter. Object oriented magnetic modelling is also carried out to provide further insight to the nature of linear magnetic anomalies in the COT. A comparison with the conjugate southern Australian margin is also undertaken.

- Chapter 8 concludes the primary findings of this thesis and outlines ideas for future work.

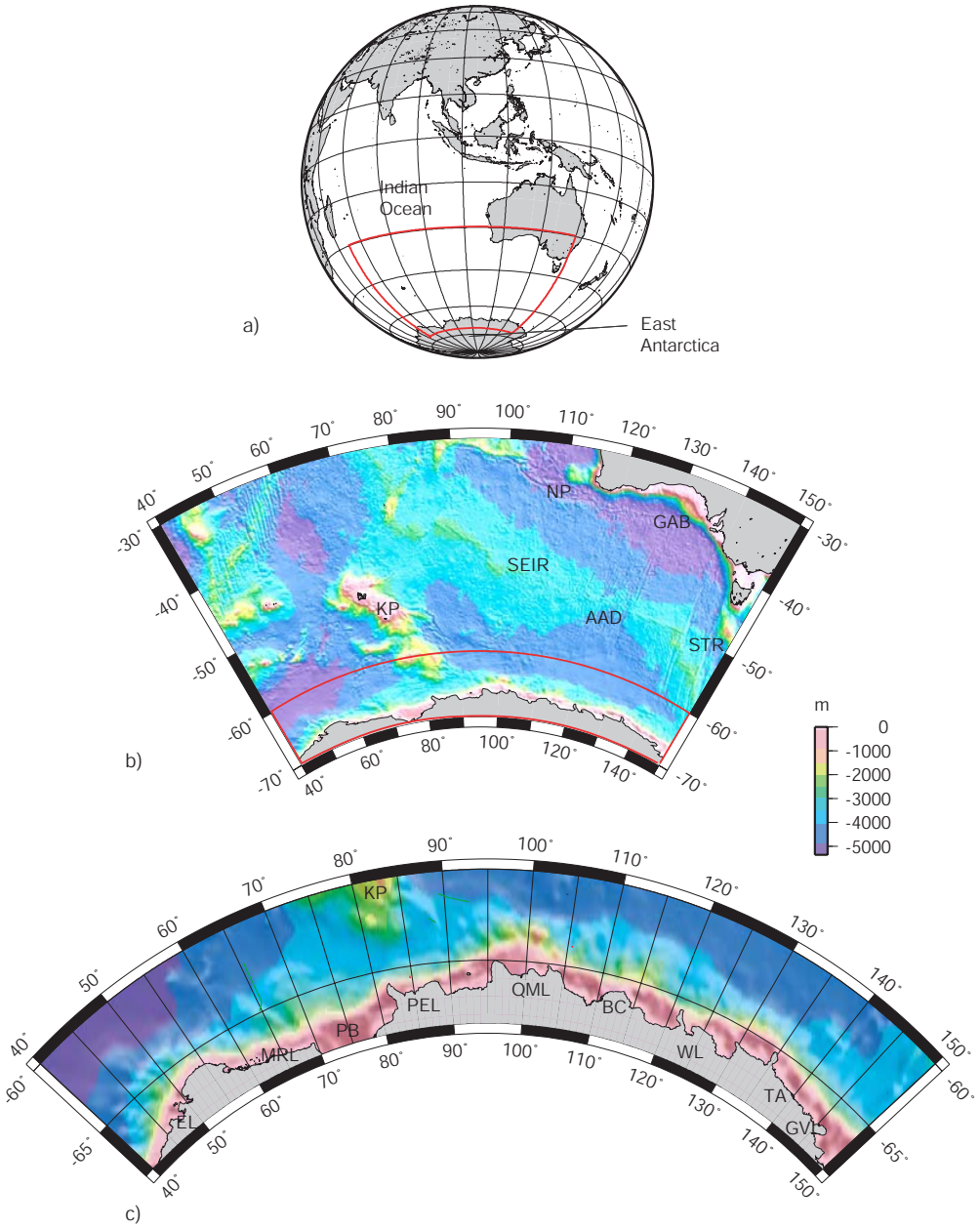

Figure 1.17: a) Location map of East Antarctica in a global context. b) Bathymetry map of the southeast Indian Ocean, the southern Australian and East Antarctic margins, and important morphological/geographical features. AAD = Australian-Antarctic Discordance, GAB = Great Australian Bight, KP = Kerguelen Plateau, NP = Naturaliste Plateau, SEIR = Southeast Indian Ridge, STR = South Tasman Rise. c) The Wilkes Land sector of East Antarctica is conjugate to the southern Australian margin. EL = Enderby Land, MRL = Mac.Robertson Land, PB = Prydz Bay, QML = Queen Mary Land, PEL = Princess Elizabeth Land, BC = Budd Coast, WL = Wilkes Land, TA = Terre Adélie, GV = George V Land. Bathymetry from Smith & Sandwell [1994].

Chapter 2

Geological and Geophysical Setting

2.1 Introduction

This chapter reviews the current state of knowledge relating to the tectonic history, geology and geophysics of Antarctica. The fragmentation and dispersal of the supercontinent Gondwana is reviewed in order to place Antarctica, in particular the Wilkes Land margin of East Antarctica, in a regional context

Due to the isolation and climate of Antarctica, and also the lack of commercial exploration and exploitation, the Antarctic continent remains a frontier realm of geology, of which very little is known. The Antarctic continent is more than 98% ice covered, and consequently the knowledge of the subglacial geology is extremely limited.

2.2 Gondwana and the Southern Continents

The notion of a continuous continental mass that once connected South America, Africa and India, was first suggested by in the late nineteenth century by Neumayr and Blanford (see Du Toit [1937] for references and historical discussion). The concept was further developed by Suess [1904], who conferred the name *"Gondwána-Land"*[1] to the prehistoric landmass. Du Toit [1937] observed that during the early twentieth century the former existence of Gondwana was to many *"...as nebulous as the mythical island 'Atlantis'"*.

The first comprehensive account of the geological basis for the existence of Gondwana was given by Du Toit [1937]. His primary aim was to provide scientific rigour to the concept of *continental drift*, as proposed by Wegener [1912] and Wegener [1915], which remained incomprehensible to most scientists of the time. Du Toit [1937] provided

[1] After *"...the ancient Gondwána flora common to all its parts"* [Suess, 1904]; although it is commonly thought that the name originates from a region of eastern India where some of the geology of the ancient continent was determined. However, as *Gondwana* translates to *"Land of the Gonds"*, Gondwana-Land would translate to "Land of the Gonds Land", which is nonsensical. Accordingly, the name Gondwana is more commonly used today, this convention is followed herein.

detailed descriptions of similarities in the faunal assemblages, sedimentology, and geological structures of the southern continents, which once comprised Gondwana, as evidence of continental drift theory. The reconstructions of Gondwana provided by Du Toit [1937], Figure 2.1, have been only slightly revised in over 65 years.

Figure 2.1: Gondwanan reconstruction of Du Toit [1937] at three intervals during the Mesozoic, 1. Early Jurassic, 2. *earliest* Cretaceous, and 3. *latest* Cretaceous.

Gondwana once formed the southern terrane of the Palaeozoic Supercontinent Pangaea, the northern terrane being Laurasia. These geologically and tectonically distinct terranes rifted apart to become isolated supercontinents during the Jurassic (e.g. Evans [2003]). Gondwana was by far the larger of the two supercontinents, with an estimated area of over 100×10^6 km^2 [Parrish, 1990]. Due to its size, the influence of the continent on global current and climate patterns would have been great. The relative positions of Gondwana and the south pole would have influenced the onset and duration of southern hemisphere glaciation, and consequently global sea level [Parrish, 1990].

The present day Antarctic continent formed the core of the Gondwanan Supercontinent, *"around which, with wonderful correspondences in outline, the remaining 'puzzle-pieces' of Gondwana can with remarkable precision be fitted"* [Du Toit, 1937]. Before the onset of breakup in the Middle Jurassic, Figure 2.2, Gondwana comprised continental crust that is now divided into a number of distinct plates. The major present-day plates that formed part of Gondwana are Antarctica, Australia, Africa, India and South America.

Figure 2.2: Gondwana tight fit reconstruction and breakup model, after Fitzgerald [2002], continent and microplate positions from Lawver *et al.* [1992] and Lawver *et al.* [1998]. AP = Antarctic Peninsula, TI - Thurston Island, MBL = Marie Byrd Land, CR = Chatham Rise, CP = Campbell Plateau, SNZ = southern New Zealand, NNZ = northern New Zealand, LHR = Lord Howe Rise, WS = Weddell Sea.

A number of major tectonic events shaped the present day continents, that once formed Gondwana, before the final breakup of the Supercontinent. The first of these is recognised as the onset of regional extension in the Early Permian, which produced a large rift and associated basins on what is now the east coast of Africa. Continuing extension led to the onset of breakup at approximately 150 Ma [Rabinowitz & LaBreque, 1979] when western Gondwana, comprising Africa and South America, separated from eastern Gondwana, comprising India, Antarctica, Australia and New Zealand [Smith & Hallam, 1970; Lawver & Scotese, 1987].

From the onset of Permian extension, through to Gondwanan breakup, large scale magmatic activity resulted in the widespread intrusion and eruption of intermediate to mafic, tholeiitic magmas. This period of extended magmatic activity is represented in southern Africa by the Karoo basalts (220-130 Ma) [Cox *et al.*, 1967], in Antarctica by the Ferrar dolerites and the Kirkpatrick basalt (180-160 Ma) [Tingey, 1991b], and in southeastern Australia by the Tasmanian dolerites (180-160 Ma) [Green *et al.*, 1978].

The separation of Greater India from East Antarctica, at ∼128 Ma, continued the west to east *unzipping* of Gondwana [Mishra *et al.*, 1999]. Following the separation of Greater India, all that remained of the former Supercontinent was the East Antarctic

terrane, the microcontinental blocks of West Antarctica and, the Australian and New Zealand terranes.

The Pacific margin of Gondwana was active during breakup, and subduction of the Phoenix Plate [Larson & Chase, 1972] continued throughout the Mesozoic. Subduction was occurring beneath the microcontinents and microplates of what are now New Zealand and West Antarctica, referred to here as Zealandia [Luyendyk, 1997] (Figure 2.2). At ∼105 Ma, subduction was replaced by an extensional tectonic regime throughout Zealandia. This was followed about 20 My later by rifting and seafloor spreading between the Campbell Plateau and West Antarctica [Luyendyk, 1997]. The change in tectonic environment is most commonly attributed to subduction of the ridge crest (ridge capture), e.g. Larter & Barker [1989], or by capture of part of the subducted/subducting Phoenix Plate by the northward moving Pacific Plate (e.g. Luyendyk [1997]).

Whatever the cause, the change to an extensional rift regime in the West Antarctic region represented one of the final tectonic events that contributed to the piecewise fragmentation of Gondwana. The rifting of Australia and Antarctica represented the final development of extensional plate margins within Gondwana. Although the exact timing of this rift event has been equivocal for some decades, it appears certain that final separation and seafloor spreading commenced in the Late Cretaceous [Cande & Mutter, 1982; Tikku & Cande, 1999; Sayers *et al.*, 2001]. The oldest oceanic crustal age estimates from the Australia-Antarctic basin range from 83-95 Ma, however, final clearance of the Antarctic Plate and the South Tasman Rise occurred much later, ∼35-29 Ma [Lawver & Gahagan, 2003; Cande & Stock, 2004].

Although the reconstruction of Gondwana is broadly well constrained (e.g. Smith & Hallam [1970], Lawver & Scotese [1987]), the exact locations of Madagascar with respect to Africa, the fit of Sri Lanka and India with East Antarctica, and the location of the Antarctic Peninsula with respect to South America have, at times, been equivocal [Lawver & Scotese, 1987]. However, advances in the identification of marine magnetic anomalies and the mapping of fracture zones in satellite altimeter derived bathymetry and gravity data have resolved most of these sources of controversy [Dalziel, 1992].

Reconstructions of Australia and Antarctica are, on a broad scale, also well constrained [Grindley & Davey, 1982]. However, a number of uncertainties remain regarding the reconstruction of the eastern Australia-Antarctic Basin (AAB) in the region of the South Tasman Rise (STR) (Figure 2.3). Although it is accepted that the STR comprises two distinct continental fragments, the East STR and the West STR, their kinematic evolution is uncertain. Due to the relatively small size of the STR it has either been ignored in some Gondwanan reconstructions, or is left in the same position relative to Tasmania as today [Royer & Rollet, 1997]. Irrespective, the STR causes a degree of

overlap with the Ross Sea Shelf or Victoria Land (e.g. Weissel *et al.* [1977], Grindley & Davey [1982]).

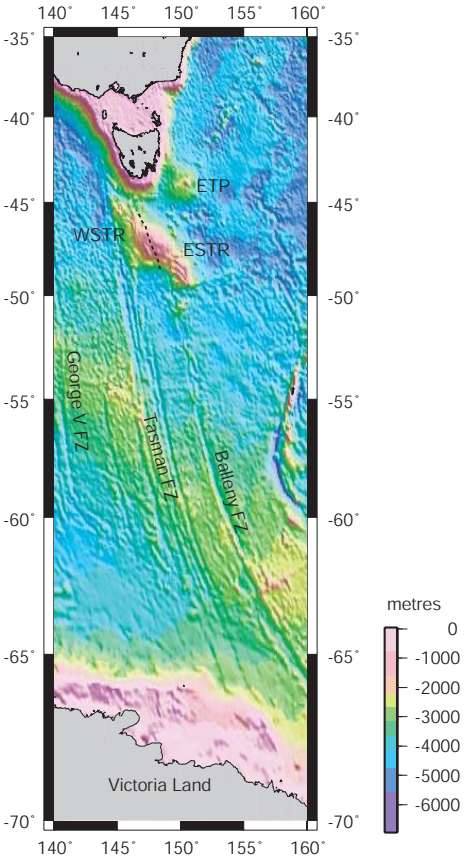

Figure 2.3: Eastern Australia-Antarctic Basin (AAB) bathymetry. Tight fit reconstructions consistently result in overlap of the East South Tasman Rise (ESTR) and West South Tasman Rise (WSTR), and Victoria Land, Antarctica. The Balleny fracture zone (FZ) marks the continuation of the East Antarctica-West Antarctica continent-continent boundary. ETP = East Tasman Plateau.

Royer & Rollet [1997] suggest a reconstruction in which the East and West STR have distinct kinematic histories in an attempt to solve the overlap problems. They suggest that the West STR was initially attached to Antarctica and underwent severe wrench deformation as the Antarctic plate moved southward relative to the Australian plate. Whereas, they suggest that the East STR rifted from southern Tasmania and the East Tasman Plateau. However, Gaina *et al.* [1998] suggest that if the likely Cainozoic extension in the western Ross Sea is considered, there is insufficient space for the STR in the total fit reconstructions of Royer & Rollet [1997]. Revised reconstructions of Tikku & Cande [1999] encounter the same overlap problems (Figure 2.4). Possible explanations for the consistent overlap problems suggested by Tikku & Cande [1999] include:

1. That the previously recognised oldest seafloor spreading anomalies are not isochrons.
2. The rotation poles for the oldest isochrons are incorrect.
3. That, as yet unidentified, post 80 Ma, continental extension has occurred in the Bass Strait region of southeastern Australia or northern Victoria Land, Antarctica.

Figure 2.4: Reconstructions of Australia and Antarctica in the region of Tasmania and Victoria Land, Antarctica for isochrons 32y, 33o, 34y, and the quiet zone boundary (QZB) anomaly. Antarctic COB (solid black line) is from Eittreim [1994], and the Australian COB (outlined white line) is digitised from the satellite free air gravity grid by Tikku & Cande [1999]. Dotted and dashed lines are the Australian and Antarctic *"continental margins"*. Figure from Tikku & Cande [1999].

The solution to the continental overlap observed in plate reconstructions of the eastern AAB remains a *"tectonic puzzlement"* [Tikku & Cande, 1999]. The acquisition of further geophysical data is required to more adequately resolve the kinematic evolution of this region. The tectonic evolution of West Antarctica also remains somewhat equivocal. However, it is not investigated further here as it is of little relevance to the region of study for this thesis.

2.3 Timing of the Antarctic-Australia Breakup

Correctly dating the onset of seafloor spreading between Antarctica and Australia is of fundamental importance to understanding the geological evolution of this conjugate margin pair. However, the timing of separation between Australia and Antarctica has been highly equivocal for the last three decades. Breakup ages from 52 to 125 Ma have been argued by workers since the early 1970's.

The continental margins of Antarctica and Australia are currently separated by the approximately 3000 km-wide Southern Ocean and southeast Indian Ocean. The Southeast Indian Ridge (SEIR), which is located approximately half-way between the continents, trends east-west, at a latitude of ∼50°S, as far as 139°E. East of this longitude, the SEIR is offset to the southeast by a zone of transform faults to nearly 65°S [Veevers, 1987]. The AAB is the only region along the length of the SEIR in which there is a recognised magnetic sequence for the oldest period of seafloor spreading from the Late Cretaceous to the early Tertiary [Cande & Mutter, 1982]. Although the anomaly sequence is complete it is far from ideal; the anomalies are generally poorly formed and exhibit significant variations in their form along strike. There is also a relative paucity of data on the Antarctic margin, forcing interpretations to include unconstrained interpolations of significant magnitude between shiptrack data.

Weissel & Hayes [1972] suggested that Australia-Antarctic separation occurred in the Early Eocene (52 Ma), based on the identification of anomaly 22 as the oldest seafloor spreading anomaly on the southern margin of Australia. A major revision of this breakup age was proposed by Cande & Mutter [1982] following their reinterpretation of southern Australian margin seafloor spreading anomalies. Cande & Mutter [1982] concluded that anomalies 19-22 of Weissel & Hayes [1972] could be better modelled as anomalies 20-34. Accordingly, they revised the age of separation from ∼53 Ma to 86-110 Ma during the long Cretaceous normal polarity epoch.

More recently, Sayers *et al.* [2001] have interpreted seafloor spreading onset at anomaly 33o time (∼79 Ma), some 15 My younger than the 95 Ma age accepted for much of the previous two decades. A full discussion of previous work on magnetic modelling in the Southern Ocean and the evolution of the revisions made to the breakup age of Antarctica and Australia is given in Chapter 3.

2.4 East Antarctica and West Antarctica: Surface, Crust, and Lithosphere

One of the broadest observations of Antarctica is the obvious division between East Antarctica and West Antarctica, Figure 2.5. The geological basis for this division was documented by some of the earliest workers in the area [Tingey, 1991b; Bentley, 1991].

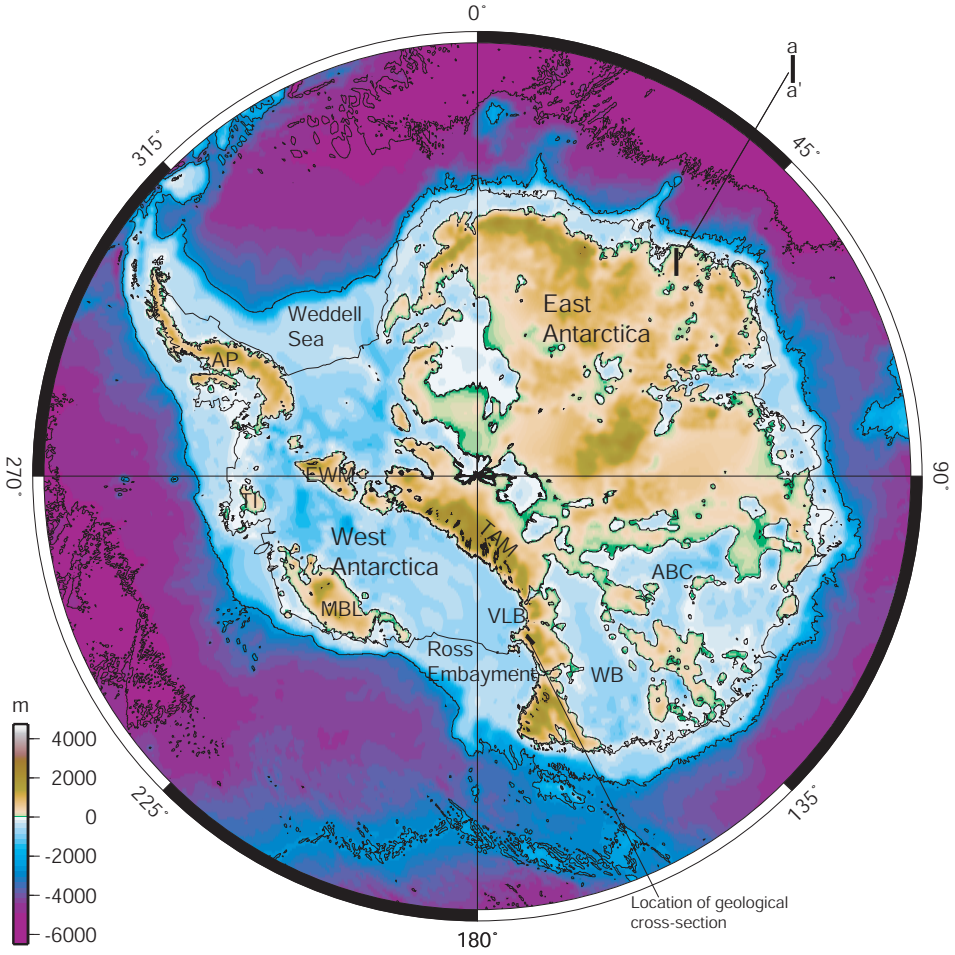

Figure 2.5: Topography of Antarctica from the BEDMAP project [Lythe *et al.*, 2000]. The Transantarctic Mountains (TAM) form the physiographic divide between East Antarctica and West Antarctica. Profile a-a' is illustrated in Figure 2.6. WB = Wilkes Basin, ABC = Aurora Basin Complex.

The boundary between East and West Antarctica is very abrupt, as seen from both the topographical divide at the Transantarctic Mountain (TAM) front, and from geophysical evidence that indicates a rapid change in crustal and lithospheric thickness [Bentley, 1991]. Seismic refraction experiments in East Antarctica indicate a depth to the *Moho* of ~38-40 km inland, Figure 2.6, decreasing to ~30 km at the coast [Kogan, 1972; Ikami

et al., 1983]. Whereas, the depth the *Moho* in West Antarctica is generally <30 km (e.g. Bentley [1983]). Gravity modelling (e.g. Groushinsky & Sazhina [1982]) also indicates greater crustal thickness in East Antarctica.

Figure 2.6: An example of a deep seismic sounding profile from East Antarctica, as located in Figure 2.5, after Ikami *et al.* [1983].

Seismic tomography reveals a marked difference in lithospheric properties between East Antarctica and West Antarctica. Figure 2.7 illustrates that East Antarctica is characterised by faster relative (to PREM, [Dziewonski & Anderson, 1981]) S-wave velocities, at a depth of ~150 km, than West Antarctica. Broadly, this represents a greater depth of cooler, continental mantle lithosphere beneath East Antarctica relative to West Antarctica. The TAM front, the physiographic divide between East Antarctica and West Antarctica, and the steepest S-wave velocity perturbation gradient correlate extremely closely.

The different geological framework of the two terranes is also apparent in the subglacial topography, Figure 2.5. East Antarctic subglacial topography is generally above sea level, the East Antarctic flank of the TAM extends for hundreds of kilometres under the East Antarctic Ice Sheet (EAIS). In contrast, the elevation drop on the West Antarctic flank of the TAM is much steeper.

East Antarctica can be divided into two main sectors, the Indian Ocean (0-90°) and Australian (90-180°) sectors, on the basis of subglacial topography. In the Indian Ocean quadrant, bedrock lies mostly above, and in extensive mountainous regions, far above, sea level. In contrast, the Australian quadrant comprises two extensive subglacial and sub-sea-level basins, the Wilkes Basin and Aurora Basin Complex (ABC), separated by rugged highlands.

Distinctive, mesa style landforms (i.e. flat-topped areas of elevated topography),

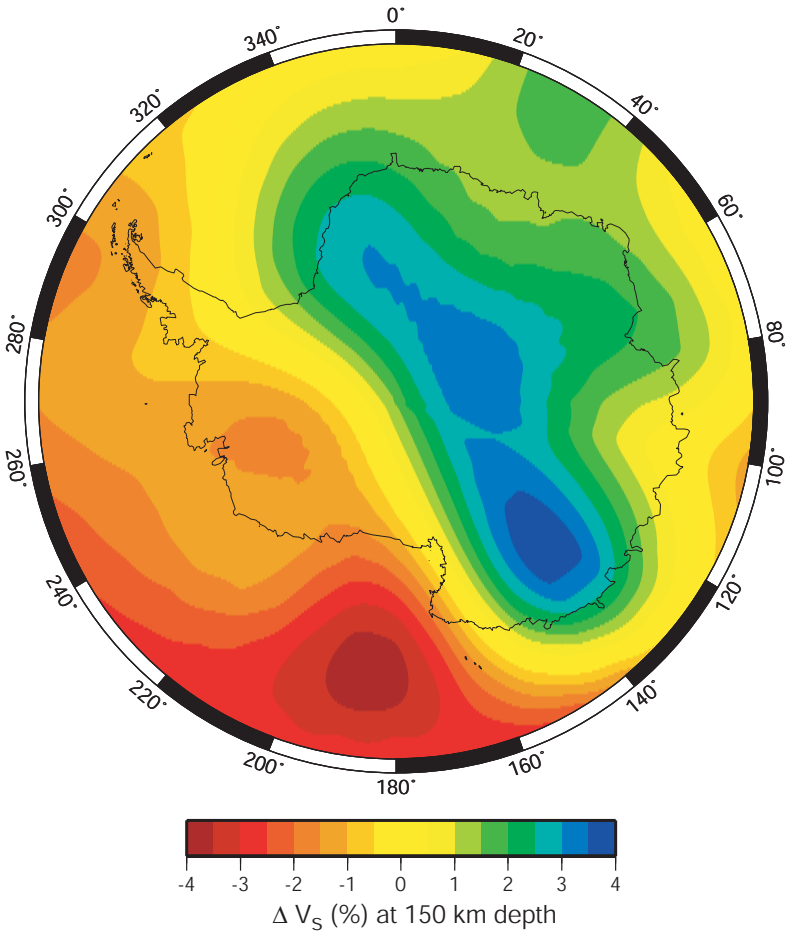

Figure 2.7: Perturbations in S-wave velocity, relative to PREM [Dziewonski & Anderson, 1981], from the S2ORTS model of Ritsema *et al.* [1999], at a depth of 150 km. The transition from fast to slow S-wave velocities correlates to the TAM front, and the boundary between East Antarctica and West Antarctica. Figure generated by K. Chambers.

identified in radio echo-sounding data, beneath the ice sheet covering Wilkes Land have been correlated with similar features observed in Queen Maud Range and in northern Victoria Land [Steed, 1980]. The Karoo Group of southern Africa is also characterised by similar landforms. Steed [1980] infers that these features are formed from eroded Beacon Supergroup sediments, and provide another link between the Gondwanan continents.

The West Antarctic subglacial topography contrasts strikingly with that of East Antarctica. A great topographic depression starts at the Ross Sea, and flanks the West Antarctic TAM front for almost their entire length. Regions of this depression lie more than 1000 m below sea level. The permanent ice sheet prevents West Antarctica from becoming an archipelago of continental islands.

Antarctic topography is very unusual relative to other continents. No other continent

exhibits a markedly bi-modal hypsometric curve [Cogley, 1984]. The bi-modal distribution of continent-wide bedrock elevation is not accounted for by isostatic compensation of the estimated ice load differences in each region. Cogley [1984] estimated deglaciated bedrock elevation modes of -450 m and 950 m (relative to mean sea level) for West Antarctica and East Antarctica respectively.

Differences in topographic, crustal, and lithospheric character and palaeomagnetic history are observed between East Antarctica and West Antarctica. This supports the notion of a continent-continent boundary at the TAM.

2.5 The Transantarctic Mountains

The Transantarctic Mountains (TAM) are located along the continent-continent boundary between West Antarctica and East Antarctica (Figure 2.5). They form the physiographic, geological, and geophysical divide between these two distinct continental terranes. The TAM provide most of the best outcrops in Antarctica, and are therefore important in understanding the geological evolution of the whole continent. The TAM form a 3500 km-long belt of elevated topography, locally reaching elevations of over 4500 m. Although the major period of uplift occurred in the Cainozoic, the structural backbone of the TAM comprises Proterozoic rocks, deformed and metamorphosed by the 500 Ma Ross Orogen [Elliot, 1975; Tingey, 1991b].

Following the uplift and granitoid intrusions associated with the Ross Orogen, Silurian to Early Devonian erosion formed the Kukri Peneplain [Gunn & Warren, 1962]. The Devonian to Jurassic, ~3 km thick, Beacon Supergroup overlies the Kukri Peneplain [Quilty, 1986; Barrett, 1991]. The Beacon Supergroup has been extensively intruded by Ferrar Group dolerites and basalts during the Jurassic [Tingey, 1991b]. A summary geological cross section of the TAM is shown in Figure 2.8.

Figure 2.8: Geological cross section of the TAM showing the geological relationship between the crystalline, metamorphic basement, the Beacon Supergroup, and the Ferrar Supergroup. The Kukri Peneplain is an angular unconformity that separates basement from the Beacon Supergroup, from ten Brink *et al.* [1997]. See Figure 2.5 for location.

The Kukri Peneplain is extensively exposed throughout the TAM, and can be used as an indicator of the pre-uplift topography of the region because the overlying Beacon Supergroup remains relatively undeformed [Quilty, 1986]. The Peneplain is interpreted to have been at depths of ∼2.5-3.5 km at the end of Beacon Supergroup deposition, to accommodate the shallow marine and fluvial deposits [Barrett, 1991]. It is now observed at elevations of over 4000 m, which gives an indication of the amount of uplift parts of the TAM have undergone. Smith & Drewry [1984] estimate an average uplift rate of 90 m/My for the last 45 My, based on geological data. Apatite fission track data indicates similar rates, 100 m/My for the last 50 My (e.g. Fitzgerald *et al.* [1986]).

The exact mechanism of uplift of the TAM continues to be debated. Various thermal and isostatic models have sought to constrain the mechanisms for the rapid and large magnitude uplift. Fitzgerald *et al.* [1986] suggested that underplating and low-angle simple shear were the primary mechanisms. Heat conduction, isostatic forces, and erosion were cited by Stern & ten Brink [1989] and ten Brink *et al.* [1997], and extensional necking of the lithosphere was proposed by van der Beek *et al.* [1995]. Due to difficulties in acquiring regional geophysical and geochemical data at the TAM, it is difficult to objectively assess the merits of each model. However, factors common to the various models, such as; a thermal gradient between the thin West Antarctic lithosphere and the thick East Antarctic lithosphere, a flexural component associated with the free-edge of the East Antarctic plate and the load of the EAIS, and upward forcing associated with valley incision within the TAM; provide a basis for explaining much of the uplift.

The TAM are characterised by a lack of folding or thrust faulting, and are generally described as a series of simple, asymmetric fault-blocks [Fitzgerald, 2002]. The TAM are interpreted to represent rift-shoulder uplifts supported by flexure of the strong East Antarctic lithosphere, that have formed in response to the divergent nature of the boundary between East and West Antarctica [Stern & ten Brink, 1989].

Rift flank uplifts are typically no more than 1000-2000 m high and exhibit half wavelengths (i.e. the distance from the axis of maximum uplift to the topographic minimum formed behind the uplift) on the order of 150 km (e.g. Steckler [1985]). In this regard, the TAM appear to be an extreme case of rift shoulder mountains as they have experienced uplift of over 4500 m and have a half wavelength of 400-500 km [Stern & ten Brink, 1989]. The significance of the TAM is also attested to by the fact that the lateral continuity of the chain is approximately 3000 km, similar to mountain ranges such as the Andes and Himalayas.

Adjacent to the West Antarctic flank of the TAM is a vast, submerged region of extended and rifted continental crust, the Ross Embayment. Ross Sea rift basins run parallel to the TAM and contain up to 14 km of sediments, over crust thinned to less

than 20 km, e.g. Melhuish *et al.* [1995] and Cooper *et al.* [1987]. Parallel to the East Antarctic flank of the TAM, but set back some 400-500 km, is the subglacial Wilkes Basin, a major basin of contentious origin and nature that will be discussed in detail later in this chapter.

2.6 West Antarctica: Tectonics and Geology

Palaeomagnetic and (limited) geological data indicate that West Antarctica comprises a number of distinct crustal blocks or lithospheric microplates. The exact number and kinematic histories of these microplates is uncertain, (e.g. Dalziel & Elliot [1982], Storey *et al.* [1998]). The Ellsworth-Whitmore Mountains crustal block (EWM), Antarctic Peninsula, Thurston Island, and Marie Byrd Land are generally accepted as the major West Antarctic microplates (Figure 2.5). In addition to these four main microplates, a number of smaller blocks are also utilised in reconstructions (see Fitzgerald [2002] for summary).

The Ross Embayment, incorporating the Ross Sea and Ross Ice Shelf, is interpreted as an area of active extension, the West Antarctic Rift System (WARS), between East Antarctica and West Antarctica [Dalziel & Elliot, 1982; Cooper *et al.*, 1987]. Except for the area beneath the Ross Sea, the WARS is not constrained in detail. A number of asymmetric grabens are imaged beneath the Ross Sea, which are interleaved by basement highs (e.g. Cooper *et al.* [1987]). The sedimentary basins within these grabens have been formed by extension since the Mid-Jurassic, however, the main phase of extension in the WARS occurred in the Late Cretaceous (e.g. Lawver & Gahagan [2003]). Post-early Oligocene extension is only inferred within a narrow zone of the Victoria Land Basin [Cooper *et al.*, 1987].

Estimates of the total amount of extension between East and West Antarctica vary widely, from 400-1800 km. The methods of estimating the extension are also varied, and include plate reconstructions (e.g. Stock & Molnar [1987]), one-layer stretching models (e.g. Bentley [1991] and Lawver & Scotese [1987]), and palaeomagnetic studies (e.g. Storey *et al.* [1998]). Palaeomagnetic studies predict greater amounts of extension relative to the other methods. Although the mechanism of extension is also poorly constrained, Fitzgerald & Baldwin [1997] suggest that extension has been primarily accommodated by low-angle, detachment faulting.

Outcrop in West Antarctica consists almost entirely of Mesozoic and Cainozoic rocks. Although sedimentary and metamorphic outcrops do occur, volcanic and plutonic rocks are far more common and comprise the majority of outcrop. The Cainozoic magmatism evident in West Antarctica is coeval with East Antarctica-West Antarctica rifting, and the main uplift phase of the TAM. The Mary Byrd Land province is the locus of more recent

volcanism. It is roughly in the centre of a belt of mid- to late-Cainozoic alkaline volcanoes that extend along the continental margin from the tip of the Antarctic Peninsula to northeast Victoria Land.

Continental basement, where observed, in West Antarctica comprises variably metamorphosed Precambrian rocks. Gneiss and schist country rock is heavily intruded by granites, felsic pegmatites, and mafic dykes. Overlying the basement are Precambrian to Mesozoic sequences of greywacke, shale, conglomerate and chert, that is variably deformed and metamorphosed. Detailed summaries of West Antarctic geology are provided by Tingey [1991b], Barker *et al.* [1991], and LeMasurier & Rex [1991].

2.7 East Antarctica: Tectonics and Geology

Geological mapping in East Antarctica is limited to sporadic outcrops along the coast, in interior highland areas, and the TAM. Mapping of such outcrop indicates a basement complex of mainly early Precambrian age, comprising primarily high-grade metamorphic gneisses and schists along with charnockitic rocks [Tingey, 1991b]. This basement underlies almost all of East Antarctica and constitutes the East Antarctic Shield. Overlying the basement sequence are Precambrian to Cambrian sedimentary rocks and some volcanic rocks which represent typically flat-lying platform deposits [Quilty, 1986].

The best exposed rock sequences are reported in the TAM. The relatively flat-lying sedimentary beds of the Beacon Supergroup, overlying the Kukri Peneplain, comprise Devonian marine rocks disconformably underlying extensive exposures of non-marine Permian and Triassic rocks [Barrett, 1991]. Sedimentation through the Permian and Triassic resulted in this 2700-3500 m sequence of sandstone, interbedded with coal and glacial sediments, in intracratonic or foreland basins parallel to the palaeo-Pacific margin [Quilty, 1986].

Extensive, plume-generated magmatism is interpreted to have accompanied the initial Gondwana breakup (e.g. Cox [1988]). Large-scale, within-plate mafic and felsic magmatic provinces in many Gondwanan continents, including Antarctica, were formed by active plume processes [Fitzgerald, 2002]. Plume magmatism is represented in Antarctica by the Ferrar Group tholeiites (Kirkpatrick Basalt and Ferrar Dolerite), which formed at approximately 180 Ma [Tingey, 1991a]. However, the Ferrar province reflects melting of more depleted lithospheric source mantle than other coeval rocks found elsewhere in Gondwana [Elliot, 1992].

The Ferrar Group forms the Antarctic segment of a long linear belt of a mafic magmatic province that extends from Tasmania and southeast Australia, to southern Africa. Peak eruption rates within this belt are inferred between 175±18 Ma [Green *et al.*, 1978]

and 182±2 Ma [Hooper *et al.*, 1993]. This short eruption time is similar to other continental flood basalt provinces [Fitzgerald, 2002]. The linear distribution of the magmatism is not compatible with classic circular plume models, and so Cox [1988] proposed a hot-line rather than a hot-spot.

[Storey & Kyle, 1999] suggest that a Gondwana 'megaplume' existed in the Weddell Sea region as a result of a spreading centre triple junction. In this model, production of magma batches associated with plume-lithosphere interaction, migrated along zones of crustal weakness forming the linear magmatic provinces. White & McKenzie [1989] suggest that the present day location of the plume is at Bouvet Island.

2.8 Antarctic Margin Physiography

Except for the Antarctic peninsula, the margins of Antarctica are exclusively passive rift margins. The margins of Antarctica likely followed a typical pattern of thermal subsidence and sediment deposition following breakup. However, they now exhibit physiographic characteristics unlike most rift margins. The morphological development of the Antarctic continental margin has been largely controlled by glacial and glacimarine processes since the development of permanent polar ice at ∼34 Ma (e.g. Exon *et al.* [2002] and Cooper & O'Brien [in press]).

Bathymetry compilations of the ocean encircling Antarctic and the marginal seas (i.e. Weddell Sea and Ross Sea) are poorly constrained relative to the margins of all other continents as a relatively limited amount of shiptrack data is available. Additionally, bathymetry derived from satellite altimetry data (e.g. Smith & Sandwell [1994]) is less reliable than at lower latitudes, due to the presence of grounded- and sea-ice on the Antarctic margins (e.g. McAdoo & Laxon [1997]).

Two compilations of bathymetry data are available for the Southern Ocean (i.e. for latitudes south of 60°S). These are the BEDMAP [Lythe *et al.*, 2000] and GEBCO 1-minute [IOC *et al.*, 2003] grids. The BEDMAP grid is a 5×5 km grid for the continent and seabed south of 60°S, which is based on a compilation of open-file shiptrack data supplemented by satellite derived bathymetry from [Smith & Sandwell, 1994]. The GEBCO data is based on shiptrack data only and has a nominal resolution of 1-minute, however, in some areas the data density is not great enough to warrant this resolution. The two grids differ locally as demonstrated for the Wilkes Land margin later in this chapter. Gross morphologic trends and characteristics can be equally well interpreted from either grid.

The Antarctic continental shelf is characterised by a number of distinct features that contrast with continental margin environments in more temperate climates. These

features include rugged topography, great depth, highly varied and commonly broad width, and its glacial setting [Anderson, 1991]. Anderson [1991] estimates an average shelf depth of ∼500 m. Near coastal, narrow troughs that exceed 1000 m depths have been observed in echo-sounding data since the earliest marine surveys and are common and characteristic of a number of regions of the Antarctic margin, (e.g. Escutia *et al.* [2000]). Some cross-shelf troughs extend seaward from the termination of major present-day glaciers and/or ice tongues, however, not all can be genetically related to the present-day glaciomorphology of the adjacent margin.

In many areas around East Antarctica, the continental shelf slopes towards the continent. This does not occur on continental margins in more temperate latitudes. Isostatic downwarping or flexure caused by the ice sheet load contributes to this, and also to the great depth of the shelf [ten Brink *et al.*, 1995]. However, glacial erosion is the primary control on the geometry, depth and rugged topography of the Antarctic continental margin. Direct evidence of glacial erosion is seen in almost all seismic profiles acquired on the margin [Anderson, 1991].

2.9 Glacial History

The sudden, widespread glaciation of Antarctica and the associated shift toward colder temperatures during the Cainozoic represents one of the most fundamental reorganisations of the global climate system recognised in the geologic record [De Conto & Pollard, 2003]. Timing the onset of Cainozoic glaciation, which has been the subject of debate since the earliest surveys of Antarctica, is important for a number of reasons. Widespread ice sheet development lowered the pre-glacial continental shelf through a combination of glacial erosion, and flexural downwarping associated with ice-loading, profoundly influencing the establishment of the present glacial maritime setting and oceanographic circulation. On a more global scale the event also triggered massive changes in global climate patterns [Kennett, 1977].

The original, and widely accepted, model of glacial onset invoked the thermal isolation of Antarctica as the catalyst for regional glaciation within Antarctica, and the onset of a global ice-house climate [Kennett, 1977]. This thermal isolation is interpreted as a function of deep seaways surrounding Antarctica. Continental palaeomagnetic data (e.g. Lawver & Gahagan [2003]) and seafloor spreading anomaly modelling (e.g. Royer & Rollet [1997]) support the notion of deepening seaways at ∼29-34 Ma between Tasmania and East Antarctica, and South America and the Antarctic Peninsula.

More recently it has been recognised that the opening of circum-Antarctic seaways is only one of a number of contributing factors to the evolution of the Cainozoic climate

(e.g. Zachos *et al.* [2001]). Coupled global climate-dynamical ice sheet modelling by De Conto & Pollard [2003] attempted to quantitatively constrain the varying contributions to the inception and growth of the East Antarctic Ice Sheet. De Conto & Pollard [2003] use climate-ice sheet simulations to investigate the effects of declining atmospheric CO_2, compared to those of the tectonic opening of Southern Ocean gateways, and timing of mountain uplift in the Antarctic interior. Their results contrast with the established paradigm of thermal isolation as a catalyst for regional glaciation, and indicate that instead, declining CO_2 may have been the primary causative mechanism. Their models of glacial expansion also do not suggest a strong feedback from the inclusion or exclusion of highland areas.

Whether a primary cause of glaciation or not, geological evidence suggests major environmental changes were associated with the opening of deep seaways around Antarctica. The two constrictions on a circum-Antarctic ocean, from Gondwanan breakup until the Late Eocene, were the southern tip of South America, and the Tasmania-South Tasman Rise system. The timing of the Tasman Gateway[2] and Drake Passage openings are considered, therefore, to have influenced the major shifts in climate patterns.

The most recent attempt to date the onset of glaciation and describe the palaeoenvironment at the time of, and following, the Tasman Gateway opening were made on Leg 189 of the Ocean Drilling Program (ODP) [Exon *et al.*, 2002]. Exon *et al.* [2002] identify a time of massive environmental change during the Late Eocene, 37-33.5 Ma. During this interval, fast seafloor spreading [Weissel & Hayes, 1972; Cande & Mutter, 1982] was moving Australia northward and the Tasmanian land bridge and its broad shelves had started to subside more rapidly.

A consequence of the deepening of the Tasmanian land bridge was that the warm shallow currents of the Pacific no longer reached the Antarctic margin. The effect of this was that cool shallow currents could penetrate from the previously isolated Australo-Antarctic Gulf (AAG) through the Tasman Gateway (Figure 2.9). The changes interpreted from well data during this interval are significant: from warm to cool climate; from poorly ventilated basins to well ventilated open sea; from dark siliciclastic to light pelagic, carbonate deposition; and from organic-rich to organic-poor sedimentation [Exon *et al.*, 2002].

Data from ODP Leg 189 indicate an abrupt change from the early Oligocene. Exon *et al.* [2002] suggest that warm tropical currents were completely cut off from some parts of the Antarctic margin by the developing ACC from this time. This likely precipitated the formation of highland glaciers, which formed the earliest components of the ice sheet

[2]Tasman Gateway describes the seaway that formed between the microcontinental blocks around the South Tasman Rise and northern Victoria Land, Antarctica.

Figure 2.9: Development of a circum-Antarctic ocean from 34-31 Ma. The northward motion of Australia allows the cool currents from the Australo-Antarctic Gulf (AAG) to penetrate the opening Tasman Gateway and isolate the Pacific margin of Antarctica from the warmer currents of the Pacific Ocean. The opening of the Drake Passage, between South America (SAM) and the Antarctic Peninsula, allows the Antarctic Circum-Polar Current (ACC) to develop. EANT = East Antarctica, AUS = Australia, NZ = New Zealand, KP = Kerguelen Plateau, BR = Broken Ridge, WS = Weddell Sea, RS = Ross Sea. Figure from Lawver & Gahagan [2003].

covering Antarctica today.

The timing and rapid onset of glaciation, extending beyond isolated highland areas, near the Eocene-Oligocene boundary (∼34 Ma), is also well constrained by ODP data from ODP Leg 188, in Prydz Bay. Palynological analyses indicate a humid and cool-cold climate persisted in the Prydz Bay region to the Late Eocene [Cooper & O'Brien, in press]. The earliest lithologic evidence of nearby highland glaciation is seen in late Eocene-age grain textures in massive sand units [Strand *et al.*, 2003]. The earliest evidence

of glacimarine erosion of the continental shelf are mid-Miocene deposits of reworked, Eocene-age, shelf environment foraminifera, encountered during drilling on the Prydz Bay continental rise [Cooper & O'Brien, in press]. The glacimarine reworking of shelf strata indicate that the ice sheet had grounded on sections of the East Antarctic continental shelf by the Mid-Miocene.

Early stages of ice sheet advance likely occurred under much less severe climatic conditions than exist at present. The cool-temperate conditions that prevailed throughout the early Tertiary, likely altered to temperate-glacial for a period before the polar-glacial environment observed today became stable. Temperate glacial environments are characterised by large sediment flux (e.g. Powell [1984]), in contrast to polar-glacial settings where sedimentation is significantly reduced (e.g. Hampton *et al.* [1987]). Polar-glaciers are typically characterised by low basal velocities and a freezing of the land surface [Eittreim *et al.*, 1995]. ODP results from Prydz Bay show a seven-fold reduction in sedimentation rates in the late Miocene (∼9 Ma), relative to peak sedimentation rates in the early Miocene, from 70 m/My to 10 m/My [Cooper & O'Brien, in press]. This reduction is interpreted to indicate close to peak glacial conditions being reached, however, as the well was located on the lower continental slope this is somewhat speculative.

Growth and development of the continental ice sheet probably lowered sea level enough to expose sections of the continental shelf to erosion by fringing elements of the ice sheet. Conceivably, this early ice sheet ablated by melting rather than iceberg calving [Anderson, 1991], and wet-based sliding would have been the dominant erosion mechanism. The combined effects of significant erosion and meltwater stream development emanating from glacier termini delivered large quantities of terrigenous sediment to the sea primarily in glacial deltaic deposits.

There is compelling evidence of subglacial till deposits on the continental shelf of a number of areas of the Antarctic margin [Anderson, 1991; Eittreim *et al.*, 1995]. This indicates that the Antarctic ice sheet grounded on the continental shelves of both West Antarctica and East Antarctica on one or more occasions since the Miocene. However, the exact timing of the glacial event(s) that led to the deposition of tills on the continental shelf is poorly constrained [Anderson, 1991]. Although near shore deposition continues today, surface geological processes have been relatively limited in the late Quaternary. The lack of any outcrops of Cainozoic sediments are an indication of this.

Estimates of present day ice thickness, primarily from airborne radar data, have been compiled by the BEDMAP project [Lythe *et al.*, 2000], Figure 2.10. These data illustrate that the regions of greatest ice thickness occur in East Antarctica, which comprises ∼90% of the ice in Antarctica [Bamber *et al.*, 2000]. A maximum ice sheet thickness of ∼4500 m is observed in East Antarctica, which is covered by an average 2500 m of ice.

Figure 2.10: Ice thickness grid of Antarctica, BEDMAP project data [Lythe *et al.*, 2000]. Greatest ice thickness is observed in East Antarctica, where 90% of all Antarctic ice is contained in the East Antarctic Ice Sheet. Figure from D. Vaughan, British Antarctic Survey.

Although on a broad scale the basal velocity of the East Antarctic Ice Sheet (EAIS) is very low relative to temperate glaciers, studies of *balance velocities* provide an insight into the dynamic nature of the EAIS [Bamber *et al.*, 2000]. The balance velocity represents the depth-averaged velocity required at any point to maintain the ice sheet in a state of balance, given a specified distribution of net surface mass flux. Balance velocity is calculated from the surface slope (estimated from satellite radar altimetry and terrestrial data) and ice thickness (as calculated by the BEDMAP project [Lythe *et al.*, 2000]). It is assumed that flow is parallel to the local topographic gradient within the ice sheet. In broad terms, the surface slope controls the spatial pattern of balance velocities, which are scaled as a function of ice thickness and the surface mass balance [Bamber *et al.*, 2000].

Bamber *et al.* [2000] calculated balance velocities for the grounded part of the Antarctic Ice Sheet, Figure 2.11. Complex flow patterns are observed throughout the continent.

Channelised flow can be clearly identified in the balance velocity distribution, however, the velocities of many of these 'channels' are lower than the typical range of ice-stream velocities of 100-2000 m/yr [Bentley, 1987]. Although lower than typical ice-stream velocities, the channels exhibit higher velocities than the surrounding ice sheet, which is characterised by balance velocities of <30 m/yr. The distinction between the slow-moving interior ice sheet and fast-moving outlet glaciers and ice streams is not as clear as has been previously believed [Bamber *et al.*, 2000].

Figure 2.11: a) Balance velocity estimates for grounded parts of the Antarctica ice sheet. b) Balance velocities for the Lambert Glacier region showing features that feed the Amery Ice Shelf. c) Balance velocities in the region of the Totten Glacier. Figure from Bamber *et al.* [2000].

Two regions of East Antarctica are characterised by large, relatively fast-flowing outlet glacier systems that are fed by complex tributary systems. The largest of these is the Lambert Glacier-Amery Ice Shelf region. The second, the Totten glacier region, exhibits similar balance velocity characteristics. However, it does not encompass as broad a catchment area as the Lambert Glacier. The Totten Glacier terminus is located at and around a topographic high on the Budd Coast sector of the west Wilkes Land coast.

2.10 Onshore Geology and Geophysics: 'Australian Sector', East Antarctica

2.10.1 Geology

The eastern extremity of the Wilkes Land sector of East Antarctica is bounded by the TAM, which form an almost complete barrier between the EAIS and the Ross Embayment and Victoria Land. The Wilkes Land sector is, in general characterised by basin development not seen in other areas of East Antarctica. The Wilkes Land coast provides little outcrop. Rare onshore outcrops comprise largely Precambrian medium- to high-grade metasediments, metavolcanics, granulites and charnockite bodies [Tingey, 1991b].

The best rock exposures in the region are found in the TAM. The sequence of outcrop generally observed comprises Precambrian basement (Robertson Bay Group) overlain by the Beacon Supergroup, which typically dip shallowly (∼5°) to the west [Tingey, 1991b]. In the eastern extremes of Wilkes Land, unmetamorphosed sedimentary rock outcrops are relatively common (by East Antarctic standards). At Horn Bluff (∼150°E) a ∼300 m high cliff capped by Ferrar Group dolerites reveals a section of Beacon Group sediments [Mawson, 1940], and Precambrian granulite facies and charnockite bodies. The latter are common throughout the East Antarctic Shield [Tingey, 1991b]. The lateral extent of the Beacon Group sediments in Wilkes Land, and East Antarctica more generally is uncertain.

The Beacon Supergroup has been identified in a number of regions of Antarctica, including the Prince Charles Mountains, Queen Mary Land, and the Shackelton Range; indicating a regional depositional system. The Devonian to Triassic aged Beacon Supergroup was one of the key factors in the first Gondwanan reconstruction of Du Toit [1937] as it is sedimentologically and petrologically very similar to the formations of the Gondwana Basin of eastern India, the Santar Katarina Supergroup in South America and, the Karroo Supergroup in southern Africa.

Gondwana reconstructions place the Queen Mary Land, Wilkes Land and Terre

Adélie-George V Land margins against the southern margin of Australia[3]. On the Australian margin, the extents of the rift system are marked by the Naturaliste Plateau, to the west, and the South Tasman Rise (STR), to the east. The conjugate features on the Antarctic margin are the Bruce Rise, in the west, and northern Victoria Land, in the east. A number of major basins occur on the southern Australian margin, including the Bremer, Bight, Duntroon, Otway, and Sorell Basins; collectively referred to as the Southern Rift System (SRS), e.g. Stagg *et al.* [1999]. A large sediment apron is also observed off the central southern Australian margin, the Ceduna Terrace. Basins of comparable magnitude have not previously been recognised on the Wilkes Land margin, and no major sediment terraces are observed.

The central conjugate margin sector is interpreted to have resulted from early northwest-southeast extension, followed by almost entirely north-south extension [Willcox & Stagg, 1990]. Spreading histories to the east and west of the central sector are more complex. The Queen Mary Land sector of the Antarctic margin occupies a complex tectonic position, where Australia-Antarctica spreading has overprinted the earlier spreading pattern of India-Antarctica. It has also been influenced by plume related emplacement of the large igneous province to the northwest, the Kerguelen Plateau [Veevers *et al.*, 1991]. In contrast, east of Wilkes Land, i.e. Terre Adélie and George V Land, the margin developed in a left-lateral rift/wrench system, e.g. Willcox & Stagg [1990]. Large fracture zones and spreading ridge offsets occur around the southeast Australian and STR margin.

2.10.2 Inland Basins: Flexure or Extension?

Two major sub-glacial basins and a number of troughs are apparent in the Wilkes Land interior. Interleaved with the areas of depressed topography are regions of rugged highlands, and relatively flat plain areas close to mean sea level (MSL) (Figure 2.12).

The Wilkes Basin broadly parallels the East Antarctic flank of the TAM, it is covered by an ice sheet of average ∼3 km thickness, and a maximum observed thickness of over 4.5 km (Figure 2.10). The basin axis is oriented broadly north-south for over 1400 km, from the coast to a latitude of ∼82°S, decreasing in width from ∼600 km at the coast to <100 km inland. The basin (as defined by the base of the EAIS) reaches depths of >1000 m relative to MSL, is characterised by relatively low base of ice gradients, and shallows towards the coast. The coastal sector of the basin exhibits greater topographic variation, and comprises a number of highland areas that locally subdivide the basin.

The eastern limits of the Wilkes basin are constrained by the TAM, whereas the western extent, and to a lesser degree the northern extents, are relatively discontinuous

[3]The Wilkes Land sector, as the largest sector conjugate to the Australian margin, is also used more generally to describe all sectors once conjugate to the southern Australian margin

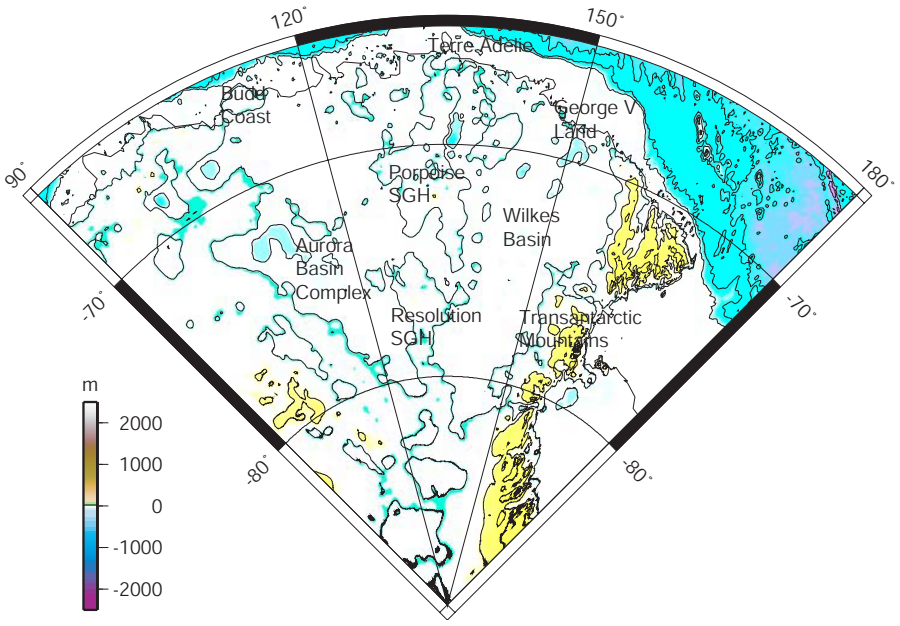

Figure 2.12: Sub-glacial bedrock topography of the 'Australian Sector' of East Antarctica. Two major basin systems dominate the topography, the Wilkes Basin and Aurora Basin Complex. SGH = sub-glacial highlands.

and interleave the bordering highlands at a number of locations. A broad correlation between increased topographical roughness (as measured by RMS deviation from mean elevation) and increased elevation is observed in the eastern sector of the basin, but this correlation decreases towards the west of the basin [Steed, 1980].

In the extreme west of the Wilkes Land interior is a secondary system of largely sub-MSL basins, the Aurora Basin Complex (ABC). The ABC, although of approximately similar proportions to the Wilkes Basin, forms a branching system of sub-basins that generally trend northwest towards the Wilkes Land coast. An even greater areal extent of >4 km thick ice is observed in the ABC relative to the Wilkes Basin. The ABC basins are generally deepest in the west, but two peripheral deeps are observed in the east. The ABC has a very sinuous outline, several sub-basins enter into bordering highland areas. Separating the Wilkes Basin and the ABC is a broadly north-south oriented region of rugged highlands, the Resolution and Porpoise Subglacial Highlands. These highlands are bounded both north and south by plains of low elevation. The southeastern end of the ABC forms a broad saddle with the southwestern limit of the Wilkes Basin, at the southern end of the Resolution Subglacial Highlands.

Geophysical data over the ABC is extremely limited. The Wilkes Basin has been the subject of much more extensive geophysical surveying. Geophysical methods have primarily been utilised to constrain the presence and thickness of sediments within the

Wilkes Basin, and to determine whether the basin has a flexural or rift-related origin.

Seismic refraction experiments in the northwest of the Wilkes Basin indicate seismic velocities typical of granitic bedrock (∼5800 m/s), which was interpreted by Bentley [1974] to indicate that there were no sedimentary deposits of significant thickness within the Wilkes Basin. Radio echo-sounding data acquired subsequent to the refraction data illustrate that the refraction experiment was located on the flank of the basin, and therefore did not sample typical basin morphology [Steed, 1980].

Drewry [1976] interpreted radio echo-sounding data, and particularly the statistical correlation of elevation and topographical roughness to infer the presence, and map the extent, of basin sediments. Drewry [1976] cited the broad spatial correlation between the Wilkes Basin and *"*...strongly negative regional free-air and Bouguer anomalies...*"* as further evidence of sediment infill within the basin. He also suggested the lower frequency magnetic anomaly data over the basin, relative to surrounding highlands, was evidence of sediments covering the basin basement rock. Drewry [1976] suggested that up to 3 km of sediments underlie the Wilkes Basin.

Steed [1980] considered that the negative gravity anomaly over the Wilkes Basin may be a result of delayed isostatic compensation to the load of the ice sheet. Although it is possible that this could, in part, contribute to the anomaly, Steed [1980] considered it unlikely to fully explain an anomaly of the observed magnitude. The possibility of a mantle source for the anomaly, associated with the uplift of the TAM, was also suggested by Steed [1980].

Stern & ten Brink [1992] interpret the Wilkes Basin as the *"outer low"* associated with the flexural origin of the TAM. The flexural model proposed by Stern & ten Brink [1992] suggests the basin is a regional, flexural downwarp, associated with the uplift of the TAM. In this model, the Wilkes Basin is analogous, although in the opposite sense, to the flexural outer rise observed at the oceanic trenches of subduction zones. Gravity modelling carried out by Stern & ten Brink [1992], comparing the gravity profiles calculated assuming a strong crust (flexural model) and a weak crust (Airy model), supports a flexural origin for the Wilkes Basin. They also propose that peripheral uplift and broad, shallow hinterland basins may be common in other cratonic areas, particularly in areas once associated with the Gondawanan Supercontinent, for example the Murray Basin of southeast Australia and the Kalahari Basin of southern Africa.

A seismic reflection and gravity profile was completed over the Wilkes Basin in the austral summer of 1993-94 (East Antarctic Seismic Traverse 1993 - EAST93) ten Brink *et al.* [1997]. Data from this survey was used by ten Brink *et al.* [1997] to constrain models to support a flexural origin for the Wilkes Basin. They also interpret the data to indicate that:

1. Ferrar flood basalts extend for at least 100 km within the Wilkes Basin.

2. The Beacon Supergroup thins gradually within the Wilkes Basin, away from the TAM, indicating deposition occurred in a foreland basin.

3. There is no evidence of incomplete isostatic rebound due to melting of the East Antarctic ice sheet since the last glacial-maximum.

ten Brink *et al.* [1997] argue against the presence of Cainozoic sediment fill within the Wilkes Basin on the basis of gravity and magnetic modelling. They model the observed gravity anomaly by the flexure of the East Antarctic plate, using a broken plate model for the continent-continent boundary between West Antarctica and East Antarctica, and the presence of *"Beacon-type"* sediments thinning away from the TAM. Their model also requires thermal uplift associated with a double thickness crust for the East Antarctic craton (45 km), relative to West Antarctica, ice loading of East Antarctica, and erosional unloading within the TAM.

Ferraccioli *et al.* [2001] do not accord with the interpretation of a flexural origin for the Wilkes Basin. Using data acquired along the International Trans-Antarctic Scientific Expedition traverse (ITASE) during the austral summer of 1998-99, Ferraccioli *et al.* [2001] infer crustal thinning beneath the Wilkes Basin. They find that at 75°S the crust thins from 37 km below the TAM to 31±2 km beneath the Wilkes Basin. This interpretation is in direct contradiction of the flexural models of Stern & ten Brink [1992] and ten Brink *et al.* [1997], which predict crustal thickening beneath the basin. Ferraccioli *et al.* [2001] interpret the Wilkes Basin as having an extensional origin, on the basis of the thinned crust. This agrees with the earlier interpretation of Steed [1980]. They also interpret the adjacent Adventure Subglacial Trench as a narrow rift basin floored by thinned (25±5 km) crust with sediment infill of 6-14 km.

Gravity and magnetic models of Ferraccioli *et al.* [2001] incorporate Beacon-type sediments within the Wilkes Basin, and low density rift sediments in the Adventure Subglacial Trench. This is, again, in direct contrast to the models of ten Brink *et al.* [1997], which included no sediment within the Wilkes Basin. The EAST93 traverse modelled by ten Brink *et al.* [1997] did not go as far west as the ITASE line, and Ferraccioli *et al.* [2001] contend that this may explain why the rift gravity signature and the presence of a sedimentary gravity signature was not identified by ten Brink *et al.* [1997].

Ferraccioli *et al.* [2001] do not dispute the flexural support of the TAM by the East Antarctic craton, as proposed by Stern & ten Brink [1992]. If the TAM have a rift-flank origin, and the crust flooring the Wilkes Basin is thinned, as inferred by Ferraccioli *et al.* [2001], then likely the Wilkes Basin is flexurally induced (at least in part), and has also been subject to extensional rifting forces. The Wilkes Basin has been correlated, on the

basis of its geophysical characteristics (and location), with the Neoproterozoic Adelaide fold belt of Southern Australia (e.g. Oliver & Fanning [1997]).

The origin of the major basin systems of the Australian Sector of East Antarctica remain poorly understood. Further geophysical data, particularly seismic reflection and refraction data, are required to determine the genetic processes involved in their formation. With the current level of data, it is not even possible to conclusively determine the presence of Cainozoic (or older) sediments within the basins, much less their tectonic origin.

2.11 Wilkes Land Margin: Offshore Geology and Geophysics

The Wilkes Land region did not become a major research focus until the early 1980's when marine geophysical and geological surveys were conducted by the Institut Francais du Pétrol (IFP) [Wannesson *et al.*, 1985], the United States Geological Survey (USGS) [Eittreim & Smith, 1987], and the Japan National Oil Company (JNOC) (e.g. Tanahashi *et al.* [1987]). These surveys acquired multi-channel seismic and potential field data on the Wilkes margin in the early 1980's.

2.11.1 Physiography

The continental shelf of the East Antarctic margin is narrow relative to West Antarctica, averaging approximately 100 km in width between 60°E and 170°E. However, variations in width from 60-200 km are observed. The average width of the Wilkes Land continental shelf is ∼125 km. This sector of the margin is characterised by a steep upper slope, relative to other East Antarctic margin sectors, and a shelf-slope break that generally occurs at depths of 400-600 m. The most striking morphological features along the Wilkes Land margin are the dendritic, large-relief (>1000 m), cross-shelf trough systems. Eittreim *et al.* [1995] suggest that these canyons, which shoal from >1000 m on the inner shelf to ∼500 m on the outer shelf, are the paths of ice streams that extended across the shelf during times of glacial maxima. Sediment banks flanking these canyons are interpreted as areas where grounded ice was relatively immobile during the glacial maxima.

Bathymetry data from the BEDMAP [Lythe *et al.*, 2000] and GEBCO 1-minute [IOC *et al.*, 2003] compilations for the Wilkes Land margin are illustrated in Figure 2.13. The BEDMAP data has been resampled at a 1-minute resolution to allow a residual map of the difference in bathymetry between the two compilations to be calculated (Figure 2.13). Broadly, the two compilations are very similar, however, locally they differ by up to ∼1000 m. The greatest disparity in the compilations occurs at the shelf break in

west Wilkes Land. This is likely a function of resampling and subsequent gridding as BEDMAP data in this region is almost entirely extracted from Smith & Sandwell [1994].

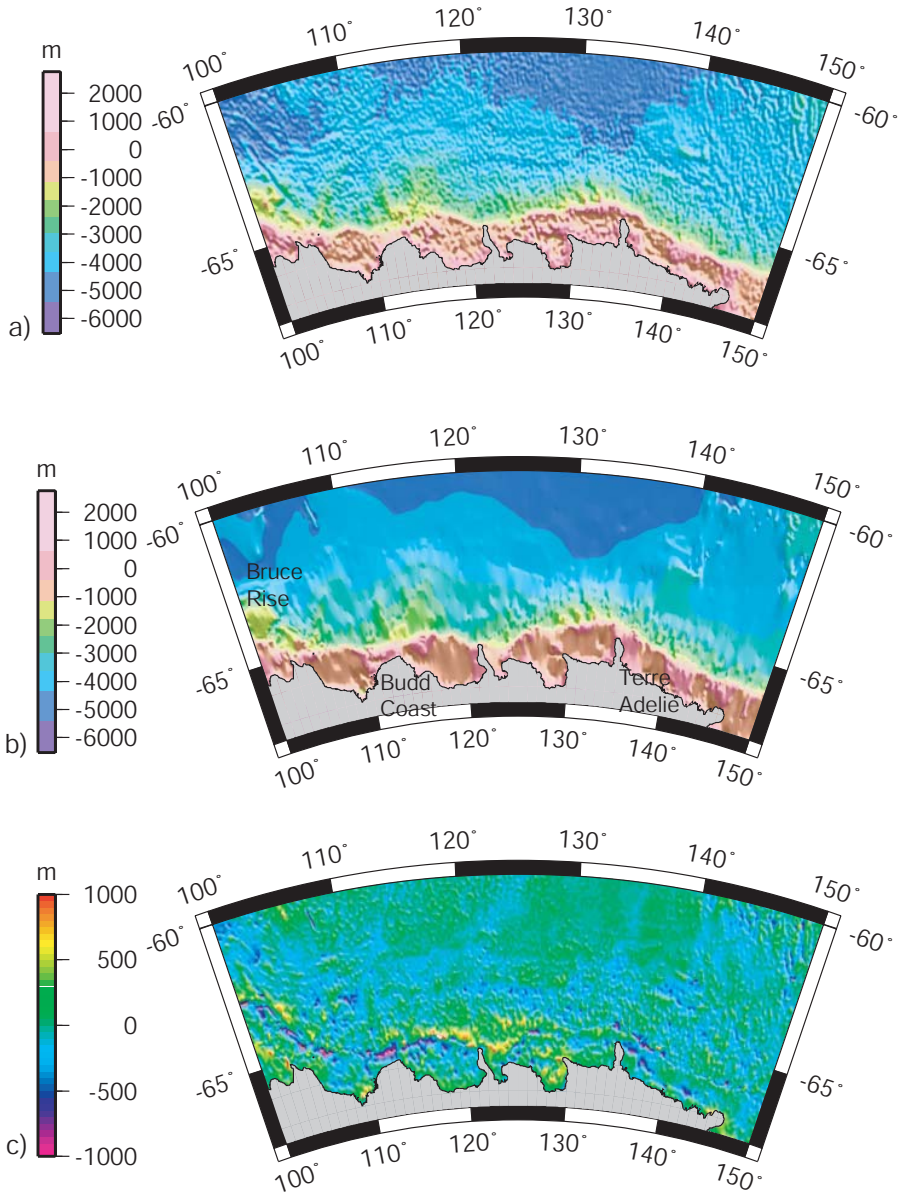

Figure 2.13: Bathymetry of the Wilkes Land margin from a) the BEDMAP project compilation, and b) the GEBCO 1-minute grid. c) The residual bathymetry (BEDMAP - GEBCO), locally the difference in the two grids reaches almost 1000 m at the shelf break off west Wilkes Land.

Seismic reflection data from the Wilkes Land continental shelf indicate significant erosion (100's m) (e.g. Eittreim *et al.* [1995]). The shelf is also over-deepened by ice sheet induced flexure of the crust (e.g. ten Brink *et al.* [1995]). In some areas the modern sea floor represents an unconformity associated with glacial erosion [Anderson,

1991]. Ice gouges are visible in sidescan sonar data to depths of over 500 m on the Wilkes Land margin, these gouges are represented by circular to subcircular depressions, 30-150 m in diameter [Barnes, 1987]. The presence of ice gouges indicate erosion and reworking of modern sediment by iceberg keels to depths of over 500 m. The upper sedimentary section has been glacially stripped on the inner shelf in some areas, exposing older strata and possibly acoustic basement [Eittreim *et al.*, 1995].

Bruce Rise, a marginal plateau at ∼100°E (Figure 2.14) marks the transition zone between the Greater India-Antarctic and Australia-Antarctic rifting events. This is the only marginal plateau recognised on the Australian sector of the East Antarctic margin. It acts as a physiographic barrier, separating the Wilkes Land margin from the Princess Elizabeth Trough and the Prydz Bay area. The plateau surface occurs at a depth of ∼1500 m, and the transition to abyssal depths at the seaward edge of the plateau is very rapid. Deep troughs also incise the continental rise to the east and west of the plateau. The Bruce Rise is interpreted to be conjugate to the Naturaliste Plateau off southwest Australia [Coleman *et al.*, 1982].

The continental shelf narrows massively at the Budd Coast, west Wilkes Land, and a clear shelf break can not be identified. In contrast, the continental shelf to the east and west of the Budd Coast is wide (>125 km), and is characterised by a distinct shelf break. The onshore Budd Coast comprises an elevated bedrock and ice surface, the Law Dome. The transition from the Law Dome to the continental slope is very rapid. This area is also the location of large-relief sediment ridges or banks, broadly oriented orthogonally to the margin. The ridges extend beyond the base of the continental slope, flanking deep troughs. Smaller magnitude, but similar geometry and character, sediment ridges occur off the Wilkes Land coast from 130-135°E, between the termini of the Dibble and Mertz Glaciers (Figure 2.14).

These networks of continental slope, cross-shelf troughs and flanking, channel-overbank deposits are interpreted by Escutia *et al.* [2000] to represent ice-sheet sourced turbidite fan systems. The Wilkes Land turbidite systems exhibit a number of systematic morphologic differences compared to most river-sourced fans, such as (after Escutia *et al.* [2000]:

1. Multiple large tributary channels across the upper and middle fan.

2. Channel relief several times greater (900 m) than typical relief (100-200 m) for channels on fans less than 300 km in diameter.

3. Steep middle-fan and lower-fan gradients.

These differences are interpreted as evidence of ice streams traversing the continental shelf and discharging sediment directly to the outer continental shelf and upper continental slope at times of glacial maxima.

The physiography of the Antarctic margin is unique, and the Wilkes Land margin

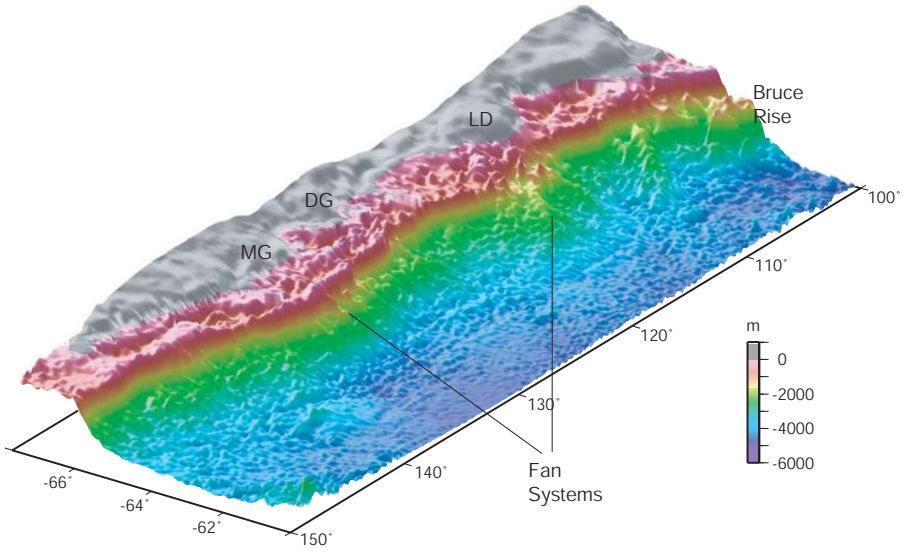

Figure 2.14: Perspective view, from the northeast, of the Wilkes Land margin physiography. The rugged topography of the shelf, comprising a number of deep canyons, is evident. The Bruce Rise forms a physiographic barrier at the western extreme of Wilkes Land. High relief sediment banks/ridges and deep canyons/channels define glacial sourced turbidite fan systems. Bathymetry from Smith & Sandwell [1994].

exhibits all of the characteristics that make it so. In addition, dynamic glacial conditions through the late Tertiary resulted in the creation of large fan systems on the Wilkes Land margin, similar in geometry to river-sourced fans, but of much greater magnitude.

2.11.2 Previous Marine Geophysical and Geological Data

Regional marine geophysical data acquired by Lamont-Doherty Geological Observatory, aboard the R/V Eltanin and Vema, 1968-1976, include bathymetric, gravity, and magnetic anomaly data from the southeast Indian Ocean, and the conjugate Australian-Antarctic margins (e.g. Weissel & Hayes [1972] and König & Talwani [1977]). These data were important in defining the broad structure of the Australia-Antarctic Basin (AAB), recognising the Australian-Antarctic Discordance (AAD), identifying Magnetic Quiet Zones (MQZ) at the continental margins, and timing the breakup of Australia and Antarctica.

Surveying since this time has tended to concentrate on the margins of Australia and Antarctica, and has included the acquisition of multi-channel seismic (MCS) data, in addition to gravity and magnetic anomaly data. The Wilkes Land margin has been surveyed sporadically since the 1980's, large portions of the margin, however, remain entirely unexplored.

The Australian-Antarctic Discordance (AAD)

The Australian-Antarctic Discordance (AAD) [Hayes & Conolly, 1972] is the portion of the Southeast Indian Ridge (SEIR) from ∼120-128°E that differs markedly in its morphologic and physical properties from the ridge flank areas immediately adjacent [Weissel & Hayes, 1972, 1974] (Figure 2.15). The AAD is characterised by extremely rugged ridge flank morphology, and closely spaced, north-south oriented fracture zones. Weissel & Hayes [1974] observed that the bathymetry of the SEIR flanks does not conform to depths expected given a simple lithospheric thermal contraction model for either the cooling plate or cooling half-space models (e.g. Parsons & Sclater [1977]. The depth of the SEIR itself is also anomalous, ∼1 km deeper than expected [Veevers, 1982].

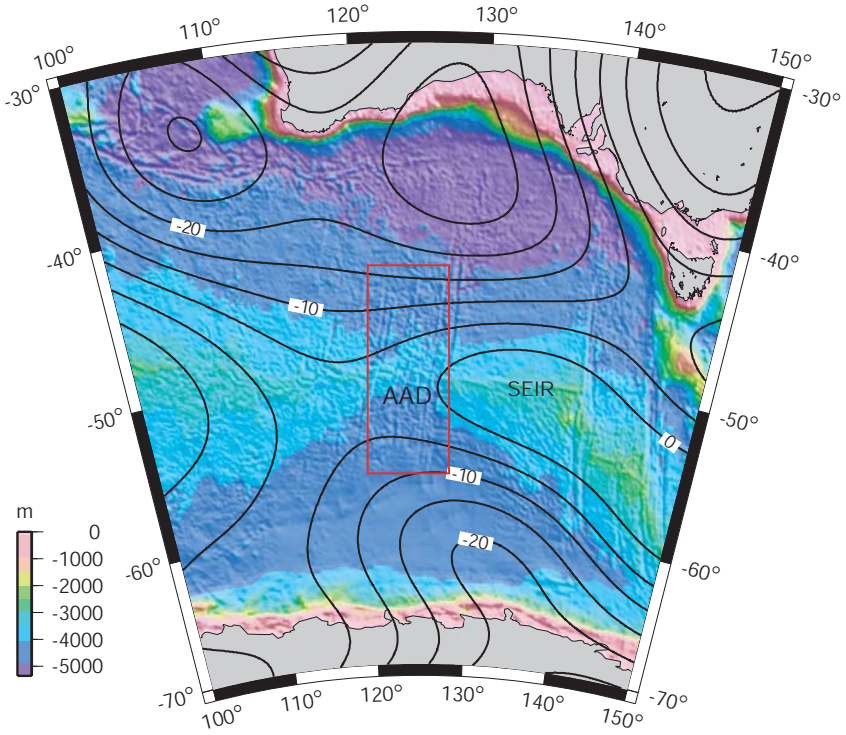

Figure 2.15: The southeast Indian Ocean between Australia and Antarctica. A broad bathymetric depression, centred on the Australian-Antarctic Discordance (AAD), is co-extensive with a broad negative anomaly in the long wavelength ($\lambda \gtrsim 2000$ km) free air gravity field (black contours). A saddle in the gravity field corresponds to the location of the AAD. Gravity contours from the model of Rapp & Pavlis [1990] and bathymetry from Smith & Sandwell [1994].

Thermal contraction models (e.g. Sclater & Francheteau [1970]) of the lithosphere predict that depth of oceanic crust is a function of age, and that crust of equal age should lie at equal depth in all ocean basins. Studies of the bathymetry of the world's ocean

basins broadly validate these models (e.g. Parsons & Sclater [1977]). However, relative to predicted depth, the Indian and Antarctic plates form a distinct regional negative depth anomaly in the region of the AAD. Maximum anomalies of 600-900 m were defined by Weissel & Hayes [1974], and anomalies in excess of 1000 m have been suggested more recently (e.g. Gurnis & Müller [2003]). The ∼2000 km wide depression extends at least 900 km from the ridge crest.

More extensive bathymetric compilations allowed Veevers [1982] to determine the regional extent of the AAD beyond the immediate area of the SEIR. Veevers [1982] defined a *"morphotectonic depression"* centred on the AAD, covering $\sim 15 \times 10^6$ km^2, that extended from the southern half of Australia to the Wilkes Land sector of Antarctica. The depth anomaly (i.e. the observed depth less the calculated depth based on a cooling plate model) of the southeast Indian Ocean is characterised by a linear, north-south trending depression, which traverses the AAB from the southern Australian margin to the Wilkes Land margin, Figure 2.16. The depth anomaly is approximately symmetrical with respect to the SEIR, which suggests the anomaly is a function of plate forming conditions at the ridge. The largest magnitude depth anomalies (>1000 m) are located close to the Australian and Antarctic margins, not at the ridge itself [Gurnis & Müller, 2003]. The AAD is, with respect to global residual oceanic bathymetry, the most prominent negative bathymetric anomaly not associated with present-day subduction [Gurnis *et al.*, 1998].

Figure 2.16: Residual topography of the southeast Indian Ocean and the Australian-Antarctic Discordance. Coloured dots represent isotopic signature of the mid-ocean ridge basalts, yellow = Pacific Ocean mantle, red = Indian Ocean mantle. Dotted line is the hypothesised trace of the isotopic boundary. Figure from Gurnis & Müller [2003].

Veevers [1982] demonstrated that the depression is co-extensive with a negative satellite free air gravity anomaly, as suggested by Weissel & Hayes [1974]. Comparison of the long wavelength gravity field ($\lambda \gtrsim 2000$ km) and the bathymetry of the southeast Indian Ocean illustrates the correlation between a saddle in the free air gravity and the location of the AAD (Figure 2.15). Although this saddle represents a relative high over the ridge, the gravity field is almost entirely negative. This contrasts with most mid-ocean ridges

where a positive free air gravity anomaly, with a wavelength of 2000-5000 km, is typically observed [Lambeck, 1972]. Weissel & Hayes [1974] suggested that the saddle in the gravity field reflects the combined effect of a typical mid-ocean ridge, and of the regional bathymetric depression.

Hayes & Conolly [1972] suggested that the observed depth anomalies are associated with a downwelling convective current in the asthenosphere. This interpretation was later supported by Weissel & Hayes [1974] and Veevers [1982] who also cited the negative, long wavelength free air gravity anomaly as evidence of downwelling mantle. Major element concentrations indicate that basalts from the AAD are consistent with lower than normal mantle temperatures [Klein & Langmuir, 1987].

Gurnis *et al.* [1998] suggest that the AAD is unique in being the only section of the present-day mid-ocean ridge system that intersects an ancient subduction zone. Gurnis & Müller [2003] infer that the SEIR, in the region of the AAD, intersects at depth lithosphere subducted by the long-lived Gondwana-Pacific/Phoenix convergent margin system. Global shear wave velocity models (e.g. Ritsema *et al.* [1999]) show a north-south trending high-velocity anomaly beneath the AAD, which Gurnis & Müller [2003] cite as evidence to support the Mesozoic subduction model for the origin of the AAD. Geochemical analyses also suggest a major change in asthenospheric-lithospheric source at the AAD, as it broadly marks the transition in tracer chemistry from 'Pacific Ocean type', to the east of the AAD, to 'Gondwana type', west of the AAD [Gurnis *et al.*, 1998] (Figure 2.16).

Antarctic and Southern Australian Margin Magnetic Quiet Zones (MQZ)

Weissel & Hayes [1971] first identified a magnetic quiet zone (MQZ) that *"begins just seaward of the continental slope and extends towards the land across the eastern continental margins of Antarctica and Australia"*. Weissel & Hayes [1972] defined the MQZ as regions where the amplitudes of local magnetic anomalies are extremely small. The seaward boundary of the MQZ is interpreted to cross-cut seafloor spreading anomalies, this indicates that the MQZ boundary itself is unlikely to be an isochron and is time-transgressive in some way Weissel & Hayes [1972].

Weissel & Hayes [1972] interpret the Antarctic MQZ to *"...presumably..."* occur over oceanic crust, and the Australian MQZ to be located both over oceanic crust and transitional crust beneath the lower continental slope. Various hypotheses have been considered to explain the origin of MQZ (e.g. Poehls *et al.* [1973]), however, König & Talwani [1977] find that these are not satisfactory to explain the presence of the Australian MQZ. They conclude that the crust below the MQZ is not typical oceanic crust. They suggest that

the crust is either:

1. Oceanic, but was never strongly magnetised or the magnetisation has been destroyed by some process since emplacement, or

2. Continental, with a low intensity of magnetisation.

Cande & Mutter [1982] used seafloor spreading modelling to demonstrate that the anomaly previously identified as chron 22 by Weissel & Hayes [1972] could be better modelled as chron 34. This revised interpretation did not require or preclude the presence of oceanic crust beneath the MQZ, and Cande & Mutter [1982] did not depart from the modes of origin suggested previously by König & Talwani [1977]. Veevers [1986], however, interpreted the MQZ to be floored by oceanic crust, as he suggested the landward boundary of the MQZ, the quiet zone boundary (QZB), represented the COB. Tikku & Cande [1999] question the validity of the interpretation of Veevers [1986], as it is unclear that the anomaly correlates directly with the COB for the entire span of the AAB.

Magnetic and gravity modelling by Sayers *et al.* [2001], based on seismic reflection data, and interpretation of seismic reflection data suggests that the Australian MQZ is floored by stretched continental crust. The COB in the model of Sayers *et al.* [2001] occurs farther seaward than previous interpretations. They, therefore, question the validity of identifying oceanic crust on the basis of magnetic anomalies only.

Seismic Reflection Data

Surveys focused on acquiring geophysical data along sections of the Wilkes Land margin were first carried out in the early 1980's by the IFP, JNOC and USGS. Each survey acquired seismic reflection, gravity anomaly, and magnetic anomaly data. Interpretations of these data, carried out independently by the individual institutions, broadly identified similar stratigraphic seqeunces. However, interpretation of the COB location, on the basis of the seismic character of the crust, differed significantly. More recent surveys have been completed by the JNOC (1993-94-95), and the Wilkes Glacial history (WEGA) project [De Santis *et al.*, 2003].

During the austral summer of 1982, the IFP survey ATC82 acquired ~3000 line-km of data off the east Wilkes Land-Terre Adélie margin, 136-154°E [Wannesson *et al.*, 1985]. Survey lines extended from the inner continental shelf (due to favourable ice conditions during the survey period) to the abyssal plain of the AAB.

The JNOC conducted two surveys in the early 1980's, survey TH82 during the 1982-83 austral summer [Tanahashi *et al.*, 1987], and the more extensive survey TH83 the following austral summer [Tsumaraya *et al.*, 1985]. Survey TH82 acquired 680 line-km of MCS data off east Wilkes Land. The TH83 survey acquired ~3700 km of MCS data, from

108-140°E). The JNOC completed a further survey on the Wilkes Land margin during 1995, TH95 [Tanahashi *et al.*, 1997]. Dredge samples were recovered during survey TH95, which indicate a cluster of seamounts off the east Wilkes Land-Terre Adélie margin have a geochemical signature indicative of a continental mantle lithosphere source [Yuasa *et al.*, 1997].

During the austral summer of 1984, the USGS research vessel *S.P. Lee* completed a survey (L184) of the east Wilkes Land margin [Eittreim & Hampton, 1987]. Over 1800 line-km of MCS data were acquired on 14 lines, from 130-146°E, which were interpreted by Eittreim & Smith [1987] and Hampton *et al.* [1987]. Icebergs and sea ice limited the southern extent of the survey and only one line extended landward of the shelf break.

The seismic stratigraphic interpretations of Wannesson *et al.* [1985], Tanahashi *et al.* [1987], Tsumaraya *et al.* [1985], and Eittreim & Smith [1987] were broadly similar. The interpreted number of sequences varied between interpretations, however, major unconformities were recognised that can be correlated. The inferred ages of unconformities, and nomenclature for their labelling, adopted during each interpretation was different. This prompted Tanahashi *et al.* [1994] to introduce a uniform nomenclature, for the major unconformities that were similarly interpreted within each data set. Figure 2.17 summarises the sequence stratigraphy of each of the above workers and correlates them to the uniform nomenclature introduced by Tanahashi *et al.* [1994]. Data acquired during survey TH95 were interpreted using the framework introduced by Tanahashi *et al.* [1994].

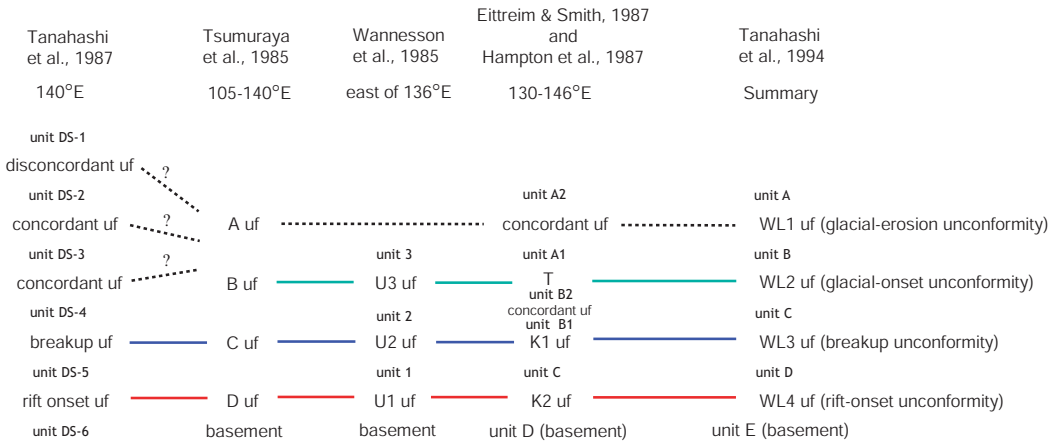

Figure 2.17: Summary of the seismic stratigraphic interpretations of MCS data acquired on the Wilkes Land margin. The summary of Tanahashi *et al.* [1994] includes the formative mechanism of the interpreted unconformities (uf).

Seismic reflection data were ubiquitously interpreted to indicate an absence of large-scale volcanism associated with rifting and breakup on the Wilkes Land margin. Various amounts of volcanism were interpreted, however, no evidence of seaward dipping reflec-

tor sequences or flood basalts was identified. Previous interpretations of the conjugate southern Australian margin had concluded that it too was non-volcanic, hence, the absence of extensive volcanism on the Wilkes Land margin had been previously predicted on this basis.

Despite the broad agreement in the interpretation of the major sedimentary sequences, widely varying estimates of the COB location and the crustal type beneath the MQZ were suggested on the basis of seismic interpretation. *Moho* reflections were interpreted in data from ATC82 and L184 data, however, relatively few strong reflections from within the crust were recorded. Hence, there is very little contrast in the recorded seismic character of the oceanic and continental crust surveyed. A basement rise off the east Wilkes Land-Terre Adélie margin added a degree of complexity to the interpretations. Sections of this high were traversed by the ATC82, TH83, L184, and TH95 surveys.

The basement high was interpreted by Wannesson *et al.* [1985] as oceanic crust, they cited the continuity of a reflector, interpreted as the *Moho*, beneath the high as evidence of oceanic crust. Hence, they interpreted the MQZ to be floored by oceanic crust, and that the lack of anomalies is due to emplacement during the Cretaceous normal polarity epoch. They interpret a COB adjacent to the foot of the continental slope. Tanahashi *et al.* [1987], in contrast, interpret the basement high to represent stretched continental or 'transitional' crust. Hence, the COB interpreted by Tanahashi *et al.* [1987] is located over 400 km seaward of that interpreted by Wannesson *et al.* [1985]. Eittreim & Smith [1987] interpret the basement high to represent volcanic build-ups associated with the earliest emplacement of oceanic crust. Hence, their interpreted COB is located at the landward edge of the high, between the interpretations of Wannesson *et al.* [1985] and Tanahashi *et al.* [1987]. Other geophysical evidence, such as potential field data and limited heat flow and sonobuoy refraction data, was not sufficient to resolve the differences in interpretation.

Seismic reflection data from survey TH95 images >1 s two-way-time (TWT) of deformed sediments overlying a section of the basement high. This was interpreted to confirm the presence of transitional crust and a COB seaward of the basement high [Tanahashi *et al.*, 1997]. Additionally, the geochemistry of dredge samples recovered from a seamount in the region were interpreted by Yuasa *et al.* [1997] to indicate that active seafloor spreading initiated seaward of the seamount location. Thus, indicating that the basement high comprises, and the majority (if not all) of the MQZ is floored by, stretched continental or transitional crust.

2.12 Summary

Relative to all other continents, the study of Antarctica has a short history. Antarctica is also the only continent where surface geological mapping is limited to less than 2% of the continental surface. These factors, combined with the absence of resource exploration and exploitation, explain why there are still many unanswered questions with regard to the geology and tectonics of Antarctica. However, much has been achieved and many important discoveries made since scientific surveying began in the early 1900's.

The Wilkes Land margin remains one of the least explored marine sectors of Antarctica. The sediment thickness and crustal structure are poorly constrained for much of the region. Surveys that have explored this margin define a number of interesting features with regards to the influence of glaciation on the physiography and sedimentation patterns on the margin. The composition and origin of basement features and the location of the COB off the Wilkes Land margin remains enigmatic. This contrasts with the conjugate southern Australian margin, which has been the subject of relatively intense study for many decades. The geological evolution and structural architecture of the Wilkes Land margin is, therefore, of great interest. Investigations of this conjugate margin pair provides a basis for further understanding the evolution of non-volcanic, passive rift margins.

Chapter 3

Seismic Reflection Data Acquisition and Processing

3.1 Introduction

Seismic reflection and refraction data are crucial in understanding the evolution of continental margins. Geoscience Australia (GA) surveys GA-228 and GA-229, the primary seismic reflection data used in this study, were completed in 2000-01 and 2001-02. Prior to this, available data acquired by surveys conducted by the Institut Francais du Pétrole (IFP) in 1982 (survey ATC82), the United States Geological Survey (USGS) in 1984 (survey L184), and the Japanese National Oil Company (JNOC) in 1982, 1983 and 1995 (surveys TH82, TH83 and TH95).

Field data from survey L184 were requested and subsequently made available by the USGS. Field data from the IFP survey ATC82 could not be obtained. However, stacked sections of Multi-Channel Seismic (MCS) data from surveys ATC82, TH82, TH83 and TH95 were obtained through the Scientific Committee on Antarctic Research (SCAR), Seismic Data Library System (SDLS) branch, at the British Antarctic Survey (BAS), Cambridge.

This chapter outlines the survey acquisition parameters and seismic processing sequence for the GA, USGS, and IFP data. The processing and interpretation of sonobuoy refraction data is also briefly outlined. The USGS MCS data were reprocessed as part of this project. This was completed in an attempt to provide increased coverage of the upper continental slope off east Wilkes Land, and to determine if imaging improvements are possible through the application of seismic processing techniques that have become common since the original processing of these data in 1984. Stacking velocities and unreversed sonobuoy refraction data were used to create velocity models to facilitate two-way-time (TWT) to depth conversion of the USGS and GA data.

3.2 Geoscience Australia Surveys GA-227, GA-228 and GA-229

3.2.1 Introduction

Geoscience Australia (GA)[1], acquired over 20 000 km of MCS, gravity and magnetic data, from 2000-2002, on the East Antarctic margin, 38-162°E. This two-season survey (GA-228 and GA-229), represents the most extensive MCS survey on the Antarctic margin. A further survey (GA-227) was completed in 2000-01 to provide bathymetric and high-speed (low-fold and small source) seismic data between the shelf edge and the southern extent of the GA-228 and GA-229 survey lines. Negotiated access to these data provides the unique opportunity to carry out an integrated geophysical study on this relatively unexplored rifted margin. The GA-228, GA-229 and GA-227 survey lines, and major geographic and morphologic features of East Antarctica are illustrated in Figure 3.1.

GA-228 and GA-229 data were acquired on transects approximately perpendicular to the Antarctic margin from the shelf edge or the surveying limits imposed by sea ice (whichever was the furthest seaward, i.e. no attempts were made to survey the continental shelf). Seismic reflection data were recorded 36 fold, and in addition, gravity and bathymetric data were recorded port-to-port and magnetic data were acquired coincident with multi-channel seismic (MCS) survey lines. Over 120 sonobuoys were also deployed during surveying, of which 99 recorded refractions and/or wide-angle reflections.

The catalyst for the acquisition of this extensive dataset was the United Nations Convention on the Law of the Sea (UNCLOS) Treaty of 1999. For Law of the Sea purposes, MCS data are required at distances of not greater than 60 nautical miles, this controlled the line density in the survey region. No tie- or cross-line was included in the survey design as under the UNCLOS treaty the lateral correlation of MCS data is not significant. No attempt was made to acquire deep seismic data landward of the shelf break in surveys GA-228 and GA-229 as these data are also not required for Law of the Sea purposes. Despite these drawbacks, this data set remains unrivalled in the realm of Antarctic geoscience and provides many exciting research opportunities.

The focus of this thesis is the Wilkes Land margin. Twelve transects across the Wilkes Land margin were completed during survey GA-228 and a number of shorter lines and line extensions were completed during survey GA-229.

[1]Formerly Australian Geological Survey Organisation (1991-2001), and the Bureau of Mineral Resources, Geology and Geophysics (pre 1991).

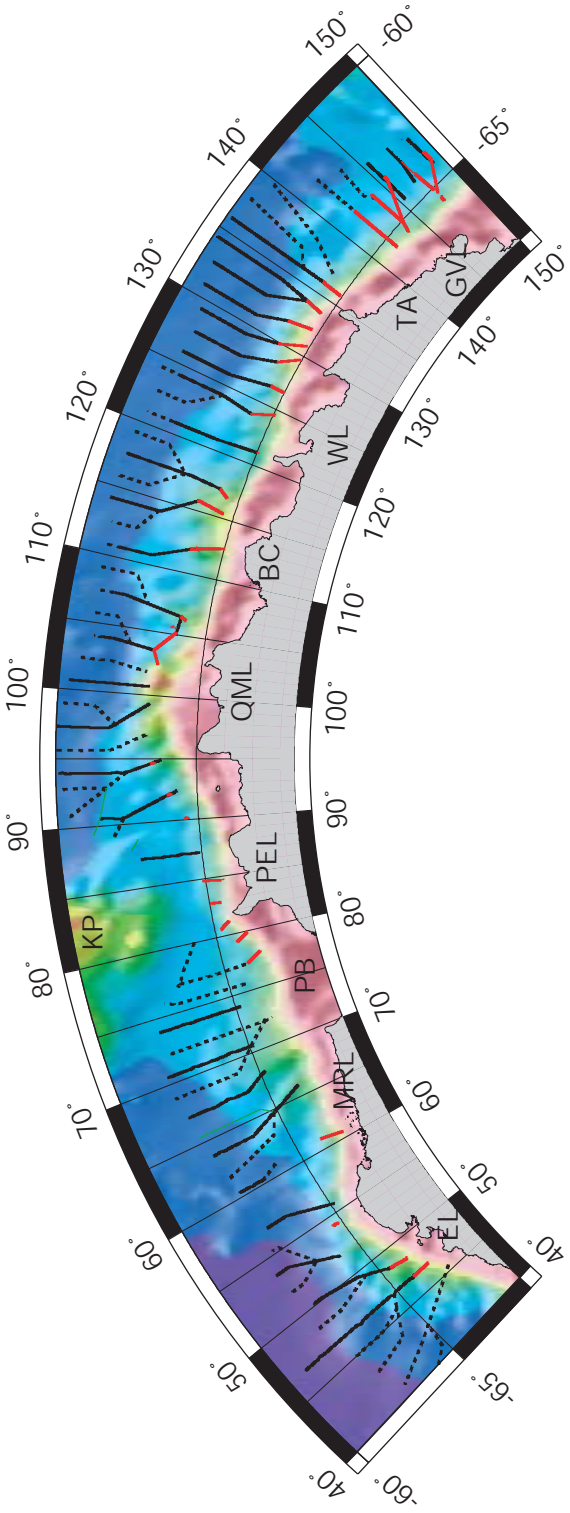

Figure 3.1: GA-228 (black), GA-229 (dashed), and GA-227 (red) survey lines on the East Antarctic margin, geographical regions are labelled. The Wilkes Land sector of East Antarctica is conjugate to the southern Australian margin. EL = Enderby Land, MRL = Mac.Robertson Land, PB = Prydz Bay, QML = Queen Mary Land, PEL = Princess Elizabeth Land, BC = Budd Coast, WL = Wilkes Land, TA = Terre Adélie, GV = George V Land.

3.2.2 Survey GA-227

A bathymetry survey was conducted by the *MV Polar Duke* off the Wilkes Land margin during the Austral summer of 2000-01, survey GA-227. The bathymetry survey lines extend from the shelf-break for 50-200 km downslope (average 80 km). A total of 3425 km of combined bathymetry and four-fold seismic data were recorded, Figure 3.1. A further 1183 km of bathymetry-only profiles were recorded when ice conditions prevented the deployment of seismic equipment. Survey equipment and parameters utilised during survey GA-227 are summarised in Table 3.1.

recording system	24 channel OYO digital recorder
streamer length	300 m
group interval	12.5 m
hydrophones per group	3
source	airguns
source volume	6 litres
SP interval	37.5 m
record length	6-9 s
echo-sounder	Simrad EA500 operating at 12 and 18 kHz

Table 3.1: Survey parameters and equipment utilised aboard the *MV Polar Duke* during bathymetry survey GA-227.

Survey GA-227 data were processed 'in house' at GA. A basic processing sequence was applied to these data as only very shallow penetration was achieved by the relatively small source and the short streamer. Normal Moveout Correction (NMO) was applied using a water bottom velocity function. Trace editing was also completed, and notch and dip filters applied. The data were subsequently stacked and migrated using a finite difference algorithm [F. Kroh, pers. comm.].

3.2.3 Surveys GA-228 and GA-229

Acquisition

Surveys GA-228 and GA-229 were completed during the austral summers of 2000-01 and 2001-02 respectively, aboard the *R/V Geo Arctic*, operated by geophysical contractors, *Fugro Geoteam AS*. The surveys acquired 10574 km and 9598 km of 36-fold MCS data respectively (a total 20172 km), along 73 lines (Figure 3.1). MCS Data were recorded 36-fold from a 3600 m streamer (comprising 288 channels) and a 60 litre tuned airgun

array, with a record length of 16 s, as detailed in Table 3.2. Survey geometry is illustrated in Figure 3.2.

recording system	288 channel MSX recorder
streamer length	3600 m
group interval	12.5 m
hydrophones per group	14
source volume	60 litres
SP interval	50 m
record length	16 s

Table 3.2: Survey equipment utilised aboard the *R/V Geo Arctic* during the deep-seismic surveys.

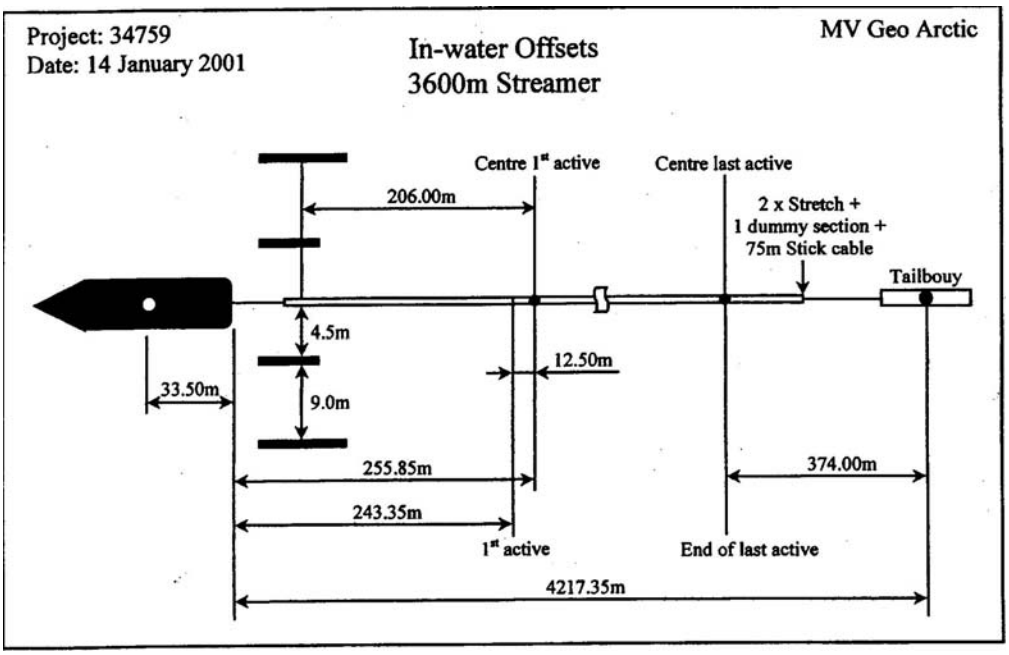

Figure 3.2: Schematic illustration of the towing configuration for surveys GA-228 and GA-229.

Twelve, approximately north-south, transects from the abyssal plain to the continental slope or lower rise of Wilkes Land (110-137°E) were completed during survey GA-228, GA-228_18 to GA-228_29. These lines are separated by ~90 km and vary in length from 300 to 450 km. A similar transect was completed during survey GA-229 off east Wilkes Land or Terre Adélie, GA-229_06, as were a number of shorter lines over the outer rise and abyssal plain which tie, at their landward extents, to GA-228 survey lines (shorter

lines were completed to satisfy particular Law of the Sea requirements).

Processing

Seismic data were processed on-board to stacked sections during both survey GA-228 and GA-229, Table 3.3 outlines the details of this processing. Brute stacks were created in real-time to allow quality control of data, and for analysis of regional geological setting.

1	reformat from SEGD to Disco format
2	designature into a minimum phase wavelet
3	bandpass filter 6-90 Hz
4	resample to 4 ms
5	trace decimations (2:1 sum with NMO)
6	amplitude recovery
7	velocity analysis at 4 km intervals
8	linear mute offset 250 to 3780 m, 0-3000 s
9	36-fold stack
10	gun and cable static correction (12 ms)

Table 3.3: Processing stream applied on-board the *R/V Geo Arctic* to seismic reflection data during surveys GA-228 and GA-229.

Pre-stack processing, involving greater parameter testing was repeated on selected portions of a number of lines from survey GA-228. This was carried out to determine to what extent imaging improvements were possible with processing under less restrictive time constraints. Processing was completed by *Robertson Research Ltd.* with supervision from Fred Kroh, Geoscience Australia. Extensive testing of the following parameters was completed; gain recovery, demultiple techniques (F-K, F-X, Radon, Radon/F-K, Radon/F-X), predictive pre-stack deconvolution, inner and outer trace muting, dip moveout, post-stack deconvolution, migration velocities, post migration signal enhancement (i.e. Tau-p filter), bandpass filters, and post-stack scaling.

A brief outline of the applied processing steps and parameters follows. The parameters were varied spatially according to water depth for processes such as mutes, predictive deconvolution, Tau-p filter, bandpass filter and percentages of reduction in migration velocity functions. The parameters outlined below are applicable for two-way time (TWT) water bottom time at 4 s.

Pre-Filter

A minimum phase Butterworth filter of 5-125 Hz, with a slope of 6 dB/octave at the low

end and out at the high end was applied to the whole data set to remove low frequency noise.

Gain Recovery

The following gain functions were applied:

$$Gain(dB) \quad = \quad 1.0(t) + 56.0$$

and

$$Gain(dB) \quad = \quad 8.0(t)$$

where t = TWT. The gain levels were held constant after 12 s and 4 s for the first and second gain functions respectively.

Designature

Far signature wavelet information was supplied via GA to convert the data into minimum phase wavelet.

Multi-Channel Filter

A symmetrical -1250 m/s to +1250 m/s pass velocity F-K filter was applied to the data using a 4^{th} power cosine taper. A 43-trace operator was utilised and automatic gain control (AGC), window size = 300 ms, was applied before and removed after filtering.

Receiver Array Simulation

A weighted 3 trace mix was performed down normal moveout (NMO) curves. Alternative traces were output to give 144 traces with a group interval of 25 m.

Common Mid-Point Gather

The 144 trace array simulated shot records were sorted into 36 fold common mid-point (CMP) gathers, with a spacing of 12.5 m.

Preliminary First Pass and First Pass Velocity Analysis

Preliminary first pass velocities were determined using interactive *Robertson's* software. Each analysis comprised an 18-CMP stacked panel, repeated 11 times with varying NMO velocity functions ranging from ±5%, ±10%, ±16%, ±24%, and ±40% increments from a central function. The central velocity function is the interpolated value of the regional velocity trend based on water depths. Analyses were performed at 12 km intervals.

A mild F-K multiple attenuation filter was applied to enhance primary energy before further analyses, using slowed preliminary velocity functions of -12% at 0 s, -16% at 3.5 s and -24% at 6 s. This was applied for analysis only. The above velocity analysis process was then repeated using the a central velocity function as determined from the preliminary first pass velocity analysis. Analyses were completed at 4 km intervals by *Robertson's* staff.

Radon Demultiple

After the application of a 300 ms removable AGC function, 4 adjacent NMO corrected (using 95% of the first pass velocities) CMP gathers were merged and transformed into the Tau-p (radon) domain. An optimum transform range of -800 to 1600 ms was used to enable a complete range of the anticipated multiples' parabolic moveout to be analysed, delineated from primaries, and filtered. Modelled multiple arrival energy was then subtracted from the super-gathers to attenuate the multiples. The filtered super-gathers were then transformed back into the space-time (x-t) domain and split into their original fold gathers and the AGC and NMO corrections removed.

F-K Multiple Attenuation

Filtering in the F-K domain was tested as a means of multiple attenuation. However, improved results were achieved by using the F-X approach, whereby the impulse response of the F-K filter is generated by populating a model F-K space with 1's and designing a filter to attenuate the required areas of F-K space. The reverse fast fourier transforms (FFT) are applied to generate the time domain impulse response of the F-K filter. The CMP gathers can then be filtered by convolution (space domain) or multiplication (frequency domain) of the impulse response and the CMP gather. NMO was performed using the same percentages of slowed primary first pass velocity as in the Radon method.

Dip Moveout

Dip Moveout (DMO) achieves partial migration, whereby traces with common midpoints, but different source-receiver offsets, relate to the same sub-surface locations after DMO, for all dips. Following DMO, all reflection events appear, for the purposes of NMO correction, to have originated from horizontal reflectors. Therefore, optimum stack response for all reflector dips can be obtained from conventional moveout corrections based on velocity functions undistorted by reflector dips.

Second Pass Velocity Analysis and NMO

Final stacking velocities were determined using a similar process to that outlined above for the first pass analysis. However, analyses were completed at 2 km intervals and were interpreted by *Robertson's Ltd.* staff and quality controlled by Fred Kroh, GA. NMO was performed using the second pass, interpreted velocity functions.

Mute

A post-NMO outer trace mute was applied to remove coherent noise from outer traces, and to reduce contamination from NMO induced stretching at far offsets.

CMP Stack

Traces within each CMP gather were summed using $1/\sqrt{N}$ stack compensation. The maximum resulting fold was 36 with a CMP interval of 12.5 m.

Statics

A +13 to +17 ms static compensation for gun and cable depths was applied.

Pre-Migration Scaling

To compensate for large lateral variations in amplitude, a dual-window AGC of 1000 and 400 ms window lengths was used for pre-migration scaling.

Migration

A 3^{rd} order 65° finite difference algorithm was utilised for migration. The migration model velocities were based on laterally smoothed stacking velocities with the percentages of reduction outline in Table 3.4.

Time (ms)	% of velocity
7,000	100
10,000	90
16,000	75

Table 3.4: Percentage velocity reduction as a function of time as used for migration of GA-228 and GA-229 data.

Post-Stack Scaling

A dual window, time variant AGC function was used for post-stack scaling prior to display. The negative effects normally associated with AGC are avoided by employing two different window lengths to determine the amplitude model (using the minimum of the two mean amplitudes determined at each sample), then conditioning the model by a weighted mix with the amplitude model derived from a single window per trace.

Comparison of on-board processed with re-processed stacked sections indicates relatively minor imaging improvements. Further multiple attenuation was achieved, however, it was determined that this could be achieved with the post-stack processing sequence outlined above. Accordingly, post-stack processing was performed on all on-board processed data (surveys GA-228 and GA-229) to produce final, time migrated, stacked sections. It was determined that no further, significant improvements could be achieved by further processing of GA survey MCS data as part of this study.

3.2.4 Sonobuoy Refraction Data

Non-reversed, expendable sonobuoys were deployed to record refraction and wide-angle reflection data during surveys GA-228 and GA-229. A total of 19 sonobuoys deployed on the Wilkes Land margin successfully recorded either refractions and/or wide-angle reflections. All sonobuoys were modelled at GA using *SIGMA* ray-tracing software developed by the Geological Survey of Canada (Seismic Image Software, 1995). The modelling methodology is outlined in detail by Stagg *et al.* [in press]. An example of sonobuoy data

recorded over stretched continental crust is shown in Figure 3.3. Wide-angle reflections and refractions were used to determine velocities in the sedimentary section. Crustal velocities were typically only indicated by refractions.

Seismic reflection data and stacking velocities were utilised in the creation of a 'first-pass' velocity model. The model was then iteratively altered to fit refractions and reflections from sonobuoy data by adjusting layer velocities and depths. Due to the excellent depth penetration of the seismic reflection data, constraints were placed on the geometries of many refractors, thereby partially offsetting the shortcomings associated with the sonobuoys being non-reversed [Stagg *et al.*, in press].

In some locations, different velocities were required at the top and bottom of a velocity layer to model both wide-angle reflections and refractions. This is because wide-angle reflections provide an interval velocity for the layer above a reflection, whereas refractions provide a velocity at a velocity boundary. However, accurately constraining these gradients is not possible with unreversed sonobuoys and in the absence of velocity-depth constraints from well data. Therefore, all modelling was conducted assuming fixed interval velocity layers rather than with velocity gradients. The result of assuming discrete interval velocities in models is that interface depths are under-estimated, by up to 15% in oceanic crust [White *et al.*, 1992].

3.2.5 Velocity Models

Semblance analyses of common mid-point (CMP) supergathers were completed every 4 km for survey GA-228 and GA-229 data as part of the on-board processing sequence (and every 2 km for re-processed data from GA-228) as outlined above. An example of a semblance plot from Line 228_26 is illustrated in Figure 3.4. Stacking velocities were converted to interval velocities using the Dix equation (Figure 3.5). A comparison of sonobuoy derived refraction velocities and interval velocities is also shown in Figure 3.5. The independently derived velocity profiles correspond very closely for the sonobuoy located over thinned continental crust. The refraction velocities modelled over oceanic crust are slightly lower than derived from semblance analysis, this may be a function of the discrete interval velocities assumed in refraction modelling (as discussed above).

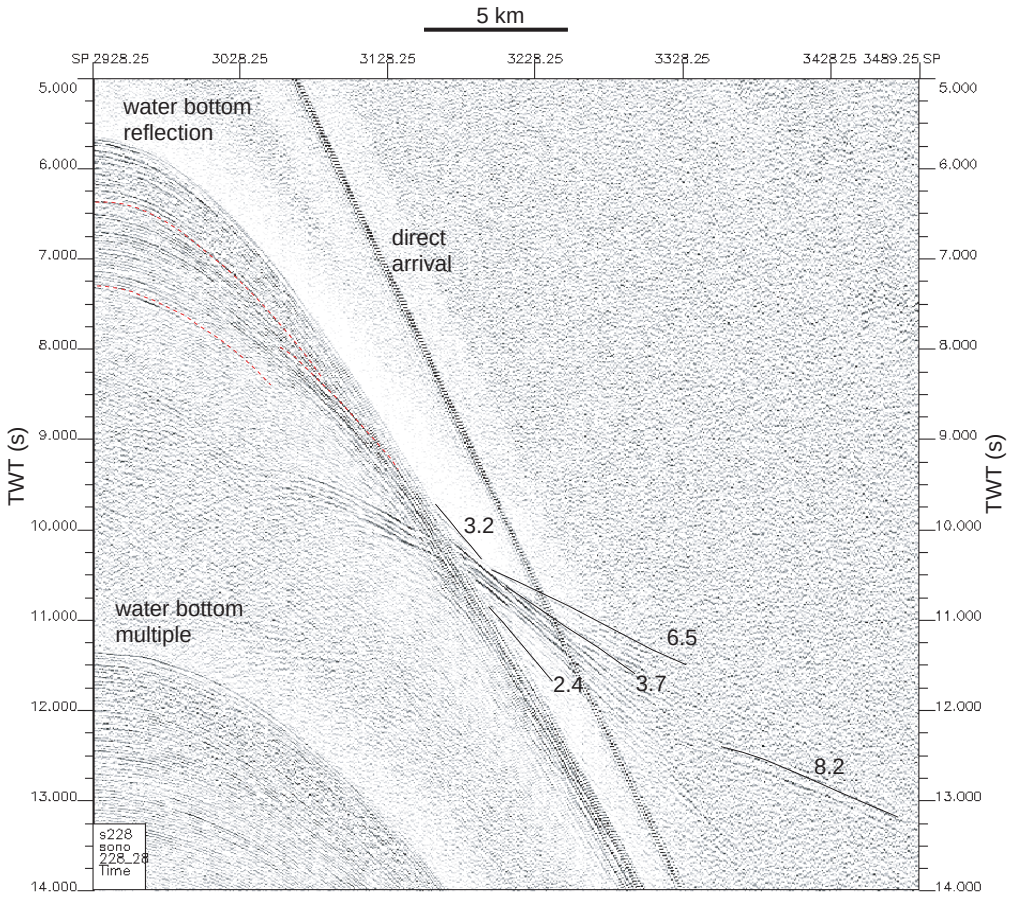

Figure 3.3: Recorded data from sonobuoy 228_21, Line 228_28. Refractions are recorded (black solid lines) along with direct arrivals, primary reflections (e.g. dashed red lines) and multiples. Refractor velocities are in $\times 10^3$m/s.

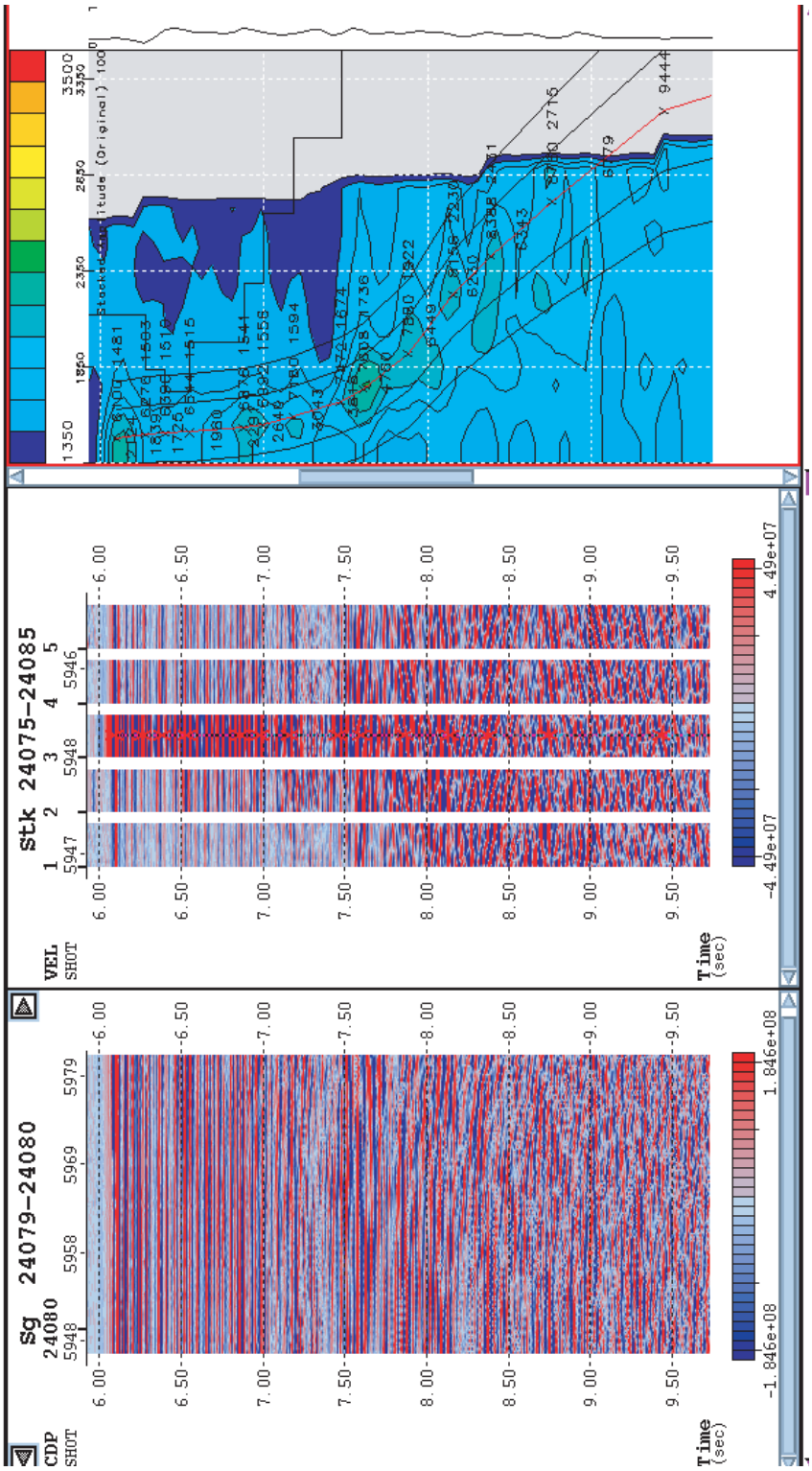

Figure 3.4: Left panel shows a 2 CMP supergather NMO corrected using the picked velocity profile, marked with X's in the right panel. The centre panel shows mini-stacks created with decreased (mini-stacks 1 and 2) or increased (mini-stacks 4 and 5) velocity functions relative to the central velocity function (mini-stack 3). The black velocity profiles, right panel, correspond to mini-stacks 1, 2, 4, and 5 from left to right respectively.

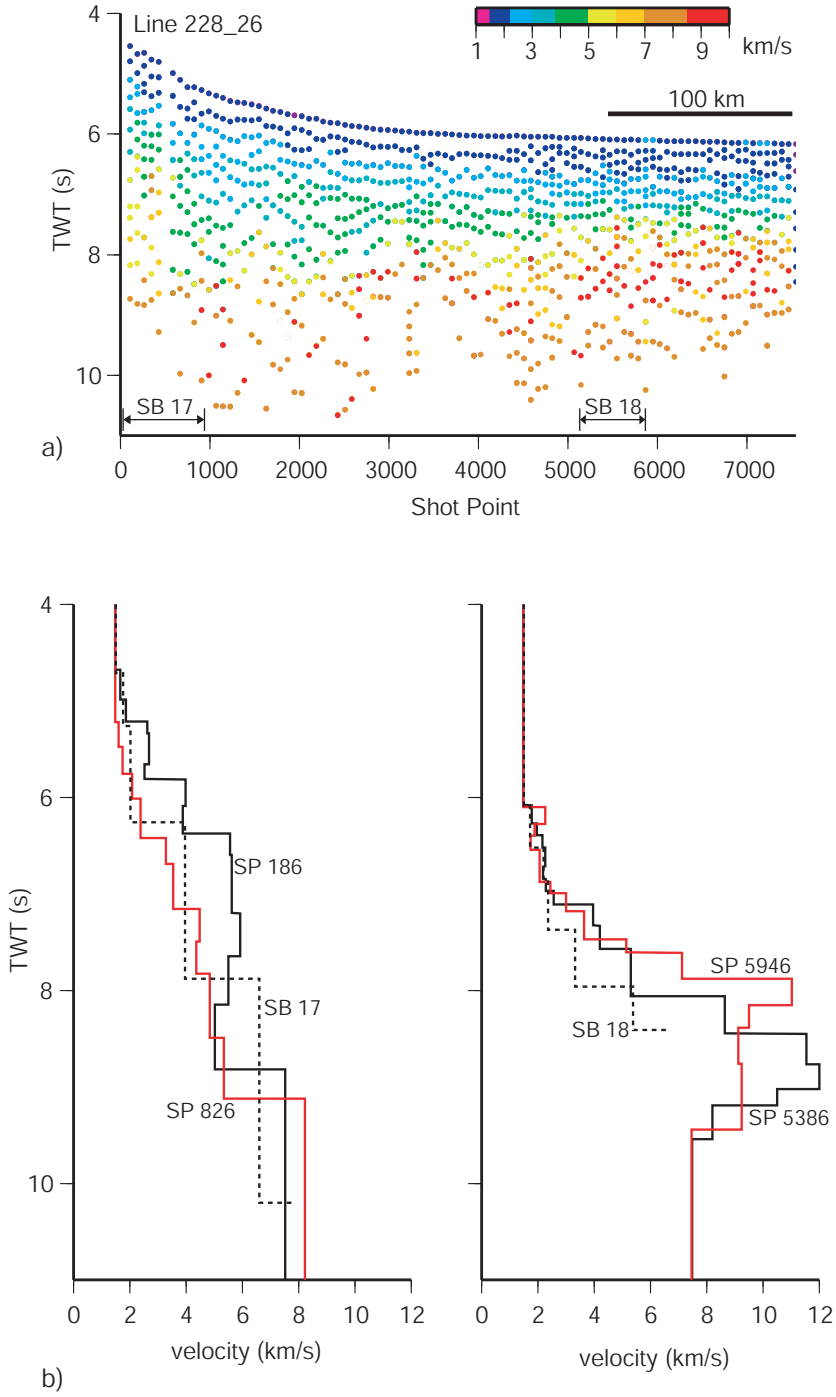

Figure 3.5: a) Interval velocities derived from stacking velocities, using the Dix equation for Line 228_26. Stacking velocities were picked from semblance analyses every 4 km. b) Comparisons of sonobuoy (SB) refraction velocity profiles, as located in (a), to two interval velocity profiles from the extreme shot points (SP) of the SB recording range. A close correlation between the velocity profiles is observed.

3.3 Institut Francais du Pétrole Survey ATC82

3.3.1 Acquisition and Processing

In January-February, 1982, IFP survey ATC82 acquired ~3000 km of MCS data on the Terre Adélie and east Wilkes Land margin of East Antarctica, between 136-154°E. Data were acquired aboard the *S/V Explora (Prakla-Seismos)* utilising a 2000 in^3 airgun array source and a 2400 m, 48 channel streamer [Wannesson *et al.*, 1985]. Details of the processing sequence are outlined in Table 3.5. Field data are not open file for this survey and requests for access made to the IFP were unsuccessful. Stacked sections of the IFP survey lines were obtained through the SDLS. As field data and velocity information was unavailable, these data are used only for interpretation in TWT and have not been depth converted.

1	Amplitude correction	
2	Predictive deconvolution	160 ms operator, 20 ms lag
3	Velocity analyses	3 per 10 km
4	Normal Moveout Correction	
5	24 fold stack	
6	Static correction	+15 ms
7	Frequency filter	Time variant, band pass filter

Table 3.5: Brief outline of the processing stream applied to Institut Francais du Pétrole survey ATC82 data.

3.4 Japanese National Oil Company Surveys

3.4.1 Acquisition and Processing

The JNOC conducted a number of marine geophysical surveys on sections of the Wilkes Land margin from 1983-1995. Data from these surveys are concentrated off east and west Wilkes Land. The quality of imaging achieved on these surveys is variable, however, crustal structure is not normally successfully imaged. Despite the lack of crustal penetration of JNOC data, they provide useful ties of sedimentary horizons between GA-228 and GA-229 survey lines. The 1995 survey (TH95), however, is extremely useful due to its location and improved imaging relative to other JNOC data. Survey TH95 was completed off the Terre Adélie sector of Wilkes Land and included dredging and piston-coring in conjunction with MCS data acquisition. JNOC surveys were conducted aboard the *R/V Hakurei-Maru*, survey equipment and data recording details from TH82 and TH83, and TH95 are summarised in Tables 3.6 and 3.7 respectively.

SOURCE	
Volume	9 litres
Shot interval	50 m
STREAMER	
Group interval	25 m
Phones per group	32
Streamer length	600 m
RECORDING	
Sample interval	4 ms
Record length	10 s
Number of channels	24

Table 3.6: Data acquisition parameter summary for the JNOC surveys TH82 and TH83.

SOURCE	
Volume	3.5 litres
Shot interval	50 m
STREAMER	
Group interval	12.5 m
Streamer length	2100 m
RECORDING	
Sample interval	4 ms
Record length	12 s
Number of channels	168

Table 3.7: Data acquisition parameter summary for JNOC survey TH95.

3.5 United States Geological Survey L184

The 1982 USGS survey off eastern Wilkes Land (survey L184) was conducted aboard the *R/V S.P. Lee* [Eittreim & Hampton, 1987]. Over 1800 km of MCS data were recorded, on 14 lines, from 130-146°E. L184 survey lines traverse the upper continental rise on a number of lines and the continental shelf on two lines.

Field data from survey L184 (pre-processed to SEGY format) were provided by the USGS to allow the data to be reprocessed and interpreted in context with the MCS data from surveys GA-228 and GA-229. This was undertaken as multiple potential benefits were identified, including:

1. The possibility of improved imaging of L184 data through the application of modern seismic processing techniques.
2. The improvement of MCS data coverage, between 130-142°E, particularly on the upper continental rise and shelf.

3.5.1 Acquisition and Processing

A typical processing sequence (e.g. Yilmaz [2001]) was tested on L184 survey data. Data were processed from field SEGY to fully time migrated sections using *ProMAX (v1998.6)*. Data acquisition parameters are summarised in Table 3.8, and the original processing sequence applied is outlined in Table 3.9.

The processing sequence applied was similar to that originally applied, except with the important addition of deconvolution. The three primary processes applied to reduce the noise content in the data were: deconvolution, stacking, and migration. Additional secondary processes were applied to improve the final data imaging. Where water-bottom multiple reflections obscure important reflectors additional multiple suppression techniques were also employed. Multiple suppression techniques were tested and applied on lines 11 and 12 only, the two lines that extend landward of the shelf break. A summary of the sequence of processing steps is listed in Table 3.10. The success of any seismic processing technique is dependent upon the user-defined parameterisation of the process. As such, a range of process parameters were tested on representative line sections before final application to entire lines. A detailed discussion of parameter testing undertaken, including comparative test panels is given in Appendix A. Limited imaging improvement was achieved via reprocessing. Multiple suppression techniques, particularly wave equation multiple rejection (WEMR), were successful in reducing the multiple energy to some degree. The quality of data imaging and the applicability of modern processing techniques are limited by the length of the streamer and the size of the source. The streamer length of 2400 m limited the amount of moveout, and a relatively small source resulted in relatively low signal to noise ratios at the longest offsets that were recorded. Hence, few of the techniques applied provided significant improvements beyond the basic processing steps applied.

3.6 Summary

All relevant, available seismic reflection data has been accessed to allow the most complete seismic interpretation possible to be completed in the following chapter. MCS data from surveys L184, GA-228 and GA-229 can also be depth converted as velocity information is available for these data.

SOURCE	
Volume	21 litres
Gun depth	10.5 m
Shot interval	50 m
STREAMER	
Length	2400 m
Group interval	100 m
Average depth	12.5 m
Group length	100 m
Phones per group	60
RECORDING	
Sample interval	2 ms
Record length	10 s
Recording filter	5-110 Hz
Number of channels	24

Table 3.8: Data acquisition parameters for the USGS L184 survey.

1	Demultiplex
2	Trace shot edit
3	Static corrections
4	CMP sort
5	Velocity analysis
6	NMO correction
7	24-fold stack
8	Bandpass filter
9	Automatic gain control

Table 3.9: Process sequence applied to the L184 data during original processing.

Reprocessing of survey L184 data indicates that the limits of imaging quality are primarily a function of the original data acquisition. Although minor improvements can be achieved through modern processing techniques, the interpretation of the data is not likely to be altered due to these small improvements. The longer streamer, greater fold, and larger source implemented during surveys GA-228 and GA-229 provides the highest

1	Preprocessing - Demultiplexing (completed externally) - Reformatting (completed externally) - Field geometry setup - Statics (DWD correction) - Trace editing - WEMR (Lines 11 and 12 only) - Geometric spreading correction
2	*F-K filtering*
3	CMP sort
4	Predictive deconvolution
5	Velocity analysis
6	NMO correction
7	- *DMO correction* - Radon filter (Lines 11 and 12 only)
8	24 fold stack
9	Deconvolution
11	Bandpass filtering
12	Migration
13	Trace mixing
14	Gain application

Table 3.10: General process sequence applied to survey L184 MCS data. Techniques that were tested but subsequently not applied are in italics.

quality MCS data off the Wilkes Land margin.

Chapter 4

Seismic Data - Interpretation

4.1 Introduction

Interpretation of GA-228 and GA-229 multi-channel seismic (MCS) data from the Wilkes Land margin was completed by scientific staff of GA[1] and the author. Interpretation of data acquired by the USGS, IFP and JNOC was subsequently undertaken in areas where these data could add value to the GA-228 and GA-229 interpretations. Figure 4.1 shows the location of all survey lines off the Wilkes Land margin. The line separation of ∼90 km in central Wilkes Land and varying coverage to the east and west does not allow the details of lateral facies and depositional environmental changes to be fully imaged. However, a range of depositional and erosional features, and facies changes are observed.

4.2 Sonobuoy Data

The MCS data interpretation presented here also integrates modelling of refraction and/or wide angle reflection data recorded with non-reversed expendable sonobuoys. Discussion of refraction velocities are included within the following interpretation sections. The locations of sonobuoy stations on the Wilkes Land margin are illustrated in Figure 4.1, and their interpreted velocities and boundary depths in two-way-time (TWT) are summarised in Table 4.1 and Figure 4.2. Unfortunately, very few sonobuoys recorded mantle velocities and accordingly there is poor control on *Moho* depth for most of the margin.

[1]Howard Stagg, Jim Colwell, Phil Symonds, Phil O'Brien, Mark Alcock, and Leesa Carson

	SB	**Lat.**	**Long.**	**Line**	V1	D1	V2	D2	V3	D3	V4	D4	V5	D5	V6	D6	V7	D7	V8	D8
A	229-26	-61.43	110.77	229_14	1.7	5.59	1.9	5.80	2.4	6.02	2.5	6.64	(3.2)	∼6.85	4.9	7.09	*5.9*	*7.73*	*7.1*	*8.06*
B	229-19	-61.67	120.87	229_10	1.7	5.65	2.0	6.10	2.5	6.51	2.8	6.96	3.7	7.37	(4.5)	∼8.02	*6.6*	*8.73*		
C	229-18	-60.9	124.23	229_09	1.7	5.93	2.4	6.44	2.7	6.98	3.4	7.29	(4.9)	∼7.86	6.1	8.04				
D	228-15	-61.83	127.6	228_24	1.7	5.88	2.0	6.23	2.4	6.63	3.4	7.45	5.4	7.74	*6.7*	*8.78*				
E	228-11	-63.95	128.28	228_24	1.7	5.05	2.4	5.74	2.6	6.16	3.4	7.19								
F	228-16	-62.92	129.34	228_25	1.8	5.83	2.4	6.65	3.0	6.94	4.1	7.34	5.4	8.27	*7.9*	*9.98*				
G	228-18	-61.63	130.97	228_26	1.7	6.09	2.2	6.52	2.3	6.87	3.3	7.37	5.4	7.96	*6.6*	*8.41*				
H	228-17	-63.88	131.85	228_26	1.8	4.71	2.0	5.26	*3.9*	*6.26*	6.6	7.88	*7.8*	*10.2*						
I	228-20	-60.82	132.65	228_27	1.8	6.16	2.2	6.58	3.1	6.75	3.9	7.54	*5.4*	*8.01*	*6.7*	*8.99*	*8.2*	*9.66*		
J	228-19	-60.69	132.65	228_27	1.8	6.17	2.5	6.67												
K	228-21	-62.87	134.33	228_28	1.8	5.67	2.0	6.22	2.4	6.42	3.1	6.71	4.5	7.42	6.5	8.70	8.2	10.21		
L	228-22	-60.73	134.33	228_28	1.8	6.12	2.1	6.49	2.8	6.77	3.0	7.13	3.8	7.40	4.9	7.87	*5.7*	*8.23*		
M	228-24	-61.79	136	228_29	1.8	5.84	2.3	6.27	3.0	6.84	3.9	7.27	4.4	8.02	*5.5*	*8.55*				
N	228-23	-60.91	136	228_29	1.8	6.01	2.2	6.62	3.5	7.26	4.9	7.65	*6.6*	*8.21*	*8.1*	*9.16*				
O	229-15	-62.97	136.83	229_07	1.9	5.29	2.1	5.78	2.7	6.22	*4.5*	*∼7.31*	5.6	∼9.75						
P	229-13	-62.22	137.42	229_07	1.9	5.6	2.0	6.02	2.3	6.41	3.3	7.09	3.6	7.23	*4.1*	*8.25*	*5.6*	*8.64*	6.6	9.69
Q	229-10	-63.89	137.47	229_06	1.9	4.67	2.0	4.99	2.7	5.76	3.5	6.52	4.0	7.04	*6.3*	*8.49*				
R	229-11	-62.98	138.5	229_06	1.8	5.07	2.0	5.37	2.1	5.75	2.5	5.94	2.9	6.29	3.8	6.87	(4.6)	∼7.21	5.4	8.74
S	229-12	-61.97	139.05	229_06	1.8	5.73	2.1	6.26	2.5	6.54	3.3	6.97	*3.6*	*7.3*	*4.1*	*8.59*	6.8	9.17		

Table 4.1: Sonobuoy locations and solutions for surveys GA-228 and GA-229. Velocity (V) units are km/s and depth (D) is recorded in two-way-time (s) below sea level. Velocities in parentheses are assumed and depths preceded by a tilda (∼) are approximate, usually because of relief on an interface. Velocity/depth pairs in italics are solutions for interfaces that are not observed in seismic reflection data and are therefore unconstrained with regard to dip.

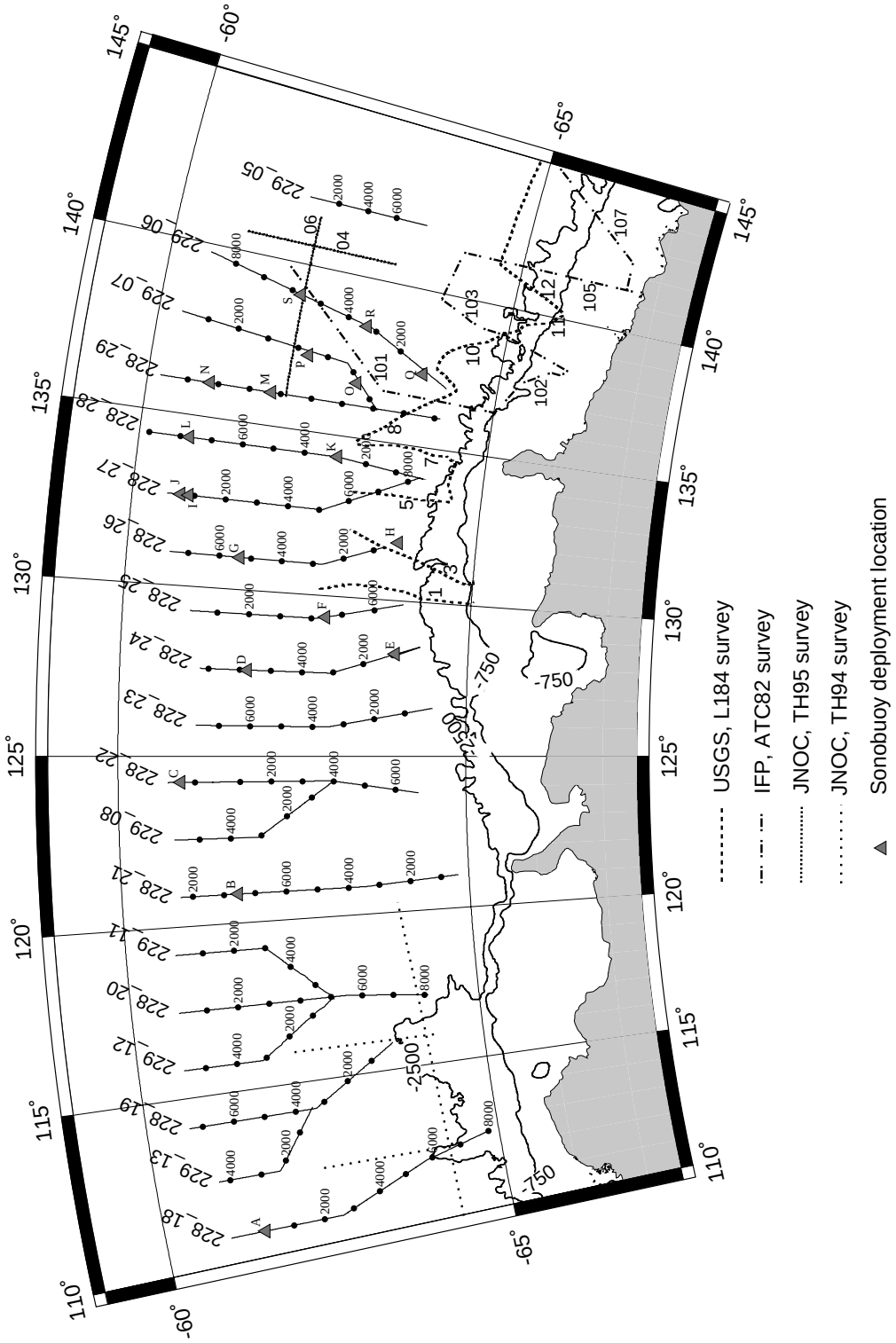

Figure 4.1: Seismic reflection survey lines from surveys GA-228, GA-229, L184, ATC82 and TH95 as labelled. Letters next to sonobuoy locations relate to Table 4.1. The 750 and 2500 m bathymetry contours from GEBCO 1-minute IOC *et al.* [2003] data are also illustrated.

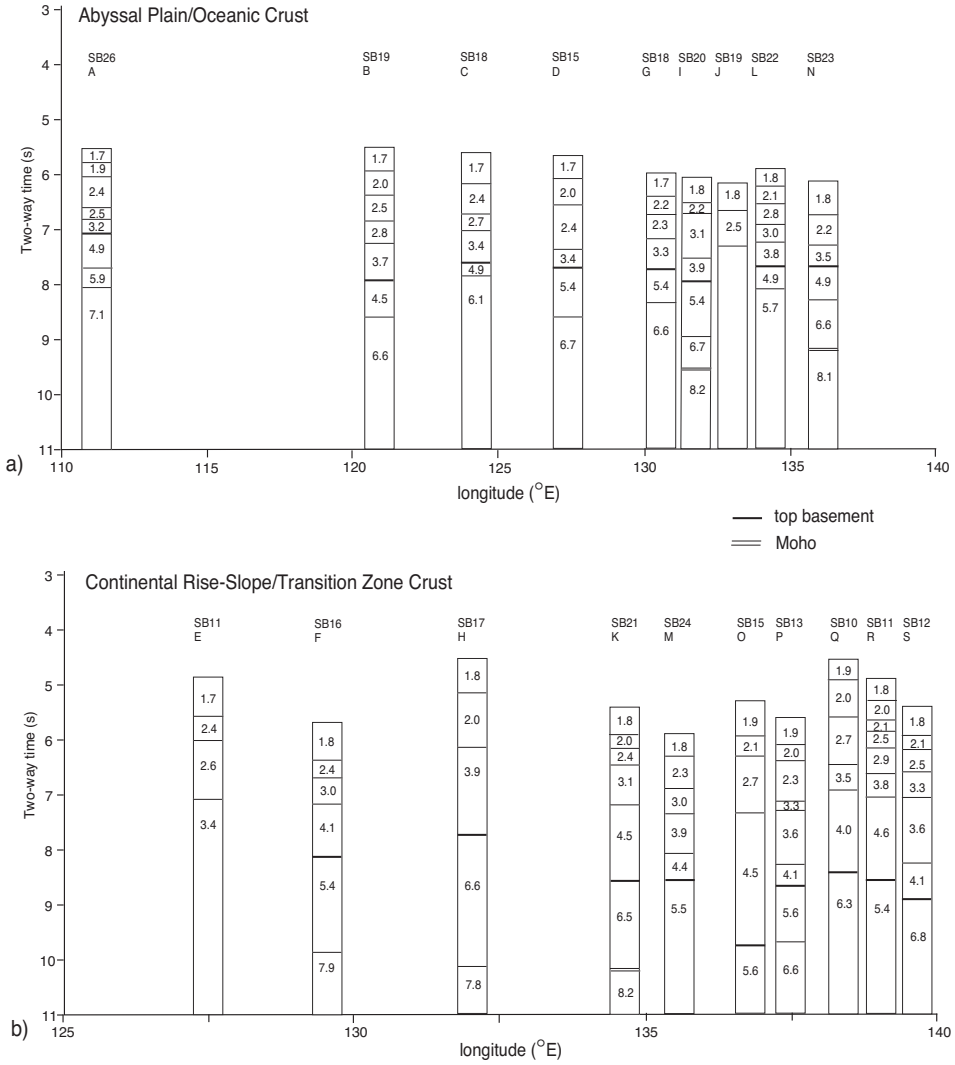

Figure 4.2: Sonobuoy refraction velocities for a) the abyssal plain, and b) the continental rise and slope. Note that the lateral scale is different in (b), as the sonobuoys are clustered off east Wilkes Land (see Figure 4.1 and Table 4.1).

4.3 Seismic Reflection Data

Regional seismic reflection profiles from the Wilkes Land margin, acquired during surveys GA-228 and GA-229, and their detailed interpretations are illustrated in Figures 4.3 to 4.16. Interpretations from USGS, JNOC and IFP data are illustrated selectively where they allow interpretation of features not imaged in GA-228 and GA-229 data. Isopachs are created using data from GA-228, GA-229 and USGS survey data, as velocity models are available for these data only (as outlined in the previous chapter). Seismic reflection data from the conjugate southern Australian margin is also utilised in interpretation, they provide images of an analogue system that has been more extensively surveyed and drilled.

Due to widespread ice coverage on the Antarctic margin, MCS data on the continental shelf is sparse. No GA-228 or GA-229 survey lines survey landward of the shelf break. The east Wilkes Land continental shelf was surveyed east of ~137° during USGS survey L184 (Lines 11 and 12) and IFP survey ATC82 (Lines 102, 103[2], 105 and 107). Lines L184_11, ATC82_102 and ATC82_105 are illustrated in Figures 4.17 to 4.19. No MCS data exists for the west and central Wilkes Land continental shelf.

A summary of the typical reflector patterns and geometry of each major sequence, with brief interpretations, is illustrated in Figure 4.20. Across margin variations in seismic character are illustrated by showing examples from the continental slope/rise and the abyssal plain environments. Examples from west and central/east Wilkes Land are also displayed to demonstrate the along margin variations in seismic character, which are important as the Wilkes Land margin sector extends over more than 1000 km.

Two major seismic sequences, bounded by regional unconformities labelled *eoc* and *tur*, are interpreted as sequences 1 and 2. The *eoc* unconformity is recognised as the base of onlapping reflectors beneath the continental slope and rise, it can be traced seawards confidently on all lines, except where pinch-outs against basement highs occur. The *eoc* unconformity is interpreted as Early- to Middle-Eocene (~50 Ma). The *tur* unconformity marks a transition between continuous, consistent amplitude and frequency reflectors above, and truncated, more chaotic reflector geometries below. The *tur* unconformity is interpreted to be early-Turonian (~85-90 Ma)

The top of Sequence 1 is defined by the present-day seafloor and its base by the *eoc* unconformity (landward) and the top of acoustic basement (seaward). Sequence 1 exhibits greater thickness relative to Sequence 2. Sequence 2 is observed beneath the continental slope and rise only, and does not extend to the deep abyssal plain. Both Sequence 1 and 2 thin seawards. These sequences can be further subdivided locally as

[2]Line 103 is not included in data placed with the SDLS and is therefore not publicly available

other distinct unconformities occur within them, which are interpreted as unlabelled blue lines on Figures 4.3 to 4.16. However, none of these minor sequence boundary can be correlated for the entire extent of the margin, due to the lack of a tie line and the large distance (average ∼90 km) between lines. The *eoc* and *tur* unconformities are identified from ∼110-145°E on the basis of seismic character and tie-lines provided by other data, however, they can not be confidently correlated further west or east.

A third sequence (Sequence 3) is identified off central and east Wilkes Land. Sequence 3 is highly variable with regard to thickness, seismic character, and to a lesser degree, seaward extent. Basement is interpreted, in general, to underlie Sequence 3 at the landward extent of data, to underlie Sequence 2 beneath the continental slope/rise transition, and to underlie Sequence 1 beneath the abyssal plain.

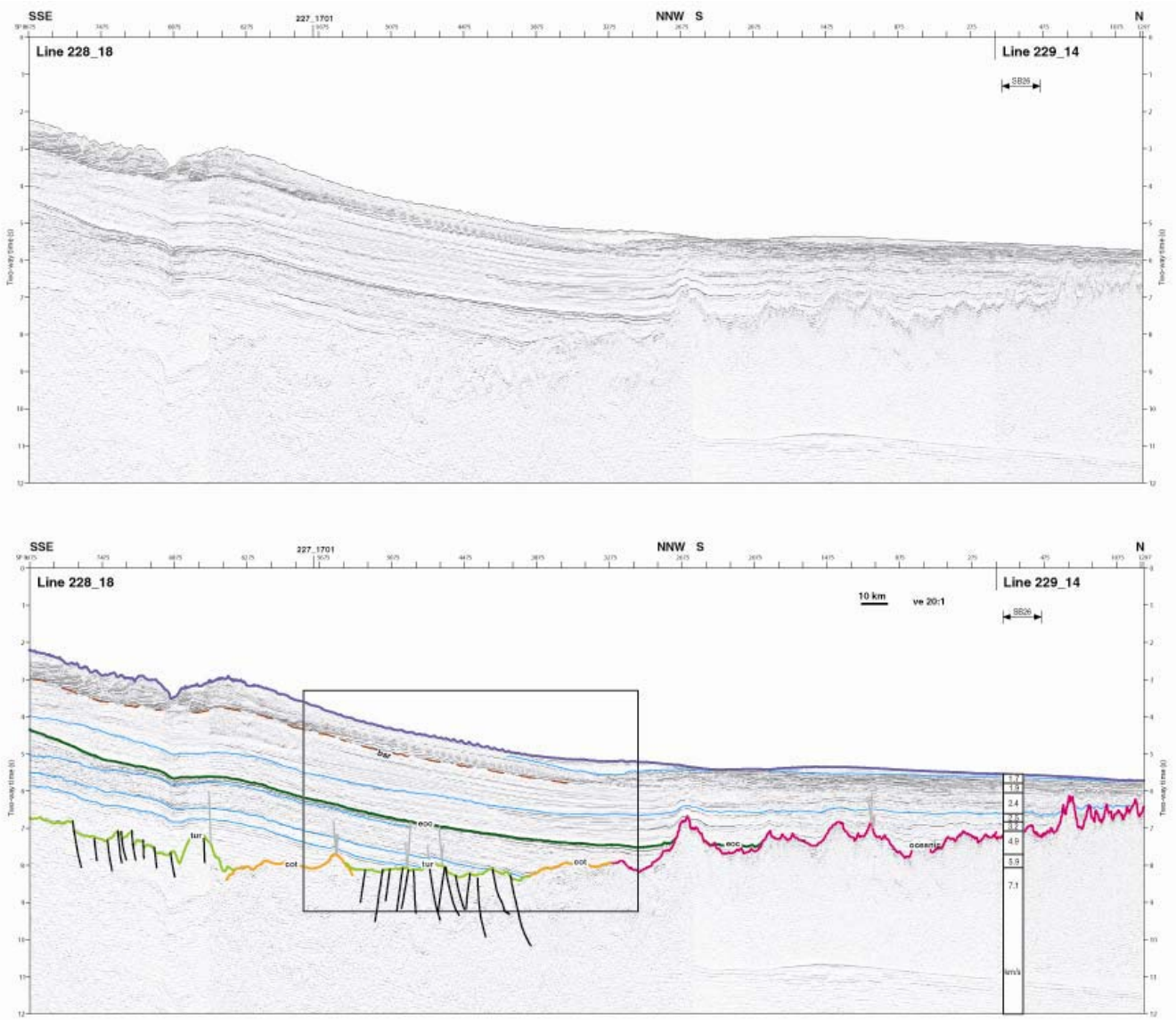

Figure 4.3. Uninterpreted and interpreted seismic reflection profiles of Line 228_18. Vertical exaggeration (ve) is calculated at the sea-floor. Boxed section is displayed in detail in Figure 4.29.

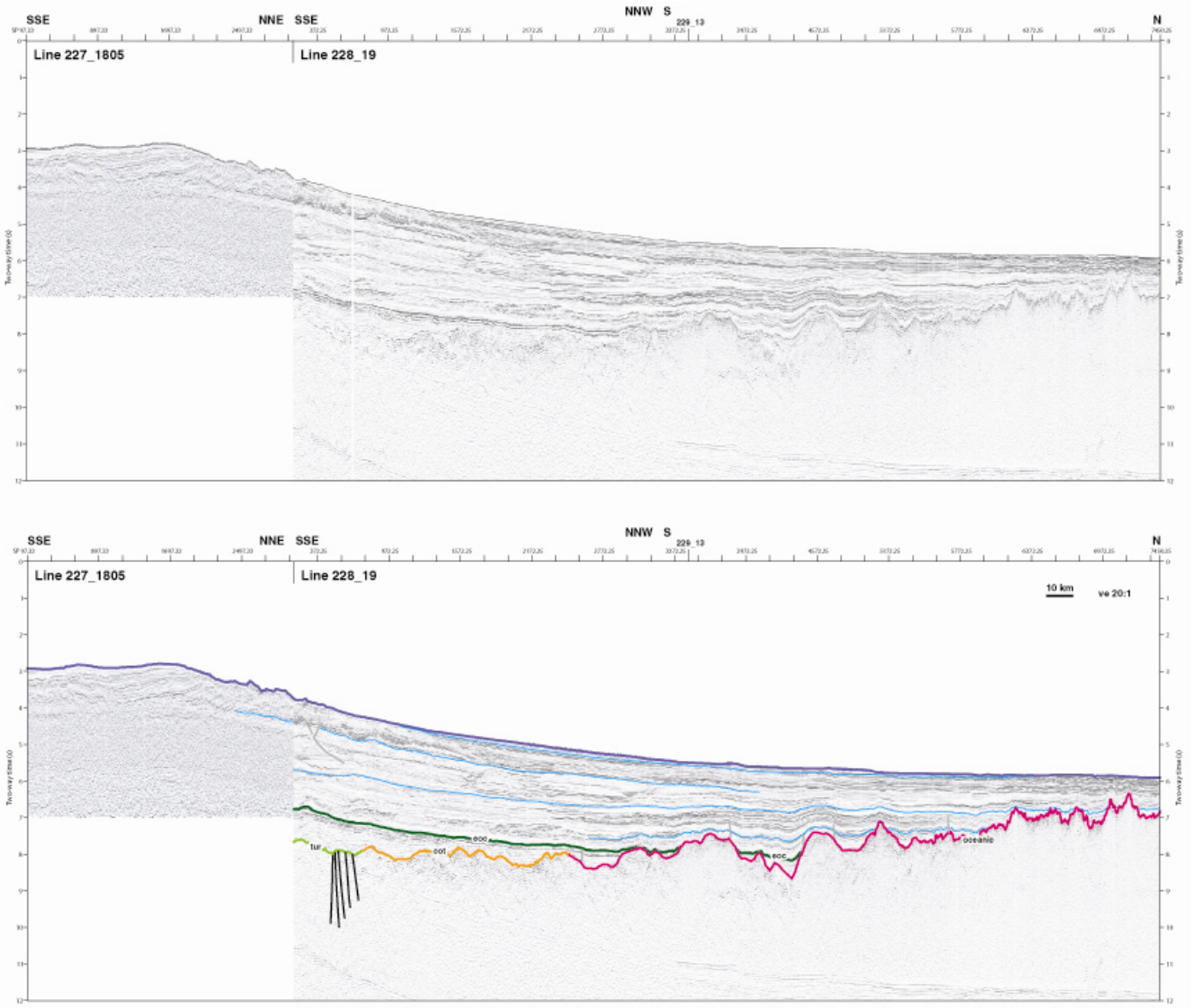

Figure 4.4. Uninterpreted and interpreted seismic reflection profiles for Line 228_19. Vertical exaggeration (ve) is calculated at the sea-floor.

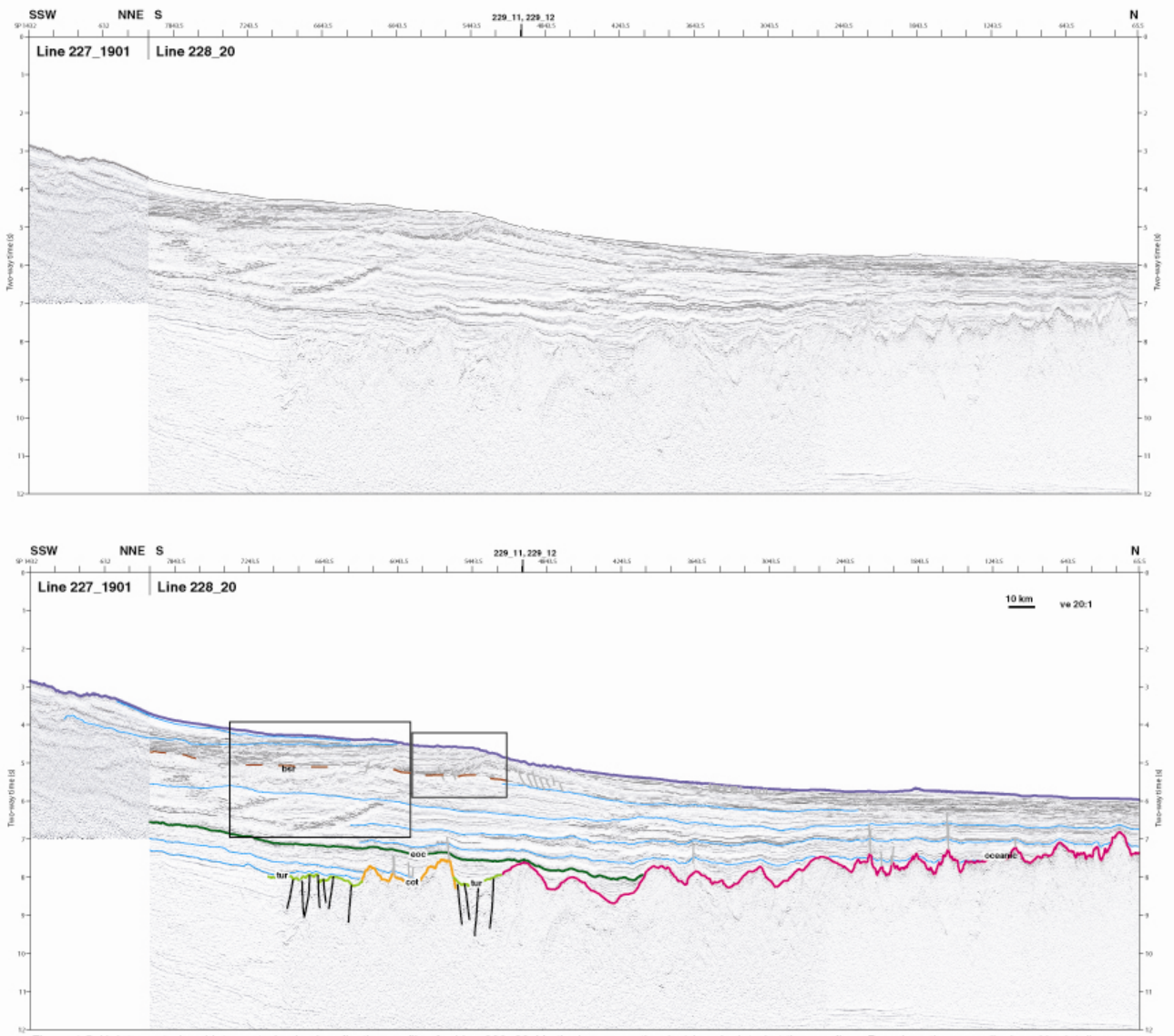

Figure 4.5. Uninterpreted and interpreted seismic reflection profiles for Line 228_20. Vertical exaggeration (ve) is calculated at the sea-floor. Boxed sections are displayed in detail in Figures 4.31 and 4.32.

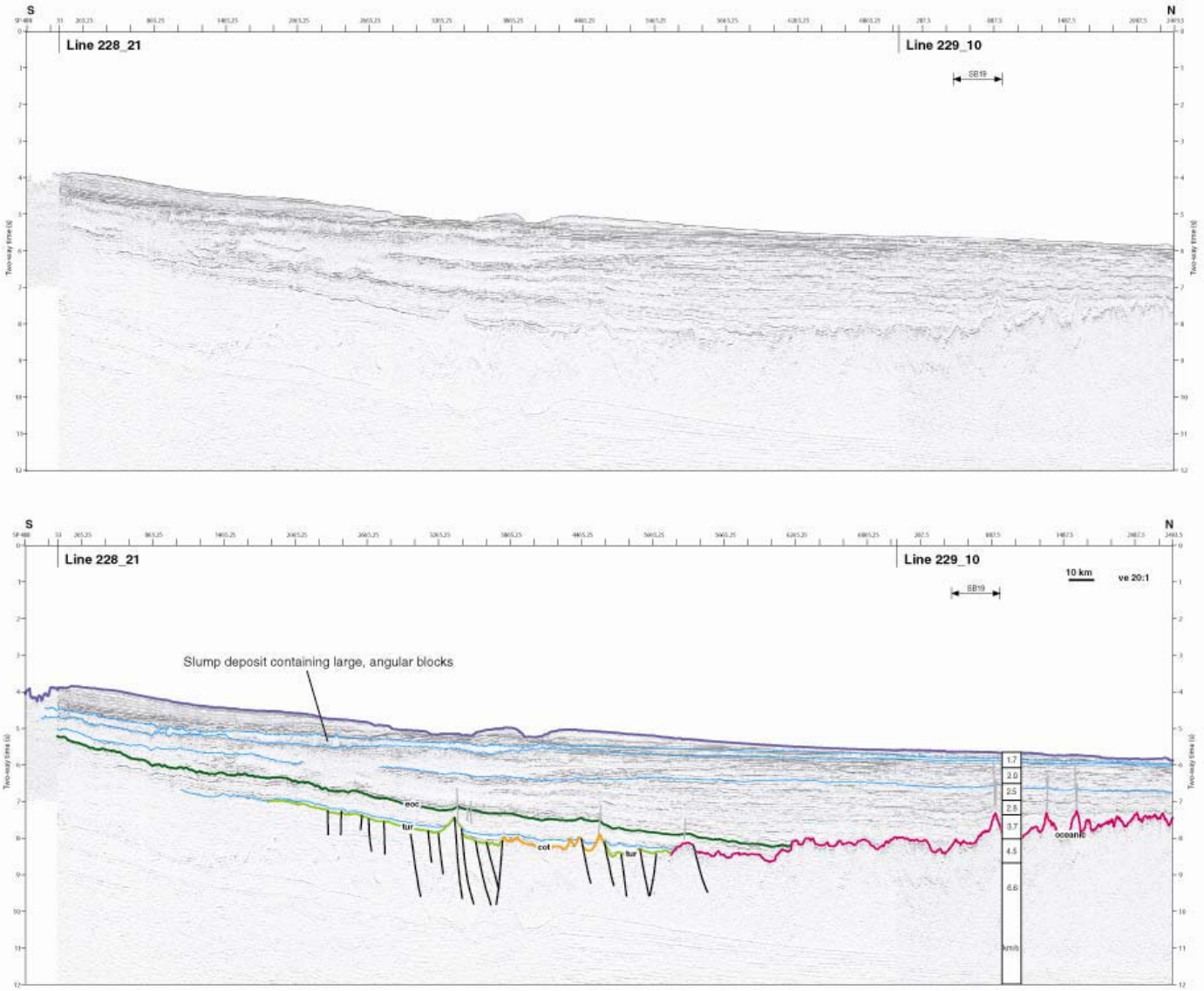

Figure 4.6. Uninterpreted and interpreted seismic reflection profiles for Line 228_21. Vertical exaggeration (ve) is calculated at the sea-floor.

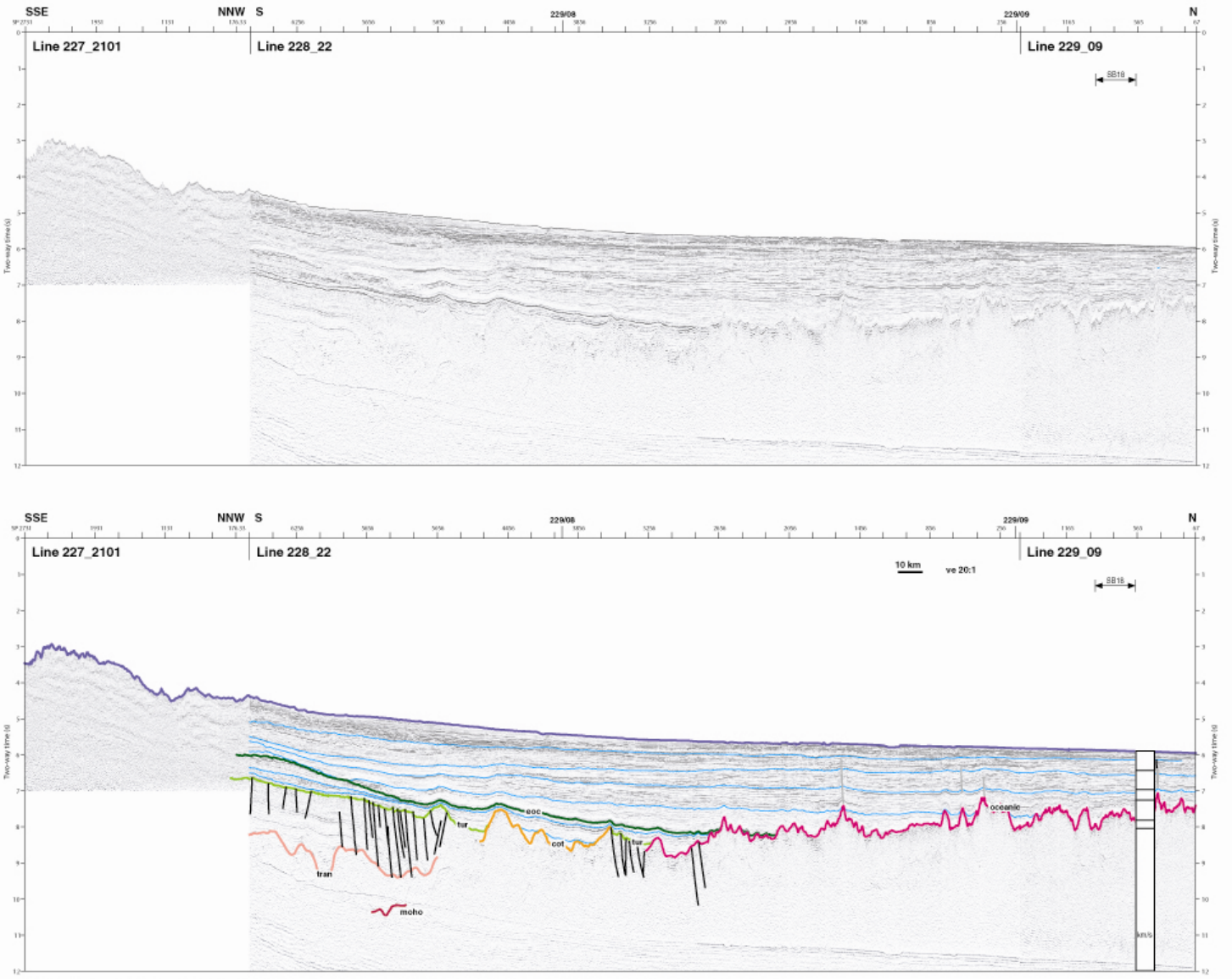

Figure 4.7. Uninterpreted and interpreted seismic reflection profiles for Line 228_22. Vertical exaggeration (ve) is calculated at the sea-floor.

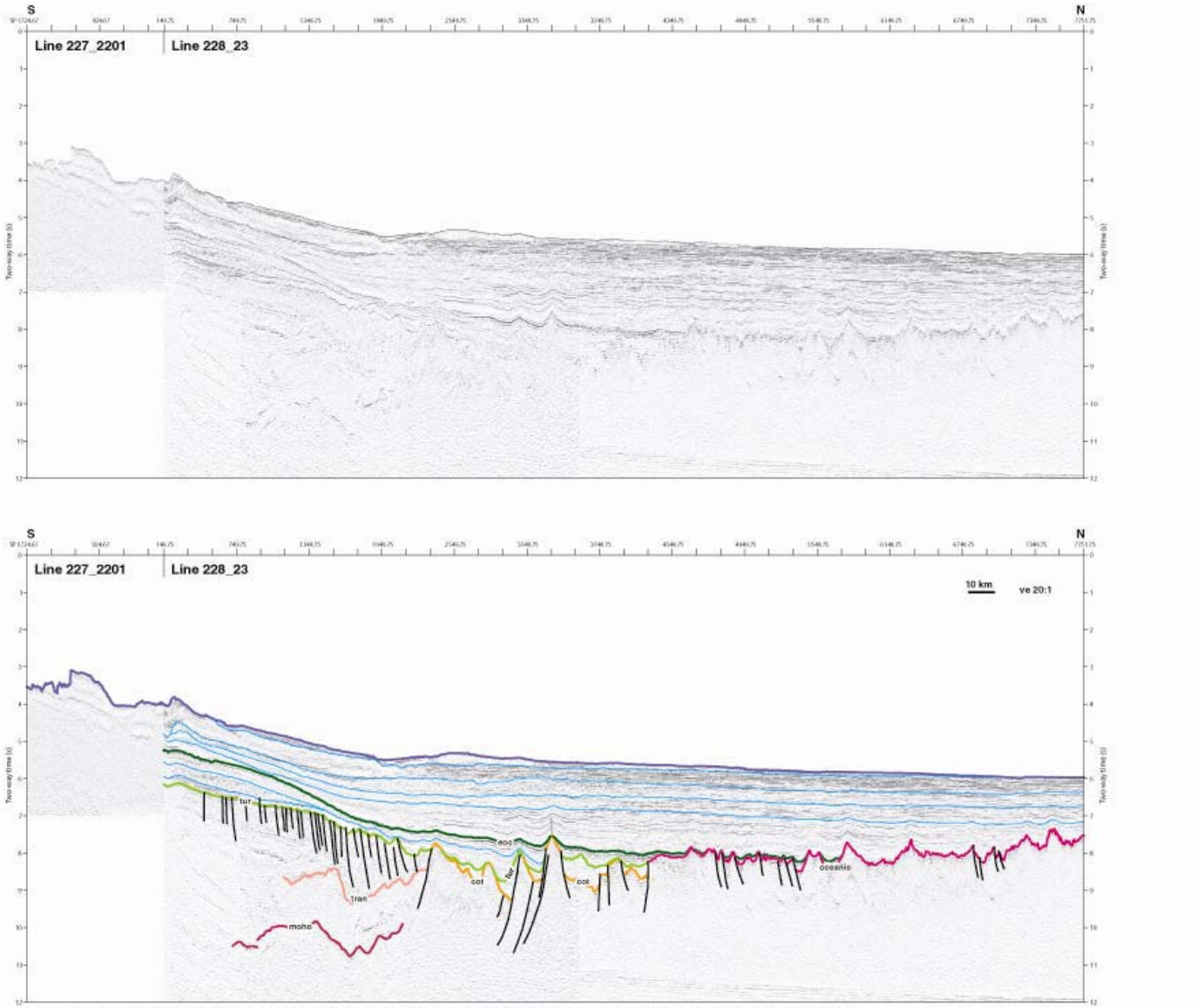

Figure 4.8. Uninterpreted and interpreted seismic reflection profiles for Line 228_23. Vertical exaggeration (ve) is calculated at the sea-floor.

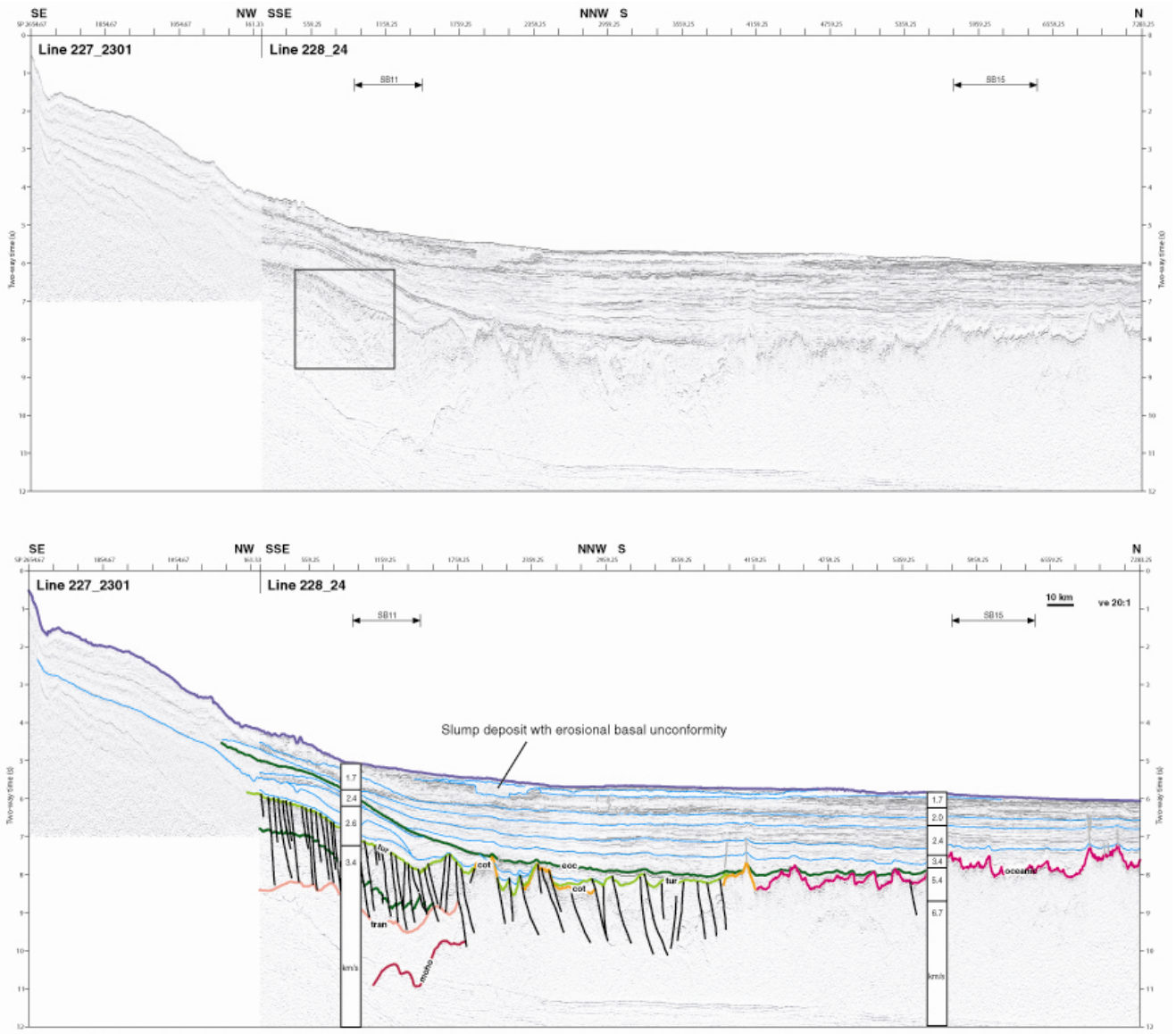

Figure 4.9. Uninterpreted and interpreted seismic reflection profiles for Line 228_24. Vertical exaggeration (ve) is calculated at the sea-floor.

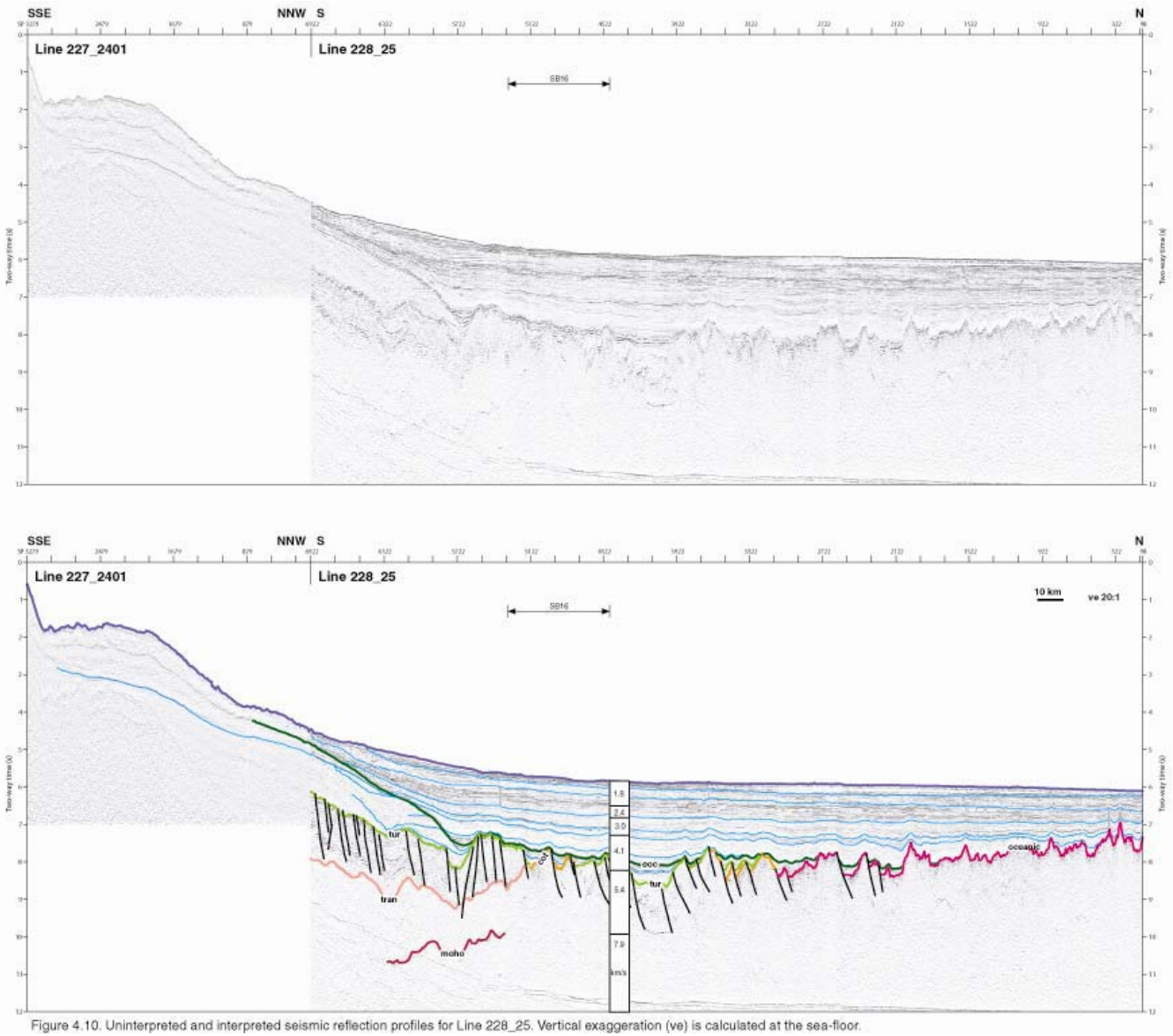

Figure 4.10. Uninterpreted and interpreted seismic reflection profiles for Line 228_25. Vertical exaggeration (ve) is calculated at the sea-floor.

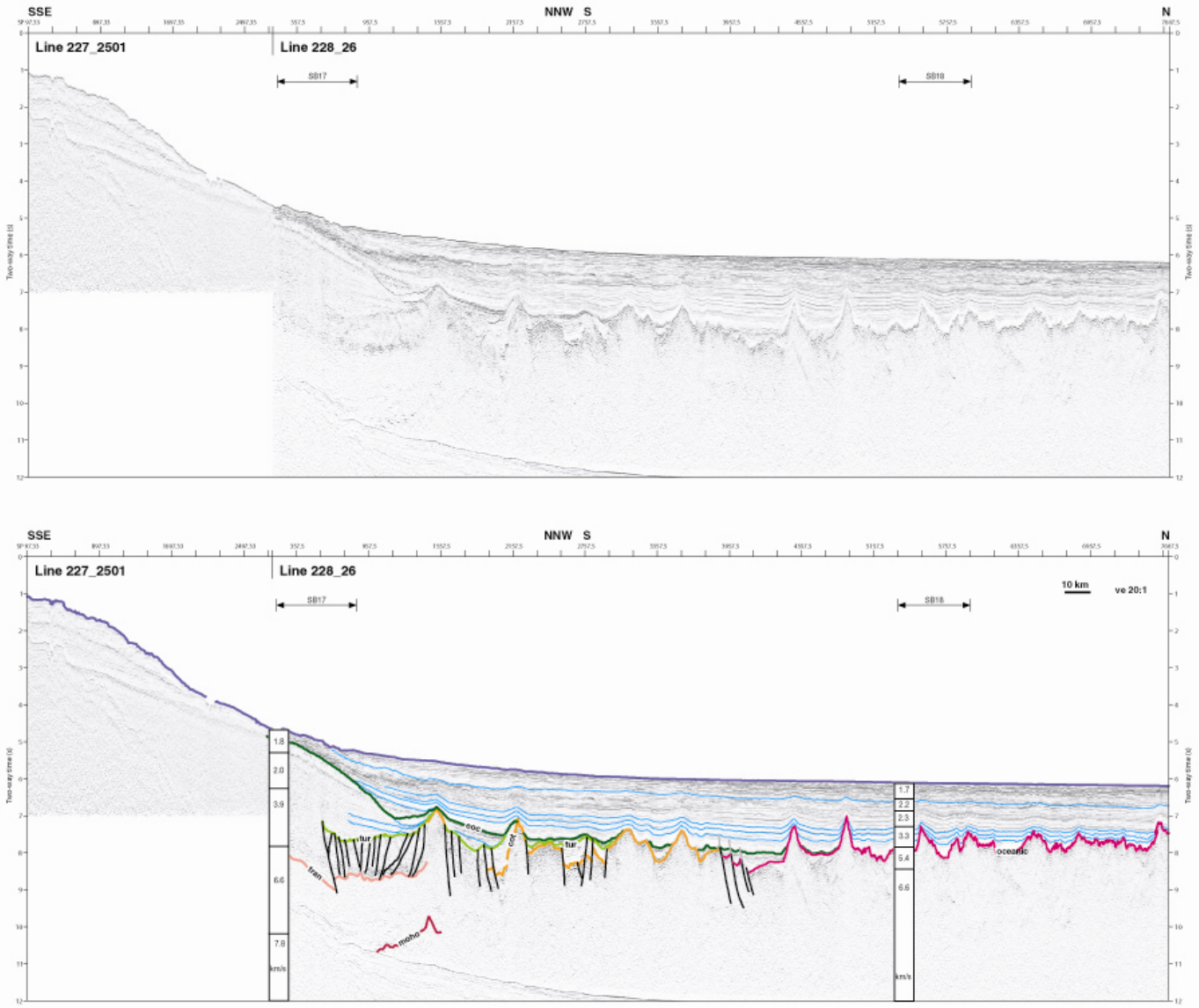

Figure 4.11. Uninterpreted and interpreted seismic reflection profiles for Line 228_26. Vertical exaggeration (ve) is calculated at the sea-floor.

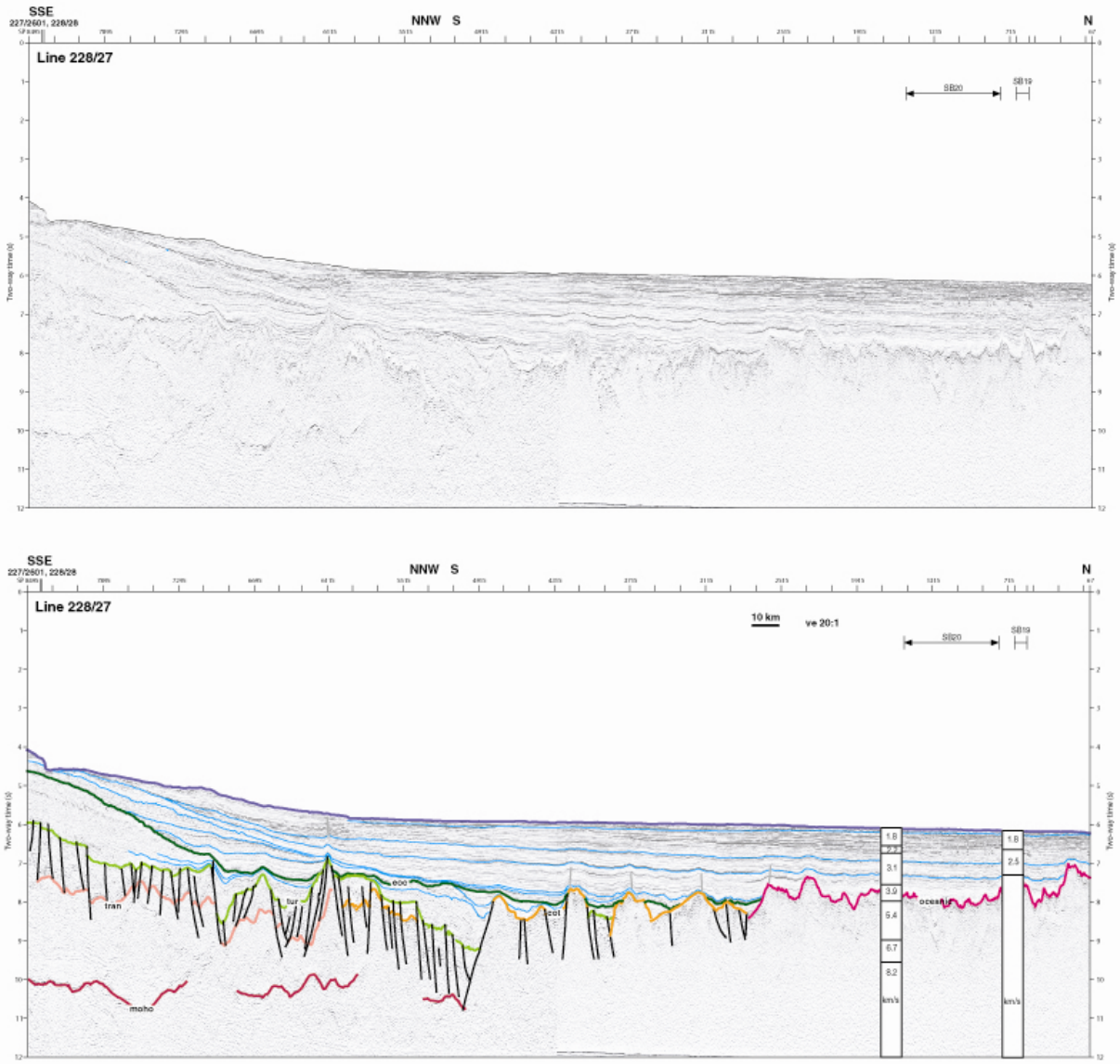

Figure 4.12. Uninterpreted and interpreted seismic reflection profiles for Line 228_27. Vertical exaggeration (ve) is calculated at the sea-floor.

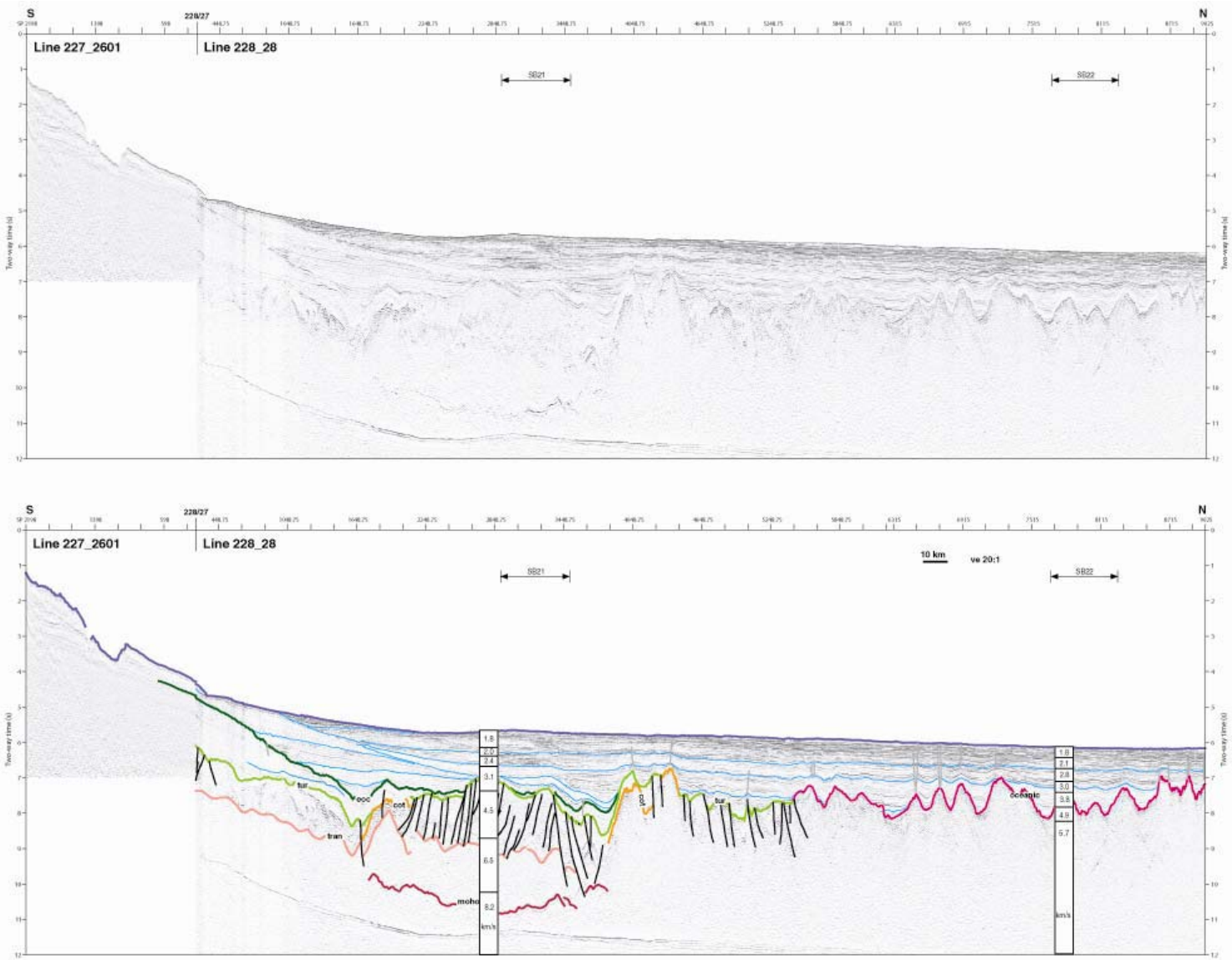

Figure 4.13. Uninterpreted and interpreted seismic reflection profiles for Line 228_28. Vertical exaggeration (ve) is calculated at the sea-floor.

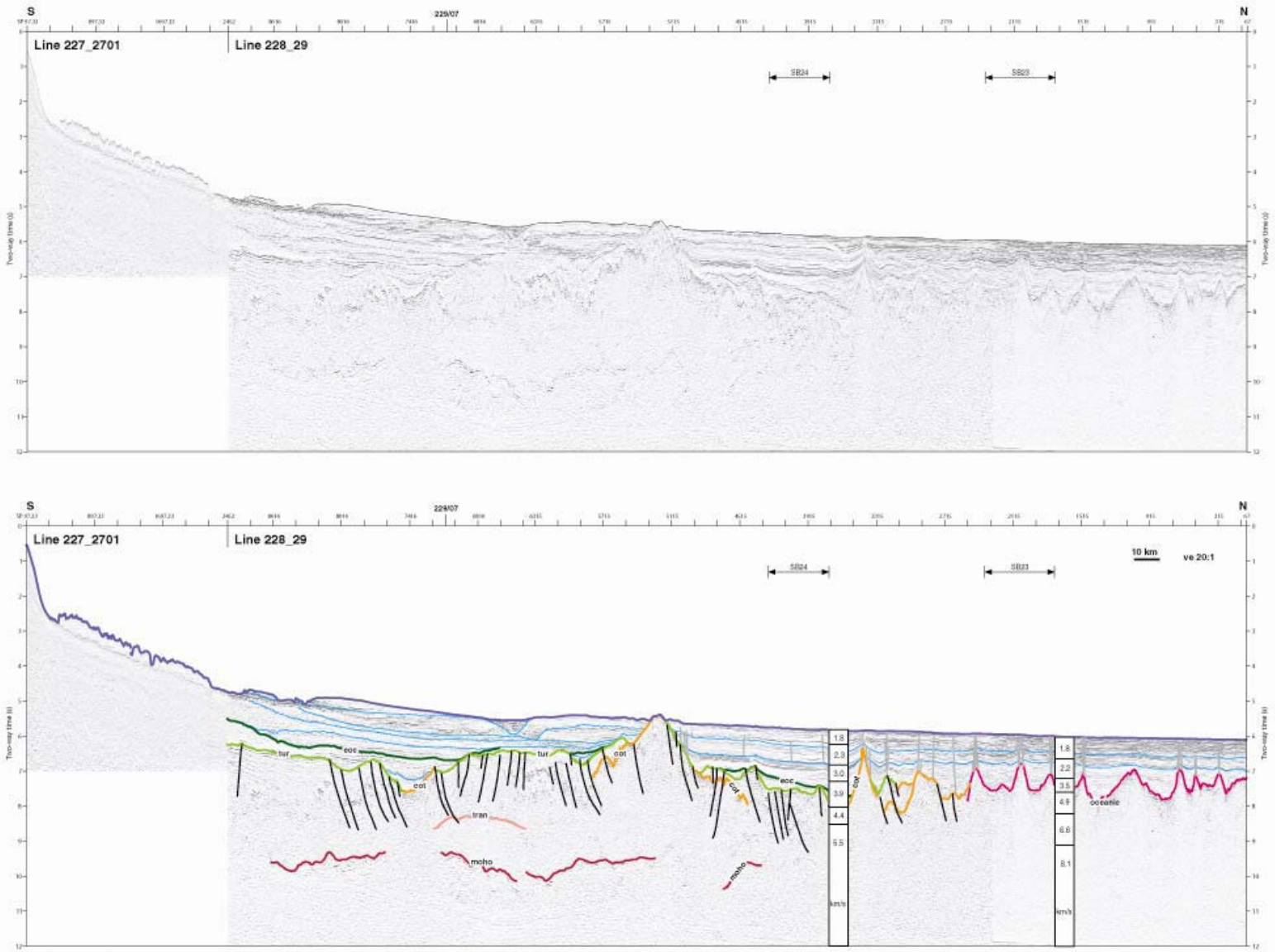

Figure 4.14. Uninterpreted and interpreted seismic reflection profiles for Line 228_29. Vertical exaggeration (ve) is calculated at the sea-floor.

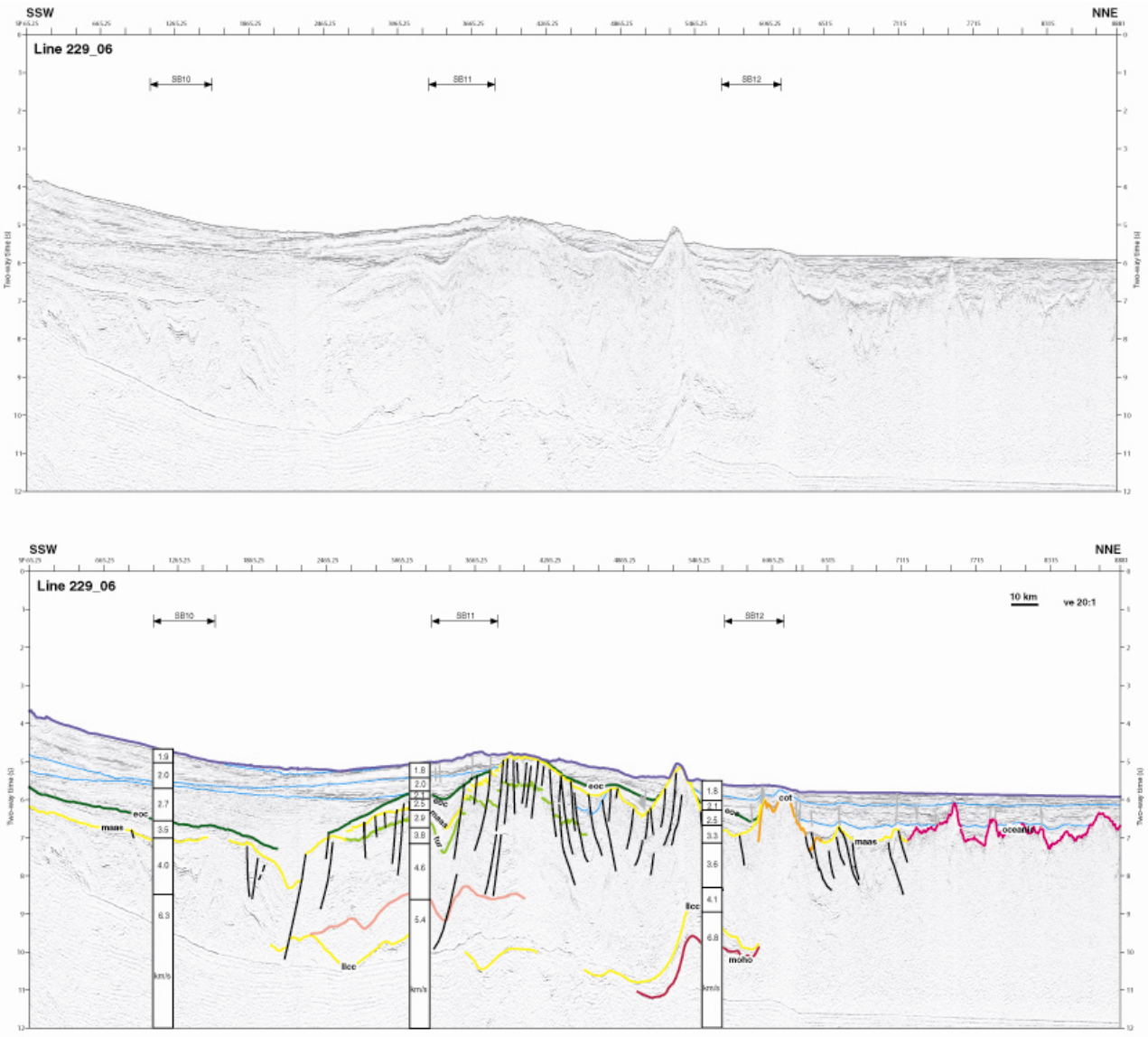

Figure 4.15. Uninterpreted and interpreted seismic reflection profiles for Line 229_06. Vertical exaggeration (ve) is calculated at the sea-floor.

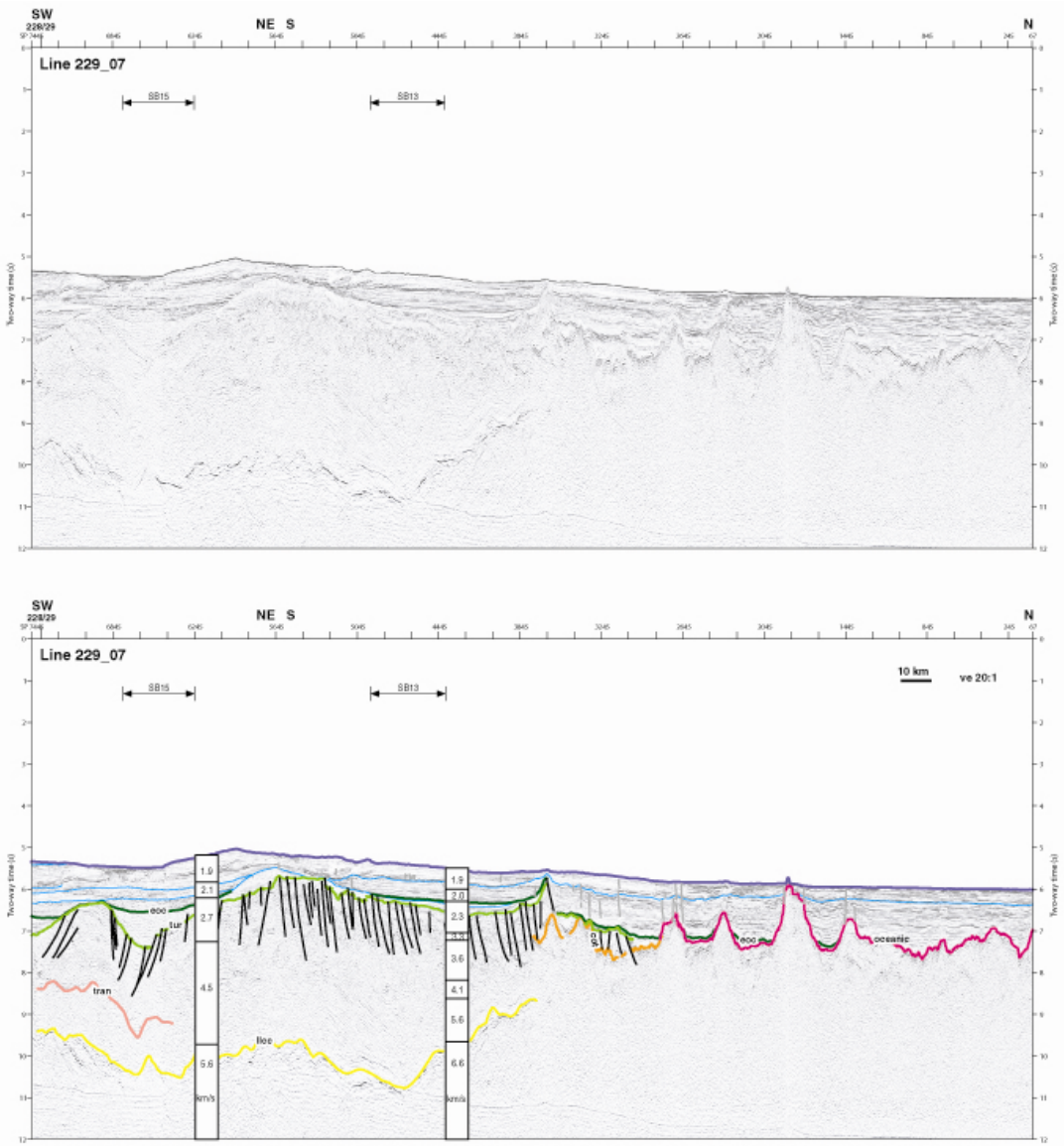

Figure 4.16. Uninterpreted and interpreted seismic reflection profiles for Line 229_07. Vertical exaggeration (ve) is calculated at the sea-floor.

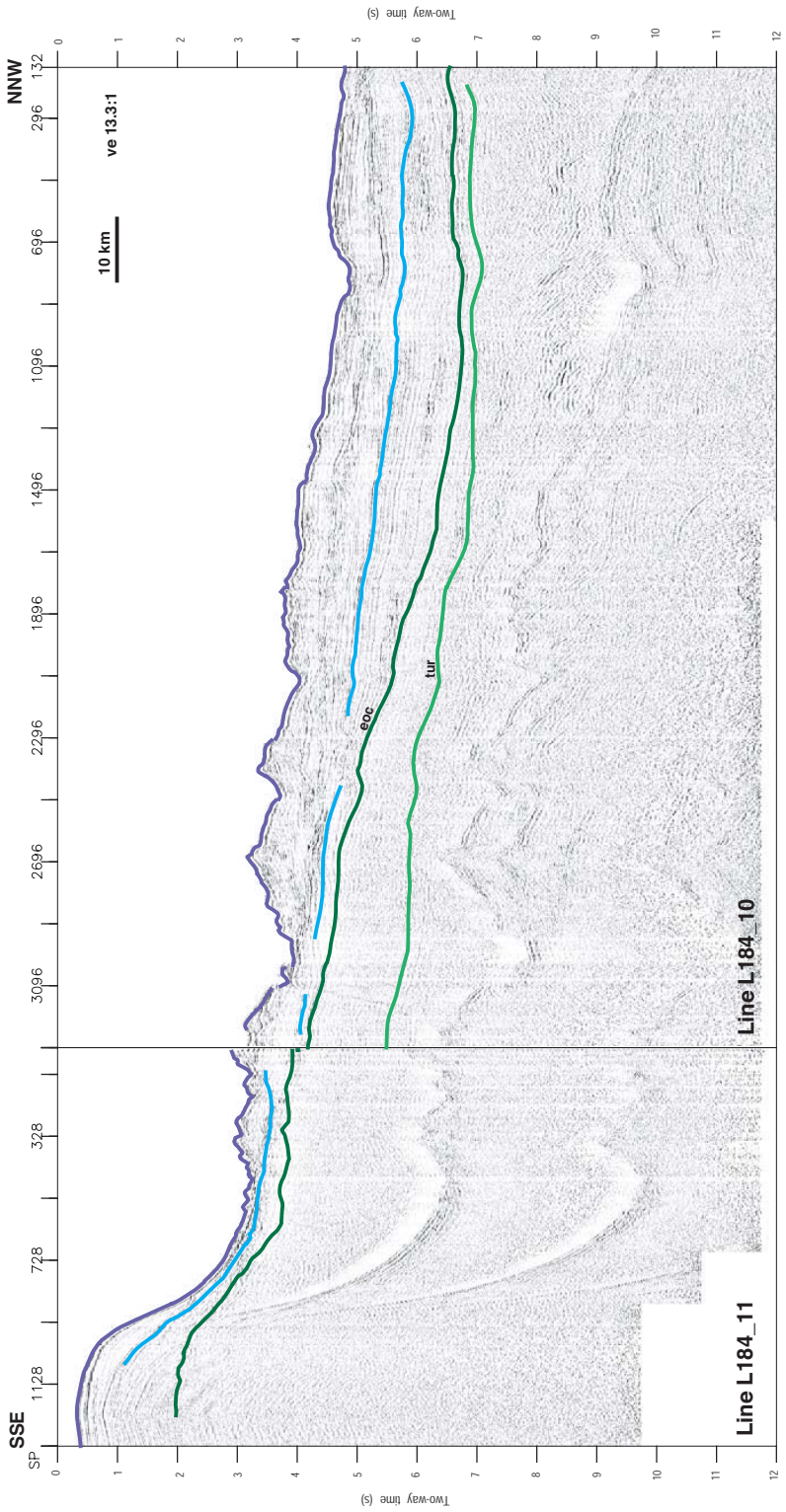

Figure 4.17: USGS, survey L184 Lines 10 and 11 as labelled. Strong multiple reflections beneath the continental slope and shelf prevent the imaging of the base of sediments.

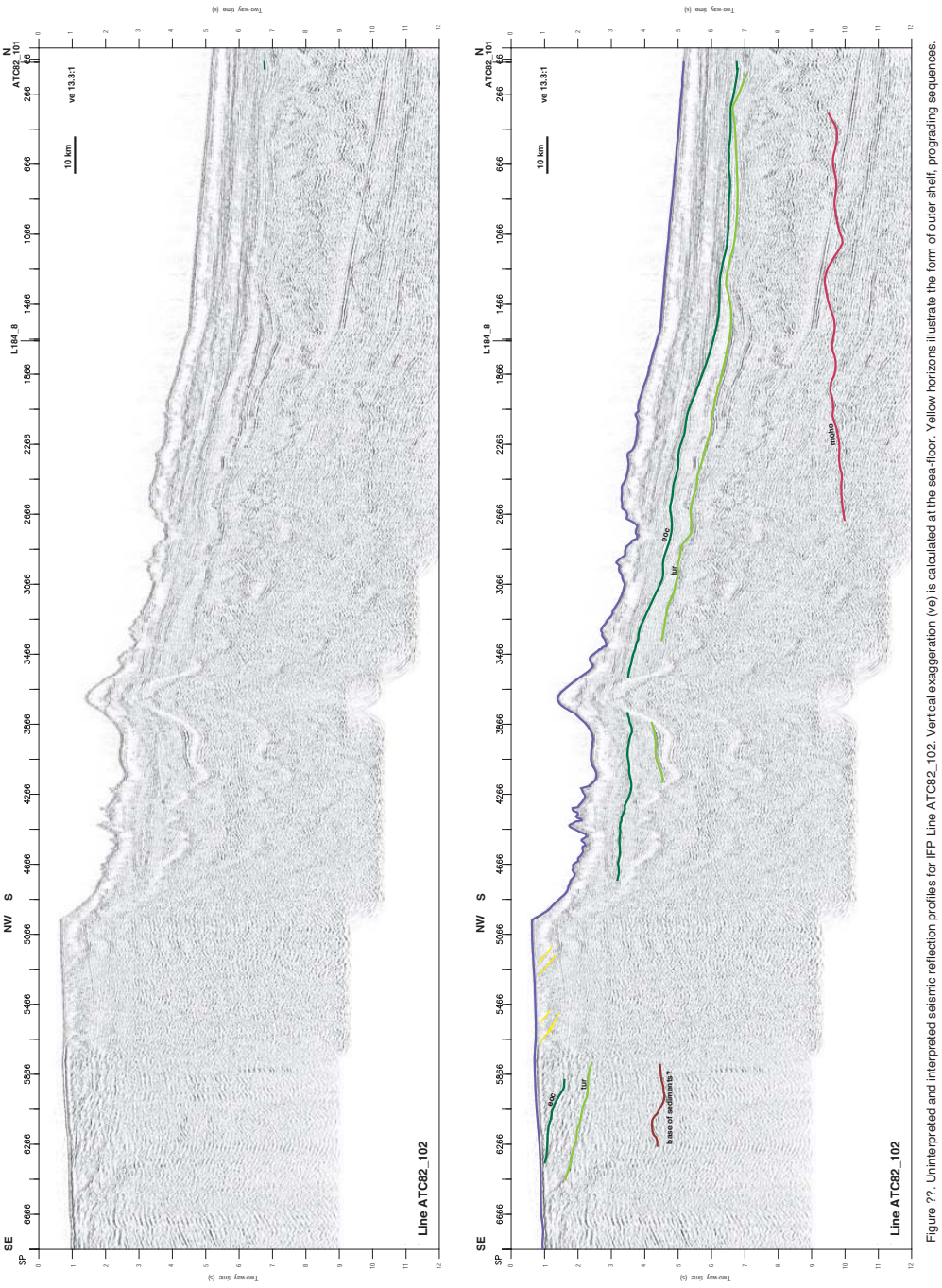

Figure ??: Uninterpreted and interpreted seismic reflection profiles for IFP Line ATC82_102. Vertical exaggeration (ve) is calculated at the sea-floor. Yellow horizons illustrate the form of outer shelf, prograding sequences.

Figure 4.18: ifp, atc82_102.

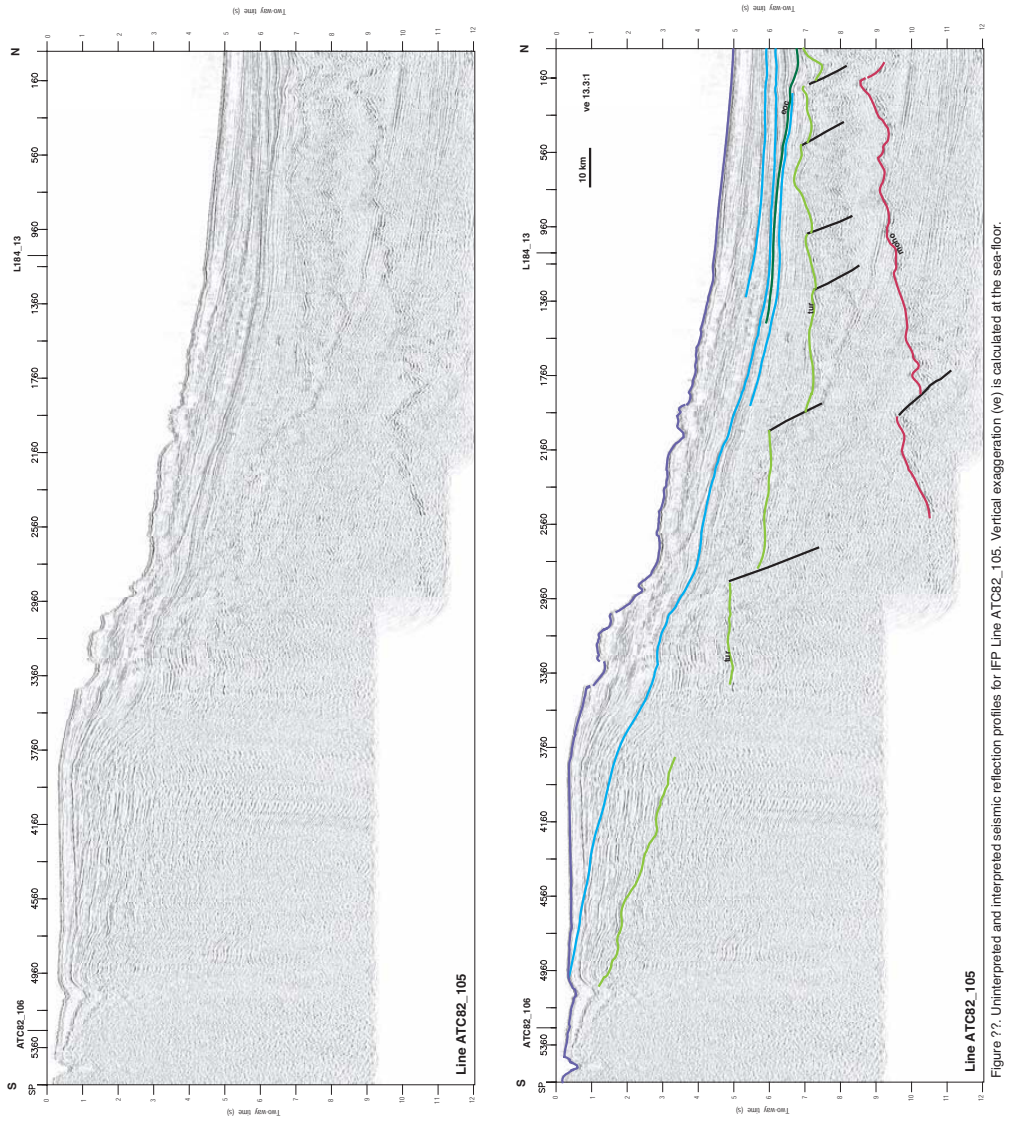

Figure ??. Uninterpreted and interpreted seismic reflection profiles for IFP Line ATC82_105. Vertical exaggeration (ve) is calculated at the sea-floor.

Figure 4.19: ifp, atc82_105.

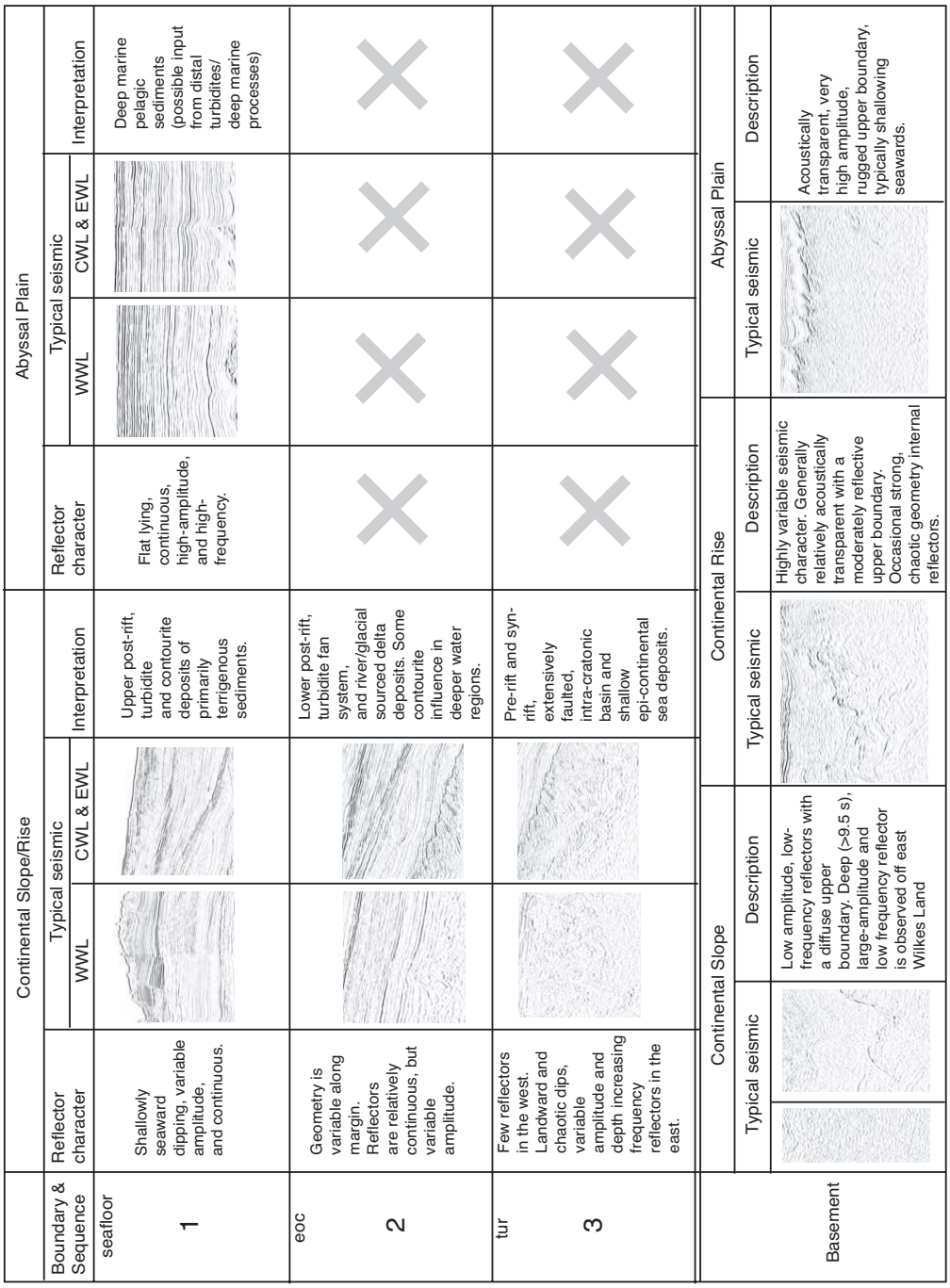

Figure 4.20: Stratigraphic summary of sequences interpreted in MCS data from the Wilkes Land margin. Variation in character and geometry of reflectors occurs along this extensive margin sector, and also across the margin with changing water depth and depositional environment.

4.4 Sequence 1: upper post-rift sediments

Reflector configuration and geometry of Sequence 1 are highly variable along the Wilkes Land margin. Changes in reflector character and structure occur on all scales. Clinoform reflectors are reported in survey ATC82 seismic profiles from east Wilkes Land beneath the outer shelf [Eittreim *et al.*, 1995]. Generally, however, reflectors grade from shallowly seaward dipping on the continental slope and rise to flat lying in the abyssal plain, mantling the underlying oceanic crust. Reflectors are also relatively continuous and broadly parallel, and exhibit consistently high amplitudes, except in low-amplitude zones below a bottom simulating reflector (BSR).

West Wilkes Land profiles, Lines GA-228_18 to GA-228_21, are characterised by reflectors relatively concordant with the underlying *eoc* unconformity, dipping shallowly seaward. Whereas, the central and east Wilkes Land profiles are characterised by relatively flat-lying reflectors that onlap the *eoc* unconformity landward, and offlap seaward onto oceanic crust. Lines GA-228_27 to GA-228_29 exhibit internal erosional unconformities and onlap surfaces, these are not observed off west Wilkes Land. The present-day seafloor, the top of Sequence 1, represents an angular unconformity for much of the margin, up to 1 s TWT of strata are abruptly truncated at high angles by canyons and channels, e.g. Line GA-228_18, Shot Points (SPs) 6700-6900.

The *eoc* unconformity represents the base of sequence 1 for all Wilkes Land margin sectors. Beneath the upper continental rise and continental shelf the unconformity exhibits evidence of erosion of up to 1.5 s of underlying sequence 2 strata, e.g. Line GA-228_25. The unconformity itself is often a relatively high amplitude reflector that is easily identified, however, the distinct onlap pattern of the overlying strata of sequence 1 is the most striking characteristic of this unconformable surface.

The thickness of seismic sequence 1 varies from 0 to >3 s TWT and is highly variable along the margin. A thick sequence (>3 s) is located off west Wilkes Land, predominantly between the shelf break and the abyssal plain. In contrast, sequence 1 is almost entirely absent from the outer continental slope off central-east Wilkes Land, e.g. Line GA-228_28. Refraction (from sonobuoys) and interval velocities (derived from semblance analysis) between 1.6 and 4 km/s (average $\approx$ 2.2 km/s) are recorded from sequence 1. The highest velocities in this range are recorded for the more deeply buried sediments off west Wilkes Land.

Sequence 1 is broadly interpreted as an onlap-fill sequence [Sangree & Widmier, 1977], composed primarily of turbidite, contourite, and hemipelagic deposits. Limited drilling on the outer rise, off the east Wilkes Land margin (DSDP sites 268 and 269), recovered sediment consisting of fine-grained turbidite facies and hemipelagic sediment in the lower

section, and coarser-grained turbidite facies, contourites and hemipelagic sediments in the upper section [Hayes & Frakes, 1975]. Reflector configuration and the geometry of erosional surfaces and channels are interpreted to represent a seaward migrating and laterally shifting turbidite fan system.

The modern continental slope, comprising an intricate network of downslope, broadly north-south oriented, canyons that transition into numerous channels on the continental rise, provides an analogue for the palaeo-fan system. Levee and overbank deposits form proximally to the channels, these are subject to downslope and geostrophic currents that preferentially entrain and transport different components of turbid sediment currents. The finest-grained components are likely transported laterally by along margin, contour hugging geostrophic currents, whereas larger, heavier sediment grains form the more proximal channel overbank and levee deposits.

Sequence 1 stratigraphy exhibits a wide range of erosive and constructional sedimentary structures, indicative of a dynamic and at times highly energetic depositional environment. No single, regional seismic stratigraphic feature is recognised as an indicator of glacial onset. The thick accumulation of post-Eocene sediments, however, is likely a direct indicator of wet-based, polythermal glacial erosion and sediment transport Powell [1984].

4.5 Sequence 2: lower post-rift sediments

Sequence 2 comprises up to 2.5 s TWT of mostly downlapping or grossly concordant reflectors of variable continuity, amplitude and frequency. The base of Sequence 2, the *tur* horizon, deepens from ∼6 s TWT beneath the outer continental slope to 8 s TWT below the abyssal plain.

Off west Wilkes Land, sequence 2 thins evenly seaward and comprises reflectors dipping shallowly seaward, downlapping onto pre-rift sediments and, transitional and oceanic crust. The overlying *eoc* horizon is relatively conformable with sequence 2 reflectors on Lines GA-228_18 to GA-228_21 and no internal unconformable reflectors are evident.

Profiles east of Line GA-228_22 exhibit greater variation in thickness and internal reflector complexity relative to west Wilkes Land. More steeply dipping, downlapping reflector sequences, are evident beneath the lower continental slope, e.g. Line GA-228_24, that grade seaward into grossly flat-lying reflectors concordant with the underlying unconformity. Internal, erosional unconformities are also inferred based on reflector termination and corresponding changes in reflector geometry. Greater amounts of stratal truncation of upper reflectors (i.e. the *eoc* unconformity) also occurs off east Wilkes Land. Sequence 2 thickens landward on Lines GA-228_26 to GA-228_28 to >2 s TWT

and is locally overlain by less than >0.5 s TWT of Sequence 1.

Sequence 2 is interpreted as a lower post-rift sequence deposited under a regime of relatively slow thermal subsidence rates associated with slow spreading from breakup until the early to middle Eocene [Cande & Mutter, 1982; Tikku & Cande, 1999]. This sequence is interpreted as post-rift for all Wilkes Land margin sectors, except off east Wilkes Land, where growth faulting is interpreted to represent syn-rift deposition.

Several phases of delta development are evidenced along the margin during deposition of this sequence. The broadly sigmoidal and downlapping reflection configuration pattern observed beneath the lower continental slope on Lines GA-228_26 to GA-228_28 is interpreted to represent continental slope (foreset) and rise (bottomset) deposits, associated with delta progradation across the broad and slowly subsiding Wilkes Land margin after breakup. Internal unconformities likely indicate sea level changes and erosion during this initially slowly subsiding environment. The non-marine and continental shelf components of this delta are not imaged in GA-228 and GA-229 survey data, however, aggradational, nearly flat-lying shelf deposits are imaged on Lines ATC82_105 and ATC82_107. Hampton *et al.* [1987] interpret toplap terminations high in the continental slope section to represent either a lowering in sea level or an excess sediment supply relative to subsidence rates that allowed sediment to by-pass the shelf and continue to grow the slope. Along margin erosional channels, e.g. Line GA-228_25, SPs 6100-6300, support the occasional seaward migration of the delta-fan channel system during the deposition of sequence 2.

The geometry of sequence 2 changes off east Wilkes Land. The *tur* unconformity does not represent the base of extensional faulting, and the *tur* horizon shallows seaward from the base of the continental slope before deepening again further seaward, e.g. Line GA-229_06. Sequence 2 is subdivided off east Wilkes Land by the *maas* horizon. Reflectors from the underlying sequence exhibit seismic character and structural similarities to the Late Cretaceous Sherbrook Group and the upper part of the Early Cretaceous Otway Supergroup of the Otway Basin, southeast Australia [Moore *et al.*, 2000]. The unconformity at the top of this sequence (*maas* horizon) is therefore interpreted as being Maastrichtian (~71-65 Ma) in age. Reflectors within the sequence, bounded below and above by the *tur* and *maas* horizons respectively, exhibit divergence towards fault footwalls, indicating that crustal extension continued between eastern Wilkes Land and the southeast Australian margin until the Maastrichtian.

Refraction velocities of 2.30 to 2.71 km/s were recorded from this sequence at sonobuoy GA-228-11 in central Wilkes Land and from sonobuoys GA-229-13 and GA-229-15 in east Wilkes Land. The range of interval velocities inferred from stacking velocity conversion shows a greater variation of 2 to 5 km/s. The higher interval velocities are inferred for

the more deeply buried sequence off west Wilkes Land.

4.6 Sequence 3: Pre-Breakup Sediments

Imaging quality of Sequence 3 is poor off west Wilkes Land relative to central and east Wilkes Land. Sequence 3 thickness reaches up to ~2.6 s TWT (~5 km) below the continental rise off central Wilkes Land, this decreases seaward and typically pinches out entirely against the landward extent of transition zone crust. The lower Sequence 3 reflectors exhibit variable amplitude and dip, and are relatively discontinuous. Upper Sequence 3 reflectors are more continuous, higher frequency, and generally lower and more consistent amplitude.

Sequence 3 is bounded above by the *tur* unconformity and below by the more diffuse *tran* horizon, interpreted as the top of crystalline basement. The *tur* horizon ubiquitously terminates against transition zone or early oceanic crust. The seaward extent to which this horizon is mapped is subjective, particularly as basement topography creates pinch-outs of the underlying reflectors on almost all lines. Many of the basement highs that cause the pinch outs are acoustically transparent, and are likely intrusive igneous bodies or possibly exhumed mantle; their character and genesis are discussed later in greater detail. Distinctly layered and truncated reflectors of Sequence 3 occur seaward of some basement highs, although they are isolated from unequivocal Sequence 3 reflectors, e.g. Line GA-228_24.

Extensive faulting is interpreted within Sequence 3, it is most easily identified in the upper sequence 3, e.g. Lines GA-228_22 and GA-228_23. Faults are almost entirely seaward dipping normal faults, along which rotation of fault blocks has occurred, Figure 4.21. Landward dipping faults, however, are also imaged.

A number of sonobuoys record the seismic velocities of Sequence 3. Velocities recorded in all but the upper-most sequence range from 3.66 to 4.61 km/s. This velocity range correlates closely to the pre-rift sequence from the conjugate southern Australian margin (e.g. Veevers [1987] and Sayers *et al.* [2001]). It also encompasses the range of seismic velocities measured from Beacon Supergroup rocks of 4.1 to 4.4 km/s [Bentley & Clough, 1972]. On the basis of seismic velocity correlations, and the extensive faulting relative to overlying sequences, Sequence 3 is interpreted to represent a pre- and syn-rift sequence that was highly stretched and deformed by extensional rifting processes. By analogy with the pre- and syn-rift geological record of southern Australia, Sequence 3 likely comprises both siliciclastic and cool-water carbonate sub-sequences. Salt sequences (common to rift margins) are not observed in well data from the southern Australian margin, and it is unlikely, given the more southerly location of the Antarctic margin, that evaporites

Figure 4.21: Detail of Line GA-228_24 illustrating reflector truncation and offset associated with faulting. Rotation along faults (e.g. dashed-dot lines), causing landward dips (e.g. dashed lines), is also evident. The top of faulted and extended crust is interpreted as the base of the post-rift sequence.

formed on the Wilkes Land margin. High amplitude, concordant but discontinuous reflectors (e.g. Line GA-228_28, SPs 1100-1600) are likely intrusive sills associated with extensive Jurassic volcanism. The Beacon Supergroup is extensively intruded by Jurassic dolerites [Quilty, 1986], and likely correlates to basal sub-sequences of Sequence 3.

No clear rift-onset unconformity, as defined by Falvey [1974], is evident within Sequence 3 on the Wilkes Land margin. This is likely a function of the complex rift history indicated by subsidence studies on the southern Australian margin [Hegarty *et al.*, 1988; Totterdell *et al.*, 2000]. Modelling indicates 1-2 km of subsidence due to an intracratonic rifting event in the Late Jurassic, 160-140 Ma. This event occurred contemporaneously with extensive igneous activity in Gondwana; represented by the Karoo province in southern Africa and the Jurassic dolerites of south-eastern Australia and Antarctica. Rifting is also inferred at this time between East Antarctica and Africa/South America, ∼150 Ma [Rabinowitz & LaBreque, 1979].

Relatively subdued thermal subsidence followed intracratonic extension and there is no evidence of oceanic crust emplacement. A second extensional rifting event, is inferred from subsidence modelling on the southern Australian margin at ∼100 Ma. Slow thermal subsidence recommences at ∼85-90 Ma and this correlates to the earliest known seafloor spreading anomalies in the Australia-Antarctic Basin (AAB) [Cande & Mutter, 1982].

Slow thermal subsidence is interpreted to relate to the slow (<5 mm/yr HSR) rates of seafloor spreading following breakup [Cande & Mutter, 1982; Tikku & Cande, 1999].

The multiple rift event history and subsequent slow thermal subsidence violates the simple assumptions of Falvey [1974]. Hence, no rift-onset unconformity is identified along the Wilkes Land margin. However, an unconformity within Sequence 3, e.g. Line GA-228_24 (dark green horizon, SPs 0-1500), is inconsistently observed on seismic profiles from central and east Wilkes Land. This horizon represents a change in seismic character from the overlying relatively high frequency, landward dipping reflectors bounded by normal faults, to the underlying, more chaotic reflection patterns. This horizon likely represents an unconformity associated with either the Late Jurassic or mid-Cretaceous rifting events and correlates to the *K2* reflector of Eittreim & Smith [1987], which they interpreted as a rift-onset unconformity. The horizon may represent the erosional, upper boundary of the Beacon Supergroup.

Evidence of syn-rift deposition is sparse, reflector divergence and growth faulting can be inferred on Line GA-229_06 only. Wilson *et al.* [2001] note similar broad absences of syn-rift sediments, as represented by stratal divergence towards fault footwalls, on the west Iberian margin also. They suggest this may be due to resedimentation of syn-rift sediments, a lack of hanging-wall rotation, or the syn-rift interval being too thin to resolve in MCS data.

Although some intrusive igneous activity is interpreted in the pre-rift sequence, very little evidence of extrusive volcanism, in the form of seaward dipping reflector sequences, is evident in the late pre-rift and syn-rift sequence. The absence of such evidence supports the contention that the southern Australia-East Antarctic rift margins are non-volcanic (e.g. Nichols *et al.* [1981] and Totterdell *et al.* [2000]).

4.7 Regional Unconformities: Ages and Correlations

Although many local unconformities are evident in seismic reflection data, only two are correlatable along the entire Wilkes Land margin. These two unconformities separate Sequences 1, 2, and 3 as described above. The *eoc* unconformity forms the base of a sequence of clearly onlapping strata. It is interpreted here to represent a change in tectonic setting of the Wilkes Land margin at early to middle Eocene time (∼50 Ma). The lower of the two regional unconformities (*tur*) is marked by a strong reflector that represents the upper limit of the pre-rift sedimentary sequence for the west and central Wilkes Land sectors. However, extension and syn-rift sedimentation continues above this unconformity off east Wilkes Land and Terre Adélie.

These unconformities are identified as U3 and U2 by Wannesson *et al.* [1985], and T

and K1 by Eittreim & Smith [1987] and Hampton *et al.* [1987] on the east Wilkes Land-Terre Adélie margin. Tanahashi *et al.* [1994] sought to simplify the nomenclature used for the Wilkes Land seismic stratigraphy and renamed the U3/T and U2/K1 unconformities as WL2 and WL3 respectively. De Santis *et al.* [2003] again redefined the nomenclature and provide a detailed stratigraphy for the post-rift sedimentary sequence of the east Wilkes Land-Terre Adélie margin. Analysis of line ties between GA-228, L184 and ATC82 survey data indicates that the WL3 and WL2 unconformities correspond to the *tur* and *eoc* unconformities respectively. The WL2 unconformity was initially interpreted by Hampton *et al.* [1987] as the result of a relative sea-level drop at ∼65 Ma. However, a second, less favoured interpretation that associated the unconformity with a global plate re-organisation at ∼42 Ma was also considered. The WL3 unconformity is interpreted by Wannesson *et al.* [1985] and Eittreim & Smith [1987] as the breakup unconformity, this accords with our interpretation that *tur* is associated with breakup.

More recent interpretations by Eittreim *et al.* [1995] and Escutia *et al.* [1997] suggest that the WL2 surface is an erosive unconformity caused by glacial downcutting at ∼40 Ma. These workers invoke fast-flowing ice streams, grounded as far as the shelf break, to erode the pre-glacial continental shelf. De Santis *et al.* [2003] suggest that the unconformity does not have a glacial origin and we accord with this re-assessment. Several lines of evidence contraindicate a glacial erosive genesis and 40 Ma timing for the *eoc* or WL2 unconformity.

The margin wide extent of the *eoc* unconformity requires that if it is associated with glacial erosion, glaciation would necessarily have been continent wide at 40 Ma. The relative importance of the contributing factors to Tertiary polar glaciation, such as declining CO_2 concentrations, opening of deep water pathways around the entire continent and the presence of high elevation areas, is not well constrained. The timing of the rapid onset of glaciation extending beyond isolated highland areas, however, near the Eocene-Oligocene boundary (∼34 Ma), is well constrained by Ocean Drilling Project (ODP) data (Legs 188) (as discussed in Chapter 2). This evidence precludes the possibility of a glacially controlled *eoc* unconformity at 40 Ma.

A further problem to a glacial origin is the continuity of the *eoc* unconformity surface, from the lower continental rise to the continental shelf, which suggests a relatively synchronous formation. To fulfil this timing criteria and invoke a glacial genesis for this unconformity, erosion on the slope and rise is required contemporaneously with a glacial advance across the shelf; there is no *a priori* reason why such events should be synchronous. Clearly the *eoc* unconformity can not have a direct glacial origin beyond the shelf break, as grounding ice on the continental slope is not feasible.

We suggest an early to middle Eocene timing, and tectonic origin for the *eoc* uncon-

formity. Comparison of Wilkes Land and southern Australian margin MCS data reveals an almost symmetric stratigraphic pattern from the breakup unconformity until the middle Tertiary. The prominent onlap surface (*eoc* horizon) is dated as early Eocene on the basis of its correlation with similar onlap surfaces in the Great Australian Bight (base Dugong sequence, Figure 4.22, [Totterdell *et al.*, 2000]), in the Otway Basin (base Nirrinda Group, [Moore *et al.*, 2000]) and in the Sorell Basin on the west coast of Tasmania (unconformity U5, [Hinz *et al.*, 1986]). The unconformity is dated in a number of wells on the southern Australian margin as early to middle Eocene (∼50 Ma) [Totterdell *et al.*, 2000]. The stratigraphic position and characteristic onlap pattern of the *eoc* boundary is compelling evidence of a synchronous event in a relatively narrow oceanic basin (<400 km, based on spreading rates of Tikku & Cande [1999]).

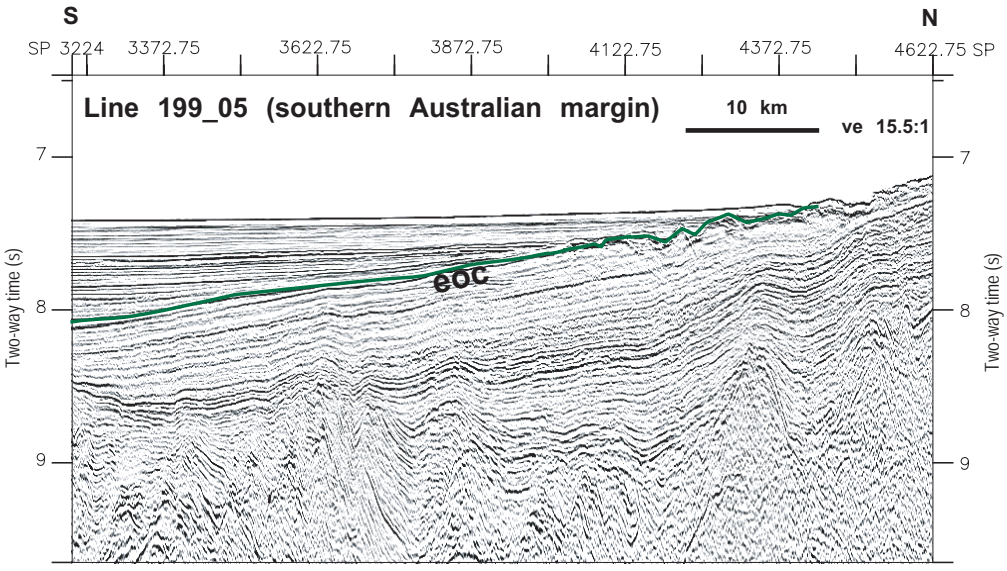

Figure 4.22: This strong onlap surface on the southern Australian margin (dark green horizon) is interpreted to correlate to the *eoc* horizon on the Wilkes Land margin. Seismic and well data from the Australian margin indicate an Early- to Mid-Eocene age for this unconformity.

The inferred timing of the *eoc* unconformity corresponds to the end of ultra-slow (∼1.5 mm/yr half rate) seafloor spreading rates, [Tikku & Cande, 1999]. Associated with this spreading rate increase is an increase in the thermal subsidence in wells on the southern Australian margin at ∼50 Ma [Totterdell *et al.*, 2000]. The result of an increased subsidence and spreading rate is a wider, deeper ocean basin that could have allowed the initiation of deep water, erosive currents and resulted in the formation of the *eoc* unconformity. Increased subsidence may have increased the gradient of the continental slope, and also have destabilised shelf and upper-continental slope sediments, resulting

in widespread slumping and erosion on the continental slope.

The *tur*, angular unconformity represents the top of extensional faulting and structuring off Wilkes Land. Accordingly, it is interpreted to represent breakup and the transition from intracratonic, continental stretching to sea floor spreading. This horizon can be correlated for over 1500 km along the margin, it is marked by a strong reflector which exhibits significant topography (0.5-1 s TWT) and fault-plane, ridge surfaces. The timing of this unconformity is constrained broadly through interpretation of seafloor isochrons as 83-95 Ma.

On the Southern Australian margin, the base of the post-rift sequence (base Hammerhead sequence of Totterdell *et al.* [2000]) is estimated as Santonian (∼85 Ma). This is underlain by the syn-rift Tiger Sequence. No clear syn-rift sequence is interpreted on the Wilkes Land margin, but the reflection and structural character of the *tur* unconformity is similar to the base Tiger sequence unconformity of Totterdell *et al.* [2000] [Colwell *et al.*, in press]. Identification of *P. mawsonii* spore-pollen in well data, from the southern Australian margin, dates the oldest sediments above this unconformity as early Turonian (∼90 Ma) [Totterdell *et al.*, 2000]. Therefore, the *tur* unconformity represents an erosional unconformity at ∼90-85 Ma.

The identification of the *tur* and *eoc* unconformities on the Wilkes Land margin allows an insight into the broad scale, post-rift depositional history of the Wilkes Land margin. The post-rift stratigraphy provides the fullest record of margin evolution since rifting. Stratigraphic interpretation of this sequence is of particular interest as it records the global transition from greenhouse to icehouse conditions, adjacent to the continent where this transition initiated. The distribution of post-rift sediments and structures imaged within Sequences 1 and 2 are discussed later in this chapter.

4.8 Continental Crust

Continental crust is interpreted at the landward extent of all MCS profiles, beneath the continental shelf and slope, and extended continental crust is interpreted to extend beneath the continental rise on a number of profiles. Strong water bottom multiple reflections, ubiquitous on the Antarctic margin Larter *et al.* [1990], prevent clear imaging through sediments in continental shelf data. However, it is possible to estimate a minimum sediment thickness in L184 and ATC82 data. Sediment thickness reaches at least 4 s TWT (∼5-7 km) below the shelf on line ATC_102, and total depth to this surface is ∼5 s TWT. Line drawings of line ATC_103 indicate a similar thickness of continental shelf sediments [Eittreim *et al.*, 1995]. Crustal or *Moho* reflections are not imaged beneath the shelf in MCS or seismic refraction data, hence no constraint on crustal structures

or the thickness of relatively unstretched continental crust is available from seismic data alone. The basement likely comprises metamorphic rocks of the continental shield, as the most common coastal and highland rock outcrops along the Wilkes Land margin are Proterozoic metamorphic rocks as discussed in Chapter 2.

Large-scale downfaulting of the crystalline basement is inferred beneath the outer continental shelf and continental slope. Combined sediment and water thicknesses of over 10 s TWT overlie the basement beneath the continental rise; >5 s TWT deeper than beneath the continental shelf. Strong water bottom multiples and a lack of data from the upper continental slope and continental shelf prevent the direct imaging of these fault structures. Basement faults at similar relative location and of similar offset are also interpreted on the conjugate southern Australian margin [Totterdell *et al.*, 2000].

Seaward of the shelf-slope fault zone, deeply subsided, stretched continental crust extends for up to 250 km. Determining the extent of continental crust is subjective, it is based on seismic character, and to a degree the presence of faulted pre-rift crust/sediments. Imaging of crustal structure in MCS data is variable along the margin. The relatively thinner sedimentary section off east Wilkes Land allows clear imaging of crustal structure. *Moho* reflections are also interpreted in MCS data from central and east Wilkes Land (Lines GA-228_23 to GA-228_29). Sonobuoy refraction data provides constraint on *Moho* depth for east Wilkes Land only, and even then only beneath stretched continental, and oceanic crust (sonobuoys GA-228-23, GA-228-21, GA-228-20). The only MCS *Moho* reflection that coincides with a refraction interpreted mantle velocity occurs on Line GA-228_28, here they correlate to within ∼0.3 s TWT.

The interpreted *Moho* is characterised by a high amplitude, long wavelength reflector beneath stretched continental or transitional crust and oceanic crust. However, on lines GA-229_06 and GA-229_07, a sequence of planar reflectors, similar in character to the *Moho* reflector occur; these are marked by the *llcc* horizon (laminated lower continental crust). Whether the top or base of these reflectors represents the *Moho* is unclear. This sequence of reflectors, therefore, indicates either altered upper mantle, or anomalous lower crust. Upper mantle reflectors are known from the Enderby margin of East Antarctica [Stagg *et al.*, in press], however, their genesis is uncertain. Refraction velocities associated with these reflectors are variable. At sonobuoys GA-229-12 and GA-229-13 refractor velocities of 6.82 and 6.57 km/s correlate to the *llcc* horizon. Landward on Line GA-229_07, however, at sonobuoy 15, a refractor velocity of 5.63 km/s correlates to the *llcc* horizon. These velocities are in the range determined for transition zone, upper mantle peridotites on the west Iberian margin [Dean *et al.*, 2000]. However, these possible 'transition zone' velocities occur beneath stretched continental crust on the east Wilkes Land margin, whereas they commonly form the top of basement between stretched continental

and oceanic crust on the Iberian margin.

Offsets in the *Moho* reflector (e.g. Line GA-228_28, shot-point (SP) 3400 and Line GA-228_27, SP 5200), indicate that faulting and brittle deformation occurred within the lower crust and upper mantle during or since rifting. The detailed orientation of these faults can not be determined, as the relatively acoustically transparent mantle and crustal character prevents faults being interpreted on the basis of reflector terminations and offset. The *Moho* reflector also exhibits some long wavelength relief. For example, on Line GA-228_27 (SPs 7900-7600) the *Moho* reflector deepens from 10 s to ∼10.75 s TWT (∼2-2.5 km) over a distance of ∼20 km, before shallowing again northwards.

Overlying the *Moho* reflector, within stretched continental crust, is an acoustically transparent zone (e.g. Line GA-228_25, SPs 5200-6900). The top of this zone is marked by an indistinct change in character (the *tran* horizon), and is interpreted as top of crystalline lower crust. Faults are typically not imaged within these lower crustal rocks, however, this again may be a function of the acoustically transparent rock character rather than an indicator of entirely non-brittle deformation. Sonobuoys GA-228-17, GA-228-21 and GA-229-11 recorded deep crustal refraction velocities of 6.60, 6.51 and 5.39 km/s respectively, coincident with the interpreted *tran* horizon. These velocities are consistent with the presence of continental crust [Stagg *et al.*, in press]. Higher velocity crustal refractions were also recorded at sonobuoys 288-16 (7.89 km/s) and GA-228-17 (7.84 km/s). These velocities are approaching typical mantle velocities of >8 km/s and likely represent altered upper mantle rocks.

The lower crustal sequence, bounded above and below by the *tran* and *Moho* horizons respectively, thins massively seaward as the *tran* horizon deepens and the *Moho* shallows. For example, on Line GA-228_24 if the *Moho* horizon is extrapolated landward, the lower crust thins from over 3 s to ∼1 s TWT (∼9 to ∼3 km) over a distance of 75 km. Large amounts of faulting in the overlying Sequence 3 accompanies the lower crustal thinning. The lack of lower crustal faulting imaged within this massive sequence indicates that much of the lower crustal thinning occurred through relatively ductile stretching.

The *tran* reflector can typically only be traced within unequivocal continental crust and wedges out against the onset of the interpreted transition zone crust. The *Moho* reflector is also not imaged as consistently seaward of the onset of transition zone crust (e.g. Line GA-228_24). A similar phenomenon is observed on the Iberian margin, where one of the identifying characteristics of transition zone crust is the lack of an identifiable *Moho* in seismic reflection and refraction data [Dean *et al.*, 2000].

4.9 Oceanic Crust

Unequivocal oceanic crust is observed at the seaward extent of all GA-228 and GA-229 seismic profiles. It is characterised by a relatively transparent acoustic character and rough, rugged topography. The velocity structure inferred from refraction modelling is also characteristic of oceanic crust. Although some variation in seismic character and crustal structure is observed, the oceanic crust remains the most uniform crustal type identified on the Wilkes Land margin. It is overlain, almost entirely, by mantled layers of high frequency reflectors, likely indicative of deep marine, pelagic deposition, with minor input from distal turbidites.

The top of oceanic crust is observed at depths of 6 to 8.5 s TWT, typically shallowing northwards. Greatest shallowing is observed on western lines (Lines GA-228_18 and GA-228_19) where the largest thickness of terrigenous sediments is observed, here oceanic crust shallows from >8 to 6.5 s TWT. This contrasts with the central Wilkes Land sector where over comparable distances the top of oceanic crust maintains a consistent depth of ∼7.5 s. The wavelength and amplitude of oceanic crust topography is also variable. Broadly speaking, the roughness of topography increases eastwards, towards the Spencer, Tasman and George V fracture zones. However, oceanic basement highs are observed on all profiles. Some are relatively broad, e.g. Line GA-228_18, SPs 2900-2200 (35 km), whereas others are very narrow, e.g. Line GA-228_26, SPs 4900-5150 (12.5 km). The wide spacing of the lines prevents correlation of any of these features along the margin.

Changes in topographic character are observed on a number of lines. For example, oceanic crust on Line GA-228_21 (including extension Line GA-229_10) exhibits relatively subdued topography from SP 6200 (Line GA-228_21) to SP 700 (Line GA-229_10), however, seaward of this point average basement depth is ∼0.5 s shallower and is characterised by rough topography. The topographic highs indicate a variable relationship between magma discharge at the South-East Indian Ridge (SEIR) spreading centre and extension and/or seafloor spreading. Volcanic buildups at the spreading centre may equally represent an increase in magma discharge or a decrease in spreading rates of the Australian and Antarctic plates. Slow seafloor spreading rates typically result in rough basement topography [Macdonald, 1982]. As changes in seafloor spreading rates are known to be variable for the Australia-Antarctic Basin from breakup until the early Eocene [Tikku & Cande, 1999], it is possible that changes in oceanic basement level (e.g. Line GA-228_19, SP ∼6000) correlate to major changes in seafloor spreading rates.

Faulting of oceanic crust is inferred on a number of lines. Faulting is likely more widespread than interpreted, however, due to the lack of internal reflectors and the

relatively homogeneous nature of oceanic crust, imaging of the faults is difficult. Faults that offset the top of oceanic crust are most easily interpreted, e.g. Line GA-228_23. Slow spreading rates are thought to be associated with greater amounts of mechanical extension within oceanic crust [Mutter & Karson, 1992], and therefore with extensional, normal faulting. Abundant evidence of large extensional faults is observed at the slow spreading Mid-Atlantic Ridge [Kong *et al.*, 1988]. As very-slow seafloor spreading rates (1.5 to 10 mm/yr half-spreading rates [Tikku & Cande, 1999]), are modelled for the Australia-Antarctic Basin for ∼50 Ma following breakup, faulting of oceanic crust is not surprising.

Reflections from the upper-most section of oceanic crust exhibit some layering, particularly adjacent to basement highs. These roughly laminar reflector sequences, e.g. Lines GA-228_23 and GA-228_24, are likely basaltic lava and pyroclastic flows, or slides of basaltic rock from adjacent crustal peaks. Again, the occurrence of these sequences indicate intermittent periods of magma discharge excess to rates of extension. Discontinuous, internal oceanic crustal reflections are also observed, e.g. Line GA-228_20. These internal reflections are most common in the oldest sections of oceanic crust. Shallowly dipping internal reflections, e.g. Line GA-228_24, SPs 4600-5300, may represent relic magma chambers, oceanic layer transitions (i.e. pillow basalts to sheeted dykes to massive gabbro), or layers of successively intruded sills. However, evidence from Cretaceous ocean crust in the Atlantic suggests it is likely that some of these internal reflectors are normal faults generated at or near the spreading axis [Morris *et al.*, 1993; Collier *et al.*, 1998].

Sonobuoy refraction data typically record two velocity layers within oceanic crust, and mantle velocities also at two locations. The uppermost crustal layer, layer 2, is characterised by velocities of 4.47 km/s (sonobuoy GA-229_19) and 4.93 km/s (sonobuoys GA-229_14, GA-229_18, GA-228_22). These velocities are at the lowest end of the 'average' velocity range for 'normal' layer 2 crust [Raitt, 1963; White, 1984; Bratt & Purdy, 1984]. At sonobuoys GA-228_15, GA-228_18 and GA-228_20, the top of oceanic crust (as determined in MCS data) correlates to a refraction velocity of 5.36 to 5.39 km/s, this velocity range is more typical of layer 2 oceanic crust.

Layer 3 oceanic crust P-wave velocities typically range from 6.5 to 7.0 km/s [Raitt, 1963; White, 1984; Bratt & Purdy, 1984]. Velocities between 6.56 and 6.72 km/s were recorded by sonobuoys GA-229_19, GA-228_15, GA-228_18, GA-228_20 and GA-228_23, indicating the presence of a distinct oceanic Layer 3. sonobuoys GA-229_18 and GA-229_26 recorded seismic velocities of 6.12 and 7.11 km/s respectively, these are outside the range of 'normal' oceanic layer 3 velocities, but are likely still representative of deep oceanic crust. The thickness of overlying layer 2 crust ranges from 1.3 to 2.6 km, which

is a typical range [Raitt, 1963; White, 1984; Bratt & Purdy, 1984].

Mantle velocities were recorded on only two sonobuoys over oceanic crust, sonobuoys GA-228_20 and GA-228_23. Velocities of 8.18 and 8.14 km/s were recorded at these locations respectively. At sonobuoy GA-228_20 the thickness of the overlying layer 3 crust is only 1.68 km, this is less than half the average layer 3 thickness of ∼4.6 km [Raitt, 1963]. The total oceanic crustal thickness indicated at this sonobuoy is 4.9 km. The thickness of layer 3 at sonobuoy GA-228_23 is 3.0 km, again significantly thinner than average layer 3 crust. The overall crustal thickness indicated at sonobuoy GA-228_23 is 4.96 km. Average oceanic crustal thickness, not affected by fracture zones and hotspots, is 7.1 km [White *et al.*, 1992]. The trend of 4.5 to 5 km thick oceanic crust inferred at sonobuoys GA-228_20 and GA-228_23 indicates oceanic crust off the Wilkes Land margin is less than 75 % the thickness of average oceanic crust.

Oceanic crust formed at spreading rates slower than <10 mm/yr is known to exhibit a sharp reduction in the thickness of crust formed [Bown & White, 1994]. Mutter & Mutter [1993] use seismic refraction data to demonstrate that variations in layer 3 thickness are the primary control on varying oceanic crust thickness. Refraction data from the Wilkes Land margin supports the hypothesis that thinner than average crust is associated with slow spreading, and also that layer 3 exhibits the greatest departure from average thickness.

The landward extent of oceanic crust can not be defined trivially. Although the seismic and morphologic features, and velocity structure of oceanic crust are characteristic, its most landward extent remains a subjective interpretation. On each seismic profile a continent-ocean transition zone is interpreted that separates unequivocal oceanic and continental crust.

4.10 Transitional Crust and the Continent-Ocean Boundary

The extent of continental and oceanic crust at continental margins is of fundamental importance to understanding rifting and plate tectonics. The continent-ocean boundary (COB), however, remains an enigmatic feature that can rarely be defined unequivocally at passive rift margins. The most diagnostic data for COB definition are seismic reflection and refraction, and gravity and magnetic anomaly data. Typically, a continent-ocean transition (COT) zone is defined at passive rift margins, which separates unequivocal continental and oceanic basement.

The width of transition zone crust of North Atlantic and Labrador Sea region rifted margins (a good analogy to the Wilkes Land and southern Australian margin due to

their non-volcanic character and slow-spreading history), varies from <10 to 170 km (see Dean *et al.* [2000] for references). The transition zone crust of the North Atlantic and Labrador Sea region is, in part, rigourously constrained by P-wave velocity structure. Where greater widths of transition zone crust are identified, the amount of extended continental crust is limited such that the sum of extended continental and transition zone crust is 100 to 200 km [Dean *et al.*, 2000]. The west Iberian margin (Galicia Bank and the southern Iberian Abyssal Plain) transition zone also includes a peridotite ridge that has been variably hydrated and serpentinised [Boillot *et al.*, 1980].

Refraction velocity data is far too sparse on the Wilkes Land margin to attempt to define a COT on the basis of P-wave velocity structure. The case for an indistinct, variable extent COT zone, however, can be demonstrated by the high quality, deep-penetrating seismic reflection data of surveys GA-228 and GA-229. The *cot* horizon is used to define the upper limit of pre-rift rocks that are not clearly continental or oceanic in structure and character. This zone represents some of the most deeply subsided crust on the Wilkes Land margin, reaching depths of up to 9 s TWT, and ranges in width from <30 to >100 km.

The belt of deeply subsided crust seaward of faulted and rotated continental crustal blocks is characterised by the presence of shallow-crustal and/or basement sub-cropping crystalline bodies. Seismically, these bodies are internally transparent relative to continental crust, however, they typically exhibit greater internal character than oceanic crust. Up to 1 s TWT of topography of the *cot* horizon is evident, through both faulting (e.g. Line GA-228_23), and crystalline basement uplift (e.g. Line GA-228_28). Imaging of the COT zone is inherently more difficult off west Wilkes Land where much greater post-rift sediment deposition has occurred. Variation in broad-scale topographic character of COT zone crust, however, can be inferred. The COT zone off west Wilkes Land is relatively subdued, whereas rough topography is observed in the COT zone off east Wilkes Land. A basement high on Line GA-228_29 penetrates the water column.

Crystalline basement highs may represent shallow, intrusive igneous bodies associated with Jurassic magmatic activity. However, it is possible that crystalline basement highs represent peridotite ridges or exhumed mantle. The coincidence in central and east Wilkes Land of the transition zone basement ridges and the termination of the *Moho* horizon in MCS data indicates that massive lower crustal thinning has occurred, unroofing the upper-mantle and forming a basement comprised of upper-mantle peridotites. A lack of typical mantle velocities, and therefore also a 'seismic *Moho*', characterises the transition zone crust of the Iberian Abyssal Plain margin [Dean *et al.*, 2000]. If the basement ridges observed off the west Wilkes Land margin are in part exhumed mantle, then they are likely serpentinised peridotite ridges similar to those interpreted off the Iberian margin.

A basement ridge on the conjugate southern Australian margin has been interpreted by Sayers *et al.* [2001] as a peridotite ridge. However, this can not be determined for the Wilkes Land margin on the basis of seismic reflection data alone.

The seaward and landward extents of the *cot* horizon, interpreted here on the basis of seismic and structural character, are interpreted to represent the extents of unequivocal oceanic and continental crust respectively. Sections of COT crust which are bound seaward by blocks of continental crust may represent abandoned seafloor spreading ridges, e.g. Line GA-228_18 and GA-228_22. The along strike extent of the COT zone is indicated in Figure 4.23. However, to consider either 'edge' of COT crust as a definitive determination of the COB is not realistic.

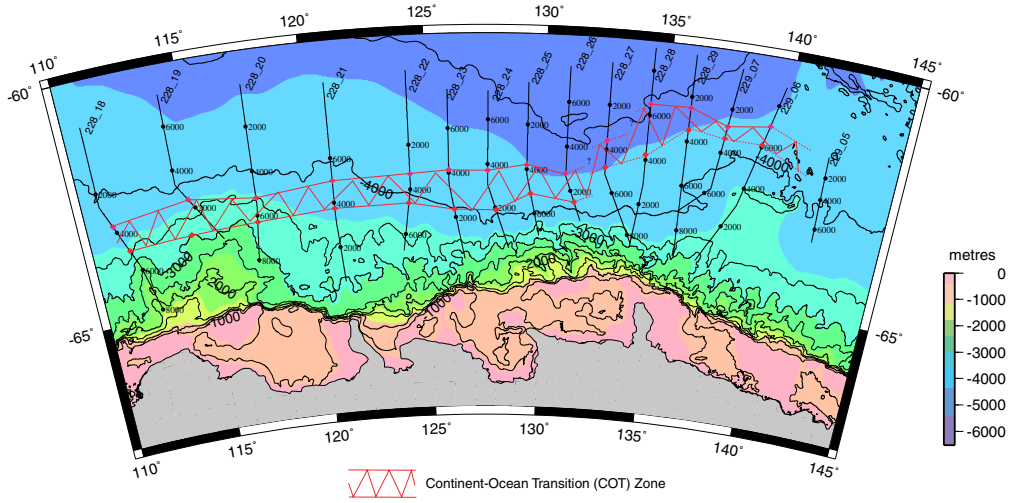

Figure 4.23: Continent-Ocean Transition (COT) zone along the Wilkes Land margin. The COB is interpreted to lie within this zone on the basis of crustal seismic character and velocity structure.

The similarity in crustal character of the crystalline bodies typical within the COT crust and oceanic crust precludes simplistic interpretation of a COB based on crustal identification. This is particularly true off west Wilkes Land due to the greater sediment thickness. Also, as radical changes in seafloor spreading rates occur for ~40 Ma post rifting, changes in oceanic crustal structure and character would be expected. Therefore, changes in crustal character may not necessarily indicate transition from stretched continental/transitional crust to oceanic crust. Initial interpretation of these data by Colwell *et al.* [in press] typically places the COB at a point of rapid change in crustal character, e.g. Line GA-228_19, SP 5000. However, on the basis of MCS data alone, there is nothing that precludes a COB up to ~180 km further landward for this transect, i.e. SP 1000. The COB interpreted by Colwell *et al.* [in press] for this line is located ~30

km seaward of the interpreted base of Eocene sediments, therefore implying an onset of seafloor spreading at <50 Ma.

The transition zone, as located in Figure 4.23, typically occurs ∼200 km from the shelf break and the COB typically <100 km further seaward. However, it steps out significantly off east Wilkes Land and Terre Adélie where the COB is located at ∼450 km from the shelf break. The interpreted width of COT crust also decreases in this region. This interpretation is discussed and defended in the following section.

4.11 Ocean Basin, Continental Crust, and Mantle Peridotites: The east Wilkes Land - Terre Adélie Margin

A group of seamounts, a basement ridge, and a broad bathymetric shallowing occurs at the edge of the abyssal plain off the east Wilkes Land margin, from 137-140°E, Figure 4.24. The seamounts and basement ridge reach heights of over 1000 m above the average ∼4000 m deep seafloor. The basement ridge forms the seaward extent of the broad zone of relatively shallowed bathymetry. The ridge reaches a maximum height at its eastern extent, and plunges to the west, continuing for ∼75-100 km above the seafloor. The seamounts and basement ridge are located south of the Spencer fracture zone, and ∼100 km west of the George V fracture zone.

An un-named, northwest-southeast trending basement structure (fracture zone?) can be inferred, from free air gravity anomaly data, directly east of the seamounts, Figure 4.25. The seamounts and basement ridge correlate to positive free air gravity anomalies. However, the regional gravity field is anomalous in this region; the broad edge-effect low, typical of the central Wilkes Land continental slope/rise transition, is replaced by a positive free air anomaly and an outer, negative free air anomaly.

MCS data have been acquired in this region by the IFP, USGS, JNOC and GA. In-situ peridotite blocks were also dredged during JNOC survey th95 from seamount B (Figure 4.24). A number of interpretations of this region of shallowed bathymetry and anomalous basement features have been presented. Wannesson *et al.* [1985] interpreted this region as an anomalous oceanic zone, similarly, Eittreim & Smith [1987] interpreted volcanic basement associated with early oceanic crust emplacement. In contrast, Tanahashi *et al.* [1997] suggest that basement in the region comprises either metamorphosed continental or igneous (but not oceanic basalt) crust.

Geochemical analyses of recovered peridotite samples indicate the seamounts have a fertile sub-continental mantle origin [Yuasa *et al.*, 1997]. The existence of sub-continental mantle material does not definitively indicate the presence of continental crust around the seamounts. However, it can be inferred that oceanic crust was not being produced in the region of the seamounts during their formation. As the seamount samples were recovered seaward of oceanic crust interpreted by Wannesson *et al.* [1985] and Eittreim & Smith [1987], the mineral chemistry analyses support the conclusions of Tanahashi *et al.* [1997].

MCS data from the IFP (ATC82) and USGS (L184) surveys do not penetrate sufficiently to image structures within pre-rift rocks. However, MCS data from the th95, GA-228 and GA-229 surveys confirm that basement is comprised of continental crust beneath this bathymetric anomaly, and that the ridge is not composed of oceanic crust.

These data indicate a stretched crystalline lower crust, overlain by up to 3 s TWT of extensively faulted pre- and syn-rift metasediments/sediments. The thickness and structures of the faulted and deformed sedimentary sequence, beneath <0.5 to 2 s TWT of deep marine sediments, precludes the possibility of oceanic crustal basement, Figure 4.26. This region of deeply subsided but clearly continental crust is labelled the Adélie Rift Block by Colwell *et al.* [in press], and we follow this protocol here.

The basement ridge is traversed by line th95_04, SPs 350-1000 (Figure 4.27) where the ridge core forms a north-facing scarp. The more gently dipping southern ridge-flank is overlain by ∼1 s TWT of sediments, which dip conformably with the underlying crystalline basement. This structure likely represents a large-scale, rotated fault, that has exposed the lower crust. The dipping sediments are overlain by an angular unconformity above which flat-lying, marine sediments onlap.

The westward, thinly sediment covered, extent of this basement ridge is traversed by Line GA-229_06, SPs 3500-4500. The ridge is significantly broader and deeper at this location and the crystalline basement occurs below an even greater thickness of pre- and syn-rift sediments (up to 3 s TWT). The top of crystalline lower crust (*tran* horizon) is not evident until a depth of ∼8-9 s TWT. Growth faulting occurs in the upper sedimentary sequence, indicating active extension during deposition. Both landward and seaward dipping fault blocks are imaged, suggesting a spatially variable locus of extension during rifting.

The landward extent of the basement ridge, on Line GA-229_06, correlates to a large-offset (∼0.5 s TWT) normal fault that penetrates through the upper-crustal, pre-rift sediments, into the laminated lower crust. This point is also the location of greatest crustal thinning imaged on this line. Assuming the thickness of the laminated lower crust is <1 s TWT (as it is farther north on this line), less than 3 s TWT of the total pre-rift crustal thickness remains. This region corresponds to a positive free air gravity anomaly that is interpreted to represent very shallow level mantle rocks associated with the crustal thinning, Figure 4.25. At the seaward extent of the basement ridge a crystalline basement high occurs in the upper-crust, and the laminated lower crust and *Moho* reflections terminate at depth. This is typical of the transition zone crust of central Wilkes Land. An isolated rift basin of 30-50 km width separates the *cot* body from oceanic crust.

Although the ridge structure becomes diffuse and less clearly imaged to the west, e.g. Lines GA-229_07, GA-228_29 and GA-228_28, the depth of the pre-rift upper surface remains elevated (average ∼6 s TWT) in the Adélie Rift Block relative to central Wilkes Land (average ∼7.5 s TWT). The Adélie Rift Block exhibits similar characteristics to the "extensional allocthons" observed in the Alps, which are interpreted to be separated from underlying exhumed mantle rocks by low-angle detachments [Manatschal, 2004].

These extensional allocthons are also interpreted to have formed within a slow spreading ridge environment.

Rough crustal topography, comprising basement highs independent of the basement ridge, is also evident in MCS data from the Adélie Rift Block. A crystalline basement high remains a consistent feature at the transition from stretched continental to oceanic crust in this region. However, the along strike extent of the basement highs is equivocal. An along-strike transect recorded during survey th95, Line th95_06, exhibits rough basement topography (Figure 4.27). This indicates that basement highs surveyed on north-south profiles may represent either ridge or seamount structures. The thickness of the post-rift sediments and height of the individual basement highs dictate whether they have a bathymetric expression.

Line th95_04 and th95_06 MCS data show seamount flank gradients of ~7.5-15%, e.g. Line th95_06, SPs 900-1400. The seamounts are characterised by a lack of coherent internal reflections. Basement highs, similar in morphology and seismic character to the observed seamounts, are observed partially or entirely sub-seafloor at a number of locations, e.g. Lines th95_06 (SPs 2900-3200), GA-228_29 (SPs 3200-3600). These features typically correlate to positive free air gravity anomalies (Figure 4.25). Interpolating between the known locations of seamounts and/or basement highs of similar character using the free air gravity data indicates an arcuate belt of similar features as illustrated in Figure 4.25. As in-situ mantle peridotites have been dredged from one of these seamounts, we suggest this belt represents a zone of extreme crustal thinning and a zone of exhumed continental mantle that forms the seaward extent of the Adélie Rift Block.

Modelling results of Pérez-Gussinyé *et al.* [2001] indicate that serpentinisation of the upper mantle occurs preferentially in cratonic rift margin environments characterised by stretching factors of 3-4. These stretching factors are observed and exceeded for most of the Adélie Rift Block. A second key factor that contributes to the presence of shallow level and exhumed, serpentinised mantle rocks is low melt production; which is also characteristic of slow spreading ridges [Bown & White, 1995]. The Adélie Rift Block exhibits many of the key factors optimal for mantle serpentinisation, as outlined by Pérez-Gussinyé *et al.* [2001]. Under these rift conditions brittle, full-crust faulting allows water to penetrate and serpentinise the mantle. Given the modelling results of Pérez-Gussinyé *et al.* [2001] and the similarities between the Adélie Rift Block and the west Iberian margin, it is likely that the upper mantle beneath the stretched continental crust of the COT zone of east Wilkes Land is, at least partially, serpentinised.

The interpreted COB location, based on MCS data and the geochemical analyses of recovered basement samples, on the east Wilkes Land margin, occurs over 450 km from

the shelf break. This is ~220 km further seaward than the interpreted COB in central Wilkes Land. This indicates that following the commencement of seafloor spreading in the central Australia-Antarctic Basin, continental crust to the east continued to stretch. Points of massive crustal thinning, as observed on Line GA-229_06, indicate that the continental crust stretched to <20% of its original thickness (assuming an initial crustal thickness of 31 km) without failing and allowing seafloor spreading to commence. This point of maximum stretching and crustal thinning occurs at a similar distance from the shelf break as the interpreted COB to the west. It is likely that this point represents a failed rift as continental crust extends seaward for up to 250 km from this point of extreme thinning before oceanic crust is encountered. Bassi [1995] demonstrates that the increased cooling associated with slow stretching causes the crust to become brittle, and the locus of maximum strain rate to move laterally and induce widened rifts. However, although widened rifts are predicted at slow rifts, modelling by Bassi [1995] also indicates it is not possible to stretch, brittle continental crust to the extent observed here.

Extensive terranes of submarine continental crust, such as the Campbell Plateau, New Zealand, and Exmouth Plateau, Australia, are well known [Nur & Ben-Avraham, 1982], however, they typically occur at relatively shallow depths (<1000 m). Stretched continental crust is inferred at greater depths at other passive rifted margins, e.g. West Iberia [Dean *et al.*, 2000], Labrador Sea [Chalmers & Pulvertaft, 2001], West Africa [Rosendahl & Groschel-Becker, 2000], East Coast U.S.A [Mohriank & Talwani, 2000], southeastern Brazil [Bassetto *et al.*, 2000], South China Sea [Huchon *et al.*, 2001], and southern Australia [Sayers *et al.*, 2001]. However, at none of these locations is the COB located at distances of greater than ~250 km from the shelf break. The Rockall Trough is an example of a failed rift that is interpreted to be floored by massively stretched continental crust (~6 km thick) that is now subsided to great depths [Pérez-Gussinyé *et al.*, 2001]. However, the width of Rockall Trough stretched crust is ~200 km, still less than half the total width of massively stretched crust off the east Wilkes Land margin.

The Wilkes Land margin, and the Adélie Rift Block in particular, share a number of similar characteristics to the west Iberian margin, e.g. slow spreading ridge, non-volcanic rifting, presence of massively thinned crust, and exhumed and serpentinised mantle peridotites. However, the zone of exhumed mantle off Wilkes Land, as interpreted from MCS and free air gravity anomaly data, is much narrower than off West Iberia. In contrast, the extent of unequivocal continental crust at abyssal depths, off east Wilkes Land in the Adélie Rift Block is greater than observed off West Iberia (or any other well-studied passive rift margin). The identification of the COB at this location adds further complexities to tectonic reconstructions in an area where continental overlap is already noted in reconstructions [Tikku & Cande, 1999; Royer & Rollet, 1997].

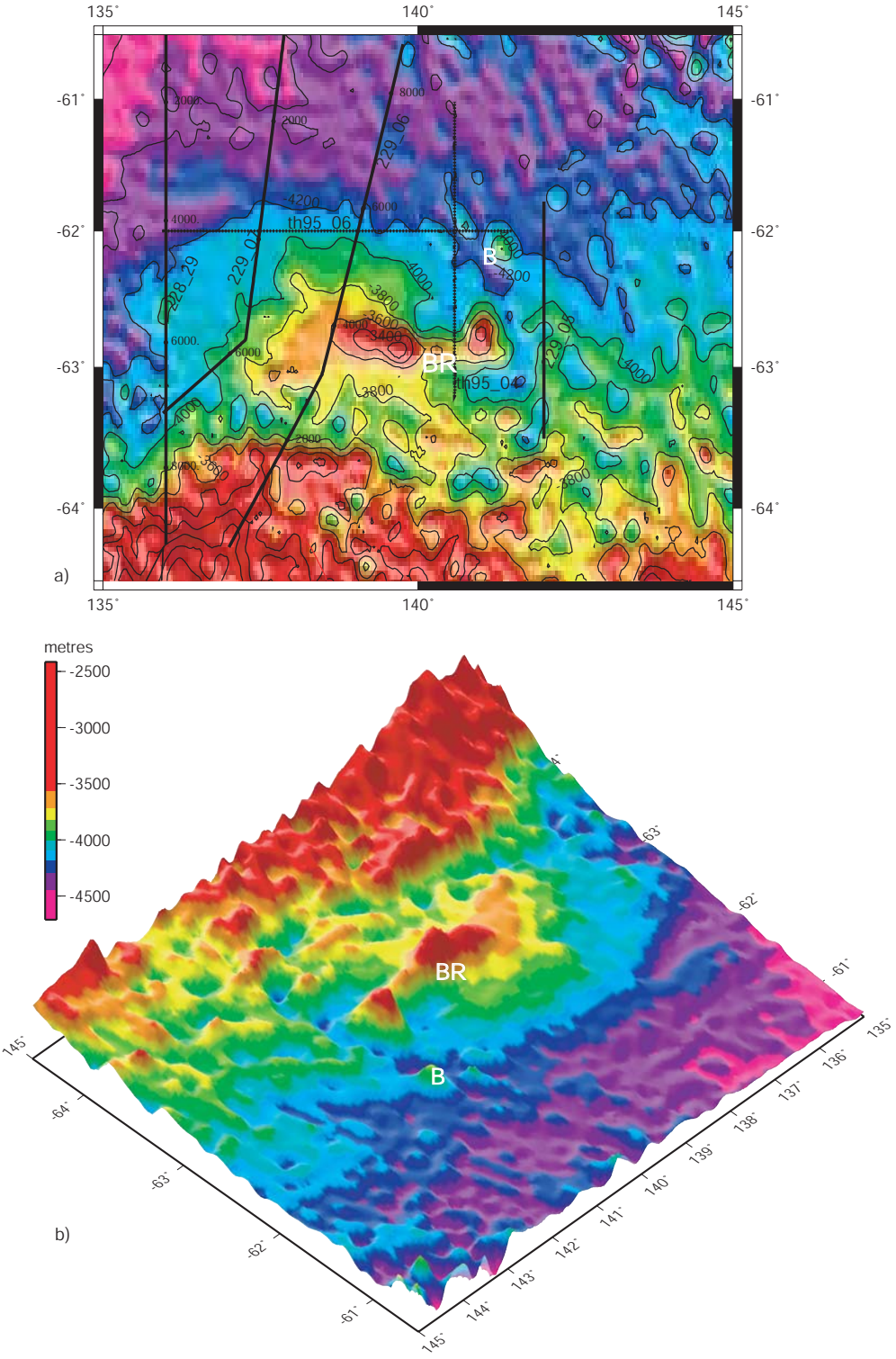

Figure 4.24: Bathymetry detail of the east Wilkes Land margin in a) map and b) perspective view. An east-west trending basement ridge (BR) and northwest-southeast trending seamounts form the seaward limit of an anomalously shallow region. B is seamount B as defined by Yuasa *et al.* [1997]. Bathymetry data from Smith & Sandwell [1994].

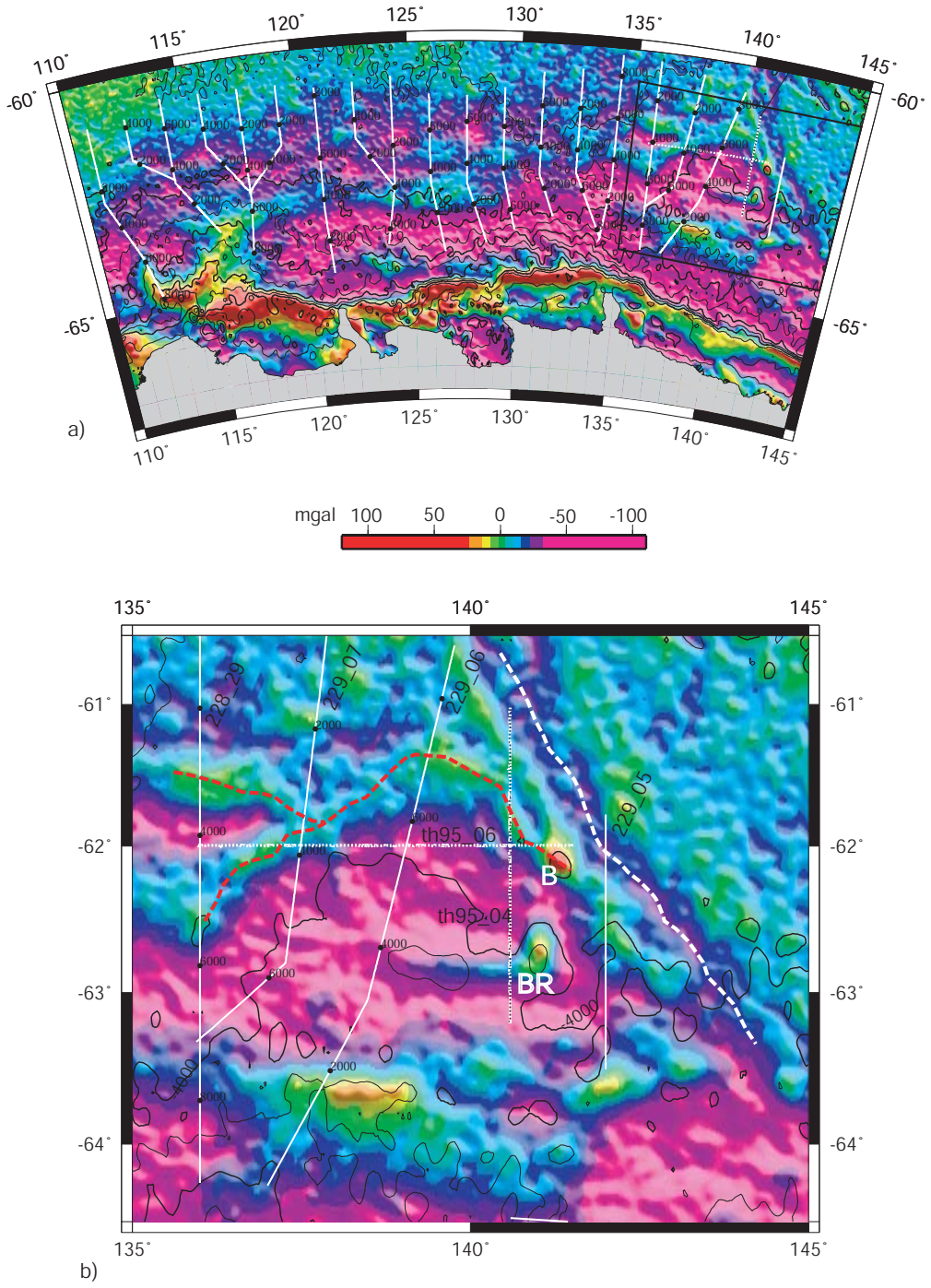

Figure 4.25: Free air gravity anomaly data overlain with bathymetry contours for a) the Wilkes Land margin, and b) the region of anomalous bathymetry off east Wilkes Land. The free air edge effect anomaly is disturbed off east Wilkes Land in the region of the basement ridge (BR) and shallowed bathymetry. B is seamount B as defined by Yuasa *et al.* [1997]. White dashed line traces the northwest-southeast trending fracture zone(?). Red dashed line traces belt of positive free air anomalies associated with outcropping or sediment covered seamounts/basement highs.

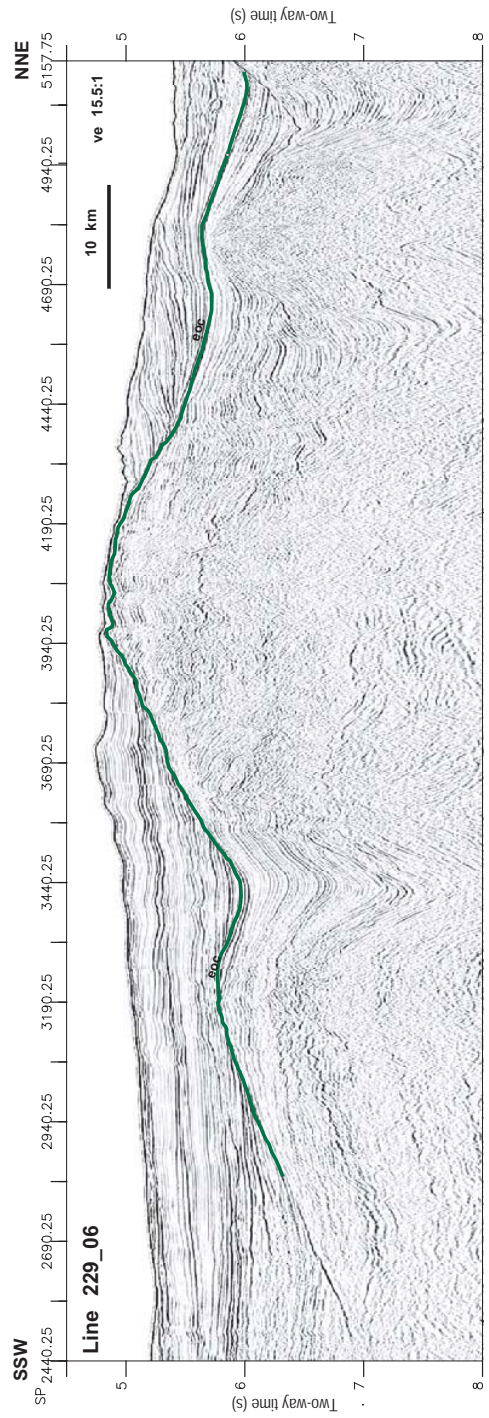

Figure 4.26: Detailed section of Line GA-229_06. The *eoc* horizon is marked for reference. Reflector geometry and structure beneath the *eoc* horizon are typical of structured sedimentary/metasedimentary rocks and precludes the possibility that the underlying crust is oceanic.

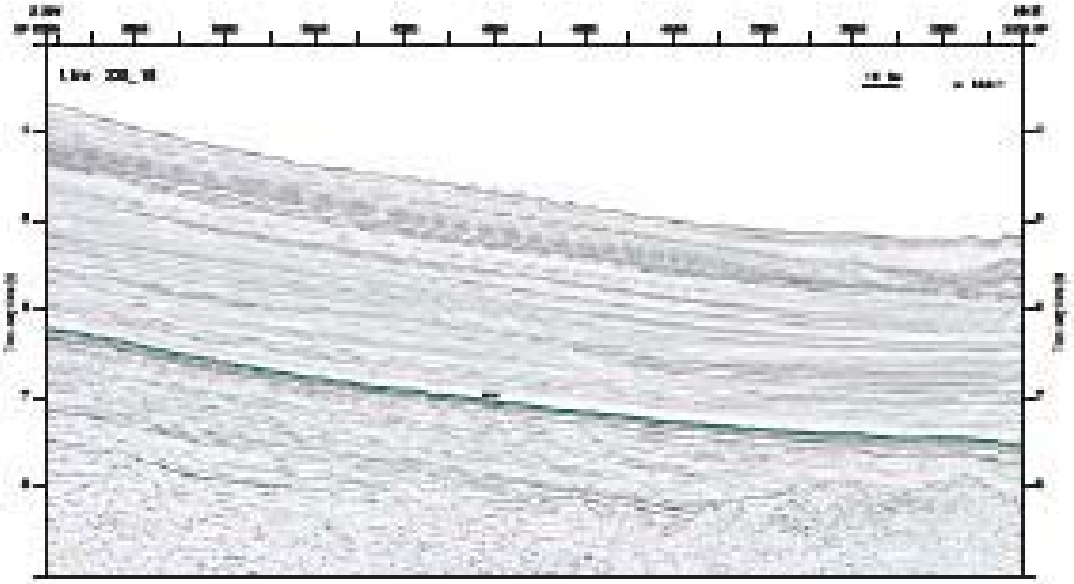

4.12 Sediment Distribution

Compilation of post-rift sediment thickness, based on the identification of the *tur* and *eoc* horizons, provides the first regional sediment isopach for the Wilkes Land margin, Figure 4.28. Although data is located on lines separated by up to 90 km, gridding of the two-dimensional sediment thickness data provides insight into the broad-scale sediment distribution. A previously unrecognised major sedimentary basin is identified off west Wilkes Land, we label this basin the Budd Coast Basin (BCB). The BCB comprises a delta and glacial sourced sediment thickness of greater than 5 s TWT (∼9 km). The volume of sediments within this basin is comparable to the major river deltas of other continents, such as the Niger and Amazon deltas.

The Sequence 2 isopach illustrates a sediment depocentre off west Wilkes Land, and a secondary, minor depocentre off east Wilkes Land. Central Wilkes Land is characterised by a thin veneer of sequence 2 sediments. The total sediment isopach demonstrates that total sediment distribution is primarily a function of variation in sequence 1 thickness. The distribution of the thickest sequence 1 sediments is distinctly asymmetric, seaward of ∼64°S the axis of thickest sediments is deflected west to east. This distinct west to east asymmetry of the BCB indicates that deep marine processes have been an important control on sediment transport and deposition on the East Antarctic margin since at least the onset of regional Antarctic glaciation. The locus of thickest sediments occurs offshore of the termination of the Totten glacier, one of the widest and highest velocity, 'fast-flow features' [Bamber *et al.*, 2000] in East Antarctica. This indicates that major ice-streams and/or flowing glaciers may be very long lived despite observations of short term (<100 years) changes in glaciomorphological features [Domack & Anderson, 1983].

The contrast in post-rift sediment volumes between sequences 1 and 2 indicates a significant change in rates of onshore erosion and sediment transport to the Wilkes Land margin. The onset of temperate-glacial climatic conditions are likely the catalyst for the much greater volumes of sequence 1 sediments. This is supported by the relative absence of Tertiary sediment on the southern Australian margin [Totterdell *et al.*, 2000], where no glaciation has occurred. If this assumption is true, then the majority of the sequence 1 thickness has been deposited since the onset of glacial conditions at ∼34 Ma. Further, as the current polar-glacial conditions can be observed to be relatively static in terms of erosion and sediment transport, we can attribute the majority of the sediment flux to have occurred prior to stable, frozen-base, glacial conditions. ODP results from the continental rise offshore from Prydz Bay show a seven-fold reduction in sedimentation rates (70-10 m/My) in the late Miocene (∼9 Ma), relative to peak sedimentation rates in the early Miocene [Cooper & O'Brien, in press]. This reduction is interpreted to indicate

close to peak glacial conditions being reached. Extrapolating the regional importance of this event suggests that the majority of Wilkes Land sedimentation occurred from ~34-9 Ma.

To infer sedimentation rates for the ~34-9 Ma interval it is necessary to estimate the thickness of sediments deposited between the *eoc* unconformity and the onset of glaciation, and since the late Miocene stabilisation of glacial extent. No unconformity or stratigraphic horizon can be recognised in regional MCS transects to be representative of glacial onset. Hence, sedimentation rates for the *tur-eoc* interval were extrapolated to 34 Ma to determine the thickness of post-*eoc* sediments not attributed to glacial erosion and/or transport. Sedimentation rates since the late Miocene of 20-25 and 10 m/My have been reported from DSDP 269 (east Wilkes Land) and ODP 1165 (Prydz Bay) sites respectively. However, this is likely to be higher during times of glacial expansion.

On the basis of the above, it is not likely that more than 250-500 m of post-*eoc* sediments is younger than late Miocene. Restricting the post-*eoc* sediment thickness, using these simple assumptions, provides an estimate of the 34-9 Ma interval sediment thickness for GA-228 survey lines that traverse the locus of thickest sediments; lines 18, 19 and 20. A thickness of 5-6 km of sediment is inferred for these lines.

Using the interval and thickness outlined above, sedimentation rates of between ~160-200 m/My are inferred for the Budd Coast Basin (BCB). This average is comparable to modern rates observed in the temperate glaciers of the Gulf of Alaska [Powell, 1984]. However, peak sedimentation rates achieved during times of glacial expansion are likely much higher than the 25 Ma average. Alley *et al.* [1989] modelled sediment flux rates of 100-1000 m^3/yr per metre width of the grounding line for Antarctic wet based glaciers, these rates are orders of magnitude higher than typical glacial sedimentation rates [Powell, 1984] and the average sedimentation rate determined here for west Wilkes Land. The peak rates modelled by Alley *et al.* [1989] could only be sustained for short periods and would overwhelm all other sources of sediment [Eittreim *et al.*, 1995].

The estimated total volume of BCB sediments (assuming a baseline sediment thickness of 2 km) is 450,000 km^3. This is comparable to the volume of the Niger Delta (500,000 km^3, Hospers [1965]), and greater than the volume of the Amazon Cone (140,000 km^3, Watts [2001]). The Amazon Cone is located on the passive rift margin of northern Brazil and formed between the Miocene and the present, ~100 Ma after rifting [Kumar, 1978]. Similarly, the BCB formed in a time interval of ~25 Ma, some 50 Ma after rifting. Hence, both the Amazon Cone and BCB represent massive loads on old, tectonically subsided, passive rift margins.

The locus of thickest sediments within the BCB occurs offshore of the Totten Glacier discharge region of west Wilkes Land. The Totten Glacier is one of the widest, fast-flow

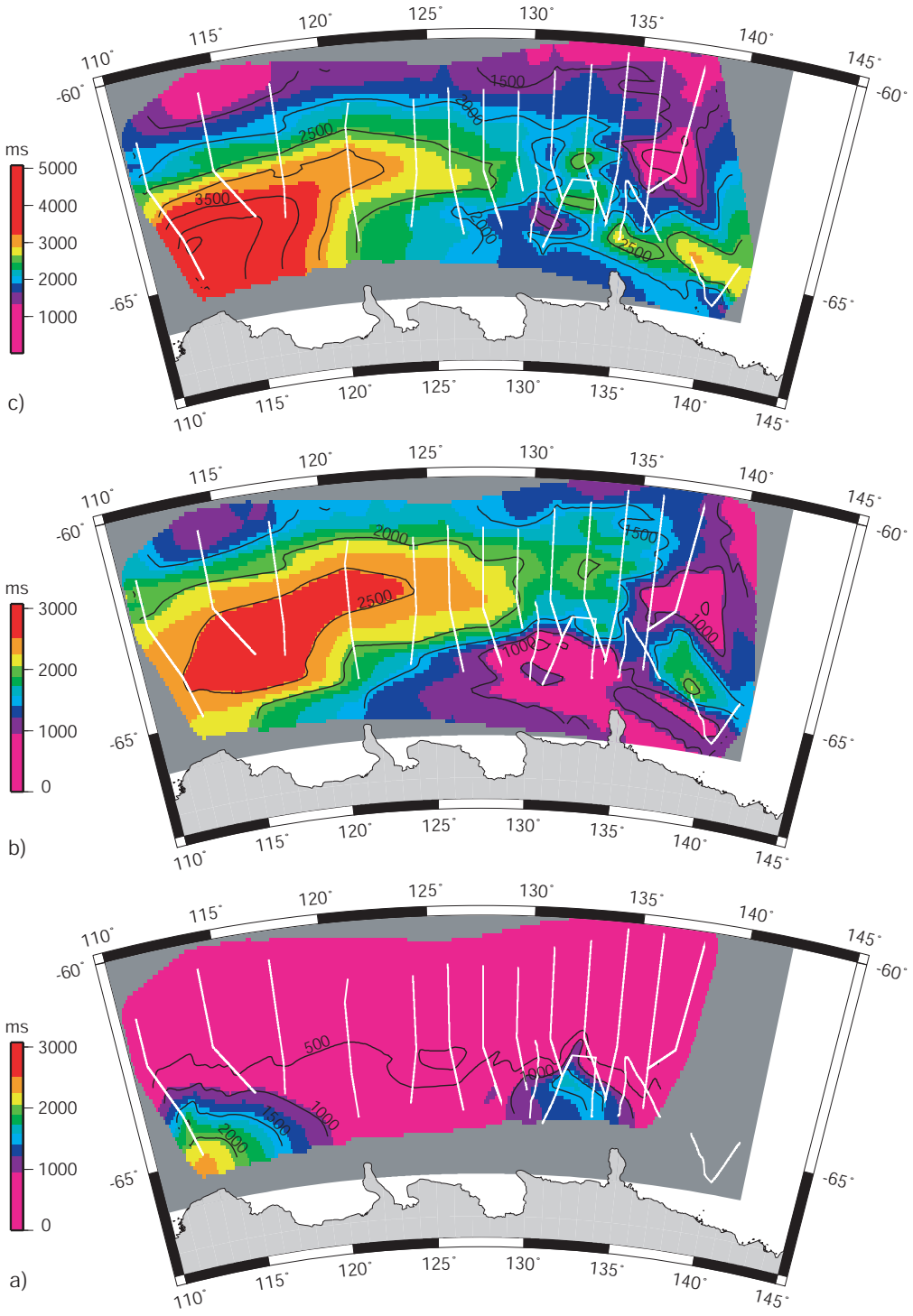

Figure 4.28: Two-way-time isopachs for a) sequence 2, b) sequence 1, and c) total post-rift sediment thickness. White lines indicate line data used in gridding. Note that isopach (c) is plotted with a different scale for improved resolution of spatial distribution.

features (outlet glaciers or ice-streams) in East Antarctica [Bamber *et al.*, 2000]. Bamber *et al.* [2000] model a peak discharge velocity of almost 800 m/y, and average velocities of greater than 50 m/y are inferred for glacier sections over 200 km wide. Analysis of the bedrock topography of the Wilkes Land interior (BEDMAP project, Lythe *et al.* [2000]) suggests that the catchment area of the Totten Glacier includes the Aurora Basin, a major depression that may be, at least in part, an erosive feature. The spatial correlation of thick offshore sediments and the Totten Glacier provides evidence that some fast-flow features maintain relatively static discharge points on long time scales (>10 My).

The west to east asymmetry of the axis of thickest sediment off Wilkes Land indicates a long-lived, marine transport process. Lateral, deep-water currents on the East Antarctic margin are interpreted as the most likely mode of along margin sediment transport. We infer that west to east deep-water currents existed for most (if not all) of the interval from ∼34-9 Ma. Measurements of bottom current velocity off the Wilkes Land margin, however, indicate an east to west direction for the geostrophic current south of ∼65°S [Bindoff *et al.*, 2000], and show no consistent trend in the deeper waters of the continental rise and abyssal plain. The only strong eastward current noted by Bindoff *et al.* [2000] occurs between 90-100°E, just south of the southern boundary of the Antarctic Circum-polar Current (ACC), where a recirculation of the westward slope current and a weak cyclonic gyre is suggested. The absence of a modern analogue current to that inferred from the distribution of Miocene sediments indicates a change in ocean circulation patterns around East Antarctica since the late Miocene.

Although the initiation of the ACC is interpreted to have occurred soon after the opening of the Tasman Gateway and Drake Passage between 34-29 Ma, the bottom water currents important in Southern Ocean and global ocean circulation likely only date back in their current (or approximately current) form to ∼9 Ma, when the ice sheet began to stabilise towards its current configuration. Therefore, palaeo-current direction could have been in the opposite sense prior to the influence of bottom water associated with continental glaciation, and these palaeo-geostrophic-currents could have provided the required transport mechanism. A second possibility is that the ACC existed south of its modern latitude range (50-60°S), from ∼34-9 Ma, and was the primary agent for the observed sediment distribution. The narrower Antarctic-Australia ocean basin and more southerly latitude of the Tasman Gateway [Lawver & Gahagan, 2003] could have forced the ACC far enough south such that it deflected the down-slope transported turbid sediment to the east off the Wilkes Land margin.

Sedimentary structures, such as wavy bedforms, do indicate the presence and influence of along margin, deep water currents. However, it is not possible to infer an absolute direction or timing of onset of these currents from two-dimensional transects of

the sedimentary section. A number of features within the post-rift sediment sequence are discussed and analysed in detail in a later section.

4.13 Sedimentary Structures

Dynamic depositional environments on the Wilkes Land margin are indicated by the range of sedimentary structures and lateral facies changes observed in MCS data. Features common to other sectors of the Antarctic margin, such as levee and channel structures, sediment drifts and mounds, and sediment waves, are evident. Down-slope gravitational and lateral-current induced forces are inferred to exert varying amounts of influence over depositional environments. Long lived, erosion-deposition cycle features, comparable to enigmatic reflectors reported by Rebesco *et al.* [1997], are imaged in fine detail. Bottom simulating reflectors (BSR) are also evident below the continental slope and rise on a number of lines.

4.13.1 Sediment Waves

Wavy bedforms are recognised in varying forms and extent along the Wilkes Land margin. The thickest and most longitudinally extensive sequence of migrating sediment waves yet discovered occurs off west Wilkes Land, Figure 4.29. This sequence is over 1.5 s TWT (∼1.5-2 km) thick and extends for ∼100 km from the continental rise to the abyssal plain. Migrating sediment waves are generally regarded as a primary indicator of contour-current deposition [Damuth, 1979]. Sediment waves in this sequence appear to migrate up-slope, however, as they are imaged in two dimensions, it is not possible to absolutely determine their direction of migration. Donda *et al.* [2003] report that sediment wave crests on channel levees observed off east Wilkes Land are generally parallel with the bathymetric contours and appear to migrate up-slope.

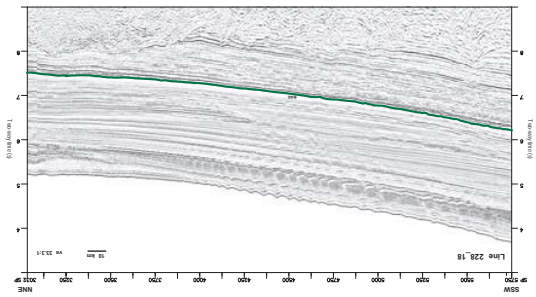

Figure 4.29: Thick sequence of sediment waves from Line GA-228_18. Waves appear to be climbing up-slope.

Contour and geostrophic currents flow in a broadly margin parallel sense, which is

grossly east-west or west-east for Wilkes Land. If the observed sediment waves formed under the influence of contour current, it suggests a long-lived (>10 My - assuming sedimentation rates derived above) interaction between deep current systems and sediment discharge from the west Wilkes Land margin. Although the presence of long lived west to east contour currents is indicated by the observed sediment distribution, the geometry of the sediment waves does not support construction due solely to west to east (or east to west) current flow.

Migrating sediment waves identical to those created by contour currents have been observed on the levees of large deep-sea channels [Embley & Langseth, 1977] and on levees of deep-sea fan valleys [Damuth, 1979], in regions interpreted to have been absent of strong or long lived contour currents. Migrating waves on channel levees, in the absence of contour currents, suggest that the channel overflow of down-slope, turbidity currents create these bed forms also. A second plausible source of down-slope currents on the Wilkes Land margin is Antarctic bottom water (ABW). ABW is saline, dense and particulate rich water produced on the Antarctic continental shelf in response to sea-ice formation [Eittreim *et al.*, 1972], it then spills over the shelf break and down the continental slope and rise. This suggests a possible alternative mode of genesis, not associated with contour currents, for sediment waves observed off west Wilkes Land. Normack *et al.* [1980] suggest that sediment waves associated with down-slope turbidity currents exhibit a down-slope decrease in amplitude, this trend is evident in this sequence of sediment waves off west Wilkes Land.

The occurrence of sediment waves in the upper-most sedimentary sequence, and the consistent form of these bedforms throughout the sequence, indicates that the genetic processes producing these bed forms have been continuous and are maintained in modern times. Whereas, comparison of modern bottom current directions and those inferred from pre-Pliocene sediment distribution indicates a change in ocean circulation patterns around the Wilkes Land margin. This ambiguity in current directions through time and the stratal patterns identified (i.e. up-slope migration and increasing amplitude) indicate that the turbidity overflow mode of genesis is more likely to represent the primary control on the observed pattern of sediment waves. This does not discount some influence from laterally flowing contour currents. Swath bathymetry of the region would allow the areal extent and true geometry of this sediment wave field to be determined, and the importance of the contrasting influences of contour current and gravity driven turbid flow to be established. If a diagonal migration direction is identified in three-dimensional data, then a contour current influence is likely.

Despite the large thickness of sediment waves imaged on Line 18, adjacent lines show little (west) or no (east) evidence of such bed forms. This is interpreted primarily as a

function of line location in relation to morphology. Whereas Line 18 traverses the ridge of a sediment levee adjacent to a major channel, adjacent lines to the east (Lines GA-228_19 and GA-228_20) are located on the flanks of levee structures, Figure 4.30. This suggests that whether their genesis is contour current or turbidity flow related, migrating sediment wave formation is also a function of morphology in glacimarine, turbidite fan systems.

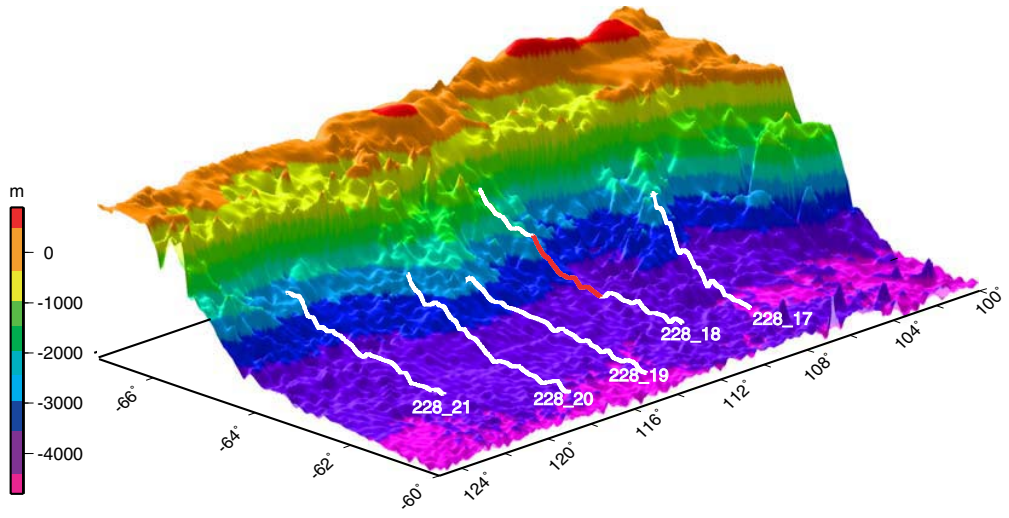

Figure 4.30: Perspective view from the northeast of the west Wilkes Land margin. The laterally isolated occurrence of the thick sequence of sediment waves on Line GA-228_18 (location marked in red) may, in part, be a function of physiography.

4.13.2 Deep, Stacked-Channel Reflections

Strong, concave reflectors are imaged on a number of lines off west Wilkes Land, e.g. Line GA-228_20, SPs 6000-7500. These reflectors occur at varying depths and on different scales, however, they share common, characteristic stratigraphic patterns. The gross geometry of these features closely resembles the enigmatic reflectors (labelled X by Larter *et al.* [1997]), identified west of the Antarctic Peninsula. Rebesco *et al.* [1997] consider the possibility that the reflectors represent bottom-current erosion, however, they reject this interpretation due to the magnitude (>1500 m) of erosion required at abyssal depths. Their favoured interpretation suggests that the reflectors represent the traces of local, diachronous hiatuses of limited temporal extent associated with the migration of abyssal currents.

We propose an alternative origin of formation for these reflectors, based on meso-scale stratigraphic relationships, involving palaeo-channel surfaces. Detailed analysis reveals that not all reflectors terminate down-dip against this 'apparently' cross-cutting reflector

surface, Figure 4.31. This suggests the reflector represents a migrating facies change from channel to overbank deposits, and comprises a 'stack' of erosional unconformities. The channel fluctuates through stages of erosion and deposition, presumably depending on the magnitude of individual turbidity currents. This removes the requirement that 1500 m of erosion occurs during a single interval and does not necessarily require bottom current erosion, the two main factors that Rebesco *et al.* [1997] used to argue against an erosional genesis.

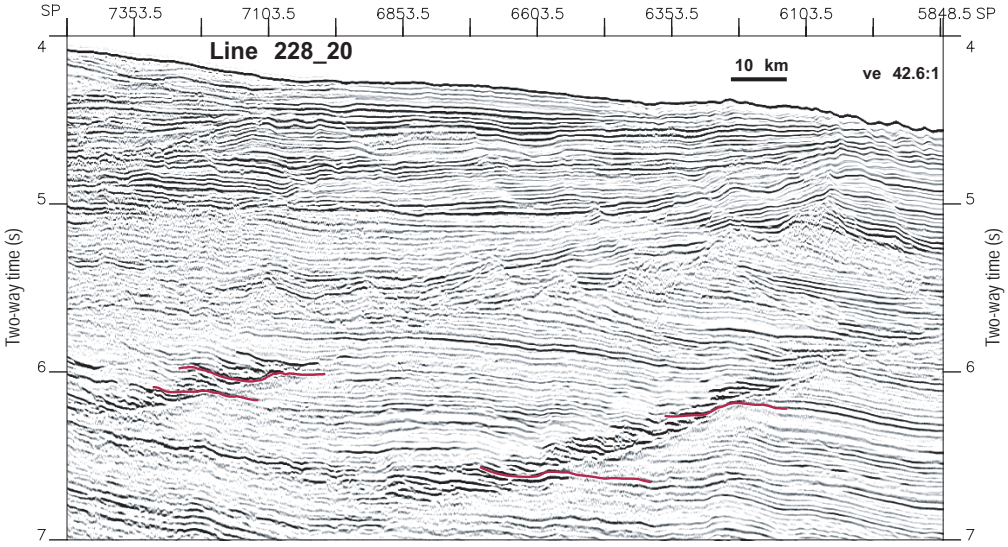

Figure 4.31: Enigmatic reflectors that appear to cross-cut the stratigraphy on Line GA-228_20. This detailed section illustrates the continuity of reflectors (e.g. red form lines) across this 'apparent erosive surface'.

The possibility that reflectors such as these represent low-angle gravity-induced slip surfaces is not supported by these data. Reflector offset, an expected association with structural, or gravity-slip origins is not evident. The erosional and onlap patterns also preclude a structural origin.

4.13.3 Multi-Scale Slumping

Three very large slump deposits are identified on the Wilkes Land margin that extend over 200 km from the base of the continental slope. These deposits exhibit a relatively transparent acoustic character and variably rough, unconformable, lower boundaries. One of these deposits is recognised as a lobe deposit, formed at the edges of a laterally spreading slump on the lower rise. The flow-axis deposit of two other slumps are also recorded from the slope to the lower rise, these deposits contains large slide blocks. Large slumps are known on almost all continental margins and also around oceanic islands,

however, they have not been reported previously on the Wilkes Land margin.

The slump-lobe deposit imaged on Line GA-228_18 exhibits a relatively conformable (i.e. only minor erosion of underlying strata) lower contact. The deposit reaches a maximum thickness of ~250 m and extends for over 50 line kilometres. It is not possible to determine the direction of propagation from this two dimensional transect or its farthest extent from the base of the continental slope.

Much more chaotic slump deposits are imaged on Lines GA-228_21 and GA-228_24. The deposit identified on Line 21 extends for over 200 km, achieving a maximum observed thickness of ~350 m at more than 100 km from the base of the continental slope. The lower contact of this deposit is rough and strongly erosive. The upper surface is also very rough and exhibits angular surface reflections from large blocks entrained by the slump. This slump clearly evidences a high-energy, and large volume displacement of sediment from the continental shelf or upper continental slope.

Smaller-scale, channel-bank slump deposits are also evident in the submarine fan system that exists on the Wilkes Land margin. Figure 4.32 illustrates a reflector interpreted as a low-angle failure surface where the sense of failure is oblique to the survey line direction. Chaotic reflector geometries are observed within channel bank and levee deposits and around palaeo-channels, where gravity-induced sediment slumping has occurred. Such processes have clearly been an almost continuous process through the life of the fan system.

4.13.4 Bottom Simulating Reflectors

Bottom simulating reflectors (BSR) are observed in MCS data on the Wilkes Land margin. They typically occur at sub-seafloor depths of ~500-700 m and represent a major change in reflector amplitude. Reflector amplitudes decrease significantly below BSR, e.g. Lines GA-228_18 and GA-228_20. BSR are recognised in many marine environments where they are commonly interpreted as the basal boundary of frozen gas hydrates. We interpret Wilkes Land BSR as representative of a diagenetic, silica phase transition. Prydz Bay ODP site 1165 results Cooper & O'Brien [in press] document a transition from sediments with diatoms (opal-A) above 606 m below sea level (mbsl), to sediments with silicified horizons (inferred opal-CT and/or chert) below this depth.

Corresponding to the depth of this silica transition are abrupt shifts in downhole logging measurements such as velocity, density, porosity and resistivity Cooper & O'Brien [in press]. The physical changes associated with this diagenetic transition cause the change in reflector amplitude noted in MCS data. The depth at which the transition occurs is a function of temperature and the ratio of terrigenous to biogenic silica concentrations,

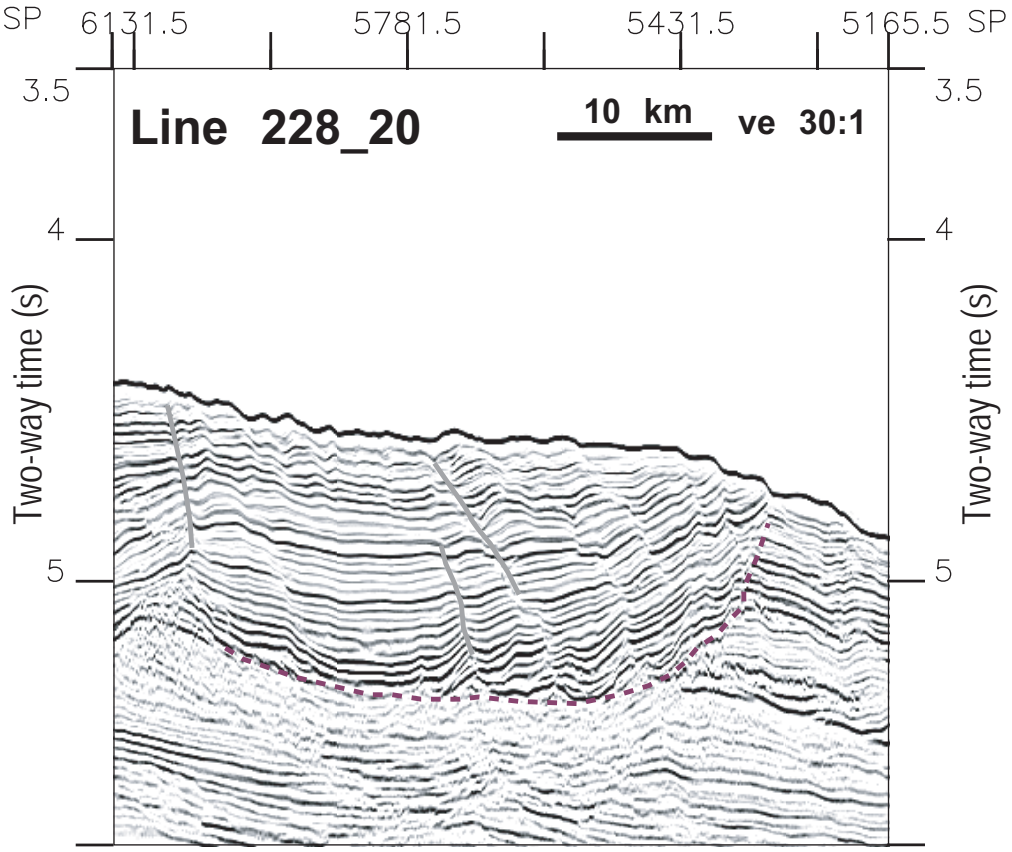

Figure 4.32: Reflector offsets along this low-angle surface (dashed form line) are interpreted as out-of-plane slumping. The surface is, in part, controlled by the location of the bottom simulating reflector which marks the change in reflector amplitude at ∼5.2 s TWT.

with higher temperatures and biogenic silica advancing the transition. The primary controls on the distribution of the BSR is unclear for the extent of the margin. Production of biogenic silica is observed to be greater on the continental rise of Prydz Bay relative to the continental slope and shelf so changes in the BSR reflectivity down dip are expected, however, the controls along strike of the margin are unclear.

Volpi *et al.* [2003] recognise the BSR as a decollement surface for slumps and slides off the Antarctic Peninsula. Evidence of this is seen off west Wilkes Land also, where we see a coincidence of the BSR and a low-angle slump surface, Figure 4.32.

4.14 Depth Conversion and Horizon Extrapolation

The horizons interpreted in MCS data were converted from TWT to depth using smoothed stacking velocity grids, as discussed in Chapter 3. Although the velocity models are pri-

marily based on stacking velocities derived from semblance analysis, constraints from sonobuoy refraction velocities were considered where available.

The interpretation of post-rift sediment thickness provides a crucial constraint in the geometry of gravity models in Chapter 6. However, the constraints on this thickness are limited landward of the lower continental slope. Therefore, it is necessary to extrapolate the landward extent of the *tur* and *eoc* horizons to create complete gravity models and allow the free air edge-effect anomaly to be modelled. These horizons were extrapolated in depth, so as not to require depth conversion where any velocity model would be unconstrained. Some constraint on horizon geometry was provided by data from JNOC surveys off west Wilkes Land, however, the central Wilkes Land sector extrapolations are largely unconstrained. The landward geometry of sequences 1 and 2 can be constrained for east Wilkes Land, from Lines GA-228_25 to GA-229_06, using ATC82 (IFP) and L184 (USGS) survey data.

An assumed zero post-rift sediment thickness at the Wilkes Land coast line provides a further constraint. This assumption is valid as outcrop on this Antarctic margin sector comprises almost entirely cratonic metamorphic rocks. The geometry of the extrapolated sediment thickness and line drawings of the interpreted, depth converted horizons for GA-228 Lines GA-228_18 to GA-228_29 are illustrated in Figures 4.33 and 4.34. These depth-sections provide geometrical constraints for gravity modelling in Chapter 6.

4.15 Summary

Seismic reflection data have allowed the architecture of the Wilkes Land rifted margin to be imaged and interpreted. On the basis of seismic character and velocity structure the limits of unequivocal continental and oceanic crust, and an interleaving zone of continent-ocean transition have been mapped. However, the location of a COB within the transition zone remains equivocal, on the basis of seismic data alone it can not be further constrained.

Regional sediment isopachs indicate a massive sediment load on the Wilkes Land margin. Most of this sediment is interpreted to have been deposited during a period of massive continental erosion and sediment transport, in response to a period of long-lived polythermal glaciation. The distribution of sediment along the margin suggests deep-marine currents have also been important in sediment transport on the Wilkes Land margin.

Through correlation with data from the conjugate Australian margin, age constraints are placed on major unconformities recognised within the sedimentary sequence. Relative age constraints are also inferred on the basis of seismic interpretation. For example, the

evidence of extension and deformation at later times in the Adélie Rift Block relative to central and west Wilkes Land. However, to further constrain the age of breakup between Antarctica and Australia, and to attempt to locate the COB, magnetic anomaly data must be analysed and correlated to seismic reflection data.

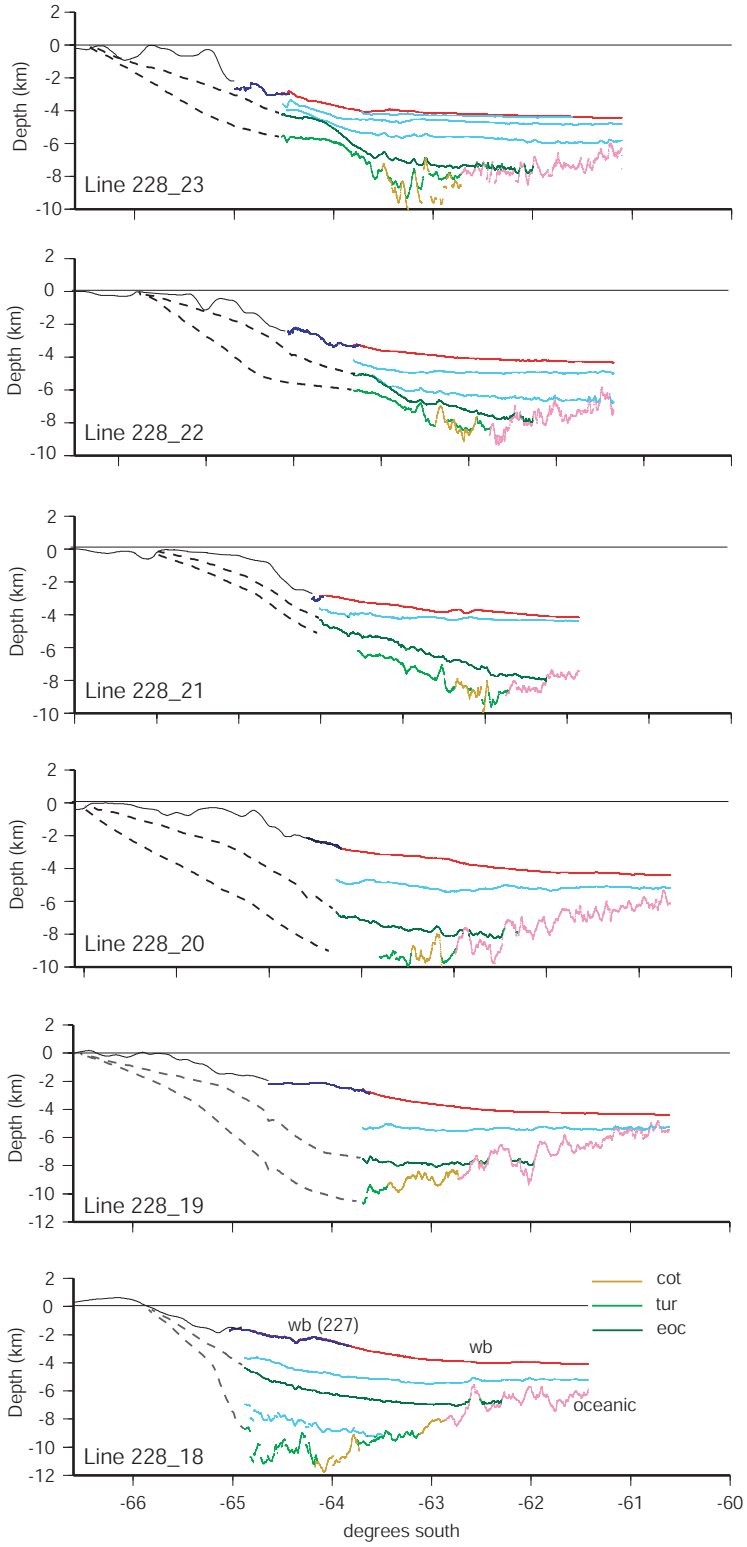

Figure 4.33: Line drawings of seismic reflection profiles GA-228_18 to GA-228_23 in depth. These sections provide constraints on the geometry of gravity models. Dashed black lines illustrate the extrapolated *eoc* and *tur* horizons.

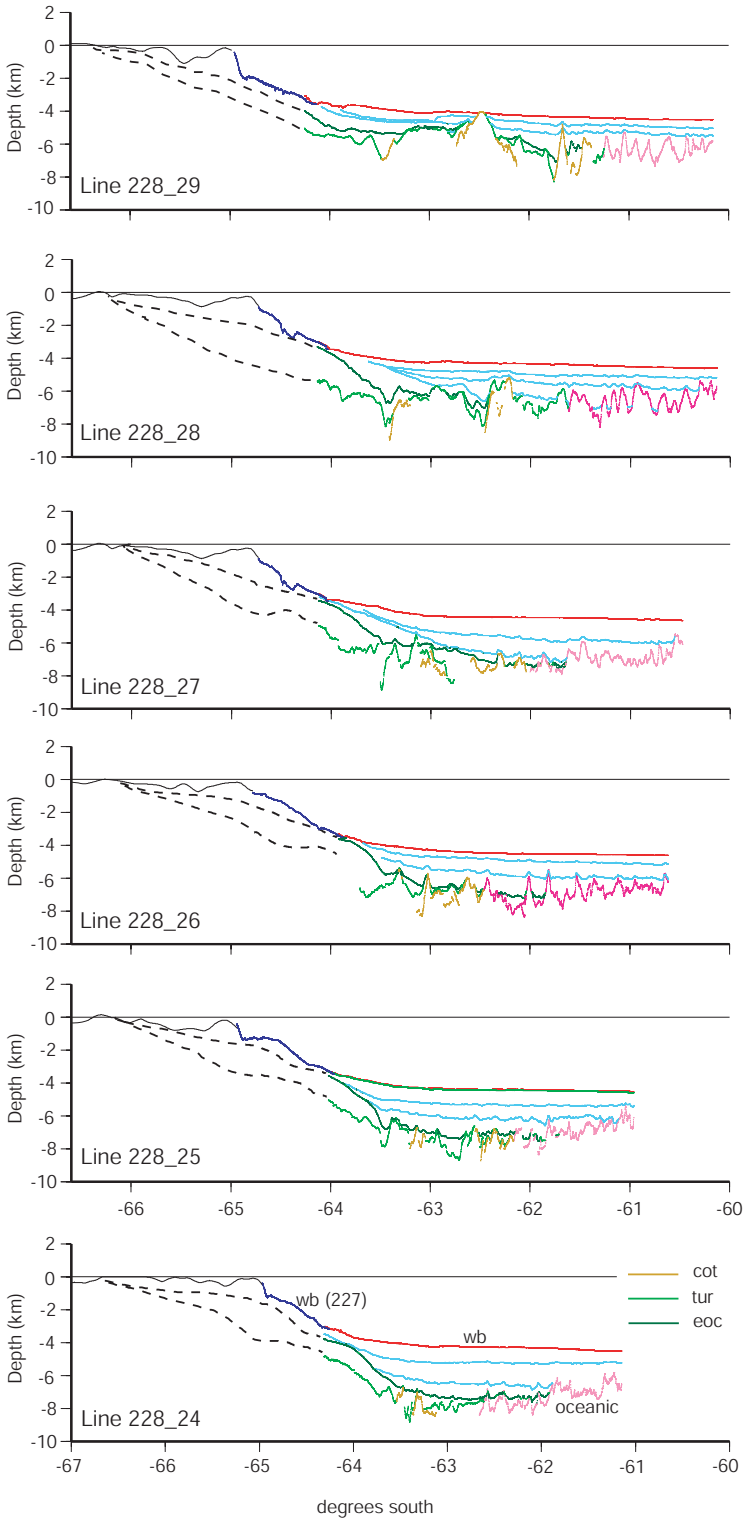

Figure 4.34: Line drawings of seismic reflection profiles GA-228_24 to GA-228_29 in depth. These sections provide constraints on the geometry of gravity models. Dashed black lines illustrate the extrapolated *eoc* and *tur* horizons.

Chapter 5

Magnetic Data and Interpretation

5.1 Introduction

Magnetic data are important in constraining marine geophysical models in continental margin environments due to the fundamentally different magnetic signature of continental and oceanic crust. Their greatest importance, however, is in dating oceanic crust through the identification of seafloor spreading anomalies and the correlation of these anomalies to the geomagnetic time-scale (e.g. Vine & Matthews [1963]). Identification of seafloor spreading anomalies on the Wilkes Land sector of the Antarctic margin, however, is difficult, primarily because of the slow and variable spreading rates at the South-East Indian Ridge (SEIR) between Australia and Antarctica prior to the onset of fast spreading in the Eocene [Cande & Mutter, 1982; Tikku & Cande, 1999].

A slow mid-ocean ridge spreading rate causes several normal and reverse polarity periods to occur in a spatially limited area. This results in the complex superposition of anomalies associated with each switch from normal to reverse field polarity. The anomaly sequence between breakup and the Eocene on the Antarctic and southern Australian margins is difficult to model and interpret. Hence, a number of questions remain regarding the identification of the oldest seafloor spreading anomaly on the Antarctic margin. Recent studies on the conjugate southern Australian margin indicate that anomaly 33o[1] represents breakup at 83 Ma [Sayers *et al.*, 2001]. This interpretation, however, conflicts with previous interpretations by Tikku & Cande [1999], Veevers [1986], and other workers as discussed below.

Magnetic data were acquired along each multi-channel seismic (MCS) line of surveys GA-228 and GA-229. An *Elsec 7706* proton precession magnetometer was utilised throughout surveying. Both total magnetic field and magnetic anomaly values (calculated using IGRF2000 [IAGA, 2000]) were provided by the geophysical contractor. The data have been filtered using a three point de-spiking and interpolation process to smooth

[1] subscripts o and y refer respectively to the old and young edges of the normal polarity period of an individual geomagnetic chron. Normal polarity periods are indicated by the subscript n, e.g. 33n refers to the entire normal polarity period of Chron 33.

irregular 'drop-outs', but have not been diurnally corrected. Accordingly, temporal magnetic field variations as well as remanent and induced magnetisations are included in the total magnetic field measurements.

Marine geophysical surveys in the Southern Ocean have been acquiring magnetic data since the 1950's. Although not as thoroughly surveyed as other ocean regions there is relatively good data coverage between the SEIR (which runs approximately east-west at 50°S) and 60°S. However, south of 60°S the coverage is much sparser. This is particularly unfortunate given that this is the region of most ambiguous seafloor spreading anomaly identification. All data used in this study are corrected to IGRF2000 [IAGA, 2000] to assure uniformity in anomaly calculation. Data are projected onto a north-south azimuth to allow consistent comparison. This orientation was chosen as it is approximately orthogonal to the trend of the SEIR between the Australian and Antarctic Plates.

The acquisition of ∼10,000 km of magnetic anomaly data along the Wilkes Land margin represents a major increase in available data in this region. The early spreading history of Wilkes Land and southern Australia, based on previously available data, remains uncertain (e.g. Tikku & Cande [1999]). Hence, spreading rate modelling was undertaken to constrain the identification of seafloor spreading anomalies in GA-228 and GA-229 data and investigate the timing of breakup between Antarctica and Australia.

5.2 Magnetic Modelling

Introduction

Magnetic modelling is crucial in the testing of seafloor spreading models, and therefore in dating sections of oceanic crust. As a potential field method it can not provide a unique solution as there are infinite source distributions possible for any given magnetic anomaly data. However, it remains a means of testing geologically reasonable hypotheses and constraining important variables, namely spreading rate and age of oceanic crust.

The magnetism of the rocks that comprise the Earth's crust is highly variable and can be acquired in a variety of ways. Magnetisation can be transient (i.e. dependent upon the presence of an ambient magnetic field), this is known as induced magnetisation. It can also be permanent (i.e. unaffected by changes in ambient field strength), this is known as remanent magnetisation. The relative importance of these two types of magnetisation is primarily a function of the local geological environment, e.g. rock type, cooling history, grain-size, metamorphic/alteration history.

When placed in a magnetic field, rocks and sediments may become magnetised by induction, a result of dipoles aligning under the presence of an ambient field. The dipole

moment per unit volume is defined as the induced magnetisation (J_i), this quantity is proportional to the strength of the ambient field (F). The constant of proportionality is defined as the magnetic susceptibility (k) such that,

$$J_i = kF$$

Susceptibilities of common minerals vary significantly, from -0.0001 (quartz) to 6 (magnetite) SI units, depending on their proportional content of paramagnetic, diamagnetic, ferromagnetic and ferrimagnetic material. Studies of induced rock magnetism primarily consider induced magnetisation of ferrimagnetic mineral grains [Dunlop, 1995].

The magnetism of the Earth's crust is largely controlled by ferrimagnetic mineral distribution. There are two such important mineral groups; the titanomagnetite series and pyrhhotite. In most rocks, particularly oceanic basalts, titanomagnetites are the primary source of magnetisation (e.g. Smith & Banerjee [1986]). Titanomagnetites exhibit a continuous solid solution between the *Fe* rich endmember (magnetite) and the *Ti* rich endmember (ulvöspinel) [Blanchard *et al.*, 1976]. The susceptibility of common rocks tends to be proportional to magnetite content and typically decreases with decreasing grain size [Stacey, 1967; Kent & Gee, 1994].

As magnetite and other ferrimagnetic minerals cool to below the Curie temperature (T_c) a large proportion of magnetic domains come to have moments which are aligned in the ambient field direction. This produces a permanent natural or Thermal Remanent Magnetisation (TRM) that persists in the absence of any external field. Many rocks with high titanomagnetite content, such as oceanic crust basalts, acquire a remanent magnetisation (J_r) as they cool. However, as oceanic crust ages, layer 2 basalts are altered and their magnetisation is reduced, although a record of the geomagnetic field is retained [Kent & Gee, 1994].

Total magnetisation (J) (i.e. the quantity measured by total field magnetometers) is the sum of induced and remanent magnetisation,

$$J = J_i + J_r$$

the induced and remanent components are both vectors and must be added accordingly. The magnitude J controls anomaly amplitude and its direction controls the anomaly shape. The ratio of the *magnitude* of J_r to J_i (i.e. J_r/J_i) is defined as the Königsberger ratio (Q).

Linear magnetic anomalies in oceanic crust that record seafloor spreading (e.g. Vine & Matthews [1963]) result almost entirely from TRM. Induced magnetisation associated with the present-day ambient geomagnetic field is also present, but the Königsberger ratio of oceanic crust tends to be large [Dunlop, 1995]. The fine grain size of titanomagnetites

in oceanic crust, resulting from initial quenching and later surface oxidation, inhibits any motion of magnetic domains within the crystal lattice and, therefore inhibits induced magnetisation. Hence, only remanent magnetisation is usually taken into account in analysis of magnetic anomalies in ocean basins.

Gee *et al.* [1989] investigated the contribution of induced magnetisation at seamounts and concluded that although remanent magnetisation is dominant, up to one-sixth of the total magnetisation may be accounted for by induced magnetisation. It is difficult to determine any departures from the assumptions regarding Königsberger ratios in oceanic basalts at passive margins as no drill-holes have as yet penetrated deeply into oceanic crust beneath thick marginal sediments. Therefore, at continental margins and other environments possibly affected by hydrothermal alteration and structural deformation, the relative contribution of remanent and induced components is less certain than in deep ocean basins.

5.2.1 Previous Work

The most detailed study of magnetic anomalies in the southeast Indian Ocean was undertaken by Weissel & Hayes [1972]. Weissel & Hayes [1971] and Weissel & Hayes [1972] divided the region south of Australia into three longitudinal zones on the basis of contrasts in magnetic, morphologic, and seismologic parameters (Figure 5.1). They investigated asymmetry in spreading, the effect of variable palaeoinclinations, and magnetic anomaly amplitude variations. Weissel & Hayes [1972] noted distinct amplitude differences among,

1. magnetic anomalies of different ages,
2. magnetic lineations of the same age but located on opposing ridge flanks, and
3. magnetic anomalies of the same age and on the same ridge flank but from the different longitudinal zones.

The oldest magnetic anomaly sequence identified by Weissel & Hayes [1972] was 19-21, with *"perhaps an indication of anomaly 22"* in the Great Australian Bight and near the Antarctic continent. Hence, they interpreted Australia-Antarctic separation to have occurred in the Early Eocene (53 Ma), based on the Heirtzler *et al.* [1968] geomagnetic reversal time scale. However, a relative paucity of data on the Antarctic margin forced interpretations of Weissel & Hayes [1972] to include unconstrained interpolations of great distance (>150 km) between shiptrack data.

The lineation identified as anomaly 22 by Weissel & Hayes [1972] does not lie adjacent to the coast on either the southern Australian or Antarctic margin, due to the presence of Magnetic Quiet Zones (MQZ) [Weissel & Hayes, 1972]. The spreading rate model of Weissel & Hayes [1972], for their zone A (128-138°E), is shown in Figure 5.2. Variable

Figure 5.1: Shiptrack magnetic anomaly data utilised by Weissel & Hayes [1971]. Zones A-C are divided on the basis of magnetic, morphologic, and seismologic properties. Earthquake epicentres are indicated by black dots.

half spreading rates of between 22 mm/yr and 38 mm/yr were interpreted based on this model. The fit between the observed and modelled profiles is good from the spreading centre to approximately anomaly 18. Spreading rate differs by only 2 mm/yr for north and south flanks (faster to the south) after anomaly 5 time. From anomaly 5 to anomaly 13 time, modelled spreading rates are faster to the north by between 5 mm/yr and 9 mm/yr. Spreading rates prior to anomaly 13 are, again, almost the same on both flanks.

A number of problems associated with the breakup age interpreted by Weissel & Hayes [1972] were noted in the mid-late 1970s and early 1980s. Boeuf & Doust [1975] and Denham & Brown [1976] interpreted foreset bedding in seismic reflection data in Upper Cretaceous strata, and suggested that they indicate the development of a marine depositional environment prior to the early Tertiary. Willcox [1978] also interpreted seismic reflection data to indicate Lower Cretaceous sediments overlying purported Eocene aged oceanic crust. König [1980] noted that the model of Weissel & Hayes [1972] did not explain the presence of a distinct, laterally extensive magnetic anomaly between anomalies interpreted as 20 and 21 by Weissel & Hayes [1972].

In particular, Cande & Mutter [1982] questioned aspects of the identification of anomaly 22 south of Australia and the fit of the model and observed data for the older

Figure 5.2: Spreading rate model of Weissel & Hayes [1972] and two-dimensional synthetic magnetic anomalies for zone A computed for selected sequences of anomalies. Representative observed profiles (indicated by arrows) shown for comparison with synthetic profiles. Note that spreading rates are in cm/yr.

part of the anomaly sequence (anomalies 19-22). On re-examination of the magnetic anomaly pattern, Cande & Mutter [1982] concluded that anomalies 19-22 were better modelled as anomalies 20-34 using a variable spreading rate, Figure 5.3. Accordingly, Cande & Mutter [1982] interpreted that breakup occurred between 86-110 Ma, during the Cretaceous Long Normal Polarity epoch (KLNP), based on the Heirtzler *et al.* [1968] geomagnetic reversal time scale. The anomaly sequence interpreted by Weissel & Hayes [1972] subsequent to anomaly 18n time was accepted by Cande & Mutter [1982].

Although the revised interpretation of the magnetic anomaly sequence suggested that breakup occurred at or before anomaly 34 time, the actual age of breakup remained uncertain. Due to the presence of the broad MQZ, of enigmatic origin, the age of breakup was difficult to estimate [Cande & Mutter, 1982]. Two alternative age constraints were suggested by Cande & Mutter [1982] based on two different geological scenarios:

1. *"If the MQZ is floored by subsided continental crust or perhaps remnants of the original pre-breakup rift valley, and if the basement high at its southern side marks the ocean/continent boundary , then we date the age of this boundary as approximately 90*

m.y. B.P. by extrapolating beyond anomaly 34 using a spreading rate of 4.5 mm/yr."

2. If the MQZ is formed in part by seafloor spreading during the Cretaceous long normal polarity period (KLNP) then *"the age of breakup could be anywhere between 112 m.y. (the age of M0) and 90 m.y."*.

The revised anomaly identifications and seafloor spreading model of Cande & Mutter [1982] included an interval of slow-spreading from 90-43 Ma. They cite the correlation of the boundaries of this period with times of global plate reorganisations, as a possible catalyst for significant spreading rate changes.

Modelling by Cande & Mutter [1982] indicated that anomalies that had been interpreted as anomalies 20-22 closely resembled a very slow spreading rate (4.5 mm/yr) model of anomalies 21-34. The key to this model was that each anomaly corresponds to the combined effect of several polarity reversals. A comparison of the models of Weissel & Hayes [1972] and Cande & Mutter [1982] is shown in Figure 5.3.

Figure 5.3: Spreading rate models of Weissel & Hayes [1972] and Cande & Mutter [1982] and two-dimensional synthetic magnetic anomalies computed for the sequence of anomalies older than 13n. Observed profiles from surveys Eltanin 37 and Eltanin 41 are shown for comparison. Model B is the preferred model of Cande & Mutter [1982]. Figure after Cande & Mutter [1982].

Geologically, there was no conclusive evidence contraindicating the interpretation of Cande & Mutter [1982]. The *"breakup unconformity"* interpreted by Falvey [1974] in the Otway Basin was reinterpreted by Cande & Mutter [1982] as an unconformity associated

with a eustatic sea level change. They correlate the unconformity with a lowering of eustatic sea level at the base Tertiary as inferred by both Vail *et al.* [1977] and Pitman [1978].

Veevers [1986] accepted the major points of the Cande & Mutter [1982] model but believed it was possible to further constrain the broad breakup age implied by the limits of the KLNP, 86-112 Ma. Veevers [1986] reinterpreted the positive magnetic anomaly that marks the oceanward edge of the MQZ, interpreted previously as anomaly 22 by Weissel & Hayes [1972] and anomaly 34 by Cande & Mutter [1982], as an edge-effect, caused by magnetic oceanic crust abutting essentially non-magnetic continental crust (i.e. the COB). Based on this interpretation of the COB location, consistently approximately 45 km landwards of anomaly 34y, and a spreading half-rate of 4.5 mm/yr, Veevers [1986] interpreted the age of breakup as 96 Ma. This age was *"...rounded to 95±5 Ma to account for uncertainties in the initial rate of spreading and the exact location of the COB"*.

The notion of a mid-Cretaceous breakup age persisted throughout the 1990s and was used ubiquitously as a basis for interpretation. Tikku & Cande [1999] reinvigorated the debate over the age of breakup for Australia-Antarctica and refined further the spreading rate model for the southeast Indian Ridge since initial separation. Reconstructions based on the revised anomaly identifications of Tikku & Cande [1999] also encountered problems involving large amounts of continental overlap involving the South Tasman Rise (STR), Tasmania, and Victoria Land (Antarctica). They offered two alternative hypotheses to account for this overlap:

1. Continental extension and/or deformation of oceanic crust in the Australia-Antarctic Basin, or

2. That magnetic anomalies older than anomaly 31 in the Australia-Antarctic Basin are not isochrons.

Tikku & Cande [1999] question the validity of the suggestion by Veevers [1986] that the seaward edge of the MQZ is the COB anomaly, since it is unclear that this distinctive magnetic anomaly is associated directly with the COB for the entire span of the Australia Antarctic Basin (AAB). Tikku & Cande [1999] also introduce a new spreading rate model, based on Cande & Mutter [1982], of the SEIR for the Late Cretaceous to early Tertiary. The major departure from the earlier model of Cande & Mutter [1982] is the introduction of a period of *"ultra-slow spreading"* (∼1.5 mm/yr) between anomaly 31o and 24o time. The inclusion of this period further improved the fit of the modelled and observed magnetic anomaly profiles. The Tikku & Cande [1999] model includes a continental edge-effect at 95 Ma, similar to that modelled by Veevers [1986], however, they do not necessarily suggest that this is representative of the COB.

Reconstructions carried out by Tikku & Cande [1999], based on their revised anomaly

and rotation interpretation, provides two particularly important indications:

1. The quiet zone boundary (QZB) anomaly is not an isochron as its rotation pole is inconsistent with those of later spreading anomalies.

2. That reconstructions using rotation poles based on anomalies 34y, 33o, and 32y result in continental overlap between Tasmania and the western STR.

Tikku & Cande [1999] suggest a number of possibilities to explain these problems:

1. The western STR is incorrectly located in recent reconstructions (e.g. Royer & Rollet [1997]).

2. There may have been substantial northeast-southwest extension in the Bass Strait region or in the conjugate area of Wilkes and Victoria Land since 80 Ma. It is also possible, though difficult to assess, that the required extension may have occurred in the poorly known Wilkes Land interior basins.

3. Like the QZB anomaly it is possible that anomalies 32y, 33o and 34y are not isochrons.

The most recent geophysical and geological interpretation of data from the southern margin of Australia, [Sayers *et al.*, 2001] further revised the Australia-Antarctica breakup age. Sayers *et al.* [2001] identify a 50-120 km continent-ocean transition (COT) zone in the Great Australian Bight using recently acquired deep seismic reflection, and gravity and magnetic data. The COT is characterised by a thin apron of post-breakup sediments overlying complexly deformed sediments and intruded crust that is bounded landward by a basement ridge and seawards by rugged basement, interpreted as oceanic crust. The COT is interpreted to be floored by extended continental lithosphere and accordingly the COB is defined between the COT and oceanic crust, the model proposed by Sayers *et al.* [2001] is shown in Figure 5.4.

In the model of Sayers *et al.* [2001], the COB is located seaward of anomaly 34y and just landward of anomaly 33o as interpreted by Tikku & Cande [1999]. Sayers *et al.* [2001] therefore conclude that the anomaly interpreted previously as 34y is not a seafloor spreading anomaly and that breakup occurred around 33o time. It should be noted, however, that the magnetic models created by Sayers *et al.* [2001] are not referenced in any way to a geomagnetic reversal time scale. Oceanic crustal segments are given positive or negative *"apparent susceptibilities"* to simulate normal or reverse remanently magnetised blocks. The block edges are *"...placed where the data demands a change in magnetic properties"*. The model includes only six reversely polarised blocks, however, the labelled anomalies (18 to 33o) corresponds to at least 15 magnetic field reversals. Despite the shortcomings of this magnetic model, the important result from this study is that anomaly 34y is interpreted to overlie stretched continental, rather than oceanic, crust.

Figure 5.4: Structural model of Sayers *et al.* [2001] (Figure 7) across the Ceduna Sub-basin in the Great Australian Bight. Stretched continental crust is interpreted to underlie the magnetic anomaly previously interpreted as a seafloor spreading anomaly associated with Chron 34.

Methodologies: Previous Studies

Conventional sea floor spreading anomaly modelling was undertaken by Weissel & Hayes [1972], Cande & Mutter [1982], Veevers [1987] and Tikku & Cande [1999]. Each of these studies utilised a constant thickness (0.5 km) magnetic source layer to represent layer 2 of oceanic crust. The upper surface of this source layer was based either on bathymetry filtered of short-wavelength features (e.g. Weissel & Hayes [1972]), or an assumed constant, crustal depth (e.g. Cande & Mutter [1982]).

The magnetic source layer was assumed by each of the above workers to be 500 m thick. This assumption is based on studies that indicate the source of magnetic anomalies over young oceanic crust is predominantly the upper 500-1000 m of oceanic layer 2 (e.g. Irving [1970] and Levi [1983]). Source layers comprised blocks of alternately normal and reverse TRM of equal magnitude. The polarities of model blocks are constrained by the geomagnetic time scale and an assumed spreading rate model. There is an assumption of zero magnetisation due to induction. This conforms to the generally valid assumption that the remanent magnetisation component is the first order control on the measured total magnetisation vector in oceanic crust.

Modelling with a flat source body of constant thickness (and constant susceptibility) results in no lateral variation in susceptibility. Accordingly the modelled induced magnetisation component is non-variable. The modelled magnetic anomalies due to such a model are entirely a result of the juxtaposition of remanently magnetised blocks with opposing directions of polarity. Weissel & Hayes [1972] explicitly state and justify using only the TRM, citing the lack of significant crustal topography and the typically high Königsberger ratios of oceanic basalts.

The rationale behind this methodology, which has been successfully applied in many of the world's ocean basins, is that a unique pattern of magnetic lineations can be generated and preserved at an active spreading ridge, and that this sequence of anomalies can be matched by a simple model based on a geomagnetic time scale and assumed spreading rates. In the simplest case where no induced component is included, a single Königsberger ratio or remanent magnetisation vector amplitude is utilised, and sharp block edges are juxtaposed, there will be a degree of misfit between the simple model and the observed data. However, even in this situation there typically exist characteristic anomalies that can be *matched* between the modelled and observed data.

The relatively simple methodology outlined above was not followed by Sayers *et al.* [2001], they instead follow an object-oriented approach to modelling. Sayers *et al.* [2001] base their models on seismic interpretations and good fits between observed and modelled profiles that are achieved. In the Sayers *et al.* [2001] model, magnetic source bodies within

the oceanic crust are *"...inferred from changes in the magnetic signal alone, in accord with standard practice"*. The magnetic sources in the models of Sayers *et al.* [2001] exhibit variable depth, thickness, susceptibility, and TRM magnitude. However, there is no basis to infer changes in magnetic properties of rocks on the basis of seismic character, and there is very little variability of seismic character in oceanic crust. Accordingly, this methodology is poorly constrained and not suited to the modelling of seafloor spreading.

Spreading around the SEIR has been primarily north-south (relative to present-day pole locations) since very early separation [Weissel & Hayes, 1972; Cande & Mutter, 1982]. If the SEIR maintained an east-west trend and the Earth's magnetic field was described by a geocentric axial dipole through the Cainozoic, then the declination of the ambient field should have been near zero throughout rifting [Weissel & Hayes, 1972]. Accordingly Weissel & Hayes [1972] assumed a direction of 0° for the horizontal component of the TRM in their modelling, this assumption has been accepted in subsequent modelling studies. [Weissel & Hayes, 1972] calculated anomalies assuming remanent inclinations of ±85°, ±74°, and ±59°, which correspond to latitudes of formation of 80°, 60°, and 40° respectively (assuming an axial dipole field). Subsequent studies by Cande & Mutter [1982] and Tikku & Cande [1999] assume a remanent inclination of ±74°.

5.2.2 Methodology: This Study

A conventional sea floor spreading modelling methodology was utilised in this study. However, as seismic reflection data constrains basement topography, the effect of including variable depth source layers was tested. Tikku & Cande [1999] were restricted to assuming a constant depth magnetic source layer at 5.5 km, as they did not have constraints on basement topography. Variations in both the remanent and induced magnetisations are introduced by including a variable magnetic source layer.

The computational method of Talwani & Heirtzler [1964] was used to compute the magnetic anomalies associated with two-dimensional irregular polygons, extending to infinity in the positive-x direction (Figure 5.5). The horizontal (ΔX) and vertical (ΔZ) magnetic field strength at any given point, associated with an arbitrary polygon, are given by,

$$\Delta X = 2(M_x.P - M_z.Q) \tag{5.1}$$

$$\Delta Z = 2(M_x.Q - M_z.P) \tag{5.2}$$

where M_x and M_z are the components of the magnetisation resolved in the x and z directions respectively, and where

$$P = \frac{(z_2 - z_1)^2}{(z_2 - z_1)^2 + (x_1 - x_2)^2}(\phi_1 - \phi_2) + \frac{(z_2 - z_1)(x_1 - x_2)}{(z_2 - z_1)^2 + (x_1 - x_2)^2} log\frac{r_2}{r_1} \tag{5.3}$$

$$Q = \frac{(z_2 - z_1)(x_1 - x_2)}{(x_2 - x_1)^2 + (x_1 - x_2)^2}(\phi_1 - \phi_2) + \frac{(z_2 - z_1)^2}{(x_2 - x_1)^2 + (x_1 - x_2)^2} log \frac{r_2}{r_1} \quad (5.4)$$

where x_1, x_2, z_1, z_2, r_1, r_2, ϕ_1 and ϕ_2 are illustrated in Figure 5.5.

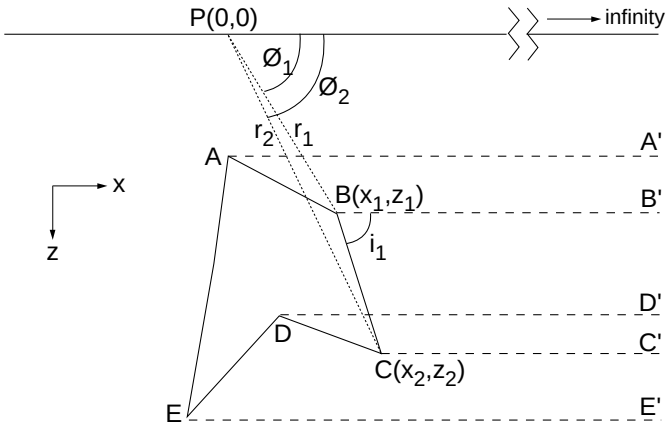

Figure 5.5: Schematic representation of an arbitrary polygon and the method of Talwani & Heirtzler [1964] for two-dimensional modelling of magnetic anomalies.

Similarly to Weissel & Hayes [1972], remanent inclinations of ±85° to ±65° were tested during modelling. A remanent inclination of ±80°, similar to the present-day inclination for the Wilkes Land margin sector of the Southern Ocean, was selected for further modelling. Remanent declination was assumed to be 0°, in accord with previous studies based on the analysis and assumptions of Weissel & Hayes [1972]. An ambient field strength of -66,000 nT was assumed, based on IGRF models [IAGA, 2000]. A remanent magnetisation amplitude of 4 Am^{-1} and magnetic susceptibility of 0.05 SI units were assumed throughout modelling, these are within the ranges specified by Telford *et al.* [1990] and typical of oceanic crust. For this ambient field, and the selected remanent magnetisation palaeoinclination and amplitude, and magnetic susceptibility, the Königsberger ratio of remanent to induced magnetisation is ∼2. The magnitude of the Königsberger ratio alters only the amplitude of calculated anomalies.

The geomagnetic reversal time-scale of Cande & Kent [1995] was used for all modelling. The age bounds of the normal polarity chrons important in discussing magnetic anomalies from the AAB, from the mid-Oligocene to the KLNP (Chron 11 to Chron 34), are detailed in Table 5.1.

Magnetic anomaly	Period (Ma)
11	29.4 - 30.1
12	30.5 - 30.9
13	33.1 - 33.5
18	38.4 - 40.1
20	42.5 - 43.8
21	46.3 - 47.9
22	49.0 - 49.7
24	52.4 - 53.3
27	60.9 - 61.3
31	67.7 - 68.7
33	73.6 - 79.1
34	83 - 118

Table 5.1: Normal magnetic polarity intervals important in the discussion of magnetic anomalies from the AAB. Intervals are from the geomagnetic reversal time-scale of Cande & Kent [1995].

Model Constraints

As there exists a greater quantity of data across the young oceanic crust flanking the SEIR relative to the older oceanic crust at the Wilkes Land margin, and as the magnetisation of oceanic crust is reduced with time (e.g. Kent & Gee [1994]), magnetic anomaly identification is easier in the central AAB relative to its margins. Accordingly, determining spreading rate variations is also easier in the central AAB. Figure 5.6 shows shiptrack plots of five separate cruises by the *R/V Eltanin* which cross the SEIR at least once. The observed magnetic anomaly and bathymetry profiles (projected as north-south profiles) for each of these crossings of the SEIR are shown in Figure 5.7. It is possible to correlate characteristic magnetic anomalies based on amplitude and form (i.e. amplitude and shape) between the profiles. These anomalies can be correlated to modelled anomalies of a synthetic profile created using an assumed spreading rate (31 mm/yr) and the geomagnetic reversal time-scale.

Characteristic magnetic anomalies are most readily correlatable on profiles acquired between 125°E and 140°E (Figure 5.7). Lack of data continuity and changes in anomaly form make it difficult to correlate anomalies east and west of the central AAB. Anomaly amplitude differs significantly between profile ELT35 (western AAB) and ELT41A (eastern AAB). Peak-to-peak amplitudes of anomalies across the SEIR and the adjacent flanks

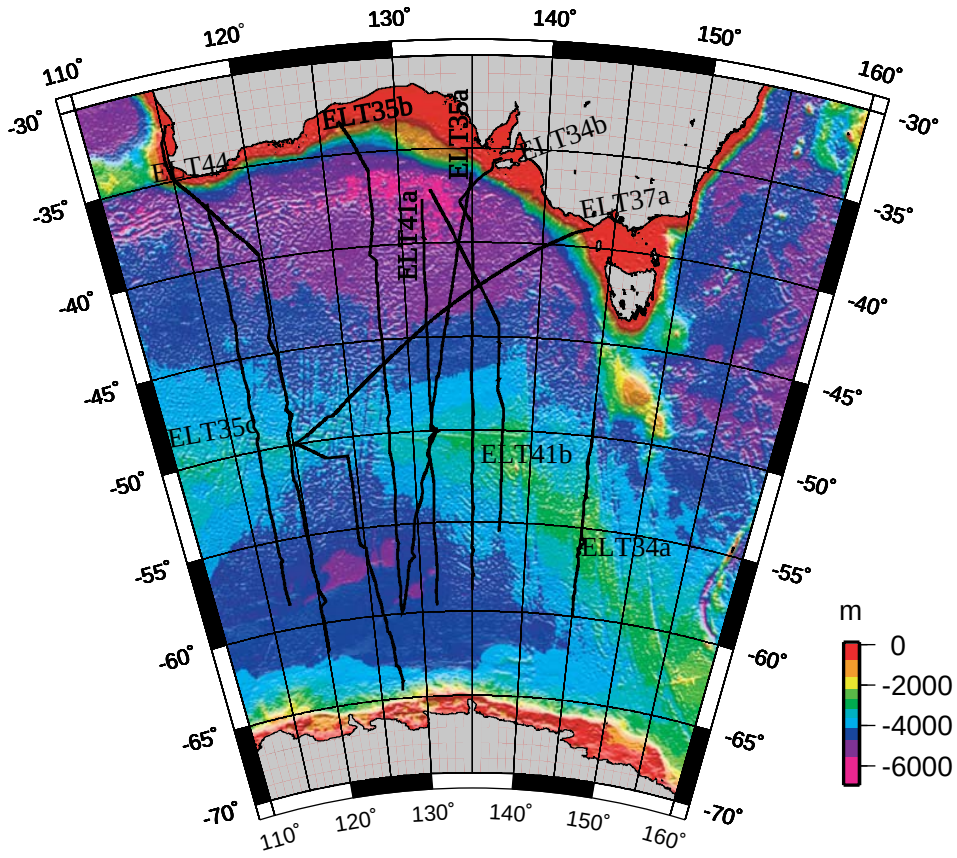

Figure 5.6: Shiptrack plot of Eltanin cruises ELT34, ELT35, ELT37, ELT41 and ELT44, each which cross the SEIR at least once. The satellite derived bathymetry [Smith & Sandwell, 1994], illuminated from the north, illustrates the position of the current spreading ridge system.

in ELT41A data reach up to 600 nT, whereas the largest amplitude anomalies in ELT35 data are ∼300 nT.

The depths to the ridge crest (and hence the minimum depth of the magnetic source layer) are not significantly different between zones A, B, and C. Likewise, the present-day ambient magnetic field is approximately equal in magnitude and inclination in each zone. Hence, it is unlikely the variable along-ridge anomaly amplitude is a function of source depth variation or differences in the present-day magnetic field. Weissel & Hayes [1972] attributed the variation in amplitude to either a thinner magnetic source layer beneath the ridge crest of zone C and/or, a contrast in the magnetic properties of the crust extruded at the ridge crest in the different zones. Weissel & Hayes [1972] provide a detailed analysis of anomaly characteristics as they relate to constant spreading rate episodes and to intervals of asymmetric spreading in the different longitudinal zones.

Despite the lateral variations in anomaly patterns, an ordered anomaly pattern oc-

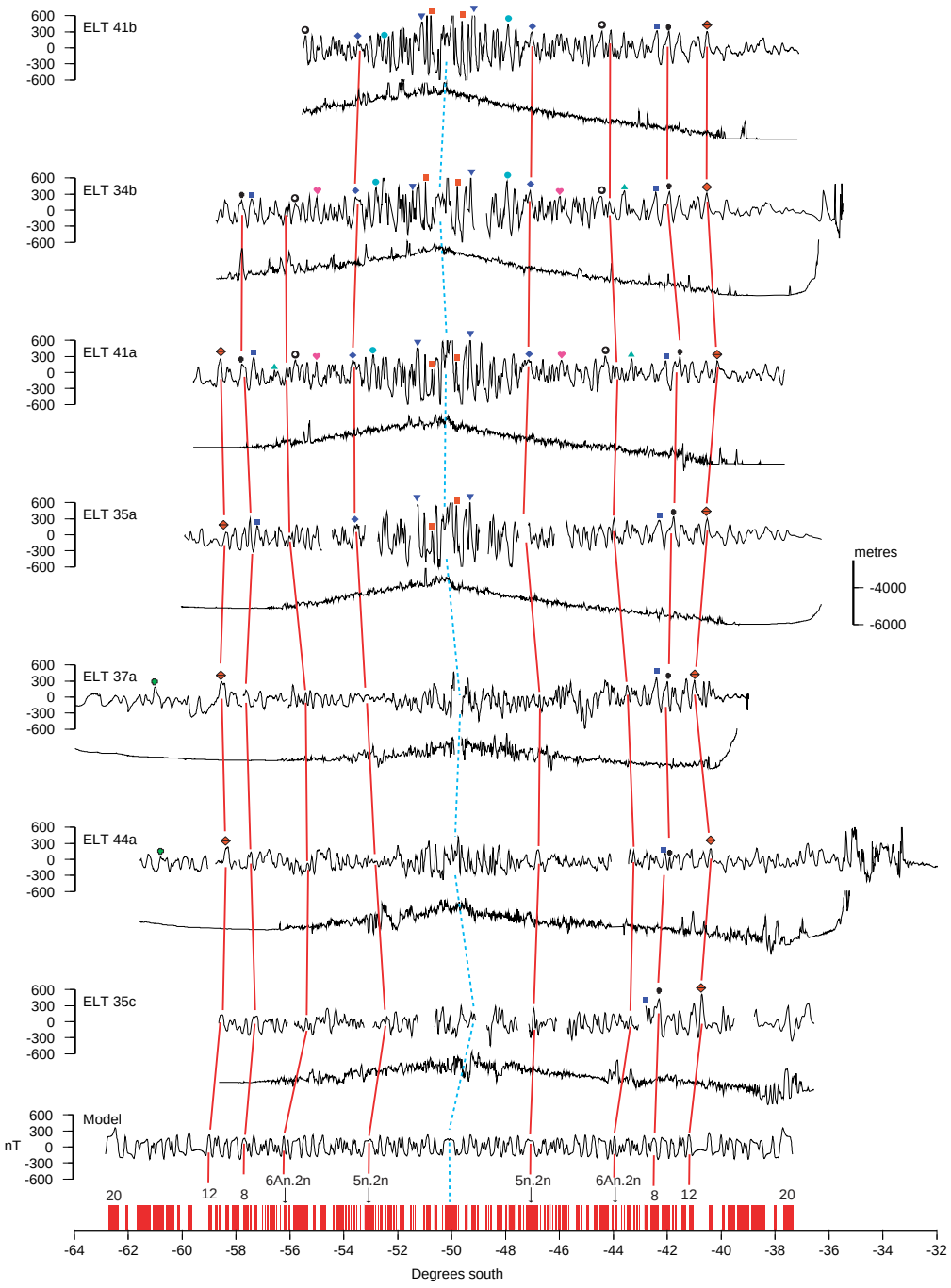

Figure 5.7: Observed magnetic anomaly and bathymetry profiles (located in Figure 5.6) across the SEIR, projected onto a north-south section and correlated to a synthetic model. Symbols and solid linking lines indicate confidently correlatable magnetic anomalies. Dashed light blue line indicates local zero age oceanic crust at the centre of the spreading ridge. Model assumes a half spreading rate of 31 mm/yr, constant depth and thickness of source layer, and a remanent magnetisation of 4 Am^{-1}.

curring north and south of the current SEIR is evident. Figure 5.8 illustrates the detailed correlation of observed and modelled anomalies for the southern flank of the SEIR from the present-day to anomaly 13n time (∼33Ma). The model was created assuming a spreading rate of 31 mm/yr, which was selected after a number of iterations with different spreading rates. The characteristic form of the anomalies labelled in Figure 5.8 are well simulated by the modelled profile, providing a high level of confidence in the spreading rate assumed in creating the model. This indicates spreading has proceeded at an average half-rate of ∼31 mm/yr since at least anomaly 13n (∼33Ma). To assess the spreading rates between anomaly 13 time and breakup, profiles extending further south are required.

To test the fit of a spreading rate model with the anomaly sequence prior to anomaly 13n, an end point within the geomagnetic time scale is required. What factors influence the choice of such an endpoint? Stratigraphic evidence of early rift basin development allows an upper (older) temporal limit for the onset of seafloor spreading. Commercial drilling results from the southern rift system of Australia (e.g.

Between 160 Ma and 118 Ma the longest single normal or reverse polarity period (i.e. time period with no reversals) is less than 2 My. 118 Ma marks the onset of the KLNP in the geomagnetic time scale (anomaly 34n), a period of ∼35 My of normal polarity with no reversals. If seafloor spreading initiated prior to this period, then an extent of relatively magnetically featureless oceanic crust flanked by positive edge-effect anomalies would be expected in observed magnetic data from the southeast Indian Ocean. No magnetic data from the southern Australian or Wilkes Land margins include evidence of such a long period without reversals. Accordingly, the *oldest* probable seafloor spreading anomaly is likely to be anomaly 34n, clearly this logic does not rule out that the oldest anomaly is not *younger* than anomaly 34n. An age of 90 Ma is assumed as a provisional endpoint here, this may be revised upwards or downwards depending on modelling results.

Extending a magnetic model to 90 Ma with a spreading rate[2] of 31 mm/yr results in,

1. a very poor anomaly fit between modelled and measured sections for the sequence of anomalies older than 17o, and

2. the southern extent of the modelled seafloor anomaly sequence (34o) occurring at a latitude of ∼74°S.

At a latitude of 74°S, anomaly 34n occurs approximately 900 km south of the Antarctic coastline. The obvious implications of this model being that spreading rates much lower than 31 mm/yr prevailed from breakup to anomaly 17o time (∼38 Ma), and/or that breakup occurred much later than 90 Ma.

[2]spreading rate implies half rates only unless explicityly stated otherwise

Figure 5.9 shows that reducing the modelled spreading rate by a factor of about two, from 31 mm/yr to 15 mm/yr, prior to 18y time still provides a poor fit between modelled and observed anomalies for the sequence older than anomaly 17, and predicts anomaly 34n to occur landward of the Antarctic coast. An average spreading rate of 6 mm/yr is required between 90 Ma and anomaly 18y time to limit the landward extent of the modelled profile to the base of the continental slope (Figure 5.9b). For the model illustrated in Figure 5.9b the positive anomaly associated with Chron 34 is aligned with the anomaly (labelled *A* in Figure 5.9) that has been previously been identified as anomaly 22 (e.g. Weissel & Hayes [1972]) and anomaly 34 (e.g. Cande & Mutter [1982]).

The *A* anomaly is a common feature in magnetic profiles from the Wilkes Land margin. It is characterised by a relatively broad (∼50 km) wavelength positive anomaly with an average peak-to-peak amplitude of 200 nT. Tikku & Cande [1999] question the interpretation of this feature as a seafloor spreading anomaly, whether the anomaly is caused by remanently magnetised oceanic crust has not been unequivocally resolved.

The indication from these relatively simple models, and assuming breakup at ∼90 Ma, is that a change in spreading rates occurred at the SEIR after anomaly 17 time. An average spreading rate of ∼6 mm/yr is implied for the interval from breakup to anomaly 17 time, whereas an average spreading rate of ∼31 mm/yr is implied from anomaly 17 time to the present-day.

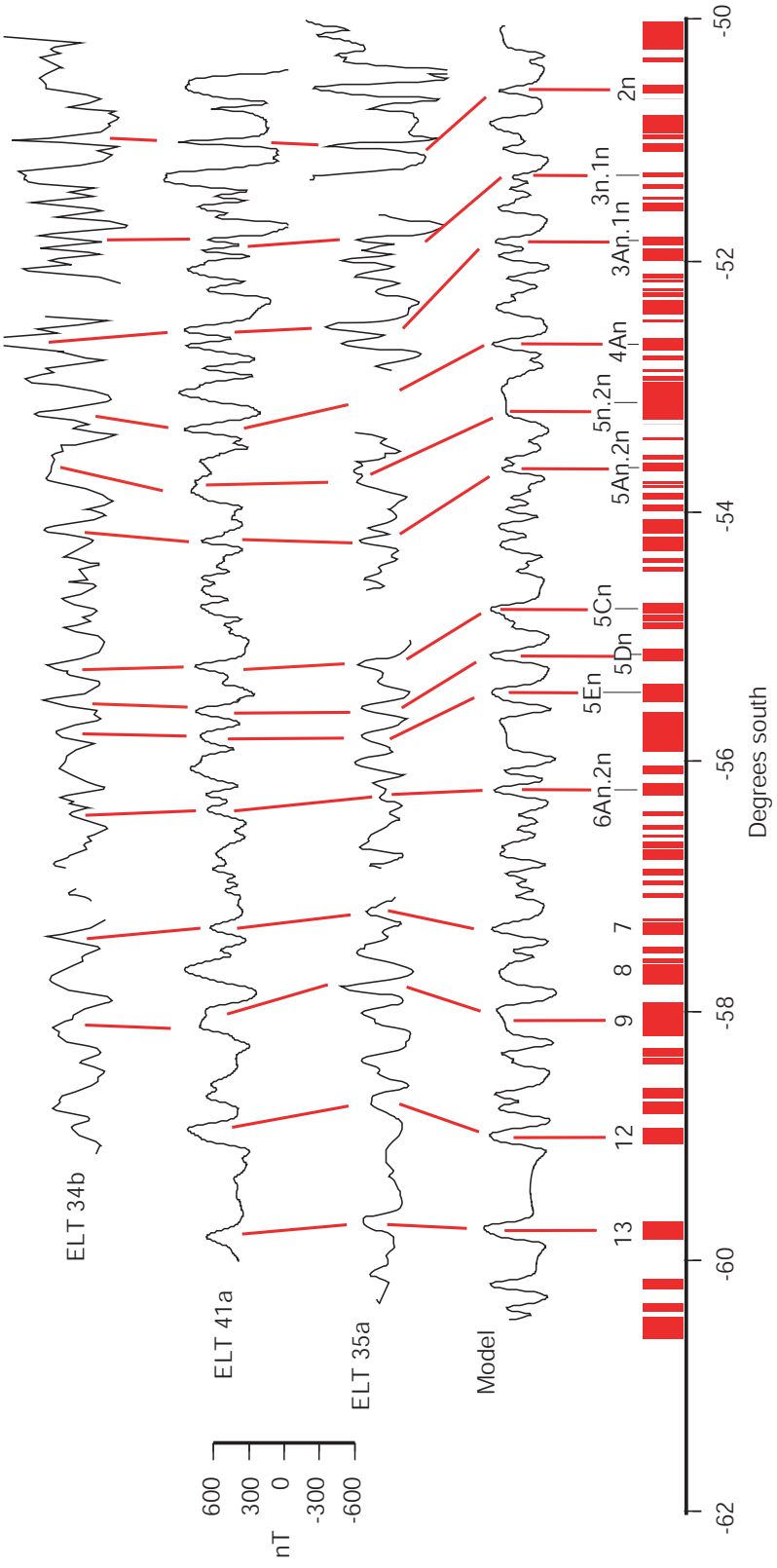

Figure 5.8: Comparison of observed and calculated magnetic anomalies over the southern flank of the SEIR. Characteristic anomaly sequences can be confidently correlated between observed and modelled profiles. Model parameters as for Figure 5.7.

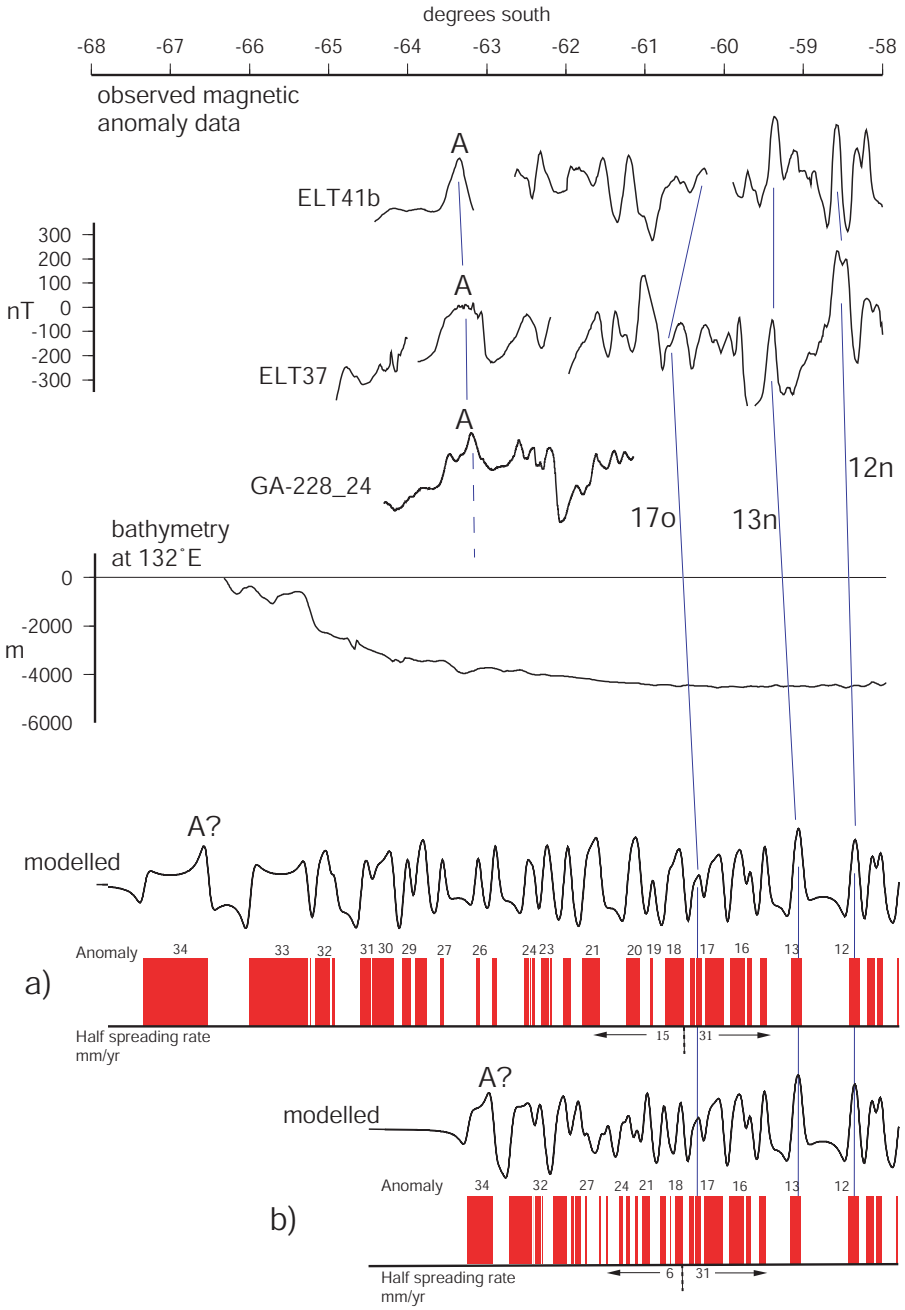

Figure 5.9: Comparison of observed and modelled magnetic anomaly profiles across the Wilkes Land margin. The anomaly sequence younger than ~17o is well modelled by a spreading rate of 31 mm/yr. b) A spreading rate of 15 mm/yr prior to 17o results in the model terminating south of the Antarctic coastline. c) For a spreading rate of 6 mm/yr prior to 17o the model terminates at the base of the continental slope. Bathymetry profile is from Smith & Sandwell [1994]. Model parameters as for Figure 5.7.

5.2.3 Variable Spreading Rate Modelling

In an attempt to improve the fit between the modelled and observed anomaly sequence older than anomaly 17o, variable spreading rates were introduced. By varying modelled spreading rates, for specific intervals of the geomagnetic time-scale, it is possible to alter the width of modelled anomalies. Hence, it is possible to improve the fit between modelled and measured magnetic anomalies. As the modelling above illustrates, spreading rates are much lower from breakup to anomaly 17o relative to anomaly 17o to the present-day. Slow spreading rates result in the interference of anomalies associated with each magnetic polarity reversal. It is possible that for very slow spreading rates, a single anomaly peak or trough may be caused by multiple bodies of alternating TRM polarity.

Initial models were extended to a time point within 34n that created a positive source body (for a given spreading rate) capable of producing an anomaly similar in character to the observed anomaly *A*. Figure 5.10 shows confidently correlated anomalies as solid lines and more contentious correlations as dashed lines for a number of lines that traverse the Wilkes Land margin. Correlation of modelled anomalies to GA-228 and GA-229 data is difficult as these survey lines terminate northwards at ∼61°S, which is ubiquitously south of the recent (∼17o to the present day) well formed anomaly sequence. The modelled data is Gaussian filtered with a 15 km full width filter (1σ ∼2.5 km) to account for the smearing effects of very slow spreading rates [Schouten & McCamy, 1972].

The spreading rate model illustrated in Figure 5.10 extends to approximately 89 Ma. The temporal end point is somewhat unconstrained in these models, as by increasing or decreasing the spreading rate before 34y (for a constant width body) the time end point can be moved back or forward in time. The spreading rate for 34y time and older is assumed to be the same as for the reversal period between 34y and 33o, which can be constrained by the modelling process.

This spreading rate model is broadly consistent with the model of Tikku & Cande [1999]. The decrease to 22 mm/yr between 18y and 18o and then 10 mm/yr from 18o to 21y mimics their spreading rate model. This model introduces a spreading rate of 7.5 mm/yr for the period between 21y and 22y, a period modelled with a spreading rate of 6.5 mm/yr by Tikku & Cande [1999]. This spreading rate model results in a modelled profile that simulates accurately observed data from anomalies 11 to 21. Survey GA-228 data terminate northwards at approximately the expected location of anomaly 18. A well-developed anomaly sequence is observed from ∼61-62°S. This sequence is characterised by a small positive anomaly on the seaward flank of the younger of two similar amplitude and wavelength, positive anomalies, which are separated by a distinct trough. This sequence can be confidently correlated with the modelled sequence for Chrons 19-20-21.

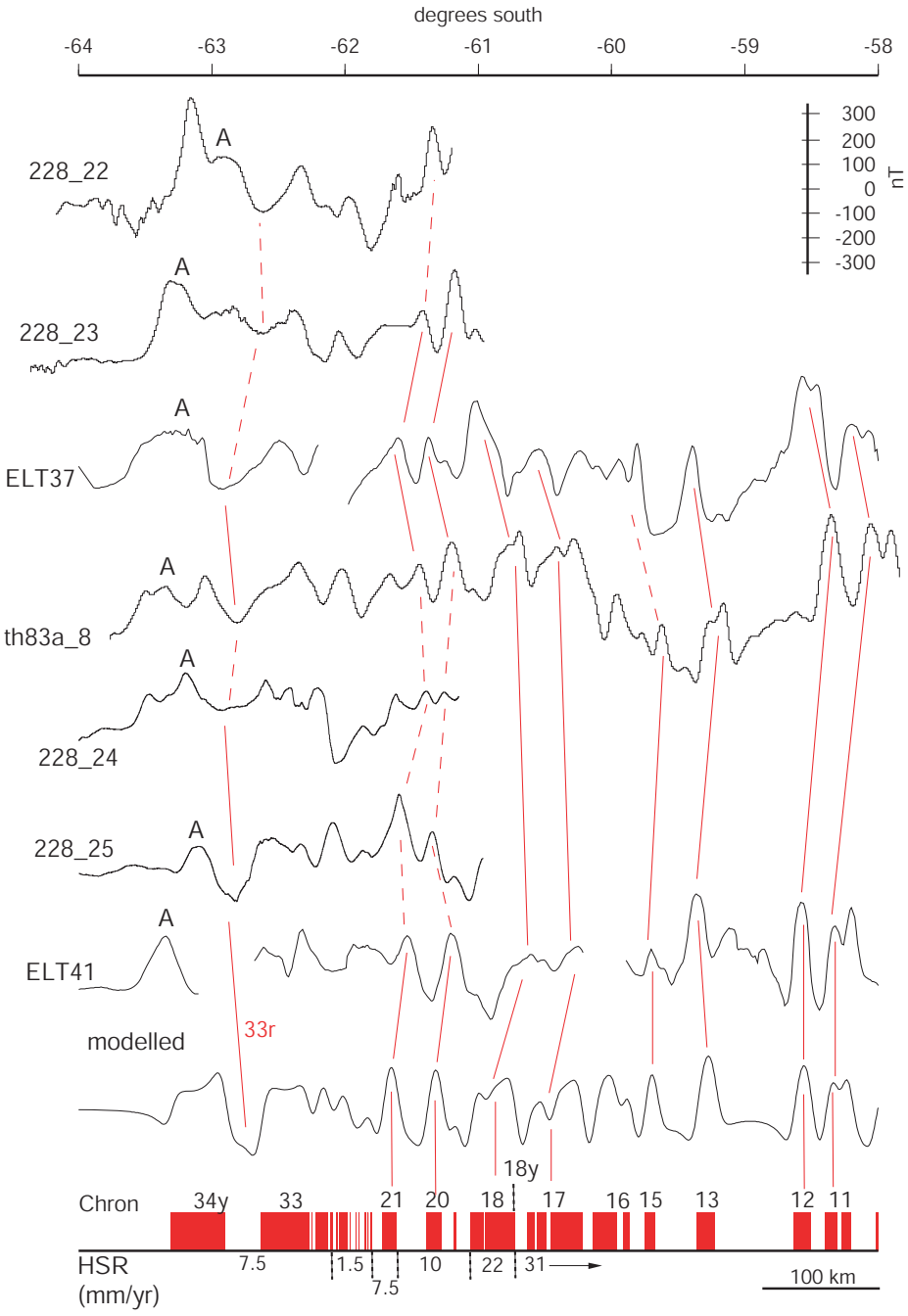

Figure 5.10: Comparison of observed and modelled magnetic anomaly profiles for a variable Half-Spreading Rate (HSR) model. The spreading rate of 31 mm/yr from present to anomaly 18y aligns the modelled characteristic sequence of anomalies 11-12-13 relative to the observed data. The 19-20-21 anomaly sequence is the oldest confidently identified sequence along the margin. Confident correlations are indicated by solid lines and estimated correlations by dashed lines.

This is the oldest anomaly sequence that can be confidently correlated for the full width of the AAB.

A very slow spreading rate of 1.5 mm/yr is introduced from 22y to 32y. This differs from the model of Tikku & Cande [1999], which only introduced such a slow rate between 24o and 31o. This spreading rate change was introduced to try and better fit the modelled and observed profiles. The model comprises a distinct double anomaly that matches the form of the observed data. However, south of anomaly 21 it becomes increasingly difficult to simulate the observed data and the quality of fit decreases significantly. Given the very slow spreading rate (1.5 mm/yr) modelled during this interval, it is not surprising that the fit is less well-developed between observed and modelled data. When such slow spreading rates occur, multiple periods of reversal are essentially 'piggy-backed' or stacked onto a relatively narrow section of oceanic crust and the complex interference of individual anomalies results.

South of the region modelled with a very slow spreading rate, the modelled spreading rate is increased to 7.5 mm/yr, which contrasts with a rate of 5 mm/yr in Tikku & Cande [1999]. The higher spreading rate improves the fit and alignment of the observed and modelled profiles south of the region of very slow spreading. The modelled positive anomaly associated with Chron 33n can be correlated to observed data on relatively few profiles, e.g. GA-228_25 (Figure 5.10). However, the trough observed at ~62.5°S can be correlated confidently between many profiles and is well simulated by the modelled trough associated with the reverse polarity interval of Chron 33 (i.e. 33r). Landward of this trough, anomaly *A* can be correlated across a number of lines. However, a large degree of variation in the form of the anomaly is observed. In this model, anomaly *A* correlates to the positive anomaly associated with Chron 34n. However, the modelled anomaly only simulates the form of a limited number of the anomalies labelled *A*, e.g. GA-228_24 and th83a_8 (Figure 5.10).

The broad correlation between modelled and observed anomalies supports the proposed spreading rate model. However, it does not vindicate the assumption that breakup occurred during Chron 34n. The next test applied to constrain breakup age is to assume breakup occurred during 33n. This would imply a breakup age of between approximately 80My and 74My. In suggesting breakup during Chron 33n, it is necessary to assess whether the full anomaly sequence, from anomaly *A* in the south through to the well constrained anomaly 21 in the north, can be modelled utilising 33n as a temporal starting point. It has already been shown that if anomaly *A* is not a seafloor spreading anomaly then the sequence of anomalies northward of this anomaly could be modelled using the spreading rate distribution outlined above.

To align the positive anomaly associated with Chron 33n to the observed anomaly

A, without shifting the well fit 19-20-21 anomaly sequence, requires increased spreading rates from anomaly 21o to 33o. Figure 5.11 shows two variable spreading rate models, both of which terminate at 33o. In the first of these models a spreading rate of 5 mm/yr is introduced between anomaly 22y and 32y, this spreading rate increase is sufficient to locate modelled anomaly 33 in line with anomaly *A*. However, the modelled trough associated with the reversal period between 32y and 31o is too narrow relative to the trough observed immediately northward of anomaly *A*. The fit of modelled to observed anomalies between this trough and anomaly 21 is also not very good. In the second spreading rate model, the spreading rate between anomaly 31o and 32y is increased to 12 mm/yr, this increases the modelled trough width to more closely approximate the observed trough. However, the fit of other anomalies is not improved relative to the first model. As the spreading rate is progressively increased, the number of individual modelled anomalies increases (i.e. there is less interference due to greater source separation), however, the observed sequence typically contains only 2-3 positive anomalies from Chron 21o to 32y.

Subsequent modelling with progressively younger terminations encounter the same problems as are evident for the 33n time ending model. The total number of anomalies modelled when spreading rates are increased (necessary to force younger age crust to reach a southern termination that allows anomaly *A* to be modelled) increases as individual anomalies begin to become distinct, this results in a calculated profile containing more anomalies than the measured profiles. In conjunction with this problem is the lack of a reversal period of great enough temporal extent (or spatial extent with reasonable spreading rates) to model the distinctive trough northward of anomaly *A*. Hence, it is possible to model anomaly *A* using several starting points, however, such starting points poorly simulate the remainder of the anomaly sequence.

This stepwise process, which has sought as much to eliminate possibilities as to vindicate any given age of breakup and temporal distribution of spreading rates, has illustrated that if anomaly *A* is a seafloor spreading anomaly, then it is associated with seafloor spreading commencing during late 34n time (approximately 90 Ma). Profiles calculated using this time point as the model terminus simulate relatively closely observed profiles, indicating that anomaly *A* is likely either associated with seafloor spreading anomaly 34, or remanently magnetised intrusive and volcanic rocks of 34n age.

Modelling thus far has assumed a constant depth to the top and bottom of the magnetised source layer. Seismic reflection data, however, reveals the actual crustal topography, showing trough to peak elevations of up to 2000 m are relatively common. One possible source of error therefore in the modelling is the contribution of a varying depth to the magnetised source layer.

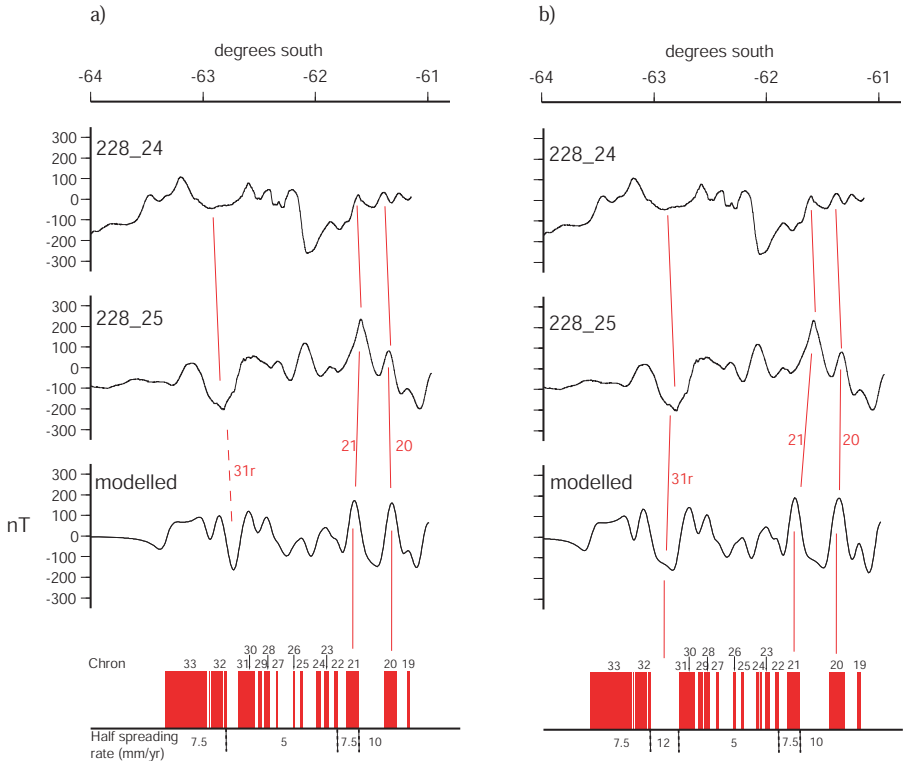

Figure 5.11: Modelled magnetic anomalies for two variable half spreading rate models. Model endpoint is anomaly 33n. There is a poor fit between observed and calculated profiles for these models. a) Modelled 31r trough is too narrow relative to observed data. b) Modelled 31r trough wavelength has been increased by increasing the spreading rate for the reversal period between 32y and 31o time, however, the overall correlation between modelled and observed anomalies is not improved. Model parameters as for Figure 5.7.

5.2.4 Variable Crustal Topography Modelling

For a variable depth magnetic source layer, lateral variations in susceptibility are introduced that did not exist in previous models. This results in an induced magnetisation component in the modelled total magnetisation. This component will remain very small, relative to the remanent component of total magnetisation, where the Königsberger ratio is large (i.e. ≥ 2). Lateral variation in the remanent component of the total magnetisation results from juxtaposed blocks of reverse and normal polarity as modelled above, however, further variation, and associated changes in the remanent magnetisation component of the modelled total magnetisation, is also introduced by the variable source depth.

The effect of incorporating basement topography on the remanent component of the total magnetisation was tested by creating a model that included both variable source depth and TRM polarity reversals. This approach requires the simple block bodies created in earlier models to have surfaces controlled by the observed crustal topography. To create models for each GA-228 and GA-229 line the interpreted basement depth was combined with the optimal spreading rate model determined previously (e.g. Figure 5.10). To minimise edge effects, a flat extension with no remanent magnetisation was added to the southern termination of the model. Figure 5.12 illustrates the small changes in the modelled field associated with a non-uniform source depth model, the topographic effect on the remanent component (that is, the effect of changing the surface of a block of any polarity) is minor. The depth variation of the crustal layer is negligible relative to the distance between the measurement surface and source layer. Accordingly, the dominant remanent magnetisation component is that resulting from the juxtaposition of remanently magnetised blocks with opposing polarity.

The induced magnetisation field component in oceanic crust is minor relative to remanent magnetisation, as the Königsberger ratio is typically large in oceanic crust as discussed previously. However, the relationship between remanent and induced magnetisation of continental crust is far more variable and complicated (e.g. Dunlop [1995]). As continental margins represent the boundary between oceanic and continental crust, variation in the magnitude of the K

To investigate the induced magnetisation associated with crustal topography, source bodies were created utilising an upper surface constrained by the depth converted basement surface (as interpreted from MCS data). The magnetic source layer was assumed to be 500 m thick and comprise a constant magnetic susceptibility. To avoid large-amplitude edge-effects, the source layer was extended to the north and south as a flat continuous body. An example of the induced magnetisation component associated with basement

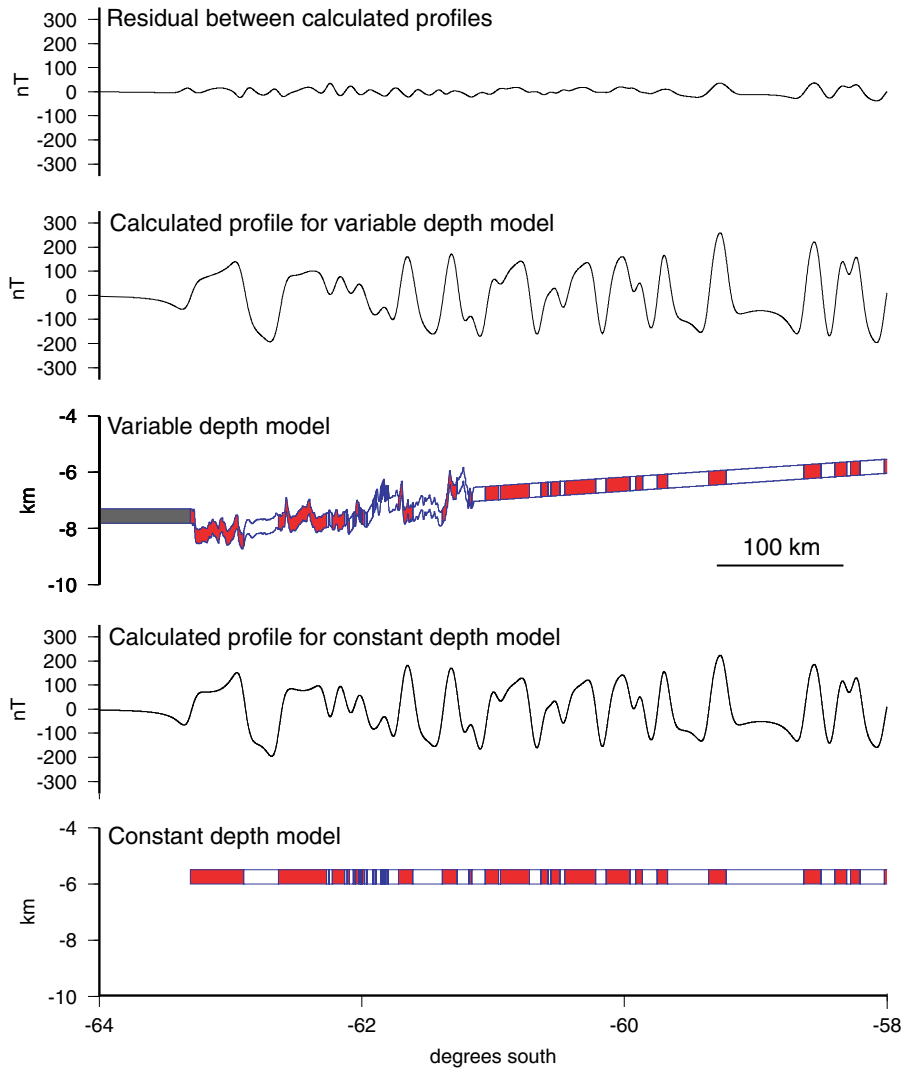

Figure 5.12: Comparison of modelled anomalies for constant and variable depth magnetic source layers. The introduction of a variable depth introduces very little variation, as illustrated by the very small signal amplitude in the residual profile. The depth variation is insignificant relative to the distance between the measurement surface and source layer. Model parameters as for Figure 5.7.

topography, calculated for three values of magnetic susceptibility (k), is shown in Figure 5.13.

Modelled induced magnetisation anomalies for susceptibilities of 0.05 and 0.1 SI are of negligible amplitude relative to observed anomalies (Figure 5.13). Only for an unrealistically large susceptibility of 0.5 SI do modelled anomalies exceed 40 nT. However, for this susceptibility, the two positive anomalies observed at ~62.5°S are well simulated by modelled anomalies. Modelling of other lines, however, provides no further evidence of a

correlation between basement topography and observed magnetic anomalies

Increasing the thickness of the magnetic source layer does not produce modelled anomalies of similar amplitude to observed anomalies, as it does not increase lateral variation in susceptibility. The depth of the source layer (∼7 km) relative to the topographic variation is such that a constant susceptibility and constant thickness source layer does not produce large amplitude anomalies. It is possible to produce induced magnetisation anomalies of greater amplitude, however, this requires variations in source layer thickness and/or susceptibility to be introduced. Unlike depth to basement, neither magnetic susceptibility or source layer thickness can be independently constrained from seismic reflection data. Other than variation in the observed magnetic data, there are no constraints on how these parameters vary, and there is no *a priori* reason to assign different susceptibility values to any specific section of oceanic crust (other than to improve the fit of a model). As there is an infinite number of source distribution solutions for any observed anomaly sequence, changing parameters such as susceptibility with no geological or geophysical basis provides no insight into anomaly identification or breakup age determination.

Modelling of the induced field component indicates that induced magnetisation anoma-

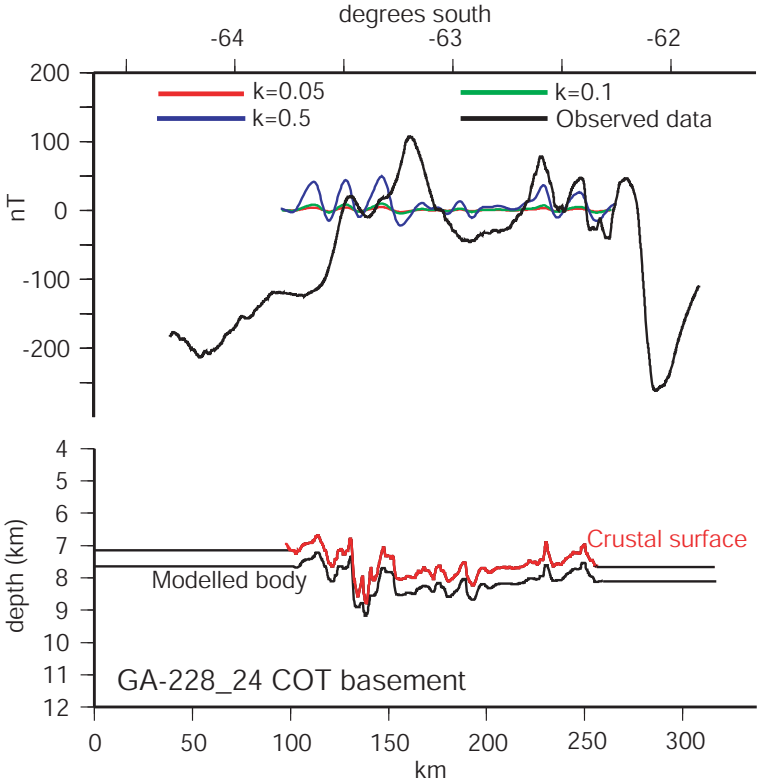

Figure 5.13: Modelled induced magnetisation anomalies and observed magnetic anomalies. Model geometry from basement depth of the continent-ocean transition zone, as interpreted from MCS data on line GA-228_24. Three values of magnetic susceptibility (k) were modelled to assess the sensitivity of the induced magnetisation to k.

lies associated with topographic variations represent a negligible component of the measured total magnetisation, for *constant susceptibility and source layer thickness*. However, the correlation of basement topographic highs with observed positive anomalies on Line GA-228_24 indicates that induced magnetisation components of the total magnetisation may be important for transition zone crust and/or altered oceanic crust in isolated instances.

5.3 Interpretation and Discussion

5.3.1 Magnetic Anomaly Compilation and Correlation

Figure 5.14 shows a compilation of open file, GA-228, GA-229, and JNOC magnetic anomaly data from 105°E and 140°E. The observed magnetic anomalies are correlated to modelled anomalies based on the spreading rate model in Figure 5.10. The variation in modelled and observed spreading rates (i.e. based on anomaly identification) since breakup is also illustrated graphically in Figure 5.16 for a number of profiles across the margin.

Figure 5.16 clearly illustrates the ultra-slow spreading rates prior to anomaly 18 time. In ∼40 My, less than 250 km of oceanic crust was created between the SEIR and Antarctica. The AAB, accordingly, was narrow (relative to its present-day width) for over 40 My following breakup. The close temporal correlation of the distinct change in spreading rates across the SEIR and the initial collision of Greater India with the Eurasian plate has been noted by previous workers, this major tectonic event may have been a catalyst for changes in spreading rate along strike of the spreading ridge system encircling the Antarctic continent.

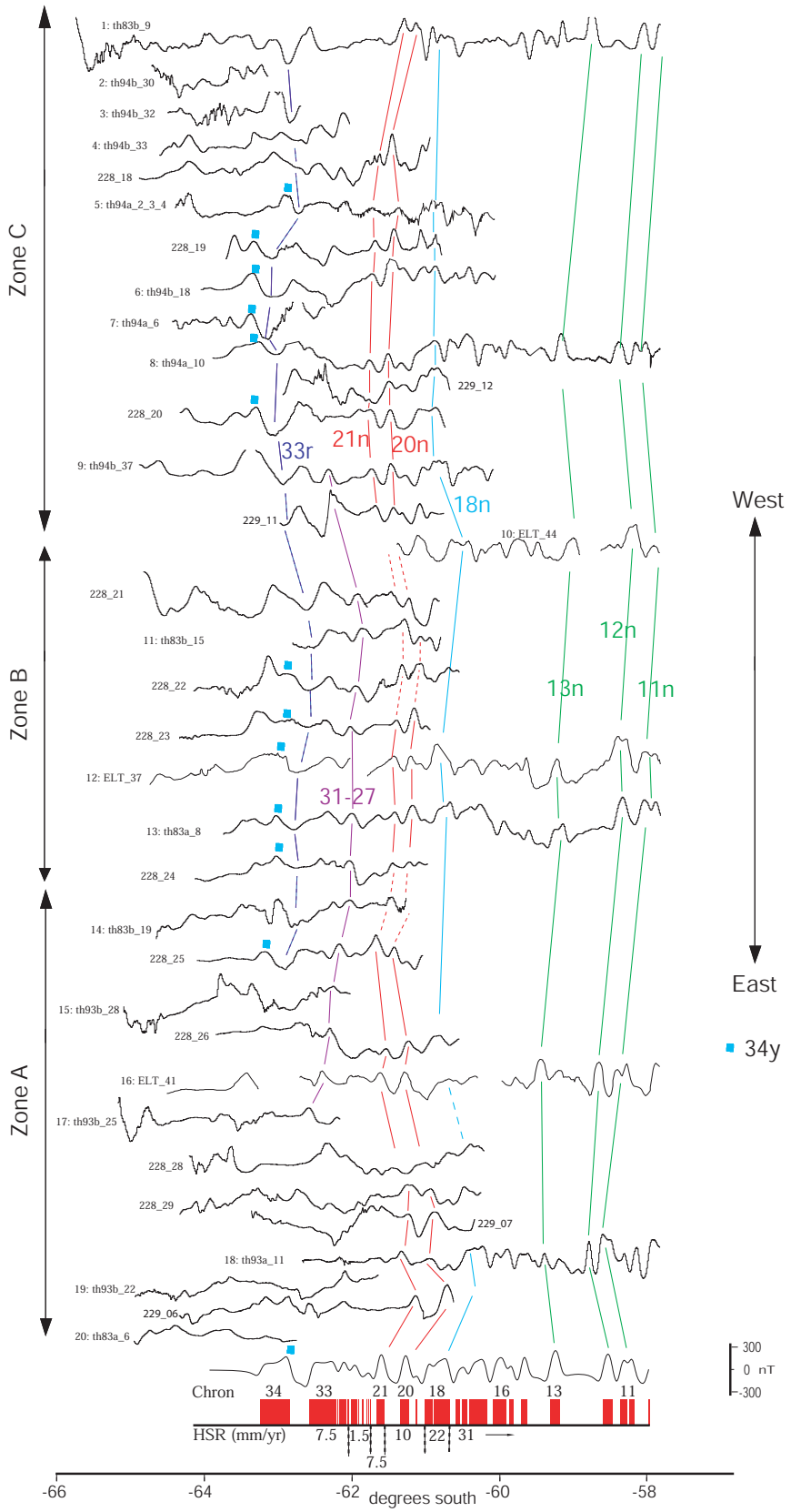
Zone C
Zone B
Zone A
1: th83b_9
2: th94b_30
3: th94b_32
4: th94b_33
228_18
5: th94a_2_3_4
228_19
6: th94b_18
7: th94a_6
8: th94a_10
229_12
228_20
33r
21n
20n
9: th94b_37
18n
229_11
10: ELT_44
228_21
11: th83b_15
12n
228_22
13n
11n
228_23
12: ELT_37
31-27
13: th83a_8
228_24
14: th83b_19
228_25
15: th93b_28
228_26
16: ELT_41
17: th93b_25
228_28
228_29
229_07
18: th93a_11
19: th93b_22
229_06
20: th83a_6
West
East
34y
300
0 nT
-300
Chron
34
33
21
20
18
16
13
11
HSR (mm/yr)
7.5
1.5
10
22
31
7.5
-66
-64
-62
degrees south
-60
-58

Figure 5.14: (*Previous page*) All GA-228, GA-229, JNOC, and Eltanin magnetic anomaly profiles across the Wilkes land margin correlated to a modelled profile. Anomaly correlations are less distinct in the eastern sector of the AAB (Zone *A* of Weissel & Hayes [1972]). Numerical identifiers for each profile correspond to location of profile in Figure 5.15.

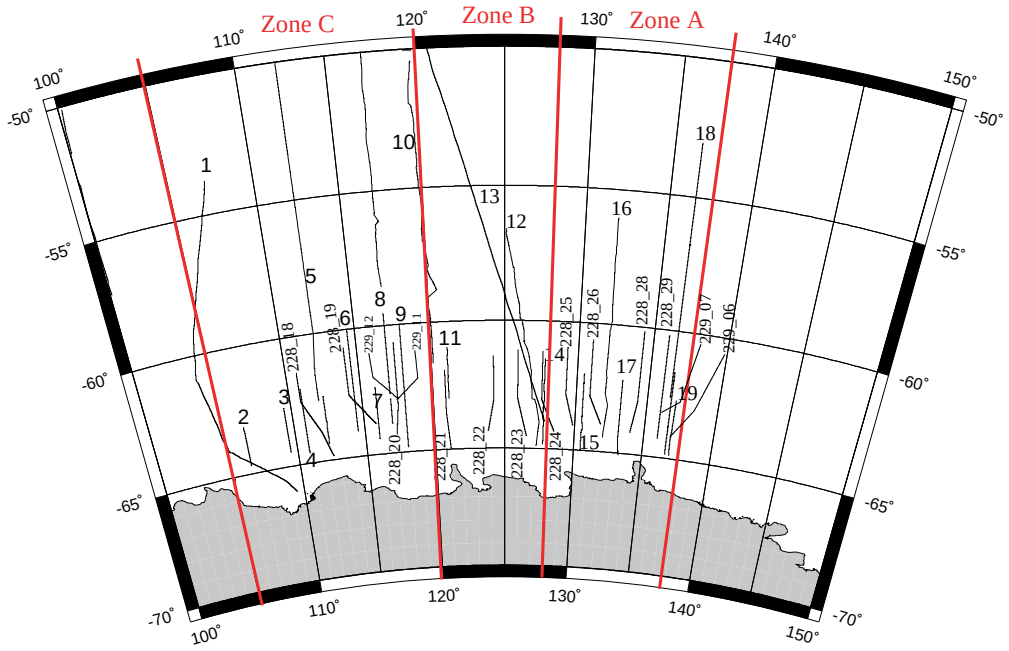

Figure 5.15: Location of GA-228, GA-229, JNOC, and Eltanin survey lines across the Wilkes land margin shown as profiles in Figure 5.14. Zones A, B and C are after Weissel & Hayes [1972] and are defined by zones of distinct morphologic, seismologic, and magnetic anomaly character at the SEIR.

The most strike continuous anomaly sequences are 11-12-13, 16-17, 18, and 19-20-21, these anomalies typically correlate very well along the margin (in all zones) and with the modelled profile for the variable spreading rate model illustrated (Figure 5.14). The anomaly sequence associated with oceanic crust emplaced between breakup and anomaly 21 time is significantly more enigmatic. The positive anomaly correlated with polarity reversals 27-31 in Figure 5.14 is continuous only in the central Wilkes Land margin sector from ~117-130°E. Landward of this peak, the negative anomaly associated with the reverse polarity interval of Chron 33 (i.e. 33r) is continuous along the width of the margin west of ~130°E, although the wavelength and amplitude of the anomaly is variable. The final anomaly identified as possibly of seafloor spreading origin is anomaly 34 (observed anomaly *A*).

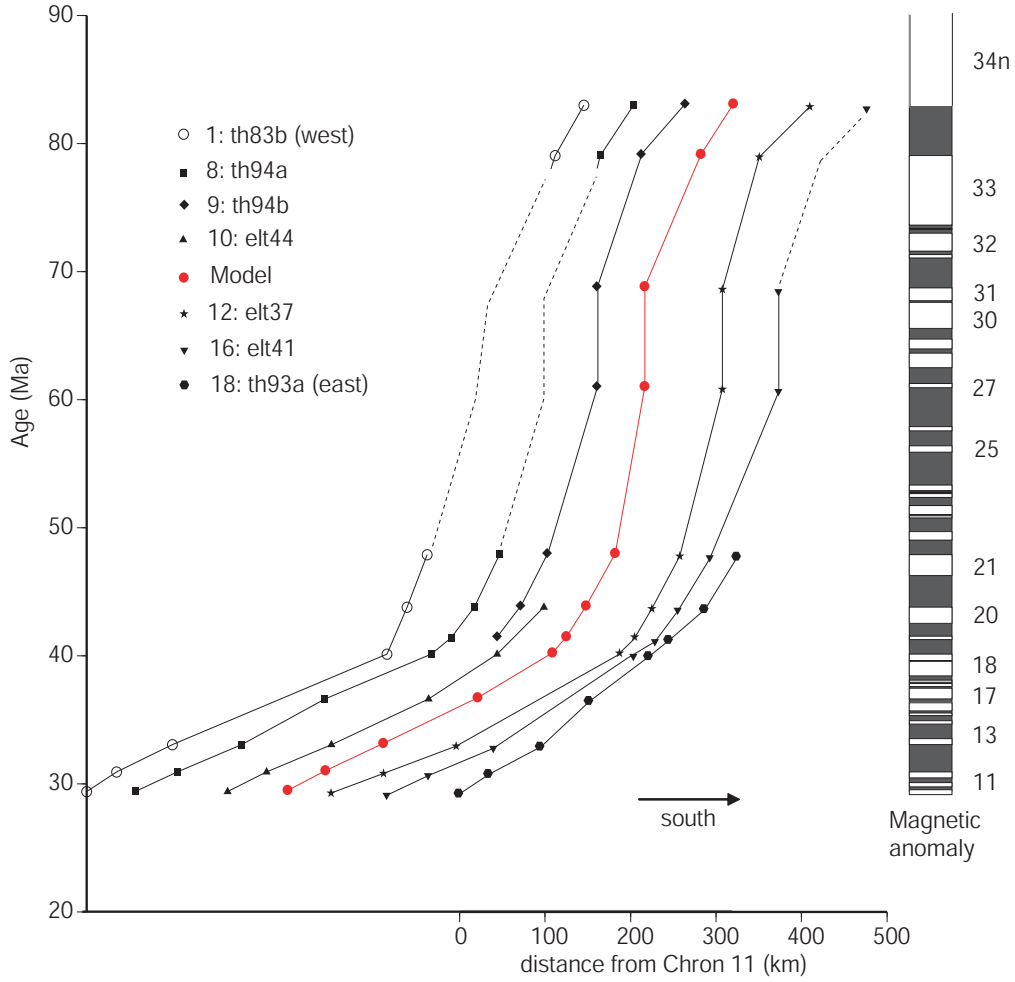

Figure 5.16: Distance of well correlated magnetic anomalies as a function of time for six observed magnetic anomaly profiles from the Wilkes Land margin (located in Figure 5.15). Profiles are normalised to anomaly 11. The almost identical trends of the modelled distance-age profile (solid circles) relative to observed trends indicates the applicability of the spreading rate model. Note that normal polarity periods are denoted by black blocks in this figure.

The location of confidently correlated magnetic anomalies on the Wilkes Land margin are shown in Figure 5.17 along with the extent of the Continent-Ocean Transition Zone (COTZ) interpreted from seismic reflection data (Chapter 4, Figure 4.23). Anomaly 34y, where it is identified in the western and central Wilkes Land sector of the AAB is located within the COTZ. The seaward edge of the COTZ off east Wilkes Land and the Adelie Rift Block (ARB) extends as far north as the Chron 21 lineation. This indicates that the earliest oceanic crust seaward of the ARB was emplaced during the Middle Eocene (~45 Ma), ~35-40 My later than in the central AAB. The onset of seafloor spreading

between the ARB and the conjugate southeastern Australian margin correlates to the end of ultra-slow spreading based on the spreading rate model presented here.

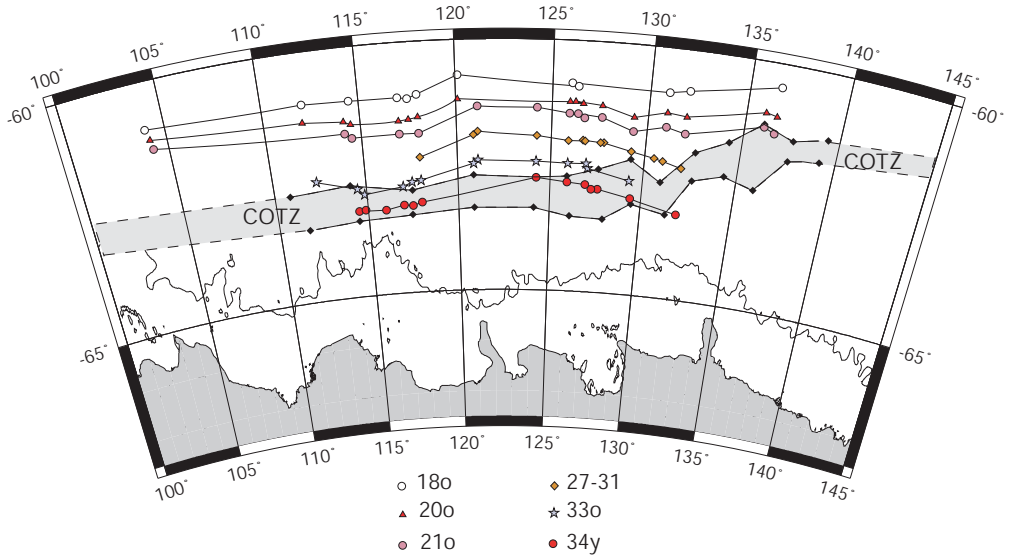

Figure 5.17: Correlatable magnetic anomaly lineations for the Wilkes Land margin and the continent-ocean transition zone (COT) as interpreted from seismic reflection data (Figure 4.23).

Anomaly '34' exhibits variable form across the margin, hence it is difficult to confidently identify it as a seafloor spreading anomaly. If it is not an anomaly associated with emplacement of oceanic crust, it is likely associated with either a regional magmatic pulse or exhumed upper mantle peridotites, which recorded the TRM of Chron 34n, prior to final breakup. An anomaly of similar form and relative location (i.e. landward of 33r) is also observed on the southern Australian margin (e.g. Veevers [1987] and Tikku & Cande [1999]).

In the central Wilkes Land sector of the AAB, anomaly 34 is most consistently formed and the fit of the modelled anomaly 34 with the observed anomaly is best. Seismic reflection data at the approximate latitude of this anomaly indicate a transition-zone not typical of continental or oceanic crust. However, given the modelled spreading rates of ~7.5 mm/yr and the subsequent hiatus in spreading, typical oceanic crust acoustic character should not be entirely expected.

The absence of correlatable magnetic anomalies over the ARB is further evidence that it comprises stretched continental crust, as suggested in Chapter 4. The magnetic anomaly pattern from the conjugate sector of the southern Australian margin is also interpreted to be devoid of anomalies older than anomaly 20 (Figure 5.18).

The more extensively studied southern Australian margin exhibits a very similar

magnetic anomaly pattern to the Wilkes Land margin, a complete discussion of these data is provided by Weissel & Hayes [1972], Veevers [1986], Veevers *et al.* [1990], and Tikku & Cande [1999]. Figure 5.19 illustrates the similarities in the anomaly pattern on the conjugate margins. Despite the greater data density from the southern Australian margin, the origin of anomaly 34 is still not conclusively established.

Figure 5.18: Interpretation of magnetic anomaly data on the southern Australian margin from Veevers *et al.* [1990]. The oldest anomaly sequence identified in the central southern Australian margin (30-34) is not evident east of ~132°E. This termination of the magnetic anomaly sequence remains, however, more than 250 km west of the Spencer fracture zone, indicating that extended continental crust is likely to abut the eastern extent of the oldest oceanic crust in the central sector of the margin.

5.3.2 Magnetic Anomaly Variability

As outlined above the magnetic anomaly sequence recorded in oceanic crust emplaced between breakup and the Middle Eocene is far from ideal. It is generally poorly repeated on profiles separated by more than a few 10s of kilometres. The variation in form along strike indicates that either this oceanic crust did not acquire strong TRM during emplacement or processes have acted to alter the original TRM since emplacement.

As oceanic crust basalt ages it is altered such that its magnetisation becomes substantially reduced [Kent & Gee, 1994]. The process of maghemitisation of titanomagnetite on the seafloor occurs throughout Layer 2A [Smith & Banerjee, 1986], generally within a few million years of extrusion. As a result, the amplitude of linear magnetic anomalies falls by about an order of magnitude from the central anomaly over an active spreading centre to older lineations over oxidised seafloor [Dunlop, 1995]. The correlation of

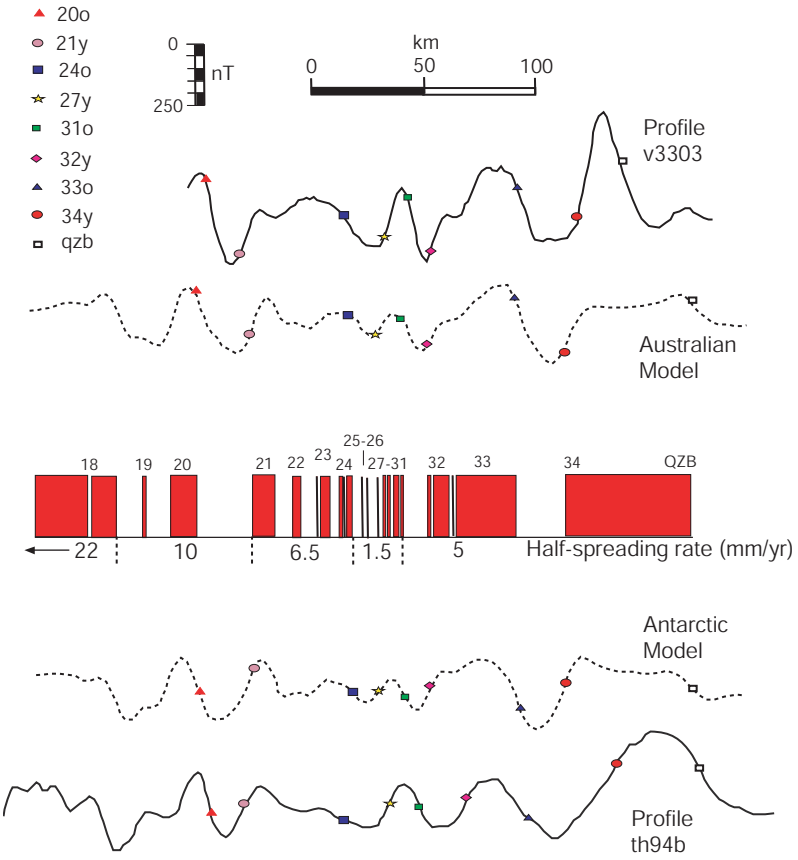

Figure 5.19: Spreading rate model of Tikku & Cande [1999] and profiles from the Wilkes and GAB margins. Synthetic magnetic profiles created using the following input parameters: top of magnetic source layer depth of 5.5 km, source layer thickness of 0.5 km, remanent inclination and declination of -74° and 0° respectively, and a 3 km Gaussian filter. Note that profile th94b is the same as th94b_37 in Figure 5.14.

anomalies older than a few million years in all ocean basins indicates that some memory of the primary TRM is retained during this alteration.

Remanent magnetisation that remains following alteration is known as Chemical Remanent Magnetisation (CRM) (e.g. Özdemir & Dunlop [1985]). CRM is phase-coupled to TRM (i.e. retains the direction of the TRM during alteration/oxidation) for fine-grained rocks only, and this explains the survival of linear magnetic anomalies [Özdemir & Dunlop, 1985; Dunlop, 1995]. Clearly then, for oceanic crust to retain an accurate geomagnetic record it must be sufficiently fine-grained.

Although young oceanic crust is typically accompanied by large-amplitude, linear magnetic anomalies, there are examples of young oceanic crust that is not. They include the northeast Pacific Ocean (e.g. Davis & Riddihough [1982], the northern Juan de Fuca Ridge (e.g. Davis & Lister [1977], and the Guaymas Basin in the Gulf of California (e.g.

Larson *et al.* [1972]). In addition to the absence of interpretable magnetic anomalies, each of these areas is overlain by sediments up to 1 km thick [Levi & Riddhough, 1986]. Larson *et al.* [1972] suggested a causal relationship between the sediment cover and the low-amplitude of observed magnetic anomalies.

Vogt *et al.* [1970] suggested that magmas crystallising under sediment will not form extrusive pillow lavas, but will cool more slowly and comprise larger grain-size and correspondingly lower TRM and CRM intensities. However, Levi & Riddhough [1986] suggest that primary cause of low-amplitude magnetic anomalies is pervasive hydrothermal alteration, which is encouraged by the blanketing of sediments over very young oceanic crust. Faults and contraction fractures typically provide pathways for sea water to interact with hot, young oceanic crust at spreading centres and encourage cooling (e.g. Lister [1972]). Sea water and magmatic fluids interact to create hydrothermal fluids that circulate and, in the absence of extensive sediment cover, vent directly into overlying cold sea water. Levi & Riddhough [1986] define this as an *"open"* system. In contrast, if there is extensive sediment cover at a spreading centre the hydrothermal circulation system is not open, and this is defined by Levi & Riddhough [1986] as a *"closed"* system.

In a closed system, hydrothermal fluids have a comparatively long residence time within the basalt, and cool more slowly while they thermally and chemically equilibrate with the basalt and overlying sediment Levi & Riddhough [1986]. This results in pervasive alteration and leaching of iron-oxides, and therefore diminishes the amplitude of lineated magnetic anomalies. Clearly, a closed system must allow sea water interaction with hot, young basalt and magmatic fluids while also preventing open circulation of these fluids.

The lack of continuity of lineated magnetic anomalies on the Wilkes Land margin is interpreted to indicate a closed system of hydrothermal circulation, at the SEIR, from breakup to the Middle Eocene. Due to the very slow spreading rates during this interval, the basin separating Australia and Antarctica would have been relatively narrow for a period of 10s of My. If sediment flux was sufficient during this interval of slow spreading, young oceanic crust, and possibly even the spreading centre itself, could have been capped by detrital sediments from the adjacent continents. Hydrothermal alteration of oceanic crust in the AAB from breakup to the Middle Eocene may, therefore, contribute to the discontinuity in lineated magnetic anomalies and the associated difficulties in interpreting the observed anomalies.

5.4 Summary

The ultra-slow early spreading rates modelled here (Figure 5.14) and the associated likely hydrothermal alteration, explains, at least in part, the variability in the observed anomaly

sequence 34-21. On the strength of magnetic evidence alone a breakup age of ~90Ma is indicated for the central sector of the Wilkes Land margin. However, uncertainty in the correlation of the observed anomaly *A* to modelled anomaly 34 prevents this being conclusively determined from magnetic anomaly data alone. The absence of the anomaly sequence 34-21 off eastern Wilkes Land, within the ARB, indicates that breakup, whenever it did initiate, was not synchronous along the extent of the margin.

Chapter 6

Gravity, Flexure and Backstripping

6.1 Gravity

6.1.1 Introduction

Observations of the Earth's gravitational field provide an important means of investigating the structure of the crust and lithosphere. Gravity observations are sensitive to both static mass distribution and dynamic processes. Gravity data interpretation suffers, however, from problems of non-uniqueness. The ambiguity of gravity interpretations can be reduced by considering independent geophysical and geological information in conjunction with gravity data. Most commonly, seismic data are used to provide constraints on model geometry and physical properties.

Two approaches to gravity interpretation of gravity data are the forward and inverse modelling methods. Inverse gravity modelling calculates body parameters directly from the observed anomaly, without requiring rigourous external constraints on source geometries. Forward modelling techniques require the definition of source geometries and properties, from which gravity anomalies can be calculated and compared to observed data.

Gravity data were acquired coincident with all GA-228 MCS survey lines using a *LaCoste and Romberg* air-sea gravimeter. A sample interval of 1 s was maintained throughout surveying. Cross-coupling corrections were calculated from beam position, beam slope, and cross and long accelerometers that were also logged using a 1 s sample rate. Drift corrections were applied based on ties to land gravity base stations in Cape Town, South Africa, and Hobart, Australia. Eötvös corrections, accounting for the vector addition of gravity meter's velocity and the Earth's rotational velocity, were applied according to,

$$E = 7.503\,V\,cos\theta\,sin\nu + 0.004154\,V^2$$

where E is in mGal, V is speed in knots, θ is latitude, and ν is the heading.

The satellite derived free air gravity field of Sandwell & Smith [1997] has been utilised to extend line data where necessary. No Bouguer Anomaly (BA) data is available for the onshore Wilkes Land margin, or indeed for much of the Antarctic continent. Accordingly, gravity models were terminated at the Antarctic coast and compared to FAA data only.

Traditionally, gravity modelling of continental margins has utilised seismic data to constrain a model geometry comprising water, sedimentary, crustal and mantle bodies. These bodies are assigned average density values based on available geophysical data (e.g. refraction velocity, stacking velocity, and well-log data). Models have typically been created assuming either Airy or flexural isostatic conditions. Models created without consideration of isostatic balance that comprise bodies of varying densities and geometry are referred to herein as *object-oriented*. Object-oriented models attempt to represent the current state of a margin and provide information on the applicability of the defined density distribution only. These models rarely represent a state of stable equilibrium and therefore implicitly argue against the theory of isostasy.

Forward modelling techniques were employed extensively throughout this study, however, inverse modelling of specific gravity anomalies was also completed to aid final interpretation. Gravity models were constrained by Multi-Channel Seismic (MCS) data, and refraction data where available. The unsurveyed margin portion, extending from the southern termination of GA-228 and GA-229 survey lines to the Antarctic coast, was modelled using extrapolated source geometries constrained with other data where possible as outlined in Chapter 4. Two-dimensional gravity methods form the basis of interpretation for this study due to the nature of the MCS data distribution (approximately parallel line data separated by up to 90km). Three-dimensional methods are investigated also, but provide for more qualitative interpretation only.

6.1.2 Parameterisation

Initial model parameters were chosen following the method of Cochran [1981]. Using a reference column through a mid-ocean ridge crest (defined as a 5 km thick crust under 2.5 km of water, underlain by 1,333°C mantle) Cochran [1981] demonstrated that the crustal parameters required to provide an internally consistent, isostatically balanced system (assuming a linear thermal gradient) for a lithospheric thickness of 125 km, were as summarised in Table 6.2. These parameters provided a defensible starting point for forward modelling, however, parameters were varied in accord with standard forward modelling practice.

Crustal thickness is poorly constrained by seismic and gravity studies for the Antarctic continent as a whole, however, where data does allow this parameter to be tested,

mantle density at 0°C (ρ_m)	3330 kg/m^3
crustal density at 0°C (ρ_c)	2800 kg/m^3
water density (ρ_w)	1030 kg/m^3
initial crustal thickness (T_c)	31.2 km
coefficient of thermal expansion	3.4×10^{-5}°C^{-1}
asthenospheric temperature	1,333°C
thermal diffusivity	0.008 cm^2/s
thermal conductivity	0.0075 cal/deg cm s

Table 6.1: Crustal parameters demonstrated by Cochran [1981] to provide an isostatically balanced system with a reference column through a mid-ocean ridge crest.

values of 30-40 km have been determined for the East Antarctic craton [Bentley, 1991]. Accordingly a range of values of 35±5 km were tested through the modelling process. It can be shown that the modelled gravity anomaly is relatively insensitive to initial crustal thickness (where crustal and mantle density are held constant) for a range of initial values, accordingly it is only possible to assess the accuracy of the initial crustal thickness value where seismic reflection and refraction data image the *Moho* discontinuity. Where large sediment accumulations occur, a lower limit of crustal thickness can be determined by establishing the minimum initial crustal thickness that requires a *Moho* depth shallower than basement depth to maintain isostatic equilibrium. For lines off west Wilkes Land, where sediment thickness is greatest, GA-228_18 to GA-228_21, a minimum initial crustal thickness of ∼35 km is necessary to ensure the modelled *Moho* remains deeper than the top of basement.

As the density of seawater is well known (1030 kg/m^3), the remaining input parameter to any gravity model is the sediment density; this varies primarily as a function of porosity and grain composition. The porosity is controlled by diagenetic processes, depth of burial, and compaction. For gravity modelling, sediments can either be decompacted and modelled with a correspondingly lower density, or considered in their compacted state and modelled with a higher density.

Seismic velocity (*P-wave* or interval) is known to correlate to density in a predictable fashion (e.g. Hamilton [1976], Hamilton & Bachman [1982]). Empirical relationships, calibrated with well-log data, provide a means of estimating density from interval velocities (determined through moveout correction of reflectors in MCS data or from refractor velocities in wide-angle data) for different marine environments and sediment compositions. Broadly, increased seismic velocity corresponds to an increase in density (Figure

6.1a). However, seismic velocity is also a function of grain-size (Figure 6.1b). The predictions of Hamilton [1976] have been confirmed to be very accurate by well-log sediment density data (e.g. Jarrard *et al.* [1989]).

Figure 6.1: Seismic or sound velocity is related to both a) density, and b) grain size for continental shelf and slope sediments. Figure from Hamilton & Bachman [1982].

Velocity-density relationships must be applied with some caution on the Wilkes Land margin, however, as the composition of sediments is inferred almost entirely from MCS data and very little well data is available to confirm interpreted lithologies. It is reasonable to assume that post-rift sediments are almost entirely siliceous (clastic near margin grading to pelagic in the abyssal plain). Due to the relatively high latitude of Antarctica since rifting, it is unlikely that there are significant carbonate reef platforms or salt layers.

The range of observed interval velocities for the post-rift sediment sequence on the Wilkes Land margin is 1700-3600 m/s (Figure 6.2) this corresponds to a density range of ~1600-2400 kg/m^3. Typically only the very upper layers exhibit interval velocities less than 2000 m/s. This full range of inferred sediment density values was tested during the modelling procedure, however, examination of interval velocity profiles indicate a *mean* sediment density of between 2100 and 2350 kg/m^3 is most applicable across and along the margin. The sensitivity to variations in sediment, crustal and mantle density, and initial crustal thickness is examined to ensure a procedure robust to reasonable levels of variation.

6.1.3 Gravity Anomaly Computation

Two-Dimensional Modelling

The line integral method of Talwani *et al.* [1959] is used to calculate gravity anomalies of two-dimensional bodies throughout this thesis. In this method, the contributions of

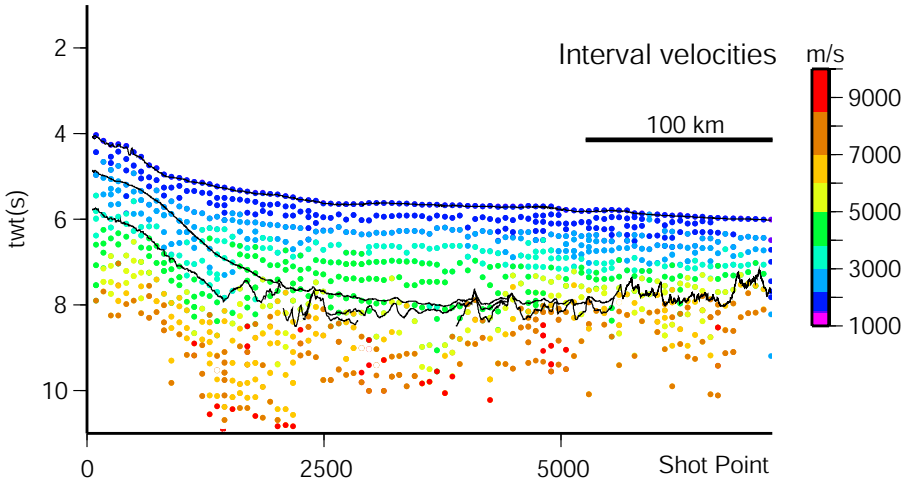

Figure 6.2: Interval velocities, converted from original seismic stacking velocities using Dix's equation, for Line GA-228_24. Base of the post rift sequence, the Eocene unconformity and the water bottom as interpreted in MCS data are superimposed (black solid lines).

a number of thin, horizontal layers, that extend infinitely in the positive-x direction, are summed to calculate the gravity anomaly of an arbitrary polygon (Figure 6.3). The gravity anomaly, Δg, of any single layer or interface, in the x,z coordinate system at point P is described by the equation,

$$\Delta g = 2G\Delta\rho(-[x_1 sin\, i + z_1 cos\, i][sin\, i\, log\frac{r_2}{r_1} + cos\, i(\phi_2 - \phi_1)] + z_2\phi_2 - z_1\phi_1)$$

where G is the universal gravitational constant, $\Delta\rho$ is the density contrast across the interface, and x_1, x_2, z_1, z_2, r_1, r_2, ϕ_1 and ϕ_2 are shown in Figure 6.3.

As the gravity field is sensitive to lateral density contrasts, the gradient of the interface between two elements is significant. For the case of $i = 0$ in Figure 6.3, no lateral density contrast exists between layers BB' and CC', and no gravity anomaly results. The wavelength of a gravity anomaly, however, is primarily controlled by the depth to a causative source body. The field strength associated with a wavenumber component (k) of the measured gravity decreases by a factor of e^{-kh}, where h is the height above the density interface. Hence, the higher frequency field components diminish as the height of observation increases. Therefore, the gravity anomaly associated with the *Moho*/crust interface has a much longer wavelength relative to anomalies associated with anomalous masses of identical dimensions closer to the surface (or level of measurement).

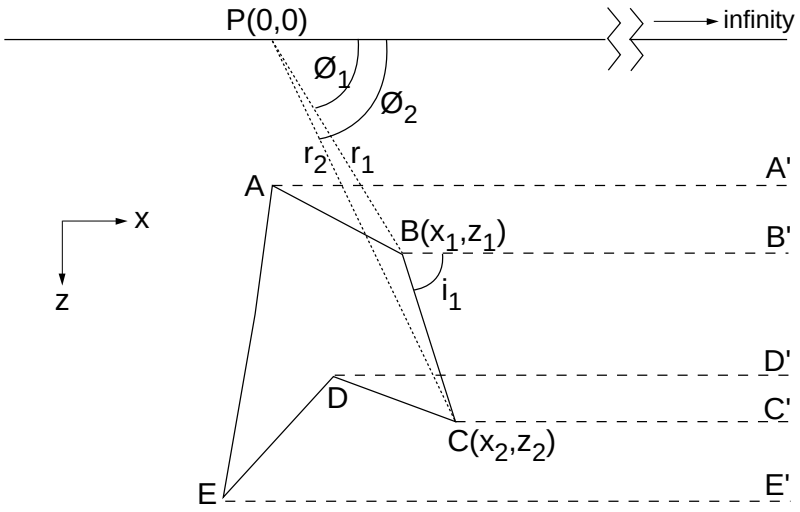

Figure 6.3: Geometry of an arbitrary polygon and the method of Talwani *et al.* [1959] for two-dimensional gravity modelling.

Three-Dimensional Modelling

Direct methods of calculating gravity anomalies associated with three-dimensional bodies are computationally intensive and time consuming [Parker, 1972]. Therefore, the method of Parker [1972] for the rapid calculation of potential anomalies is utilised here to calculate the gravity anomaly associated with density contrasts across three-dimensional surfaces, in this way bodies are simulated by two or more surfaces. Parker [1972] demonstrates that for the gravity anomaly, Δg,

$$\mathcal{F}[\Delta g] \quad = \quad -2\pi G e^{-|k|z_0} \sum_{n=1}^{\infty} \frac{(|k|)^{n-1}}{n!} \mathcal{F}[\Delta\rho(z_1^n - z_2^n)] \tag{6.1}$$

where $\mathcal{F}[\ ]$ represents the Fourier transform of the enclosed variable, G is the universal gravitational constant, k is the wavenumber and $\Delta\rho$ is the density contrast across the surface. The gravity anomaly is calculated at some surface, $z = z_0$, where z is depth, and the upper and lower surfaces of the body of anomalous mass are at depths of $z = z_1$ and $z = z_2$ respectively (Figure 6.4). Although the Fourier transform comprises infinite terms of Taylor's expansion series, terms for n>4 are of negligible magnitudes and are disregarded in gravity anomaly calculation.

6.1.4 Data

The marine satellite derived gravity field of Sandwell & Smith [1997] is routinely used in geophysical studies. However, special consideration must be given to the use of these data at high latitudes because, i) shiptrack data is sparse, providing less possibilities

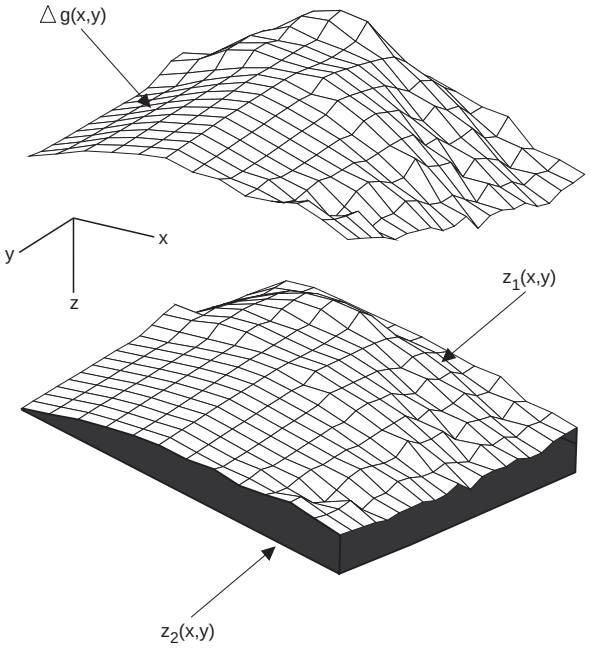

Figure 6.4: Three-dimensional calculation of the gravity anomaly for a layer bounded by z_1 and z_2, based on the Fourier transform methods of rapid calculation of potential field data [Parker, 1972].

for calibration with measured data, and ii) the perennial coverage of the ocean (at polar latitudes) with ice. Complex radar echoes from sea ice confuse trackers onboard altimeter satellites and produce noisy height estimates [McAdoo & Laxon, 1996].

McAdoo & Laxon [1997] derived a high-resolution gravity grid for the poorly charted and ice covered oceanic sector of West Antarctica, from 145-360°E. They incorporated ERS-1 altimetry data, which has a more steeply inclined orbit relative to Geosat and is therefore capable of observing to higher latitudes, in their grid. McAdoo & Laxon [1997] utilised the full 20 Hz ERS-1 wave-form (WAP) data set rather than the ocean product (OPR) data set. This allowed the data to be reprocessed and the height noise significantly reduced [Laxon & McAdoo, 1994]. However, no equivalent data is available for the Wilkes Land sector of East Antarctica.

Comparison of free-air satellite derived gravity anomaly data with GA-228 shiptrack data illustrates the close similarity of the two fields (Figure 6.5a). The close correlation of shiptrack and satellite derived free-air anomaly (FAA) data decreases at higher latitudes (Figure 6.5b). Data acquired by the *R/V S.P. Lee* (survey L184) extends as far south as 66°S, at these latitudes shorter wavelength anomalies observed in shiptrack data are not observed in satellite derived data. This is a function of the problems associated with high latitude satellite altimetry data and the complexities associated with sea ice, as outlined

above. The extents of ice during the austral winter and summer, as shown in Figure 6.6, illustrate that even during times of minimum ice extent, much of the positive peak of the edge-effect anomaly remains ice covered.

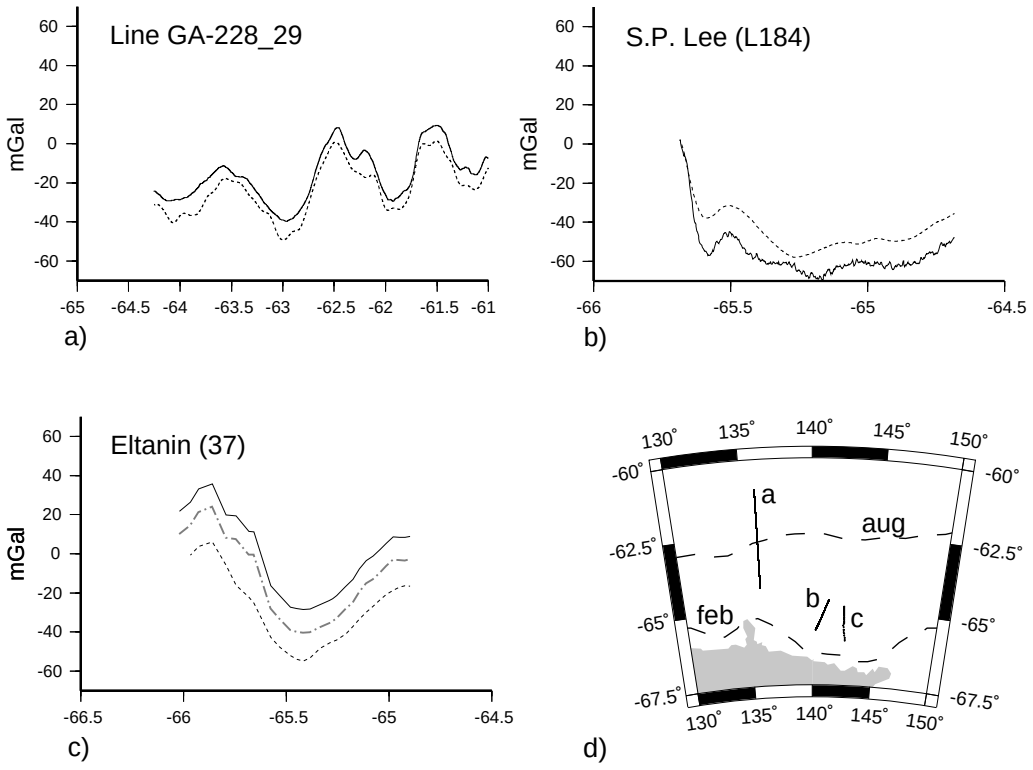

Figure 6.5: Profile comparisons of shiptrack observed (solid) and satellite derived (dashed) free air gravity anomaly data off the Wilkes Land margin for, a) GA-228 survey data, b) *R/V S.P. Lee* survey L184 data, c) *R/V Eltanin* survey 37 data (grey dashed line is shiptrack measured data following correction as discussed in text), and d) Location of profiles for a, b and c, and the August (austral winter) and February (austral summer) ice extents (from R. Larter, BAS).

The most striking feature of Figure 6.5a is the shift between satellite derived and shiptrack data of 5-10 mGal. Comparison of satellite derived FAA data with shiptrack data from survey of L184 [Childs & Stagg, 1987] exhibits the converse relationship (Figure 6.5b). Further confusion is added by the fact that McAdoo & Laxon [1997] demonstrated that L184 shiptrack gravity anomaly data is offset by $\sim$+30 mGal relative to their high-resolution grid; thus, data that is negatively offset relative to satellite derived data on the Wilkes Land margin is positively offset relative to the high-resolution satellite derived data on the West Antarctic margin. Earlier surveys by the *R/V Eltanin* (1968-1972) measured gravity anomaly data that, similarly to the GA-228 and GA-229 data, is shifted positively relative to the satellite derived FAA data (Figure 6.5c). However, the Generic

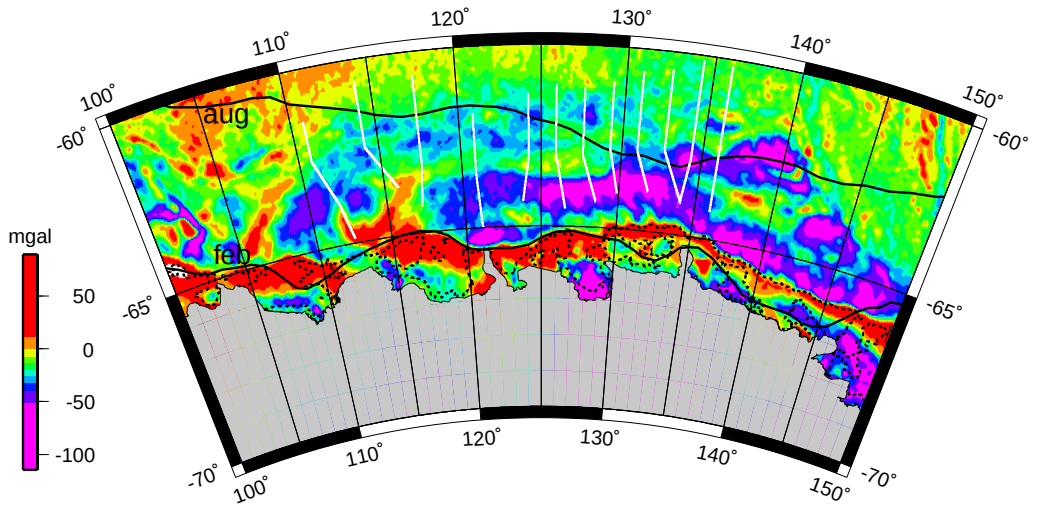

Figure 6.6: August (winter) and February (summer) ice extents (from R. Larter, BAS) for the Wilkes Land margin in solid black. Dashed black represents the 500 m bathymetric contour (GEBCO 1m), and white lines are GA-228 survey lines from 18 (west) to 29 (east). The 500 m contour correlates to the location of the steepest gradient of the edge-effect positive anomaly and also to the minimum (February) ice extent also. Gravity data from Sandwell & Smith [1997].

Mapping Tools (GMT[1]) default (version 3.4) correction file[2] provides corrections for many of the *R/V Eltanin* data, which decrease the magnitude of the positive shift relative to satellite FAA data (Figure 6.5c).

As no tie-line exists between the GA-228 survey lines there are no internal cross over errors, therefore, external cross over error analysis provides the only means of assessing the accuracy of gravity data acquired during the GA-228 survey. Figure 6.7a illustrates the location of shiptrack gravity data for the Wilkes Land margin, a total of 940 external cross over errors were determined between all datasets, the mean value of which was 0.07 mGal with a standard deviation of 11.58. Figure 6.7b illustrates their distribution. Figures 6.7c-f illustrate the external cross over error distribution between groups of surveys (e.g. all *USNS Eltanin* survey data) and all other data. Predictably (given the offsets relative to satellite FAA data) the *USNS Eltanin* and *R/V S.P. Lee* data are respectively positively and negatively shifted relative to the mean for all external cross over errors. *USNS Eltanin* data is corrected where possible. Only 47 cross over errors

[1]http://www.soest.hawaii.edu/gmt

[2]The GMT database contains open-file marine geophysical data. This data can be extracted in 'raw' or 'corrected' format, however, details of the correction are not provided, likely they are associated with different theoretical gravity formulae used in data reduction and referencing to the Potsdam network rather than to the IGSN71 network of base stations.

were determined for GA-228 gravity data, the mean of these errors is 0.93 mGal with a standard deviation of 12.72.

The JNOC survey dataset represents the closest analogue to the GA-228 survey in terms of navigation (i.e. both are GPS controlled) and exhibits a similar mean external cross over error and standard deviation. By examining internal cross over errors for the JNOC cruises we can therefore make some inferences about the level of accuracy achieved by survey GA-228. Internal cross over error analysis of the JNOC cruises of 1983, 1993, and 1994 indicates that mean errors are less than 0.47 mGal for each survey and standard deviations range from 2.06 to 3.65. These low standard deviations, relative to external cross over errors, indicates that the data acquired in each of these surveys is of high quality. A similar reduction in standard deviation could be expected for GA-228 internal cross over errors, were they to exist, and accordingly we can infer an accuracy of better than ± 5 mGal in GA-228 gravity data.

Long Wavelength Analysis and Removal

Gravity models created throughout this study include upper mantle and shallower bodies only, therefore gravity anomalies of very long wavelengths are not modelled. Measured gravity data, however, comprises both the shorter wavelength signals due to crustal density anomalies and longer wavelengths due to density anomalies within the mantle and the curvature of the geoid. If long wavelength anomalies contribute unequally across the study area then it is necessary to remove these from observed data to allow direct comparison with modelled gravity anomalies. Utilising the geopotential coefficient model of Rapp & Pavlis [1990] it is possible to isolate gravity anomaly data of any given waveband by using the simple (and approximate) relationship between spherical harmonic degree and order (of the coefficient model) and gravity signal wavelength by

$$\lambda \;=\; 360 \times \frac{111}{n} \tag{6.2}$$

where λ is wavelength in km, and n is the spherical harmonic degree and order.

The threshold value over which all greater wavelengths are removed is ultimately a subjective choice. The gravity field for a number of degree and order values equivalent to wavelengths from ~5000-2000 km are shown in Figure 6.8. The magnitude of the long wavelength components illustrated do not exceed 25 mGal, but are almost entirely negative. The negative regional FAA reflects the negative depth anomalies associated with the ~2000 km wide Australia-Antarctica Depression (AAD), which extends at least 900 km from the ridge crest.

Hayes & Conolly [1972] suggested that the AAD and observed depth anomalies are associated with a downwelling convective current in the asthenosphere. To remove the deep,

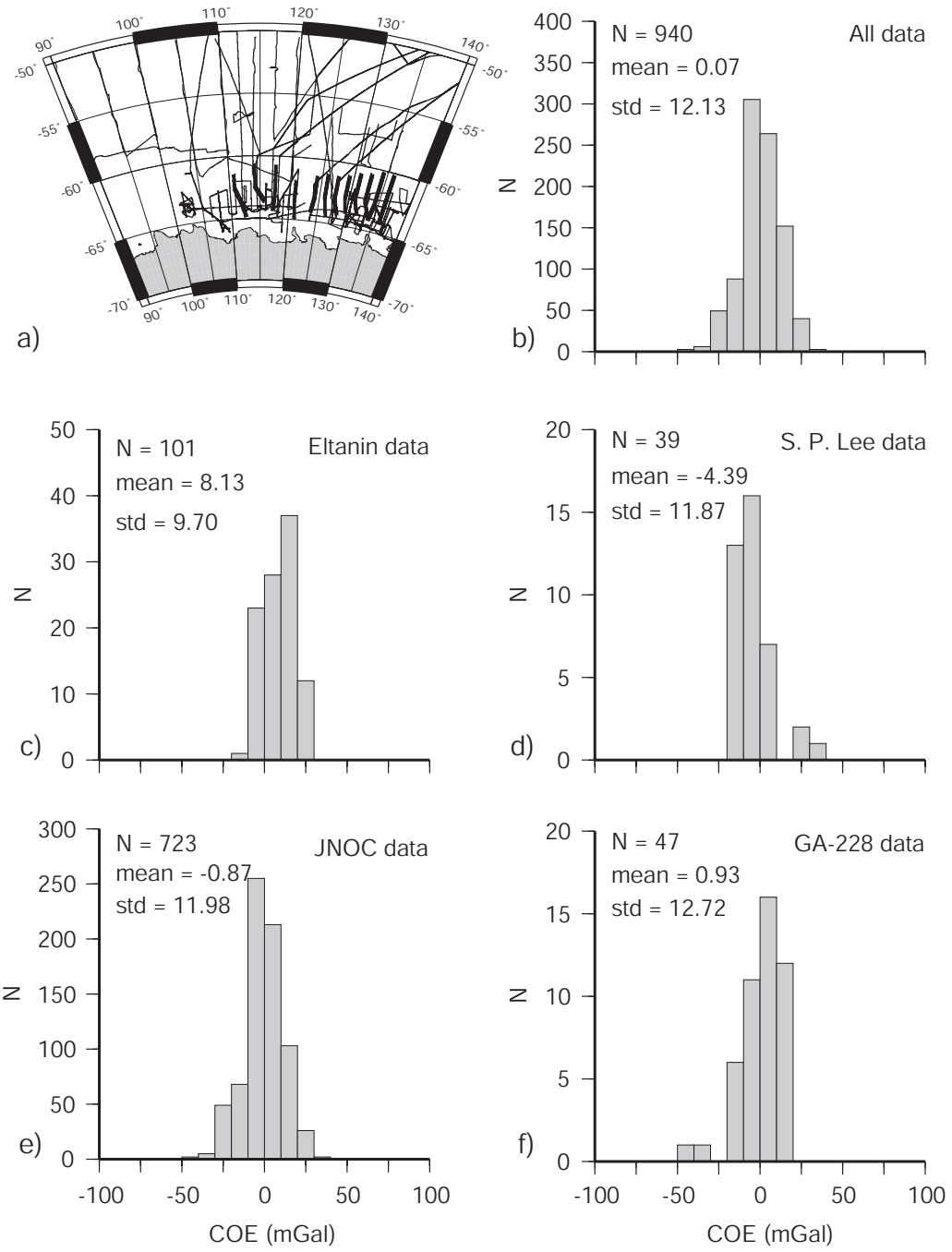

Figure 6.7: External cross over error analysis of shiptrack gravity data for the Wilkes Land margin. a) Shiptrack plot of all open access, JNOC and GA-228 (bold) gravity data. Distribution of cross over error magnitudes for b) all data, c) Eltanin data (after correction where possible), d) USGS S.P. Lee data, e) Japanese National Oil Company (JNOC) data, and f) Geoscience Australia survey GA-228.

asthenospheric contribution to the regional negative gravity field, wavelengths greater than ∼3333 km ($n = 12$) were subtracted from the total field satellite derived FAA data. All subsequent analysis and comparisons of observed gravity data (shiptrack and satellite derived), throughout this study, have had components equal and greater to degree and order 12 removed.

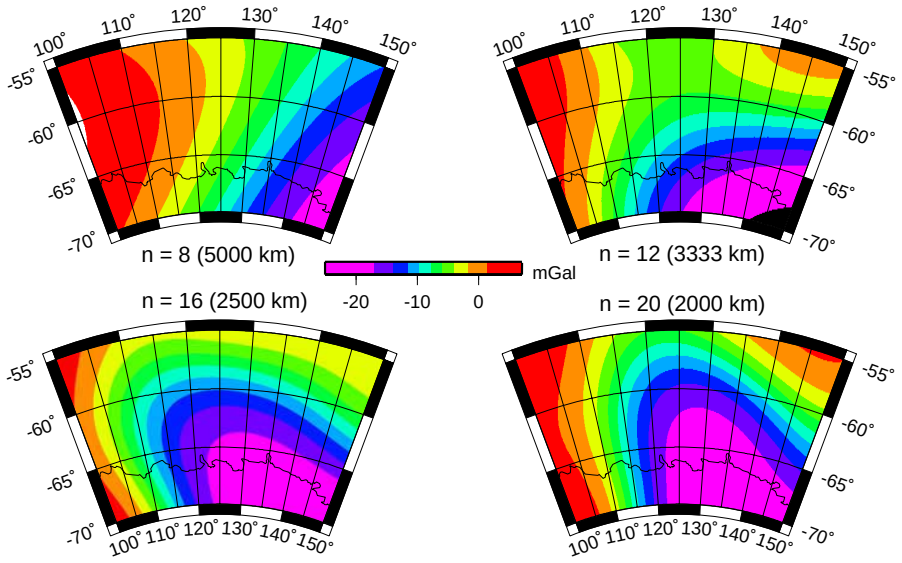

Figure 6.8: Comparison of the long wavelength gravity field [Rapp & Pavlis, 1990] in the Wilkes Land margin region, for four different degree and order values, n. Approximate minimum included wavelengths are bracketed. The long wavelength fields are almost entirely negative for the extent of the Wilkes Land margin.

Wilkes Land Edge Effect Gravity Anomaly

A number of features of the edge effect anomaly, as imaged in the satellite derived FAA gravity data, are worthy of note prior to quantitative analysis and modelling. One of the most prominent features of the marine free-air gravity field (e.g. Figures 6.6 and 6.9b) is the *edge effect* observed at the continental margin. This anomaly typically consists of a gravity high over the shelf break and a low over the continental slope/rise. This high-low 'couple' is observed along much of the Wilkes Land margin. The edge effect high exceeds 60 mGal in the eastern sector only and the low is typically no more negative than -40 mGal. North-south profiles extracted from the satellite FAA field (Figure 6.10) illustrate the variation in the edge effect anomaly along the margin.

In the central sector the edge effect anomaly is relatively consistent in form and magnitude. To the west and east, however, significant departures from this form are evident. In the western sector, at ∼112°, the edge effect high is shifted abruptly southwards by

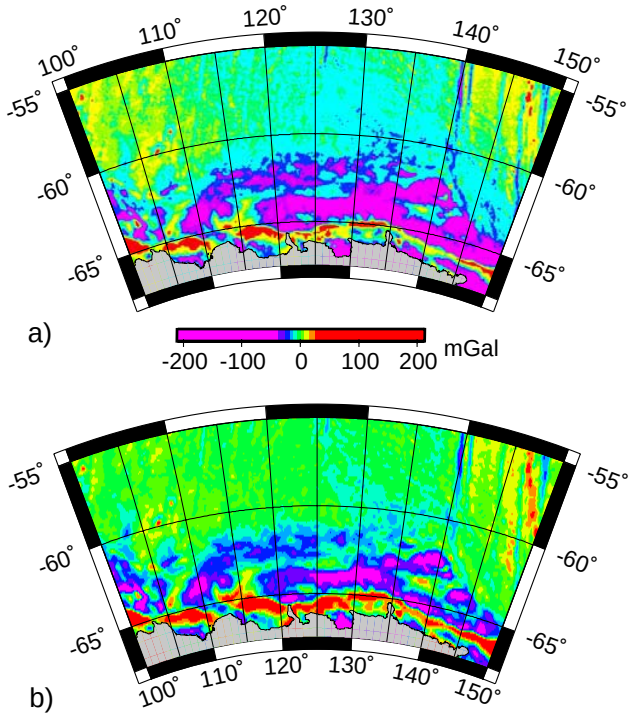

Figure 6.9: Comparison of a) total satellite derived gravity anomaly field of Sandwell & Smith [1997], and b) residual gravity field after subtracting the long wavelength gravity field to degree and order $n = 12$ (i.e. wavelengths ~3333 km).

more than 100 km. This edge effect discontinuity occurs at the prominent Budd Coast headland, formed by the Law Dome. The physiography of this margin sector is unusual, it is characterised by a very narrow continental shelf and an absence of a clear shelf-break. The absence of a shelf break explains the discontinuity in the edge effect high.

The outer continental rise sector of the Budd Coast Basin (BCB), as defined in Chapter 4, broadly correlates to the east-west positive FAA at ~62.5°S, from ~115-130°E (Figure 6.11). This indicates that the basin sediments are, at least in part, uncompensated.

To the east, between ~132-142°E, the relatively broad edge effect low is replaced by an *outer high* and the low is split into two limbs encircling this anomalous high. This anomaly was discussed in Chapters 4 and 5 due to its coincidence with anomalous seismic reflection and magnetic anomaly data. The eastern sector of the Wilkes Land margin is characterised by much thinner sediment loads, decreasing to less than 1 km in some areas.

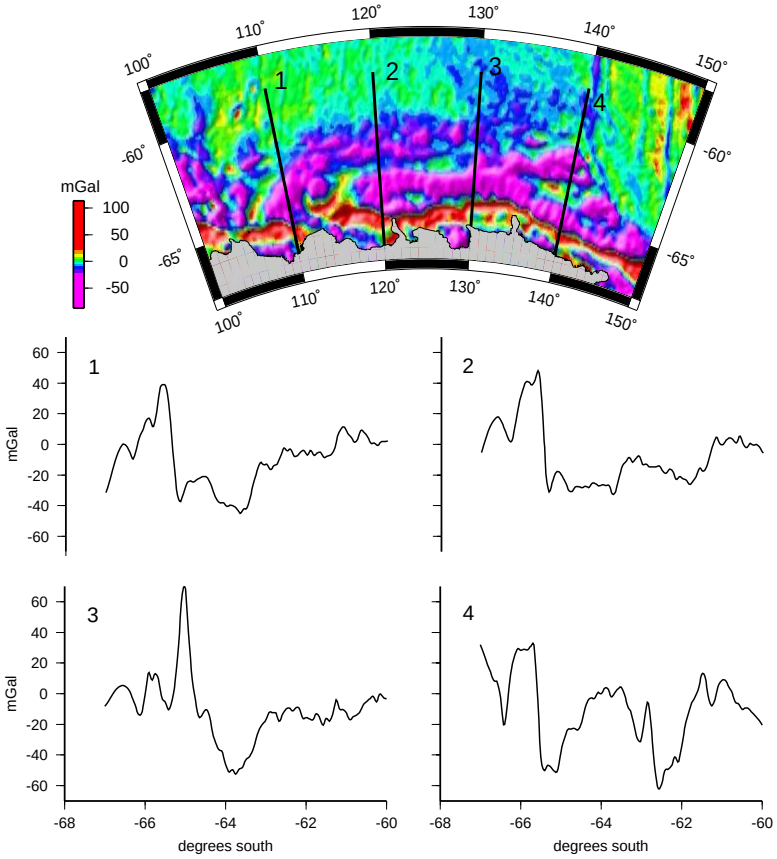

Figure 6.10: Four north-south profiles extracted from satellite derived free air gravity anomaly data, located as per black solid lines on map above. The edge effect anomaly is best developed in the central sector (profile 3) between 122-132°E.

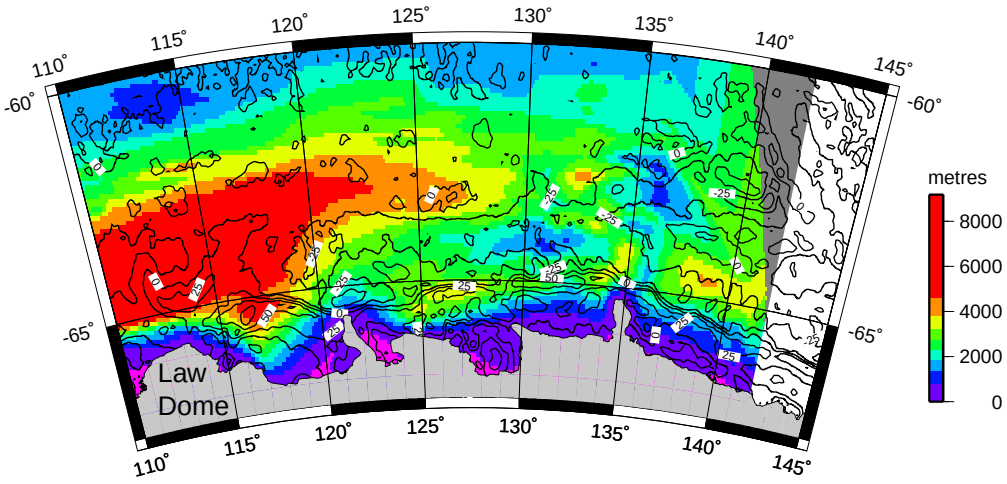

Figure 6.11: Total sediment isopach overlain by satellite derived FAA contours [Sandwell & Smith, 1997]. The edge effect low is deflected by the thick sediments off the western sector of the Wilkes Land margin. The correlation between sediment thickness and positive gravity anomalies indicates that the sediments are, at least in part, uncompensated.

6.2 Backstripping, Flexure and Process-Oriented Modelling

6.2.1 Backstripping and Flexure

Backstripping is a method developed by Watts & Ryan [1976] to "correct" a stratigraphic sequence for the disturbing effects of sediment and water loading, and hence isolate the unknown tectonic driving forces responsible for the rift basin subsidence. By applying this technique Watts & Ryan [1976] were able to determine the depth at which basement would be in the absence of the driving loads of water and sediments (i.e. the *tectonic subsidence*). Sawyer [1985] defined the *Total Tectonic Subsidence* (TTS) as the difference between the pre-rifting continental crust elevation and the present, sediment unloaded or backstripped basement depth.

To determine the TTS we consider the deflection of an elastic plate in response to the loading effect of a sediment layer (S) and the loading effect of water due changes in sea level (Δ_{sl}), Figure 6.12. The general equation for the deflection of an elastic plate (Equation 1.1), therefore, becomes

$$D\frac{d^4w}{dx^4} + (\rho_m - \rho_{infill})gw = (\rho_s - \rho_w)gS + \rho_w g\Delta_{sl} \tag{6.3}$$

where D is the flexural rigidity (Equation 1.2), w is the deflection of the plate (i.e. flexure), ρ_m and ρ_{infill} are the densities of the mantle and the material that infills the deflection respectively, ρ_s is the average density of the sediment load, and ρ_w is the density of water. Solving this equation using Fourier transforms provides,

$$\begin{aligned} \hat{W}[Dk^4 + (\rho_m - \rho_{infill})g] &= (\rho_s - \rho_w)g\hat{S} + \rho_w g\hat{\Delta_{SL}} \\ \hat{W} &= \phi\left[\hat{S}\frac{(\rho_s - \rho_w)}{(\rho_m - \rho_{infill})} + \hat{\Delta_{sl}}\frac{\rho_w}{(\rho_m - \rho_{infill})}\right] \end{aligned} \tag{6.4}$$

where the hat above an upper-case variable denotes the Fourier transform of the lower case variable, k is wavenumber, and ϕ is the flexural parameter,

$$\phi = \left[1 + \frac{Dk^4}{(\rho_m - \rho_{infill})g}\right]^{-1} \tag{6.5}$$

For the case of Airy isostasy (i.e. D=0), $\phi = 0$, and the solution to Equation 6.4 reduces to,

$$w = S\left[\frac{(\rho_s - \rho_w)}{(\rho_m - \rho_{infill})}\right] + \Delta_{sl}\left[\frac{\rho_w}{(\rho_m - \rho_{infill})}\right] \tag{6.6}$$

Figure 6.12 illustrates that a sedimentary layer (S) may be considered as the sum of a load (y) and its flexure (w), i.e. $S = y + w$. We also see that the TTS (Y) is the sum of the load and water depth, i.e. $Y = y + W_d$. Therefore, by setting $\rho_{infill} = \rho_w$, the

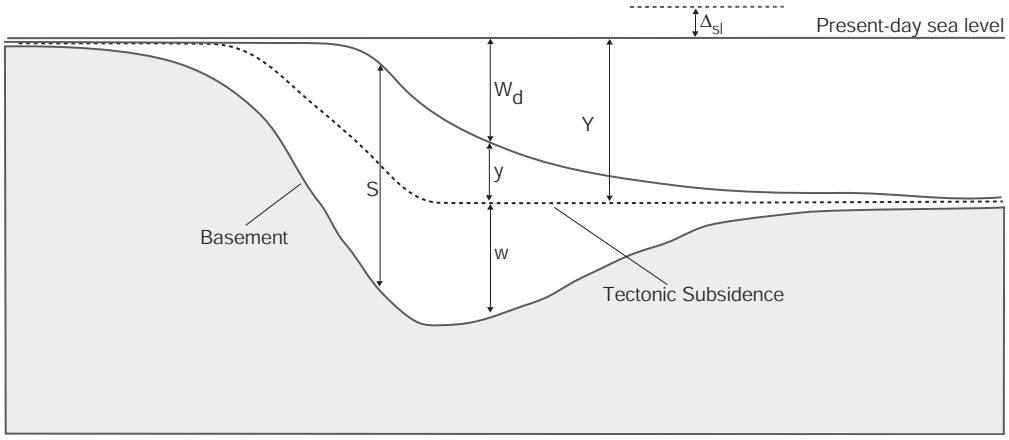

Figure 6.12: Schematic representation of the backstripping process. A sedimentary layer of thickness S can be considered as the sum of a load, y, and its flexure, w. The total tectonic subsidence (TTS), $Y = y + W_d$, is shown as a dashed line.

TTS for Airy isostasy ($D = 0$) is given by,

$$\begin{aligned} Y &= S - w + W_d \\ &= S - \left[S \left(\frac{(\rho_s - \rho_w)}{(\rho_m - \rho_w)} \right) + \Delta_{sl} \left(\frac{\rho_w}{(\rho_m - \rho_w)} \right) \right] + W_d \end{aligned} \tag{6.7}$$

The TTS for the flexural case is, following the logic above, given by,

$$Y = S - \mathcal{F}^{-}1 \left[\phi \hat{S} \left(\frac{(\rho_s - \rho_w)}{(\rho_m - \rho_w)} \right) + \hat{\Delta_{SL}} \left(\frac{\rho_w}{(\rho_m - \rho_w)} \right) \right] + W_d \tag{6.8}$$

where $\mathcal{F}^{-}1$ represents the inverse Fourier transform.

6.2.2 Stretching Factor (β) and Rifted Crust Structure

Combining the backstripping process with kinematic rift models (e.g. McKenzie [1978]) allows a quantitative estimation of crustal thinning in rift basins. Crustal structure and the stretching factor (β) can be determined from the backstripped basement (TTS) by assuming a state of isostasy during rifting.

For Airy isostatic compensation during rifting, subsidence is compensated locally by crustal thinning, and conversely uplift is compensated by crustal thickening. Assuming Airy isostasy during rifting implies a zero-strength lithosphere. Strength, or layers of increased strength, within the lithosphere introduce a flexural component to the compensation of a rift basin.

Dynamic modelling of Braun & Beaumont [1989], using a finite element model with a depth dependent rheology, showed that thinning or *necking* occurs preferentially at the depth of the lithospheric strength maxima. Kooi *et al.* [1992] define the *depth of*

necking as a surface which, in the absence of gravity or buoyancy forces, would not move vertically during extension. For a given depth of necking (Z_{neck}) and stretching factor (β), Weissel & Karner [1989] showed that the kinematic rift basin depth (S_t), as shown in Figure 6.13, is given by

$$S_t = (1 - \frac{1}{\beta})Z_{neck} \tag{6.9}$$

and that the $Moho$ occurs at a depth of T_c/β below S_t, where T_c is the initial, zero-elevation, crustal thickness.

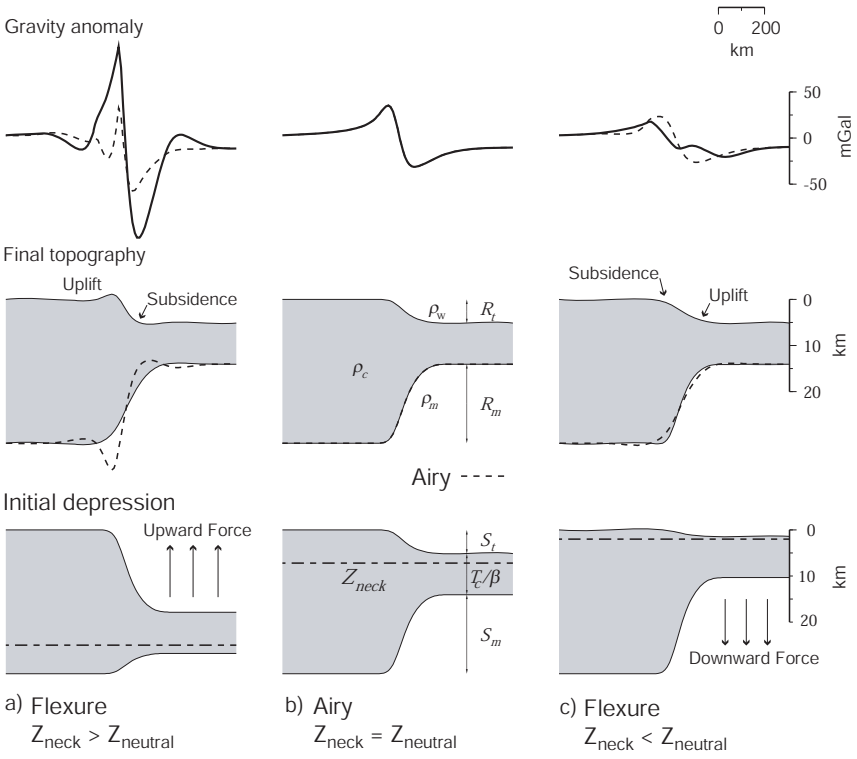

Figure 6.13: Schematic illustration of the effect of including a depth of necking, Z_{neck}, in rift modelling. The forces associated with an a) oversized, and c) undersized basin, and their effects on the initial and final rift topography and gravity anomaly are illustrated. b) shows the Airy or $Z_{neck} = Z_{neutral}$ solution for comparison. Reproduced from Watts [2001] after Watts & Stewart [1998].

The isostatic inequilibrium associated with the initial, kinematic basin depth causes vertical forces which act to restore isostatic equilibrium. The balance of upward and downward forces, q_{net}, associated with the replacement of crust by mantle and air/water respectively, is given by (for a water filled basin),

$$q_{net} = [S_m(\rho_m - \rho_c) + S_t(\rho_w - \rho_c)]g \tag{6.10}$$

where ρ_m, ρ_c, and ρ_w are the densities of the mantle, crust and water respectively. The final basin depth (R_t) and *Moho* upwarp (R_m) is controlled by the distribution of q_{net} and the strength of the lithosphere during rifting.

For any given combination of crust, mantle, and infill density, and initial crustal thickness, there exists a unique Z_{neck} for which $q_{net} = 0$, we call this $Z_{neutral}$. For $Z_{neck} = Z_{neutral}$, the basin geometry is equivalent to that predicted by Airy compensation. For $\rho_c = 2800\,kg/m^3$, $\rho_m = 3300\,kg/m^3$, $\rho_w = 1030\,kg/m^3$, and $T_c = 35\,km$, $Z_{neutral} =\sim 7.7$ km. Weissel & Karner [1989] demonstrated that for $Z_{neck} < Z_{neutral}$ a shallow basin with increased *Moho* relief forms, and conversely for $Z_{neck} > Z_{neutral}$ a deep basin with subdued *Moho* relief forms (Figure 6.13).

Watts & Stewart [1998] directly related the TTS to β, accounting for both Z_{neck} and a finite syn-rift strength (Te_{rift}),

$$\beta^{-1} = \frac{q_{net}(x) - [Y - Z_{neck}](x)\,\psi(x)}{Z_{neck}\,\psi(x) + q_0} \tag{6.11}$$

where

$$\psi(x) = Dk^4 + (\rho_m - \rho_w)g$$

Equation 6.11 allows the β distribution to be determined directly from the backstrip, taking into account the possibility of strength during rifting. Once β is determined, it is a simple matter to compute the $Moho$ configuration [Watts & Stewart, 1998].

6.2.3 Process-Oriented Modelling

The observed gravity anomaly at a continental margin can be considered as the result of all dynamic and geological processes that have shaped it through time. These include rifting, volcanism, sedimentation, and magmatic underplating [Watts & Fairhead, 1999]. The 'Process-oriented' method models the gravitational contribution of individual geological processes, with an aim of better understanding the causes of edge-effect variations. This method contrasts with object-oriented modelling, where the density structure that best explains the observed gravity anomaly is determined.

Object-oriented modelling is useful in determining the physical properties of the lithosphere, however, the non-uniqueness of any model is amplified by the sensitivity to user input. Object-oriented methods also provide little insight into the effect that geological processes may play in the evolution of a margin. The process-oriented method is a powerful forward modelling technique as it allows the long term mechanical properties of the lithosphere to be constrained, by considering the geological processes that have shaped the margin through time. Additionally, the direct methods by which the process-oriented

method models the gravity anomalies, using defined formative processes, helps to address the problems of non-uniqueness inherent to gravity modelling.

Process-oriented modelling describes a three-stage process (Figure 6.14) that is particularly applicable in rifted continental margin environments where spectral techniques are incapable of extracting T_e estimates due to large sedimentary accumulations. The foremost and most basic assumption of this technique is that prior to rifting there existed a crust of uniform average thickness, T_c, that was stretched during rifting to create a subsided and water filled, rift basin.

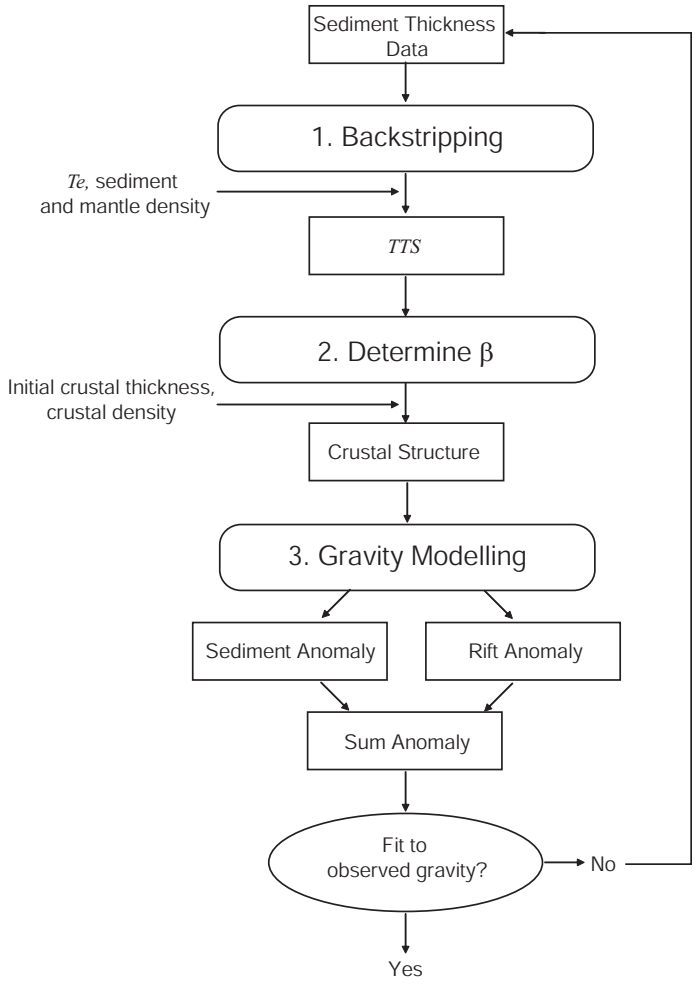

Figure 6.14: Flow chart of the three stages involved with process-oriented modelling.

The first stage of the process-oriented method involves backstripping sediments within the rift basin to determine the *TTS*. The second stage requires the determination of the stretching factor (β), assuming either Airy or flexural isostasy during rifting. The third stage involves the calculation of gravity anomalies that can be summed and compared to the observed gravity anomaly. The model gravity anomaly is considered to be the sum

of the gravity effects of all the processes operating at the margin. The three-stages of the process-oriented method are iterated until an optimal fit between modelled and observed gravity anomalies is achieved.

The third stage of the process-oriented method applied here models the competing gravity effects of rifting and sedimentation. Hence, the gravity anomalies associated with rifting, the *rift anomaly*, and sedimentation, the *sediment anomaly*, are calculated independently and summed to create the *sum anomaly*.

The rift anomaly (Figure 6.15a) is the anomaly associated with the changes in crustal thickness resulting from the rifting process, without the disturbing effect of sediment loading. It comprises the negative contribution of water replacing crust ($\rho_w - \rho_c$) and the positive contribution of mantle replacing crust ($\rho_m - \rho_c$). The depth of the basin is defined by the TTS surface and the depth to the *Moho* by the β factor distribution determined in stage 2. The anomaly is characterised by a landward high, over the seaward edge of unstretched crust, and a flanking low, over the stretched crust. The geometry of this anomaly represents the greater wavelength of the positive mantle anomaly due to its greater depth.

The sediment anomaly (Figure 6.15b) is the anomaly associated with sedimentation within the rift basin and its compensation. It comprises a positive component due to the replacement of water by denser sediments (i.e. $\rho_s - \rho_w$) and negative components due to their compensation, which occurs at the basement (i.e. $\rho_s - \rho_c$) and at the *Moho* (i.e. $\rho_c - \rho_m$). As the compensation occurs at greater depths than the sediment load, the wavelengths of the corresponding gravity anomalies (flexure and *Moho* flexure anomalies in Figure 6.15b) are greater relative to that of the sediment load. Hence, the sedimentation anomaly comprises a single high with flanking, lower amplitude, lows.

The sum anomaly (6.15d) is simply the sum of the rift and sediment anomalies. This is because the sum anomaly is a result of mass additions (or subtractions) to the original, uniform thickness crust and the gravity effect of these anomalies have been calculated *in situ*. The sum anomaly represents the gravity contribution of the crustal thickness changes associated with a dynamic rifting process, and the subsequent modification of the rift structure by sedimentation. The addition of the sediment anomaly to the rift anomaly shifts the positive peak oceanward over the new prograded shelf break. The relative importance of the component anomalies depends upon the thickness and geometry of the sedimentary sequence and on the T_e structure.

The form of the sum anomaly can differ significantly for low and high T_e margins. Figure 6.16 illustrates two simple margin models with different T_e structures. The "weak" margin is characterised by a double edge effect anomaly, comprising two relatively lower amplitude and shorter wavelength positive anomalies over the original and new shelf

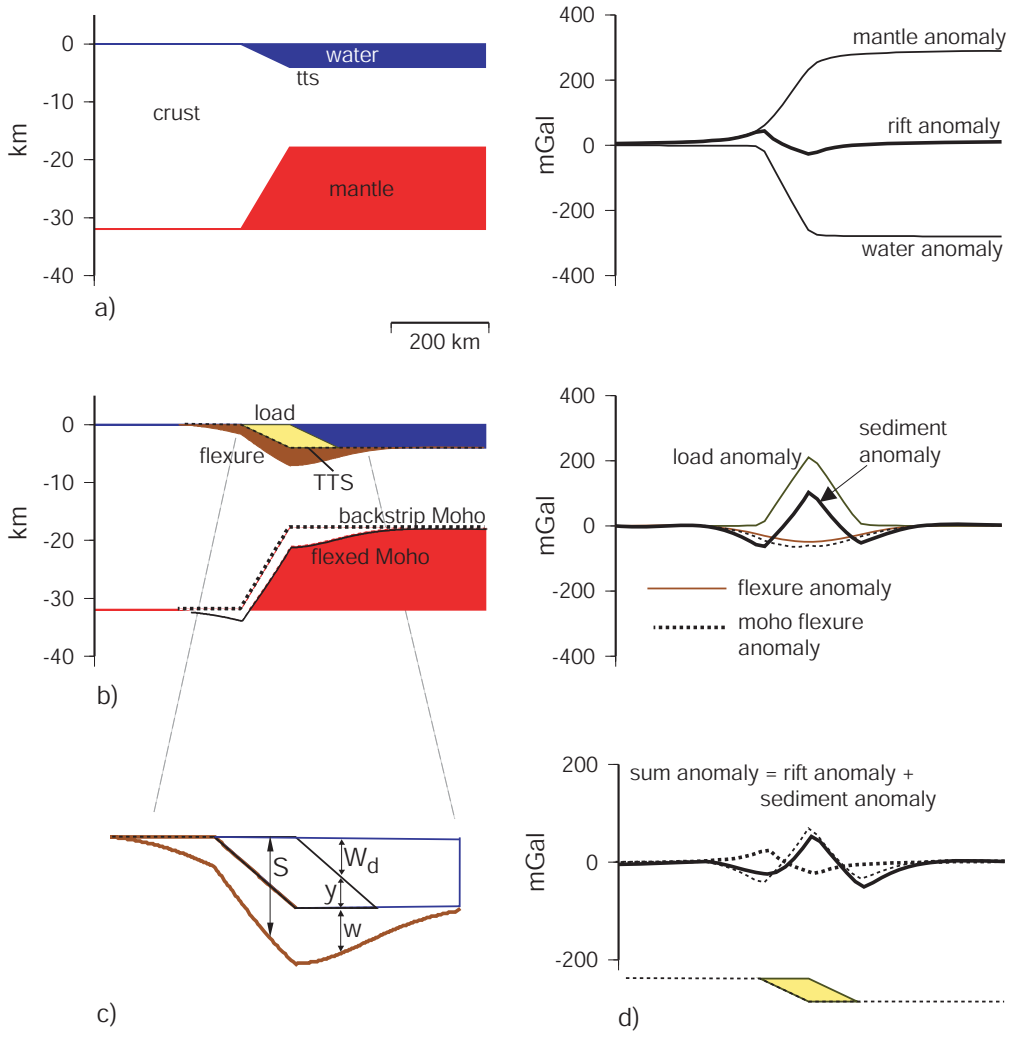

Figure 6.15: Schematic representation of important components and principles of process oriented gravity modelling. a) Original rift margin structure and associated rift anomaly. b) Present day margin structure, loaded with flexurally compensated sediments, and the sediment anomaly. The Total Tectonic Subsidence (TTS), determined from backstripping, is the crucial surface for defining load and flexure in the process-oriented method. c) Detailed section of sediment sequence and the relationship between load and flexure. d) Sum gravity anomaly (solid black) and component rift and sediment anomalies (dashed black).

breaks. Whereas the "strong" margin exhibits the more typical single edge effect anomaly, of greater amplitude and wavelength, with the peak amplitude reached over the locus of the thickest sediments [Watts & Marr, 1995]. The terms strong and weak here are not meant to characterise the actual margin strengths, which requires knowledge of the maximum stresses required to cause failure. Rather, the terms are used to describe the

lithosphere's ability to support long term loads. In the case of the strong margin, much of the load is supported by lithospheric strength. In contrast, the load at a weak margin is primarily supported by the underlying fluid substratum [Watts & Marr, 1995].

The above simple examples demonstrate that the form of the edge effect anomaly is a strong function of the strength of the underlying lithosphere. Although the gravity signal of the original margin structure is modified by sediment loading for both the weak and strong cases, the strength of the lithosphere determines the form of this modification [Watts & Marr, 1995].

Figure 6.16: Simple models of a) *weak*, low T_e, and b) *strong*, high T_e - margins and their associated process oriented, sum free air gravity anomalies. A marked difference in the modelled gravity anomaly is observed for these two models, indicating a strong dependence of the gravity signal on T_e.

6.2.4 Isostatic Anomalies

Residual gravity anomalies that remain after subtracting the isostatically modelled gravity field from the observed field are labelled *Isostatic Anomalies* (IA). If Airy isostasy is

assumed in modelling, then the term Airy isostatic anomaly is used. If regional isostatic compensation is assumed in modelling, then the residual anomalies are labelled flexural isostatic anomalies.

If geometries and properties of a model are perfectly constrained, but isostatic anomalies remain, it indicates that a load is somehow "undercompensated" or "overcompensated" in the sense that there is a deficiency or excess of mass involved in its compensation [Stewart, 1998]. If Airy isostatic anomalies remain it may indicate that loads are supported by the flexural strength of the lithosphere so that compensating masses may be offset from the load, however, integration of such isostatic anomalies over the region of compensation should tend to zero. Two further explanations of both Airy and flexural isostatic anomalies are.

1. A load may not have been present or absent for a sufficient period to allow a region to achieve isostatic equilibrium, accordingly isostatic gravity anomalies will be measured over the region. For example, areas subject to Pleistocene glaciation not completely adjusted to the removal of ice loads (e.g. Walcott [1973]).

2. The presence of density anomalies within the lithosphere, even if compensated, can also cause isostatic anomalies (Figure 6.17). A mass excess within the crust may be completely locally compensated, however, if there is no associated topographic expression then neither the mass or its compensation is accounted for in an isostatic model. Hence, an isostatic anomaly exists despite perfect isostatic balance within the lithosphere.

The process-oriented method allows isostatic anomalies to be computed that account for flexural compensation, accordingly we take isostatic anomalies to represent density anomalies or departures from the assumed isostatic regime. Density anomalies in the post-rift sedimentary sequence are likely to be directly resolved by changes in reflection character and/or by zones of anomalous seismic velocity. In the absence of such observations it is reasonable to assume that inferred density anomalies are intra- or sub-crustal. Typically, the wavelength of an isostatic anomaly will indicate whether it is likely that the causative source is at crustal or mantle levels. The process-oriented method, therefore, allows the density structure of the crust to be interrogated without the interfering effects of other geological processes (e.g. rifting, sediment loading).

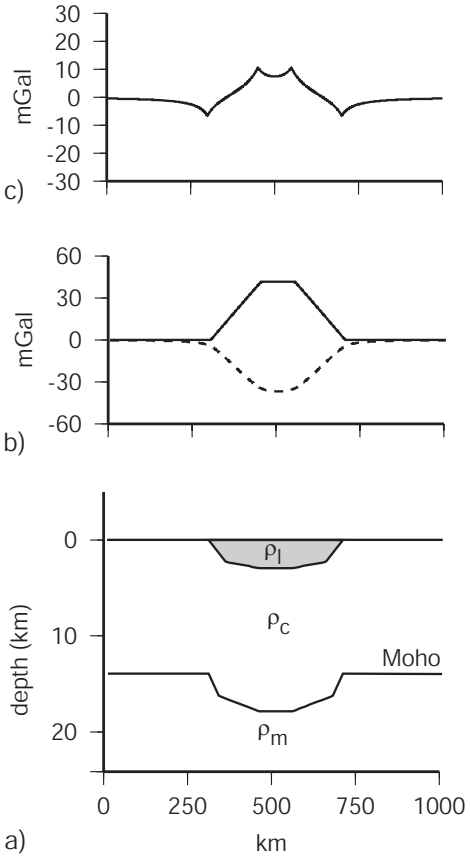

Figure 6.17: a) A mass anomaly (ρ_l) within the crust (ρ_c), that is perfectly locally compensated at the crust/mantle (ρ_m) boundary. b) the free-air anomalies associated with the mass anomaly (solid) and its compensation (dashed). c) The isostatic anomaly that exists in this situation despite perfect local isostatic compensation.

6.3 2-Dimensional Gravity Modelling on the Wilkes Land Margin

6.3.1 Airy Isostatic Models

Classic Airy Modelling

The conceptually simplest gravity model utilised in margin studies is the *"classic-Airy"* model which considers the observed basin topography to be supported by crustal thickness variations. The crustal thinning required to Airy compensate a basin is calculated, assuming some initial, zero-elevation crustal thickness (T_c), from the observed water depth (T_w). This is achieved by mass balancing the base of an unstretched crustal column with a water, stretched-crust, and mantle column (Figure 6.18). That is,

$$\rho_c T_c = \rho_w T_w + \rho_c t_c + \rho_m T_m \tag{6.12}$$

Where ρ_w, ρ_c and ρ_m are the densities of water, crust and mantle respectively. Solving this for either T_m or t_c allows the *Moho* geometry to be defined, e.g.

$$T_m = T_w \frac{\rho_c - \rho_w}{\rho_m - \rho_c} \tag{6.13}$$

The gravity effect of the topography is calculated, using a density contrast of $\rho_w - \rho_c$, for the water filled rift basin. The gravity effect of the compensation is calculated assuming a density contrast of $\rho_m - \rho_c$. These competing gravity contributions are summed to calculate the classic-Airy gravity anomaly.

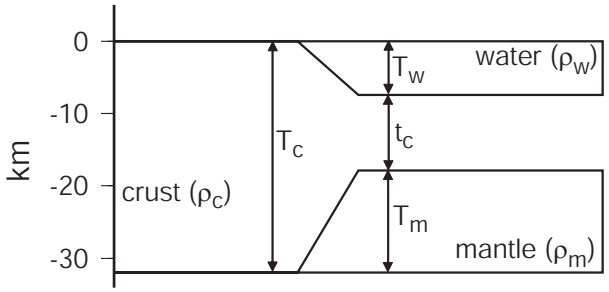

Figure 6.18: Schematic representation of parameters important in determining the crustal structure for a rift basin of depth T_w.

As this type of model makes no corrections for the effects of sedimentation on the total gravity field, it is more likely to yield close fits to observed data for regions of low sediment thickness. The difference between the observed FAA and the gravity effect of the topography and its Airy-type compensation is the Airy isostatic anomaly, as discussed previously.

The Airy isostatic anomaly was used by early workers as a means of identifying the COB location in a number of rift margin basins, [Rabinowitz & LaBrecque, 1977; Talwani & Eldholm, 1973], although it was subsequently demonstrated that the outer

high observed in Airy isostatic anomaly profiles, interpreted to represent the COB, could be explained by considering flexural compensation of sediment loads [Karner & Watts, 1982].

Classic-Airy models were created for survey lines GA-228_18 to GA-228_29 and GA-229_06 using MCS derived bathymetry supplemented by GEBCO 1 minute bathymetry data between the Antarctic coast and the survey line terminations. The models for selected lines and their calculated gravity fields are plotted and compared to the satellite and shiptrack gravity fields in Figures 6.19 and 6.20. The location of the edge effect anomaly is correctly located in the modelled sections. However, the fit between the observed edge effect low and corresponding section of the modelled profile is poor. In general, the long wavelength positive gradient observed seaward of the edge effect low is matched by the modelled profiles, however, the shorter wavelength components included in observed data are not simulated in these simple models.

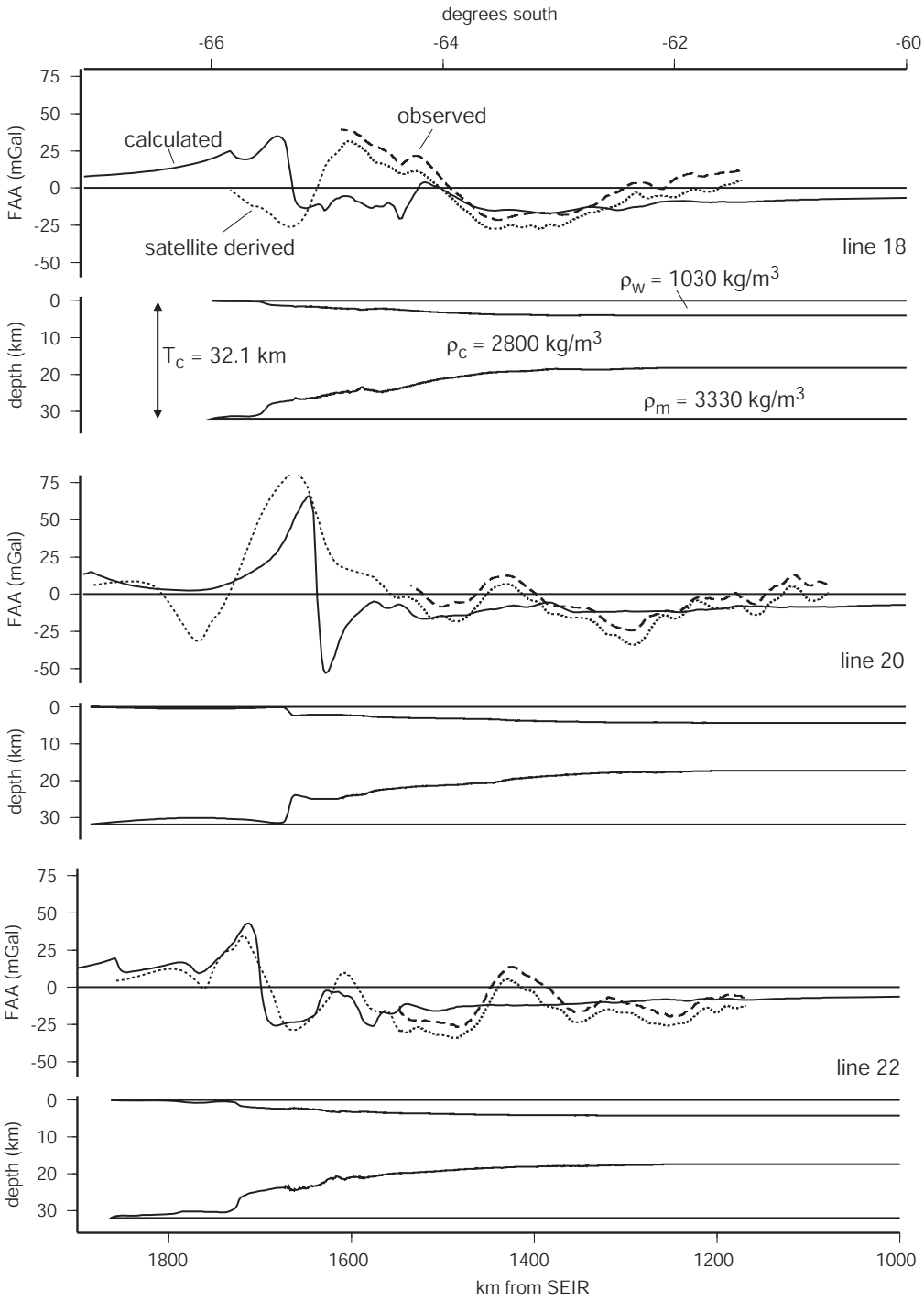

Figure 6.19: Classic Airy isostatic gravity models for survey lines GA-228_18, GA-228_20 and GA-228_22, and corresponding modelled free air gravity anomalies (solid black) compared to observed free air gravity (dashed black) and satellite derived (dotted black) free air gravity from Sandwell & Smith [1997].

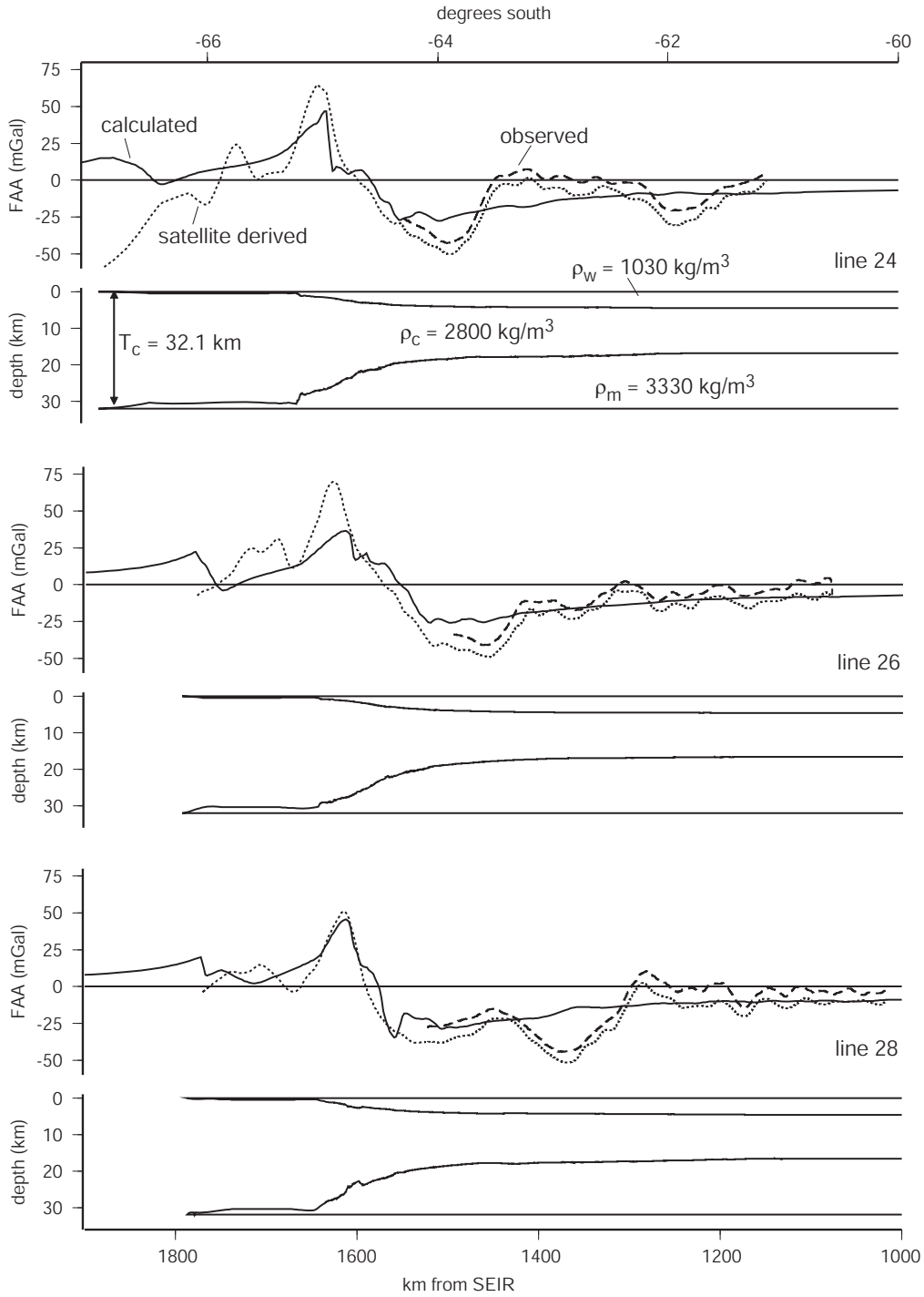

Figure 6.20: Classic Airy isostatic gravity models for survey lines GA-228_24, GA-228_26 and GA-228_28, and corresponding modelled free air gravity anomalies (solid black) compared to observed free air gravity (dashed black) and satellite derived (dotted black) free air gravity from Sandwell & Smith [1997].

Sediment Corrected Airy Modelling

The classic-Airy model can be adjusted to incorporate sediment thickness data where available. This process essentially provides a simple sediment correction by adding a third model body that is assumed to be replacing crust and completely locally compensated (Figure 6.21). Similarly to the classic-Airy approach, the depth to *Moho* can be calculated to maintain a state of Airy isostatic balance by considering

$$\rho_c T_c = \rho_w T_w + \rho_s t_s + \rho_c t_c + \rho_m T_m \tag{6.14}$$

where variables are as for Equation 6.12 and ρ_s and t_s are the density and thickness of sediment respectively. Solving this for either T_m or t_c allows the *Moho* geometry to be defined by

$$T_m = \frac{A(\rho_c - \rho_w) + t_s(\rho_w - \rho_s)}{\rho_m - \rho_c} \tag{6.15}$$

where $A = T_w + t_s$ (Figure 6.21).

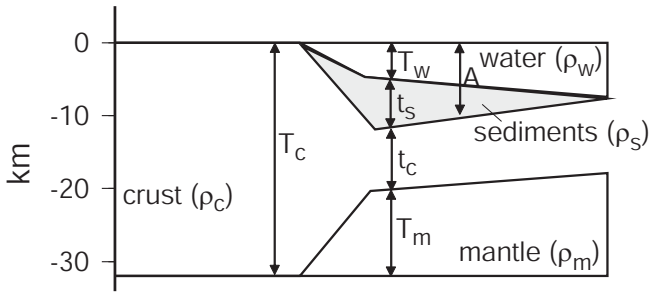

Figure 6.21: Schematic representation of parameters important in determining the crustal structure for a rift basin of depth T_w with a sedimentary section of thickness t_s.

The gravity calculations required for the sediment corrected Airy model are as for the classic-Airy model, with a further negative contribution associated with the sediment body ($\rho_s - \rho_c$). Sediment corrected Airy models were created for survey lines GA-228_18 to GA-228_29 and GA-229_07 using the same procedure as for the classic-Airy case, however, a sediment body defined by depth converted MCS data was included.

In general, the addition of an Airy compensated sediment body does not improve the fit between the calculated and observed FAA relative to the classic-Airy models (Figure 6.22). In each of the sediment corrected Airy model profiles the amplitude of the edge effect anomaly is decreased relative to the classic-Airy models (except for Line GA-228_18. The biggest misfit between calculated and measured gravity anomalies is observed on line GA-228_18, where the locus of thickest sediments corresponds to a large amplitude positive FAA. The classic and sediment corrected Airy models both predict a negative anomaly at this location, this indicates that the sedimentary sequence, at least in part, is not Airy or locally compensated.

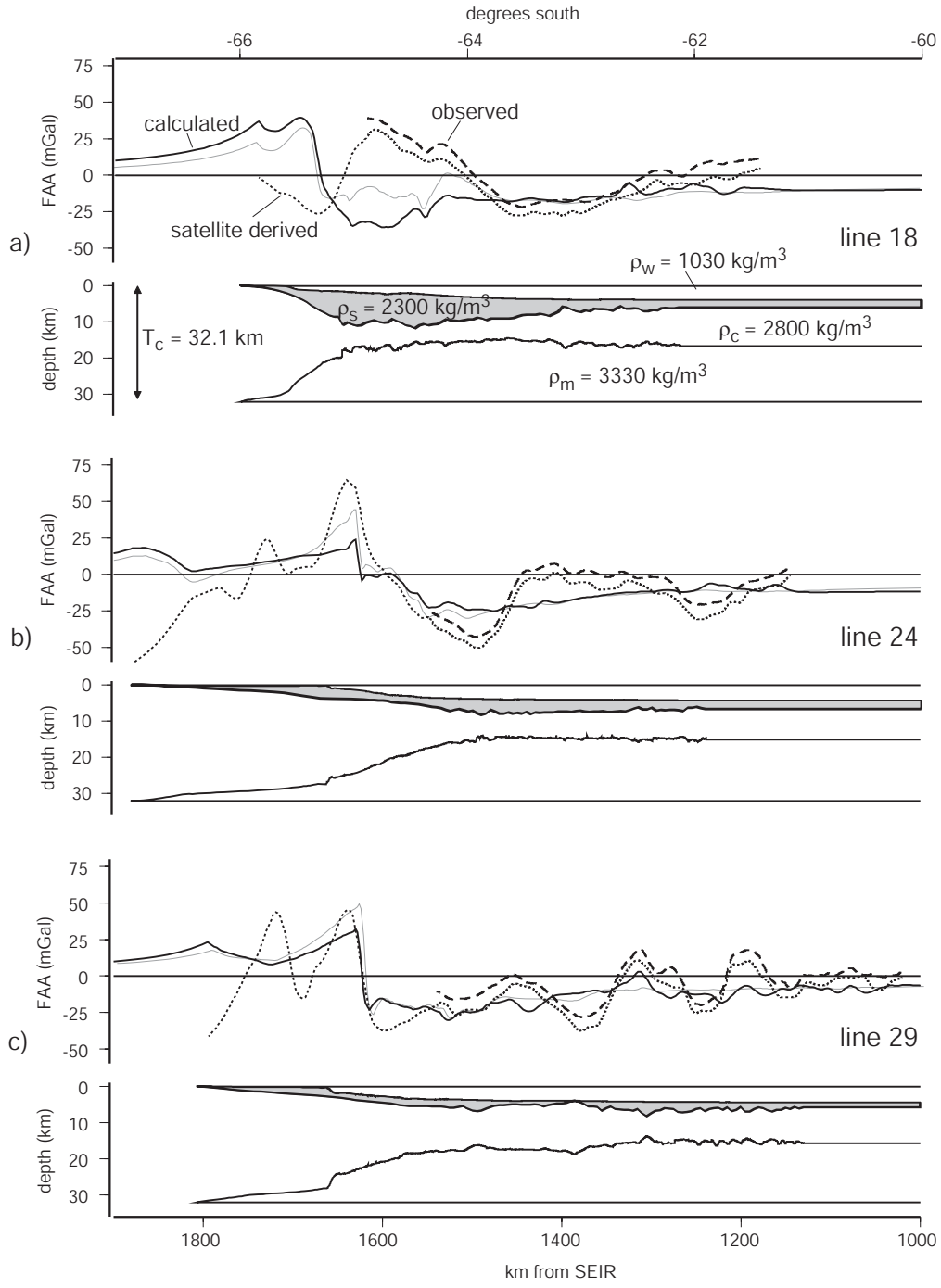

Figure 6.22: Sediment corrected Airy isostatic gravity models for survey lines GA-228_18, GA-228_24 and GA-228_29, sediment bodies are shaded grey. Corresponding free air gravity anomalies (solid black), shiptrack (dashed black) and satellite (dotted black) derived free air gravity data are shown above the modelled crustal section. The classic-Airy calculated anomaly profile is illustrated for comparison as a thin, grey line.

Summary of Airy Modelling

Results of classic-Airy modelling indicate that the broad trends of the observed gravity field are controlled by basin topography and its compensation. The results of the sediment corrected Airy models indicate that it is unlikely that sediments are locally compensated, and that flexural compensation of the sediment load is important at the Wilkes Land margin. This is particularly evident for west Wilkes Land, where large misfits between calculated and observed FAA correlate to the locus of the thickest sediments along the Wilkes Land margin.

6.3.2 Two-Dimensional Process Oriented Modelling

Introduction

The correlation of large positive free air gravity anomalies and the locus of thickest sediments off west Wilkes Land is taken to indicate that the sediment load is flexurally compensated, implying a finite crustal strength. Process oriented modelling is used here to investigate the flexural strength of the crust and its relationship with observed gravity anomalies.

Initial process oriented modelling was conducted utilising a single backstrip (i.e. backstripping the entire sediment thickness in a single step), with non varying T_e values in stage 1. Airy compensation was assumed in determining stretching factors and rifted crustal structure in stage 2 (i.e. no strength during rifting). This makes the implicit assumption that during rifting (i.e. heating and stretching) the lithosphere is massively weakened and local compensation is applicable, and that as the thermal anomaly decays (e.g. McKenzie [1978]) the lithosphere regains strength such that sediment loading may be supported by flexure of the lithosphere. Kusznir & Park [1987] demonstrated that the geothermal gradient exerts the strongest control on lithospheric strength and that a decreasing thermal perturbation correlated to increasing lithospheric strength, which provides support for this assumption in stage 2.

The process-oriented method is illustrated for line GA-228_21 using a constant T_e of 15 km in Figure 6.23. Each of the component anomalies associated with the rift and sediment anomalies are shown before summing and comparison with the observed signal. The procedure is as for the synthetic example above.

Modelling is repeated for a range of T_e estimates to determine the T_e that provides the best fit between calculated and observed gravity anomalies. Specific observed anomalies may be best fit by different T_e models. This is demonstrated in Figure 6.24 where a star marks regions of best fit on different calculated profiles. Some sections are equally well fit by almost all T_e values, and others again are not well fit by any of the calculated

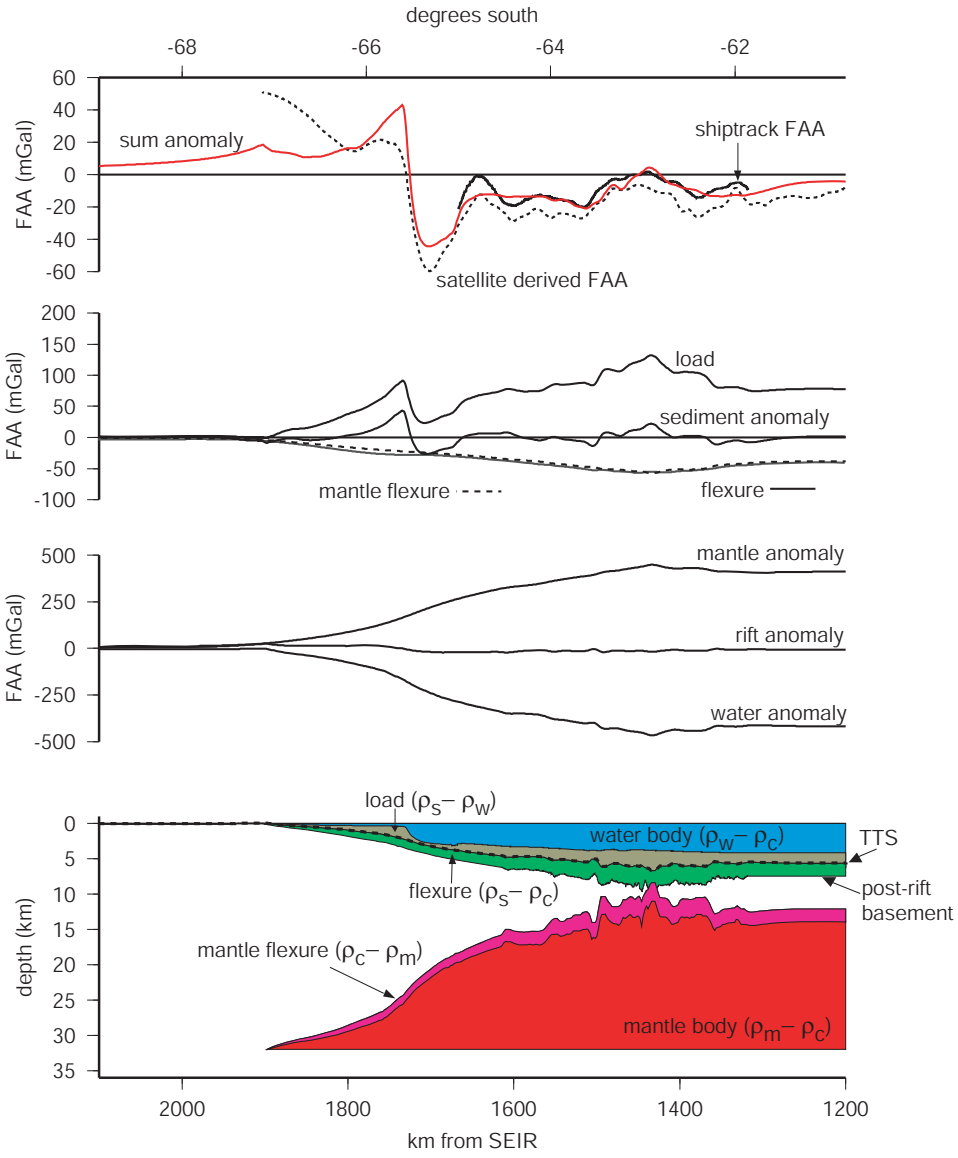

Figure 6.23: The process oriented method demonstrated for line GA-228_21 using a T_e of 15 km.

profiles. These relationships provide information regarding spatial variation in T_e. Spatial variation can be important in defining along margin segmentation (e.g. Watts & Stewart [1998]) or inferring the location of the COB (e.g. Watts [1988]).

A more quantitative way of assessing the fit of calculated and observed anomalies is to calculate and analyse the flexural isostatic anomaly. Where the flexural isostatic anomaly is defined as the *difference* between the calculated and observed anomalies as outlined previously. Sections of low and high isostatic anomaly indicate good and poor fit between calculated and observed data respectively. Hence, the standard deviation (SD) or root mean square (RMS) of the flexural isostatic anomaly profiles is another means of

determining the best fitting calculated T_e profile.

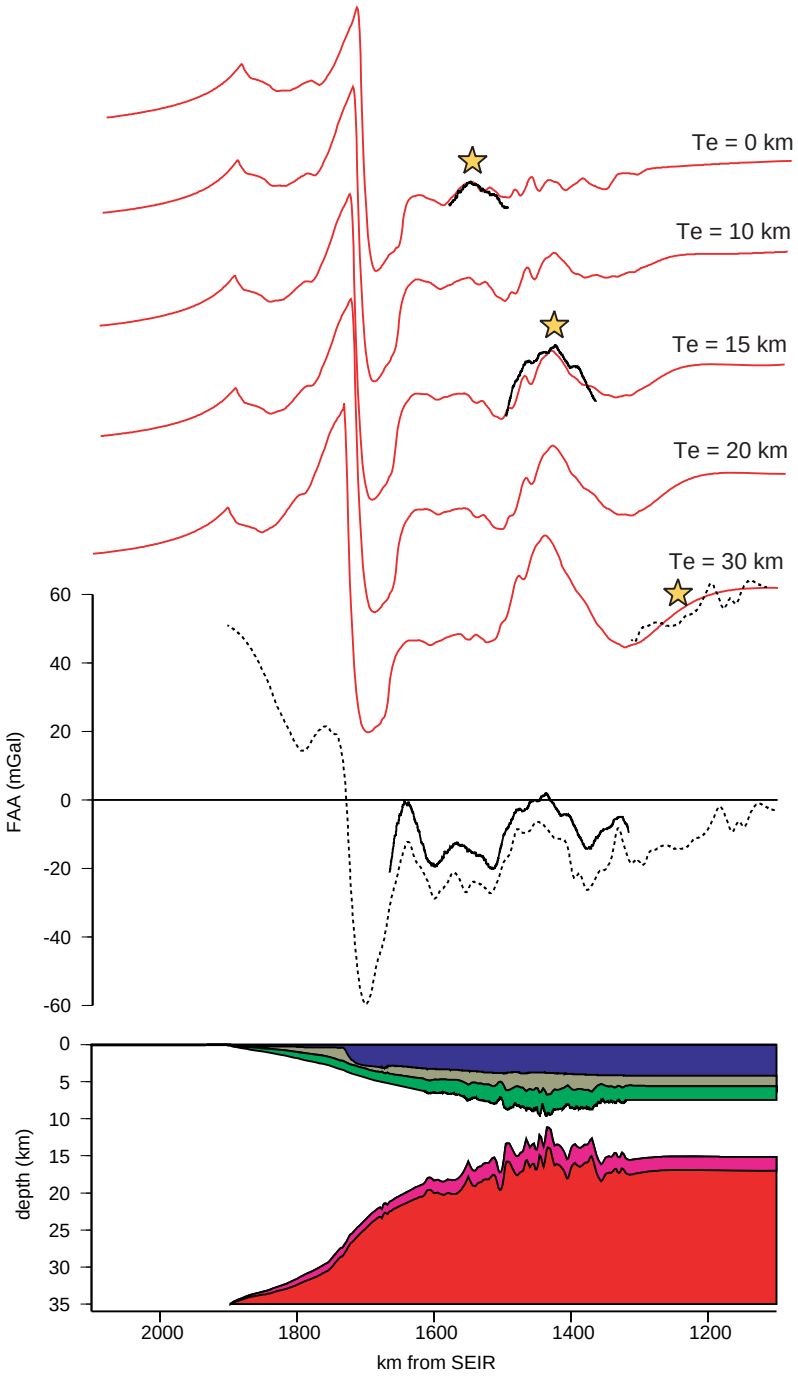

Figure 6.24: Comparison of observed FAA data to modelled profiles for a range of T_e values. Specific sections of observed data are best fit by different T_e models as marked by a yellow star, the observed data is overlain the modelled to emphasise these correlations (shiptrack = solid, satellite derived = dashed).

Sensitivity Analysis

An analysis of the sensitivity to variations in model parameters, namely ρ_s, ρ_c, ρ_m, T_c and T_e was undertaken. Figure 6.25 illustrates the variation in the RMS of the flexural isostatic anomaly for varying model parameters for lines GA-228_18 and GA-228_29. Lines GA-228_18 and GA-228_29 are subjected to the greatest and smallest magnitudes of sediment loading respectively, and are therefore representative of the extremes of model sensitivity.

Figure 6.25 demonstrates the greater sensitivity to parameter variation for line GA-228_18 models relative to line GA-228_29. Plots of RMS as a function of ρ_c, ρ_s, ρ_m and T_c illustrate that the model is relatively insensitive to variation in these parameters for $\rho_c < 2900kg/m^3$. Except for the case of a low density mantle ($\rho_m < 3200kg/m^3$) where the limit of sensitivity for crustal density is $\rho_c = 2800kg/m^3$. This indicates an upper bound on crustal density of 2800-2900 kg/m^3. The sensitivity of the model, for $\rho_c < 2900kg/m^3$ is much higher for variation in T_e relative to density or T_c variation. Although this is more profound for line GA-228_18 it is still evident for line GA-228_29. This indicates that models are more sensitive to parameter variation for greater sediment thicknesses, however, the greater relative sensitivity to T_e variation is evident for the range of sediment thicknesses observed along the Wilkes Land margin.

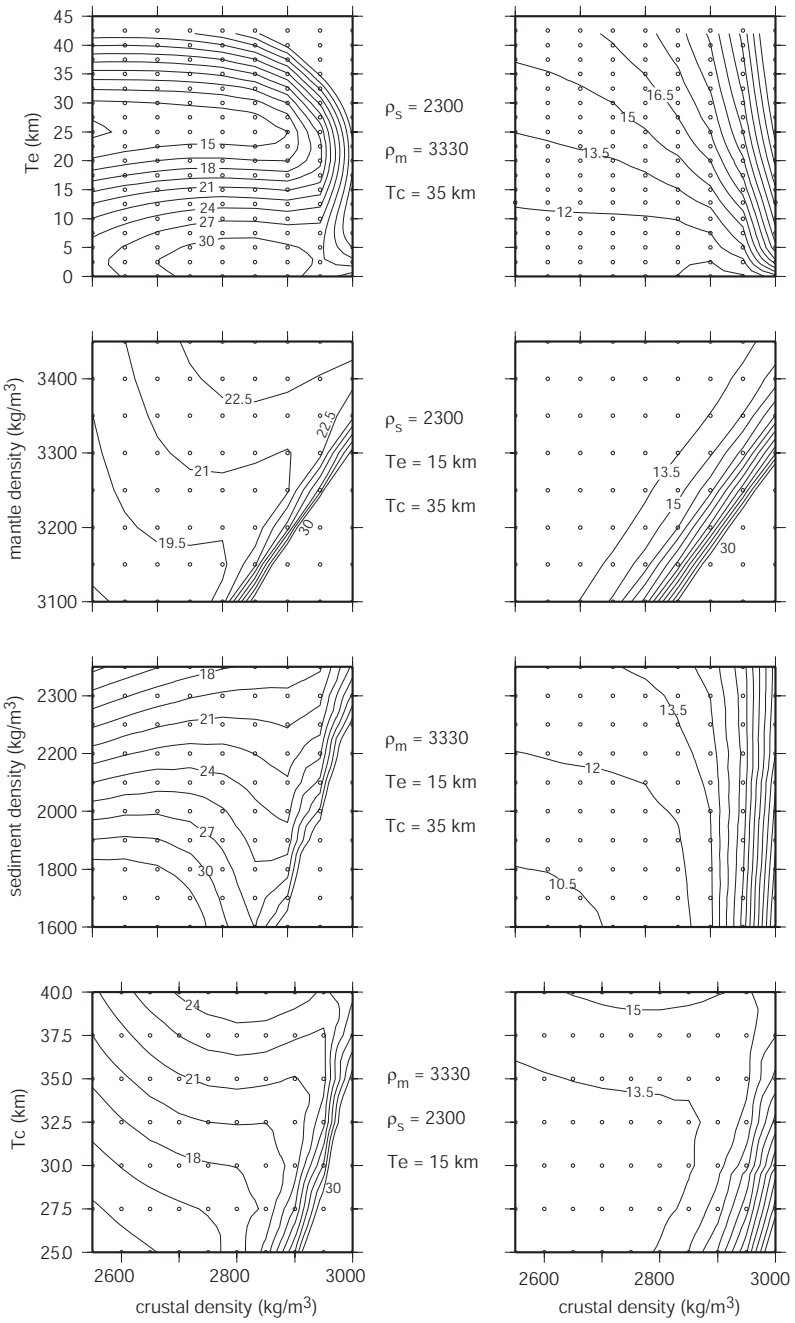

Figure 6.25: Sensitivity of isostatic anomaly to model parameters for lines GA-228_18 and GA-228_29 (left and right panels respectively) as a function of crustal density (ρ_c). Contour interval is 1.5 mGal and RMS values of greater than 30 mGal are excluded. The RMS of the flexural isostatic anomaly is more sensitive to variation in T_e relative to other model parameters (for $\rho_c < 2900\,kg/m^3$). Mantle, crustal, and sediment density denoted by ρ_m, ρ_c, and ρ_s respectively, all in units of kg/m^3.

Modelling

Utilising the parameters constrained via the initial modelling and sensitivity analysis (Table 6.2) process-oriented modelling was completed for lines GA-228_18 to GA-228_29 and GA-229_06. The depth converted MCS reflectors and their landward extrapolations (as detailed in Chapter 4) were used to constrain model geometries. A range of T_e and crustal thickness values were tested for each line and RMS values calculated for each associated isostatic anomaly profile to assess the fit with the observed gravity data. Figures 6.26 to 6.32 shows for each line the model created with T_e=15 km and calculated profiles, for a range of T_e values, compared to the shiptrack and satellite free air gravity. The greatest sensitivity to T_e is on the western lines, and specifically over the greatest sediment thicknesses associated with the Budd Coast Basin. The calculated profiles for lines GA-228_27 to GA-228_29 are similar for all T_e values tested, this is not surprising given that the T_e is extracted by analysing load induced flexure. Where the crust has not been significantly loaded (sediment thickness of these eastern-most lines rarely exceeds 2 km) the backstrip is relatively insensitive to T_e.

Parameter	**Range and Units**
Initial crustal thickness, T_c	29 - 35 km
Crustal density, ρ_c	2800 kg/m^3
Sediment density,ρ_s	2300 kg/m^3
Mantle density, ρ_m	3330 kg/m^3
Water density, ρ_w	1030 kg/m^3

Table 6.2: Parameters utilised in process oriented modelling.

The initial crustal thickness parameter, T_c, was varied to comply with two simple principles. Firstly, the T_c must be great enough such that the *TTS* surface remains shallower than the modelled *Moho* surface, i.e. there are no negative β values. Regions where the present day basement is at great depth or the sea floor is anomalously deep require greater values of T_c as a significant shallowing of the *Moho* is necessary to compensate for deep, water filled basins. Secondly, that the modelled flexed *Moho* depth correlates with any *Moho* velocities extracted from refraction data and also to the depth of inferred *Moho* reflections from MCS data. Less confidence can be placed in *Moho* depths indicated by MCS reflections as the conversion of these from time to depth could introduce errors of up to several km due to poor constraints on velocity models, used for depth conversion, at greater depth. The refraction and reflection inferred *Moho* horizons are overlain on the models in Figures 6.26 to 6.32. A summary of the characteristic features

of models from the western, central and eastern Wilkes Land margin sectors, and their associated gravity anomalies follows.

Figures are constructed as follows: Models constrained by MCS data (lower panels), which include mantle (red), water (blue), sediment load (olive), crustal flexure (green) and *Moho* flexure (purple) bodies. MCS inferred *Moho* depths are indicated by thick blue lines, sonobuoy (SB) inferred mantle velocity refractor depths are indicated by a thick black line over the width that the sonobuoy recorded. Calculated gravity anomalies for a range of T_e values (red = 0 km to blue = 45 km) are compared to shiptrack (black solid) and satellite derived (black dashed) gravity anomaly data (middle panels). The isostatic anomaly (IA) for each T_e estimate is calculated for the length of shiptrack constrained data (upper panels). The RMS of the isostatic anomaly is plotted as a function of T_e (inset graphs), this provides an indication of the fit between calculated and observed anomalies.

West Wilkes Land

Lines GA-228_18 to GA-228_22 (Figures 6.26 to 6.28):

The observed edge effect anomaly is distorted off west Wilkes Land due to the lack of a distinct shelf break and the presence of uncompensated sediment banks as noted previously. This explains the poor fit between the modelled and satellite derived edge effect anomalies for Line GA-228_18. The poor fit between modelled and satellite derived edge effect anomalies on Lines GA-228_19 and GA-228_20 is more likely a function of uncertainties in sediment thickness and bathymetry, and poor quality satellite derived FAA data (due to the perpetual ice coverage of the continental shelf in this region). The edge effect is better modelled on Lines GA-228_21 and GA-228_22, however, the modelled edge effect is insensitive to T_e for these lines so no inferences regarding T_e are possible.

Broadly, models of Lines GA-228_19, GA-228_20 and GA-228_22 are relatively insensitive to variations in T_e, as demonstrated by the lack of clear minima in the RMS v T_e plots. However, for Line GA-228_19, models for higher T_e estimates (30-45 km) predict a positive anomaly over the locus of thickest sediments that simulates the peak amplitude and negative gradient flank of the broad positive observed anomaly. Seaward of this, the peak-trough-peak at ~62°S is almost perfectly matched by the T_e=0 km profile, indicating the presence of a T_e discontinuity at approximately this location.

Lines GA-228_18 and GA-228_21 are for more sensitive to T_e variations, as demonstrated by the RMS v T_e plots, and the observed data are well fit by calculated anomalies relative to other lines. A wide (>200 km), positive anomaly, with a peak amplitude of ~60 mGal, is located at the southern end of Line GA-228_18, over the locus of thickest

sediments. Calculated anomalies are very sensitive to T_e variation in this region. Low T_e estimates predict no anomaly, whereas for $T_e = 45$ km the calculated anomaly exhibits a peak amplitude ∼30 mGal greater than the observed anomaly. For $T_e = 30$ km, however, the calculated anomaly is almost identical to the observed anomaly in both shape and amplitude, and there is a clear minima in the RMS for this T_e. This high sensitivity to T_e and good fit between observed and calculated anomalies indicates that flexural compensation is important in this region and that the lithosphere is characterised by $T_e = 30$ km.

A clear minima in the RMS is evident for $T_e = 15$ km for models of Line GA-228_21. However, variations in T_e can be inferred across the margin. Seaward of the edge effect low, three distinct positive anomalies, of varying amplitude and width, are evident in observed data. The first (most landward) of these peaks is relatively narrow (∼50 km) and has an amplitude of almost 20 mGal, calculated profiles fail to predict this anomaly for any T_e estimate. The next distinct observed anomaly comprises a smaller peak amplitude of ∼10 mGal and a width of ∼75 km, this anomaly is matched very well by the $T_e = 0$ km modelled profile, which predicts both the amplitude and width very closely. Higher T_e profiles exhibit no predicted anomalies in this section. Further seaward is the broadest (∼120 km) and largest amplitude (>25 mGal) of the three anomalies. The observed anomaly is only fit in amplitude and width by the $T_e = 15$ km modelled profile, lower and higher T_e values lead to under and over estimations of amplitude respectively.

Crustal thickness is not constrained by seismic data in this region. The only interpreted *Moho* reflections occur on Line GA-228_22, where a laterally non-continuous reflector is observed beneath the outer continental rise at a depth of ∼15 km. For an initial crustal thickness (T_c) of 32 km, the depth of the modelled flexed *Moho* occurs within 1 km of the interpreted *Moho* reflector depth. Lines to the west of GA-228_22 are modelled with a $T_c = 35$ km, a lower T_c requires mantle compensation to occur at a shallower depth than basement, which violates the modelling principles outlined previously.

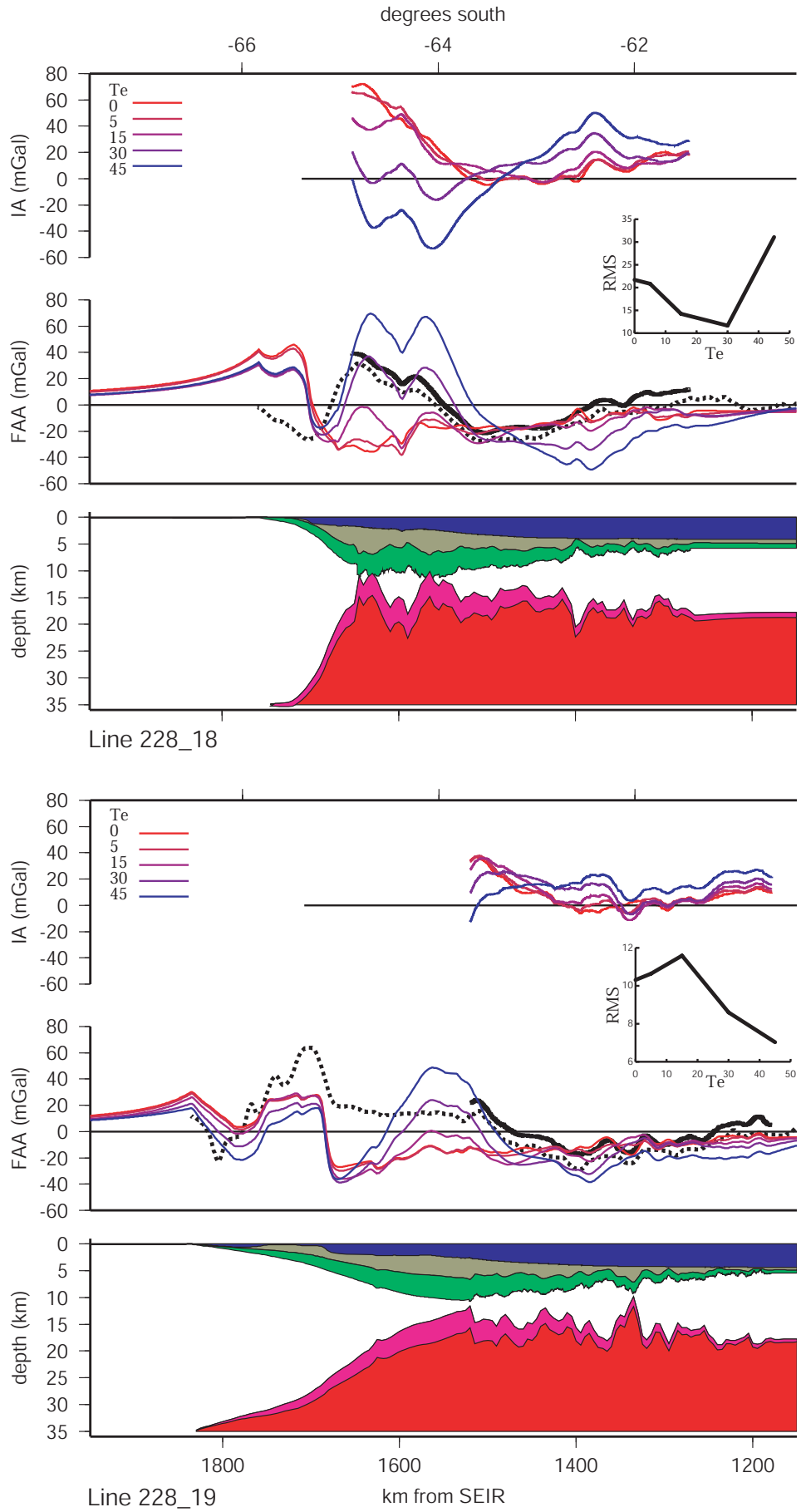
degrees south
-66
-64
-62
IA (mGal)
FAA (mGal)
depth (km)
Te
0
5
15
30
45
RMS
Te
Line 228_18
Line 228_19
1800
1600
1400
1200
km from SEIR

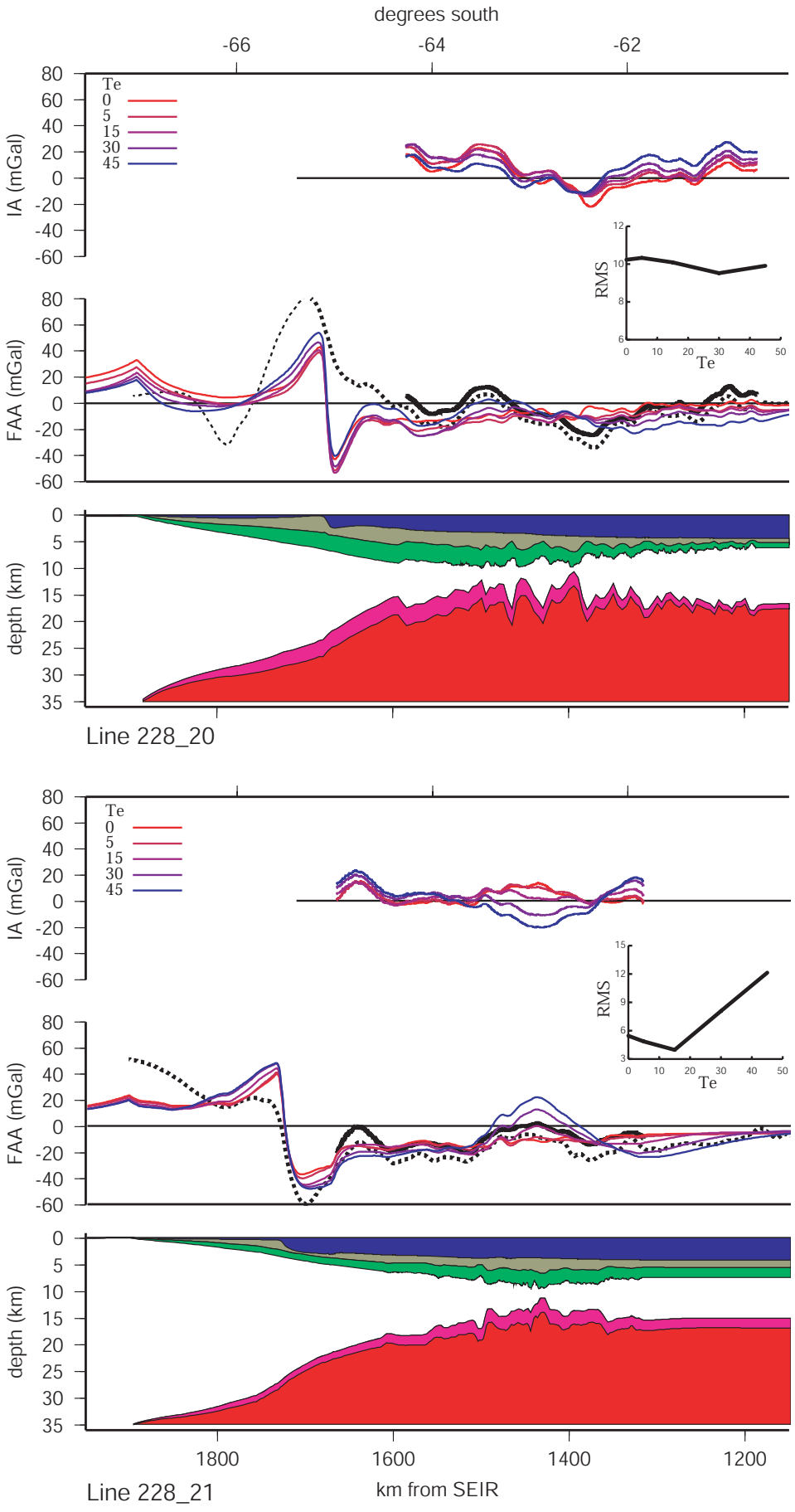

Figure 6.27: Lines GA-228_20 and GA-228_21 process-oriented modelling.

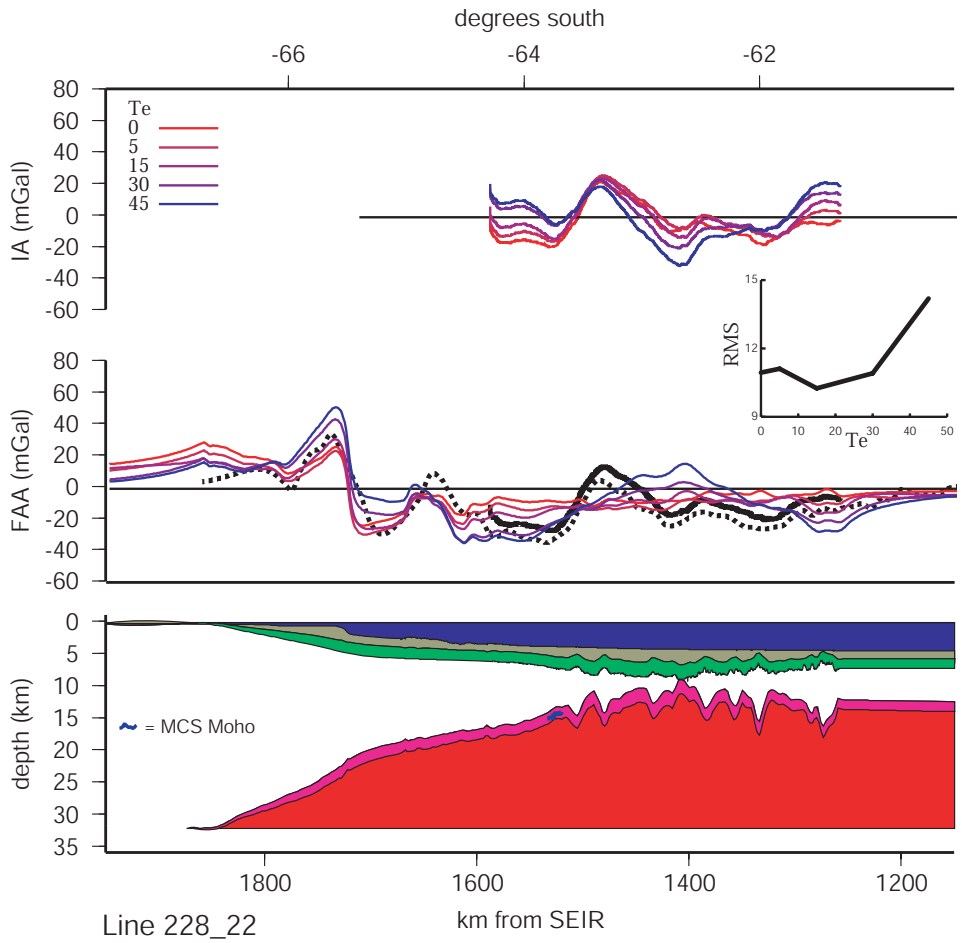

Figure 6.28: Line GA-228_22 process-oriented modelling.

Central Wilkes Land

Lines GA-228_23 to GA-228_26 (Figures 6.29 to 6.30):

The edge effect anomaly is characterised by a consistent amplitude and wavelength high-low couple in central Wilkes Land relative to the western and eastern sectors. Although not traversed by GA-228 and GA-229 shiptracks, some constraint on sediment thickness was provided by data from the *S. P. Lee* L184 survey data. The satellite derived edge effect anomaly is well simulated by calculated anomalies for each of the models from this margin sector. However, the peak positive amplitudes are only modelled for Line GA-228_23. This may be a function of incorrect assumptions regarding sediment thickness or uncertainties in the satellite derived FAA data. The edge effect is ubiquitously best modelled using high T_e estimates.

Broadly, the T_e = 30 km models provide the best simulation of observed anomalies in this sector. The fit of the observed positive anomalies seaward of the edge effect

low on Lines GA-228_23 and GA-228_24 is very sensitive to T_e, providing a high level of confidence in the inference of a high T_e. Additionally, the RMS v T_e plots exhibit clear minima for $T_e = 30$ km for all lines except Line GA-228_26, for which models are relatively insensitive to T_e.

The flexural isostatic anomaly profiles for Lines GA-228_23, GA-228_25 and GA-228_26 are characterised by a positive anomalies at the location of greatest crustal thinning. The origin of these anomalies is discussed further in Chapter 7.

Crustal structure and *Moho* depth is better constrained by seismic data for this sector relative to the western margin sector. *Moho* reflections are interpreted in seismic reflection data from all lines in this sector except Line GA-228_23. Although of limited lateral extent, their depths correlate to the depth of the modelled flexed *Moho* for $T_c = 31$ km.

Mantle velocities were also modelled from two sonobuoy stations in this sector on Lines GA-228_25 and GA-228_26. On Line GA-228_25, modelled sonobuoy data indicates a *Moho* depth of ∼12.5 km, which correlates almost exactly with the depth of both the seismic reflection interpreted *Moho* and the modelled flexed *Moho*. This further supports that $T_c = 31$ km for this margin sector. The sonobuoy modelled *Moho* depth for Line GA-228_26 correlates to the flexed *Moho* depth at its landward extent, however, the sonobuoy is located in a region of high *Moho* gradient according to Airy isostasy. The depth of the sonobuoy inferred *Moho* may be predicted too deep due to a dipping refractor, or alternatively the compensation may not be entirely local in this region. The misfit between modelled and observed gravity anomalies in this region would be improved if the mantle peak implied by Airy isostasy, but not supported by the limited seismic data, was not actually present.

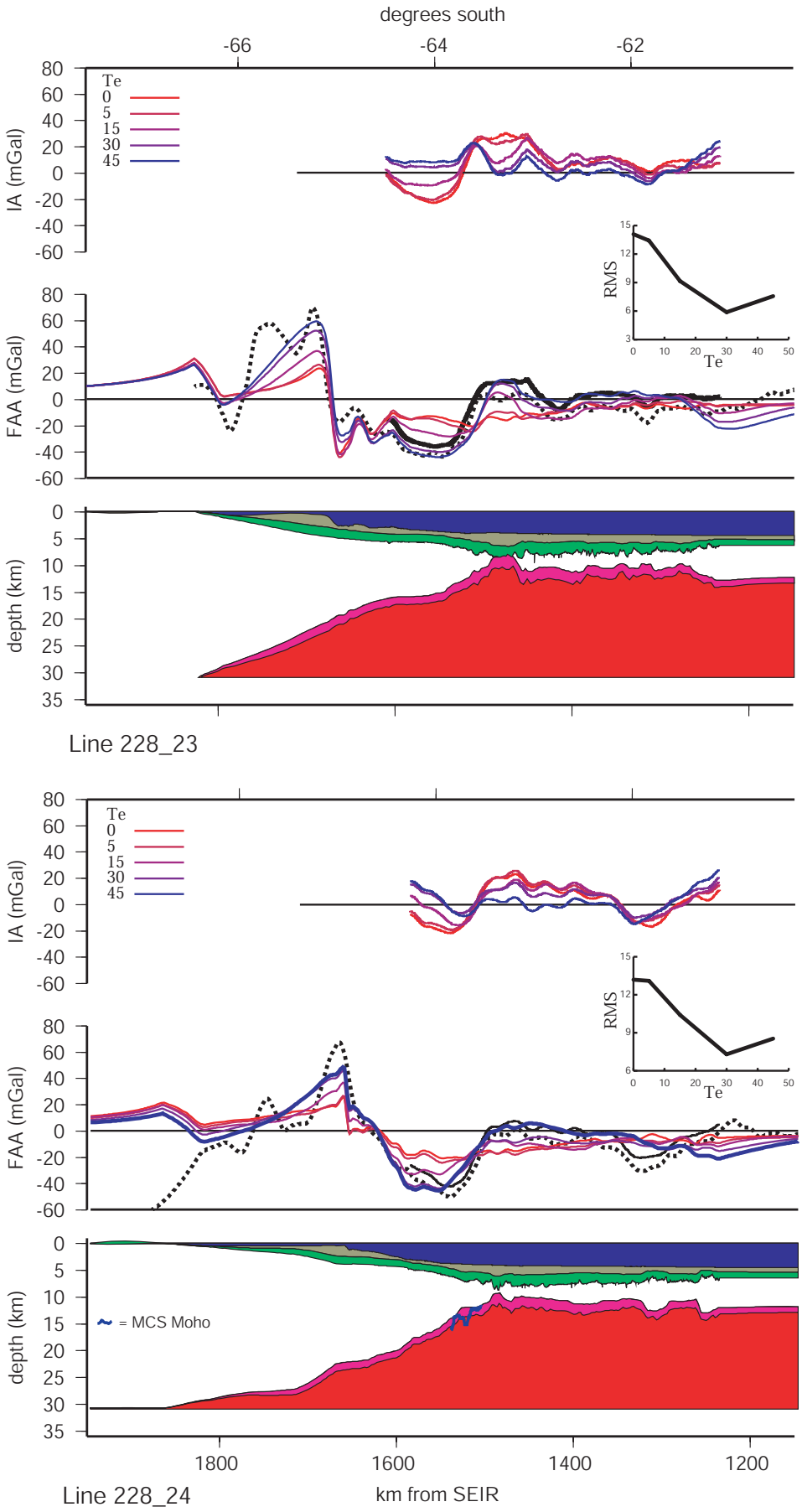

Figure 6.29: Lines GA-228_23 and GA-228_24 process-oriented modelling.

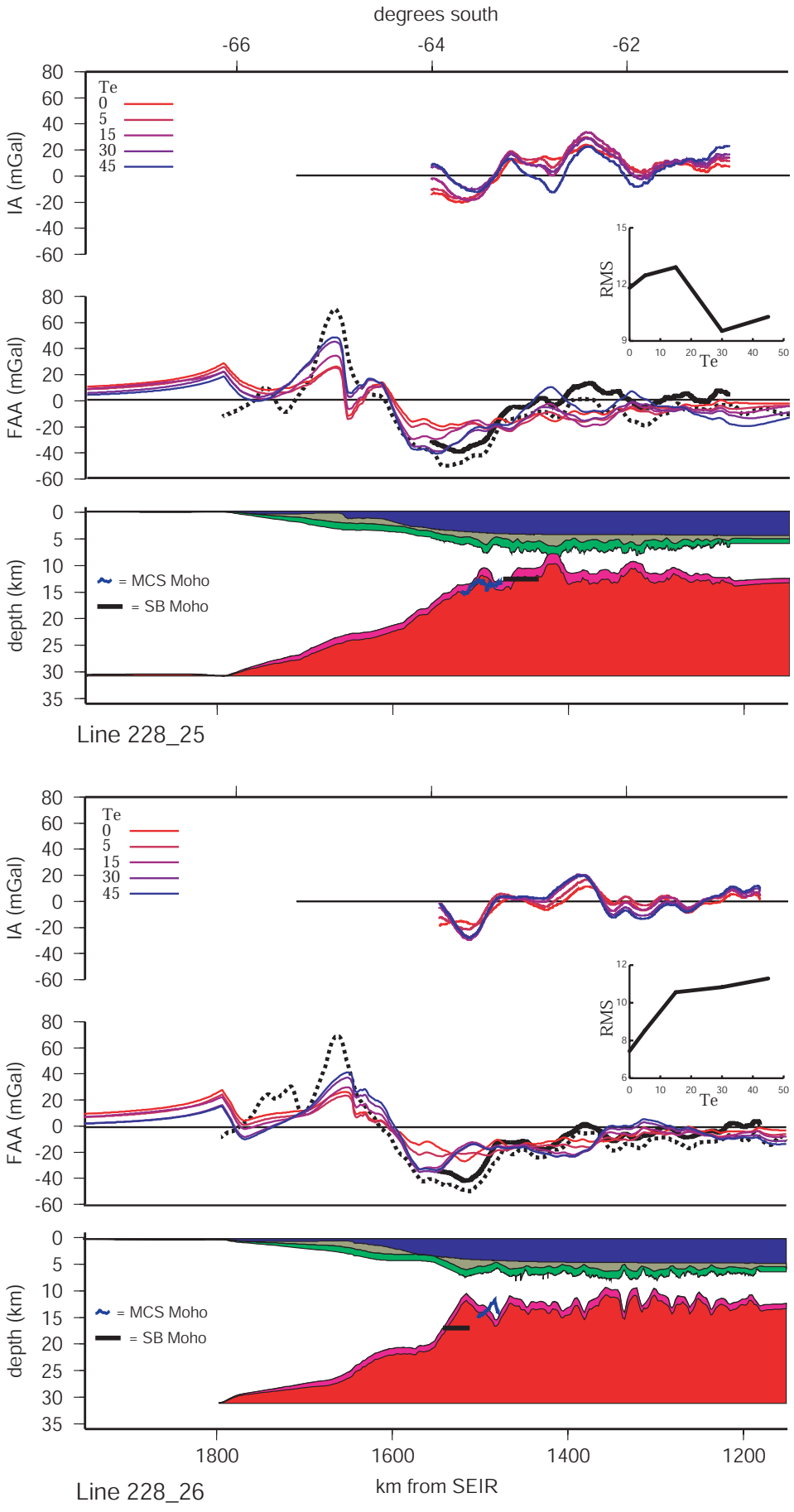

Figure 6.30: Lines GA-228_25 and GA-228_26 process-oriented modelling.

Eastern Wilkes Land

Lines GA-228_27 to GA-228_29 (Figures 6.31 to 6.32):

A relatively consistent edge effect anomaly extends along the margin in the eastern sector. The satellite derived edge effect anomaly is best simulated by models for T_e estimates of 30-45 km, particularly along the landward projections of Lines GA-228_27 and GA-228_28, which both exhibit T_e sensitivity in the region of the edge effect.

Calculated anomalies (for the shiptrack data constrained portion of the model) are relatively insensitive to T_e for Lines GA-228_27 and GA-228_28. The calculated anomalies, however, do account for most of the observed anomalies. Similarly to lines from the central sector, a positive isostatic anomaly is observed on Line GA-228_28 just seaward of the point of greatest crustal thinning.

A greater sensitivity to T_e is evident for models of Line GA-228_29, however, it is difficult to infer which T_e provides for the best fit between calculated and observed anomalies. This is primarily due to large amplitude basement topography and a relatively thin sediment cover. The positive anomaly immediately seaward of the edge effect low on this line is best modelled for a high T_e. However, the observed positive anomaly further seaward (at $\sim$62.5-62°S), which correlates to a basement high, is poorly simulated for high T_e. This poor fit is a result of the negative gravity effect of a deepening $Moho$ to compensate for the basement high. If the basement high is not locally compensated then the observed anomaly is well simulated by the high T_e calculated anomaly. Additionally, the seismic reflection interpreted $Moho$ correlates well for most of this line with the modelled flexed $Moho$, however, it does not predict a crustal thickening associated with this basement high.

The correlation between seismic constraints on $Moho$ depth and the modelled flexed $Moho$ is excellent in this margin sector for T_c = 29 to 30 km. The sonobuoy derived $Moho$ depth over oceanic crust on Lines GA-228_27 and GA-228_29 correlates very closely to the modelled flexed $Moho$ depths. The seismic reflection interpreted $Moho$ on Line GA-228_27 correlates closely to the depth of the modelled flexed $Moho$, except for at the point of maximum crustal thinning where the model predicts a mantle peak that is not observed in seismic data. This may indicate that the corresponding basement feature is not locally compensated, this would account for the negative isostatic anomaly that is associated with the elevated $Moho$. The geometry of the modelled flexed $Moho$ and the seismic reflection interpreted $Moho$ on Line GA-228_28 is remarkable, providing a high level of confidence in the assumed T_c and the assumption of Airy isostasy during rifting.

One exception in this margin sector, to the generally close correlation between the depth of the modelled flexed $Moho$ and the seismic reflection inferred $Moho$, occurs on

Line GA-228_29. The basement high at ~62.5°S corresponds to a modelled increase in crustal thickness, however, the interpreted *Moho* reflections do not deepen beneath this basement feature. This misfit in modelled and observed *Moho* depth and the positive isostatic anomaly that correlates to this feature may indicate non-local compensation.

Adélie Rift Block

Line GA-229_06 (Figure 6.32):

The satellite derived edge effect high is modelled equally well for all T_e estimates for this line, however, the edge effect low is poorly modelled. A positive anomaly seaward of the edge effect low correlates to the point of maximum crustal thinning interpreted from seismic reflection data. Seaward of this anomaly, over the basement high interpreted as the western edge of the Adélie Rift Block, a broad negative gravity anomaly is observed. The calculated anomaly is very sensitive to T_e in this region. This broad negative is very well simulated by the calculated anomaly profile for T_e = 45 km. However, similarly to Line GA-228_29 this is largely due to the negative gravity effect of crustal thickening associated with the basement high. There is no constraint on $Moho$ depth from sonobuoy data and only a very limited seismic reflection interpreted $Moho$ reflection for this line. Hence, it is difficult to assess whether the best fit for the high T_e model is actually representative of a rigid lithosphere, or simply an artifact of the assumption that basement features on all scales are locally compensated. A T_c of 30 km was assumed for this line.

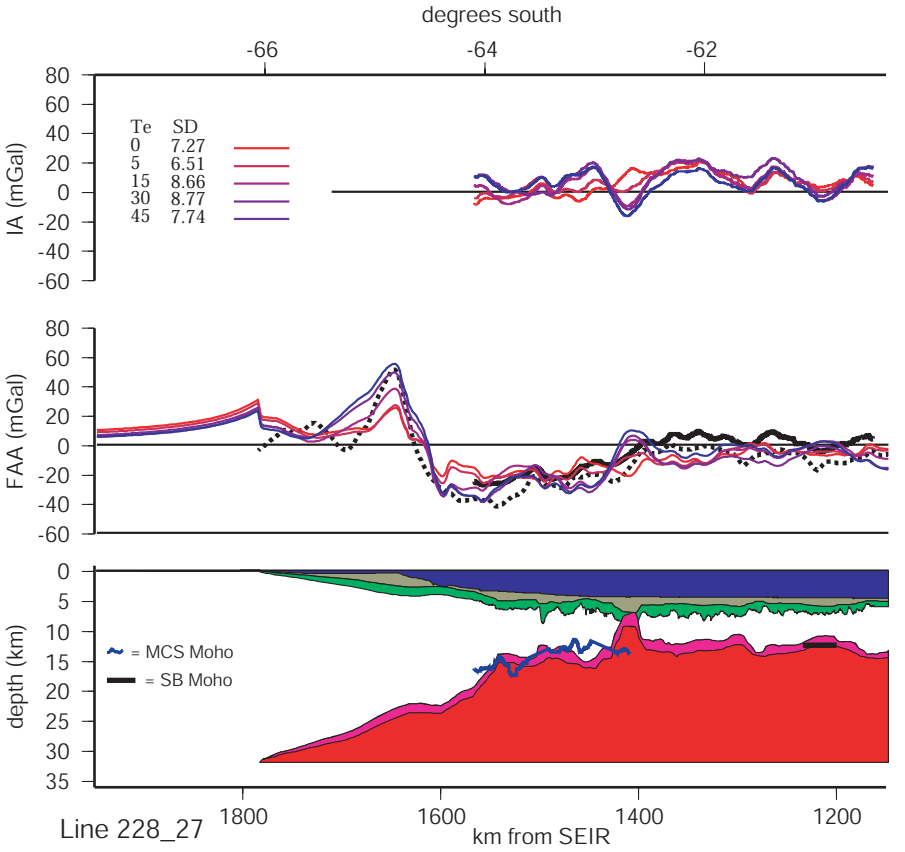

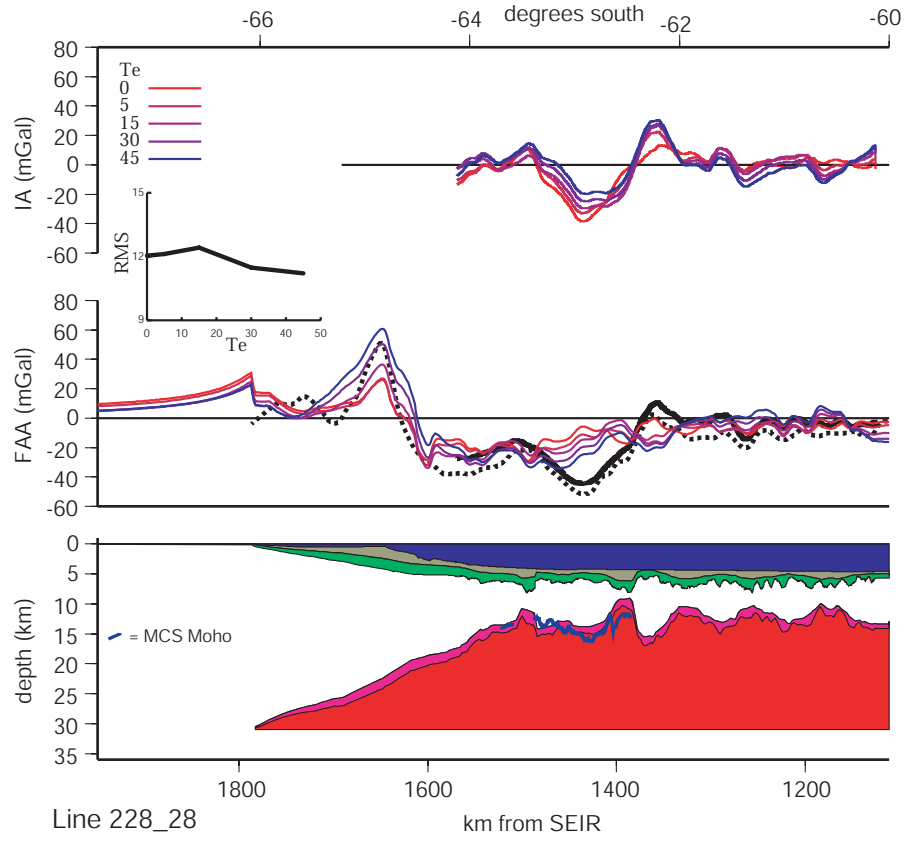

Figure 6.31: Lines GA-228_27 and GA-228_28 process-oriented modelling.

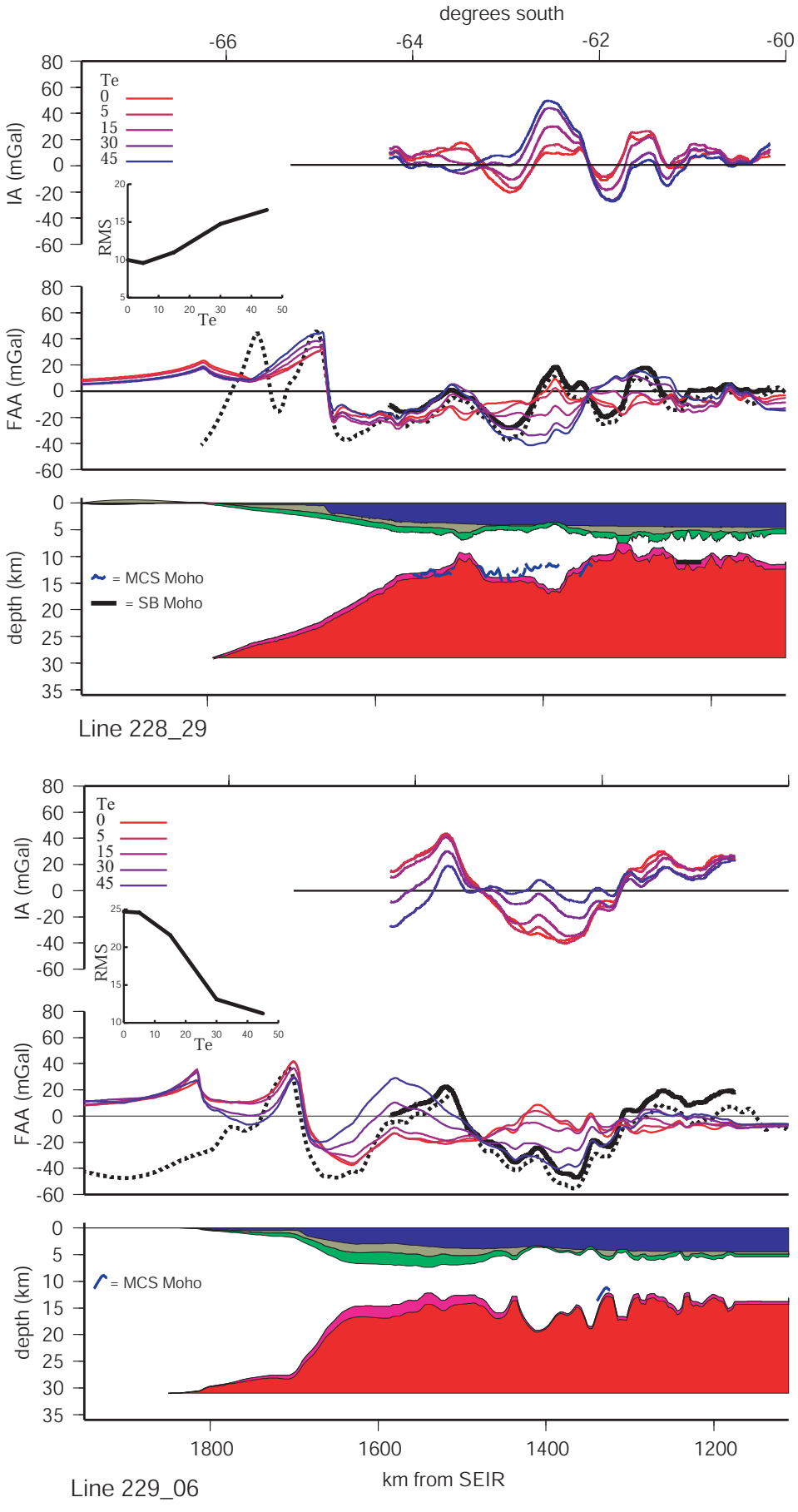

Figure 6.32: Lines GA-228_29 and GA-229_06 process-oriented modelling.

6.3.3 Strength During Rifting

The initial modelling detailed above assumed Airy isostasy during rifting, i.e. stretching factors were determined in stage 2 assuming local compensation. We now test the effect of incorporating strength during rifting (Te_{rift}) and a depth of necking (Z_{neck}) in the determination of stretching factors in stage 2 of process-oriented modelling. As outlined in section 6.2.2, Te_{rift} and the depth of Z_{neck} controls the rift crustal structure, and hence effects the rift and sediment anomalies in process oriented modelling.

Whereas Z_{neck} describes the depth to the strength maxima, Te_{rift} defines the 'strength' of the lithosphere during rifting. This strength controls the distribution of restoring forces associated with kinematic isostatic inequilibrium. For $Te_{rift} = 0$ km, the crust does not resist the restoring forces and the observed gravity anomaly is identical to the Airy case regardless of Z_{neck}. If there is strength during rifting (i.e. $Te_{rift} > 0$), then the basin geometry is modified by flexure.

Process oriented modelling was repeated for each of the survey lines on the Wilkes Land margin utilising strength during rifting. A range of parameters were tested during this process to assess if the fit between calculated and observed gravity anomaly profiles could be improved by the introduction of strength during rifting. It is clear, however, that no combination of model parameters would produce improved results by incorporating strength during rifting. The modelled gravity anomaly profiles for a range of T_e, Z_{neck} and Te_{rift} values for line GA-228_25 are illustrated in Figure 6.33. We see that the $Te_{rift} = 0\,km$ is identical for all depths of Z_{neck} tested, as predicted by the theory. A Z_{neck} depth of less than ~7.2 km predicts a subdued edge effect and a large positive anomaly over the deepest section of the rift basin due to an elevated *Moho*. For $Z_{neck} = 7.2\,km$ the modelled anomaly profile does not vary with Te_{rift} due to the equal magnitude upward and downward restoring forces. For Z_{neck} $7.2\,km$ the predicted amplitudes and wavelengths of the edge effect high and low anomalies are greatly increased. There is also a poor correlation between refraction and MCS reflection inferred *Moho* depths and the flexed *Moho* determined for models incorporating Z_{neck} and Te_{rift}.

These tests incorporating strength during rifting and depth of necking indicate that the Antarctic-Australia breakup is more likely to have occurred under Airy state isostatic balance, and that there was no specific zone of lithospheric strength that mechanically resisted the rifting process. This is somewhat surprising given the geological evidence that suggests a relatively low geotherm during breakup (e.g. lack of evidence of volcanism, low magma discharge rates associated with slow seafloor spreading, low strain rates associated slow extension).

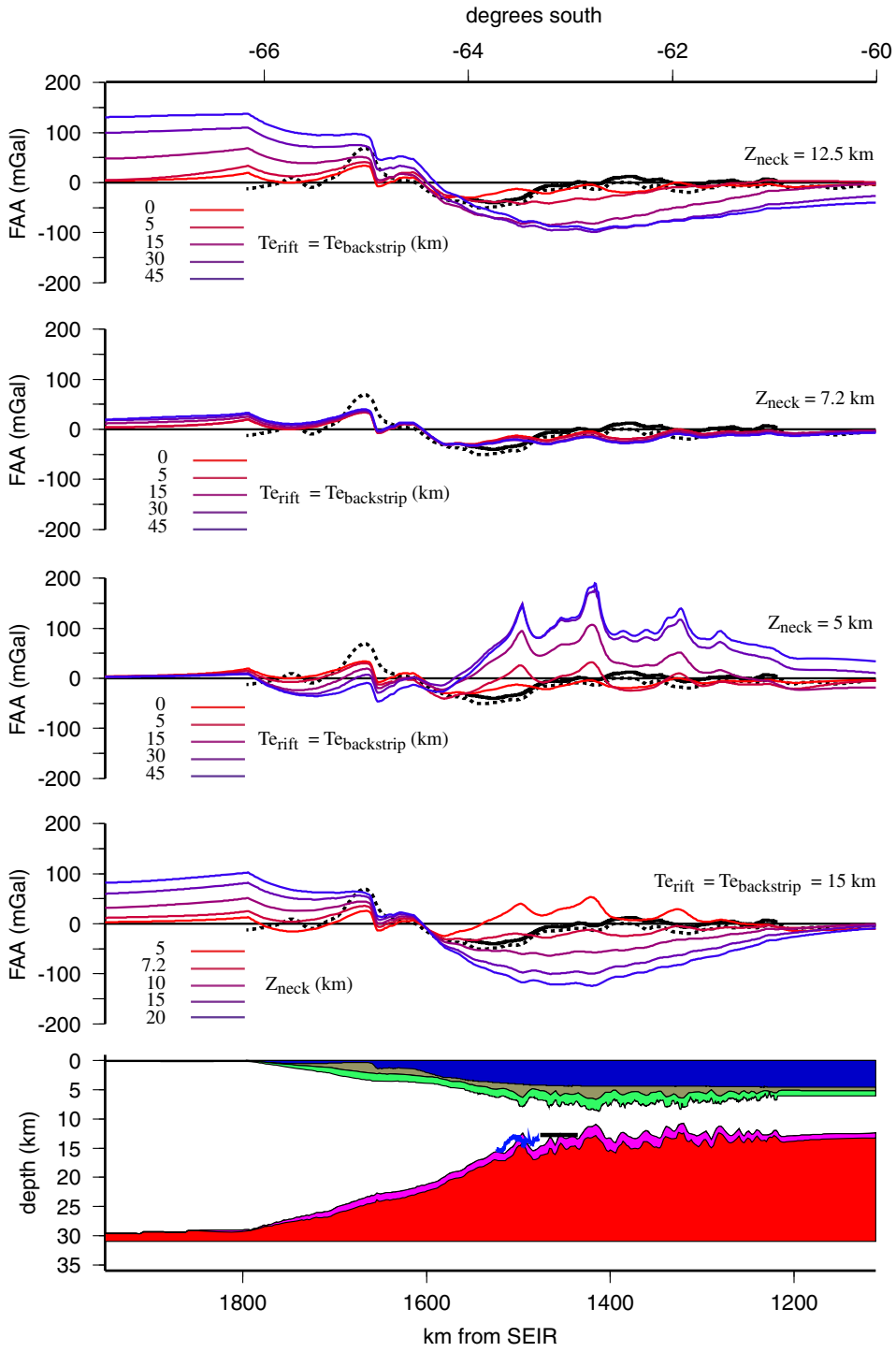

Figure 6.33: Demonstration of the effect of incorporating strength during rifting for line GA-228_25.

6.3.4 Multi-Layer Backstripping

Until this point, sediment loads have been backstripped in one step. However, typically seismic stratigraphy allows any sedimentary sequence to be divided into distinct strati-

graphic units. In many margin environments well-log and core data can then be used to constrain the physical properties of each unit. It is possible to test temporal variations in T_e by backstripping individual stratigraphic units, and summing the subsidence due to each layer to determine the *TTS*. By backstripping layers individually it is also possible to use different sediment density parameters for each layer. Multi-layer backstripping produces a significantly different *TTS* only if T_e changes are introduced for each layer backstrip and if the depositional geometry varies for each or some of the individual units backstripped.

The crust may respond to post-rift cooling, associated with the increased distance to the spreading centre, by increasing in strength and accordingly T_e as in oceanic crust (e.g. Watts [1978]). Alternatively, sediment blanketing during thermal subsidence may result in a reduction in lithospheric strength, as suggested by Beaumont *et al.* [1982]. Hence, sediments may be loaded on crust that comprises a T_e that varies with time since rifting.

The only regionally correlatable stratigraphic horizons, for which age estimates are constrained, on the Wilkes Land margin are the *Turonian* and *Eocene* unconformities, as outlined in Chapter 4. The sedimentary sequence is, therefore, most logically divided, for backstripping purposes, into two units by the *Eocene* unconformity. Two-layer backstripping and process oriented modelling was undertaken for each of the Wilkes Land seismic transects to test whether varying the backstrip T_e and/or the densities of the two units improved the fit of calculated and observed anomalies.

Process-oriented modelling utilising a two-layer backstrip provides negligible improvement in the fit between calculated and observed gravity anomalies. A range of T_e estimates and sediment densities were tested for each backstrip and the calculated gravity anomaly compared to observed data. Results did not suggest any systematic variation in T_e between the time of loading of Sequence 1 and Sequence 2 (where Sequences 1 and 2 are as defined in Chapter 4). Additionally, no systematic spatial variation in T_e was evident from backstripping with a spatially varying T_e. Initial variable T_e functions tested were based on inferred T_e structure from single-layer backstrip process-oriented modelling. Additionally, T_e functions which followed the depth to oceanic isotherms from 150-600°C were tested, as studies of flexure in the oceans demonstrate that T_e follows the depth to the 450°C [Watts, 1978].

These results do not directly indicate that T_e has not changed through time or that the density of the two sediment layers is equal, it simply indicates that the *average* values assumed in the single backstrip case were representative of the average margin T_e and sediment density, and that as a result the *TTS* is not significantly different for a one- or two-layer backstrip. Another significant factor controlling the similar results from

the two approaches is the sediment load distribution, on most lines the thickness of the Sequence 1 is much greater than the Sequence 2 thickness. Hence, the sediment load driven subsidence of Sequence 1 contributes most strongly to the total sediment driven subsidence, and the TTS is not significantly altered by backstripping Sequence 2 with a different T_e. Also due to the greater average thickness of Sequence 1, the best fitting average T_e for a single-layer backstrip will be approximately equal to the best fit T_e for Sequence 1 in the multi-layer backstrip.

The consequences of calculating the gravity anomaly associated with each loading step for the multi-layer backstrip were also investigated. This requires the calculation of many more individual sediment anomaly components and therefore allows greater flexibility with regards to the density of individual loading events and water/sediment/crustal replacements. Again the differences were negligible, primarily as the overall geometry is not altered significantly (for the same reasons as outlined for the multi-layer backstrip). Also, the density differences can only be varied intuitively, and therefore are difficult to alter significantly without violating the simplicity of the process oriented method by introducing arbitrary density anomalies.

6.3.5 Two-Dimensional Modelling Summary

The models illustrated here represent simplified geological models that include a limited number of bodies and uniform density contrasts. These models have been constructed utilising knowledge of the processes that have shaped the margin through time, but no attempt has been made to find by "trial and error" the number of bodies of variable density that will best fit the observed gravity anomaly. Two-dimensional process-oriented models account for a significant component of the observed gravity anomaly and provide insights into the structure and strength distribution of the Wilkes Land margin.

A relatively consistent spatial trend of crustal strength variations is indicated, these are summarised in Table 6.3 and illustrated in Figure 6.34. Although across margin variation in T_e can be inferred, there is little evidence for along margin segmentation of T_e. The edge effect anomaly is best fit by models of higher T_e ($\sim$30 km) for all lines in central and east Wilkes Land, indicating that the relatively unstretched continental crust has either retained strength during the rifting process or regained strength since rifting. The poor fit between calculated and observed edge effect anomalies and the relative insensitivity to T_e variation on western Wilkes Land models (lines GA-228_18 to GA-228_20) makes it difficult to determine if the T_e is systematically lower relative to the east as inferred on lines GA-228_21 and GA-228_22.

Tests incorporating strength during rifting do not support the maintenance of crustal

rigidity during rifting. Therefore the high T_e estimates of ~30 km inferred for much of the Wilkes Land margin are interpreted to indicate that rigidity or strength has been recovered over time since rifting. It is also evident that the greater thickness of Sequence 1 sediments results in a T_e estimate from backstripping that is representative of margin strength some 30-40 Ma after rifting. Multi-layer backstrips are, therefore, relatively insensitive to temporal T_e variations.

Zones of low T_e are inferred on a number of lines. This is interpreted to indicate that sections of continental and/or transitional crust have been weakened significantly by the rifting process and failed to regain strength since rifting. The consistency of these zones along the margin supports the interpretation of a zone of weakened transitional crust, defined on the basis of flexural rigidity, interleaving continental and oceanic crust.

Although the most oceanward sections of observed data are generally most poorly fit by calculated anomalies, the gradients observed are simulated most accurately by modelled data for higher T_e values (15-30 km). The inferred oceanward increase in T_e is representative of the transition to oceanic crust which is known to exhibit a simple relationship of increasing T_e and increasing age of the lithosphere at the time of loading [Watts, 1978].

Table 6.3 also summarises the T_c inferred for each line, although these initial average crustal thicknesses are approximate only, they indicate a distinct trend of decreasing crustal thickness from west to east. Although there are no independent constraints on *Moho* depth for western Wilkes Land, the thick sedimentary sequences observed require a compensation depth of at least 35 km to prevent rift models inferring that there was significant amount of mantle material shallower than the water bottom of the initial rift basin. *Moho* depth is better constrained for east Wilkes Land where MCS and sonobuoy refraction data provide an independent indication of depth on a number of lines. If initial crustal thickness is held at 35 km for east Wilkes Land, then there is a poor correlation between the modelled and observed/inferred *Moho* depths. The correlation is improved if initial crustal thickness is reduced to between 29 and 32 km. More seismic refraction data is required to confirm this trend, however, it seems clear that there is a distinct change in the depth of compensation and the initial, pre-rift crustal thickness between east and west Wilkes Land.

Line	T_e **at shelf break (km)**	**low** T_e **zone***	**Oceanward increasing** T_e	T_c **(km)**
18	-	200, 100	yes	35
19	-	280, 100	-	35
20	-	-	yes	35
21	15	135, 100	yes	35
22	15	-	no	32
23	30	no	-	31
24	30	-	yes	31
25	30	-	-	31
26	30	240, 120	yes	31-32
27	30	120, 100	-	32
28	30	250, 200	no	31
29	-	-	no	29
229_06	-	-	no	31

*Distance from shelf break (km), width (km)

Table 6.3: Summary of interpreted T_e structure and T_c based on process-oriented modelling results.

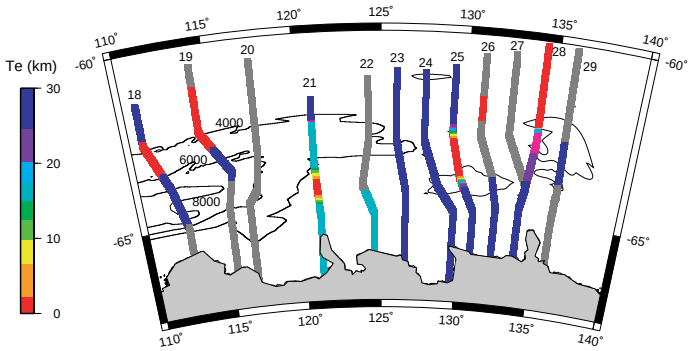

Figure 6.34: Inferred T_e for each survey transect plotted over sediment thickness contours. A relatively consistent trend of T_e distribution is exhibited northward from the margin, however, it is difficult to confidently infer east-west segmentation of crustal strength or rigidity.

The greatest sensitivity to T_e is exhibited by lines west of GA-228_24. Although lines east of GA-228_24 exhibit lower sensitivity to variation in T_e, the RMS of the flexural isostatic anomalies for these lines is significantly lower than for free air gravity anomaly data. This indicates that even if process-oriented modelling does not allow the crustal

rigidity distribution to be uniquely determined, it remains a useful means of further reducing free air anomaly data in a geologically rigourous manner that is not overly sensitive to user input. The isostatic anomaly profiles exhibit a number of features that correlate between survey lines, further gravity modelling using seismic and magnetic data constraints may provide insight to the origin, geometry, depth and physical properties of the causative features of these isostatic anomalies.

6.4 3-Dimensional Gravity Modelling on the Wilkes Land Margin

6.4.1 Introduction

Three-dimensional (3D) modelling, in general, offers some advantages over two-dimensional (2D) modelling. Typically in 2D models, bodies are assumed to extend infinitely out of plane. No such assumptions are made in 3D modelling. This may be significant in regions of rapid lateral change of bathymetry, sediment thickness, basement depth, or crustal thickness. However, for the Wilkes Land margin the sediment isopach is not truly 3D, but rather a gridded series of widely spaced, parallel line data. Hence, it is difficult to assess the accuracy of 3D process-oriented modelling as there exist large uncertainties in the along margin variation in sediment thickness. However, analyses of 3D flexural isostatic anomalies provides a useful tool for qualitative interpretation.

6.4.2 Airy Isostatic Model

As for the 2D case, the conceptually and computationally simplest type of 3D isostatic anomaly is the classic-Airy isostatic anomaly. The GEBCO 1M data [IOC *et al.*, 2003] is the most extensive bathymetric data compilation that is not supplemented by satellite derived bathymetry estimates for the Wilkes Land margin, and, therefore, is used as the basis of the 3D classic-Airy model.

The modelling methodology is identical to the 2D classic-Airy model considered previously. The calculated gravity anomaly is simply the sum of the anomalies resulting from the replacement of crust by water and mantle, where the model geometry is constrained by the present-day bathymetry and its Airy-type compensation. The 3D calculations were carried out in the Fourier domain as outlined previously, accordingly care was taken to ensure that the input grids extended far enough in every direction such that spurious edge effects associated with tapering of data were not superimposed on data in the region of interest. The Airy isostatic anomaly was calculated by subtracting the calculated gravity anomaly data from the satellite derived free air gravity grid of Sandwell & Smith

[1997].

The calculated classic-Airy model FAA, satellite derived FAA, and Airy isostatic anomaly maps are shown in Figure 6.35. The amplitude of the edge effect anomaly is significantly reduced in the isostatic anomaly map, particularly in the central Wilkes Land area, relative to the satellite derived free air data. There is a large amplitude positive isostatic anomaly situated off the west Wilkes Land margin between ∼112°E and ∼120°E, this anomaly correlates to the location of uncompensated sediment banks and the thick sediments of the Budd Coast Basin. Similarly to the 2D case, the classic-Airy model does not predict the complexity of observed gravity anomalies, and large isostatic anomalies remain oceanward of the edge effect low.

6.4.3 3D Process Oriented Modelling

Three-dimensional process-oriented modelling is identical in methodology to 2D process-oriented modelling, except that it is carried out using a sediment thickness grid rather than a sediment thickness profile. Hence, any errors introduced in the creation of the 3D sediment thickness grids, associated with the large line spacing and lack of data from the upper continental rise to the continental shelf, are propagated through the backstripping and gravity modelling process. Uncertainty in the sediment thickness grid introduces the largest source of unconstrainable error. Despite this obvious limitation, there is still significant benefit in calculating 3D flexural isostatic anomalies as they provide a means of quantitative and qualitative interpretation of the crustal structure of the Wilkes Land margin.

Three-dimensional modelling was undertaken using a single backstrip of the post-rift sediment thickness grid (Chapter 4) assuming a range of constant T_e values. Densities of water, sediment, crust and mantle are as for 2D modelling (Table 6.2). An initial crustal thickness of 35 km was assumed. However, tests indicate that the isostatic anomaly is relatively insensitive to variation of this parameter.

Figure 6.36 illustrates the rift, sediment and sum anomalies calculated for $T_e = 30$ km, compared to satellite derived FAA data. The right hand panels in Figure 6.36 show profiles extracted through the corresponding grid, along line GA-228_25, compared to the 2D solution obtained earlier using the line integral method. The profiles extracted compare almost exactly to the 2D profiles illustrating the assumptions of loads and bodies of infinite lateral extent in the 2D modelling introduced only negligible error. The slight differences that are apparent result from the resampling of the 2D data during gridding. Data spacing along the 2D profiles is ∼0.05 km, whereas the 3D grid spacing is 5 minutes (∼9 km in the north-south plane and between ∼4 to 4.5 km in the east-west plane). It

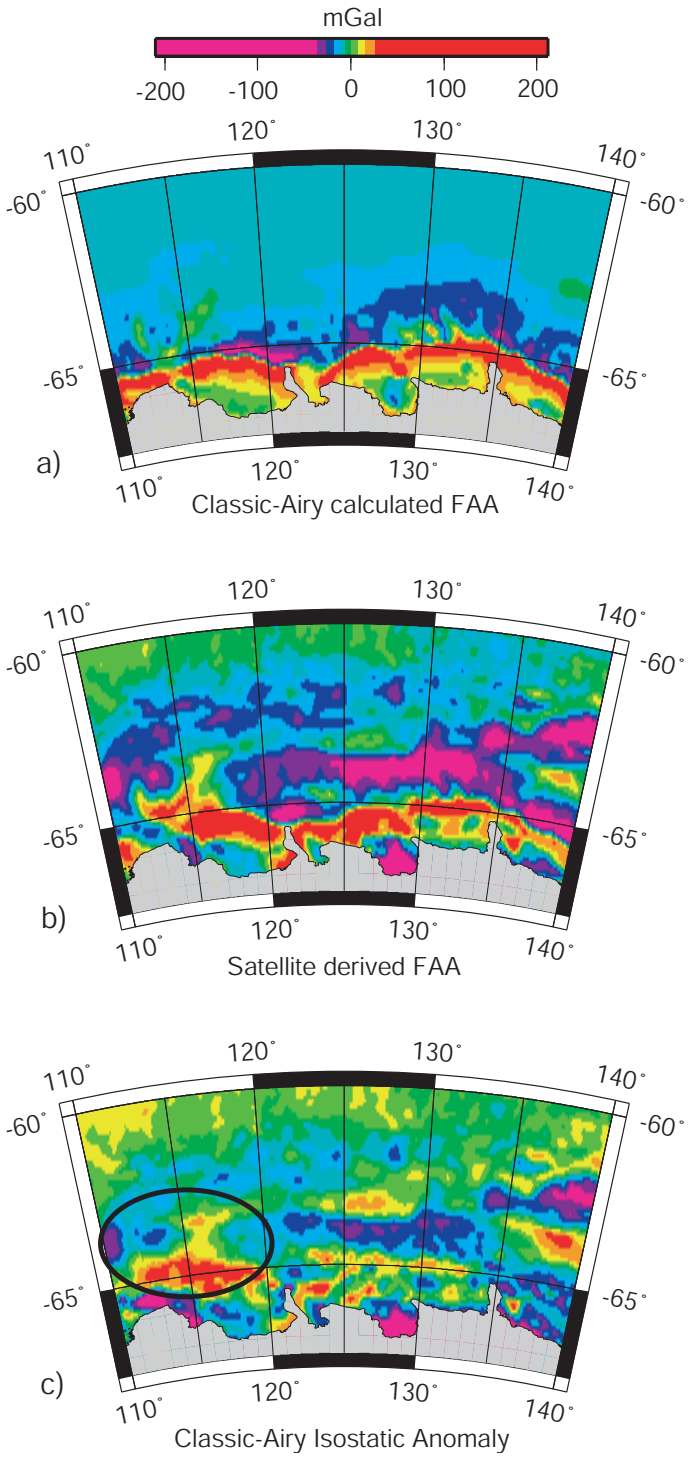

Figure 6.35: a) Classic-Airy model FAA. b) Satellite derived FAA from Sandwell & Smith [1997]. c) Classic-Airy isostatic anomalies for the Wilkes Land margin, the edge effect anomaly has been decreased in amplitude, however, large amplitude isostatic anomalies remain oceanward of the edge effect low. The Budd Coast Basin is circled in (c).

is necessary to alias the data during resampling to some degree due to the asymmetry in the north-south (∼0.05 km shot point spacing) and east-west (∼90 km line separation) data spacing. If gridding is completed using the maximum north-south data resolution then spurious interpolations are introduced in the east-west direction.

Flexural isostatic anomaly grids for T_e=0,5,10,20,30 and 45 km were created by subtracting the calculated sum anomalies from the satellite derived FAA. Flexural isostatic anomaly maps for T_e=0,5,10,20,30 and 45 km are displayed in Figure 6.37, some isostatic anomalies are common to each isostatic anomaly map indicating an insensitivity to T_e. The anomaly associated with the Adélie Rift Block (132-140°E) and the large positive amplitude anomaly off the west Wilkes Land margin are examples of isostatic anomalies that are not reduced more efficiently by any particular T_e. It must be noted that both these areas of large amplitude isostatic anomalies are outside the extents of MCS data, hence the errors are possibly related to insufficient data constraints. The positive isostatic anomaly off West Wilkes Land is located immediately landward of the southern extents of lines GA-228_19 and GA-228_20, where large sediment accumulations are observed. If the assumed landward extrapolations of these sediments are inaccurate then errors are introduced and isostatic anomalies result.

Isostatic anomalies within the areas directly constrained by MCS data are most effectively reduced for higher T_e estimates (30-45 km). The positive isostatic anomalies along ∼65°S are associated with misfit between calculated and observed edge effect anomalies. These isostatic anomalies are most reduced for high T_e. The isostatic anomalies outlined in Figure 6.37 are interpreted to represent flexurally compensated sediments of the BCB. These anomalies are relatively large for low T_e (0-10 km), however, they are effectively reduced for higher T_e estimates. Therefore, 3D modelling results accord with those of 2D modelling and indicate that the Wilkes Land margin is, in general, characterised by a high (for a rifted margin) T_e. The results of 3D modelling do not indicate any along margin segmentation of T_e.

The correlation between thick sediments and high T_e indicates that there is not necessarily a positive correlation between zones of weakened lithosphere and large scale sediment accumulation. This positive correlation has been suggested by Beaumont *et al.* [1982] and demonstrated for the northeast U.S. margin by Wyer [2003].

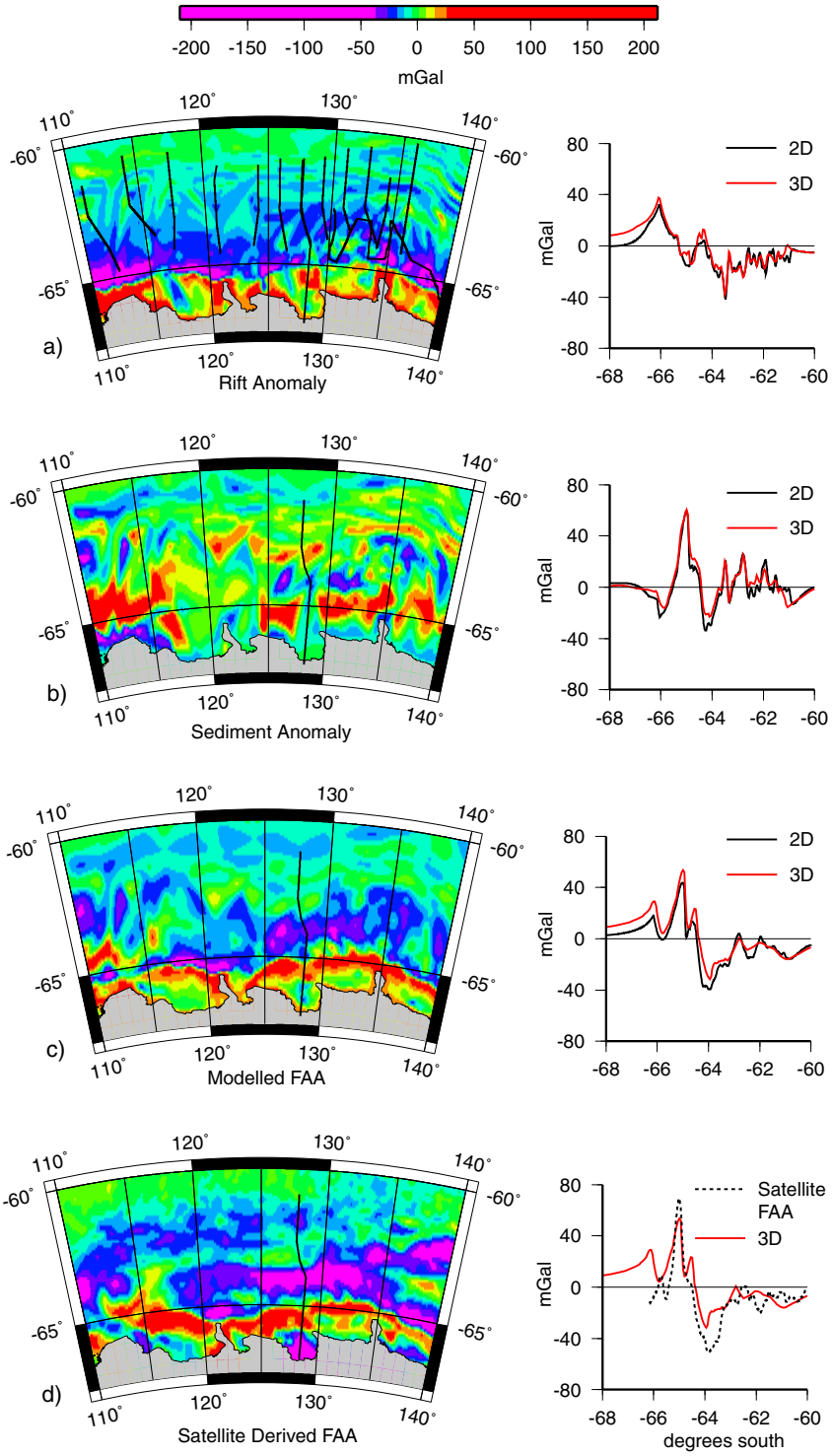

Figure 6.36: Gravity anomaly maps of the process oriented, T_e=30 km, a) rift anomaly, b) sediment anomaly, c) sum modelled free air anomaly, and d) the satellite derived free air gravity anomaly data. Right hand panels show profiles extracted through the associated grid (red) along line GA-228_25 compared to the 2D line integral solutions (black). Profile location is plotted on each map (black solid line) and the location of MCS data is plotted on the rift anomaly map.

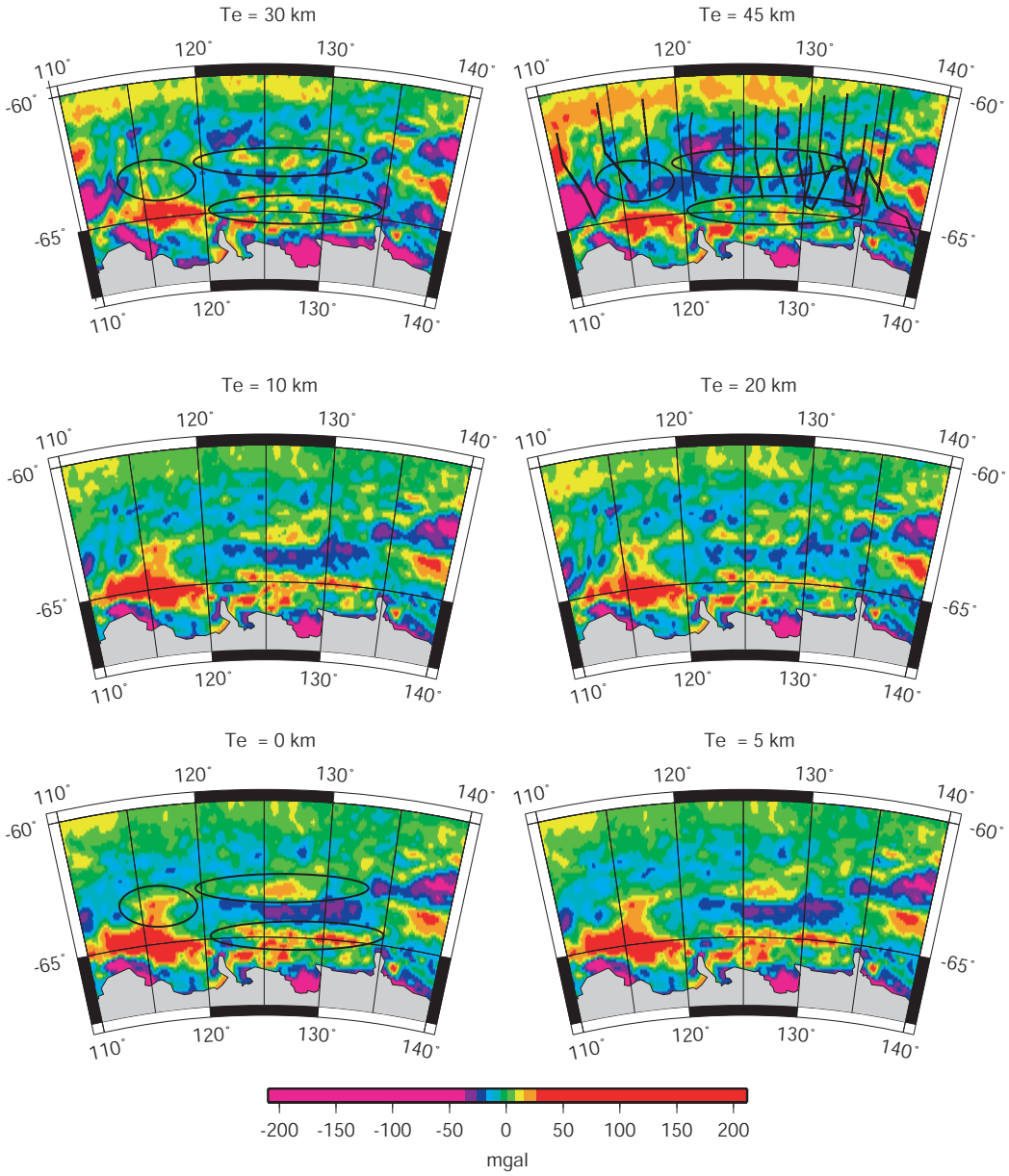

Figure 6.37: Isostatic anomaly maps for T_e as labelled. The amplitude of isostatic anomalies associated with the Budd Coast Basin (BCB) and the edge effect (as outlined for T_e =0,30 and 45 km) are most effectively reduced for the high T_e estimates. MCS line data locations are overlain on the T_e=45 km isostatic anomaly map.

6.4.4 Spectral Analysis

Computing the power spectra of the satellite derived FAA and isostatic anomaly data provides another technique of analysing gravity anomalies. By transforming the space domain anomaly data into the frequency domain (i.e. Fourier transform), power spectra can be analysed as a function of frequency or wavelength. Power spectra illustrate the wavelengths at which the greatest power or energy (spectral peaks) of a signal are associated. The differences in power spectra can be interpreted in terms of the applicability of T_e estimates and the fit between calculated and observed anomalies.

As no data is available for onshore Wilkes Land it is necessary to restrict the spectral analysis to the offshore region only. The southern limit of data included in spectral analyses can be considered as the Antarctic coastline or the extent of sea ice due to uncertainty in satellite derived free air gravity anomaly data over ice covered regions (section 6.1.4), both possibilities were tested.

Figure 6.38 illustrates the three-dimensional power spectra of the satellite derived FAA, classic-Airy isostatic anomaly, and flexural isostatic anomalies for T_e=0, 15 and 30 km. The spectra were calculated for both the entire offshore region (i.e. limited by the coastline) and also for the region offshore of the austral summer ice extents. The correlation between the shelf break, edge effect high and sea ice extent is significant with regards to inclusion in spectral analyses. The coastline limited power spectrum of free air anomaly data shows peak amplitudes at wavelengths of ∼300 and 500 km, the ice extent limited spectrum illustrates peaks at identical wavelengths, however, the amplitude of the ∼300 km peak is reduced by more than half. As the ice limited spectrum effectively excludes input from the edge effect high the ∼300 km peak can be correlated with the edge effect high.

The spectra for the coastline limited analyses indicate that power associated with the edge effect high is reduced in both the classic-Airy and flexural isostatic anomalies from ∼38 to ∼20 mGal^2. The greater amplitude and longer wavelength power peak observed in the FAA spectrum is reduced most efficiently in the classic-Airy isostatic anomaly, from >40 to <10 mGal^2, however, this peak is also reduced by more that half in the flexural isostatic anomaly spectra. This peak is interpreted to correlate to power associated with the edge effect low. The spectra created using the sea ice extent as the basis of data exclusion suggest that the edge effect low power is effectively reduced in both the classic-Airy and flexural isostatic anomalies.

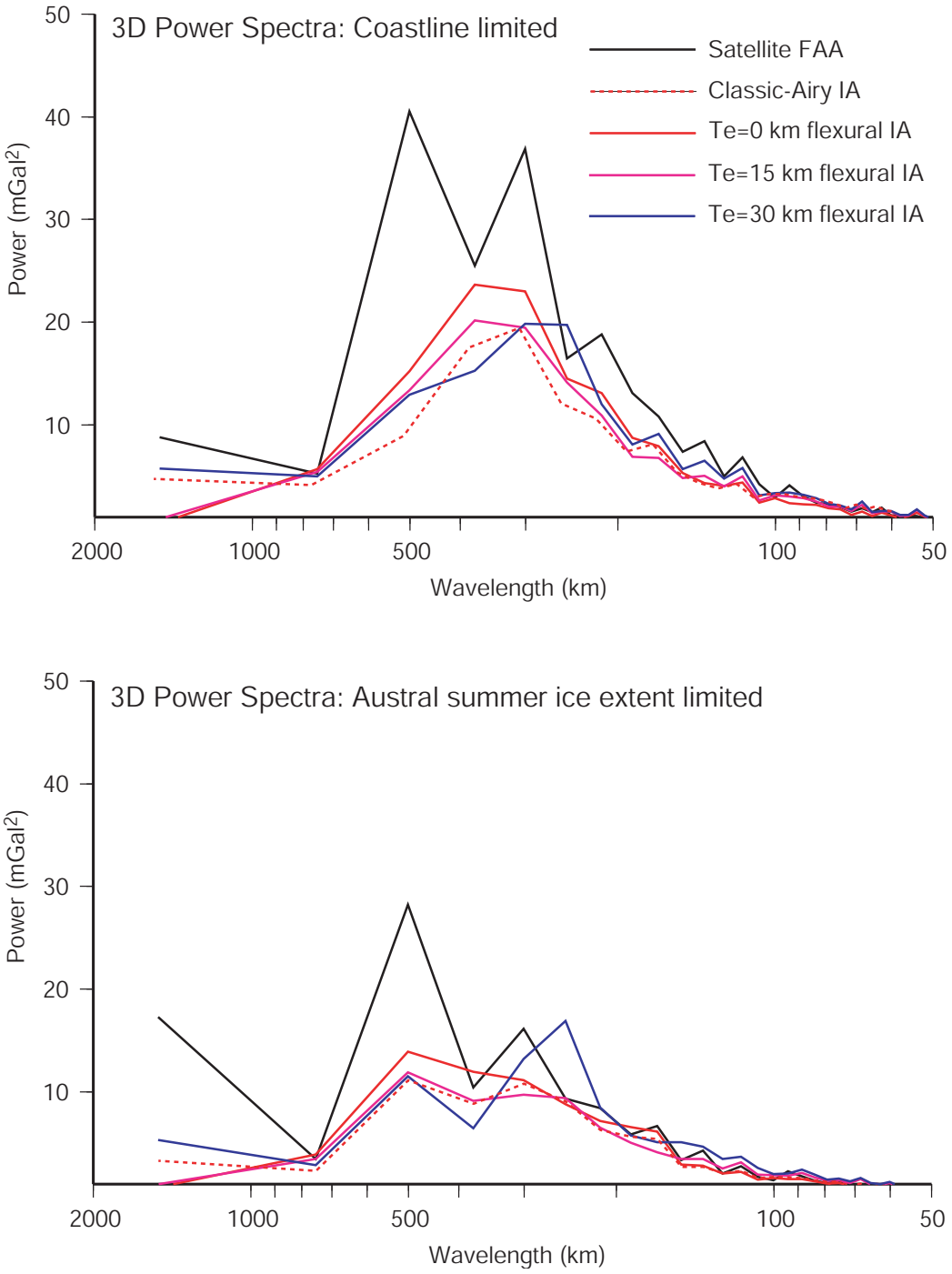

Figure 6.38: Three dimensional (3D) power spectra of satellite free air anomaly (FAA), Airy and flexural isostatic anomaly (IA) data for a) coastline limited analyses, and b) Austral summer sea ice extent limited analyses. Long wavelength power associated with the edge effect anomaly is significantly reduced in IA data relative FAA data.

6.5 Summary

Despite the limitations of gravity data and the extent of seismic reflection data on the Wilkes Land margin, 2D and 3D process-oriented gravity modelling provides important results. The T_e structure of the margin has been, for the first time, estimated and constrained via modelling. The high T_e inferred for most of the margin contrasts with other rift margins, which are typically characterised by low T_e. Crustal structure has been constrained and the variation in stretching factor across and along the margin can now be determined. The close correlation between modelled and seismic data inferred $Moho$ depths, and the results of incorporating syn-rift strength and a depth of necking, broadly validate the assumption of Airy isostasy in determining crustal structure.

The results presented here further demonstrate the ability of process-oriented modelling to constrain the gravity anomaly contributions of individual geological processes in a continental margin environment. This, in turn, allows density anomalies and breakdowns in isostatic assumptions to be investigated without the interfering effects of other geological processes.

Chapter 7

Discussion

7.1 Introduction

This chapter comprises four main sections. The first two sections address key issues that arise from the studies undertaken in previous chapters. In the first section, one of the main aims of this chapter and thesis is addressed, namely, the integration of the results of interpretation and modelling of the seismic reflection and refraction, magnetic and gravity data. The interpretation of these data has led to a number of questions with regard to the location of the COB and the nature of the COT. Here we use combined magnetic and gravity modelling to infer serpentinised peridotites associated with exhumed mantle within the COT.

In the second section we summarise the subsidence history of the margin. Following backstripping, the pattern of crustal thinning can be inferred. Oceanic crust is observed to occur at anomalously great depth off the Wilkes Land margin, even once adjusted for the thick sediment load associated with Tertiary glaciation. The effect of ice-induced subsidence is also discussed with regards to alteration of the continental shelf, and possibly continental rise, morphology.

The third section comprises a study of the conjugate margin structure. A fundamental question of rift studies is to determine whether conjugate margins can be classified as symmetrical or asymmetrical with regard to crustal thinning patterns, width of extended crust, volcanism, subsidence history, segmentation, and long-term thermo-mechanical properties. Process-oriented gravity modelling is undertaken on the southern Australian margin to allow comparison with interpretation of the Wilkes Land margin.

The strength of extended continental crust is discussed in the fourth section of this chapter. The permanent mechanical alteration of continental crust and the transient changes in the geotherm associated with rifting alter the YSE of the extended continental crust and, therefore, potentially its T_e structure.

7.2 Mantle Exhumation in the Continent-Ocean Transition Zone

The existence of serpentinised mantle peridotites in the Continent-Ocean Transition (COT) zone at the West Iberian rifted margin has been established through dredging and drilling (e.g. Boillot *et al.* [1980], Pinheiro *et al.* [1996]). Seismic refraction data have also been used to constrain the presence and extent of serpentinised peridotite (e.g. Dean *et al.* [2000]). Serpentinised peridotites have also been interpreted within the COT zone of the southwest Greenland (e.g. Chian & Louden [1994]). Figure 7.1, a schematic cross-section through the south-west Greenland margin, illustrates the suggested mode of occurrence of serpentinised mantle within the COT zone. At this margin, serpentinised mantle is interpreted beneath thinned continental crust and as top basement where total crustal separation has occurred [Pérez-Gussinyé *et al.*, 2001].

Figure 7.1: Cross-section through the south-west Greenland margin illustrating the presence of serpentinised peridotites within the COT zone. Figure from Pérez-Gussinyé *et al.* [2001], after Chian & Louden [1994].

A basement ridge complex, interpreted as a combination of serpentinised peridotites and mafic rock associated with mantle upwelling, has also been identified off the Great Australian Bight (GAB) margin of southern Australia [Sayers *et al.*, 2001]. However, the interpretation of this basement ridge, which is only based on seismic character and gravity and magnetic modelling, is yet to be tested by drilling or seismic refraction.

Minshull *et al.* [1998], Dean *et al.* [2000] and other workers suggest that serpentinisation is facilitated if there are readily available pathways for seawater to reach the upper mantle, and if the upper mantle is cool. These conditions are commonly satisfied at fracture zones on slow spreading ridges, in COT zones, and at the axes of extinct rifts. However, in each of these environments Minshull *et al.* [1998] observe that serpentinisation sufficient to significantly lower the seismic velocity and density of mantle peridotites

does not penetrate beyond ~5 km into the crust. The slow spreading (<10 mm/yr HSR) and inferred low-temperature (as evidenced by a lack of volcanic rocks and the great depth of the AAB oceanic crust) breakup of Australia and Antarctica, therefore, makes the Wilkes Land margin a likely location for the occurrence of serpentinised peridotites.

A number of basement highs, characterised by a relatively transparent internal acoustic character, were identified in seismic reflection data from the COT zone off the Wilkes Land margin (as discussed in Chapter 4). Some of these basement highs protrude through the post-rift sediments and have a bathymetric expression off east Wilkes Land and Terre Adélie, where they correlate to positive free air gravity anomalies.

In-situ, but altered, peridotite blocks have been dredged from one of the basement highs that forms a seamount at the seaward extent of the Adélie Rift Block (ARB) (Seamount B, Figures 4.24 and 4.25). Geochemical analyses of these dredged peridotite samples indicate the seamount comprises upper-mantle peridotites that have a fertile, sub-continental mantle origin [Yuasa *et al.*, 1997].

Sediment-covered basement features in central and eastern Wilkes Land, similar to the seamounts dredged in the ARB, correlate to Flexural Isostatic Anomalies (FIA), and in some cases, magnetic anomalies also. Forward modelling and inversion of FIA and forward modelling of magnetic anomalies was undertaken to constrain the geometry and physical properties of the possible sources of these anomalies and determine if exhumed and potentially serpentinised mantle peridotites could be inferred outside of the ARB.

The density and seismic velocity, and magnetic susceptibility, of mantle peridotites varies with degree of serpentinisation (e.g. Horen *et al.* [1996], Oufi & Cannat [2002]). The relationship between density and degree of serpentinisation being far more systematic than variations in magnetic susceptibility. Table 7.1 summarises the density and seismic (P wave) velocity of variably serpentinised peridotite samples recovered from ophiolites. The density and seismic velocity of peridotites decreases systematically as the degree of serpentinisation increases.

% serpentinisation	ρ (kg/m^3)	V_p (m/s)
3	3260	7759
15	3200	7346
35	3030	6744
45	2930	6355
75	2710	5864

Table 7.1: Relationship between degree of serpentinisation, density, and seismic velocity. After Horen *et al.* [1996].

The magnetic susceptibility (k) of serpentinised peridotites does not linearly correlate to degree of serpentinisation [Oufi & Cannat, 2002]. Instead, k remains subdued in partially serpentinised peridotites and then increases rapidly as a threshold degree of ~75% alteration is reached. This is related to the formation of magnetite during the serpentinisation process. A wide range of k and Königsberger ratios (Q) were determined by Oufi & Cannat [2002] based on the analysis of samples from ODP drilling. A k range of 0.01 to 0.15 is demonstrated and a Q range from 0 to 10. The grain size distribution and serpentinite micro-structure controls the importance of remanent magnetisation, for larger grain-size the contribution of remanence after alteration is decreased [Dunlop, 1995; Oufi & Cannat, 2002].

Figure 7.2 illustrates the spatial correlation on Line GA-228_22 of a COT zone basement high, a FIA, and a large amplitude magnetic anomaly that occurs on the 'anomaly 34y' lineation (see Figure 5.14). The FIA and observed magnetic anomalies are well fit by the calculated anomalies for the two-dimensional body illustrated, constrained by the depth to basement interpreted from depth converted seismic reflection data. A positive density contrast of 300 kg/m^3 (equivalent to an absolute density of 3100 kg/m^3 as the FIA was calculated assuming a crustal density of 2800 kg/m^3). A density of ~3100 kg/m^3 correlates to a serpentinisation of ~25%. A magnetic susceptibility of 0.1 SI units was assumed in modelling. The calculated magnetic anomalies are assumed to be due to induction in the present-day geomagnetic field only (i.e. very low Königsberger ratio). Ambient magnetic field properties assumed in modelling are as for the present day Wilkes Land margin, i.e. field strength = 66,000 nT, inclination = -80°, and declination = -3° [IAGA, 2000].

The base of the body illustrated in Figure 7.2 does not correlate with the depth to the flexed $Moho$ from process-oriented modelling. By lowering the density of the body and increasing its thickness these surfaces can be forced to correlate more closely without altering the quality of fit between calculated and observed anomalies. However, as there is no constraint on depth to $Moho$ in the COT zone and we infer higher density basement in the COT, the depth to the flexed $Moho$ calculated assuming a crustal density of 2800 kg/m^3 is likely too deep. Therefore, this apparent 'misfit' is not corrected here. Without further constraint on depth to $Moho$ it was considered arbitrary to alter density or thickness of bodies to conform to a flexed $Moho$ calculated assuming Airy isostasy.

A similar spatial correlation of FIA and magnetic anomalies, and rugged COT zone topography, occurs close to the point of maximum crustal thinning on Line GA-228_23 (Figure 7.3). The geometry of the bodies required for calculated gravity anomalies to fit the FIA correlate closely to the basement surface and flank a shallow point in the modelled flexed $Moho$. Densities of 3120 and 3100 kg/m^3 were assumed for the two bodies, again

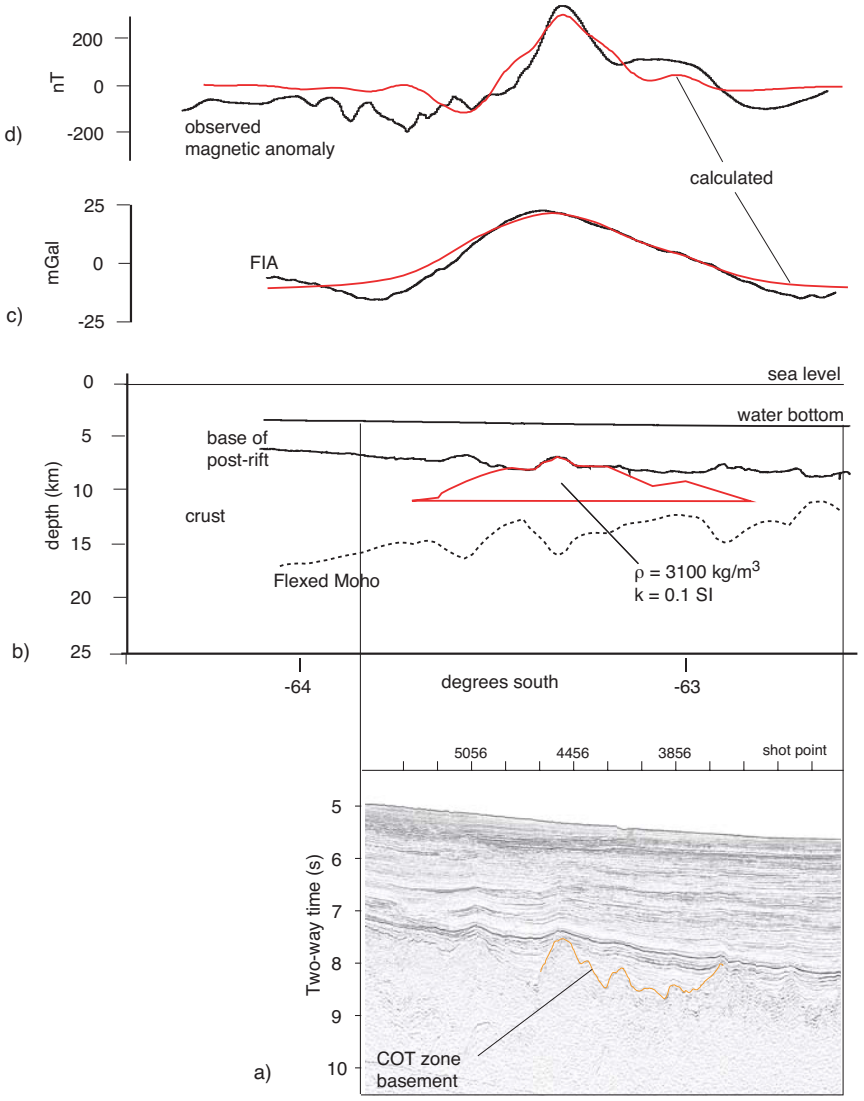

Figure 7.2: a) Seismic reflection data from Line GA-228_22. b) Crustal structure from process-oriented modelling (dashed black) and modelled body geometry (red) with density (ρ) and magnetic susceptibility (k) as labelled. c) FIA and calculated gravity anomaly for body in (b). d) Observed magnetic anomalies compared to calculated anomalies assuming induction only for the body in (b).

suggesting ~25% serpentinisation of exhumed peridotites. The geometry of these bodies do not provide a calculated magnetic anomaly that accurately fits the observed magnetic anomaly. However, slight variations of the body geometries assumed in the gravity model, with an upper surface still constrained by the basement depth, provides for an accurate fit between calculated and observed anomalies assuming magnetic susceptibilities of 0.09 and 0.04 SI. The magnetic sources required to predict calculated anomalies of similar magnitude to observed anomalies, assuming induction only, are of much greater thickness

(∼2 km) than the typical thickness of layer 2 oceanic crust.

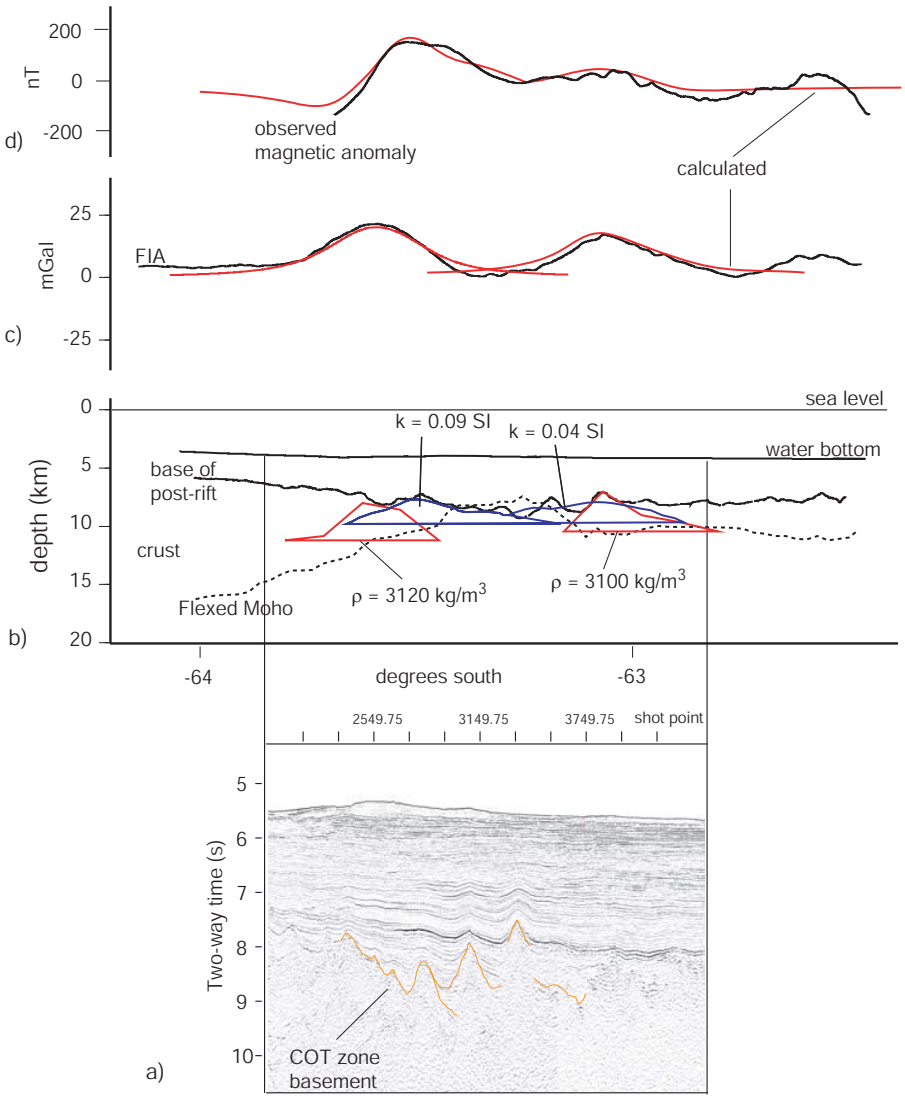

Figure 7.3: a) Seismic reflection data from Line GA-228_23. b) Crustal structure from process-oriented modelling (dashed black) and modelled body geometries for gravity (red) and magnetic (blue) modelling with density (ρ) and magnetic susceptibility (k) as labelled. c) FIA and calculated gravity anomaly for red bodies in (b). d) Observed magnetic anomalies compared to calculated anomalies assuming induction only for blue bodies in (b).

Figure 7.4 illustrates the coincidence of an interpreted zone of COT zone crust and a positive FIA for Line GA-228_26. Forward modelling of the FIA indicates the presence of a relatively broad mass excess in the upper crust with a density of 3100 kg/m^3. Again, this is interpreted to indicate the presence of serpentinised peridotites associated with exhumation of the upper mantle within the COT zone. The magnetic anomaly pattern

for this line is very complex landward of 62.5°S (see Figure 5.14). The FIA at this location does not occur on the lineation of 'anomaly 34y', rather it occurs within the COT zone interpreted from seismic reflection data. Results from modelling of Line GA-228_27 are very similar (Figure 7.5). There is no spatial correlation of magnetic and FIA, but a mass excess correlated to the basement surface, with a density of 3050 kg/m^3, is inferred from gravity modelling.

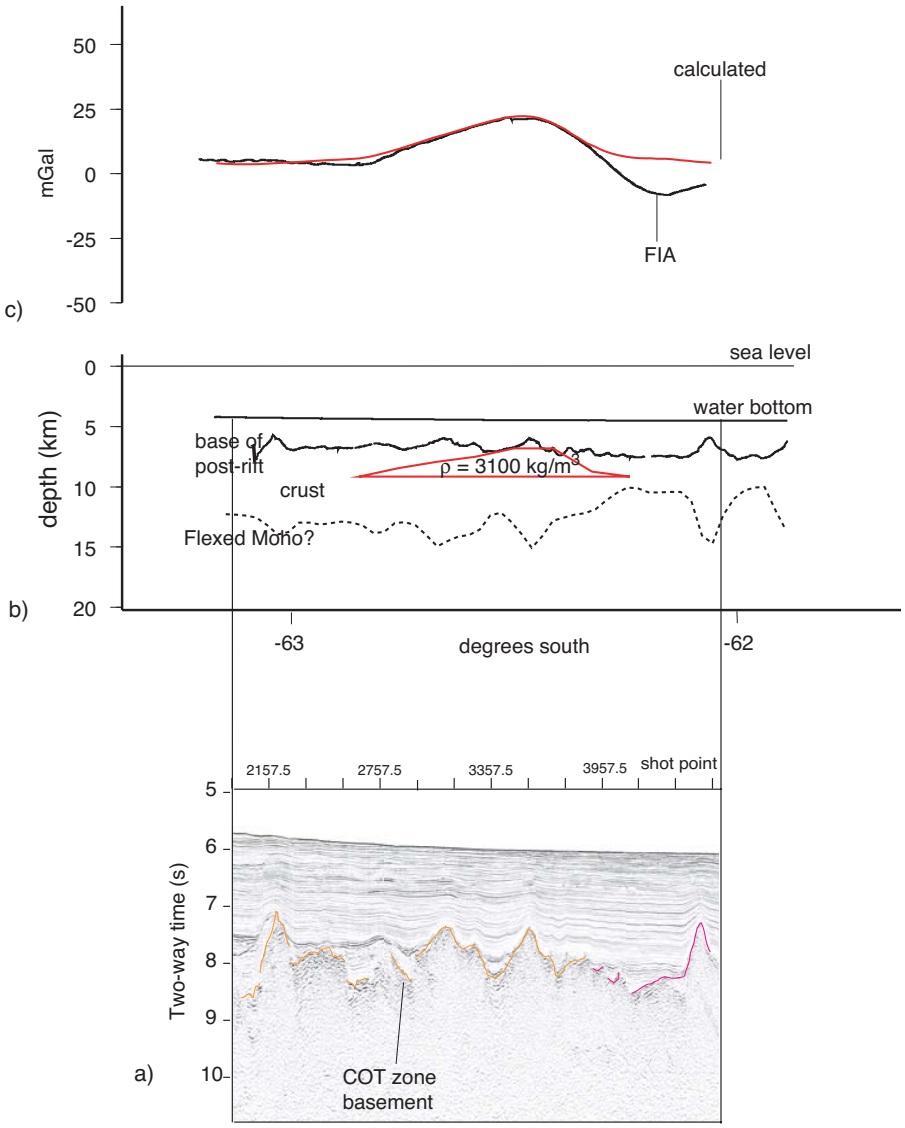

Figure 7.4: a) Seismic reflection data from Line GA-228_26. b) Crustal structure from process-oriented modelling (dashed black) and modelled body geometry (red) with density (ρ) as labelled. c) FIA and calculated gravity anomaly for body in (b).

A FIA occurs over the basement high located at the seaward limit of the interpreted COT zone for Line GA-228_29 (Figure 7.6). No observed magnetic anomalies correlate

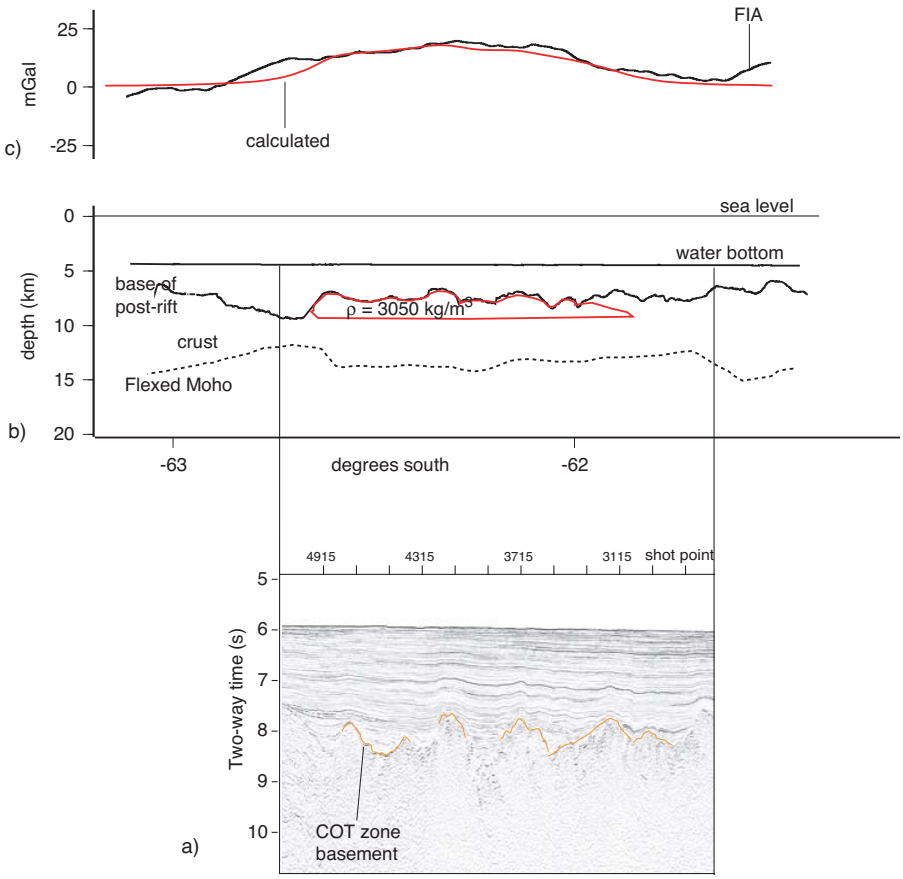

Figure 7.5: a) Seismic reflection data from Line GA-228_27. b) Crustal structure from process-oriented modelling (dashed black) and modelled body geometry (red) with density (ρ) as labelled. c) FIA and calculated gravity anomaly for body in (b).

to this basement high and FIA. Forward modelling, constrained by the geometry of the basement high, indicates a density for this feature of 3100 kg/m^3.

The consistency of the spatial correlation of positive FIA and basement features within the COT zone, which modelling indicates have a density of ~3100 kg/m^3, indicates the presence of serpentinised upper-mantle peridotites. This has already been established for the ARB off the eastern Wilkes Land margin, however, these results indicate their presence along margin from the ARB. The serpentinised, peridotite ridges occur both at the landward (e.g. Lines GA-228_22 and GA-228_23) and seaward extents (e.g. Line GA-228_29) of the COT zone. Despite variation in the geometry of the interpreted COT zones and ridges, the gross structure is similar to the schematic section from the south-west Greenland margin discussed above (Figure 7.1).

Coincident magnetic and gravity modelling indicates that magnetic anomalies that occur on the 'anomaly 34y' lineation (Figure 5.14) are likely not associated with *normal*

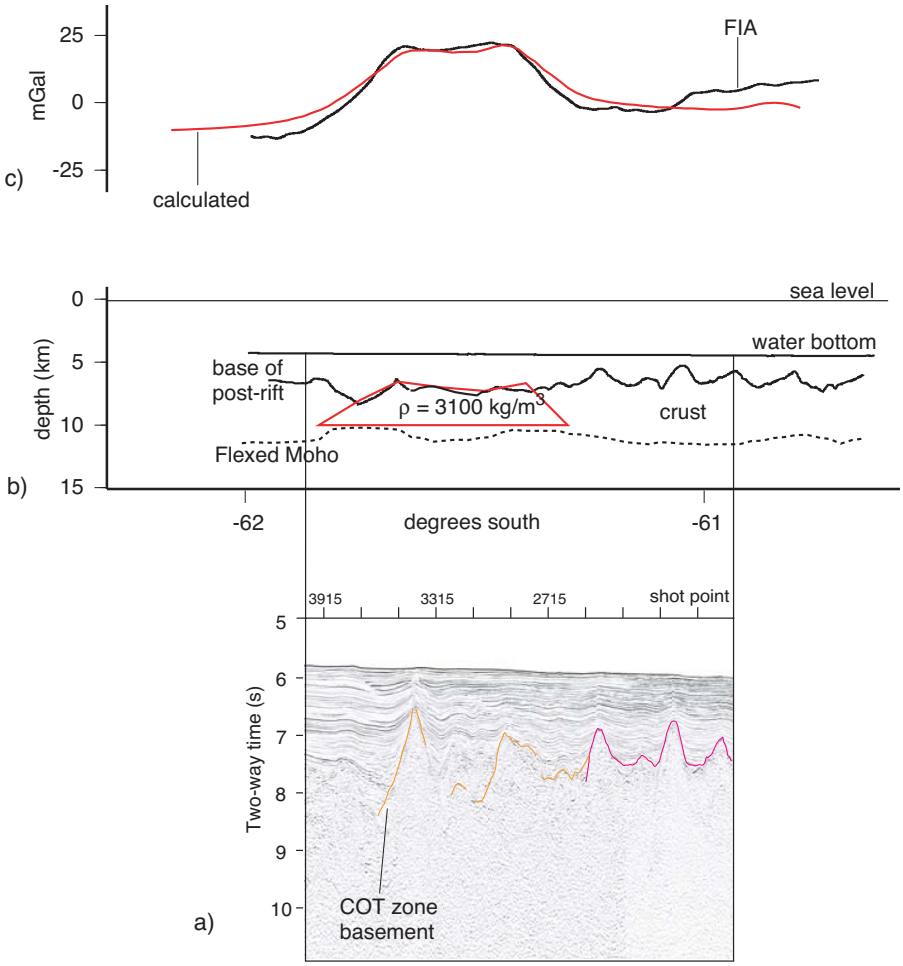

Figure 7.6: a) Seismic reflection data from Line GA-228_29. b) Crustal structure from process-oriented modelling (dashed black) and modelled body geometry (red) with density (ρ) as labelled. c) FIA and calculated gravity anomaly for body in (b).

oceanic crust. It was demonstrated in Chapter 5 that the observed magnetic anomalies did not correlate to basement topography for a constant thickness magnetic source layer. However, it is clear from the modelling undertaken here that there is a strong correlation between basement topography and the observed magnetic anomalies for a non-constant thickness source body. The additional correlation with positive FIA provides for greater confidence in reinterpreting the magnetic anomalies previously identified as anomaly 34y to be associated with serpentinised upper-mantle peridotites, exhumed during continental extension. The observed magnetic lineation is likely a function of the approximately contemporaneous exhumation of upper mantle segments along the Wilkes Land margin.

The massive extension and rupture of the upper- and lower-crust is indicated by the presence of exhumed, altered mantle at the base of the post-rift sediments for much of the

COT zone off the Wilkes Land margin. As outlined previously, many of the factors considered important in allowing mantle serpentinisation and exhumation at rifted margins occur at the Wilkes Land margin. Namely, low extension rates and low mantle temperatures, which both contribute to low melt generation, a key factor in allowing mantle exhumation [Pérez-Gussinyé *et al.*, 2001]. Figure 7.7 illustrates the temporal evolution for a 'West Iberia type' margin and the mode of mantle hydration and serpentinisation suggested by Pérez-Gussinyé *et al.* [2001]. However, a décollement surface at the crust-mantle boundary (CMB), similar to that suggested by Pérez-Gussinyé *et al.* [2001] (for which there is evidence in seismic reflection and refraction data at the Iberian margin [e.g. Krawczyk *et al.* [1996]]), is not apparent in seismic data from the Wilkes Land margin. This indicates that mantle exhumation may occur due to crustal separation without full-crust penetrating detachment surfaces.

Figure 7.7: Schematic representation of the temporal evolution at a central rift zone for a 'West Iberia Type' margin. For stretching factors of 4 or greater the whole crust is brittle and crust-cutting faults allow hydration and serpentinisation of the upper mantle. A similar mechanism is interpreted at the Wilkes Land margin, however, no evidence of major detachment or décollement surfaces are evident in seismic reflection data from the Wilkes Land margin. Figure from Pérez-Gussinyé *et al.* [2001].

Further investigation with wide-angle seismic refraction techniques are required to determine if the COT zone inferred here shares the same characteristic velocity structure as observed off the Iberian margin. However, the presence of exhumed mantle peridotites at the Wilkes Land margin can be interpreted on the basis of seismic reflection data interpretation and, gravity and magnetic modelling.

These results provide further support to the suggestions of Tikku & Cande [1999] and Sayers *et al.* [2001] that 'anomaly 34y' and its interpreted lineation (e.g. Figures 5.10 and 5.14) is not a seafloor spreading anomaly as it overlies extended continental crust

and exhumed upper-mantle lithosphere. This has a number of important implications for the breakup history of Australia and East Antarctica. Due to the lack of a confidently identifiable magnetic anomaly sequence prior to the Eocene, and the recognition that 'anomaly 34y' may not be a seafloor spreading anomaly, it is very difficult to constrain the timing of the onset of seafloor spreading between Antarctica and Australia. Additionally, it is apparent that a boundary between continental and oceanic crust is not present at the Wilkes Land margin, arguably a COB should therefore be defined at the boundary between exhumed continental lithosphere mantle and oceanic crust. Although the COB can be defined in this fashion, determination of a stretching factor (β) within the COT has little meaning as a total absence of continental crust is inferred within this zone.

The re-interpretation of the genesis of 'anomaly 34y' does not, however, require the interpreted COT zone to be re-assessed. This is because it was originally defined herein (Figure 4.23) as the zone interleaving crust of clear continental and oceanic affinity. The presence of exhumed mantle, interpreted to represent continental lithosphere, does not constitute unequivocal continental crust, therefore, the interpreted COT zone is robust to the results of the above modelling.

7.3 Extension and Subsidence at the Wilkes Land margin

7.3.1 Extension and Crustal Thinning

Thermal contraction, following heating of the lithosphere, and crustal thinning associated with erosion have been demonstrated to contribute to subsidence at rifted margins (e.g. Sleep [1971]). However, lateral extension of the crust and upper-mantle is now believed to be the primary causative process responsible for the creation of rift-type basins in passive margin settings. McKenzie [1978] developed a model in which extension is responsible for both the thermal anomaly and crustal thinning necessary for a sedimentary basin to form (as discussed in Chapter 1). McKenzie [1978] defined the ratio of initial to extended crustal and lithospheric-mantle thickness as the stretching factor (β). In this uniform stretching model, there exists a unique subsidence history for any given value of β. Accordingly, defining β at rifted margins has important consequences for understanding the subsidence history and margin evolution.

The McKenzie [1978] model, however, does not account for lateral heat conduction or lithospheric flexure associated with syn- and post-rift processes, and assumes instantaneous rifting. These processes were demonstrated to alter the theoretical subsidence and evolution of a basin beyond the simple controls that the degree of stretching imparts (e.g. Steckler & Watts [1981], Watts *et al.* [1982], Cochran [1983]).

Modelling by Cochran [1983] demonstrated that incorporating a finite rift interval in concert with the effects of lateral heat conduction and lithospheric flexure predicted markedly different subsidence and uplift histories relative to the uniform stretching model of McKenzie [1978]. Specifically, Cochran [1983] predicted that post-rift subsidence could be as much as 25% less than predicted by the method of McKenzie [1978] for a rift interval of 20 Ma.

The subsidence history at rifted margins is usually constrained by backstripping sedimentary sequences, observed in core and well-log data, in conjunction with palaeontological data that provides information on water depth through time (e.g. Steckler & Watts [1978]). By comparing backstripped curves of tectonic subsidence through time with theoretical curves based on the models of, for example, McKenzie [1978] and Cochran [1983], it is possible to deduce information on basin forming mechanisms. However, as no well data is available on the Wilkes Land margin, this is not possible here.

Stewart *et al.* [2000] used *pseudo-well* analyses, to supplement data from a single well, to investigate the subsidence history and palaeowater depths at the Namibian rift margin. Pseudo-wells can be 'created' at any point where the sediment thickness is constrained, and can be flexurally or Airy backstripped if a sediment thickness profile or grid is available. In this way each seismic-stratigraphic unit is backstripped and the cumulative backstrip compared to theoretical subsidence plots to infer palaeowater depths.

The tectonic subsidence can be calculated for only three points at the Wilkes Land margin, as there are age constraints on only two seismic-stratigraphic sequences. Therefore, the resulting tectonic subsidence 'curve' is poorly defined (Figure 7.8). Figure 7.8 compares the cumulative backstrip and TTS, for two pseudo-wells on Line GA-228_23, to theoretical curves of tectonic subsidence based on the model of Cochran [1983]. An initial crustal thickness of 31 km, a rift age of 100 Ma, and a rift duration of 15 Ma were assumed in the calculation of the theoretical tectonic subsidence curves, based on subsidence curves inferred from wells on the southern Australian margin (e.g. Hegarty *et al.* [1988]). The difference between the cumulative backstrip and the theoretical subsidence curve can be inferred to represent palaeowater depths. For the margin region constrained by seismic reflection data, pseudo-well analyses indicate that the water depth has exceeded 1.5 km since at least 83 Ma.

Although the subsidence history can not be constrained in detail, the TTS is constrained from backstripping. Studies of TTS are advantaged relative to studies of crustal thinning as they involve no assumption about initial crustal thickness. Henning *et al.* [2004] use variations in TTS depth to infer the presence and thickness of serpentinised mantle in the COT zone off west Iberia. In their study, local compensation of sediments is assumed. Additionally, complete alteration to serpentinite is assumed for the zone of

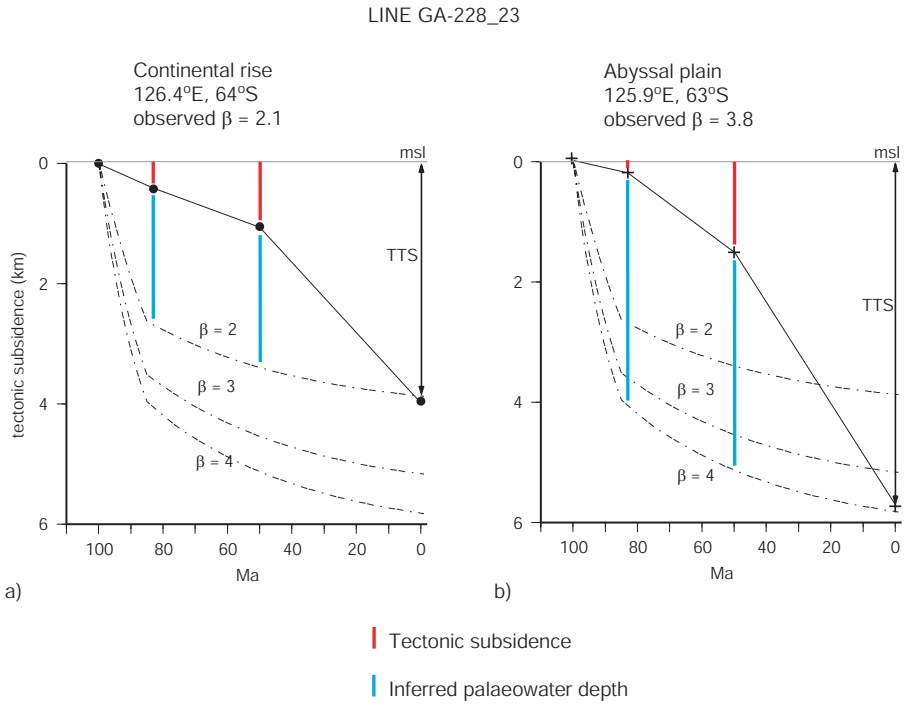

Figure 7.8: The difference between the cumulative backstrip curve (solid) and the theoretical subsidence curve (dashed) provide an estimate of palaeowater depth for two pseudo-wells on Line GA-228_23. The observed β values are taken from the gravity model crustal structure for this line and correlate very closely to the theoretical subsidence predicted by the model of Cochran [1983].

altered mantle (i.e. a density of 2550 kg/m^3). Despite these limitations, they find a correlation between TTS and the presence of serpentinised peridotites determined from drilling, dredging, and seismic refraction experiments. Analysis of the TTS off Wilkes Land do not show any clear correlation between TTS and the COT zone. Given the lack of seismic refraction data to independently constrain the extent of exhumed mantle and the degree to which it has been serpentinised, it is not possibly to quantitatively analyse the TTS data with regard to possible thicknesses of serpentinised mantle.

In addition to the importance in understanding basin evolution, the β distribution at rifted margins is one of the most useful parameters by which dynamic models of rifting can be constrained (e.g. Bassi [1991], Bassi [1995], Pérez-Gussinyé *et al.* [2001]). Whether or not lithospheric necking occurs and the degree to which conjugate margins are symmetrical is a strong function of the crustal thinning pattern (e.g. Buck *et al.* [1999]). Additionally, estimates of β are integral to inferring strain rate during rifting at ancient passive margins, a parameter believed to strongly influence the final width of extended continental crust (e.g. Bassi [1995]). Pérez-Gussinyé *et al.* [2001] also demonstrate that

β is a critical factor in the serpentinisation of the upper-mantle during rifting.

The pattern of thinning at the Wilkes Land margin has been investigated by using the crustal structure parameters determined from process oriented modelling (i.e. TTS and initial crustal thickness), which were demonstrated to correlate closely to the independent crustal structure data available (i.e. seismic reflection and sonobuoy refraction inferred $Moho$ depths). Figure 7.9 plots β as a function of distance from the landward or inner limit of the COT zone (herein referred to as the Continent-Transition Boundary [CTB]), as defined from seismic reflection data interpretation (Figure 4.23). The dashed lines beyond the inner limit of the COT zone show the β distribution as far as the outer limit of the COT zone. It is not clear, however, that β has any physical meaning in a COT zone where top basement comprises, in part, exhumed mantle peridotite and there is a complete absence of continental crust. Evidence from the West Iberian margin suggests that there is a gradation in the vertical seismic velocity in the COT zone, rather than a sharp change associated with a continental or oceanic lithosphere crust-mantle boundary [Dean *et al.*, 2000]. This further suggests that the determination of β within the COT zone is of limited value.

Bathymetry profiles for each β profile are included to allow any relationships with the present-day margin morphology to be assessed. The 13 GA-228 and GA-229 lines are divided into western, central, and eastern sectors for analysis in Figure 7.9. Although this is partly undertaken to improve the clarity of the images, these regions are also distinct in terms of free air gravity anomaly patterns, post-rift sediment distribution and, more importantly, inferred initial crustal thickness as outlined in Chapter 6.

The greatest amount of crustal extension in the western margin sector is inferred for Lines GA-228_18 and GA-228_19. However, there are no independent constraints on crustal thickness for this sector and the greatest sediment thickness is also observed. Due to the large sediment thickness a deep basement is observed and, therefore, a large degree of crustal thinning is required to compensate for this. Therefore, large β values are inferred, however, if a greater initial crustal thickness value was assumed (i.e. >35 km) the points of maximum necking would not be as radically thinned.

The pattern of crustal thinning for Lines GA-228_20 to GA-228_26 are very similar. A total width of extended continental crust of ~350 km is observed, and the distance from the shelf-break to the inner limit of the COT is ~150-200 km. The β increases approximately linearly from unity at the coast, to ~2.5 at 100 km landward of the CTB. A sharp increase in β occurs towards the CTB, and maximum values of ~5 are reached at or just landward of the CTB.

The pattern of crustal thinning in the eastern Wilkes Land and Terre Adélie margin sector is far more variable. Lines GA-228_27 and GA-228_28 exhibit a relatively similar

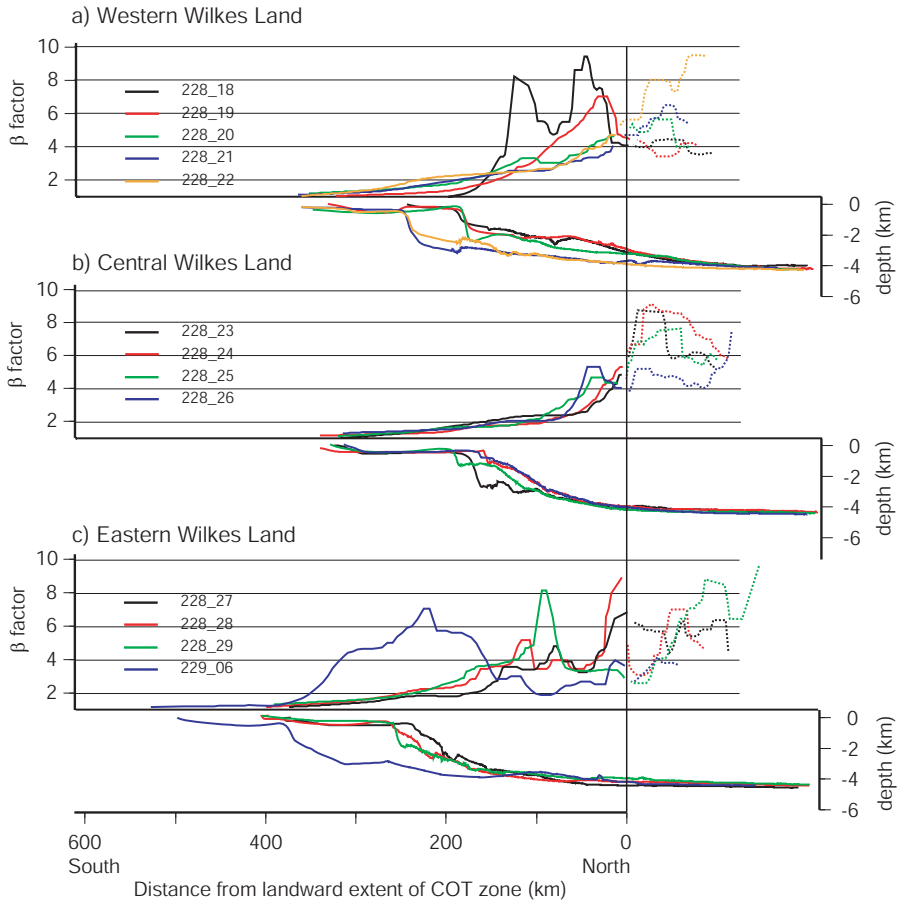

Figure 7.9: Degree of crustal stretching (β) as a function of distance from the inner limit of the COT zone (Figure 4.23) a) western, b) central, and c) eastern Wilkes Land. Bathymetry data are illustrated in the lower panels beneath the β profiles.

pattern to central Wilkes Land transects, except that peak β values exceed 6 and 8 on these lines respectively. Both these lines also indicate a zone of increased crustal thinning ($\beta > 4$) at ~100 km landward of the CTB. The peak β on Line GA-228_29 (~8) occurs coincident with this zone of increased crustal thinning, not at the CTB. The total width of extended continental crust for Lines GA-228_27 to GA-228_29 is almost 400 km, and the shelf-break to CTB distance is 225-275 km.

The β distribution for Line GA-229_06, across the ARB, is markedly different relative to the transects from margin sectors to the west. The total width of extended continental crust on this line is over 500 km, and the shelf-break to CTB separation is almost 400 km. The width of crust characterised by $\beta > 4$, almost 200 km, is also much greater than in other margin sectors. The region of maximum β occurs more than 150 km landward of the inferred CTB. A $\beta < 4$ characterises the limit of extended continental crust, lower than for all other lines except GA-228_29. This indicates that the point of eventual

crustal rupture for eastern most Wilkes Land and Terre Adélie occurred seaward of the point of maximum crustal extension.

Figure 7.10 compares the β distribution inferred for the central Wilkes Land margin (Line GA-228_24) with the inferred β results of backstripping, gravity modelling and crustal restoration studies at other passive, rift-type margins. Results from the margins of South Africa, Nova Scotia, Gabon, eastern U.S.A., Brazil (Campos Basin), Goban Spur, Carolina, and Valencia Trough (western Mediterranean) are included from a compilation by Watts & Fairhead [1997]. Results from the Otway Basin are after the published wide-angle refraction data of Finlayson *et al.* [1998]. Results from West Iberia are courtesy of T. Cunha (unpubl., Uni. of Oxford), and results from the Great Australia Bight (GAB) margin are from this study.

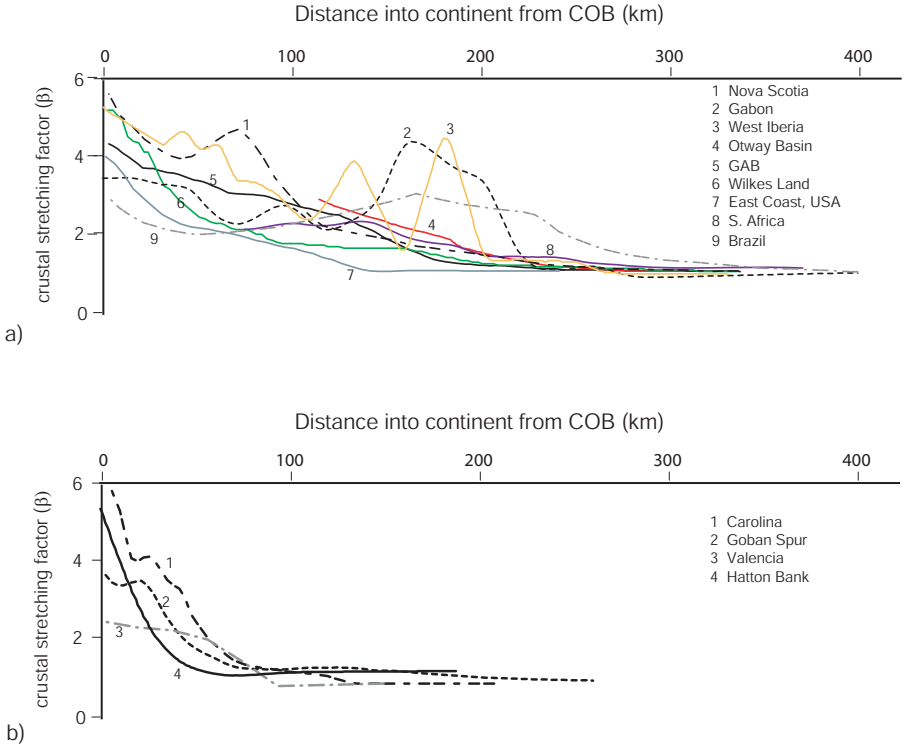

Figure 7.10: Comparison of crustal extension, as determined from a variety of methods, as a function of distance from the COB. a) Rifts where extended crust occurs up to and beyond 200 km landward of the COB, and b) narrow rifts where extension is focused within 100 km of the COB. The results from West Iberia and Gabon indicate that the locus of extension can occur at large distances from the point of eventual crustal rupture.

The results in Figure 7.10 are broadly divided on the basis of width of extended crust. The crustal thinning pattern from Wilkes Land is clearly more comparable to the patterns observed for the wider rift margins. The results from the West Iberia, Nova

Scotia, and Gabon margins indicate that crustal thinning is not confined to the region of the COB, but can occur up to 150-200 km landward of the COB. These results are similar to the observed crustal thinning pattern for eastern Wilkes Land and Terre Adélie.

The two examples of conjugate margin pairs included in Figure 7.10 (i.e. Brazil-Gabon and West Iberia-Nova Scotia) are all wider rifts that exhibit non-uniform stretching. The reasons for the large variations in crustal thinning patterns at rifted margins are not well understood. As outlined in Chapter 1, rift margin evolution is a complex function of the geotherm, rheology, lithospheric strength, extension and strain rates, and thermal processes.

Modelling (e.g. Bassi [1991], Bassi [1995], Buck *et al.* [1999]) and geological observations (e.g. Taylor *et al.* [1995], Pérez-Gussinyé *et al.* [2001]) indicate that wider rifts, with variable loci of extension, and a broad COT zone are associated with lower strain rates, which allow greater heat loss and, therefore, rheological hardening during rifting and a corresponding increase in strength. Whereas, narrow rift margins are associated with rapid extension, high strain rates, and, therefore, less heat loss and a greater propensity for melt generation and magmatism. Davis & Kusznir [2002], however, demonstrate that there is a continuum of rifted margin widths from ∼50 km to almost 500 km. This emphasises that the large number of factors involved in controlling rift margin formation can interact over a wide range and produce the great variety of rifted margin styles and structures observed.

7.3.2 Oceanic Crust Depth Anomalies

The rate and magnitude of oceanic crust subsidence does not depend on extension, as for rifted continental crust, but rather on thermal contraction and, therefore, time since emplacement or age (e.g. Sclater & Francheteau [1970]). Therefore, where the age of oceanic crust is constrained, normally by the correlation of magnetic anomalies with the geomagnetic reversal time scale, its depth can be relatively accurately predicted.

Parsons & Sclater [1977] demonstrated a linear relationship between the depth to oceanic crust and $\sqrt{t}$, where t is the age of the oceanic crust, which applies for $t < 60$ Ma. They showed that for older crust that this relationship breaks down, and that depth decays exponentially with age toward a constant asymptotic value. Parsons & Sclater [1977] predict oceanic crust to subside according to the following relationship for $0 < t < 60$ Ma,

$$D_t = 2500 + 350\sqrt{t} \tag{7.1}$$

and for $t > 60$ Ma,

$$D_t = 6400 - 3200e^{(\frac{-t}{62.8})} \tag{7.2}$$

Where D_t (metres) is the depth of oceanic crust at time t. The data used by Parsons & Sclater [1977] to derive these relationships were taken from the Atlantic and north Pacific Oceans only. However, Marty & Cazenave [1989] demonstrated that data from almost all oceanic plates are characterised by similar trends for young oceanic crust. In contrast to Parsons & Sclater [1977], they suggest that there is no asymptotic flattening and that oceanic crust continues to subside proportional to $\sqrt{t}$ indefinitely. Using an algorithm to remove small-scale consructional features on oceanic crust, Hillier & Watts [2005], however, confirm the plate-like subsidence of oceanic crust and asymptotic flattening in general accord with Parsons & Sclater [1977].

Where oceanic crust is sediment loaded it will have subsided to a greater depth than predicted by Equations 7.1 and 7.2. Therefore, to compare observed and predicted oceanic crust depths it is necessary to backstrip sediments to determine the depth to which the crust would have subsided in the absence of sediments. The difference in the observed (backstripped where sediment loaded) and predicted depth of oceanic crust is termed a *depth anomaly*.

Figure 7.11 compares the observed and predicted depths of oceanic crust for western, central and eastern Wilkes Land as a function of crust age. The observed depths are based on the anomaly identifications summarised in Figure 5.14. Predicted depths are calculated for both Equations 7.1 (curve 1) and 7.2 (curve 2), the depths predicted by these two equations do not diverge until after ~60 Ma. A third predicted depth curve is plotted based on Equation 7.2, with a constant shift of -600 m added (curve 3).

Figure 7.11 illustrates a consistent trend of deeper than predicted oceanic crust for the extent of the Wilkes Land margin. The only data points which do not conform to this trend are for Chron 33r aged crust on Line GA-228_20 and for Chron 20 and 21 aged crust on Line GA-229_06. The spurious result for Line GA-228_20 is likely associated with greater error due to the large sediment accumulation and uncertainty in identifying anomaly 33r on this line, it is possible that basement comprises transition zone rather than oceanic crust at this location. The correlation between the predicted depths for curves 1 and 2 and the observed depth for Chrons 20 and 21 on Line GA-229_06 may indicate that the ARB represents the eastern extent of anomalously deep oceanic crust. However, there is insufficient data to confidently infer this.

The magnitude of depth anomalies range from 200-800 m. There is no clear correlation between the age of the oceanic crust and the magnitude of the depth anomaly. Predicted depth curve 3, shifted -600 m relative to curve 2, provides the best fit to observed depths. This indicates that the depth anomalies are likely associated with a greater depth of zero-age crust at the SEIR relative to the Atlantic mid-ocean ridge and the Pacific spreading ridge system.

Figure 7.12 illustrates the distribution and magnitude of inferred depth anomalies off the Wilkes Land margin. There is no clear correlation between latitude and/or longitude and the magnitude of the inferred depth anomalies. However, the greatest magnitude anomalies are observed from ~120-136°E.

The results of this study, with regards the magnitude and approximate lateral extent, accord with previous interpretations of depth anomalies in the AAB associated with the Australia-Antarctica Discordance (AAD). The cause of the great depth of oceanic crust associated with the AAD has not been determined absolutely. Hayes & Conolly [1972] suggested that the observed depth anomalies are associated with a downwelling convective current in the asthenosphere. This interpretation was later supported by other workers (e.g.

Gurnis *et al.* [1998] suggest that the great depth of the AAD is associated with the Mesozoic subduction of Pacific ocean crust beneath the eastern margin of Australia. Geochemical data supports the notion of distinct mantle sources east and west of the AAD (Figure 2.16). This is cited by Gurnis *et al.* [1998] as evidence of the intersection at depth of the present-day SEIR and the ancient subduction zone which is plunging westwards.

Although the origin of the AAD remains enigmatic, the evidence for oceanic crust at anomalously great depths is well established. The results of this study provide some of the first regional estimates of the depth of unloaded oceanic crust along the extent of the Wilkes Land margin. With further improvements in dating of the oceanic crust and definition of the three-dimensional sediment distribution, it will be possible to better constrain the spatial and temporal extents of the AAD.

7.3.3 Ice Loading and Flexure

In addition to subsidence associated with the extension of continental crust and the cooling of oceanic crust, and sediment loading, high latitude margins are subject to load induced (e.g. glaciers and ice-sheets) subsidence and uplift. The East Antarctic Ice Sheet (EAIS) covers almost all of East Antarctica. Ice thicknesses of up to 4500 m occur locally and an average of 2500 m is observed for East Antarctica. The EAIS is isostatically supported almost entirely by the continental lithosphere of East Antarctica.

The flexural compensation of the EAIS explains, in part, the great depth of the continental shelf of Antarctica (e.g. ten Brink *et al.* [1995]). Although the ice sheet does not directly load the continental shelf (except during glacial maxima), the flexural response of the lithosphere results in a deepened continental shelf. Kagami [1995] suggested that the flexural response may extend beyond the continental shelf and manifest itself as crustal

upwarping beneath the continental rise (Figure 7.13).

A domed or upwarped basement has been observed in seismic reflection data off eastern Wilkes Land in a number of studies (e.g. Eittreim & Smith [1987], Tanahashi *et al.* [1987]). The landward extents of Lines GA-228_23 and GA-228_24 exhibit an upwarp of the *tur* unconformity that correlates to the doming identified in other studies. Kagami [1995] suggests that the region that is now upwarped originally subsided to a greater depth and was characterised by normal faults and seaward increasing subsidence. He suggested that the weight of the ice sheet was the main factor that contributed to an adjustment in the basement structure and resulted in upwarping.

A simple two-dimensional model, as illustrated in Figure 7.14, demonstrates that the upwarped structure observed in seismic reflection data is not associated with flexure due to ice sheet loading. Three-dimensional models were also tested, however, as the thickness of the EAIS does not vary rapidly laterally, the results are almost identical to two-dimensional models. A range of T_e estimates were tested and a spatially varying T_e model, varying from 100 km inland to 30 km at the margin, was also tested.

The model comprises a 3000 m thick ice sheet that terminates at the inner-limit of a 100 km wide continental shelf. This thickness of ice is representative of the ice-thickness for most of the EAIS in the Wilkes Land region. Ice sheet induced flexure deepens the inner limit of the continental shelf by ∼200-400 m depending on the T_e assumed in modelling. Whether or not a landward dipping continental shelf results is a function of the depth assumed for the shelf break. Although the downwarping of the continental shelf is as much as 400 m, the magnitude of the flexural bulge is less than 50 m for all T_e estimates tested. Therefore, it is unlikely that the 1-2 km of doming that is observed on the Wilkes Land margin is associated with ice sheet development in the Tertiary.

Three-dimensional flexural modelling of the Antarctic lithosphere, due to the load of the EAIS, was also carried out. The results of this modelling indicate that due to the long wavelength represented by the load of the EAIS, it is effectively locally compensated. Accordingly, there is very little difference in the modelled flexure predicted for a wide range of T_e estimates. The results proximal to the margins of Antarctica, where variations in flexure occur with changes in T_e, are almost identical to the simple two-dimensional model detailed above.

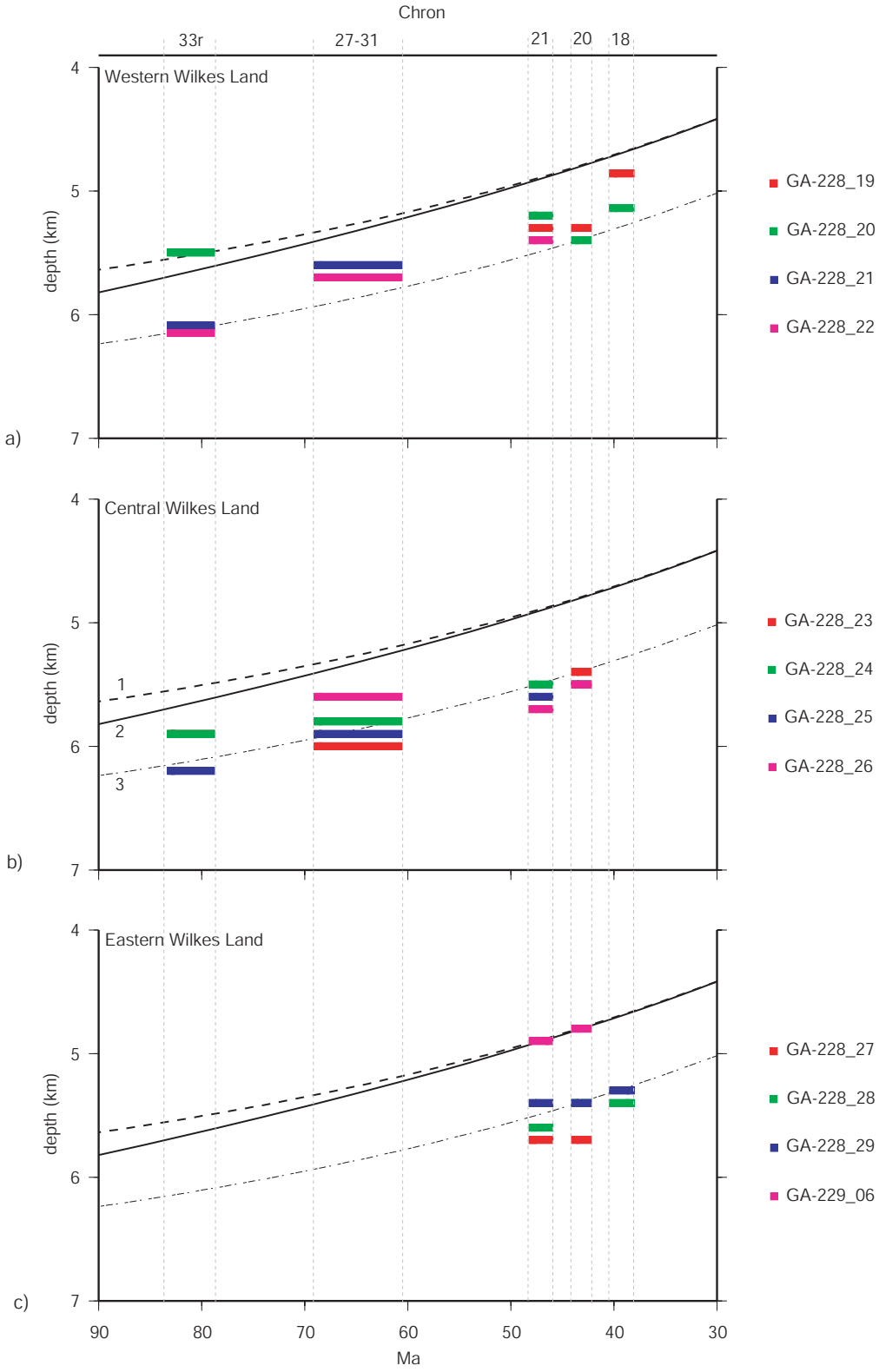

Figure 7.11: Comparison of predicted and backstripped depths of top of oceanic crust layer 2 for a) western, b) central, and c) eastern Wilkes Land. The predicted depth curves are based on Parsons & Sclater [1977] for $0 < t <\sim 70$ Ma (curve 1) and for $t >\sim 70$ Ma (curve 2), where t is the age of oceanic crust. Curve 3 is for $t >\sim 70$ Ma shifted by -600 m, this curve provides a better fit to the observed depths.

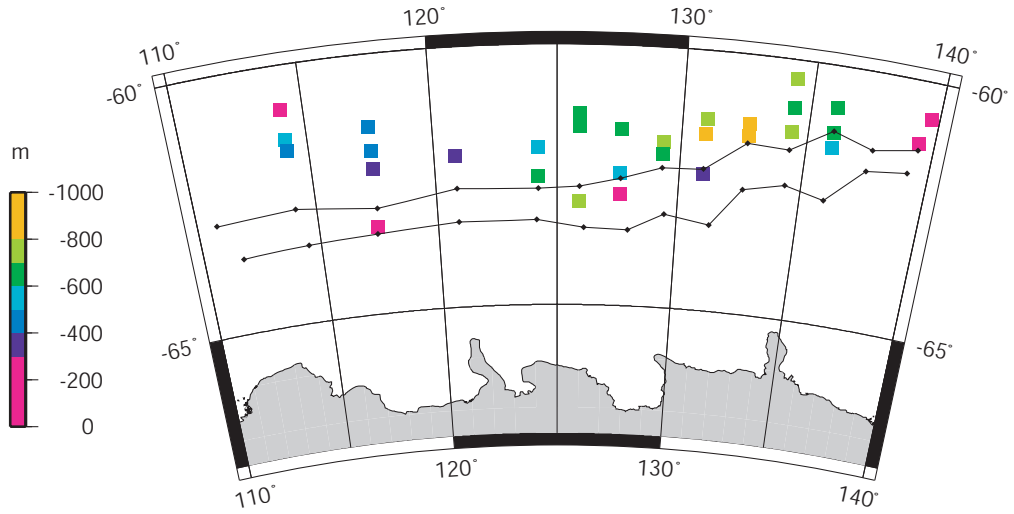

Figure 7.12: Depth anomalies calculated using the theoretical subsidence of Parsons & Sclater [1977] and the backstripped depth of oceanic crust observed on GA-228 and GA-229 survey lines. There is no spatial correlation of depth anomaly magnitude. The COT zone interpreted from MCS data (Figure 4.23) is shown (black solid lines).

Figure 7.13: The Kagami [1995] schematic model for upward arched basement at the Wilkes Land margin. Kagami [1995] attributed the uparched basement to the flexural compensation of ice sheet loading. OC = oceanic crust, M = mantle.

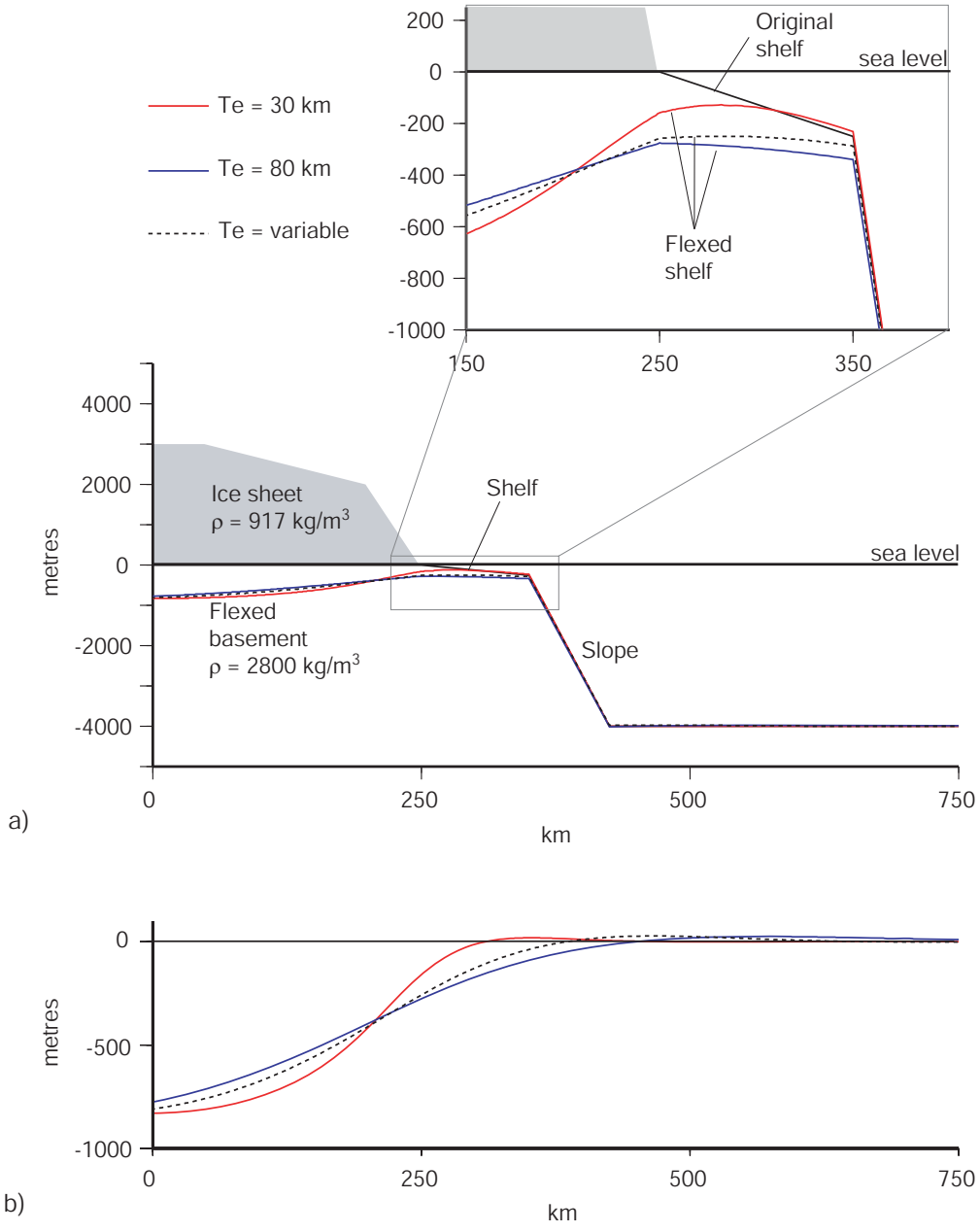

Figure 7.14: a) Model of ice sheet induced flexure and its modifying effect on a simplified margin morphology. The inset figure demonstrates the minor contribution of ice sheet loading to the great depth of the Antarctic continental shelf, except for the inner shelf. b) The flexure associated with the ice sheet load illustrated in (a), the amplitude of the flexural bulge does not exceed 50 m.

7.4 Conjugate Margin Structure

7.4.1 Regional Setting

Australia is a low elevation, stable continental mass where active volcanoes are absent and large earthquakes rare. The majority of the land mass comprises the Australian Precambrian Shield (e.g. Ludbrook [1980]). The Shield is a composite of blocks that became stable during the Proterozoic and have not been subjected to major tectonism since (Figure 7.15). The oldest rocks occur within the Pilbara and Yilgarn Blocks of Western Australia. The *Tasman Line* (e.g. Murray *et al.* [1989]) broadly divides the western terrane of Precambrian blocks from the Phanerozoic fold belt systems of eastern Australia [Direen & Crawford, 2003]. The southern margin of Australia comprises a number of distinct blocks, from the Yilgarn Block in the west to structurally complex Cambrian terranes of western Tasmania in the east (e.g. Meffre *et al.* [2000]).

Figure 7.15: Major structural elements of Australia, from Ludbrook [1980]. The Tasman Line represents the structural boundary between the Australian Precambrian Shield to the west and the Phanerozoic fold belt systems to the east.

The basins of the southern margin are largely a product of protracted extension throughout eastern Gondwana from the Jurassic to the Cretaceous, which led to the development of the Southern Rift System (SRS) [Willcox & Stagg, 1990]. The extension resulted in the final breakup of what are now the Australian and Antarctic Plates in the Late Cretaceous, as discussed previously. The SRS, comprising the Great Australian Bight (GAB), Otway, and Sorell Basins, extends for more than 4000 km, from the Naturaliste Plateau in the west to the South Tasman Rise (STR) in the southeast (Figure 7.16). The Bass Strait region represents a major splay of the SRS that separates the continental crust of the Australian mainland and Tasmania.

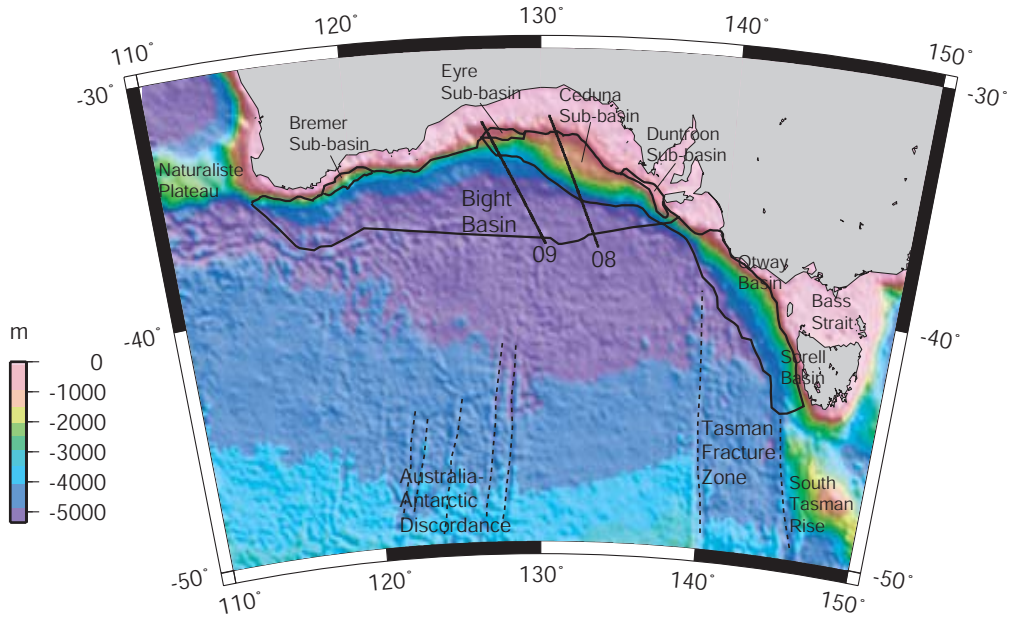

Figure 7.16: Location of the Bight Basin (with component sub-basins), Otway Basin, and Sorell Basin, which together form the Southern Rift System (SRS). Transects 08 and 09 are the location of seismic reflection profiles illustrated in Figure 7.17.

The GAB basin, or Bight Basin [Totterdell *et al.*, 2000], is the most areally significant of the SRS basins, extending from the southwest tip of Australia to ∼140°E. The Bight Basin contains five main depocentres; they are, from west to east, the Bremer, Recherche, Eyre, Ceduna, and Duntroon sub-basins [Totterdell & Bradshaw, 2004]. The Bight Basin underlies the continental shelf and slope, including two bathymetric terraces, in water depths ranging from 200 to over 4000 m. The largest and thickest depocentre, the Ceduna Sub-basin, comprises a sedimentary sequence of >15 km thickness [Totterdell *et al.*, 2000]. The breakup unconformity within the Bight Basin is interpreted as the approximately Turonian aged base of the Tiger Super-Sequence [Totterdell *et al.*, 2000].

To the east of the Bight Basin are the Otway and Sorell Basins, which are located in

a region where continental separation failed to continue eastward but was instead offset to the south by the Tasman Fracture System west of Tasmania [Moore *et al.*, 2000]. The breakup unconformity within the Otway and Sorell basins was interpreted as the top of the Sherbrook Group (∼64 Ma) by Moore *et al.* [2000].

The STR occurs ∼200 km south of Tasmania approximately along strike of the Tasman Fracture System from the Sorell Basin. It consists of a triangular core of Palaeozoic basement, flanked by basins containing up to 6 km of sediments Stagg *et al.* [1999]. Willcox *et al.* [1989] correlated the seismic sequences in these basins, on the basis of seismic character, to the Otway Basin. They inferred that the STR may have been conjugate to the Otway Basin prior to the Late Cretaceous.

Sediment Distribution

The SRS, particularly the Bight Basin, is characterised by very thin Cainozoic sediments. Because of the arid climate and low elevation of most of southern Australia, the SRS has been sediment starved throughout the Tertiary. Even the great thickness of sediments in the Ceduna Sub-basin was deposited almost entirely throughout the Jurassic and Cretaceous. Figure 7.17 illustrates the thickness of seismic-stratigraphic units, based on the interpretation of Totterdell *et al.* [2000], for two profiles across the GAB margin.

Both transects are characterised by very thin Tertiary sequences, of less than 1000 m. However, the thickness of Cretaceous sediments on Lines 08 and 09 is markedly different. Line 08, which traverses the Ceduna Terrace and Sub-basin, is characterised by a thick (up to 6000 m) Turonian to Santonian (syn-rift?) sequence, and a similarly thick Santonian to Tertiary, lower post-rift sequence. A hiatus in sedimentation is inferred for most the Palaeocene and the erosional upper surface of the lower post-rift sequence is unconformably overlain by the basal units of the Eocene and younger upper post-rift sediments. In contrast, the maximum syn- and post-rift sediment thickness on Line 08 is less than 2000 m.

Figure 7.18 illustrates the total sediment isopach for the Bight Basin [Totterdell & Krassay, 2003]. The great thickness of sediments in the Ceduna Sub-basin is evident, however, a large proportion of this is pre- and syn-rift. No regional post-rift sediment thickness grid is available for the entire Bight Basin due to data limitations.

The great thickness of sediments within Ceduna Sub-basin is attributed to deposition by high sediment flux, delta progradation [Totterdell *et al.*, 2000; Totterdell & Bradshaw, 2004]. Basins outside of this region received relatively low sediment input throughout the Late Cretaceous. Since the Early Tertiary the entire Bight Basin and the Otway basin have been sediment starved, although sedimentation continues in the Sorell Basin

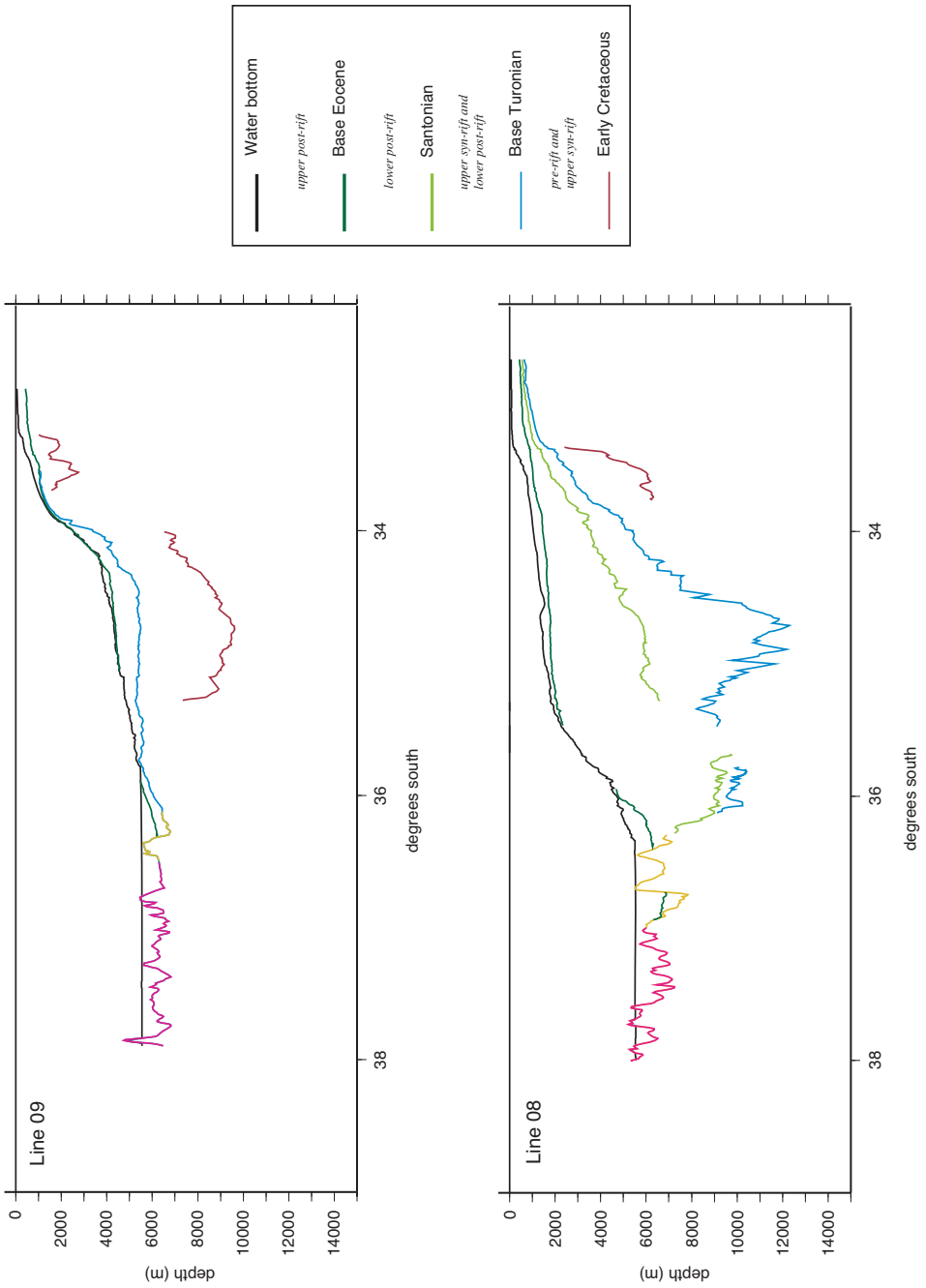

Figure 7.17: Seismic-stratigraphy from Totterdell *et al.* [2000] for two seismic reflection profiles across the Bight Basin, as located in Figure 7.16. Profile 08 traverses the Ceduna Sub-basin, whereas profile 09 is located to the west and is characterised by a much thinner sedimentary sequence.

off western Tasmania.

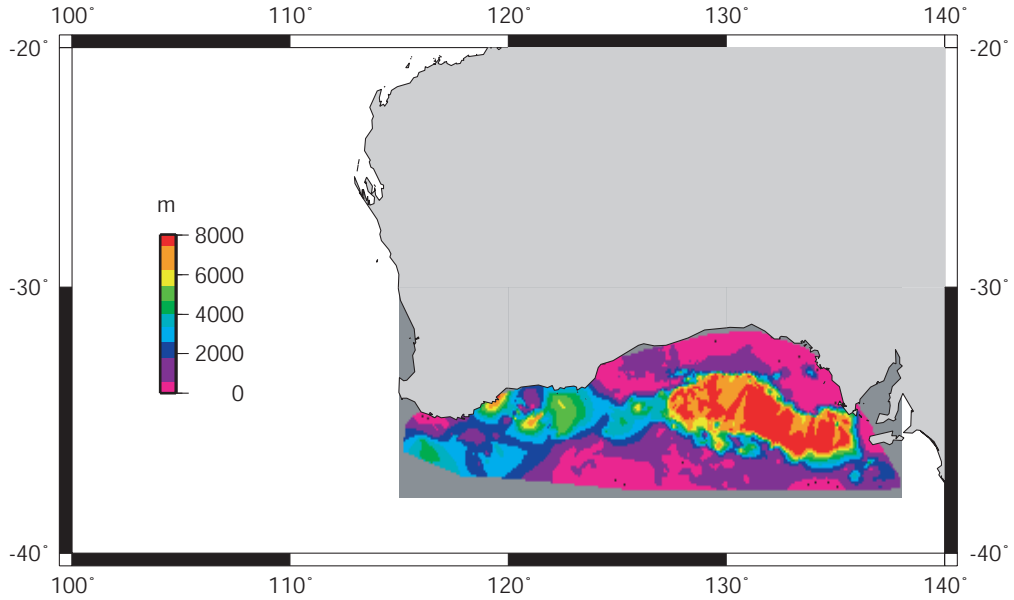

Figure 7.18: Total sediment isopach (including pre-, syn- and post-rift sediments) for the Bight Basin of the southern Australian margin. The Ceduna Sub-basin is the locus of thickest sediments. Data from Geoscience Australia [Totterdell & Krassay, 2003], resolution is nominally ∼3 minute.

Crustal Structure

Constraints on crustal structure and thickness for the Australian continent and its margins are sparse. However, Collins *et al.* [2003] estimate that ∼73% of onshore continental Australia is characterised by a crustal thickness of 35-41 km using seismic refraction data. Data from the onshore sector of the southern Australian margin is particularly sparse. Figure 7.19 illustrates velocity depth curves from the Yilgarn Block of southwest Australia, and from Tasmania. A shallower depth to *Moho* is inferred for Tasmania relative to the far west of Australia. Crustal thickness estimates for the southern margin vary along-strike from 30-35 km (e.g. Collins *et al.* [2003], Brown *et al.* [2003]).

Figure 7.19: Velocity-depth curves for the Yilgarn Block (southwest Australia) and Tasmania (see Figure 7.15 for location of the blocks). Grey shading marks the range of *Moho* depths for each location. After Collins *et al.* [2003].

Estimates of *Moho* depth offshore of the southern Australian margin are based on sonobuoy refraction and seismic reflection data only. Ocean Bottom Seismometer (OBS) data exists for a small portion of the Otway Basin margin only. Figure 7.20 shows the location of sonobuoy data, where *Moho* velocities have been interpreted, from Geoscience Australia Survey 199 [Sayers *et al.*, 2001] and *Vema* Cruise 33 [Talwani *et al.*, 1978]. The depth to the sea floor and *Moho* are summarised for each of these sonobuoy locations in Table 7.2.

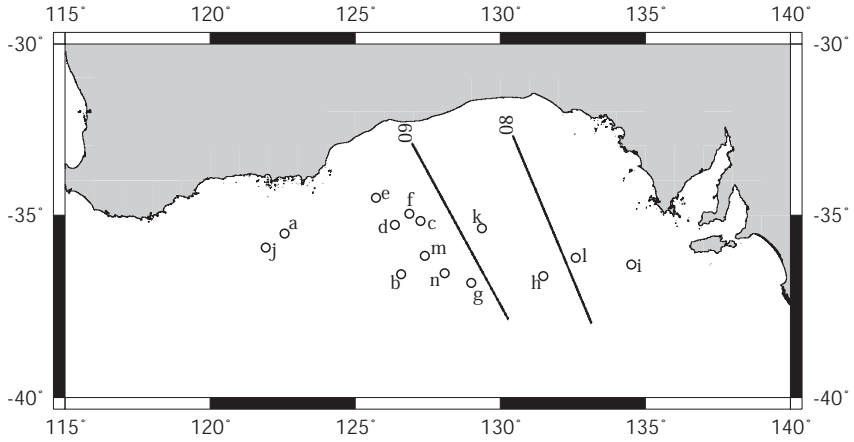

Figure 7.20: Sonobuoy locations for the Bight Basin (circles), with labels referring to Table 7.2. Profiles 08 and 09 are as illustrated in Figure 7.17.

7.4.2 Process-Oriented Modelling

Two-dimensional process-oriented modelling was undertaken for profiles 08 and 09 across the Bight Basin. Three-dimensional modelling was also conducted, on both the total sediment thickness and on sediment thickness grids adjusted to exclude pre- and syn-rift sediments. The applied methodology and parameters were identical to that outlined in Chapter 6, unless specifically stated otherwise (i.e. densities etc. as per Table 6.2).

Two-Dimensional Process Oriented Modelling

Figures 7.21 and 7.22 illustrate the results of process-oriented modelling for Lines 09 and 08 respectively. An initial, zero-elevation, crustal thickness (T_c) was selected such that the depth the flexed *Moho* was broadly in accord with the depth to *Moho* interpreted from off-line sonobuoys projected onto the 08 and 09 profiles. As the calculated gravity is relatively insensitive to T_c, this is the only constraint available.

Modelling on Line 09 is not sensitive to T_e as there is only a very thin post-rift sedimentary sequence in this region. The results are not altered by including the syn-

SB	cruise	station	long.	lat.	wb (km)	*Moho* (km)
a	*Vema* 33	6	122.57	-35.52	4.69	13.5
b	*Vema* 33	8	126.59	-36.65	5.59	12.0
c	*Vema* 33	11	127.25	-35.16	5.0	14.4
d	*Vema* 33	12	126.37	-35.27	5.05	13.0
e	*Vema* 33	13	125.72	-34.50	4.03	13.8
f	*Vema* 33	15	126.86	-34.95	4.57	16.7
g	*Vema* 33	16	129.00	-36.89	5.61	11.2
h	*Vema* 33	19	131.48	-36.71	5.61	11.7
i	*Vema* 33	21	134.52	-36.39	5.0	15.6
j	*Vema* 33	27	121.91	-35.91	5.05	13.0
k	*Vema* 33	36	-35.37	129.36	5.03	15.8
l	*Vema* 33	40	132.60	-36.20	5.03	15.8
m	GA 199	2	127.40	-36.15	5.5	15.7
n	GA 199	5	128.08	-36.62	5.5	14.1

Table 7.2: Sonobuoy (SB) data which have recorded mantle velocities in the Bight Basin, southern Australia, as located in Figure 7.20. wb = water bottom.

rift sediments (Tiger Supersequence Totterdell *et al.* [2000]), along with the post-rift sediments, in modelling. The edge effect high is well simulated by the calculated profiles for all T_e estimates tested. However, the magnitude of the edge effect low is not reached for any T_e estimate. The positive seaward gradient exhibited by the observed data is simulated by the calculated profiles, however, inferring the T_e via process-oriented modelling is not possible for this line.

Although T_e can not be constrained for Line 09 due to a lack of sediment loading since rifting, the number of sonobuoy stations where mantle velocities have been interpreted in the vicinity (within ∼100 km) of this line allow T_c to be constrained. For $T_c > 31$ km the flexed *Moho* is almost ubiquitously deeper than the sonobuoy inferred *Moho* depths. For $T_c = 31$ km, the modelled flexed *Moho* depth occurs within the range of *Moho* depths inferred from sonobuoys.

Survey 199 Line 08 is much more sensitive to T_e variation in process-oriented modelling. This is primarily because of the greater sediment thickness relative to Line 09 to the west. Due to the relatively shallow submarine extension of the Ceduna Terrace, there are effectively two edge effect anomalies across this line, one at the shelf break proper, and another further seaward at the change in slope across the terrace at ∼35°S. The large magnitude positive anomaly that correlates with the change in slope of the terrace

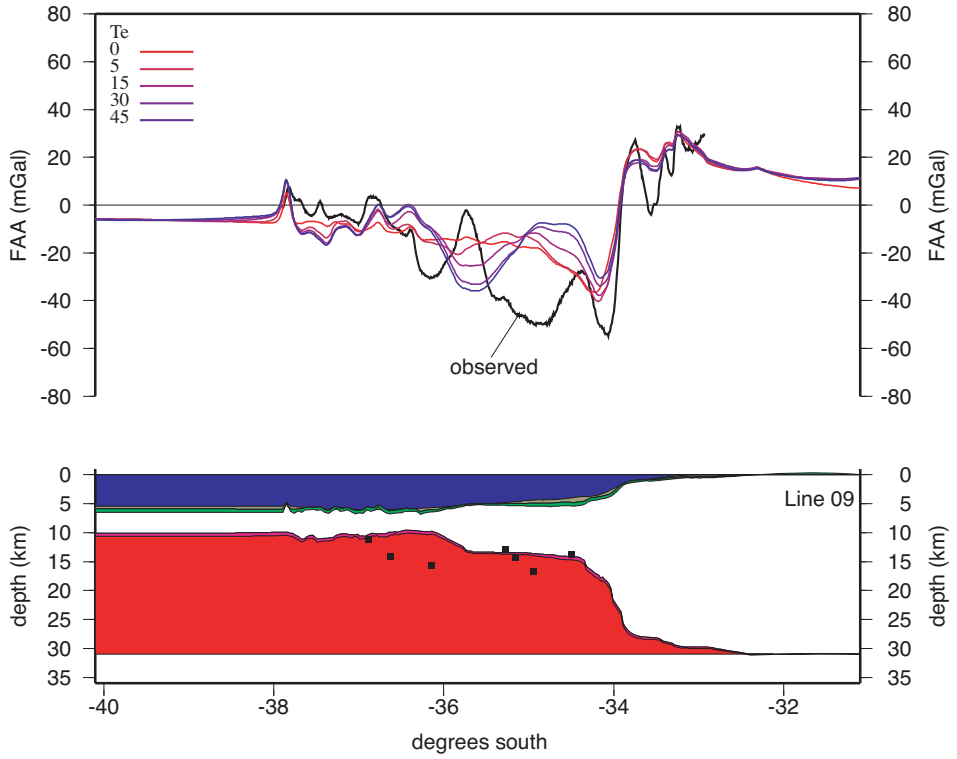

Figure 7.21: Process-oriented modelling for GA survey Line 09, as located in Figure 7.20. Black squares indicate the depth to *Moho* inferred from sonobuoy data projected laterally onto this section. Observed data is shiptrack measured gravity. Crustal section is for $T_e = 15$ km.

is also coincident with the locus of thickest sediments on this line.

Modelling with low T_e ($\leq$10 km) under-estimates the magnitude of the positive anomaly over the thickest sediments and over-estimates the magnitude of the edge effect high. Conversely, for high T_e ($\geq$30 km) the edge effect high is under-estimated and the high over the thickest sediments is over-estimated (along with the low seaward of this high). However, for T_e=15 km a good fit is achieved between calculated and observed anomalies. The shape and amplitude of the observed anomalies are almost perfectly simulated by the calculated profile. This indicates that the lithosphere underlying this region of the Bight Basin is characterised by T_e=15 km.

Although the T_e can be well-constrained for Line 09, it is more difficult to determine T_c due to the lack of seismic refraction and/or reflection data that images the *Moho* in this region. A slightly higher T_c of 33 km was assumed in modelling of this line, however, it is not possible to confidently infer T_c more accurately than by the range of $31 < T_c < 35$ km. The T_c does not exert a strong influence on the calculated gravity anomaly profile, however, the determination of crustal stretching factors is strongly dependent upon the

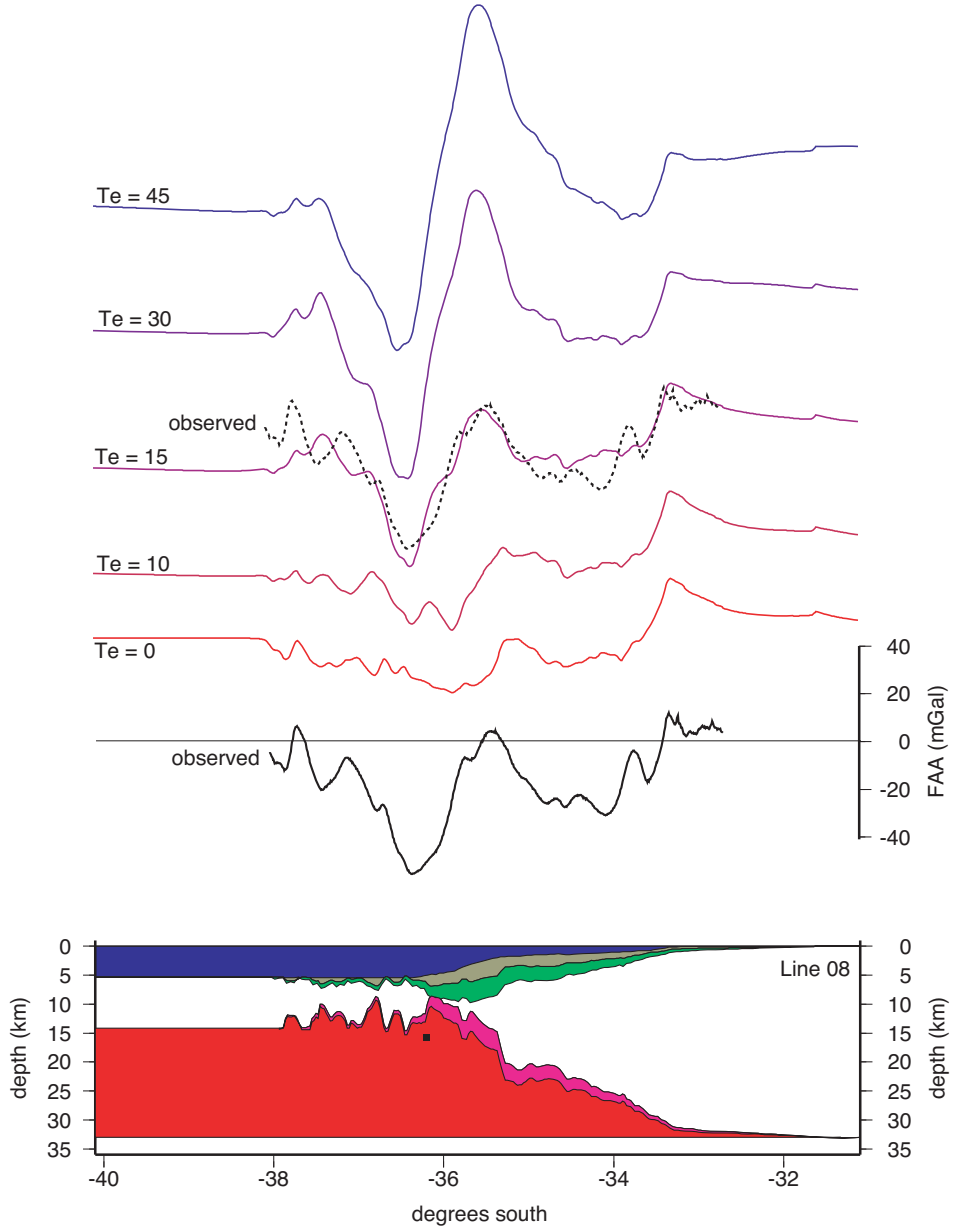

Figure 7.22: Process-oriented modelling for GA survey Line 08, as located in Figure 7.20. Black square indicates the depth to *Moho* inferred from sonobuoy data projected laterally onto this section. Observed data is shiptrack measured gravity. The calculated anomaly profile for T_e=15 km accurately simulates all features of the observed data. Crustal section is for $T_e = 15$ km.

assumed T_c.

Three-Dimensional Process Oriented Modelling

Three-dimensional gravity modelling was undertaken. The classic-Airy model isostatic anomaly was calculated for the entire southern Australian margin region using GEBCO 1 minute bathymetry [IOC *et al.*, 2003]. However, process-oriented modelling was conducted for the Bight Basin region of the margin only, as a sediment thickness grid is not available beyond this region.

Figure 7.23 shows the satellite derived free air gravity field [Sandwell & Smith, 1997] for the southern Australian margin[1], the classic-Airy modelled free air gravity field, and the classic-Airy isostatic anomaly. The free air field is characterised by a continuous, but relatively subdued, edge effect high and a broad, large amplitude edge effect low. The classic-Airy model simulates the broad character of the observed free air gravity field, however, it fails to predict the full extent of the observed edge effect low and some small sections of the edge effect high (e.g. 115-125°E).

The Ceduna Terrace region correlates to a positive free air anomaly in the classic-Airy model, however, the observed field is largely negative, except for the seaward edge of the Terrace. The classic-Airy isostatic anomaly map illustrates that although a large amount of the observed free air gravity field can be explained by the Airy compensation of the water filled basin, there is sufficient complexity such that a simple Airy model, which does not account for the presence of sediments, is inadequate.

Three-dimensional process-oriented modelling was undertaken for the Bight Basin. However, although the total sediment thickness is known for this region, the relative thickness of pre-, syn- and post-rift sediment is not constrained. Analysis of survey 199 Line 08 illustrated that in the Ceduna Sub-basin, the locus of thickest sediments in the Bight Basin, the pre- and syn-rift sediments comprised up to half of the total sediment thickness. Backstripping and gravity modelling of the total sediment thickness is, therefore, clearly not comparable to the methodology adopted for the Wilkes Land margin where only post-rift sediments were considered.

Process-oriented modelling was initially conducted using the total sediment isopach, clipped to a maximum thickness equivalent to the maximum observed post-rift sediment thickness (∼8000 m) (case 1). This is obviously an over-estimation of the *average* post-rift sediment thickness. Therefore, modelling was subsequently undertaken assuming a ratio of 1:1 for pre- and syn-rift, and post-rift sediment thickness (i.e. half the total sediment thickness was assumed to be post-rift) (case 2). Figure 7.24 illustrates flexural isostatic anomaly maps of the Bight Basin region, for three T_e estimates, for both

[1] After removal of wavelengths greater than ∼3333 km ($n = 12$) according to the geopotential coefficient model of Rapp & Pavlis [1990]

sediment thickness cases considered.

For T_e=0 km, the results for sediment thickness cases 1 and 2 are very similar. Neither are fully devoid of the residual edge effect low, and both almost entirely account for the edge effect high. For higher T_e the results for cases 1 and 2 diverge further. The differences are most evident in the region of the Ceduna Sub-basin and the thickest sediments. Larger isostatic anomalies are associated with the greater sediment thickness of case 1. The differences are substantial for T_e=30 km, a large amplitude negative anomaly occurs in the region of the Ceduna Sub-basin for both cases, however, the amplitude and size of the anomaly is much greater for case 1. Lower T_e models clearly more accurately simulate the observed gravity data.

Although in general a low T_e ($\sim$15 km) is inferred for the Bight Basin region, specific regions are best fit by higher and lower T_e estimates. For example, the positive linear FIA off the south-west margin sector is effectively reduced by different T_e estimates in different lateral segments. Circled areas in Figure 7.24 illustrate that the margin may be segmented to some degree with regards to T_e structure. To confirm this, a detailed knowledge of the thickness of post-rift sediments is required for the entire Bight Basin region.

Spectral analyses of flexural isostatic anomalies and the satellite derived FAA (Figure 7.25) confirm that the Bight Basin region is characterised by low T_e ($\leq$15 km). Two distinct peaks are evident in the FAA power spectrum, at wavelengths of $\sim$400 and 650 km, which reach amplitudes 50 and 90 mGal^2 respectively. These peaks are reduced in the power spectra of the flexural isostatic anomalies for sediment thickness case 1 for T_e=0 and 15 km, however, for T_e=30 km the peaks are of greater magnitude relative to the FAA spectrum. This indicates that for the maximum possible post-rift sediment thickness in the Bight Basin region, the $T_e << 30$ km. For sediment thickness case 2, the peaks in the flexural isostatic anomaly power spectra are reduced relative to the FAA spectrum for T_e=0, 15 and 30 km. However, the longer wavelength peak amplitude of the T_e=0 and 15 km power spectra is less than half that of the T_e=30 km spectrum. This indicates that even for the minimum likely post-rift sediment thickness, a $T_e < 30$ km best characterises the Bight Basin.

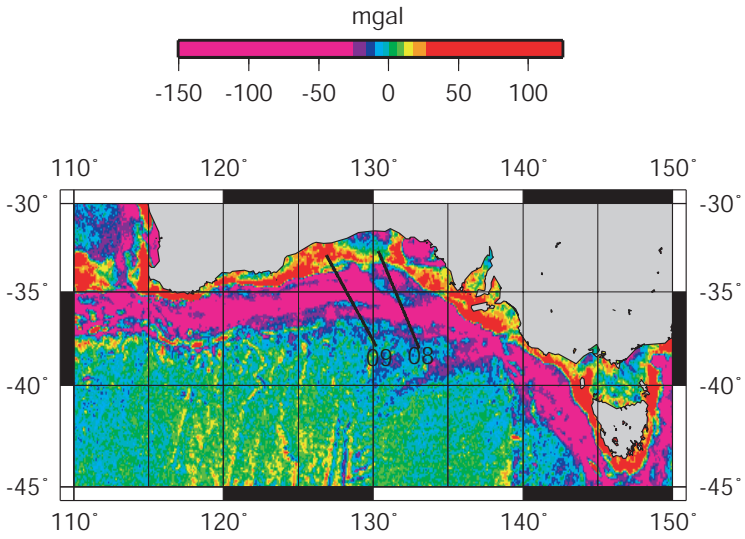

a) Observed free air anomaly

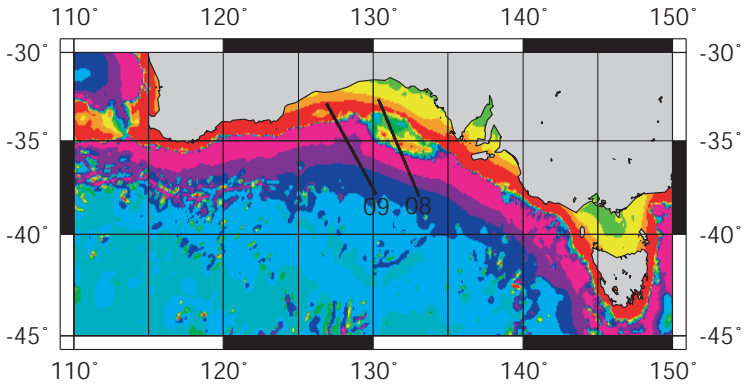

b) Classic-Airy modelled free air anomaly

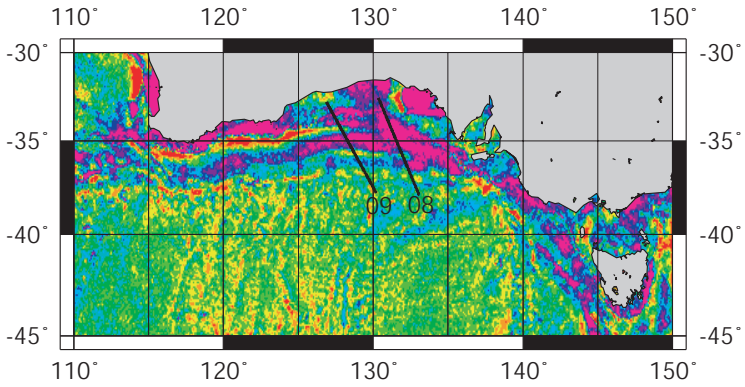

c) Classic-Airy model isostatic anomaly

Figure 7.23: a) Satellite derived free air anomaly map of the southern Australian margin [Sandwell & Smith, 1997]. b) Classic-Airy modelled free air anomaly map based on GEBCO 1 minute bathymetry [IOC *et al.*, 2003]. c) Classic-Airy isostatic anomaly map, which illustrates the failure of the classic-Airy model to predict the large amplitude edge effect low.

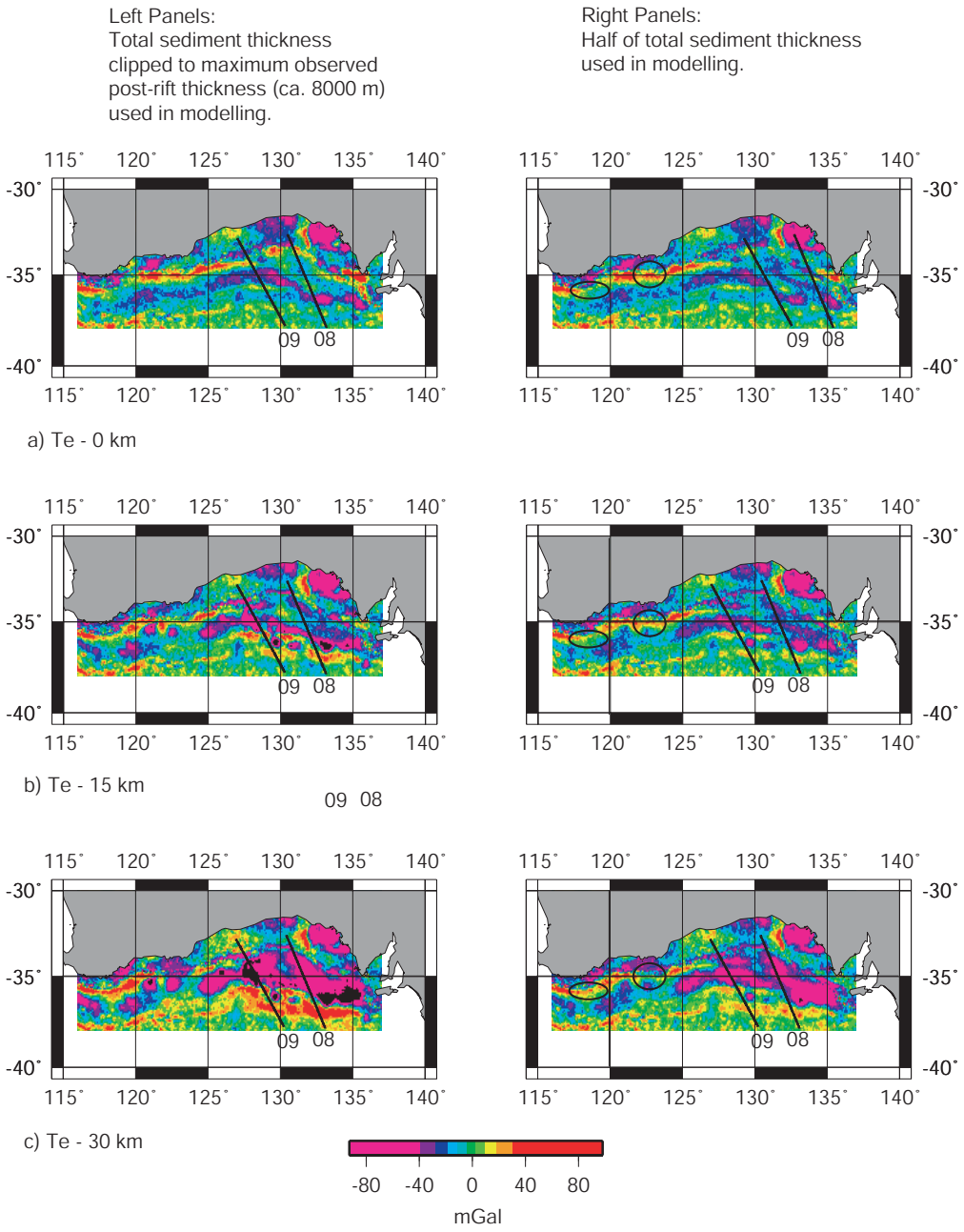

Figure 7.24: Flexural isostatic anomaly maps of the Bight Basin region for a) T_e=0 km, b) T_e=15 km, and c) T_e=30 km. Left panels were calculated assuming the maximum possible post-rift sediment thickness. Right panels were calculated assuming that half of the total sediment thickness comprises post-rift sediments, a more realistic assumption. The broad trends for both cases are similar.

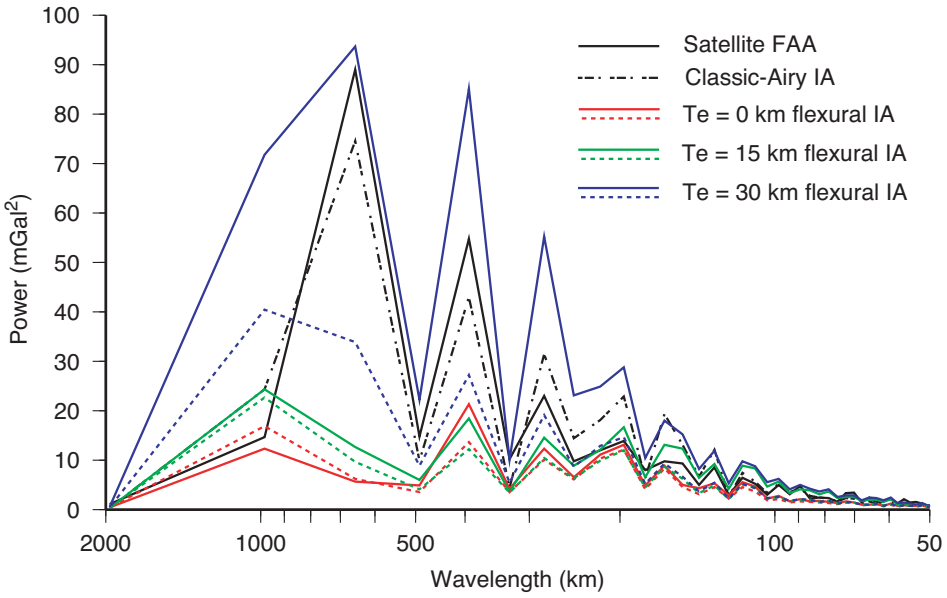

Figure 7.25: Spectral analyses of free air anomaly and isostatic anomaly data for the Bight Basin region. Solid and dashed flexural isostatic anomaly (IA) spectra are of data in the left and right panels of Figure 7.24 respectively. Power peaks are observed in the satellite derived free air anomaly (FAA) spectrum at ~400 and 650 km, these are effectively reduced for flexural IA spectra for low T_e estimates ($\leq$15 km).

7.4.3 Conjugate Margin Comparisons

Figure 7.26 illustrates the present-day bathymetry of the southern Australian and Wilkes Land margins reconstructed to Chron 18o (~40 Ma), using the rotation pole of Royer & Rollet [1997]. A tighter closure is not attempted as older anomaly lineations are, in general, poorly defined. The major differences in the conjugate margin morphology primarily reflect the disparate environments dominant on each continent throughout the Tertiary. The rugged and very deep continental shelf of Wilkes Land, for instance, is a function of extensive glacial erosion and flexural downwarping associated with the East Antarctic Ice Sheet.

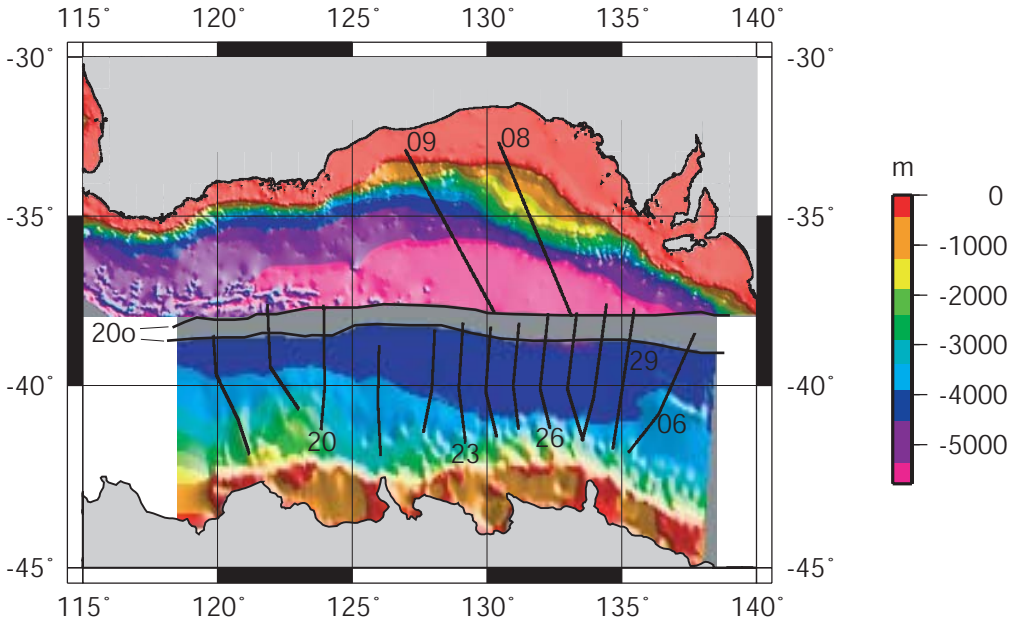

Figure 7.26: Bathymetry of the Wilkes Land and southern Australian margins reconstructed to Chron 18o (~40 Ma) and clipped at Chron 20o (~44 Ma). Reconstruction is based on the rotation pole of Royer & Rollet [1997] (rotation pole: 14.32°N, 31.75°E, and rotation angle: 23.77°).

The abyssal plain of the southern Australian margin occurs at a much greater depth (~1000 m) relative to the Wilkes Land margin. To determine whether this is a function of crustal structure or sediment thickness, and to assess the symmetry of this conjugate margin pair, conjugate profiles of bathymetry, sediment thickness, TTS, crustal structure, and inferred crustal thinning, also clipped to anomaly 20, are compared in Figure 7.27. Comparisons of the FAA and magnetic anomaly profiles are illustrated in Figure 7.28. We see in Figure 7.26 that survey 199 Lines 08 and 09, across the Bight Basin, are approximately conjugate to Lines from GA-228_22 to GA-228_27 on the Wilkes Land

margin.

The difference in abyssal plain bathymetry is, in part, explained by the thinner Tertiary sedimentary sequence on the southern Australian margin Figure 7.27a. Although the bathymetry is deeper on the southern Australian margin, the basement depth is, in general, comparable with or shallower than the sediment loaded basement of the Wilkes Land margin. Comparing the backstripped basement surfaces (i.e. the TTS) in Figure 7.27b, illustrates that the sediment corrected basement depths are comparable across Lines GA-228_22/GA-228_23 and 09. However, the TTS on Lines GA-228_26/GA-228_27 is some 1500 m shallower than the conjugate Line 08. The large calculated TTS may have contributed to the greater thickness of syn-rift and post-rift sediments observed in the region of the Ceduna Sub-basin by allowing greater accommodation space during early rift stages.

Due to the lack of constraints on $Moho$ depth on the southern Australian margin it is difficult to determine the accuracy of the calculated crustal stretching factor (β) profiles (Figure 7.27c). Therefore, establishing whether or not the pattern of extension is symmetrical across the conjugate margin sectors is difficult. Broadly, extension increases relatively linearly towards the COT across Lines GA-228_22/GA-228_23 and 09, whereas across Lines GA-228_26/GA-228_27 and 08 a sharp increase in β is observed close to the COT.

The free air anomaly pattern across this conjugate margin pair is not symmetric as illustrated in Figure 7.28a. The edge effect anomaly is subdued on the southern Australian margin relative to the Wilkes Land margin. Although both margins are characterised by almost entirely negative free air anomalies, the pattern of anomalies is not symmetric. However, this is primarily a function of the differences in the sediment distribution and morphology of the opposing margins.

The inconsistent patterns of magnetic anomaly lineations have been discussed in detail for the Wilkes Land margin in Chapter 5. Similar problems in identification of anomalies older than Chron 21 occur on the southern Australian margin (e.g. Veevers [1986], Tikku & Cande [1999]). There is very poor correlation in the magnetic anomaly pattern between Lines GA-228_26/GA-228_27 and 08 (Figure 7.28b). However, the correlation between Lines GA-228_22/GA-228_23 and their symmetry with Line 09 is improved.

In particular, the large amplitude positive magnetic anomaly at the landward extent of Lines GA-228_22/GA-228_23, attributed to upper mantle peridotite ridges, is mirrored at a similar distance landward from anomaly 20 on Line 09. This magnetic anomaly corresponds to a positive free air gravity anomaly (Figure 7.27d) and the location of the basement ridge interpreted by Sayers *et al.* [2001] as a serpentinised peridotite ridge. This symmetry indicates that the magnetic anomaly lineations previously attributed to

Chrons 22 [Weissel & Hayes, 1972] and 34 [Cande & Mutter, 1982] likely have a common origin, but one that is not associated with *normal* seafloor spreading.

The results of this study suggest that the southern Australian and Wilkes Land margins are broadly symmetrical. The total width of extended continental crust at each margin is comparable, as are the basement depths when corrected for sedimentation. This suggests that this conjugate margin pair formed in a similar way to the Iberian non-volcanic rifted margin; that is, via largely pure-shear deformation at the lithosphere scale [Brun & Beslier, 1996]. Additionally, there is no substantial evidence for upper-crustal detachment surfaces and/or lithosphere-penetrating shear zones as predicted by simple shear models which predict asymmetric rifting (e.g. Wernicke [1985]). The inferred widespread presence of upper mantle peridotites in the COT zone, of the Wilkes Land and southern Australian margins, is also analogous to the rifted Iberian margin.

This conjugate margin pair was previously interpreted as asymmetric and the product of a mixed-mode simple and pure shear extension mechanism by Etheridge *et al.* [1989] and Lister *et al.* [1991]. They interpreted the southern Australian margin as an 'upper plate' margin and the opposing Wilkes Land margin as a 'lower plate' margin. This interpretation was questioned by Sayers *et al.* [2001] on the basis of the structure of the Great Australian Bight margin of southern Australia. The additional constraints provided here, through modelling and interpretation of data from the Wilkes Land margin, supports the reassessment of Sayers *et al.* [2001] that this conjugate margin pair is most appropriately considered as the product of lithosphere-scale pure shear.

Figure 7.27(next page): Comparison of a range of observed and derived parameters for the central Wilkes Land and Bight Basin conjugate margins. Seaward ends of profiles are truncated at anomaly 20. Line labels for (b)-(d) are as in (a). Total tectonic subsidence (TTS), crustal structure and β in (b) to (d) are calculated assuming a T_e of 30 km for the Wilkes Land transects and 15 km for the Bight Basin transects. Blue circles in (b) are the expected depth of Chron 20 ($\sim$43 Ma) aged oceanic crust based on Parsons & Sclater [1977]. The boxed regions in (c) outlines the COT zone.

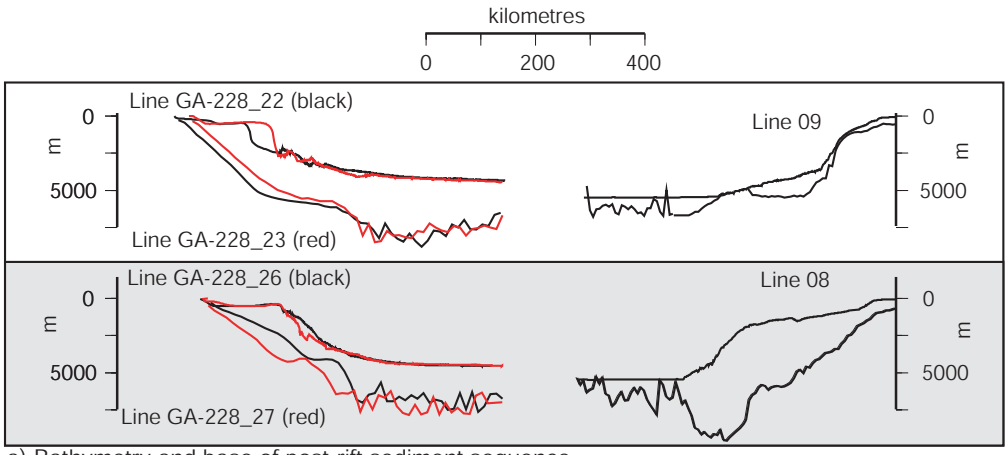

a) Bathymetry and base of post-rift sediment sequence

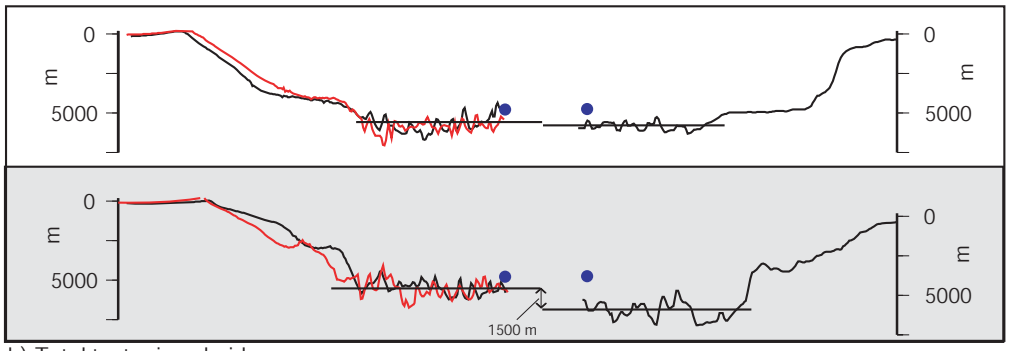

b) Total tectonic subsidence

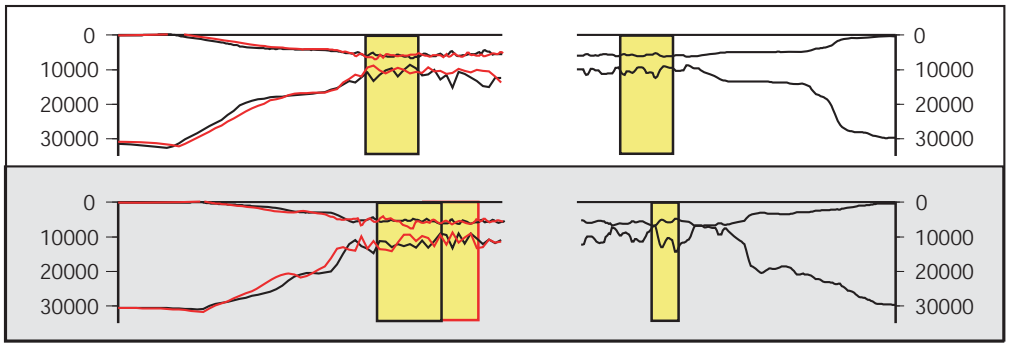

c) Crustal structure after rifting assuming Airy isostatic compensation

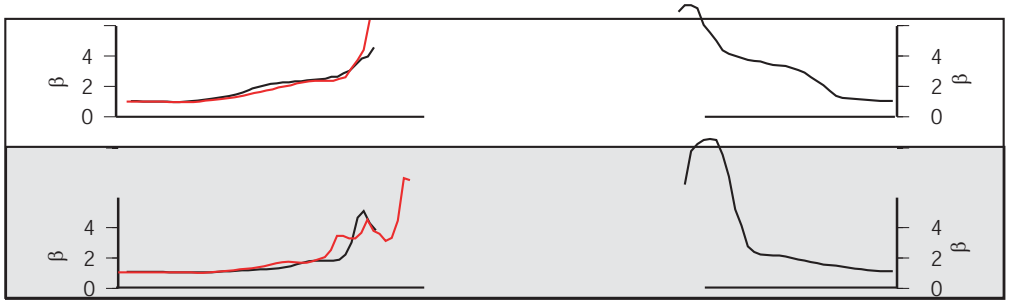

d) Crustal stretching factor (β) to the inner limit of the COT

Figure 7.27: Caption on previous page.

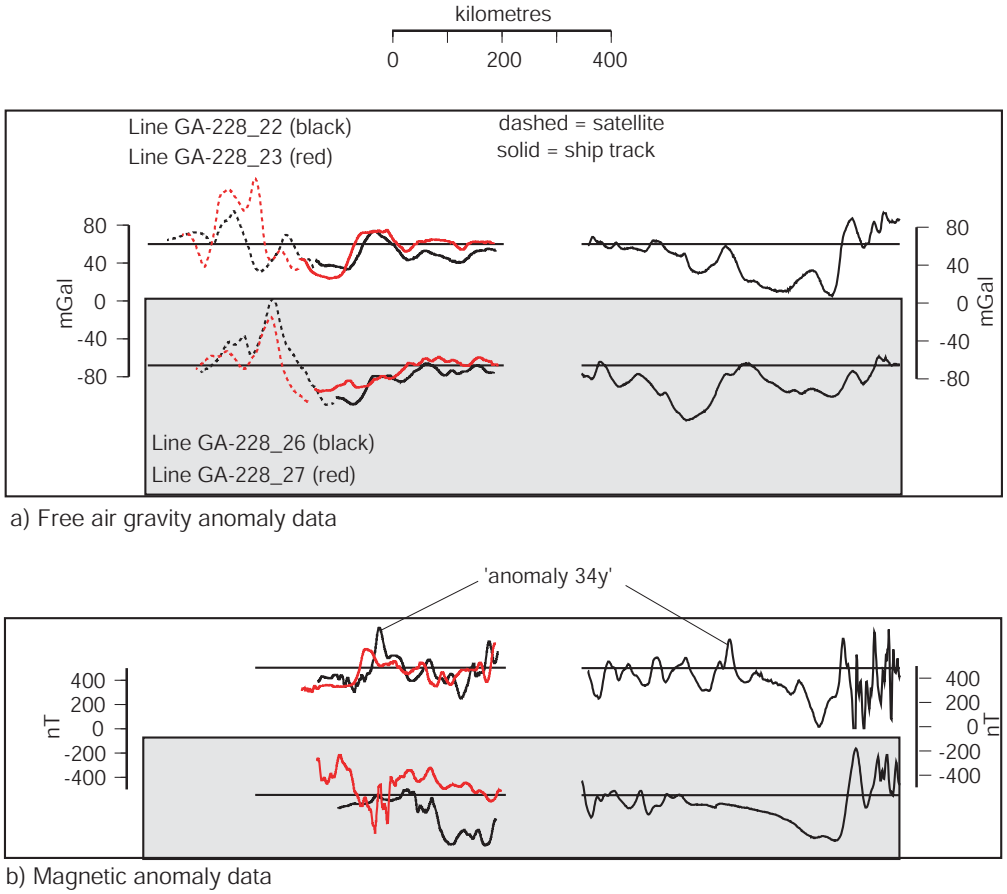

Figure 7.28: Comparison of a) FAA, and b) magnetic anomaly data across the central Wilkes Land and Bight Basin conjugate margins. Seaward ends of profiles are truncated at anomaly 20. Line labels for (b) are as in (a).

7.5 Strength of Extended Continental Lithosphere

Rifted continental crust is permanently mechanically altered by extensional thinning. A rifted margin comprises not only altered continental crust, but also relatively unaltered continental crust and oceanic crust. Despite the apparent complexity of lithospheric structure at rifted margins, a single T_e estimate, that provides the best overall description of observed flexural behaviour, is normally reported in T_e studies. These T_e estimates typically being based on gravity modelling of the edge effect anomaly or comparison of observed and theoretical flexural subsidence.

Previous estimates of T_e at rifted margins vary widely. They range, for example, from a low of 5-10 km for the Valencia Trough [Watts & Torné, 1992] and Baltimore Canyon Trough [Watts, 1988] to a high of 40-60 km for the West Greenland margin [Keen & Dehler, 1997]. These single T_e estimates at rifted margins represent, however, the *average* response of the lithosphere to sediment loading. They do not refer to a particular crustal type or time since rifting. These estimates may be biased downwards relative to their present day rigidity if lithospheric rigidity was very low during syn-rift and early post-rift sedimentation.

It is, therefore, difficult to use these data to constrain the T_e structure of stretched continental crust and determine whether or not it is able to recover strength with time. However, it is difficult to constrain T_e for discrete time intervals and therefore assess any possible bias in T_e estimates at rifted margins. The difficulty in constraining discrete T_e estimates is primarily a function of relatively continuous sedimentation, that occurs at almost all continental margins, within the developing rift basin from the onset of subsidence to the present-day. Only where discrete loading events can be identified and timed can estimates of the T_e of the lithosphere during a discrete interval be constrained.

The Amazon Cone is one example of a discrete sediment load where constraints exist on both the magnitude of the sediment load and timing of deposition. ODP results (e.g. Damuth [1975]) indicate a mid- to late-Miocence (8-12 Ma) age for the Cone. This load, therefore, occurs on a rifted margin that formed some 140 Ma previously during the opeing of the central Atlantic Ocean [Rabinowitz & LaBreque, 1979]. Cochran [1973] estimated that $T_e = 31.1$ km in the region of the Amazon Cone.

A second and similar example of a large sediment load that was deposited in a discrete interval are the sedimentary basins of the Bay of Bengal, India. Although rifting initiated during the Jurassic, large amounts of the observed sediment thickness have been deposited since the Eocene, due to uplift within the Himalayas [Krishna *et al.*, 2000]. Gravity modelling by Krishna *et al.* [2000] suggests that $T_e = 30$ km in the Krishna-Godavari Basin region of the Bay of Bengal.

A further example of a discrete loading event on rifted continental lithosphere where T_e has been estimated is the West Taiwan Basin. Lin & Watts [2002] demonstrated that T_e = 13 km in this region on the basis of flexural and gravity modelling of the orogenic loading, associated with the development of the basin, on the rifted lithosphere of the South China Sea. They relate this T_e estimate to the rigidity of the rifted margin lithosphere ∼23-51 Ma after rifting.

Process-oriented modelling on the Wilkes Land and Bight Basin margins indicates that they are characterised by a different average T_e. Whereas an average T_e of 30 km most effectively reduces the magnitude of flexural isostatic anomalies for the Wilkes Land margin, an average T_e of ∼15 km is inferred from modelling at the Southern Australian margin.

The southern Australian-Wilkes Land conjugate margin pair are unique in that they have almost opposite sedimentation or loading histories, i.e. the southern Australian margin has been sediment starved throughout the Tertiary while areas of the Wilkes Land margin were subject to very large sediment loads. The low T_e inferred for the southern Australian margin, therefore, indicates that immediately following rifting and through the Late Cretaceous, the lithosphere was relatively weak. However, the high T_e inferred for the Wilkes Land margin indicates that the lithosphere was relatively strong by the mid-Tertiary when the major loading event on this margin occurred. The asymmetry of the southern Australian and Wilkes Land margins, in terms of inferred T_e, may therefore not reflect absolute difference in T_e, rather it demonstrates that the T_e has increased through time.

The examples of the Amazon Cone, the Bay of Bengal, the Taiwan foreland, and the Wilkes Land-southern Australian margins suggest that continental lithosphere does regain strength with time following rifting. Figure 7.29 illustrates the relationship of increasing T_e with increasing time elapsed between rifting and load emplacement. A similarly crude positive correlation between T_e and the age of the lithosphere at time of loading has been established for the continents (e.g. Burov & Diament [1995]). This result accords with the numerical modelling of Burov & Poliakov [1995]. They suggest that lithospheric rigidity initially decreases during rifting but regains strength during the post-rift interval. However, it has proved difficult to assign a single isotherm that describes the rigidity-time relationship as is possible for oceanic lithosphere.

The results compiled here (Figure 7.29) accord approximately with the 450°C isotherm, however, a paucity of data prevents this relationship being defined absolutely. The 450°C isotherm best describes the T_e evolution of oceanic crust, where $T_e = 3\sqrt{t}$ and t is My. This suggests that there may be a thermal control on T_e in continents and at rifted continental margins, but that other factors (such as post-rift sedimentation, geotherm during

rifting, strain rates, and rheology) may also play an important role.

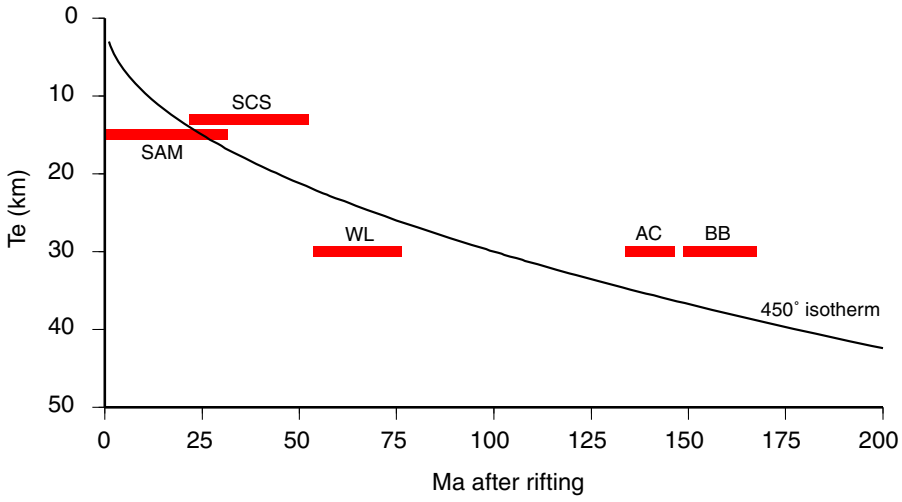

Figure 7.29: Plot of T_e as a function of elapsed time between rifting and load emplacement for discrete loads on rifted continental margin lithosphere. AC = Amazon Cone, BB = Bay of Bengal, SAM = Southern Australian Margin, SCS = South China Sea, WL = Wilkes Land. See text for references.

It has been suggested that sediment blanketing at continental margins contributes to lithospheric weakening and, therefore, a long-term reduction in T_e. The suggested processes by which this occur include (after Wyer [2003]):

1. Increasing the mean crustal temperature through insulation (e.g. Steckler & Ten Brink [1986]).

2. Increasing the depth to the *Moho* and, therefore, increasing the temperature at the base of the crust (e.g. Lavier & Steckler [1997]).

3. Reducing the lithostatic pressure at brittle depths in the yield strength envelope (e.g. Steckler & Ten Brink [1986]).

The results of Lavier & Steckler [1997] demonstrate that a sediment thickness of 3-5 km is sufficient to reduce T_e significantly. However, Karner [1991] illustrates that only if sedimentation rates are unrealistically high during the rift or early post-rift phase of basin development may T_e be reduced to near zero values by sediment blanketing. Even then, during subsequent cooling, he predicts that T_e will increase with time and that sediment blanketing alone can not cause T_e to remain low for long (>50 Ma) periods of time. Additionally, a clear correlation of high T_e (~30 km) off west Wilkes Land and the thick sediments of the Budd Coast Basin is indicated in this study. Therefore, the occurrence of thick sediments does not ubiquitously correlate to a low T_e.

Whether some rifted margins maintain or regain strength during and after rifting, while others remain weak, has not been firmly established. However, evidence from this

study suggests that the lithosphere does regain strength following rifting, and that low T_e estimates at other margins are biased by analytical methodology. It is possible, however, that the complex interaction of the controlling parameters (e.g. geotherm, rheology, etc.) and post-rift sedimentation could contribute to the wide range of T_e estimates at different rift margins.

Chapter 8

Conclusions and Future Work

8.1 Conclusions

8.1.1 Introduction

The aim of this study has been to present the data acquired during surveys GA-228 and GA-229, and, where appropriate, interpretations and modelling results of these data. This chapter aims to summarise the main results of this work, and suggest possible areas of further research.

The strength of this study is its utilisation of all available data for the Wilkes Land margin, and the application of both process- and object-oriented modelling methods. In Chapter 4, interpretation of deep-penetrating seismic reflection data provide for the first regional seismic stratigraphic summary for this Antarctic margin sector. Magnetic anomaly compilation, modelling and interpretation was undertaken in Chapter 5 to further constrain the breakup age of Antarctica and southern Australia. Due to a number of factors, however, magnetic lineations in the AAB are poorly formed and difficult to interpret for oceanic crust older than ∼48 Ma (Chron 21o). The interpreted and depth converted seismic reflection data provide the key input to process-oriented gravity modelling in Chapter 6. Process-oriented modelling was undertaken to constrain the individual gravity contributions of different geological processes at this rifted continental margin. The process-oriented gravity modelling results have also allowed the long-term rigidity of the Wilkes Land margin lithosphere to be inferred. Chapter 7 integrates the results of the preceding chapters and demonstrates that the geophysical characteristics of the COT zone off Wilkes Land are consistent with the presence of exhumed and partially serpentinised upper-mantle peridotites as top basement. The subsidence history of the margin is also inferred as far as possible in Chapter 7. Finally, a comparison between the conjugate Wilkes Land and southern Australian margins is carried out in Chapter 7.

8.1.2 Conclusions

The primary and most important results of this study are summarised here in conclusion to this thesis.

• Seismic reflection data indicate the presence of up to 5 s TWT (∼8-9 km) of post-rift sediments on the Wilkes Land margin. These sediments are divided into two major sequences by a regional unconformity, interpreted to be Eocene aged (∼50 Ma), on the basis of comparison with seismic reflection data from the southern Australian margin.

1. The younger of the two major post-rift sequences (Sequence 1) comprises a much greater thickness relative to the older Sequence 2. This is interpreted to represent the high sediment fluxes associated with the period of polythermal glaciation from ∼34-9 Ma.

2. The asymmetric distribution of Sequence 1 sediments indicates that deep-marine processes were important in lateral, along-margin sediment transport. A west to east direction of movement is inferred by the sediment distribution. This direction is opposite to the present-day marginal currents along the continental slope and rise.

3. Seismic reflection data also indicate a zone of anomalous crust between unequivocal continental and oceanic crust. This interpreted Continent-Ocean Transition (COT) zone is typically <100 km wide, and its inner-limit located ∼150-200 km from the shelf break.

4. A seaward excursion of ∼200 km is observed in the COT zone off east Wilkes Land and Terre Adélie. This is based on the identification of stretched continental crust beneath a region of anomalously shallow bathymetry characterised by a number of seamounts at its seaward edge. This region is interpreted to represent a sunken marginal plateau or a microcontinental block. 5. As the Wilkes Land margin is characterised by a diffuse COT zone, and a lack of volcanic rocks and evidence of magmatic influence during rifting, it can be classified as non-volcanic.

• Interpretation and modelling of magnetic anomaly data demonstrates a complex pattern of seafloor spreading anomalies.

1. A lineation previously associated with Chron 34 (the Cretaceous Long Normal Quiet period) is interpreted to overlie the COT zone interpreted from seismic reflection data.

2. Accurately constraining the breakup age of Antarctica and Australia on the basis of seafloor spreading anomaly identification is not possible due to the ambiguity in the magnetic anomaly lineation patterns.

3. That breakup was not synchronous along the margin is demonstrated by the interpretation of magnetic anomaly data in concert with interpretation of seismic reflection data. The earliest seafloor spreading anomaly seaward of the Adélie Rift Block is anomaly 21. This indicates that east Wilkes Land is characterised by a Tertiary breakup age, whereas, central and west Wilkes Land is interpreted to have rifted from southern

Australia during the Late Cretaceous.

4. Seafloor spreading rates are interpreted to vary between 1.5 and 10 mm/yr HSR prior to Chron 18 time (∼38-40 Ma), when normal seafloor spreading rates (20-35 mm/yr) begin.

• Process-oriented gravity modelling reveals that the Wilkes Land margin lithosphere was characterised by a relatively high T_e (∼30 km) during the loading of sediments associated with polythermal glaciation from ∼34-9 Ma.

• Two-dimensional modelling of coincident flexural isostatic anomalies and magnetic anomalies indicate the presence of high density (∼3100 kg/m^3) and susceptibility (0.05-0.1 SI units) source, which is spatially correlated to basement ridge structures within the COT zone. This is interpreted to indicate the presence of partially serpentinised (∼25%) upper-mantle peridotites, which were exhumed during extension prior to the initiation of seafloor spreading. A number of magnetic anomalies that occur on the 'anomaly 34y' lineation are unlikely to be associated with seafloor spreading anomalies, and therefore do not necessarily represent isochrons.

• The pattern of crustal thinning across the central Wilkes Land margin is broadly similar to other passive rift margins from around the world. However, the great width of highly extended crust associated with the microcontinental block off Terre Adélie is unusual in that the locus of greatest extension occurs ∼200 km landward of the point of eventual breakup.

• Depth anomalies are evident for backstripped oceanic crust along the Wilkes Land margin. The magnitude of the depth anomalies varies from 200-800 m. The greatest magnitude depth anomalies are observed to the south and south-east of the present day location of the AAD. The continuity of the depth anomalies to the oldest likely oceanic crust indicates that the cause of the great depth of the AAD is long-lived.

• The conjugate southern Australian margin is characterised by a much thinner Tertiary sediment thickness relative to the Wilkes Land margin. However, large thicknesses of sediment are observed in seismic reflection data from the Ceduna Sub-basin.

1. Two-dimensional process-oriented modelling indicates a T_e of 15 km for the region of the Ceduna Sub-basin.

2. Three-dimensional process-oriented modelling also supports the notion of a low ($\leq$15 km) for the Bight Basin region of the southern Australian margin, conjugate to Wilkes Land.

3. This apparent asymmetry in T_e is interpreted to represent the strengthening of the rifted lithosphere through time. The southern Australian margin was largely loaded in the Late Cretaceous and Early Tertiary, whereas the Wilkes Land margin was loaded from ∼34-9 Ma, some 50 to 70 Ma after rifting. As process-oriented modelling reveals

the T_e at the time of loading, the results from the Wilkes Land and southern Australian margins suggest that the rifted lithosphere was weak initially following rifting, but has regained strength through time.

4. Despite the apparent asymmetry in T_e structure, the Wilkes Land and southern Australian margins are broadly symmetric with regards to width of extended continental crust and inferred crustal structure. Depth anomalies are evident from oceanic crust on both margins, supporting the notion that the cause of the great depth of oceanic crust is imparted at the spreading ridge.

8.1.3 Future Work

An essential requirement in improving the understanding of the breakup of Australia and Antarctica is the acquisition of wide-angle refraction data along both margins. The limited constraints on crustal thinning and initial crustal thickness do not allow the ambiguity of gravity models to be reduced to the extent that would be possible if the $Moho$ structure was known from refraction surveying. Also, wide-angle data will allow the velocity structure of the margin to be determined, and the presence of a COT zone and serpentinised mantle rocks within the basement confirmed.

Additionally, a seismic reflection transect that ties the north-south profiles of surveys GA-228 and GA-229 would allow the seismic stratigraphy to be characterised in greater detail. If this was completed in conjunction with a well-placed drilling survey, it would be possible to constrain the ages of the major horizons evident in seismic reflection data. This would also allow constraints on the subsidence history of the margin, which as yet can only be inferred from comparison with the southern Australian margin or through entirely theoretical studies.

A detailed MCS survey off west Wilkes Land would be beneficial as this would allow the three-dimensional geometry of the thick sequence of sediment waves to be constrained. This may be important in understanding the palaeocirculation patterns off East Antarctica.

The acquisition of further magnetic data will allow some improvement in the identification of seafloor spreading anomaly lineations. However, given the complex patterns evident in available data, it is unlikely that magnetic anomaly data will ever allow the unambiguous definition of breakup age and the location of a COB.

Finally, the acquisition of onshore geophysical data, namely seismic refraction, gravity, and magnetic anomaly data, in the Wilkes Land sector of East Antarctica will allow more complete comparison with the conjugate Australian margin. The lack of comprehensive onshore datasets is a problem almost unique to Antarctica.

Despite the obvious need for further data in Wilkes Land, and East Antarctica in general, it is unlikely that a marine geophysical survey on the magnitude of surveys GA-228 and GA-229 will be repeated for several decades. The only likely means of acquiring well and core data from the Wilkes Land margin is through a successful application to the IOPD program. Although site selection will require further surveying, primarily an along-margin tie line, a number of potentially optimal sites for drilling can be identified in GA-228 and GA-229 data.

The lower slope of the central Wilkes Land margin, e.g. landward extents of Lines GA-228_24 and GA-228_25, provides an appealing drilling target. The relatively thin post-rift sequence there and the identification of a number of distinct unconformities would allow the full post-rift stratigraphy to be sampled and described.

Basement highs identified off east Wilkes Land and within the Adélie Rift Block (ARB) also provide drilling targets as they occur under relatively small amounts of post-rift sediments and are of somewhat equivocal composition. The broad high on Line GA-229_06 would also potentially provide greater constraints on the subsidence of the ARB and the final stages of breakup between Australia and Antarctica.

Bibliography

Airy, G. B. 1855. On the computation of the effect of the attraction of the mountain masses, as disturbing the apparent astronomical latitude of stations in geodetic surveys. *Phil. Trans. Roy. Soc. Lond.*, **145**, 101–104.

Alley, R. B., Blankenship, D. D., Rooney, S. T., & Bentley, C. R. 1989. Sedimentation beneath ice shelves - the view from ice stream B. *Marine Geology*, **85**, 101–120.

Anderson, J. B. 1991. The Antarctic Continental Shelf: Results from Marine Geological and Geophysical Investigations. *Pages 285–326 of:* Tingey, R. J. (ed), *The Geology of Antarctica*. Clarendon Press, Oxford.

Bamber, J. L., Vaughan, D. G., & Joughin, I. 2000. Widespread Compled Flow in the interior of the Antarctic Ice Sheet. *Science*, **287**, 1248–1250.

Barker, P. F., Dalziel, I. W. D., & Storey, B. C. 1991. Tectonic development of the Scotia Arc region. *Pages 215–244 of:* Tingey, R. J. (ed), *The Geology of Antarctica*. Clarendon Press, Oxford.

Barnes, P. W. 1987. Morphologic Studies of the Wilkes Land Continental Shelf, Antarctica-Glacial and Base to Iceberg Effects. *Pages 175–194 of:* Eittreim, S. L., & Hampton, M. A. (eds), *The Antarctic Continental Margin Geology and Geophysics of Offshore Wilkes Land*. Houston, Texas, USA: Circum-Pacific Council for Energy and Mineral resources.

Barrett, P. J. 1991. The Devonian to Triassic Beacon Supergroup of the Transantarctic Mountains and correlative in other parts of Antractica. *Pages 120–152 of:* Tingey, R. J. (ed), *The geology of Antarctica. Oxford Monographs on Geology and Geophysics*. Clarendon Press.

Bassetto, M., Alkmim, F. F., Szatmari, P., & Mohriak, W. U. 2000. The Oceanic Segment of the Southern Brazilian Margin: Morpho-Structural Domains and Their Tectonic Significance. *Pages 235–260 of:* Mohriank, W., & Talwani, M. (eds), *Atlantic Rifts and Continental Margins*. AGU.

Bassi, G. 1991. Factors controlling the style of continental rifting from numerical modelling. *Earth and Planetary Science Letters*, **105**, 430–452.

Bassi, G. 1995. Relative importance of strain rate for the mode of continental extension. *Geophysical Journal International*, **122**, 195–210.

Beaumont, C., Keen, C. E., & Boutilier, R. 1982. On the evolution of rifted continental margins: comparison of models and observations for the Nova Scotian margin. *Geophysical Journal of the Royal Astronomical Society*, **70**, 667–715.

Behn, M. D., & Lin, J. 2000. Segmentation in gravity and magnetic anomalies along the U.S. East Coast passive margin: Implications for incipient strucure of the oceanic lithosphere. *Journal of Geophysical Research*, **105(B11)**, 25,769–25,790.

Bentley, C. R. 1974. Crustal structure of Antarctica. *Tectonophysics*, **20**, 229–240.

Bentley, C. R. 1983. Crustal Structure of Antarctica from Geophysical Evidence-A Review. *Pages 491–497 of:* Oliver, R. L., James, P. R., & Jago, J. B. (eds), *Antarctic Earth Science*. Australian Academy of Science, Canberra.

Bentley, C. R. 1987. Antarctic ice streams; a review. *Journal of Geophysical Research*, **92**, 8843–8858.

Bentley, C. R. 1991. Configuration and Structure of the Subglacial Crust. *Pages 335–358 of:* Tingey, R. J. (ed), *The Geology of Antarctica*. Clarendon Press, Oxford.

Bentley, C. R., & Clough, J. W. 1972. Antarctic subglacial structure from seismic refraction measurements. *Pages 683–692 of:* Adie, R. J. (ed), *Antarctic geology and geophysics*. Universitetsforlaget.

Bindoff, N. L., Rosenberg, M. A., & Warner, M. J. 2000. On the circulation and water masses over the Antarctic continental slope and rise between 80 and 150°E. *Deep-Sea Research II*, **47(12-13)**, 2299–2326.

Blanchard, D. P., Rhodes, J. M., Dungan, M. A., Rodgers, K. V., Donaldson, C. H., Brannon, J. C., Jacobs, J. W., & Gibson, E. K. 1976. The Chemistry and Petrology of Basalts From Leg 137 of the Deep-Sea Drilling Project. *Journal of Geophysical Research*, **81(23)**, 4231–4247.

Boeuf, M. G., & Doust, H. 1975. Structure and development of the southern margin of Australia. *APEA Journal*, **15(1)**, 33–43.

Boillot, G., Grimaud, S., Mauffret, A., Mougenot, D., Kornprobst, J., Mergoil-Daniel, J., & Torrent, G. 1980. Ocean-continent boundary off the Iberian margin: A serpentinite diapir west of the Galicia Bank. *Earth and Planetary Science Letters*, **48**, 23–34.

Bown, J. W., & White, R. S. 1994. Variation with spreading rate of oceanic crustal thickness and geochemistry. *Earth and Planetary Science Letters*, **121**, 435–449.

Bown, J. W., & White, R. S. 1995. Effect of finite extension rate on melt generation at rifted continental margins. *Journal of Geophysical Research*, **100**, 18,011–18,029.

Bratt, S. R., & Purdy, G. M. 1984. Structure and variability of oceanic crust on the flanks of the East Pacific Rise between 11° and 13°N. *Journal of Geophysical Research*, **89**, 6111–6125.

Braun, J., & Beaumont, C. 1989. A physical explanation of the relation between flank uplifts and the breakup unconformity at rifted continental margins. *Geology*, **17**, 760–764.

Brown, B. J., Müller, R. D., Struckmeyer, H. I. M., Stagg, H. M. J., & Symonds, P. A. 2003. Formation and evolution of Australian passive margins: implications for locating the boundary between continental and oceanic crust. *Pages 223–244 of:* Hillis, R. R., & Müller, R. D. (eds), *Evolution and Dynamics of the Australian Plate. Geological Society of Australia Special Publication 22 and Geological Society of America Special Paper 372.*

Brun, J. P., & Beslier, M. O. 1996. Mantle exhumation at passive margins. *Earth and Planetary Science Letters*, **142**, 161–173.

Buck, W. R., Lavier, L. L., & Poliakov, A. N. B. 1999. How to make a rift wide. *Philosophical Transactions of the Royal Society of London*, **357**, 671–693.

Burov, E. B., & Diament, M. 1995. The effective elastic thickness (Te) of continental lithosphere: What does it really mean? *Journal of Geophysical Research*, **100(B3)**, 3905–3927.

Burov, E. B., & Poliakov, A. 1995. Erosion and rheology controls on synrift and postrift evolution: Verifying old and new ideas using a fully coupled numerical model. *Journal of Geophysical Research*, **100(B3)**, 16,461–16,481.

Cande, S. C., & Kent, D. V. 1995. Revised calibration of the geomagnetic polarity timescale for the Late Cretaceous and Cenozoic. *Journal of Geophysical Research*, **100:B4**, 6093–6095.

Cande, S. C., & Mutter, J. C. 1982. A revised identification of the oldest sea-floor spreading anomalies between Australia and Antarctica. *Earth and Planetary Science Letters*, **58**, 151–160.

Cande, S. C., & Stock, J. M. 2004. Cenozoic reconstructions of the Australia-New Zealand-South Pacific sector of Antarctica. *Pages 5–18 of:* Exon, N., Kennett, J. P., & Malone, M. (eds), *The Cenozoic Southern Ocean: Tectonics, Sedimentation and Climate Change Between Australia and Antarctica: Geophysical Monograph Series (151).* AGU.

Chalmers, J. A., & Pulvertaft, T. C. R. 2001. Development of the continental margins of the Labrador Sea - a review. *Pages 77–106 of:* Wilson, R. C. L., Whitmarsh, R. B., Taylor, B., & Froitzheim, N. (eds), *Continental Margins: A Comparison of Evidence from Land and Sea. Special Publication 187.* London: Geological Society London.

Chian, C., & Louden, K. E. 1994. The continent-ocean transition across the southwest Greenland margin. *Journal of Geophysical Research*, **99**, 9117–9135.

Childs, J.R., & Stagg, H. M. J. 1987. The Deep Crustal Structure of the Wilkes Land Continental Margin. *Pages 90–99 of:* Eittreim, S. L., & Hampton, M. A. (eds), *The Antarctic Continental Margin Geology and Geophysics of Offshore Wilkes Land.* Houston, Texas, USA: Circum-Pacific Council for Energy and Mineral resources.

Cochran, J. R. 1973. Gravity and magnetic investigations in the Guiana Basin, Western Equitorial Atlantic. *Geol. Soc. Am. Bull.*, **84**, 3249–3268.

Cochran, J. R. 1981. Simple models of diffuse extension and the pre-seafloor spreading development of the continental margin of the Northeastern Gulf of Aden. *Pages 155–165 of: Proceedings 26^{t}h International Geological Congress, Geology of continental margins sumposium*. Oceanol. Acta.

Cochran, J. R. 1983. Effects of finite rifting times on the development of sedimentary basins. *Earth and Planetary Science Letters*, **66**, 289–302.

Cochran, J. R., & Martinez, F. 1988. Evidence from the northern Red Sea on the transition from continental to oceanic rifting. *Tectonphysics*, **153**, 25–53.

Coffin, M. F., & Eldholm, O. 1994. Large igneous provinces: Crustal structure, dimensions and external consequences. *Review of Geophysics*, **32**, 1–36.

Cogley, G. J. 1984. Deglacial hypsometry of Antarctica. *Earth and Planetary Science Letters*, **67(3)**, 284–296.

Coleman, P. J., Michael, P. J., & Mutter, J. C. 1982. The origin of the Naturaliste Plateau, SE Indian Ocean; implications from dredged basalts. *Journal of the Geological Society of Australia*, **29**, 457–468.

Collier, J. S., Henstock, T. J., Pierce, T. J., & Watts, A. B. 1998. A detailed geophysical study in the Canary Basin (eastern Atlantic): Implications for the internal structure of 130 Ma oceanic crust. *Geophysical Journal International*, **135**, 943–963.

Collins, C. D. N., Drummond, B. J., & Nicoll, M. G. 2003. Crustal thickness patterns in the Australian Continent. *Pages 121–128 of:* Hillis, R. R., & Müller, R. D. (eds), *Evolution and Dynamics of the Australian Plate. Geological Society of Australia Special Publication 22 and Geological Society of America Special Paper 372*.

Colwell, J. B., Stagg, H. M. J., Direen, N. G., Bernadel, G., & Borissova, I. in press. The structure of the continental margin off Wilkes Land and Terre Adelie, East Antarctica. *In:* Futterer, D. (ed), *Antarctic Contributions to Global Earth Science, Proceedings 9th International Symposium on Antarctic Earth Sciences, Potsdam*.

Cooper, A. K., & O'Brien, P. in press. Leg 188 Synthesis: Transitions in the Glacial History of the Prydz Bay Region, East Antarctica, from ODP Drilling. *Chap. 1 of:* Cooper, A. K., O'Brien, P. E., & Richter, C. (eds), *Proceedings of the Ocean Drilling Program, Scientific Results Volume 188*.

Cooper, A. K., Davey, F. J., & Behrendt, J. C. 1987. Seismic stratigraphy and structure of the Victoria Land Basin, Western Ross Sea, Antarctica. *Pages 27–76 of:* Cooper, A. K., & Davey, F. J. (eds), *The Antarctic Continental Margin: Geology and Geophysics of the Western Ross Sea*. Houston, Texas, USA: Circum-Pacific Council for Energy and Mineral resources.

Cox, K. G. 1988. The Karoo Province. *Pages 239–271 of:* MacDougall, J. D. (ed), *Continental flood basalts*. Kluwer Academic Publishers.

Cox, K. G., Macdonald, R., & Hornung, G. 1967. Geochemical and petrographic provinces in the Karoo basalts of southern Africa. *American Mineralogist*, **52(9,10)**, 1451–1474.

Dalziel, I. W. D. 1992. Antarctica; a tale of two supercontinents. *Annual Review of Earth and Planetary Science Letters*, **20**, 501–526.

Dalziel, I. W. D, & Elliot, D. H. 1982. West Antarctica: problem child of Gondwana. *Tectonics*, **1**, 3–19.

Damuth, J. E. 1975. Echo character of the western equatorial Atlantic floor and its relationship to the dispersal and distribution of terrigenous sediments. *Marine Geology*, **18**, 17–45.

Damuth, J. E. 1979. Migrating sediment waves created by turbidity currents in the northern South China Basin. *Geology*, **7**, 520–523.

Davis, E. E., & Lister, C. R. B. 1977. Tectonic structures on the Juan de Fuca Ridge. *Geological Society of America Bulletin*, **88**, 346–363.

Davis, E. E., & Riddihough, R. P. 1982. The Winona Basin: Structure and tectonics. *Canadian Journal of Earth Sciences*, **19**, 767–788.

Davis, M., & Kusznir, N. 2002. Are buoyancy forces important during the formation of rifted margins. *Geophsical Journal International*, **149**, 524–533.

De Charpal, O., Guennoc, P., Montadert, L., & Roberts, D. G. 1978. Rifting, crustal attenuation and subsidence in the Bay of Biscay. *Nature*, **275**, 706–711.

De Conto, R. M., & Pollard, D. 2003. A coupled climate-ice-sheet modeling approach to the Early Cenozoic history of the Antarctic ice sheet. *Palaeogeography, Palaeoclimatology, Palaeoecology*, **198(1-2)**, 39–52.

De Santis, L., Brancolini, G., & Donda, F. 2003. Seismo-stratigraphic analysis of the Wilkes Land continental margin (East Antarctica): influence of glacially driven processes on the Cenozoic deposition. *Deep-Sea Research II*, **50(8-9)**, 1563–1594.

Dean, S. M., Minshull, T. A., Whitmarsh, R. B., & Louden, K. E. 2000. Deep structure of the ocean-continent transition in the southern Iberia Abyssal Plain from seismic refraction profiles: The IAM-9 transect at 40°20'N. *Journal of Geophysical Research*, **105(B3)**, 5859–5885.

Denham, J. I., & Brown, B. R. 1976. A new look at the Otway Basin. *APEA Journal*, **16(1)**, 91–98.

Direen, N. G., & Crawford, A. J. 2003. The Tasman Line: where is it, what is it, and is it Australia's Rodinian breakup boundary. *Australian Journal of Earth Sciences*, **50**, 491–502.

Domack, E. W., & Anderson, J. B. 1983. Marine geology of the George V continental margin: combined results of Deep Freeze 79 and the 1911-14 Australasian Expedition. *Pages 402–406 of:* Oliver, R. L., James, P. R., & Jago, J. B. (eds), *Antarctic Earth Sciences*. Canberra: Australian Academy of Science.

Donda, F., Brancolini, G., Santis, L. De, & Trincardi, F. 2003. Seismic facies and sedimentary processes on the continental rise off Wilkes Land (East Antarctica): evidence of bottom current activity. *Deep-Sea Research II*, **50(8-9)**, 1509–1527.

Drewry, D. J. 1976. Sedimentary Basins of the East Antarctic Craton from Geophysical Evidence. *Tectonophysics*, **36**, 301–314.

Du Toit, A. L. 1937. *Our Wandering Continents*. Oliver and Boyd.

Dunlop, D. J. 1995. Magnetism in rocks. *Journal of Geophysical Research*, **100(B2)**, 2161–2174.

Dziewonski, A. M., & Anderson, D. L. 1981. Preliminary Reference Earth Model. *Physics of the Earth and Planetary Interiors*, **25**, 297–356.

Ebinger, C. J., Karner, G. D., & Weissel, J. K. 1991. Mechanical strength of extended continental lithosphere: constraints from the western rift system, Africa. *Tectonics*, **10**, 1239–1256.

Eittreim, S. L., & Hampton, M. A. 1987. *The Antarctic Continental Margin Geology and Geophysics of Offshore Wilkes Land*. Circum-Pacific Council for Energy and Mineral resources.

Eittreim, S. L., & Smith, G. L. 1987. Seismic Sequences and Their Distribution on the Wilkes Land Margin. *Pages 15–43 of:* Eittreim, S. L., & Hampton, M. A. (eds), *The Antarctic Continental Margin Geology and Geophysics of Offshore Wilkes Land*. Houston, Texas, USA: Circum-Pacific Council for Energy and Mineral resources.

Eittreim, S. L., Gordon, A. L., Ewing, M., Thorndike, E. M., & Bruchhausen, P. 1972. The nepholoid layer and observed bottom currents in the Indian-Pacific Antarctic Sea. *Pages 19–35 of:* Gordon, A. L. (ed), *Studies in Physical Oceanography*. New York: Gordon and Breach.

Eittreim, S.L. 1994. Transition from continental to oceanic crust on the Wilkes-Adelie margin of Antarctica. *Journal of Geophysical Research*, **99**, 24,189–25,205.

Eittreim, S.L., Cooper, A. K., & Wannesson, J. 1995. Seismic stratigraphic evidence of ice-sheet advances on the Wilkes Land margin of Antarctica. *Sedimentary Geology*, **96**, 131–156.

Eldholm, O., Sundvor, E., & Myhre, A. M. 1979. Continental margin off Lofoten-Vesteralen. *Marine Geophysical Research*, **4**, 3–35.

Eldholm, O., Skogseid, J., Planke, S., & Gladczenko, T. P. 1995. Volcanic margin concepts. *Pages 1–16 of:* Banda, E., Torné, M., , & Talwani, M. (eds), *Rifted Ocean-Continent Boundaries*. Dordrecht: Kluwer Academic Publishers.

Elliot, D. H. 1975. Tectonics of Antarctica: a review. *American Journal of Science*, **275**, 45–106.

Elliot, D. H. 1992. Jurassic magmatism and tectonism associated with Gondwanaland breakup: an Antarctic perspective. *Pages 165–184 of:* Storey, B., Alabaster, T., & Pankhurst, P. J. (eds), *Magmatism and the Causes of Gondwana Break-up*. London: Geol. Soc. Special Publ.

Embley, R. W., & Langseth, M. G. 1977. Sedimentation processes on the continental rise of northeastern South America. *Marine Geology*, **25**, 279–297.

Emery, K. O. 1980. Continental margins - classification and petroleum prospects. *AAPG Bulletin*, **64**, 297–315.

Escutia, C., Eittreim, S. L., & Cooper, A. K. 1997. Cenozoic Sedimentation on the Wilkes Land Continental Rise, Antarctica. *Pages 791–795 of:* Ricci, C. A. (ed), *The Antarctic Region: Geological Evolution and Processes*. Siena: Terra Antarctica Publication.

Escutia, C., Eittreim, S. L., Cooper, A. K., & Nelson, C. H. 2000. Morphology and Acoustic Characteristic of the Antarctic Wilkes Land Turbidite Systems: Ice-Sheet-Source versus River-Sourced Fans. *Journal of Sedimentary Research*, **70, No.1**, 84–93.

Etheridge, M. A., Symonds, P. A., & Lister, G. S. 1989. Application of the Detachment Model to Reconstruction of Conjugate Passive Margins. *Pages 23–40 of:* Tankard, A. J., & Balkwill, H. R. (eds), *Extensional Tectonics and Stratigraphy of the North Atlantic Margins*. The American Association of Petroleum Geologists and The Canadian Geological Foundation.

Evans, D. A. D. 2003. True polar wander and supercontinents. *Tectonophysics*, **1-4**, 303–320.

Exon, N., *et al.* 2002. Drilling Reveals Climatic Consequences of Tasmanian Gateway Opening. *EOS Transactions*, **83; No 23**, 253–259.

Falvey, D. A. 1974. The development of continental margins in plate tectonic theory. *Australian Petroleum Exploration Association Journal*, **14**, 95–106.

Ferraccioli, F., Coren, F., Bozzo, E., Zanolla, C., Gandolfi, S., Tabacco, I., & Frezzotti, M. 2001. Rifted(?) crust at the East Antarctic Craton margin: gravity and magnetic interpretation along a traverse across the Wilkes Subglacial Basin region. *Earth and Planetary Science Letters*, **192**, 407–421.

Finlayson, D. M., Collins, C. D. N., Lukaszyk, I., & Chudyk, E. C. 1998. A transect across Australia's southern margin in the Otway Basin region: crustal architecture and the nature of rifting from wide-angle seismic profiling. *Earth and Planetary Science Letters*, **288**, 177–189.

Fitzgerald, P. G. 2002. Tectonics and landscape evolution of the Antarctic plate since the breakup of Gondwana, with an emphaisis on the West Antarcti Rift System and the Transantarctic Mountains. *Royal Sociey of New Zealand Bulletin*, **35**, 453–469.

Fitzgerald, P. G., & Baldwin, S. L. 1997. Detachment fault model for the evolution of the Ross Embayment. *Pages 555–564 of:* Ricci, C. A. (ed), *The Antarctic region: geological evolution and processes*. Sienna: Terra Antarctica Publications.

Fitzgerald, P. G., Sandiford, M., Barrett, P. J., & Gleadow, A. J. W. 1986. Asymmetric extension associated with uplift and subsidence in the Transantarcitic Mountains and the Ross Embayment. *Earth and Planetary Science Letters*, **81**, 67–78.

Forsyth, D. W. 1985. Subsurface loading and estimates of the flexural rigidity of continental lithosphere. *Journal of Geophysical Research*, **90**, 12,623–12,632.

Foucher, J.-P., Le Pichon, X., & Sibuet, J.-C. 1982. The ocean-continent transition in the uniform lithosphere stretching model: role of partial melting in the mantle. *Philosophical Transactions of the Royal Society of London*, **A305**, 27–43.

Fowler, S. R., White, R. S., Spence, G. D., & Westbrook, G. K. 1989. The Hatton Bank continental margin – II: Deep structure from two-ship expanding spread seismic profiles. *Geophysical Journal International*, **96**, 295–309.

Gaina, C., Müller, R. D., Royer, J. Y., Stock, J., Hardebeck, J., & Symonds, P. 1998. The tectonic history of the Tasman Sea: A puzzle with thirteen pieces. *Journal of Geophysical Research*, **103**, 12,413–12,433.

Gee, J., Staudigel, H., & Tauxe, L. 1989. Contribution of induced magnetization to magnetization of seamounts. *Nature*, **342**, 170–173.

Green, R., Schmidt, P. W., & McDougall, I. 1978. Palaeomagnetic and potassium-argon dating studies of the Tasmanian dolerites; discussion and reply. *Journal of the Geological Society of Australia*, **25(5-6)**, 365–367.

Grindley, G. W., & Davey, F. J. 1982. The Reconstruction of New Zealand, Australia and Antarctica. *Pages 15–29 of:* Craddock, C. (ed), *Antarctic Geoscience*. University of Wisconsin Press.

Groushinsky, N. P., & Sazhina, N. B. 1982. Some features of Antarctic crustal structure. *In:* Craddock, C. (ed), *Antarctic Geoscience*. University of Wisconsin Press.

Gunn, B. M., & Warren, G. 1962. Geology of Victoria Land between the Mawson and Mulock Glaciers, Antarcitca. *New Zealand Geological Survey Bulletin*, **71**, 157.

Gurnis, M., & Müller, R. D. 2003. Origin of the Australian-Antarctic Discordance from an ancient slab and mantle wedge. *Pages 417–430 of:* Hillis, R. R., & Müller, R. D. (eds), *Evolution and Dynamics of the Australian Plate. Geological Society of Australia Special Publication 22 and Geological Society of America Special Paper 372.*

Gurnis, M., Müller, R. D., & Moresi, L. 1998. Cretaceous Vertical Motion of Australia and the Australian-Antarctic Discordance. *Science*, **279**, 1499–1504.

Hamilton, E. L. 1976. Variations of density and porosity with depth in deep-sea sediments. *Journal of Sedimentary Petrology*, **46, No. 2**, 280–300.

Hamilton, E. L., & Bachman, R. T. 1982. Sound velocity and related properties of marine sediments. *Journal of Acoustic Society of America*, **72(6)**, 1891–1904.

Hampton, M. A., Eittreim, S. L., & Richmond, B. M. 1987. Seismic Sequences and Their Distribution on the Wilkes Land Margin. *Pages 75–87 of:* Eittreim, S. L., & Hampton, M. A. (eds), *The Antarctic Continental Margin Geology and Geophysics of Offshore Wilkes Land*. Houston, Texas, USA: Circum-Pacific Council for Energy and Mineral resources.

Hatton, L., Worthington, M. H., & Makin, J. 1986. *Seismic Data Processing - Theory and Practice*. Blackwell Scientific Publications.

Hayes, D. E., & Conolly, J. R. 1972. Morphology of the southeast Indian Ocean. *Pages 125–145 of:* Hayes, D. E. (ed), *Antarctic Oceanology II: The Australian-New Zealand Sector, Antarctic Research Series, 19*. Washington: AGU.

Hayes, D. E., & Frakes, L. A. 1975. General synthesis Deep-Sea Drilling Project Leg 28. *In:* Hayes, D. E., & Frakes, L. A. (eds), *Initial reports of the Deep-Sea Drilling Project*. Washington, D. C.: U. S. Government Printing Office.

Heezen, B. C. 1974. Atlantic-Type Continental Margins. *Pages 13–24 of:* Burke, C. A., & Drake, C. L. (eds), *The Geology of Continental Margins*. Springer-Verlag.

Hegarty, K. A., Weissel, J. K., & Mutter, J. C. 1988. Subsidence history of Australia's southern margin: constraints on basin models. *AAPG Bulletin*, **72 (5)**, 615–633.

Heirtzler, J. R., Dickson, G. E., Herron, E. M., & Pitman III, W. C. 1968. Marine magnetic anomalies, geomagnetic field reversals, and motions of the ocean floor and continents. *Journal of Geophysical Research*, **73(6)**, 2119–2136.

Henning, A., Sawyer, D., & Templeton, D. C. 2004. Exhumed upper mantle within the ocean-continent transition on the northern West Iberia margin: Evidence from prestack depth migration and total tectonic subsidence analyses. *Journal of Geophysical Research*, **109(B5)**. doi:10.1029/2003JB002526.

Hillier, J., & Watts, A. B. 2005. Relationship between depth and age in the North Pacific Ocean. *Journal of Geophysical Research*, **110(B02405)**. doi:10.1029/2004JB003406.

Hinz, K., Willcox, J. B., Whiticar, M., Kudrass, H., Exon, N. F., & Feary, D. 1986. The west Tasmanian margin: an underrated petroleum province? *Pages 395–410 of:* Glenie, R. C. (ed), *Second southe-eastern Australia oil exploration symposium*. PESA.

Holbrook, W. S., Purdy, G. M., Sheridan, R. E., Glover, III, L., Talwani, M., Ewing, J., & Hutchinson, D. 1994. Seismic structure of the U.S. Mid-Atlantic continental margin. *Journal of Geophysical Research*, **99**, 17871–17891.

Hooper, P. R., Rehacek, J., & Duncam, R. A. 1993. The basalts of Lesotho, Karoo Province, Southern Africa (abstract). *EOS, Transactions of the American Geophysical Union*, **74**, 553.

Horen, H., Zamora, M., & Dubuisson, G. 1996. Seismic waves velocities and anisotropy in serpentinized peridotites from Xigaze ophiolite: Abundance of serpentine in slow spreading ridge. *Geophsyical Research Letters*, **23(1)**, 9–12.

Hospers, J. 1965. Gravity field and structure of the Niger Delta, Nigeria, West Africa. *Geological Society of America Bulletin*, **76**, 407–422.

Huchon, P., Nguyen, T. N. H., & Chamot-Rooke, N. 2001. Propogation of continentl break-up in the southwestern South China Sea. *Pages 31–50 of:* Wilson, R. C. L., Whitmarsh, R. B., Taylor, B., & Froitzheim, N. (eds), *Continental Margins: A Comparison of Evidence from Land and Sea. Special Publication 187.* London: Geological Society London.

Hudec, M. R., & Jackson, M. P. A. 2002. Structural segmentation, inversion, and salt tectonics on a passive margin: evolution of the Inner Kwanza Basin, Angola. *Geological Society of America Bulletin*, **114**, 1222–1244.

Hutchinson, D. R., Grow, J. A., Klitgord, K. D., & Swift, B. A. 1982. Deep structure and evolution of the Carolina Trough. *Pages 129–152 of:* Watkins, J. S., & Drake, C. L. (eds), *Studies in Continental Margin Geology.* AAPG Memoir 34. Tulsa, OK: American Association of Petroleum Geologists.

IAGA, Working Group 8. 2000. International Geomagnetic Reference Field 2000. *Geophysical Journal International*, **141(1)**, 259–262. International Association of Geomagnetism and Aeronomy (IAGA) Division V.

Ikami, A., Ito, K., & Kaminuma, K. Shibuya K. 1983. Crustal structure of the Mizuho Plateau, Antarctica, revealed by explosion seismic measurements. *In:* Oliver, R. L., James, P. R., & Jago, J. B. (eds), *Antarctic Earth Science.* Australian Academy of Science, Canberra.

IOC, IHO, & BODC. 2003. *Centenary Edition of the GEBCO Digital Atlas.* Published on CD-ROM on behalf of the Intergovernmental Oceanoographic Commission and the International Hydrographic Organization as part of the General Bathymetric Chart of the Oceans; British Oceanographic Data Centre, Liverpool.

Irving, E. 1970. Oxidation and magnetic properties of basalt; review and discussion. *Canadian Journal of Earth Sciences*, **7**, 1528–1538.

Jarrard, R. D., Dadey, K.A., & Busch, W.H. 1989. Velocity and Density of Sediments of Erik Ridge, Labrador Sea: Control by Porosity and Mineralogy. *Pages 811–835 of:* Srivastava, S. P., Arthur, M.A., & Clement, B. (eds), *Proceedings of ODP Scientific Results, 105.* Ocean Drilling Program.

Jones, E. J. W. 1999. *Marine Geophysics.* Wiley.

Kagami, H. 1995. Topogrpaphic character of the East Antarctic continental margin off Wilkes Land. *Pages 181–192 of: Proceedings of the National Institute for Polar Research Symposium on Antarctic Geoscience*. Japan: NIPR.

Karner, G. D. 1991. Sediment blanketing and the flexural strength of extended continental lithosphere. *Basin Research*, **3**, 177–185.

Karner, G. D., & Watts, A. B. 1982. Gravity anomalies and flexure of the lithosphere at mountain ranges. *Journal of Geophysical research*, **88**, 10,449–10,477.

Karner, G.D., & Watts, A.B. 1983. Gravity Anomalies and Flexure of the Lithosphere at Mountain Ranges. *Journal of Geophysical Research*, **88**(B12), 10449–10477.

Keen, C., Peddy, C., De Voogd, B., & Matthews, D. H. 1989. Conjugate margins of Canada and Europe: results from deep reflection profiling. *Geology*, **17**, 173–176.

Keen, C. E., & Dehler, S. A. 1997. Extensional styles and gravity anomalies at rifted continental margins: Some North Atlantic examples. *Tectonics*, **16**, 744–754.

Keen, C. E., Loncarevic, B. D., Reid, I., Woodside, J., Haworth, R. T., & Williams, H. 1990. Tectonic and geophysical overview. *Pages 31–85 of:* Keen, M. J., & Williams, G. L. (eds), *Geology of the Continental Margin off Eastern Canada*. The Geology of North America, vol. 2. Ottowa: Geol. Surv. of Can.

Kennett, J. 1982. *Marine Geology*. Prentice-Hall.

Kennett, J. P. 1977. Cenozoic evolution of Antarctic glaciation, the Circum-Antarctic Ocean, and their impact on global paleoceanography. *Journal of Geophysical research*, **82**, 3843–3859.

Kent, D. V., & Gee, J. 1994. Grain Size-Dependent Alteration and the Magnetization of Oceanic Basalts. *Science*, **265**, 1561–1563.

Klein, E. M., & Langmuir, C. H. 1987. Global correlations of ocean ridge basalt chemistry with axial depth and crustal thickness. *Journal of Geophysical Research*, **92(8)**, 8089–8115.

Kogan, A. L. 1972. Results of deep seismic soundings of the earth's crust in East Antarctica. *Pages 485–489 of:* Adie, R. J. (ed), *Antarctic geology and geophysics*. Universitetsforlaget.

Kong, L. S. L., Detrick, R. S., Fox, P. J., Mayer, L. A., & Ryan, W. B. F. 1988. The morphology and tectonics of the Mark area from the Sea Beam and Sea MARK I observations, Mid-Atlantic Ridge 23°N. *Marine Geophysical Research*, **10**, 59–90.

König, M. 1980. *Geophysical Investigations of the Southern Continental Margin of Australia and the Conjugate Sector of East Antarctica*. Ph.D. thesis, Lamont Doherty Earth Observatory, Columbia University, NY, USA. unpublished.

König, M., & Talwani, M. 1977. A geophysical study of the southern continental margin of Australia: Great Australian Bight and western sections. *Geological Society of America Bulleting*, **88**, 1000–1014.

Kooi, H., Cloetingh, S., & Burrus, J. 1992. Lithospheric necking and regional isostasy at extensional basins1. Subsidence and gravity modeling with an application to the Gulf of Lions Margin (SE France). *Journal of Geophysical research*, **97**, 17,553–17,571.

Krawczyk, C. M., Reston, T. J., Beslier, M., & Boillot, G. 1996. Evidence for detachment tectonics on the Iberia Abyssal Plain rifted margin. *Pages 603–615 of:* Whitmarsh, R. B., Sawyer, D. S., Klaus, A., & Masson, D. G. (eds), *Proceedings of the Ocean Drilling Program, Scientific Results 149*. Ocean Drilling Program.

Krishna, M. R., Chand, S., & Subrahmanyam, C. 2000. Gravity anomalies, sediment loading and lithospheric flexure associated with the Krishna-Godavari basin, eastern continental margin of India. *Earth and Planetary Science Letters*, **175**, 223–232.

Kumar, N. 1978. Sediment Distribution in Western Atlantic Off Northern Brazil - Structural Controls and Evolution. *AAPG Bulletin*, **62(2)**, 273–294.

Kusznir, N. J., & Egan, S. S. 1990. Simple-shear and pure-shear models of continental extensional sedimentary basin formation: application to the Jeanne d'Arc Basin, Grand Banks of Newfoundland. *Pages 305–322 of:* Tankard, A. J., & Blakwill, H. R. (eds), *Extensional Tectonics of the North Atlantic Margins*. Am. Assoc. Pet. Geol., Mem. 46.

Kusznir, N. J., & Park, R. G. 1987. The extensional strength of the continental lithoshpere: its dependence on geothermal gradient, and crustal composition and thickness. *Pages 35–52 of:* Coward, M. P., Dewey, J. F., & Hancock, P. L. (eds), *Continental Extensional Tectonics*. Geological Society of London Special Publication.

Lambeck, K. 1972. Gravity anomalies over ocean ridges. *Geophysical Journal of the Royal Astronomical Society*, **30**, 37–53.

Larson, P. A., Mudie, J. D., & Larson, R. L. 1972. Magnetic anomalies and fracture zone trends in the Gulf of California. *Geological Society of America Bulletin*, **83**, 3361–3368.

Larson, R. L., & Chase, C. G. 1972. Late Mesozoic evolution of the western Pacific Ocean. *Geological Society of America Bulletin*, **83**, 3627–3644.

Larter, R. D., & Barker, P. F. 1989. Effects of ridge crest-trench interaction on Antarctic-Phoenix spreading: forces on a young subducting plate. *Journal of Geophysical Research*, **17**, 19,583–19,607.

Larter, R. D., Cunningham, A. P., & Hardy, R. J. J. 1990. The sea-floor multiple problem in multichannel seismic reflection data acquired on the Antarctic continental shelf: its causes and treatment. *Pages 187–193 of:* Cooper, A. K., & Webb, P. N. (eds), *International Workshop on Antarctic Offshore Seismic Stratigraphy (ANTOSTRAT): Overview and Extended Abstracts*. USGS.

Larter, R. D., Rebesco, M., Vanneste, L. E., Gamboa, L. A. P., & Barkere, P. F. 1997. Cenozoic tectonic, sedimentary and glacial history of the continental shelf west of Graham

Land, Antarctic Peninsula. *Pages 1–27 of:* Cooper, A. K., Barker, P. F., & Brancolini, G. (eds), *Geology and Seismic Stratigraphy of the Antarctic margin, Part 2. Antarctic Research Series. 71.* American Geophysical Union.

LASE Study Group. 1986. The structure of the U.S. East coast passive margin from large aperature seismic experiments (LASE). *Marine and Petroleum Geology*, **3**, 234–242.

Lavier, L. L., & Steckler, M. S. 1997. The effect of sedimentary cover on the flexural strength of continental lithosphere. *Nature*, **389**, 476–479.

Lawver, L. A., & Gahagan, L. M. 2003. Evolution of Cenozoic seaways in the circum-Antarctic region. *Paelaeogeography, Palaeoclimatology, Paleaecology*, **198**, 11–37.

Lawver, L. A., & Scotese, C. R. 1987. A Revised Reconstruction of Gondwanaland. *Pages 17–24 of:* McKenzie, G. D. (ed), *Geophys. Monogr. 40.* American Geophysical Union.

Lawver, L. A., Gahahgan, L. M., & Coffin, M. F. 1992. Development of paleoseaways around Antarctica. *Pages 7–30 of: The Antarctic paleoenvironment: a perspective on global change.* Washington D.C.: American Geophysical Union. Antarctic Research Series Volume 56.

Lawver, L. A., Gahahgan, L. M., & Dalziel, I. W. D. 1998. A tight fit–Early Mesozoic Gondwana: a plate tectonic perspective. *In: Origin and evolution of continents. Memoirs of the National Institute of Polar Research.* Tokyo: NIPR.

Laxon, S., & McAdoo, D. 1994. Arctic Ocean Gravity Field Derived From ERS-1 Satellite Altimetry. *Science*, **265**, 621–624.

LeMasurier, W. E., & Rex, D. C. 1991. The Marie Byrd Land volcanic province and its relation to the cainozoic West Antarctic Rift System. *Pages 249–281 of:* Tingey, R. J. (ed), *The Geology of Antarctica.* Clarendon Press, Oxford.

Levi, S. 1983. Paleomagnetism and rock magnetism of submarine basalts from the Galapagos spreading centre near 86°W. *Pages 429–435 of: Initial reports of the Deep Sea Drilling Project: Volume 70.* Washington D.C.: U.S. Government Printing Office.

Levi, S., & Riddhough, R. 1986. Why are marine magnetic anomalies suppressed over sedimented spreading centers. *Geology*, **14**, 651–654.

Lin, A. T., & Watts, A. B. 2002. Origin of the West Taiwan basin by orogenic loading and flexure of a rifted continental margin. *Journal of Geophysical Research*, **107(B9)**.

Lin, J., & Phipps Morgan, J. 1992. The spreading rate dependence of three-dimensional mid-ocean ridge gravity structure. *Geophysical Research Letters*, **19**, 13–16.

Lister, C. R. B. 1972. On the thermal balance of a mid-ocean ridge. *Royal Astronomical Society Geophysical Journal*, **26**, 515–535.

Lister, G. S., Etheridge, M. A., & Symonds, P. A. 1991. Detachment models for the formation of passive continental margins. *Tectonics*, **10**, 1038–1064.

Ludbrook, N. H. 1980. *A Guide to the Geology and Mineral Resources of South Australia*. Dept. of Mines and Energy South Australia.

Luyendyk, B. P. 1997. Slab capture versus ridge collision as an explanation for Cretaceous extension and rifting of east Gondwana. *Pages 467–474 of:* Ricci, C. A. (ed), *The Antarctic Region: Geological Evolution and Processes, Proceed. VII Symp. on Antarctic Earth Sci.* Siena.

Lythe, M. B., Vaughan, D. G., & the BEDMAP Consortium. 2000. BEDMAP - bed topography of the Antarctic. 1:10,000,000 scale map. *BAS (Misc) 9*.

Macdonald, K. C. 1982. Mid-ocean ridges: Fine scale tectonics, volcanic and hydrothermal processes within the plate boundary zone. *Annu. Rev. Earth Planet. Sci.*, **10**, 155–190.

Maggi, A., Jackson, J.A., McKenzie, D., & Priestley, K. 2000. Earthquake focal depths, effective elastic thickness, and the strength of the continental lithosphere. *Geology*, **28**(6), 495–498.

Manatschal, G. 2004. New models for evolution of magma-poor rifted margins based on a review of data and concepts from West Iberia and the Alps. *International Journal of Earth Science*, **93**, 432–466.

Marty, J. C., & Cazenave, A. 1989. Regional variations in subsidence rate of oceanic plates: a global analysis. *Earth and Planetary Science Letters*, **94**, 301–315.

Mawson, D. 1940. Sedimentary Rocks. *Australasian Antarctic Expedition 1911-14 Scientific Reports*, **Series A, IV(II)**, 347–367.

McAdoo, D., & Laxon, S. 1996. Satellite Gravity in the Weddell Sea. *Pages 155–164 of:* Storey, B. C., King, E. C., & Livermore, R. A. (eds), *Weddell Sea Tectonics and Gondwana Breakup*. Geological Society Special Publication NO. 108.

McAdoo, D., & Laxon, S. 1997. Antarctic Tectonics: Constraints From an ERS-1 Satellite Marine Gravity Field. *Science*, **276**, 556–560.

McKenzie, D. 1978. Some Remarks on the Development of Sedimentary Basins. *Earth and Planetary Science Letters*, **40**, 25–32.

McKenzie, D. P. 2003. Estimating Te in the presence of internal loads. *Journal of Geophysical Research*, **108(B9)**, 10.1029/2002JB001766.

McKenzie, D. P., & Fairhead, J. D. 1997. Estimates of the effective elastic thickness of the continental lithosphere from Bouguer and free air gravity anomalies. *Journal of Geophysical Research*, **102**, 27,523–27,552.

Meffre, S., Berry, R. F., & Hall, M. 2000. Cambrian metamorphic complexes in Tasmania: tectonic implications. *Australian Journal of Earth Sciences*, **47(6)**, 971–985.

Melhuish, A., Henrys, S. A., Bannister, A., & Davey, F. J. 1995. Seismic profiling adjacent to Ross Island: Constraints on late Cenozoic stratigraphy and tectonics. *Journal of Geophysical Research*, **94**, 10,473–10,500.

Menzies, M. A., Klemperer, S. L., Ebinger, C. J., & Baker, J. 2002. Characteristics of volcanic rifted margins. *Pages 1–14 of:* Menzies, M. A., & Baker, J. (eds), *Volcanic Rifted Margins*. Geological Society of America Special Publication.

Michon, L., & Merle, O. 2003. Mode of lithospheric extension: Conceptual models from analogue modeling. *Tectonics*, **22(4)**, 1028.

Minshull, T. A., Muller, M. R., Robinson, C. J., White, R. S, & Bickle, M. J. 1998. Is the oceanic Moho a serpentinisation front? *Pages 71–80 of:* Mills, R. A., & Harrison, K. (eds), *Modern Ocean Floor Processes and Geological Record*. Geological Society of London Special Publication.

Mishra, D. C., Sekhar, D. V. Chandra, Raju, D. Ch. Venkata, & Kumar, V. Vijaya. 1999. Crustal structure based on gravity-magnetic modelling constrained from seismic studies under Lambert Rift, Antarctica and Godavari and Mahanadi rifts, India and their interrelationship. *Earth and Planetary Science Letters*, **172**, 287–300.

Mohriank, W., & Talwani, M. (eds). 2000. Inferences Regarding Initiation of Oceanic Crust Formation From the U.S. East Coast Margin and Conjugate South Atlantic Margins. *Pages 211–234 of:* Mohriank, W., & Talwani, M. (eds), *Atlantic Rifts and Continental Margins*. M. Talwani and V. Abreu: AGU.

Moore, A. M. G., Stagg, H. M. J., & Norvick, M. S. 2000. Deep-water Otway basin: a new assessment of the tectonics and hydrocarbon prospectivity. *APPEA Journal*, **40**, 66–84.

Morris, E., Detrick, R. S., Minshull, T. A., Mutter, J. C., White, R. S., Su, W., & Buhl, P. 1993. Seismic Structure of Oceanic Crust in the Western North Atlantic. *Journal of Geophysical Research*, **98(B8)**, 13,879–13,903.

Murray, C. G., Scheibner, E., & Walker, R. N. 1989. Regional geological interpretation of a digital coloured residual Bouguer gravity image of easter Australia with a wavelength cut-off of 250 km. *Australian Journal of Earth Sciences*, **36**, 423–449.

Mutter, C. Z., & Mutter, J. C. 1993. Variations in thickness of layer 3 dominate oceanic crustal structure. *Earth and Planetary Science Letters*, **117**, 295–317.

Mutter, J., Talwani, M., & Stoffa, P. 1982. Origin of seaward-dipping reflectors in oceanic crust off the Norwegian margin by subaerial seafloor spreading. *Geology*, **10**, 137–157.

Mutter, J. C., & Karson, J. A. 1992. Structural processes at slow-spreading ridges. *Science*, **257**, 627–634.

Neidell, N. S., & Taner, M. T. 1971. Semblance and other coherency measures for multichannel data. *Geophysics*, **36**, 482–497.

Newman, P. 1993. Divergence effects in a layered earth. *Geophysics*, **38**, 481–488.

Nichols, I. A., Ferguson, J., Jones, H., Marks, G. P., & Mutter, J. C. 1981. Ultramafic blocks from the ocean floor southwest of Australia. *Earth and Planetary Science Letters*, **56**, 362–374.

Normack, W. R., Hess, G. R., Stow, D. A. V., & Bowen, A. J. 1980. Sediment waves on the Monterey fan levee: a preliminary physical interpretation. *Marine Geology*, **37**, 1–18.

Nur, A., & Ben-Avraham, Z. 1982. Oceanic Plateaus, the Fragmentation of Continents, and Mountain Building. *Journal of Geophsyical Research*, **87(B5)**, 3644–3661.

Oliver, R. L., & Fanning, C. M. 1997. Australia and Antarctica: precise correlation of Palaeoproterozoic Terrains. *Pages 163–172 of:* Ricci, C. A. (ed), *The Antarctic Region: Geological Evolution and Processes*. Sienna: Terra Antarctica Publication.

Oufi, O., & Cannat, M. 2002. Magnetic properties of variably serpentinized abyssal peridotites. *Journal of Geophysical Research*, **107(B5)**, EPM3–20.

Özdemir, Ö., & Dunlop, D. J. 1985. An experimental study of chemical remanent magnetizations of synthetic monodomain titanomaghemites with initial thermoremanent magnetizations. *Journal of Geophsyical Research*, **90**, 11,513–11,523.

Parker, R. L. 1972. The rapid calculation of potential anomalies. *Geophysical Journal of the Royal Astronomical Society*, **31**, 447–455.

Parrish, J. T. 1990. Gondwanan Paleogeography and Paleoclimatology. *Pages 15–26 of:* Taylor, T. N., & Taylor, E. L. (eds), *Antarctic Paleobilology*. Springer-Verlag.

Parsons, B. E., & Molnar, P. 1976. The origin of outer topographic rises associated with trenches. *Geophysical Journal of the Royal Astronomical Society*, **45**, 707–712.

Parsons, B. E., & Sclater, J. G. 1977. An analysis of the variation of ocean floor bathymetry and heat flow with age. *Journal of Geophysical Research*, **82**, 803–827.

Pérez-Gussinyé, M., Reston, T., & Morgan, J. Phipps. 2001. Serpentinization and magmatism during extension at non-volcanic margins: the effect of initial lithospheric structure. *Pages 551–576 of:* Wilson, R. C. L., Whitmarsh, R. B., Taylor, B., & Froitzheim, N. (eds), *Continental Margins: A Comparison of Evidence from Land and Sea. Special Publication 187*. London: Geological Society London.

Perez-Gussinye, M., Lowry, A. R., Watts, A. B., & Velicogna, I. 2004. On the recovery of effective elastic thickness using spectral methods: Examples from synthetic data and from the Fennoscandian Shield. *Journal of Geophysical Research*, **109(B10409)**. doi:10.1029/2003JB002788.

Pinheiro, L. M., Wilson, R. C. L., Pena dos Reis, R., Whitmarsh, R. B., & Ribeiro, A. 1996. The western Iberia Margin: a geophysical and geological overview. *Pages 3–27 of:*

Whitmarsh, R. B., Sawyer, D. S., Klaus, A., & Masson, D. G. (eds), *Proceedings of the Ocean Drilling Program, Scientific Results 149*. Ocean Drilling Program.

Pitman, W. C. 1978. The relationship between eustacy and stratigraphic sequences of passive margins. *Geological Society of America Bulletin*, **89**, 1389–1403.

Poehls, K. A., Luyendyk, B. P., & Heirtzler, J. R. 1973. Magnetic smooth zones in the world's oceans. *Journal of Geophysical Research*, **78**, 6985–6997.

Powell, R. D. 1984. Glacimarine processes and inductinve lithofacies modelling of ice shelf and tidewater glacier sediments based on Quaternary examples. *Marine Geology*, **57(1)**, 1–52.

Pratt, J. H. 1855. On the attraction of the Himalaya Mountains, and of the elevated regions beyond them upon a plumb-line in India. *Philosophical Transactions of the Royal Society of London*, **145**, 53–101.

ProMAX. 1998a. *2D Advanced Techniques User Training Manual*. Landmark.

ProMAX. 1998b. *2D Seismic Processing and Analysis*.

Quilty, P. 1986. Australia's Antarctic Basins - Identification and Evolution. *Petroleum Exploration Society of Australia*, **8**, 20–46.

Rabinowitz, P. D., & LaBrecque, J. L. 1977. The isostatic gravity anomaly: A key to the evolution of the ocean-continent boundary. *Earth and Planetary Science Letters*, **35**, 145–150.

Rabinowitz, P. D., & LaBreque, J. L. 1979. The Mesozoic south Atlantic Ocean and evolution of its continental margins. *Journal of Geophysical Research*, **84**, 5973–6002.

Raitt, R. W. 1963. The crustal rocks. *Pages 85–102 of:* Hill, M. N. (ed), *The Sea*. Interscience.

Rapp, R. H., & Pavlis, N. K. 1990. The Development and Analysis of Geopotential Coefficient Models to Spherical Harmonic Degree 360. *Journal of Geophysical Research*, **95, B13**, 21,885–21,911.

Rebesco, M., Larter, R. D., Barker, P. F., Camerlenghi, A., & Vanneste, L. E. 1997. The history of sedimentation on the continental rise west of the Antarctic Peninsula. *Pages 29–49 of:* Cooper, A. K., Barker, P. F., & Brancolini, G. (eds), *Geology and Seismic Stratigraphy of the Antarctic margin, Part 2. Antarctic Research Series. 71.* American Geophysical Union.

Ritsema, J., van Heijst, H. J., & Woodhouse, J. H. 1999. Complex shear wave velocity structure imaged beneath Africa and Iceland. *Science*, **286**, 1925–1928.

Rosendahl, B. R., & Groschel-Becker, H. 2000. Architecture of the Continental Margin in the Gulf of Guinea as Revealed by reprocessed Deep-Imaging Seismic Data. *Pages 85–104 of:* Mohriank, W., & Talwani, M. (eds), *Atlantic Rifts and Continental Margins*. AGU.

Royer, J., & Rollet, N. 1997. Plate tectonic setting of the Tasmanian region. *Australian Journal of Earth Science*, **44**, 543–560.

Sandwell, D. T., & Smith, W. H. F. 1997. Marine gravity anomaly from Geosat and ERS 1 satellite altimetry. *Journal of Geophysical Research*, **102(B5)**, 10,039–10,054.

Sangree, J. B., & Widmier, J. M. 1977. Seismic stratigraphy and global changes of sea level. Part 9. Seismic interpretation of clastic depositional facies. *Pages 165–184 of:* Payton, C. E. (ed), *Seismic stratigraphy - applications to hydrocarbon exploration. AAPG Memoir 29.* AAPG.

Sawyer, D. 1985. Total tectonic subsidence: A parameter for distinguishing crust type a the U.S. Atlantic continental margin. *Journal of Geophysical Research*, **90**, 7751–7769.

Sayers, J., Symonds, P. A., Direen, N. G., & Bernadrel, G. 2001. Nature of the continent-ocean transitionon the non-volcanic rifted margin of the central Great Australian Bight. *Pages 51–77 of:* Wilson, R. C. L., Whitmarsh, R. B., Taylor, B., & Froitzheim, N. (eds), *Continental Margins: A Comparison of Evidence from Land and Sea. Special Publication 187.* London: Geological Society London.

Schouten, H., & McCamy, K. 1972. Filtering Marine Magnetic Anomalies. *Journal of Geophysical Research*, **77;35**, 7089–7099.

Sclater, J. G., & Francheteau, J. 1970. The implications of terrestrial heat flow observation on current tectonic and geochemical models of the crustal and upper mantle of the earth. *Geophysical Journal of the Royal Astronomical Society*, **20**, 509–542.

Sleep, N. H. 1971. Thermal effects of the formation of Atlantic continental margins by continental breakup. *Journal of the Royal Astronomical Society*, **24**, 325–350.

Smith, A. G., & Drewry, D. J. 1984. Delayed phase change due to hot asthenosphere causes Transantarctic uplift? *Nature*, **309**, 536–538.

Smith, G., & Hallam, A. 1970. The Fit of the Southern Continents. *Nature*, **225**, 139–144.

Smith, G. M., & Banerjee, S. K. 1986. Magnetic Structure of the Upper Kilometer of the Marine Crust at Deep Sea Drilling Project Hole 504B, Eastern Pacific Ocean. *Journal of Geophysical Research*, **91(B10)**, 10,337–10,354.

Smith, W. H. F., & Sandwell, D. T. 1994. Bathymetric prediction from dense satellite altimetry and sparse shipboard bathymetry. *Journal of Geophysical Research*, **99(B11)**, 21,083–10,824.

Stacey, F. D. 1967. The Koenigsberger Ratio and the Nature of Thermoremanence in Igneous Rocks. *Earth and Planetary Science Letters*, **2**, 67–68.

Stagg, H. M. J. 1985. The structure and origin of Prydz Bay and the Mac.Robertson Shelf, East Antarctica. *Tectonophysics*, **114**, 315–340.

Stagg, H. M. J., Willcox, J. B., Symonds, P. A., O'Brien, G. W., Colwell, J. B>, Hill, P. J., s. Clee, C, Moore, A. M. G., & Struckmeyer, H. I. M. 1999. Architecture and evolution of the Australian continental margin. *AGSO Journal of Australian Geology & Geophysics*, **17(5/6)**, 17–33.

Stagg, H. M. J., Colwell, J. B., Direen, N. G., O'Brien, P. E., Brown, B. J., Bernadel, G., Borissova, I., & Ishihara, T. in press. Geology of the continental margin of Enderby and Mac. Robertson Lands, East Antarctica: insights from a regional data set. *In:* Jokat, W. (ed), *Proceedings Workshop East-West Antarctic Tectonics and Gondwana Break-up: 60W to 60E, Potsdam, 2003.* Marine Geophysical Researches.

Steckler, M. S. 1985. Uplift and extension at the Gulf of Suez: indication of induced mantle convection. *Nature*, **317**, 135–139.

Steckler, M. S., & Ten Brink, U. S. 1986. Lithospheric strength variation as a control on new plate boundaries: examples from the Gulf of Suez. *Earth and Planetary Science Letters*, **79**, 120–132.

Steckler, M. S., & Watts, A. B. 1978. Subsidence of the Atlantic-type continental margin off New York. *Earth and Planetary Science Letters*, **41**, 1–13.

Steckler, M. S., & Watts, A.B. 1981. Subsidence history and tectonic evolution of Atlantic-type continental margins. *Pages 184–19 of:* Scrutton, R.A. (ed), *Dynamics of Passive Margins, Geodynamics Series, Vol. 6.* Washington D.C.: American Geophysical Union.

Steed, R. 1980. *Geophysical investigation of Wilkes Land, Antarctica.* Ph.D. thesis, University of Cambridge, U. K. unpublished.

Stern, T. A., & ten Brink, U. S. 1989. Flexural Uplift of the Transantarctic Mountains. *Journal of Geophysical Research*, **94, B8**, 10,315–10,330.

Stern, T. A., & ten Brink, U. S. 1992. Rift flank uplifts and hinterland basins: comparison of the Transantarctic Mountains with the Great Escarpment of Southern Africa. *Journal of Geophysical Research*, **97**, 569–585.

Stewart, J. 1998. *Gravity Anomalies and Lithospheric Flexure: Implications for the Thermal and Mechanical Evolution of the Continental Lithosphere.* Ph.D. thesis, University of Oxford, U. K. unpublished.

Stewart, J., Watts, A. B., & Bagguley, J. G. 2000. Three-dimensional subsidence analysis and gravity modelling of the continental margin offshore Namibia. *Geophysical Journal International*, 724–746.

Stock, J., & Molnar, P. 1987. Revised history if early Tertiary plate motion in the southwest Pacific. *Nature*, **325**, 495–499.

Storey, B. C., Dalziel, I. W. D., Garrett, S. W., Grunow, A. M., Pankhurst, R. J., & Vennum, W. R. 1998. West Antarctica in Gondwanaland: crustal blocks, reconstruction and breakup processes. *Tectonophysics*, **155**, 381–390.

Storey, B.C., & Kyle, P.R. 1999. The Weddell Sea region: a plume impact site and source for Gondwana magmas during the initial stages of Gondwana breakup. *Page 292 of:* Skinner, D. N. B. (ed), *8th International Symposium on Antarctic Earth Sciences, 5-9 July 1999, programme and abstracts.* Victoria University of Wellington, New Zealand.

Strand, K., Passchier, S., & Nasi, J. 2003. Implications of quartz grain microtextures for onset of Eocene/Oligocene glaciation in Prydz Bay, ODP Site 1166, Antarctica. *Paelaeogeography, Palaeoclimatology, Paleaoecology*, **198**, 101–112.

Suess, E. 1904. *The face of the earth (Das Antlitz der Erde).* Oxford University Press.

Symonds, P. A., Eldholm, O., Mascle, J., & Moore, G. F. 2000. Characeristics of Continental Margins. *Pages 25–63 of:* Cook, P. J., & Carleton, C. (eds), *Continental shelf limits: the legal and scientific interface.* Oxford University Press.

Talwani, M., & Eldholm, O. 1972. The continental margin off Norway: A geophysical study. *Geological Society of America Bulletin*, **83**, 3573–3606.

Talwani, M., & Eldholm, O. 1973. The boundary between continental and oceanic crust at the margin of rifted continents. *Nature*, **241**, 325–330.

Talwani, M., & Heirtzler, J. R. 1964. Computation of magnetic anomalies caused by two dimensional structures of arbitrary shape. *Computers in the Mineral Industries*, **9(1)**, 464–480.

Talwani, M., Worzel, J. L., & Landisman, M. 1959. Rapid computation for two dimensional bodies with application to the Mendocino submarine fracture zone. *Journal of Geophysical Research*, **64**, 19–59.

Talwani, M., Mutter, M., Houtz, R., & Konig, M. 1978. The Crustal Structure and Evolution of the Area Underlying The Magnetic Quiet Zone on the Margin South of Australia. *Pages 151–175 of:* watkins, J., Montadert, L., & Dickenson, P. (eds), *Geological and Geophysical Investigations of Continental Margins. Memoirs. American Association of Petroleum geologists. 29.* AAPG.

Tanahashi, M., Saki, T., Oikawa, N., & Sato, S. 1987. An Interpretation of the Multichannel Seismic Reflection Profiles across the Continental Margin of the Dumont d'Urville Sea, off Wilkes Land, east Antarctica. *Pages 1–13 of:* Eittreim, S. L., & Hampton, M. A. (eds), *The Antarctic Continental Margin Geology and Geophysics of Offshore Wilkes Land.* Houston, Texas, USA: Circum-Pacific Council for Energy and Mineral resources.

Tanahashi, M., Eittreim, S., & Wannesson, J. 1994. Seismic stratigraphic sequences of the Wilkes Land margin. *Terra Antarctica*, **1**, 391–393.

Tanahashi, M., Ishihara, T., Yuasa, M., Murakami, F., & Nishimura, A. 1997. Preliminary reoport of the TH95 geological and geophysical survey results in the Ross Sea nd Dumont D'Urville Sea. *Pages 36–58 of: Proceedings NIPR Symp. Antarctic Geoscience*. NIPR.

Taylor, B., Goodliffe, A., Martinez, F., & Hey, R. 1995. Continental rifting and initial sea-floor spreading in the Woodlark basin. *Nature*, **374**, 534–537.

Telford, W. M., Geldart, L. P., & Sherriff, R. E. 1990. *Applied Geophysics: Second Edition*. Cambridge University Press.

ten Brink, U. S., Schneider, C., & Johnson, A. H. 1995. Morphology and stratal geometry of the Antarctic Continental Shelf: Insights from models. *Pages 1–25 of:* Cooper, A. K., Barker, P. F., & Brancolini, G. (eds), *Geology and Seismic Stratigraphy of the Antarctic Margin: Antarctic Research Series, Volume 68*. American Geophysical Union.

ten Brink, U. S., Hackney, R. I., Bannister, S., Stern, T. A., & Makovsky, Y. 1997. Uplift of the Transantarctic Mountains and the bedrock beneath the East Antarctic ice sheet. *Journal of Geophysical Research*, **102, B12**, 27,603–27,621.

Tikku, A. A., & Cande, S. C. 1999. The oldest magnetic anomalies in the Australian-Antarctic Basin: Are they isochrons? *Journal of Geophysical Research*, **104, B1**, 661–677.

Tingey, R. J. 1991a. Mesozoic tholeiitic igneous rocks in Antarctica: The Ferrar (Super) Group and related rocks. *Pages 153–170 of:* Tingey, R. J. (ed), *The Geology of Antarctica*. Clarendon Press, Oxford.

Tingey, R. J. 1991b. The Regional Geology of Archaean and Proterozoic rocks in Antarctica. *Chap. GEBCO, pages 1–58 of:* Tingey, R. J. (ed), *The Geology of Antarctica*. Clarendon Press, Oxford.

Totterdell, J. M., & Bradshaw, B. E. 2004. The structural framework and tectonic evolution of the Bight Basin. *Pages 41–61 of:* Boult, P. J., Johns, D. R., & Lang, S. C. (eds), *Eastern Australasian Basins Symposium II*. Petroleum Exploration Society of Australia.

Totterdell, J. M., & Krassay, A. A. 2003. *Sequence stratigraphic correlation of onshore and offshore Bight Basin successions*. Geoscience Australia Record.

Totterdell, J. M., Blevin, J. E., Struckmeyer, H. I. M., Bradshaw, B. E., Colwell, J. B., & Kennard, J. M. 2000. A new sequence framework for the Great Australian Bight: starting with a clean slate. *APPEA Journal*, **4**, 95–117.

Tsumaraya, Y., Tanahashi, M., Saki, T., Machihara, T., & Asakura, N. 1985. Preliminary report of the marine geophysical and geological surveys off Wilkes Land, Antarctica in 1983-1984. *Pages 48–62 of: Memoirs of National Institute of Polar Research Issue 37*. National Institute of Polar Research, Japan.

Tucholke, B. E., & Lin, J. 1994. A geological model for the structure of ridge segments in slow spreading ocean crust. *Journal of Geophysical Research*, **99**, 11,937–11,958.

Vail, P. R., Mitchum, R. M., & Thompson, S. 1977. Seismic stratigraphy and global changes of sea level, 4. *Pages 83–97 of: Seismic Stratigraphy-Application to Hydrocarbon Exploration.* American Association of Petroleum Geology Memoirs.

van der Beek, P. S., Cloetingh, S., & Andriessen, P. 1995. Mechanisms of extionsional basin formation and vertical motion at rift flanks: constraints from tectonic modeling and fission track thermochronology. *Earth and Planetary Science Letters*, **121**, 417–433.

Veevers, J. J. 1982. Austrlian-Antarctic depression from the mid-ocean to adjacent continents. *Nature*, **295(5847)**, 315–317.

Veevers, J. J. 1986. Breakup of Australia and Antarctica estimated as mid-Cretaceous (95Ma) from magnetic and seismic data at the continental margin. *Earth and Planetary Science Letters*, **77**, 91–99.

Veevers, J. J. 1987. The Antarctic Continental Margin Geology and Geophysics of Offshore Wilkes Land. *Pages 45–73 of:* Eittreim, S. L., & Hampton, M. A. (eds), *The Antarctic Continental Margin Geology and Geophysics of Offshore Wilkes Land.* Houston, Texas, USA: Circum-Pacific Council for Energy and Mineral resources.

Veevers, J. J., Stagg, H. M. J., Willcox, J. B., & Davies, H. L. 1990. Pattern of slow seafloor spreading (<4 mm/year) from breakup (96 Ma) to A20 (44.5 Ma) off the southern margin of Australia. *BMR Journal of Australian Geology and Geophysics*, **11**, 499–507.

Veevers, J. J., McA. Powell, C., & Roots, S. R. 1991. review of seafloor spreading around Australia. I. Synthesis of the patterns of spreading. *Australian Journal of Earth Sciences*, **38**, 373–389.

Vening Meinesz, F. A. 1932. Comments on Isostasy. *Page 27 of:* Bowie, W. (ed), *Comments on Isostasy.* National Research Council.

Vine, F. J., & Matthews, D. H. 1963. Magnetic anomalies over oceanic ridges. *Nature*, **199**, 947–949.

Vogt, P. R., Anderson, C. N., Bracey, D. R., & Schneider, E. D. 1970. North Atlantic magnetic smooth zones. *Journal of Geophysical Research*, **75**, 3955–3968.

Volpi, V., Camerlenghi, A., Hillenbrand, C. D., Rebesco, M., & Ivaldi, R. 2003. The effect of biogenic silica on sediment consolidation and slope instability, Pacific margin of the Antarctic Peninsula. *Basin Research*, **15**, 339–354.

Walcott, R. 1972. Gravity, flexure, and the growth of sedimentary basins at a continental edge. *Geol. Soc. Am. Bull.*, **83**, 1845–1848.

Walcott, R. 1973. Structure of the Earth from glacio-isostatic rebound. *Annual Review of Planetary Physics*, 15–38.

Wannesson, J., Pelras, M., Petitperrin, B., Perret, M., & Segoufin, J. 1985. A geophysical transect of the Adelie Margin, East Antarctica. *Marine and Petroleum Geology*, **2**, 192–201.

Watts, A. B. 1978. An analyisis of isostasy in the world's oceans: 1. Hawaiian-Emperor Seamount Chain. *Journal of Geophysical Research*, **83**, 5989–6004.

Watts, A. B. 1988. Gravity anomalies, crustal structure and flexure of the lithosphere at the Baltimore Canyon Trough. *Earth and Planetary Science Letters*, **89**, 221–238.

Watts, A. B. 2001. *Isostasy and Flexure of the Lithosphere*. Cambridge University Press.

Watts, A. B., & Burov, E. B. 2003. Lithospheric strength and its relationship to the elastic and seismogenic layer thickness. *Earth and Planetary Science Letters*, **213**, 113–131.

Watts, A. B., & Fairhead, J. D. 1997. Gravity anomalies and magmatism along the western continental margin of the British Isles. *Journal of the Geological Society of London*, **154**, 523–529.

Watts, A. B., & Fairhead, J. D. 1999. A process-oriented approach to modeling the gravity signature of continental margins. *The Leading Edge*, **Feb**, 258–263.

Watts, A. B., & Marr, C. 1995. Gravity anomalies and the thermal and mechanical structure of rifted continental margins. *Pages 65–94 of:* et al., E. Banda (ed), *Rifted Ocean-Continent Boundaries*. Kluwer Academic Publishers.

Watts, A. B., & Ryan, W. B. F. 1976. Flexure of the lithosphere and continental margin basins. *Tectonophysics*, **36**, 25–44.

Watts, A. B., & Torné, M. 1992. Subsidence history, crustal structure and thermal evolution of the Valencia Trough: A young extensional basin in the western Mediterranean. *Journal of Geophysical Research*, **97**, 20,021–20,041.

Watts, A.B., & Stewart, J. 1998. Gravity anomalies and the segmentation of the continental margin offshore West Africa. *Earth and Planetary Science Letters*, **156**, 239–252.

Watts, A.B., Karner, G.D., & Steckler, M.S. 1982. Lithospheric flexure and the evolution of sedimentary basins. *Philosophical Transactions of the Royal Society of London*, **305**, 249–281.

Wegener, A. 1912. Die Enstehung der Kontinente. *Petermanns Mitteilungen*, 185–195,253–256,305–309.

Wegener, A. 1915. *Die Ehtstehung der Kontinente*. Friedrich Vieweg & Sohn. (*First English translation in 1924 from the 3rd (1922) German edition*).

Weissel, J. K., & Hayes, D. E. 1971. Asymmetric Seafloor Spreading South of Australia. *Nature*, **231(5304)**, 518–522.

Weissel, J. K., & Hayes, D. E. 1972. Magnetic anomalies in the Southeast Indian Ocean. *Page 196 of:* Hayes, D. E. (ed), *Antarctic Oceanology II. The Australian-New Zealand Sector.* American Geophyscial Union, Antarctic Research Series, 19.

Weissel, J. K., & Hayes, D. E. 1974. The Australian-Antarctic Discordance: New results and Implications. *Journal of Geophysical Research*, **79(17)**, 2579–2587.

Weissel, J. K., & Karner, G. D. 1989. Flexural uplift of rift flanks due to mechanical unloading of the lithosphere during extension. *Journal of Geophysical Research*, **94**, 13,919–13,950.

Weissel, J. K., Hayes, D. E., & Herron, E. M. 1977. Plate tectonics synthesis, the displacements between Australia, New Zealand, and Antarctica since the Late Cretaceous. *Marine Geology*, **25**, 231–277.

Wernicke, B. 1985. Uniform-sense normal simple shear of the continental lithosphere. *Canadian Journal of Earth Science*, **22**, 108–125.

White, R. S. 1984. Atlantic oceanic crust: Seismic structure of a slow spreading ridge. *Pages 34–44 of:* Gass, I. G., Lippard, S. J., & Shelton, A. W. (eds), *Ophiolites and oceanic lithosphere.* Geological Society of London.

White, R. S., & McKenzie, D. 1989. Magmatism at rift zones: the generation of volcanic continental margins and flood basalts. *Journal of Geophysical Research*, **94**, 7685–7729.

White, R. S., McKenzie, D., & O'Nioins, R. K. 1992. Oceanic crustal thickness from seismic measurements and rare earth element inversions. *Journal of Geophysical Research*, **97(B13)**, 19,683–19,715.

Willcox, J. B. 1978. The Great Australia Bight - a regional interpretation of graivty, magnetic, and seismic data from the Continental Margin Survey. *Bureau of Mineral Resources, Australia. Report 201.*

Willcox, J. B., & Stagg, H. M. J. 1990. Australia's southern margin: a product of oblique extension. *Tectonophysics*, **173**, 269–281.

Willcox, J. B., Baillie, P., Exon, N., Lee, C. S., & Thomas, B. 1989. *The geology of western Tasmania and its continental margin - with particular reference to petroleum potential.* Geoscience Australia Record.

Wilson, R. C. L., Manatschal, G., & Wise, S. 2001. Rifting along non-volcanic passive margins: stratigraphic and seismic evidence from the Mesozoic successions of the Alps and western Iberia. *Pages 429–452 of:* Wilson, R. C. L., Whitmarsh, R. B., Taylor, B., & Froitzheim, N. (eds), *Continental Margins: A Comparison of Evidence from Land and Sea. Special Publication 187.* London: Geological Society London.

Worzel, J. L. 1968. Advances in marine geophysical research of continental margins. *Can. J. Earth Sci.*, **5**, 963–983.

Wyer, P. 2003. *Gravity anomalies and segmentation of the Eastern USA passive continental margin*. Ph.D. thesis, University of Oxford, U. K. unpublished.

Yilmaz, Ö. 2001. *In:* Doherty, S. M. (ed), *Seismic Data Analysis: Processing, Inversion, and Interpretation of Seismic Data*. SEG, Investigations in Geophysics, No. 10.

Yuasa, M., Niida, K., Ishihara, T., Kisimoto, K., & Murakami, F. 1997. Peridotite Dredged from a Seamount off Wilkes Land, the Antarctic: Emplacement of Fertile Mantle Fragment at Early Rifting Stage between Australia and Antarctica during the Final Breakup of Gondwanaland. *Pages 725–730 of:* Ricci, C. A. (ed), *The Antarctic Region: Geological Evolution and Processes*. Terra Antarctica.

Zachos, J. C., Quinn, T. M., & Salamy, K. A. 2001. Trends, rhythms, and aberrations in global climate 65 Ma to present. *Science*, **292**, 251–266.

Appendix A

USGS Survey L184 Seismic Reflection Data Processing

A.0.4 Processing Sequence Summary

In the following sections a typical processing sequence (e.g. Yilmaz [2001]) is tested and demonstrated on L184 survey data. Data were processed from field SEGY to fully time migrated sections using *ProMAX (v1998.6)*. Acquisition parameters and the original processing sequence applied are outlined in Chapter 3.

A.1 Survey L184 Data Processing

A.1.1 Preprocessing

Data received for this study had been transcribed from field tapes, demultiplexed and re-written as SEGY. Subsequently, the significant preprocessing steps remaining to be applied were field geometry setup, deep-water delay (DWD) correction, trace editing, and geometric spreading correction.

Field Geometry Setup

Limited field geometry information was included within the SEGY headers of these data. Separate navigation files including location and time information were provided separately as ASCII text files. Thus, shot and receiver locations prescribed during the geometry setup were relative only. CMP binning was performed and the relative locations of CMPs assigned based on shot-receiver geometries initialised during setup. The CMP binning process assigns all traces at the midpoint of a given shot-receiver pair to one CMP.

Deep Water Delay Correction

Data were recorded in water depths varying from less than 400 m (∼0.5 sec TWT) to over 4000 m (∼5 sec TWT) during this survey. Data acquired in deeper water had a deep water delay (DWD) of 1-3 s applied, this simply delays the start of data recording after shot firing. The DWD was recorded in the observer's log and could be easily confirmed via single trace analyses. A near trace display of the data prior to DWD correction is shown in Figure A.1, the water bottom reflection is offset at a number of shot locations by 1 s intervals.

To correct for the DWD, and ensure that the water bottom was not offset for each change in the DWD, static corrections were applied. The amount of the DWD was added to each section of the line it was applied to, however, firstly the record length was increased by the magnitude of the maximum DWD to ensure that no data were lost once the record start point was reset. The correction transforms the variably offset water bottom reflector to its true TWT position (Figure A.1).

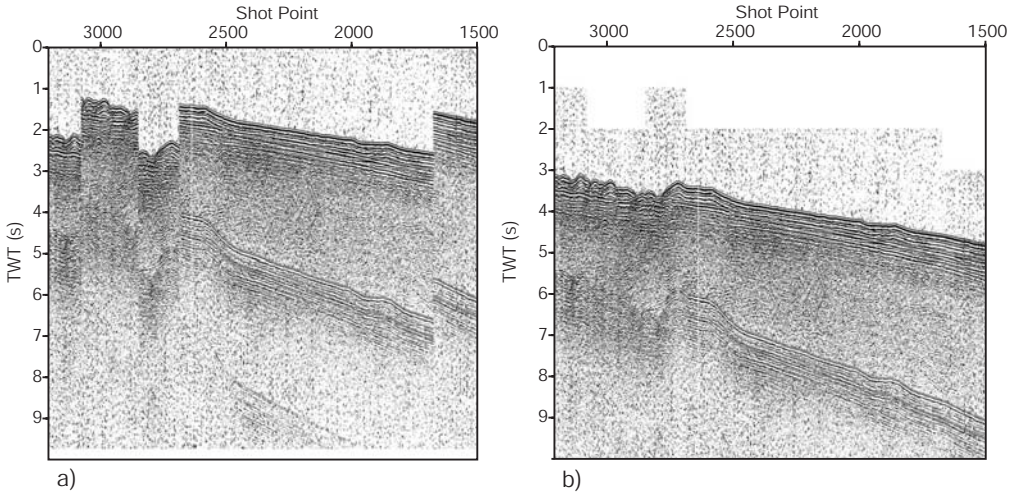

Figure A.1: Near trace display (channel 1) a) before correction, and b) after correction of the deep-water delay (DWD).

Trace Editing

Trace data were edited to remove noisy and/or spiky traces and to check that no traces had been recorded with reverse polarity. Trace statistics were calculated for the entire raw trace dataset to assist in the editing process. They allow statistical outliers, typically associated with traces exhibiting high noise levels and spikes, to be identified without checking every trace individually.

The interactive trace statistic analysis used to locate noisy traces is illustrated in Figure A.2. The histograms represent energy decay, first-break energy, dominant data frequency, frequency deviation, pre first-break average energy, pre first-break average frequency, average trace energy, and spikiness. The mean and standard deviation of these quantities are also displayed on the histograms. The data frequency and average trace energy histograms were most useful in interactively selecting traces which were particularly noisy or spiky. Undesired traces were deleted from the dataset.

True Amplitude Recovery

Seismic energy decays as it propagates from its source. In a homogeneous halfspace energy is lost due to both spherical divergence (frequency independent) and attenuation (frequency dependent) [Yilmaz, 2001]. The Earth generally acts as a low pass filter and attenuates higher frequency signals most rapidly. Seismic energy decreases proportional to $1/r^2$ and amplitude proportional

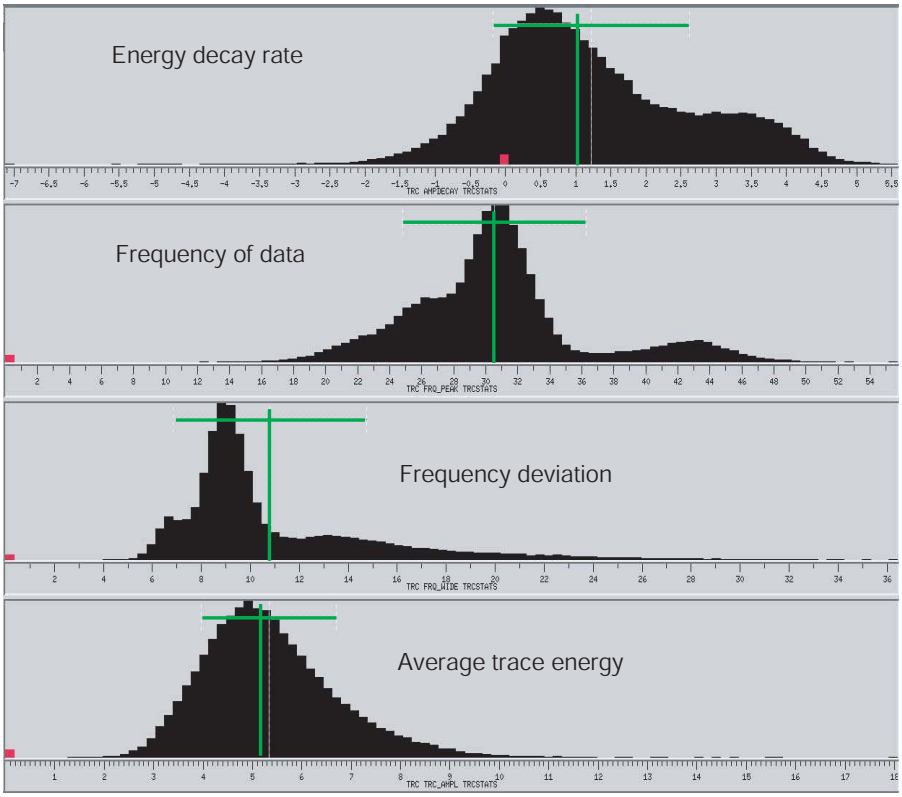

Figure A.2: Analysis of the trace statistics (calculated using the *ProMAX* database statistics functionality) for the entire seismic line allows statistically outlying traces to be interactively selected and edited. Histograms represent different trace attribute variations of amplitude, frequency and energy as labelled. Vertical green lines represent the mean and horizontal green lines show the standard deviation. The red traces have been selected from the entire dataset (black) and can be viewed in a different but interactively connected window.

to $1/r$, where r is the radius of the wavefront. True Amplitude Recovery (TAR) is a process applied to seismic data to compensate for these effects.

For a layered Earth, amplitude decay is a function of the RMS velocity of primary reflections and the two-way travel time (TWT); it can be described approximately by $1/(v^2.t)$, where t is the TWT and v is the RMS velocity at time t [Newman, 1993]. This function was used to correct for spherical divergence in this dataset.

TAR was first applied to all shot data using a simple, assumed velocity function. Due to the high energy multiple reflections affecting this dataset TAR was applied to a depth such that amplitude recovery was not performed on or below the water bottom multiple. To apply TAR only above the water bottom multiple ensures that the high energy multiple is not amplified further through the application of this time dependent gain function. Selected shot gathers following the application of spherical divergence correction are shown in Figure A.3. Primary reflection amplitude is increased. However, undesirable noise in the data is also boosted. As

higher frequencies are also subject to greater attenuation by the Earth, the recovery of higher frequency data is not as successful as for lower frequencies.

This initial TAR function was removed following velocity analysis and repeated with the interpreted RMS velocity structure. The imaging differences associated with this change are relatively minor.

A.1.2 Pre-Stack Processing

Deconvolution

The signal recorded in seismic reflection surveying is a function of the source wavelet, the Earth impulse response function, and random background noise [Yilmaz, 2001]. The convolution model for seismic reflections can be expressed as,

$$x(t) \quad = \quad w(t) * e(t) + n(t)$$

where *x(t)* denotes the recorded seismic signal, *w(t)* is the seismic source wavelet, *e(t)* is the Earth response function, *n(t)* represents random noise, and the * denotes convolution in the time domain or multiplication in the frequency domain.

The Earth impulse response function imposes some undesirable effects on the data such as attenuation (particularly of higher frequencies) and multiple reflections. Deconvolution attempts to recognise these effects as linear filters and apply appropriate inverse filters to remove them. Deterministic inverse filtering is only applicable where the form of the seismic source wavelet is known explicitly and it is assumed to propagate through the subsurface without distortion. When the form of the source wavelet is unknown more sophisticated deconvolution techniques, such as predictive deconvolution, are required [Yilmaz, 2001].

Predictive deconvolution attempts to predict repeated sequences in a given time series associated with the form of the original source signal. It is assumed the components of the signal to be removed (i.e. original source signature and noise) follow a repeatable pattern with a linear offset or lag. Applying predictive deconvolution requires the definition of three main parameters
i) one or many time gates over which to apply the deconvolution,
ii) the active operator length, and
iii) the gap or minimum lag.
The choice of the deconvolution gate length defines how much of the original time series is deconvolved. An optimum time gate excludes the early parts of any record affected by energy from direct arrivals and also the deeper parts of a record where incoherent noise dominates.

There is no theoretical minimum or maximum operator length which controls the limits of this parameter [Hatton *et al.*, 1986]. Short operators often yield spikey amplitude spectra. Whereas, amplitude spectra created with longer operators begin to approximate the spectrum of the impulse response. However, increasing operator length does not indefinitely improve the success of deconvolution; typically more and more spurious spikes are actually introduced beyond some optimum operator length [Yilmaz, 2001]. Selecting an appropriate operator length can be quantitatively assessed by examining autocorrelograms of the recorded seismic wavelet. The autocorrelation of the unknown source wavelet should resemble the first transient zone in the

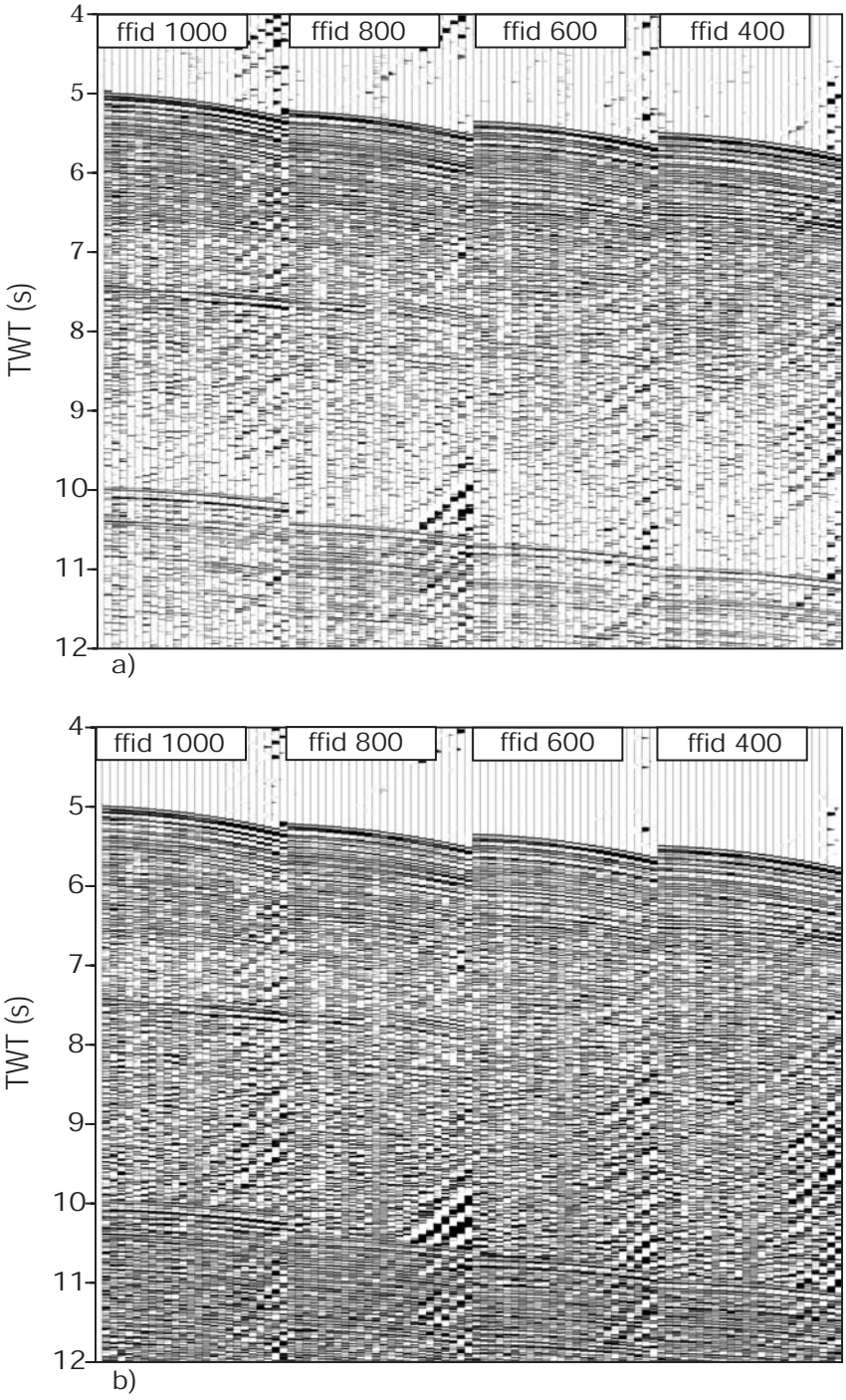

Figure A.3: Comparison of four shot gathers (ffid = field file identifier) a) before any correction for spherical divergence, and b) following the application of true amplitude recovery (TAR) to correct for spherical divergence. Noise and signal are both amplified by this gain function.

autocorrelation [Yilmaz, 2001]. Hence, if the extent of the seismic source wavelet can be inferred then an operator length can be chosen to include only autocorrelation lags associated with the seismic source wavelet. In practice then, the operator length is generally chosen to include the first distinct energy packet in the autocorrelation.

Analyses of autocorrelograms allows an absolute minimum operator length of 100 ms to be inferred. However, it is likely that in practice the optimal operator length is greater than 100 ms.

Prediction lag controls the resolution of the deconvolution output and the power distribution of the output frequency spectrum. A unit prediction lag, that is where the prediction lag is chosen to be equal to the sampling interval (2 ms for this dataset), is equivalent to spiking deconvolution and implies the highest resolution. Any larger prediction lag implies less than full resolution. In reality, the signal-to-noise ratio controls how close to unity the prediction lag can be forced [Yilmaz, 2001]. Deconvolved signals using a unit prediction lag contain high frequencies, this may actually degrade signal-to-noise ratios in situations where high frequency energy is mostly noise [ProMAX, 1998b]. As the prediction lag is increased the amplitude spectra become increasingly band-limited and approximate more closely the input wavelet, i.e. the deconvolution process has no effect on the data.

The effect of varying the prediction lag from unity to approximately equal to operator length is demonstrated by the power spectra shown in Figure A.4. A unit lag operator length (2 ms) creates a very broadband deconvolved power spectrum with significant spikiness. Similarly, a lag of 6 ms fails to remove major spikes in the output spectrum between 20-40 Hz and fails to preserve the overall spectral shape of the input data. The very long prediction lag of 90 ms has little effect on the data, the output power spectrum for this lag resembles the control power spectra. The optimum prediction lag is ∼20-30 ms, for these lag values the high frequency end of the spectrum is suppressed, spikiness is decreased from the original power spectra, and the overall shape of the input power spectra is maintained.

Varying the operator length, using a constant prediction lag, has a lesser relative effect on the deconvolved power spectra. Figure A.5 illustrates the effect of varying the deconvolution operator length from 100-500 ms. The power spectra indicate that the output is largely inssensitive to changes in operator length between 200-400 ms. An operator length of 100 ms does not boost the power enough for some mid range frequencies leaving a relatively spikey output spectrum. Operators of 500 ms and greater begin to alter the input spectral range to an extent where unacceptable amounts of noise are introduced, boosting the power of higher frequency components.

Predictive deconvolution is required on this dataset as the airgun source signal was not explicitly recorded. A deconvolution time gate was defined every 25 shots and excludes data deeper than 8.5 sec TWT in the record and also excludes the earliest part of the signal in shallow water where direct wave energy is superimposed on primary reflected energy in the recorded signal. Analysis of the power spectra indicate appropriate parameters for the application of predictive deconvolution are an operator distance of 200-300 ms and a prediction lag of ∼24 ms.

Utilising the parameters indicated by the spectral analyses as initial values, a selection of CMP gathers were deconvolved and analysed in the time-space (t-x) domain. The imaging of CMP gathers in the t-x domain shows very little sensitivity to variations in operator length.

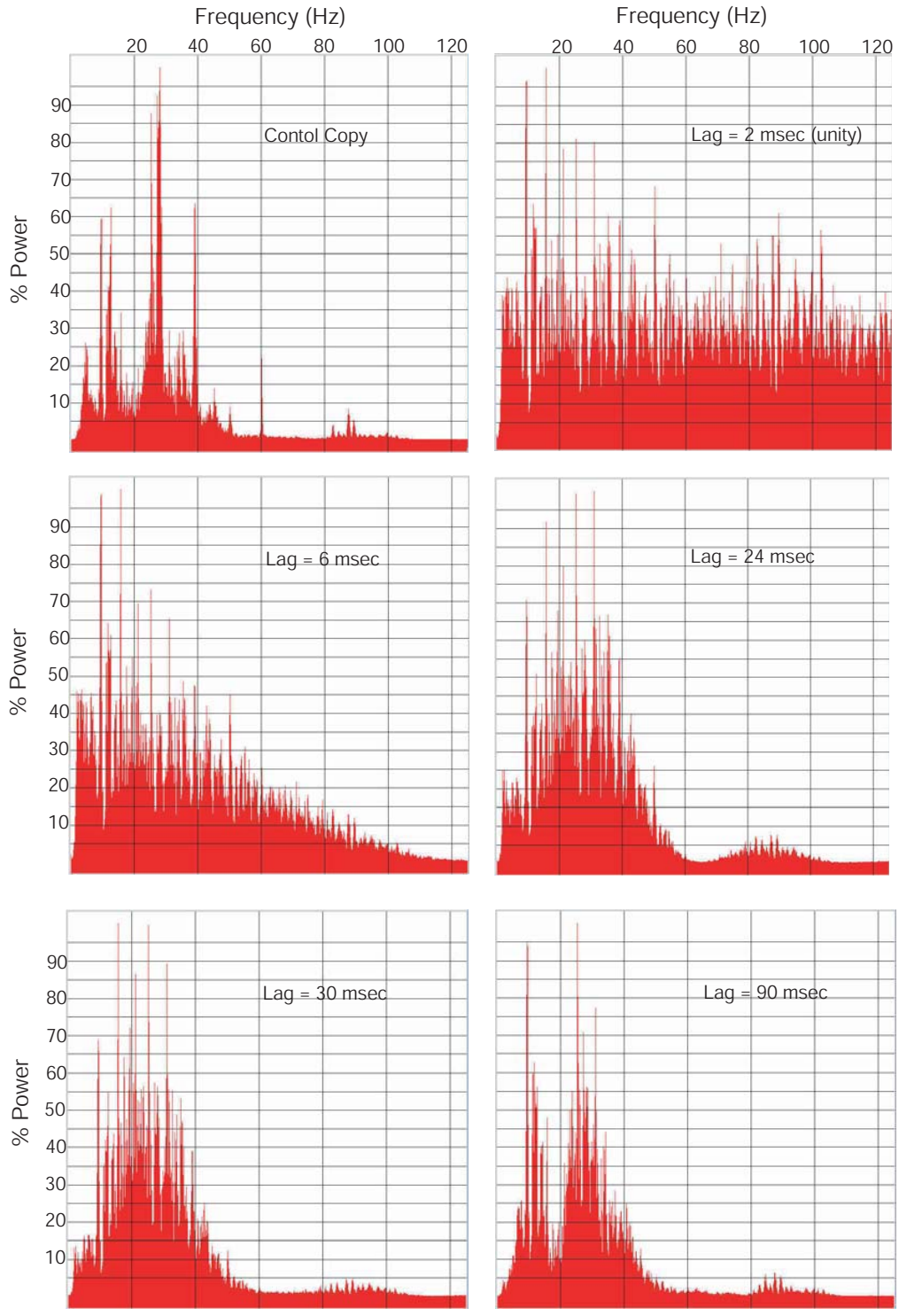

Figure A.4: Comparison at CMP 800 of original power spectra and five spectra calculated following predictive deconvolution with different prediction lag values and a constant operator distance of 200 ms. Short lags (i.e. unity) retain the significant spikiness of the original spectra, whereas long lags are band limited and do not significantly alter the original spectra. A lag distance of 24-30 ms is appropriate for these data.

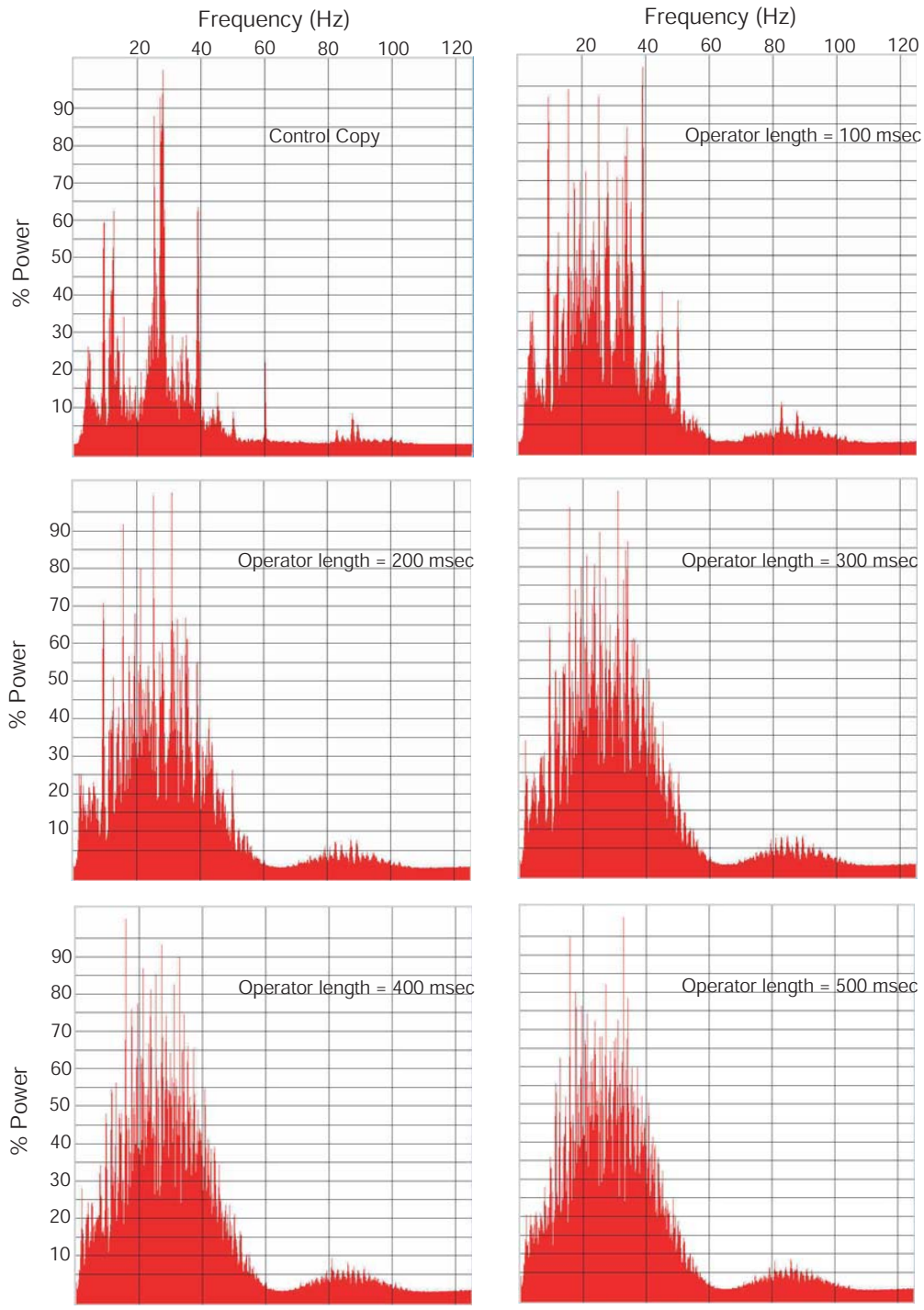

Figure A.5: Comparison at CMP 800 of original power spectra and five spectra calculated following predictive deconvolution with different operator distances and a constant prediction lag of 24 ms.

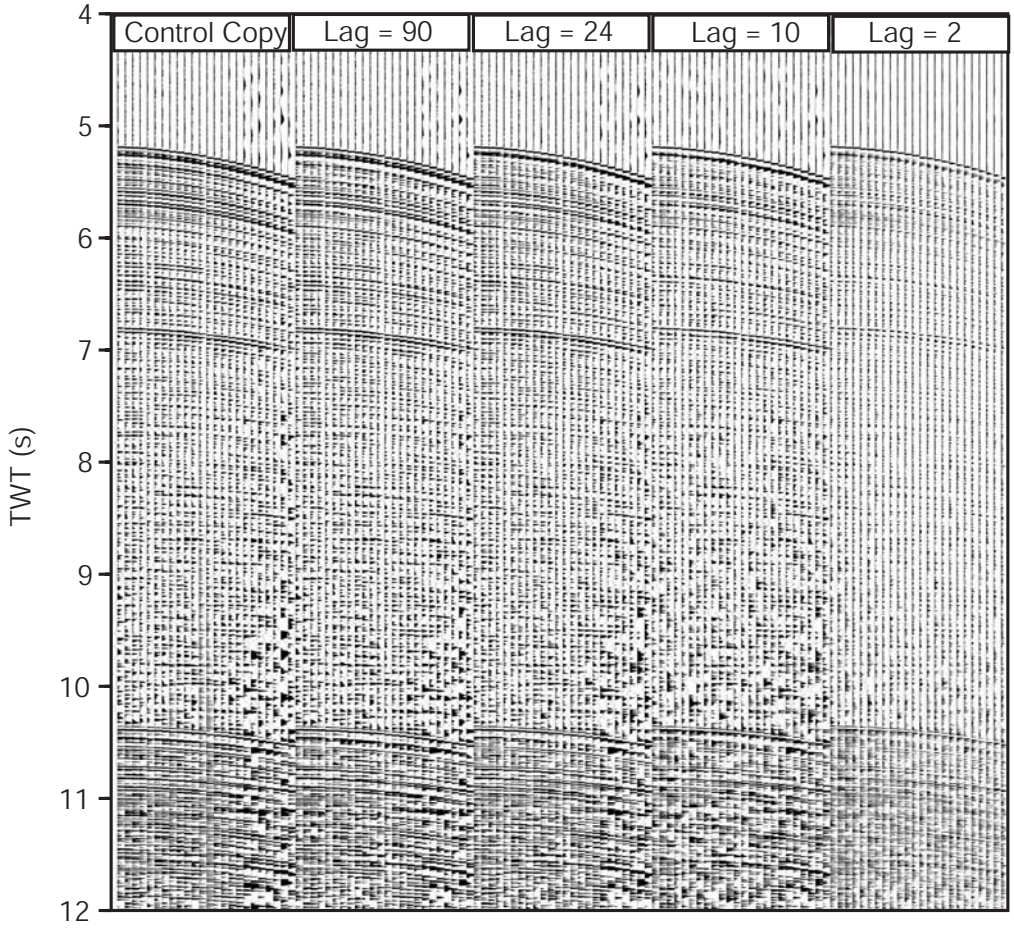

Figure A.6: Comparison of CMP 800 following deconvolution with prediction lags as labelled and an operator distance of 250 ms. Although imaging of the subtle differences is difficult, analysis of these gathers and corresponding amplitude spectra (Figure A.4) indicate a prediction lag of 24 ms provides the best data enhancement.

Variations in prediction lag have a greater impact on CMP gathers. Figure A.6 illustrates the effect on CMP 800 of varying prediction lag from 2-90 ms for an operator distance of 250 ms. The unity prediction lag does not enhance the signal amplitude relative to the noise and produces a 'washed-out' output gather. The 90 ms lag does not alter the imaging relative to the control copy, indicating that this lag is too great. Deconvolution applied with lags between 12-30 ms produce very similar output gathers, from this analysis alone it would be difficult to select an appropriate value for the prediction lag.

Imaging the subtle changes affected by altering prediction lag and particularly operator distance in shot gathers is very difficult. Utilising power spectra calculated for differing parameters provides a far more quantitative assessment of parameter selection. Following the parameter testing process, predictive deconvolution was applied to the entire line using an operator distance of 250 ms and a prediction lag of 24 ms.

Velocity analysis and Normal Moveout (NMO) correction

Semblance velocity analysis [Neidell & Taner, 1971] was carried out to create stacking velocity sections at regular intervals along each line. Stacking velocities allow correction of moveout associated with the hyperbolic moveout, in t-x space, of events associated with flat reflectors. Velocity analysis using semblance is based on the calculation of a velocity spectrum that represents a measure of signal coherency as a function of velocity and two-way zero offset time. A number of acquisition factors affect velocity analysis. Spread length has a significant control on velocity analysis as short streamers which do not provide far offset information exhibit little moveout and poor resolution in the velocity spectrum, this is particularly problematic at greater seafloor depths where moveout is the smallest. The fold of a dataset also constrains the resolution of the velocity spectrum, lower folds typically allow less accurate stacking velocity determination. Departures from hyperbolic moveout, generally associated with dipping reflectors, also negatively impact on the quality of velocity spectra [Yilmaz, 2001].

Semblance analyses were performed on super-gathers created by combining nine adjacent CMPs at a maximum spacing of four kilometres, more frequent analyses were completed in areas of rapid change in bathymetry or basement depth. The velocity spectrum typically shows high levels of coherence up until the arrival of the first water bottom multiple (Figure A.7). The short streamer of only 2400 m used to acquire this data and the fold of only 24 does not allow significant moveout differences between primary energy reflections and the water bottom multiple which makes accurately defining stacking velocities below this multiple reflection difficult. Refraction and wide-angle reflection velocity data were available on some lines from sonobuoys deployed during surveying [Childs & Stagg, 1987]. Where available these data were considered during semblance analyses to provide improved constraints.

Figure A.7 shows the semblance velocity analysis for CMP 640 without NMO applied, and with NMO applied using the displayed velocity profile. Typically, RMS velocity increases with depth. However, the semblance shows maximum coherence at relatively lower velocities at and below the arrival of the first water bottom multiple due to the greater energy contained in the water bottom multiple relative to primary reflections. Quality control of stacking velocities was carried out by applying NMO to the relevant CMP supergather as the velocities were picked. Further real time quality control was achieved by viewing the two-dimensional velocity field as it was created with a brute stack displayed in the background (Figure A.8). This allows spuriously high or low velocity picks to be readily identified and re-examined where necessary.

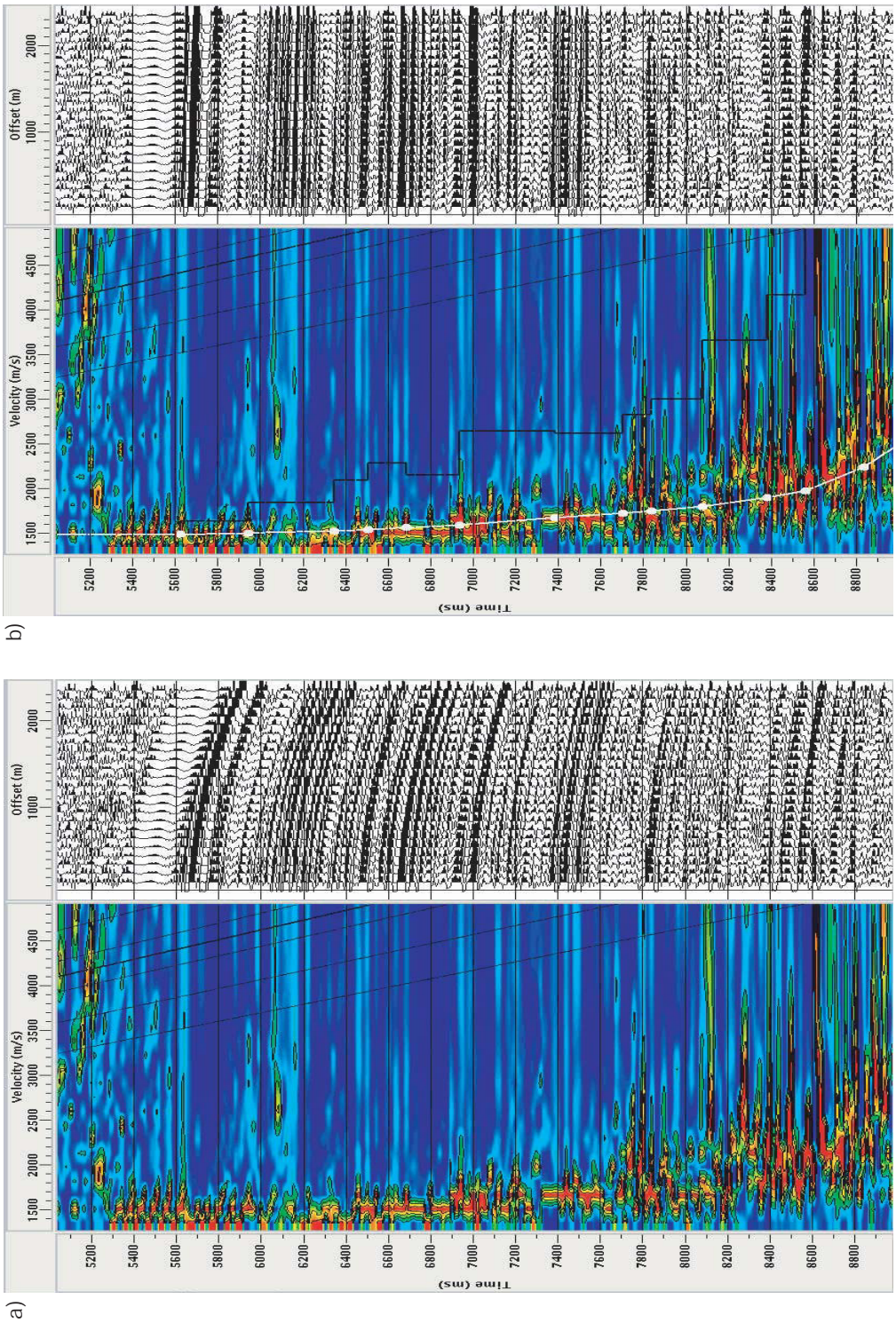

Figure A.7: a) Semblance analysis and corresponding CMP super-gather composed of 9 adjacent CMP gathers at CMP 640, and b) estimated velocity function, and NMO corrected CMP super gather. RMS velocity profile (white) and interval velocities, derived from conversion of RMS velocities using the Dix equation, (black) are shown.

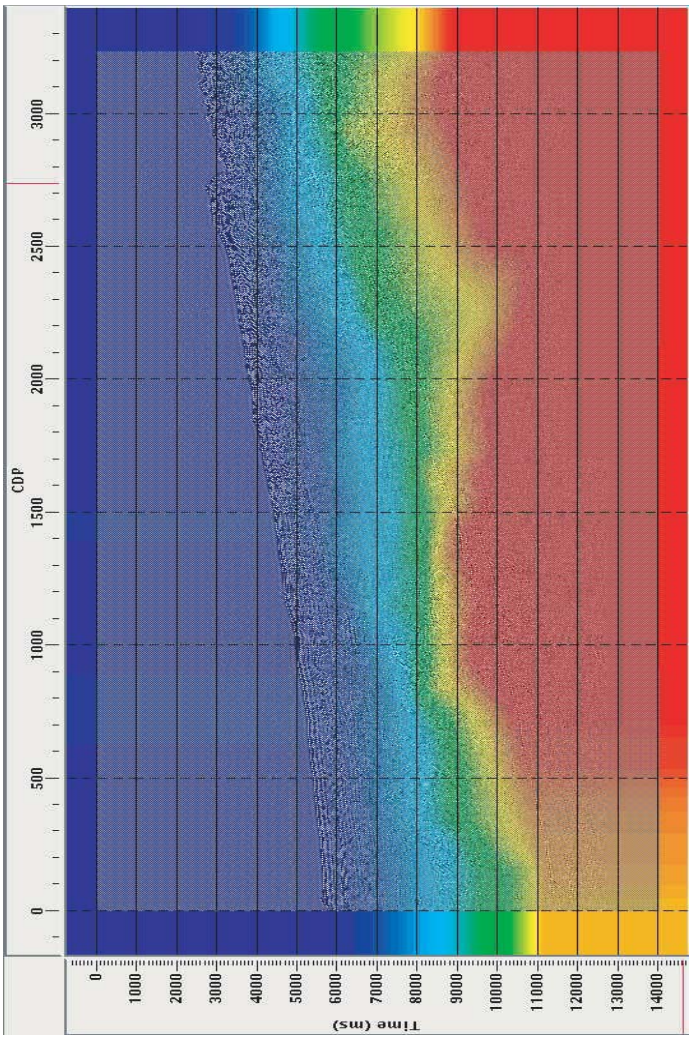

Figure A.8: Interactive velocity volume viewer used to quality control stacking velocities picked every 4 km. Colours represent velocity, red = 4000 m/s and blue = 1480 m/s. Brute stack of seismic data (calculated using an assumed velocity-depth profile) is visible as the image background.

The NMO correction was applied using the stacking velocities. The NMO correction applies a time variant stretching to each input trace to correct for offset and simulate a zero offset section. For a single horizontal layer the NMO correction is, after Yilmaz [2001]

$$\begin{aligned} \Delta t_{nmo} &= t(x) - t(0) \\ &= t(0)[(1 + [x/v_{nmo}t(0)]^2)^{0.5} - 1] \end{aligned}$$

where *t(x)* is the time at offset x, *t(0)* is the time at zero offset, and v_{nmo} is the normal moveout velocity.

As the NMO correction is a time dependent stretching of time data dimension, the frequency content of reflections can be altered, literally stretched from an actual wavelength to a greater apparent wavelength. The adverse effects of stretching are most apparent at early times for larger

offsets. To minimise the stretching effects of the NMO all samples in a gather for which stretching exceeds a threshold value of 30% were muted.

Dip Moveout

Dip moveout (DMO) is a form of partial prestack migration whereby each data sample is migrated to its zero offset position. This process collapses the smear associated with CMP stacking of dipping reflectors. Testing of DMO on these data indicates that very little benefit in data imaging is achieved through the application of this process. This is most likely a function of the geometry of the survey. The appropriate offset bin interval of 100 m (2×shot interval) [**?**] equals the channel spacing for this survey. Typically, offset bins would include more than 3 channels of data. Further DMO processing was not applied due to the minimal impact of this technique.

Common Mid Point (CMP) Stacking

Common midpoint (CMP) stacking is the single most important step in improving data imaging. The stacking process takes advantage of the acquisition practice of 'redundant recording', a process whereby a single point on any given reflector is imaged by multiple shot-receiver combinations, the number of these combinations is the fold of the data. Theoretically the signal to noise ratio is increased by a factor of $\sqrt{N}$ for a survey with an N-fold stack, however, in practice this value is always somewhat lower than $\sqrt{N}$ [Yilmaz, 2001]. A CMP stack is created by combining traces in each CMP gather to form a stacked trace at the midpoint location of that gather, and then combining (stacking) each of these CMP traces. The fold of the data in this survey was 24.

As well as increasing the signal to noise ratio, CMP stacking also attenuates coherent noise such as multiples. Multiples spend more of their travel time in the low velocity water column relative to primaries with the same arrival time, and hence usually have lower stacking velocities than the primaries and do not align on the NMO corrected gather, subsequently they are severely attenuated by the stacking process [Hatton *et al.*, 1986].

A.1.3 Post-Stack Processing

Post-Stack Deconvolution

Post stack deconvolution can improve data imaging for two main reasons. Firstly, it restores higher frequency components of the data which are attenuated by the CMP stacking process. Secondly, the stacked section approximates a zero-offset section, hence predictive deconvolution has the potential to compress the source wavelet more efficiently than when applied to CMP gathers [Yilmaz, 2001].

Parameter testing demonstrated that post stack deconvolution was again more sensitive to variation in prediction lag relative to changes in operator length. An operator distance of 250 ms was selected following testing of this parameter. A stacked section of 1000 CMP gathers (1500-2500) was deconvolved using a number of prediction lags of 2-90 ms, Figure A.9. It is not possible to optimally diplay each of the test panels in hardcopy without altering the gain and display settings between each panel, a process that would effectively remove the imaging differences resulting from deconvolution with different parameters. A lag of 2 ms introduces significant amounts of high frequency noise, particularly after the arrival of the first water bottom multiple. The sections deconvolved with lags of 10, 16 and 24 ms have similar results on the imaging quality of the section; the first water bottom multiple is suppressed relative to the control copy and the imaging of reflectors between 4-7 ms is also improved. The 90 ms lag is too long to have any noticeable effect on imaging relative to the control copy. A prediction lag of 16 ms and an operator length of 250 ms were selected for the deconvolution of the entire line.

Frequency Filtering

Application of frequency filtering is standard practice in seismic processing [Yilmaz, 2001]. It is applied here after deconvolution to remove noise introduced by the deconvolution process. Frequencies outside the 5-120 Hz range were not recorded during acquisition, thus, any signal outside of this range must be noise introduced by previous processing steps.

The frequency dependent absorption of seismic energy results in deeper arrivals comprising a lower frequency power peak relative to shallow arrivals. Hence, higher frequency bands of signal are confined to the shallow part of the section. The time-variant nature of the seismic signal bandwidth requires the application of frequency filters that are time variant. Time variant filters allow a band-pass filter with different frequency cut-offs to be applied to the data in different time sections. Typically the high frequency cut-off will be greater for shallow data, relative to deeper data which is subject to greater natural attenuation of high frequency data. Test panels, Figure A.13, illustrate the effect of varying the frequency pass gate of the band-pass filter. The optimally filtered test panel shows much greater reflector fidelity throughout the section. The individual reflectors in the upper sequence are more clearly defined and deep reflectors are much clearer due to the removal of high frequency noise at greater depths.

After analysis of test panels it was evident that a low frequency tapered cut-off from 5-12 Hz was appropriate for both the early and late time gates. The high frequency cut off tapered from 70-77 Hz in the upper time gate for optimal data enhancement. For the later time gate a lower

high frequency cut-off of 40-60 Hz was optimal. When applied to the entire line the filter was designed to be spatially variant as well as time variant to ensure that as the depth of the water bottom changed approximately the upper 3 s of data were included in the early time gate.

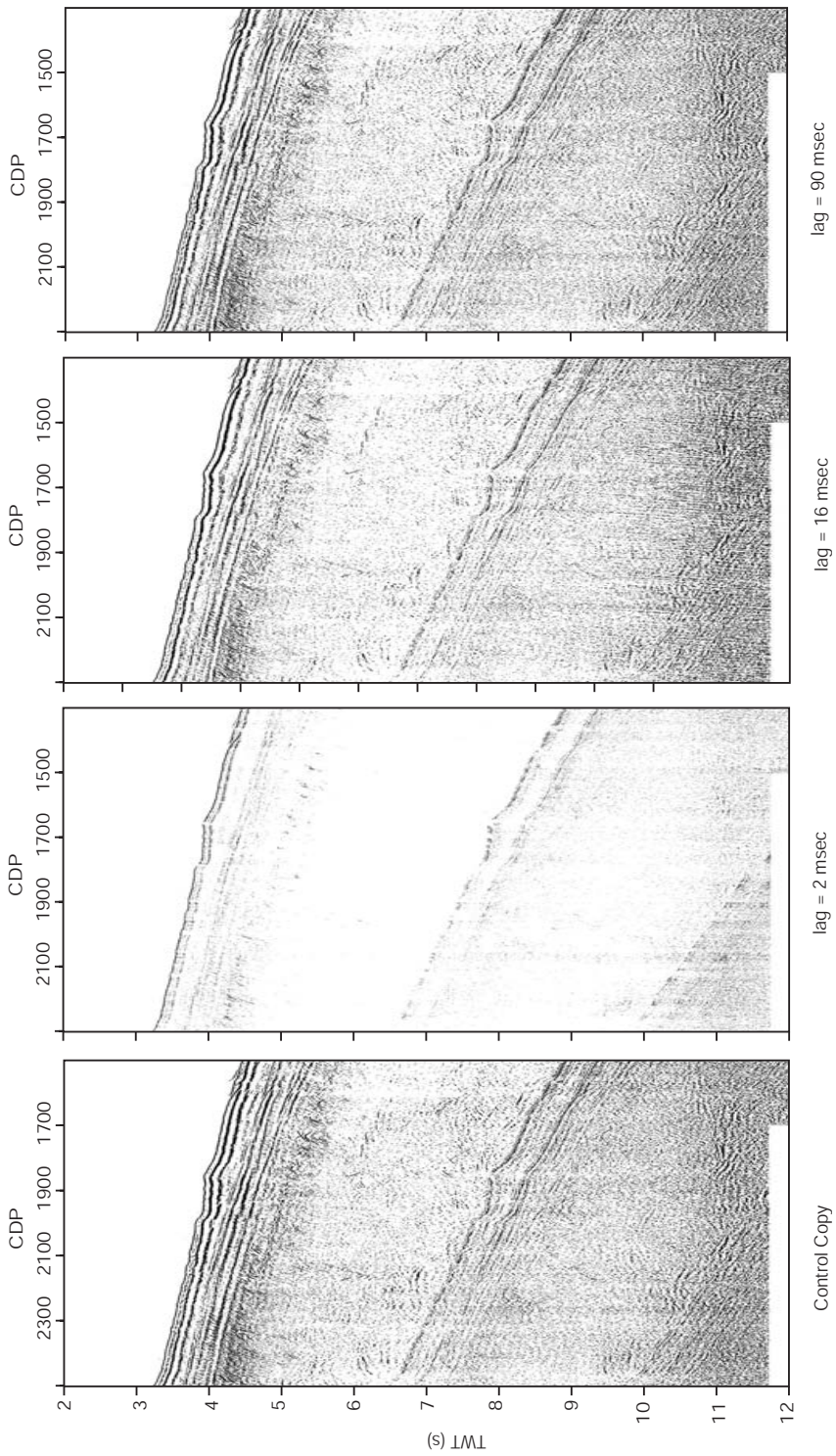

Figure A.9: Comparison of the effect of predictive deconvolution on a stacked section of line L184-5 utilising varying prediction lag lengths, as labelled. Display settings are equal for each panel resulting in non-optimal imaging for the 2 ms lag panel. A lag of between 10-24 ms provides best data imaging improvements.

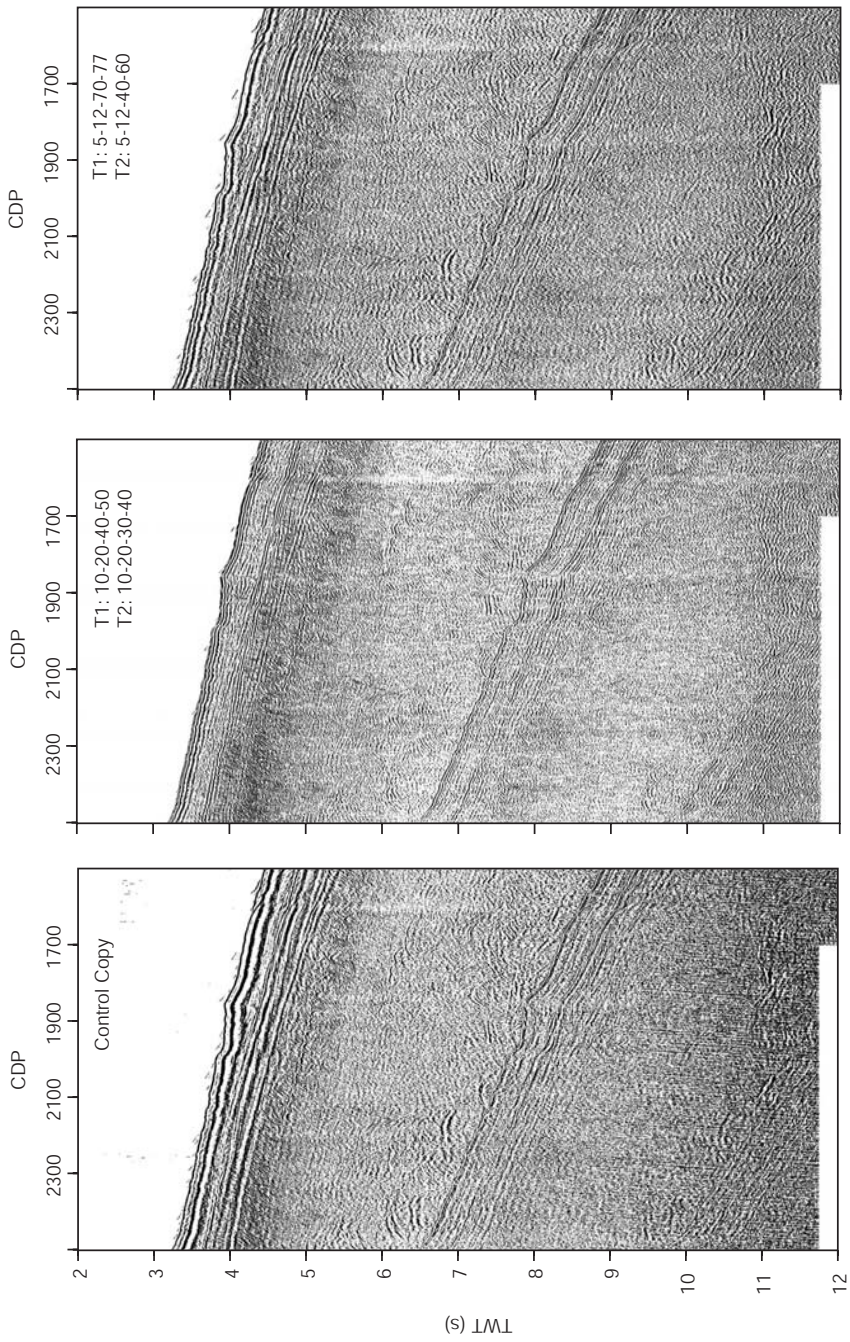

Figure A.10: Test panels for band-pass frequency filtering of CMP gathers 1500-2500. T1 and T2 are time gates from 0-6 s and 6-12 s respectively. The optimal frequency gates reduce the high frequency noise at later times without removing the high frequency signal component at early times.

A.1.4 Migration

Migration is typically the final step in a standard seismic processing sequence. The two major aims of migration are, i) to position reflectors in their correct subsurface position in t-x space, and ii) to collapse diffractions associated with geological discontinuities [Yilmaz, 2001]. Migration attempts to correct the position of reflectors by compensating for the assumption in the CMP stacking process that all reflectors are horizontal and continuous. Obviously in a geologic environment all reflectors do not meet these assumptions and are subsequently imaged in an incorrect subsurface location.

Using simple geometric constructions it can be shown that a number of basic principles are always true of migrated data. The dip angle of the reflector in a geological section is greater than in the recorded time section, that is; migration steepens reflectors. The length of a reflector in a geological section is shorter than in a time section, that is; migration shortens reflectors. A reflector in a geologic section is positioned up dip of its image in a time section, hence; migration moves reflectors up dip.

Accurate velocity information is paramount to the effectiveness of the migration process. Typically a means of direct velocity analysis, independent from the indirect velocities of semblance analysis (i.e. refraction or sonic logs) is utilised in creating the velocity field for migration. This is particularly true of depth migration. As semblance analysis was the only major source of velocity information for this data, depth migration was not attempted.

Many algorithms exist for performing time migration. Common migration algorithms include phase shift, Stolt Frequency-Wavenumber (FK), Kirchoff, fast explicit finite difference (FD), and steep dip explicit FD. Important factors in selecting the optimal migration technique include the required computational time (which can differ by factors of more than 20), the accuracy of velocity structure, and expected dip angles (steepness). Detailed descriptions of the technical differences between algorithms are not included here (see Yilmaz [2001] for detailed analysis), however, test panels of a section of the stacked data illustrate the different results obtained via different migration algorithms A.11.

Comparable results were produced by the FK, phase-shift, and reverse-time migration techniques. Whereas Kirchoff and steep-dip algorithms reduced the amplitude of important reflectors significantly. The three former methods collapse diffractions and improve dipping reflector resolution between the sea-floor and the first water-bottom multiple. The phase-shift algorithm provides optimal imaging enhancement.

Below the first water-bottom multiple the improvements introduced by migration relative to the control panel are negligible, this is due to inaccuracies in the velocity function below the very strong water-bottom multiple. The deep reflector between 10-12 sec is over-migrated by each algorithm, indicating that the velocity used for migration at this depth is too high. Phase-shift migration was re-applied with a velocity scaling factor of 80%, Figure A.12. The resulting migration does not over-migrate the deep reflector. Final migration was conducted using the phase-shift algorithm with and without velocity scaling.

A.1.5 Trace mixing and Display

Trace mixing is a technique commonly applied to amplify coherent events in seismic data and improve the signal to noise ratio. It is effective as from trace to trace coherent reflections should interfere more constructively than incoherent noise. Mixing large number of traces causes lateral smearing and provides the practical limitation for the enhancement possible from this technique.

The two important parameters in this processing step are the number of traces being mixed, and the weighting given to each of the mixed traces. After testing several mixing combinations, Figure **??**, a three trace mix with a 1:2:1 weighting distribution was deemed most appropriate for maximum imaging improvement. The 5 and 9 trace mixes remove signal as well as noise and smear high-amplitude, non-continuous reflectors.

A comparison of the processed and migrated stacked section, and a pre-processed only stack (after NMO at 1480 m/s) is shown in Figure A.14. Both sections have had automatic gain control (AGC) applied to optimise data imaging. AGC is applied post processing only and prior to display as it can not be removed through the application of any filter-inverse mathematical function as with other types of gain applications. The final stacked section exhibits improved signal to noise ratio and imaging of reflectors relative to the brute stack. Imaging of the sedimentary section is improved and deep reflectors become visible in the migrated section relative to the brute stack.

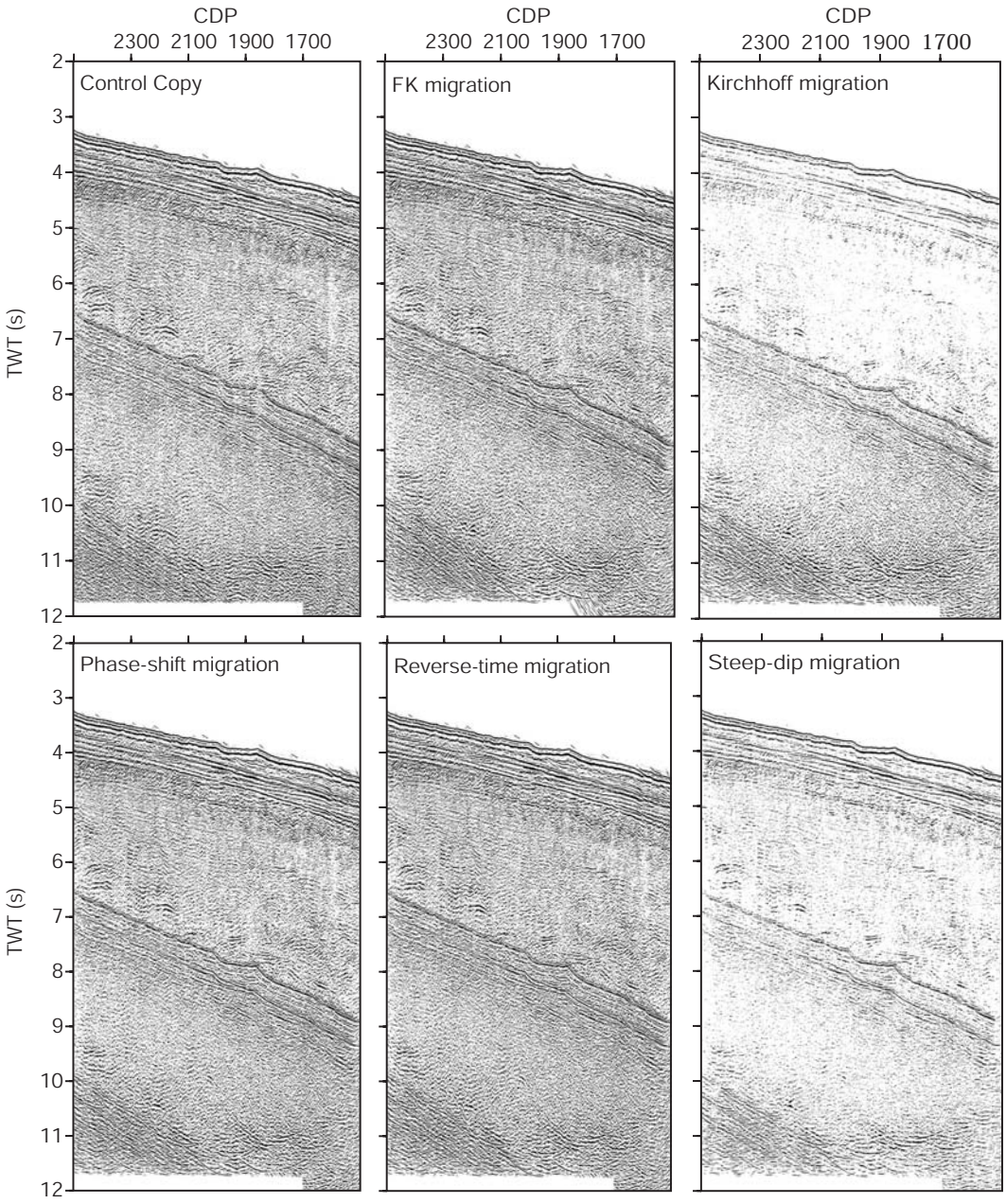

Figure A.11: Test panels of migration algorithms as labelled with no gain applied before display. Phase-shift, FK, and reverse-time migrations provide similar imaging enhancements. Deep reflectors are all overmigrated as indicated by the introduction of upward-inflected 'smiles' relative to the control panel.

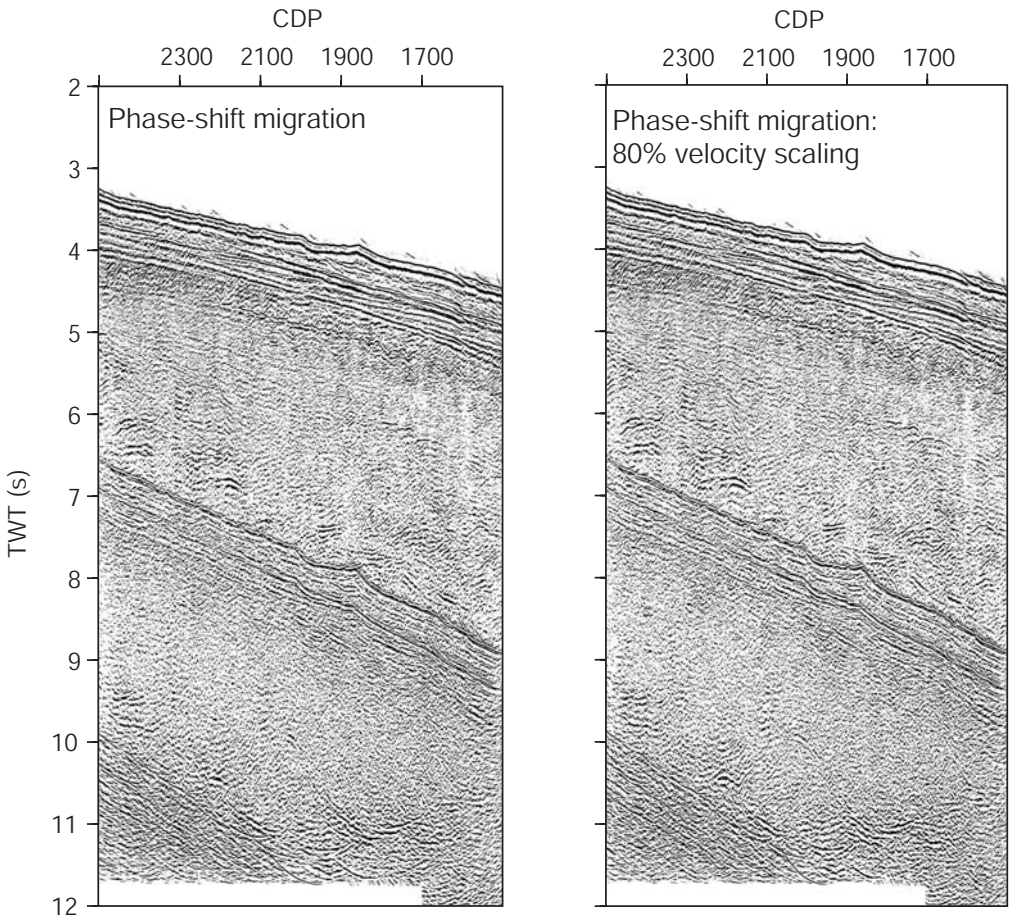

Figure A.12: Phase-shift migrated section with no and 80% velocity scaling applied as labelled. The scale-reduced velocities do not overmigrate deep reflectors between the first and second water-bottom multiples.

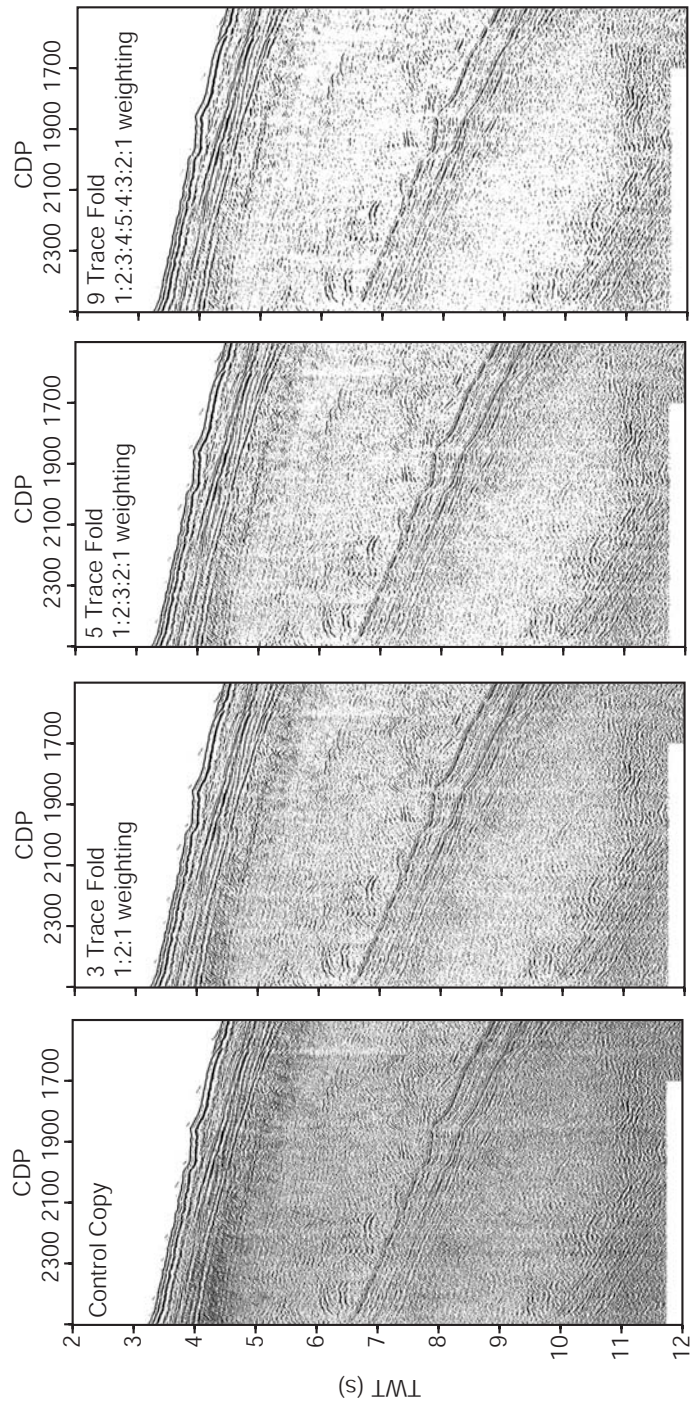

Figure A.13: Test panels for trace mixing stacked data between CMP gathers 1500-2500. 3, 5, and 9 trace mixes are tested with differing weighting distributions. The 3 trace fold with a 1:2:1 weighting provides optimal imaging enhancement.

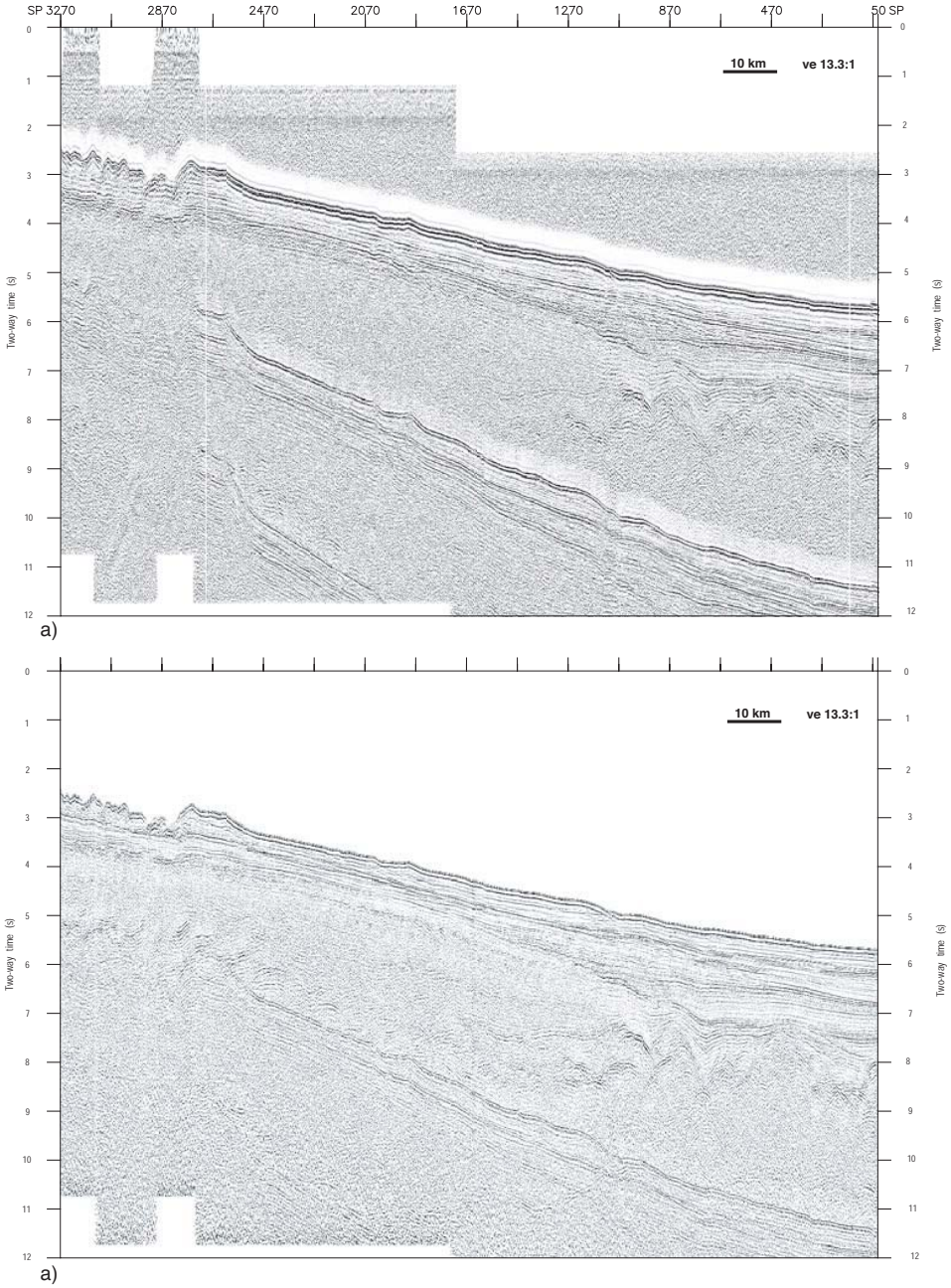

Figure A.14: Stacked sections of L184-5 data a) after basic pre-processing and NMO correction at water velocity, and b) following the processing sequence outlined herein. Definition of reflectors is greatly improved in the fully processed section and the amplitude of the water bottom multiple is massively reduced.

A.2 Multiple Suppression

Two L184 survey lines, L184-11 and L184-12, traverse the outer part of the continental shelf. Data from both these lines exhibit large amplitude water bottom multiples at similar TWT depths to primary reflectors. A number of processing steps were tested on these lines in an attempt to reduce the amplitude of the water bottom multiple relative to the primary reflectors. Strong multiples are common on the Antarctic margins, MCS data acquired over the Antarctic continental shelf at a number of locations including Prydz Bay [Stagg, 1985], the Ross Sea [Cooper *et al.*, 1987], and the Antarctic Peninsula margins [Larter *et al.*, 1990] are effected by strong water bottom multiples also.

The primary geological factors specific to the Antarctic Margins that cause exceptionally strong water bottom multiples are, after Larter *et al.* [1990]:
i) The overdeepened continental shelf, a result of isostatic loading by the proximal Antarctic ice sheet , and ii) Overcompacted sediments on the shelf, a result of loading by grounded ice sheets during periods of glacial maxima and ice sheet migration across the shelf.
The geophysical consequences of these factors are water bottom multiples of longer wavelengths (relative to shallower continental shelves at lower altitudes) and greater amplitude water bottom reflections (and hence multiples also) due to the increased acoustic impedance difference between the water and shallow sediments due to their ice load increased compaction.

Traditional methods of decreasing the amplitude of the water bottom multiple on continental shelves include deconvolution (pre- and post-stack) and CMP stacking. Long predictive deconvolution operators applied pre-stack have little effect except for near channel traces as the multiple is not truly periodic at larger offsets. The stacking process utilising primary velocities distorts the phase of the water bottom multiple and ensures that post-stack deconvolution fails to remove large amounts multiple energy. CMP stacking is typically the most powerful method of removing significant amounts of multiple energy, however, this too fails to remove much of the multiple energy on Antarctic margins [Larter *et al.*, 1990].

A number of multiple suppression techniques were applied to the MCS data from lines L184-11 and L184-12 to investigate possible imaging benefits. These lines had the standard processing sequence outlined above applied, in addition, techniques such as wave equation multiple rejection (WEMR), frequency-wavenumber domain (f-k) filtering, Radon filtering, and near trace mutes (NTM) were tested.

Wave Equation Multiple Rejection

Wave Equation Multiple Rejection (WEMR) is designed specifically to attenuate water bottom multiples in marine data. The process uses water depths and f-k extrapolation to model water bottom multiples which can then be subtracted from the original data [ProMAX, 1998a]. This process must be applied prior to TAR as the data can not have had any amplitude altering steps previously applied.

The WEMR algorithm requires water depth information in the trace headers and an accurately picked top mute just above the seafloor. As water depth values were not included in the

trace headers of this dataset they were picked off a near trace stacked section, with normal moveout (NMO) correction applied at water velocity. Water depth values were then projected from the picked horizon file into the trace header, with the application of the appropriate conversion from TWT to depth in metres.

A comparison of a section of stacked data with and without the application of WEMR, Figure A.15, with normal moveout applied at water velocity (1480 m/sec), shows the impact of the WEMR filter. The amplitude of the primary multiple reverberation is reduced somewhat by the process, however, significant multiple energy remains. Although computationally expensive, WEMR was applied to both lines 11 and 12 as they are relatively short and the improvement, although minor, was evident.

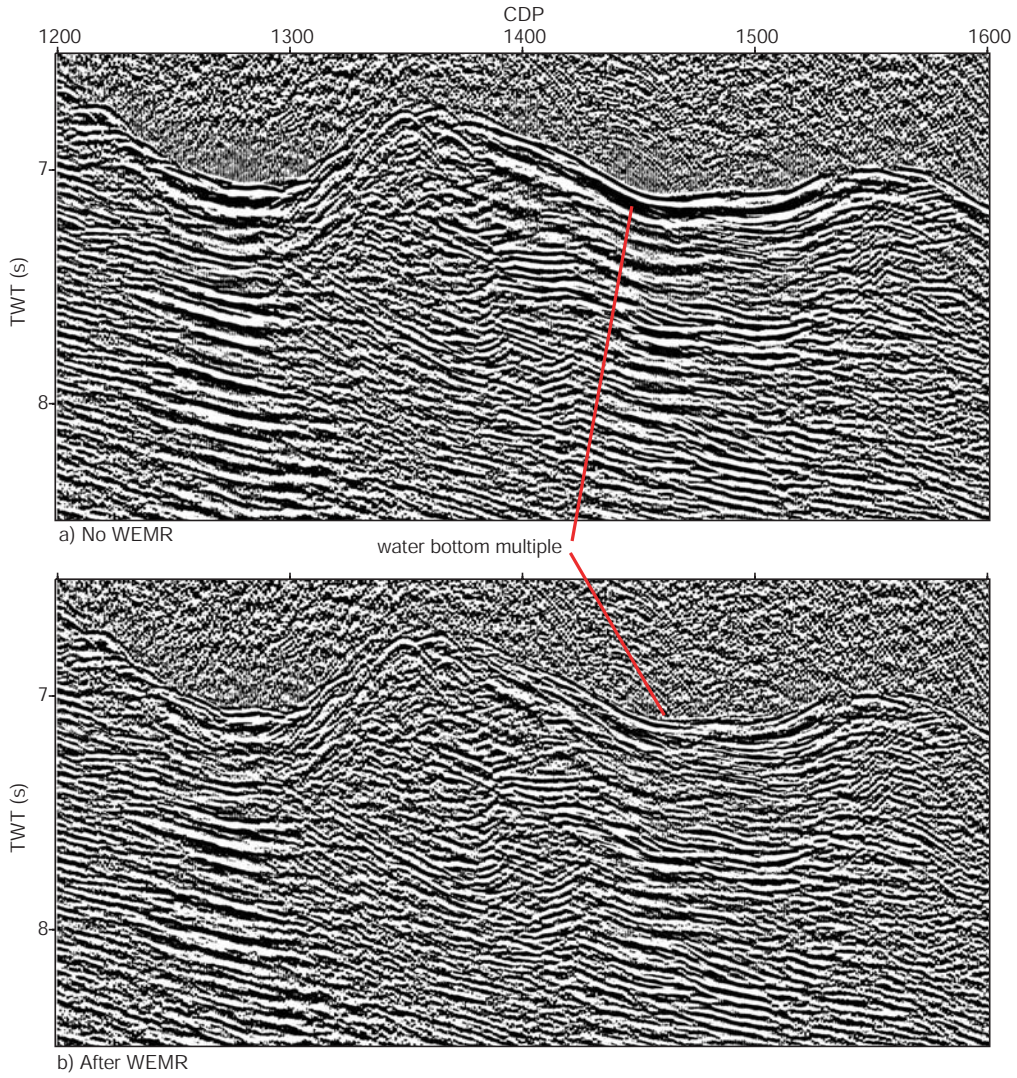

Figure A.15: Comparison of a stacked (nmo at 1480 m/sec)section of Line 12, a) with no multiple suppression, and b) following the application of wave equation multiple rejection (WEMR) filtering. The amplitude of the first water bottom multiple is reduced by the application of WEMR, although significant amounts of multiple energy remain.

F-K Filtering

Decreasing the amplitude of the water bottom multiple using f-k filtering was not possible without eliminating important primary data. Far offsets could be filtered with some success, however, the relative benefit of this is much less than that gained by stacking far offsets. The non-zero dip of much of the sedimentary section on the outer-shelf and upper-rise also create difficulties in attempting to apply f-k filtering, because the NMO correction will cause dipping primary events to appear as multiple data when mapped into f-k space. After extensive testing it was evident that f-k filtering was not an appropriate method of multiple suppression for this data set.

Radon Filtering

Radon analysis involves transforming seismic data from time-distance (t-x) space into time-moveout (t-mo) space. Following NMO correction with a primary velocity field all primary reflectors exhibit zero moveout (ideally), that is they are entirely flat in t-x space, however, multiples still exhibit moveout and resemble parabolas in t-x space. Radon analysis models an input gather using the Radon transform, and maps events of an image or data set with different characteristics (in this case curvatures) into different locations of a new space, the Radon model [ProMAX, 1998a]. Accordingly as primaries exhibit zero moveout and multiples exhibit non-zero moveout they are separated in t-mo space. When the modelled data is displayed in t-mo space multiples and primaries plot as points rather than lines, Figure A.16.

Data points occur in the t-mo space at equal times to coherent reflectors in t-x space. Water bottom multiples plot at predictable times after the primary water bottom reflection, and at positive moveouts. The filter in Figure A.16 is designed to remove this multiple energy and pass the primary energy which plots close to the zero moveout axis.

It is difficult to image the minor improvement produced by Radon filtering the data from these two lines in the t-x domain. However, a small reduction in the amplitude of multiples was evident, particularly on the southern end of Line L184-11 on the continental shelf. Accordingly, both lines were Radon filtered prior to CMP stacking.

Near Trace Mute

Far offset multiple energy is far more effectively suppressed by the stacking process and filter application than near offset multiple energy. At near offsets multiple energy is far more difficult to remove as the moveout of the multiple reflections, relative to primary reflectors, is much smaller. A near trace mute can help eliminate remaining multiple energy at near offsets. A surgical mute with an upper surface just above the arrival of the first water bottom multiple is generally most appropriate. For near trace muting to improve imaging, the acoustic source utilised during surveying must have been sufficient to produce coherent, reflectors at far offsets.

Obviously a near trace mute can not distinguish between primary and multiple energy, hence, primary and multiple energy alike are muted. A near trace mute was not necessary for Line L184-12 as the multiple energy was efficiently removed by the previous processing steps and by stacking. However, as Line L184-11 still contained significant multiple energy a near trace

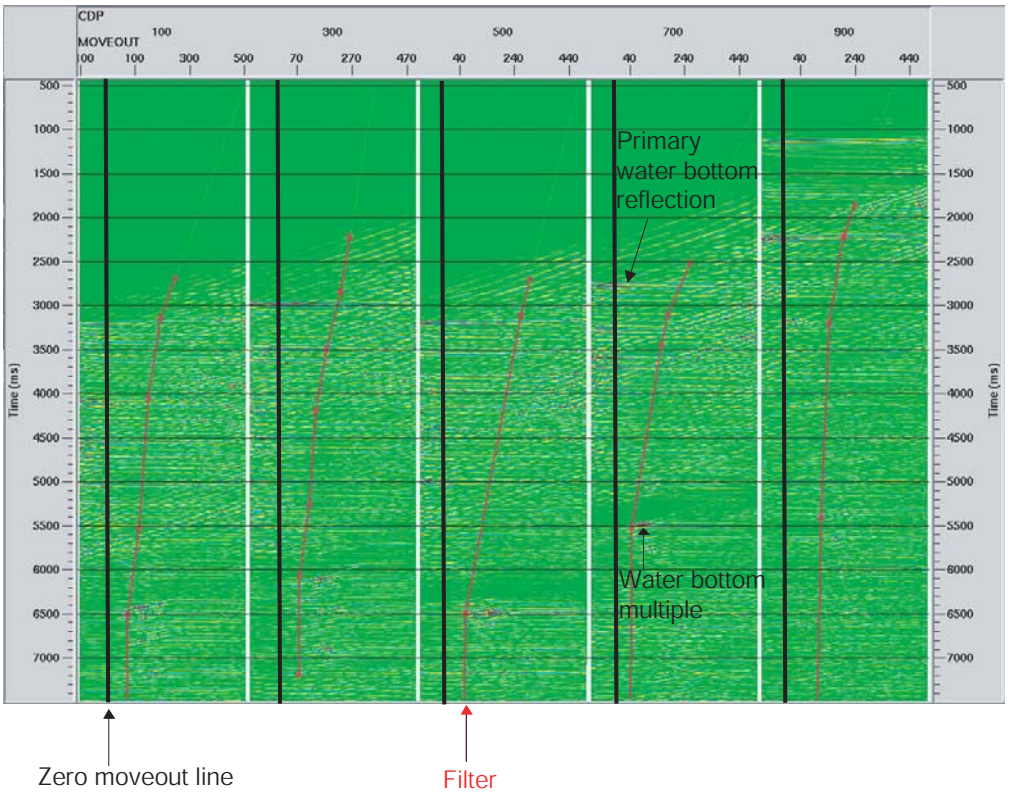

Figure A.16: Five NMO corrected CMP gathers in time-moveout (t-mo) space. Non-zero data in t-mo space corresponds to parabolic/curved events in t-x space, that is multiples. The filter mutes information to the positive direction (right) of the red line.

mute was tested on CMP gathers prior to stack. Significant amounts of multiple energy can be removed, however, the amplitude of important primary reflectors are also significantly reduced by the muting process, particularly in the shallow waters of the continental shelf. The overall signal-to-noise ratio was worsened by the application of the near trace mute, accordingly it was not applied before the final stack.